Exploring Problems in Inorganic Solid-State Systems with Wavefunction-Based Molecular Spectroscopy Methods

Dissertation

zur

Erlangung des Doktorgrades (Dr. rer. nat.)

der

Mathematisch-Naturwissenschaftlichen Fakultät

der

Rheinischen Friedrich-Wilhelms-Universität Bonn

vorgelegt von

Anneke Dittmer

aus

Verden (Aller)

July 2023

Angefertigt mit Genehmigung der Mathematisch-Naturwissenschaftlichen
Fakultät der Rheinischen Friedrich-Wilhelms-Universität Bonn

Erstgutachter:	Prof. Dr. Frank Neese
Zweitgutachter:	Prof. Dr. Thomas Bredow
Tag der Promotion:	28. November 2023
Erscheinungsjahr:	2024

For my grandfather Karl-Heinz Oetting, in loving memory.

If I had to do it all over again? Why not, I would do it a little bit differently. - Freddie Mercury

Summary

The present work explores the possibilities of computational protocols that combine an electrostatic embedding approach to model inorganic crystalline solid-state systems with molecular theory methods for accurate calculation of spectroscopic properties. It highlights the potential of multistep protocols that combine methods ranging from DFT to single- and multireference wavefunction-based methods to explore and understand spectroscopic observations at the theoretical level.

A generalized protocol for modeling bulk properties of inorganic solid-state systems using an electrostatic embedding approach within the ORCA program suite is presented. The protocol involves applying a quantum mechanical method to a specific quantum cluster that represents a part of a solid-state system. The quantum cluster is embedded in a point charge field that accounts for the long-range electrostatic effects of the solid-state system. This approach allows the quantum cluster to operate as if it were in the bulk of a solid-state system. In particular, a newly developed automated electrostatic embedding approach within the QM/MM framework in ORCA, called Ionic-Crystal-QM/MM, is presented.

Two benchmark studies are performed to evaluate the applicability of the electrostatic embedding approach and molecular methods for the calculation of bulk properties of inorganic solid-state systems. The first study focuses on the calculation of NMR nuclear shielding constants using DFT functionals and MP2. The second study investigates the calculation of band gaps using TD-DFT with a variety of DFT functionals and bt-PNO-STEOM-CCSD. Both studies show that the electrostatic embedding approach gives robust results as long as the quantum cluster is carefully embedded in a sufficiently large and charge-optimized point charge field and the quantum cluster itself is converged with respect to the desired property. When this is the case, the molecular methods can obtain the calculated bulk properties with an accuracy comparable to that expected for the calculation of equivalent molecular properties using the same methods. In addition, the band gap study gives results comparable to those obtained from periodic studies. The accuracy of the calculated properties compared to the experimental data increases with the level of theory used and gives a satisfactory agreement with the experimental results for the

applied post-Hartree-Fock methods in both cases.

With the developed and tested electrostatic embedding approach, the antiferromagnetic cobalt oxide Co(II,III)$_3$O$_4$, a spinel structure with tetrahedrally coordinated Co(II) and octahedrally coordinated Co(III) sites, is studied in terms of its band gaps and $K\beta_{1,3}/K\beta'$ mainline and $K\beta_{2,5}/K\beta''$ valence-to-core (VtC) X-ray emission (XES) spectra. To gain a better understanding, the antiferromagnetic derivative Al$_2$Co(II)O$_4$ and the diamagnetic derivative Co(III)$_2$ZnO$_4$ are also studied. Both studies combine different DFT and multiconfiguration/multireference wavefunction-based approaches. The latter class of methods is able to explicitly treat the antiferromagnetic coupling within the materials by considering "neutral" and "ionic" antiferromagnetic states.

Each study provides significant insight into the properties of the cobalt oxides under investigation. For example, it is found that the band gaps of Co(II,III)$_3$O$_4$ are dominated by ligand field transitions local to the antiferromagnetically coupled Co(II) sites. The $K\beta_{1,3}/K\beta'$ mainline XES study shows that significant intensity contributions to the spectra can originate from final states with electron excitations within the $3d$ orbitals, and the $K\beta_{2,5}/K\beta''$ XES study shows that the presence of "ionic" antiferromagnetic states can lead to double peak features in the spectrum.

List of Publications

Published parts of this thesis

1. Dittmer, A., Izsák, R., Neese, F. Maganas, D. Accurate Band Gap Predictions of Semiconductors in the Framework of the Similarity Transformed Equation of Motion Coupled Cluster Theory. *Inorg. Chem.* **58**, 9303–9315 (2019).
   doi: 10.1021/acs.inorgchem.9b00994

2. Dittmer, A., Predicting Band Gaps of Semiconductors with Quantum Chemistry. *EPJ Web of Conferences* **246**, 00006 (2020).
   doi: 10.1051/epjconf/202024600006

3. Dittmer, A., Stoychev, G., Maganas, D., Auer, A. Neese, F. Computation of NMR Shielding Constants for Solids Using an Embedded Cluster Approach with DFT, Double-Hybrid DFT, and MP2. *J. Chem. Theory Comput.* **16**, 6950–6967 (2020).
   doi: 10.1021/acs.jctc.0c00067

Publications in progress

1. Dittmer, A., DaCosta Leyser, T., Sivalingam, K., Maganas, D., DeBeer, S. Neese, F. Revisiting the Band Gap problem in bulk Co_3O_4 solid with the eyes of theoretical spectroscopy.

2. Dittmer, A., Chen, M., Peredkov, S., Angel, S., Rüdiger, O., Schulz, S., DeBeer, S., Maganas, D. Neese, F. A Combined Experimental and Embedded Cluster Computational study of the X-ray emission spectroscopy of Co_3O_4, Co_2ZnO_4, and Al_2CoO_4 solid systems. The case of Valence to Core XES.

3. Dittmer, A., Chen, M., Peredkov, S., Angel, S., Rüdiger, O., Schulz, S., DeBeer, S., Maganas, D. Neese, F. A Combined Experimental and Embedded Cluster Computational study of the X-ray emission spectroscopy of Co_3O_4, Co_2ZnO_4, and Al_2CoO_4 solid systems. The case of $K\beta$ Mainline XES.

Further publications

The publications listed below are not part of this thesis.

1. Kleemiss, F. Justies, A., Duvinage, D., Watermann, P., Ehrke, E., Sugimoto, K., Fugel, M., Malaspina, L., Dittmer, A., Kleemiss, T., Puylaert, P., King, N., Staubitz, A., Tzschentke, T., Dringen, R., Grabowsky, S. Beckmann, J. Sila-Ibuprofen, *J. Med. Chem.* **63**, 12614-12622 (2020).
   doi: 10.1021/acs.jmedchem.0c00813

2. Fugel, M., Dittmer, A., Kleemiss, F. Grabowsky, S. On the Role of Hydrogen Bonding in Gas-Phase S_N2 Reactions at Silicon. *J. Phys. Chem. A* **125**, 4070-4078 (2021).
   doi: 10.1021/acs.jpca.1c00601

Acknowledgments

First of all, I would like to thank Frank Neese for his guidance, for giving me the opportunity and trust to work on various interesting research projects, and for providing me with exciting possibilities beyond the daily research routine.

I am very grateful to Dimitrios Manganas for the best mentorship I could have asked for and for giving me the freedom and confidence to manage my projects independently. I thank him for taking the time to discuss problems and ideas with me in depth, and for always being there to offer advice and encouragement when I needed it.

I would like to thank all the people I have worked with on various projects, namely Christoph Riplinger, Alexander Auer, Georgi Stoychev, Róbert Izsák, Min-min Chen, Olaf Rüdiger, and Serena DeBeer. Special thanks to Christoph Riplinger for turning our ideas into ORCA implementations and giving me the opportunity to continue my passion for computational chemistry at FACCTs. Also, many thanks to Alexander Auer for his support beyond our NMR project and for giving me the chance to participate in the Fermi School of Physics.

A big thank you to all my colleagues in the Neese and DeBeer departments for creating a great working environment. Special thanks to Frank Wennmohs for his frequent advice.

This work was funded by the Max-Planck Society and carried out at the Max-Planck-Institut für Kohlenforschung in Mülheim an der Ruhr. I am very grateful to them for providing the space and financial support to complete my research. I would also like to thank all the administrators, especially Andrea Bosserhoff and Annette Krappweis.

Many thanks to Thomas Bredow for agreeing to be my second reviewer and for taking the time to talk science with me during my visit to Bonn.

I would like to thank Pauline Colinet, Van Anh Tran, Erna Wieduwilt, and Sören Dittmer for taking the time to read parts of my thesis and thus contributing to its readability. I would also like to thank Pauline and Anh for many inspiring conversations and Erna for her constant encouragement.

I am deeply grateful to my family and friends for their unwavering support

throughout my studies. I would especially like to thank my parents Jörg and Ute, my grandmothers Annegret and Wilma, and my siblings Marieke and Sören as well as Julia.

I would like to thank Miranda Wilson for her friendship, support, and sofa.

Last but not least, I would like to thank my partner Edem Pascal Oumata for always being there for me.

Contents

1 Introduction **1**

I Theory and Models of Crystalline Solid-State Systems **7**

2 A Tale of Two Systems: Basic Descriptions of Molecules and Crystals **12**

2.1 Electrostatic Interactions in Molecules and Crystals 13

2.2 A Brief Journey from Orbitals to Bands and Back 16

2.2.1 Orbitals 16

2.2.2 From Orbitals to Bands 18

2.2.3 Bands 19

2.2.4 From Bands to Orbitals 21

2.2.5 A Detour to Many-Electron States 22

2.3 Quantum Meets "Classical" Mechanics 23

3 How to Model a Crystal with the Electrostatic Embedded Cluster Approach **26**

3.1 General Workflows and Input File Structures 29

3.1.1 Creating Electrostatic Embedded Cluster Models Manually and with ORCA_CrystalPrep 29

3.1.2 The "Simple" Electrostatic Embedding Approach 32

3.1.3 Ionic-Crystal-QM/MM 35

3.2 Insights into the Quantum Cluster, the Boundary Region, and the Point Charge Field 39

3.2.1 Different Approaches to a Quantum Cluster (QC) 39

3.2.2 The Role of the Boundary Region (BR) 44

3.2.3 The Quest for the "Best" Charge Model 48

4 Limits and Possibilities of the Electrostatic Embedding Approach **57**

II Computational Spectroscopy: From Ground to Excited States 64

5 A Quick Introduction to Spectroscopy 68

6 Ground States 72
6.1 Wavefunction-Based Methods 72
6.1.1 Hartree-Fock 72
6.1.2 CI - Configuration Interaction 75
6.1.3 ICE-CI – Iterative-Configuration Expansion Configuration Interaction 77
6.1.4 Multiconfigurational Methods: CASSCF and RASSCF 77
6.1.5 Many-Body Perturbation Methods: MP2, NEVPT2, CASPT2 . 78
6.1.6 Coupled Cluster (CC) Methods: CCSD, DLPNO-CCSD, and MR-CC 81
6.2 Density Functional Theory 82
6.2.1 LDA Functionals 84
6.2.2 (Meta-)GGA Functionals 84
6.2.3 Hybrid Functionals 84
6.2.4 Double-Hybrid Functionals 85
6.3 Remarks to the Ground State Methods 85

7 Nuclear Magnetic Resonance Spectroscopy 87

8 Electronic Spectroscopy: UV/Vis and X-ray Spectroscopy 90
8.1 Band Gaps 92
8.2 X-ray Emission Spectroscopy 100

III Benchmark Studies of Spectroscopic Properties in Solid-State Systems 103

9 Introduction to the Solid-State Benchmark Study Set 107

10 Benchmarking NMR Shielding Constants for Solid-State Systems: A Comparative Study Using DFT, Double-Hybrid DFT, and MP2 113
10.1 The Context and Aim of the NMR Study 113
10.2 General Computational Details 115
10.3 Dependence of the Nuclear Shielding Constants on Different Model Parameters 116
10.3.1 Influence of the Electrostatic Embedding Environment 117
10.3.2 Convergence of the Cluster Size 120

10.4 Influence of the Level of Theory on Nuclear Shielding Constants . . . 125
10.4.1 Basis Set Size 125
10.4.2 Residual Error of MP2 and Double-Hybrid DFT with Respect to CCSD(T) 127
10.4.3 Relativistic Effects 129
10.5 Method dependence of the Computed Nuclear Shielding Constants and Comparison to Experiment 132
10.5.1 Method Dependence of Halide Nuclear Shielding Constants . 132
10.5.2 Method Dependence of Alkali Metal Nuclear Shielding Constants 134
10.5.3 Method Dependence of Magnesium and Zinc Nuclear Shielding Constants 136
10.5.4 Chemical Shifts: Comparison to Experiment 137

11 Shedding Light on Band Gap Predictions for Solid-State Systems: A Comparative Study Using TD-DFT and bt-PNO-STEOM-CCSD 142
11.1 The Context and Aim of the Band Gap Study 142
11.2 General Computational Details 144
11.3 Influence of the Model Parameters on the Optical Band Gap 145
11.4 Influence of the Basis Set Size on the Optical Band Gap 147
11.5 Organic Semiconductors: The Case of Anthracene 148
11.6 Inorganic Semiconductors: The Cases of LiCl and ZnS 150
11.7 Performance Evaluation of TD-DFT and bt-PNO-STEOM-CCSD . . . 154

12 Conclusions of the NMR and Band Gap Benchmark Studies: Key Insights and Findings 158

IV Unraveling the Spectroscopic Response of Multimetallic Oxide Solid-State Systems 163

13 Introduction to Co_3O_4 and Its Derivatives 168
13.1 The Crystal Structures and Models of the Cobalt Oxides 168
13.1.1 The Crystal Structures of the Cobalt Oxide Derivatives 168
13.1.2 The Electrostatic Embedding Models of the Cobalt Oxide Derivatives 170
13.2 A brief Introduction to Antiferromagnetically Coupled Metal Centers 172
13.2.1 An Antiferromagnetic Coupling Model 172
13.2.2 Methods to Address Antiferromagnetic Coupling 177

13.2.3 Antiferromagnetic Coupling, Multiplet Effects, and More in the Cobalt Oxides . . . 179

14 The Quest for the Band Gap(s) of Co_3O_4 181

14.1 The Context and Structure of the Band Gap Study . . . 181
14.2 Literature Overview . . . 183
14.2.1 Experiments . . . 183
14.2.2 Calculations . . . 188
14.3 Computational Details . . . 194
14.4 Theoretical Considerations on the Excited States . . . 195
14.4.1 Single-Center Co Models . . . 195
14.4.2 Multicenter Co Models . . . 196
14.5 Convergence and Characterization of Excited States with TD-DFT . . 198
14.5.1 Co_2ZnO_4 . . . 198
14.5.2 Al_2CoO_4 . . . 200
14.5.3 Co_3O_4 . . . 202
14.5.4 Comparison of Single-Reference Methods (DFT, CIS, EOM-CC) and Literature . . . 204
14.6 Towards a Multireference Model . . . 209
14.6.1 Co_2ZnO_4 . . . 209
14.6.2 Al_2CoO_4 . . . 212
14.6.3 Co_3O_4 . . . 218
14.6.4 Comparison of Different Multireference Methods . . . 220
14.7 Conclusions . . . 223

15 Uncovering the Spectral Features of Secret Final States in the $K\beta_{1,3}/K\beta'$ Mainline X-ray Emission Spectra of Co_3O_4, Co_2ZnO_4, and Al_2CoO_4 226

15.1 The Context and Structure of the Study . . . 226
15.2 Computational Details . . . 228
15.3 Experimental Spectra . . . 230
15.4 Cluster Size Convergence . . . 232
15.5 One-Electron $K\beta_{1,3}/K\beta'$ Mainline XES Spectra Results . . . 234
15.6 An Introduction to the $K\beta_{1,3}/K\beta'$ Mainline XES Intensity Mechanism 236
15.6.1 Radiative and Non-Radiative XES Cross Sections . . . 236
15.6.2 $K\beta_{1,3}/K\beta'$ Mainline Emission Pathways . . . 239
15.7 CASCI $K\beta_{1,3}/K\beta'$ Mainline XES Spectra Results . . . 242
15.7.1 Co_2ZnO_4 . . . 242
15.7.2 Al_2CoO_4 . . . 251
15.7.3 Co_3O_4 . . . 257

15.8 Conclusions 258

16 Decoding the Hidden Spectra Behind the $K\beta_{2,5}/K\beta''$ Valence-to-Core X-ray Emission Processes of Co_3O_4, Co_2ZnO_4, and Al_2CoO_4 261

16.1 The Context and Structure of the Study 261
16.2 Computational Details 262
16.3 Experimental Spectra 263
16.4 Cluster Size Convergence 266
16.5 One-Electron $K\beta_{2,5}/K\beta''$ VtC XES Results 267
16.6 Analysis of the Intensity Mechanism of the $K\beta_{2,5}/K\beta''$ VtC XES Spectra for Multicenter Systems 271
16.6.1 The Valence-to-Core X-Ray Emission Spectrum of an isolated tetrahedral Cu(II) site 272
16.6.2 Nature of Core-Ionized Initial States in Cu(II) Multicenter Model Systems 274
16.6.3 Nature of the $K\beta_{2,5}/K\beta''$ VtC XES Spectra Final States in Cu(II) Multicenter Model Systems 279
16.6.4 Nature of Initial States and Electronic Structure of Co(II) and Co(III) Centers in Al_2CoO_4 and Co_2ZnO_4, and a Hypothetical Larger Multicenter Model - "5t12o" 283
16.7 CASCI $K\beta_{2,5}/K\beta''$ VtC XES results 289
16.7.1 Co_2ZnO_4 289
16.7.2 Al_2CoO_4 291
16.7.3 Co_3O_4 299
16.8 Conclusions 300

17 Conclusions 304

Appendices 309

A Additional Information Part I 310

B Additional Information Part III 314

C Additional Information Part IV 337

List of Abbreviations 371

List of Figures 373

List of Tables 392

Bibliography **396**

1 Introduction

The combination of a range of spectroscopic methods with carefully calibrated theoretical spectroscopy results is widely used in (bio)inorganic chemistry and catalysis.[1–8] A successful example of this approach is the characterization of unusual reactive species in model systems (e.g., Fe(V)[6] and Fe(VI)[7] centers in coordinate complexes), which has helped elucidate the structure and oxidation states in enzymes. Among others, a unique carbide center was identified in the active site of the nitrogen-activating enzyme nitrogenase,[5], and the structure and oxidation states of the oxygen-evolving complex in photosynthesis were characterized.[1, 3] Moreover, this approach has shown great potential to bridge the worlds of homogeneous and heterogeneous catalysis by simultaneously interpreting the spectroscopic response of vanadium-based oxidation catalysts.[9]

For the successful application of theoretical methodologies to interpreting spectroscopic responses in real-life chemical problems, it is paramount that the theoretical methods be properly calibrated. The error bars of the theoretical predictions must be known from studying a series of known and understood systems. Therefore, in all cases described above, the predictions made by the theoretical methods are valid only within the confidence intervals defined by the calibration procedures.[10] In particular, the application of ab initio wavefunction-based methods showed higher success than density functional theory (DFT) in studying molecular systems accurately.

For solids and surfaces, the situation is much worse than for molecules, and the available methods are limited. In recent decades, density functional theory has been widely used to study electronic band structure in the context of periodic calculations or non-periodic embedded cluster calculations to predict solid-state properties.[11–15]

A variety of DFT approaches (one-electron energies or Δ-SCF), linear-response DFT approaches such as the many-body Green's function (GW) approximation, the Bethe-Salpeter equation, and time-dependent density functional theory (TD-DFT) provide access to a wide range of solid-state properties with accuracy that depends strongly on the functionals.[11–13, 16–18] It has been shown that in periodic DFT

calculations, both the local and semi-local density functionals and the generalized gradient approximation (GGA or meta-GGA), the most favorable functionals for solids, vastly underestimate the magnitude of fundamental solid-state properties. Examples of such properties are the adsorption energies of small molecules on surfaces or the band gap energies.[12, 13, 15] One of the main reasons for this underestimation is the self-interaction error inherent in DFT functionals.[19]

Hybrid functionals, global or screened, are known to perform better. Global hybrid functionals, such as B3LYP, B3PW91, and PBE0, or screened hybrid functionals in DFT approaches using plane waves, such as HSE, are able to reduce the mean absolute errors, for example, in the band gap calculations from about or more than 1.0 eV and to roughly 0.4 eV.[11, 12] These errors are very similar to the errors of the many-body perturbation GW approach.[11, 12]

Meanwhile, various specialized functionals have been developed, such as the SCAN meta-GGA functional, which minimizes self-interaction and improves the efficiency of solid-state property calculations toward the accuracy of hybrid functionals and GW methods.[14, 15] Diagrammatically derived functionals based on the random phase approximation (RPA) have also been used to calculate solid-state properties. However, due to the high computational cost, they are limited to small sizes of solid-state systems.[20]

In contrast, ab initio wavefunction-based reference calculations have until recently been either unintelligible for the large system sizes required for solid-state bulk or surface problems, or too demanding to be routinely applied.[21–28] Nonetheless, several important applications for ground and excited states have been introduced at the level of periodic Monte Carlo coupled cluster (CC) and full configuration interaction (Full-CI).[22, 24, 25, 28] In addition, band structure calculations of several semiconductors have recently been carried out with periodic equation-of-motion-based coupled-cluster theory (EOM-CC).[29, 30]

It has been demonstrated that the severe limitations arising from the steep scaling of wavefunction-based methods with system size can be overcome by exploiting the relatively short-range nature of the dynamic correlation through local correlation techniques.[31] This has allowed the treatment of several surface problems in the framework of the second-order periodic local Møller-Plesset perturbation theory (MP2).[32–37] Also, for non-metallic solid-state systems, the size of the system to be treated quantum mechanically can be effectively reduced by using embedded cluster models that treat long-range electrostatics and polarization at the molecular mechanical level.[38–43] The approach has been successful in performing CCSD(T) level calculations for surfaces.[10, 23]

By describing the quantum region of these embedded cluster models at the level

of the domain-based local pair orbital version of the CCSD(T) approach, i.e. DLPNO-CCSD(T),[44] the adsorption energies for a number of small molecules on the rutile TiO2(110) surface can be calculated with errors smaller than 0.04 eV (1 kcal/mol) with respect to the available experimental values.[23] In combination with excited state methods, local correlation methods are much less explored. PNOs for excited states can be generated from correlated excited state methods based on either configuration interaction or pair-cluster schemes such as CIS(D), CC2 and ADC2,[45–47] leading to state-specific PNO-CI and PNO-CC based methods. More recently, the ground-state PNO scheme has been combined with equation-of-motion-based techniques such as EOM-CC and STEOM-CC, leading to the back-transformed (bt) bt-PNO-EOM-CCSD and bt-PNO-STEOM-CCSD methods, as well as STEOM-DLPNO-CCSD, which provide a balanced description for valence, charge transfer (CT), and Rydberg states in optical spectroscopy.[48, 49] In particular, bt-PNO-STEOM-CCSD has been able to describe the excited states of a wide variety of chemical systems, providing errors below $\sim$0.2 eV for valence, Rydberg, and CT states.[48–50] In the field of solid-state problems, the bt-PNO-STEOM-CCSD and STEOM-DLPNO-CCSD can provide band gap energies for a number of organic and inorganic semiconductors,[51] as well as values for Eu-doped phosphors[52] with errors on average in a similar order of magnitude compared to the available experimental data as the excited state calculations in molecular systems. This topic will be fully explored in the course of this thesis.

In practice, tackling spectroscopic events in solid-state systems is a major undertaking due to the complex multiplet structures involved in the various spectroscopic processes. The multiplet structure is particularly interesting for the accurate calculation of complete X-ray spectra, including emission and absorption. For example, the K'_β and $K_{\beta_{1,3}}$ mainline features in X-ray emission (XES) spectra cannot be accurately expressed by single-reference methods, which cannot capture the multiplet effects. Therefore, one-electron DFT methods cannot capture such complex features. However, DFT has proven useful in many valence-to-core (VtC) XES computational problems. Multireference methods that treat complete or restricted active spaces (CAS or RAS) with CI, such as CASCI and RASCI, must be applied to the mainline XES problem. These have often only been successfully applied to monometallic systems.[53, 54] In addition to an explicit treatment of the multiplet structure of the final state manifold, a successful computational protocol must account for spin-orbit coupling effects and metal-ligand covalency, which significantly affect the intensity distribution and energetic positions of the computed spectral features.

Another major complication arises when the systems under study have antiferromagnetically coupled open shell centers. This is often approached by break-

ing the spin symmetry and performing the target spectroscopy calculations using a determinant of the broken-symmetry (BS). The methods based on single reference wavefunctions or DFT are usually only applicable to some spectroscopic problems. At the same time, the corresponding multireference option, while rigorous, quickly becomes unmanageable in terms of computational complexity.[55–57]

In density functional theory (DFT), time-dependent DFT (TD-DFT) is typically used on top of a BS-DFT solution to address spectroscopic problems in such antiferromagnetic systems.[58–62] Nevertheless, it should be emphasized that BS-DFT gives only a crude representation of the antiferromagnetic coupling and, like any particle/hole-based theory, does not correctly capture multiplet effects. Recent advances in approximate CI wavefunction-based methods based on the density matrix renormalization group (DMRG)[63], the iterative configuration expansion (ICE-CI)[64, 65] or the full configuration interaction quantum Monte Carlo (FCIQMC)[66] in the treatment of large active spaces, while instrumental for the calculation of the magnetic anisotropy or the low-lying valence excitation spectrum of multimetallic centers,[67–70] have yet to be applied to problems in solid-state spectroscopy.

The goal of this work is to develop robust computational protocols that combine an electrostatic embedded cluster approach to model inorganic crystalline solid-state systems with molecular theory methods to accurately calculate spectroscopic bulk properties compared to experiments and thereby better understand the underlying mechanisms. The work is divided into four parts to achieve this goal and to understand the path from the bare electrostatic embedding approach to accurate theoretical solid-state spectroscopy.

Starting on page 8, the first part of this thesis presents a comprehensive and robust protocol for modeling inorganic crystals using the electrostatic embedded cluster approach. This protocol is designed, explained, established, and automated within the ORCA suite of programs. The part consists of three chapters that provide a detailed understanding of the approach. In the first chapter, a comparison is made between crystalline solid-state systems and molecules to identify their differences and similarities. These insights serve as the basis for rationalizing the electrostatic embedded cluster approach. The second chapter presents the approach used in this thesis. First, general protocols and tools are outlined, followed by an explanation of the underlying principles and additional details. In particular, the automated Ionic-Crystal-QM/MM method available in the ORCA program suite is introduced. The final chapter of this first part critically examines the strengths and limitations of the electrostatic embedded cluster approach, specifically in comparison to the more conventional method of treating solid-state systems with periodic boundary conditions.

The second part, which begins on page 65, provides an introduction to various computational ground and excited state methods as well as theoretical concepts applied in the subsequent spectroscopic studies.

The third part, starting on page 104, focuses on two benchmark studies that evaluate the effectiveness of the electrostatic embedded cluster protocol in combination with molecular theory methods. The first benchmark study examines the NMR spectroscopic nuclear shielding constants for a number of embedded crystals, including rock salt and zinc blende structures with different nuclei such as (earth) alkali metals, transition metals, and halides. The second study examines the optical band gaps of similar systems. The goal of both studies is to demonstrate that accurate results comparable to experimental data can be obtained by carefully applying the electrostatic embedded cluster approach and ensuring convergence of the model size with respect to the desired property. In particular, the study on nuclear shielding constants evaluates the performance of different DFT functionals (including (meta-)GGA, hybrid, and double-hybrid functionals) as well as MP2, showing that higher levels of theory lead to increased accuracy and comparable errors to molecular studies using similar methods. Likewise, the optical band gap study evaluates the accuracy of a similar set of DFT functionals within the TD-DFT framework as well as the post-Hartree-Fock method bt-PNO-STEOM-CCSD in comparison to experimental data and periodic DFT calculations.

The fourth part, starting on page 164, uses the knowledge gained in the previous three parts to investigate the real-world challenges posed by the cobalt oxide Co_3O_4. The first chapter of this part introduces the antiferromagnetic spinel structure of $Co(II,III)_3O_4$ and its derivatives, namely the diamagnetic $Co(III)_2ZnO_4$ and the antiferromagnetic $Al_2Co(II)O_4$. These derivatives represent the octahedral Co(III) and tetrahedral Co(II) sites of Co_3O_4, respectively. The chapter also presents the corresponding electrostatic embedded cluster models and discusses the significance and theory behind the antiferromagnetic nature of the system. In the second chapter of this part, the focus shifts to a review of the nature of the optical band gaps in Co_3O_4. The investigation emphasizes the role of the different cobalt sites and the influence of antiferromagnetic coupling in their origin, using a combination of broken-symmetry TD-DFT and various (multireference) wavefunction-based methods. The third and fourth chapters of this part deal with the analysis of the $K\beta_{1,3}/K\beta'$ mainline and $K\beta_{2,5}/K\beta''$ valence-to-core X-ray emission spectra of the three cobalt oxide derivatives. This is accomplished through the development of a unified one-electron and CASCI (complete active space configuration interaction) protocol. The goal is to gain a comprehensive understanding of specific experimental features in these X-ray emission spectra in the context of the character of the contributing final states,

the involvement of the different cobalt sites, and the influence of antiferromagnetic coupling.

The primary focus of all the studies presented in this thesis revolves around the investigation of the bulk properties of inorganic crystalline solid-state systems. The rationale behind this focus is that bulk properties offer greater accessibility compared to surface properties, as they exclude surface effects such as bond shortening. Within the bulk, forces and bonds are more uniform and "homogeneous" in nature. These properties facilitate property calculations on smaller cluster sizes, allowing the use of more accurate methods and the development of robust protocols with broad applicability to bulk properties. As a potential future direction, these established protocols can be extended to address surface effects and relevant challenges in areas such as heterogeneous catalysis.

Part I

Theory and Models of Crystalline Solid-State Systems

[. . .] the solid is a molecule, a big one, to be sure, but just a molecule. – Roald Hoffmann[71]

Introduction to Part I

Over the last centuries, theories related to molecules and solid-state materials have developed separately and become independent disciplines.[71] As a result, different approaches and techniques have emerged for the computational analysis of molecular and solid-state properties. In particular, solid-state materials are often studied using calculations with periodic boundary conditions along with plane wavefunction basis sets, while molecules are analyzed in a discrete environment using Gaussian basis sets. Although Gaussian basis sets can also be used in periodic systems, they are much more computationally expensive in this setting.[72, 73]

Furthermore, as the computational resources required to analyze discrete systems are generally lower, more diverse computational methods are available to study the ground and excited states of molecules that cannot be easily adapted to periodic calculations of solid-state systems.[73] This is particularly true for wavefunction-based methods, which are generally more accurate than density-based methods typically applied in periodic calculations.[74]

To make the variety of molecular methods available to solid-state properties, solid-state systems can be modeled using electrostatic embedding approaches. These approaches are not a new idea but have been developed in parallel with the periodic protocols.[72] The electrostatic embedding approaches for modeling solid-state systems are similar to the QM/MM approach commonly used to study extended macromolecular structures, such as proteins. The protocols involve modeling a specific part of the solid-state system at the quantum mechanical level using methods developed for molecules. Meanwhile, the long-range structure is simulated using "classical" mechanics by introducing point charges to account for the long-range electrostatic structure of the solid. Over time, various electrostatic embedding methods have been developed, ranging from simple ones that introduce a few point charges around an atomic cluster to more complex multilevel schemes. These models can be polarizable or static. [23, 38, 40–43, 72, 75–81] The following discussion refers only to the latter.

Despite the existence of various embedding schemes, electrostatic embedding approaches have not been widely adopted for solid-state systems. One possible ex-

planation may be the lack of a widely accepted generalized protocol that can be applied in a "black box" fashion, as most periodic protocols are. Moreover, issues related to solid-state systems have historically been the realm of physicists. Electrostatic embedding approaches are emerging and present in the field of chemists. Thus, applying the electrostatic embedding approach to a solid-state system views it more through the lens of a chemist who looks at quantum mechanical systems typically from the perspective of the local structure rather than the extended one.[71]

The placement of molecules in the domain of chemists and solid-state systems in that of physicists adds another layer to the differences in their theory and computation. The methods and theories often use inconsistent language. This can lead to confusion, especially when studying the same properties of molecules and solid-state systems, which are expressed in different terms, making it difficult to study either in an interdisciplinary context or to apply methods developed for one field to the other. As a result, many research opportunities remain unexplored. In particular, Hoffmann's work, such as "Solid and Surfaces - A Chemists View of Bonding in Extended Structures",[82] has bridged the gap between the languages used in both fields, making solid-state theory accessible to (molecular) chemists. His work will be used as one of the foundations for the upcoming chapters and the protocols developed within them.

This part of the thesis intends to present an electrostatic embedding approach for modeling crystalline solid-state systems with ORCA based on previous research[23, 80] as well as protocols[51, 83] developed as part of this thesis. The distinction between amorphous and crystalline solid-state systems (crystals) is essential at this point. The former may have local symmetry elements but no long-range order, while the latter are highly symmetric and characterized by long-range order.[84] There are both organic and inorganic crystals, and this work will focus on ideal inorganic crystals. These systems are well-ordered systems with a strong ionic character.

The introductory chapter "A Tale of Two Systems: Basic Descriptions of Molecules and Crystals" in this first part, starting on page 12, serves as a foundation for the electrostatic embedding approach. It discusses the differences and similarities between molecules and solids and explains how a solid can be "approximated" as a "molecule".

The first half of the following chapter, "How to model a Crystal with the Electrostatic Embedding Approach" presents protocols for the electrostatic embedding approach, starting on page 26. In particular, it provides instructions for constructing an electrostatic embedding model manually and using the ORCA_CrystalPrep tool. It also gives instructions for performing electrostatic embedding calculations

using a "standard" ORCA input file and employing the Ionic-Crystal-QM/MM utility introduced in ORCA 5.0. ORCA_CrystalPrep and Ionic-Crystal-QM/MM were developed with the goal of paving the way for the development of "black box" protocols for electrostatic embedding approaches for crystalline solid-state systems. In the second half of the chapter, starting on page 39, various aspects of the electrostatic embedding model are examined, and recommendations for a reliable protocol are given.

The last chapter of this first part, "Limits and Possibilities of the Electrostatic Embedding Approach", starting on page 57 compares aspects of the developed electrostatic embedding approach with periodic boundary approaches. Examples of the strengths and weaknesses of the approaches are given.

2 A Tale of Two Systems: Basic Descriptions of Molecules and Crystals

The basis of the electrostatic embedded cluster approach is the idea to transfer and extend the description of molecules to crystals. For this purpose, the question "What is the difference between molecules and crystals?" must first be answered.

A molecule is a discrete system with a countable number of atoms and therefore, electrons. When the molecule is in a vacuum and thus, not interacting with its environment, most effects are mainly short-range. A crystal can be thought of as a periodic system with an uncountable number of atoms and electrons. Long-range effects, mostly electrostatic, become essential. Electrons in a molecule are described by molecular orbitals and those in solid-state systems by bands. Symmetry elements may or may not be present in some molecules. Crystals are by definition symmetric and consist of periodically repeating units that are translationally symmetric with respect to each other. They are called unit cells, and each represents the overall symmetry of the crystal.[84] A large number of repeating unit cells is called a "supercell". Figure 2.1 schematically illustrates the evolution from a unit cell to ever larger supercells and on to an "infinite" crystal.

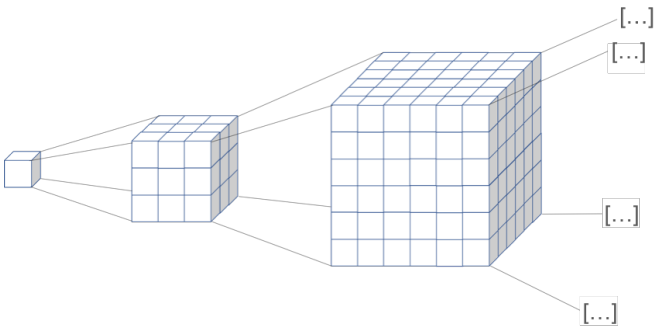

Figure 2.1: A schematic representation from a unit cell (= one cube) to ever larger supercells to an "infinite" crystal.

Although molecules and crystals appear to be very different, they are subject to

the same underlying physical laws. In the following sections, this will be demonstrated through an examination of electrostatic effects and the description of electrons in the two types of systems.

2.1 Electrostatic Interactions in Molecules and Crystals

As a first approximation, one can assume that the long-range effects in a crystal are purely electrostatic. This section shows that the principles of electrostatics do not differ between a molecule and a crystal, and that the long-range electrostatic effects acting on the bulk of a crystal can be approximated for a finite system size.

If the simple diatomic molecule sodium chloride (NaCl) is assumed to be purely ionic, Figure 2.2 describes the potential energy of the interaction between the cation Na^+ and the anion Cl^-. An ionic interaction can be viewed as a combination of repulsive and attractive terms. The repulsive term is mainly Pauli repulsion, based on the Pauli exclusion principle, which states that two electrons cannot be in the same quantum state.[85] The attractive term is the electrostatic potential, also called the Coulomb potential.[86]

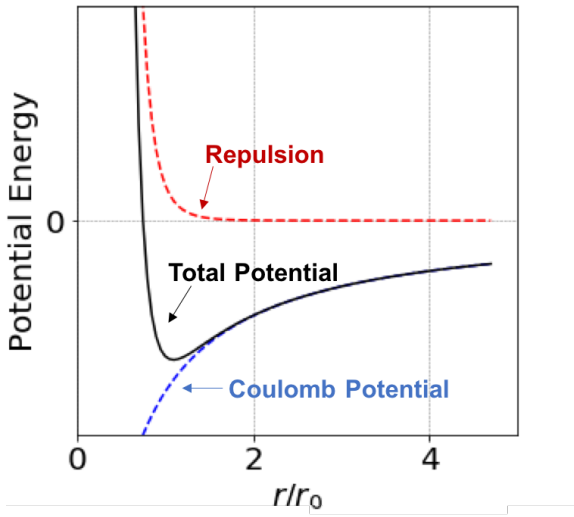

Figure 2.2: Total potential energy (black), Coulomb potential (blue), and repulsion potential (red) of an interaction between a cation and an anion as a function of their distance r/r_0, where r_0 is their equilibrium distance.

When the distance r between Na^+ and Cl^- is small, repulsion is the dominant term because the electrons of the two ions are forced to approach the same state. This interaction is short-range, and at the equilibrium distance r_0 it is close to zero. The equilibrium distance refers to the optimal distance between the two ions where the

molecule is most stable. Therefore, at r_0, the total potential V_0 can be approximated as in Equation 2.1 with the Coulomb potential.

$$V_0 = V_{Coulomb} + V_{Pauli} \approx V_{Coulomb} = -\frac{q_1 q_2}{4\pi\varepsilon_0 r_0} = -\frac{e^2}{4\pi\varepsilon_0 r_0} \tag{2.1}$$

Here, ε_0 is the vacuum permittivity, and q_1 and q_2 are the magnitudes of the Na^+ and Cl^- charges, respectively, resulting from the electron transferred from Na to Cl. Accordingly, in both cases the charge has the magnitude of an electron, which allows $q_1 q_2$ to be written as e^2. The total potential is negative because the charges of the two ions are opposite and thus, the interaction is attractive.

Since the only two pieces of information about the ions relevant to the Coulomb potential are their respective total charges and the distance between them, the interaction can be approximated as one between two point charges e and $-e$ at distance r_0. Hence, the Coulomb potential, which is a component of "classical" mechanics, completely describes the system.

Figure 2.3 considers a one-dimensional array of charges. The Coulomb potential arises not only from attractive interactions between opposite charges, but also from repulsive interactions between identical charges. As the distance r between any two charges increases, the strength of their interaction decreases in proportion to r^{-1}.

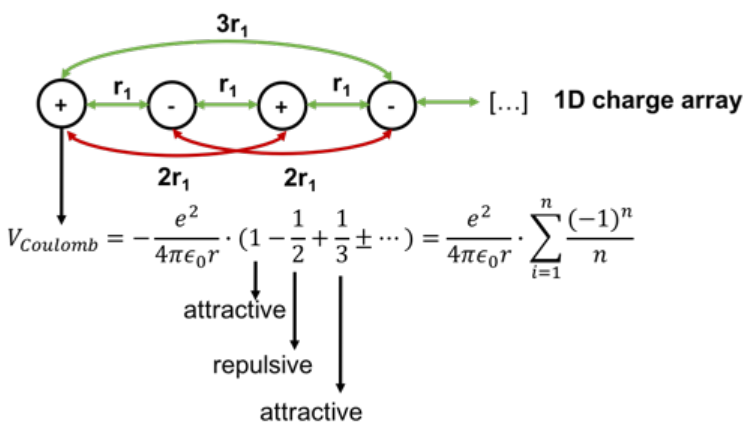

Figure 2.3: One-dimensional charge array with alternating positive and negative charges and the resulting Coulomb potential of the first charge on the left. Figure inspired by ref. [87].

This principle can be applied to a three-dimensional field of point charges, which represents a purely ionic crystal. NaCl crystallizes in the rock salt structure, which means that a Na+ or Cl- ion - or in this approximation, a representative point charge - has six direct neighbors with opposite charges, all at a distance of r_2. Figure 2.4a shows the structure along with a unit cell and a supercell. Due to the restrictive

environment, r_2 is smaller than r_0 for its diatomic counterpart. Considering the six direct neighbors, the resulting Coulomb potential of any point charge is that of a charge interacting with not one, but six opposite charges simultaneously.

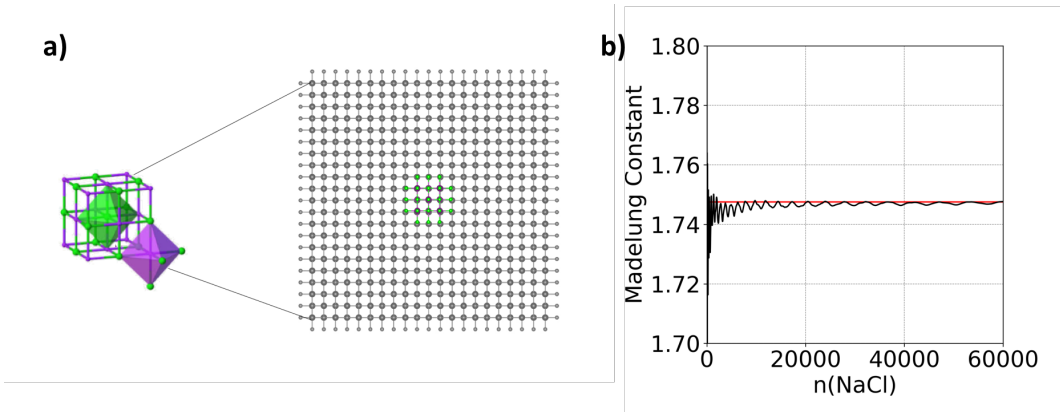

Figure 2.4: a) Unit cell and supercell of NaCl in the rock salt structure. **b)** The Madelung constant of an ion in the center of a rock salt supercell with increasing supercell size in terms of the number of Na^+ and Cl^- ions.

At a distance of $\sqrt{2}r_2$ there are twelve charges equal to the one in the center. Therefore, another Coulomb potential must be added to the equation describing this type of repulsive interaction between identical charges with the respective number of charges and their distance. This series of attractive and repulsive interactions with more and more distant charges continues. Equation 2.2 gives the resulting Coulomb potential V_{RS} of any point charge in an "infinite" rock salt crystal.

$$V_{RS} = -\frac{\alpha_{RS} e^2}{4\pi\varepsilon_0 r_0} \tag{2.2a}$$

$$\alpha_{RS} = 6 - \frac{12}{\sqrt{2}} + \frac{8}{\sqrt{3}} \pm ... = 1.747756 \tag{2.2b}$$

The Madelung constant[88] α determines the electrostatic potential of a single ion in a crystal depending on the overall crystal lattice type. For any ion in an "infinite" rock salt structure, regardless of its position or charge, α_{RS} is about 1.75.[89] If the solid is not considered infinite, but has a defined size, the Madelung constant for ions on or near the surface of the crystal is different from that for ions in bulk positions. Therefore, only those ions that are surrounded by enough other ions to approach the correct Madelung constant can be considered to have bulk properties from an electrostatic point of view. The scheme shown in Figure 2.4b suggests that

this is approximately true if about 7,500 other ions - or in this approximation, point charges - surround the ion in question. This is also true for other types of crystals that differ from the rock salt structure.

2.2 A Brief Journey from Orbitals to Bands and Back

Both concepts of electrons in molecules, described by molecular orbitals, and in solids, represented by bands, are based on the principle that a quantum mechanical system with n electrons can be completely described by its wavefunction ψ. In the following, these ideas are explored for molecules and crystals, with the Born-Oppenheimer approximation providing a framework in which the wavefunction depends only on the positions of the electrons and not on the motion of the nuclei.[90]

2.2.1 Orbitals

The (electronic) wavefunction ψ of n electrons is defined by $3n$ coordinates - three spatial coordinates [$r = (x, y, z)$] per one electron i. Even for a "simple" system like an atom, this wavefunction gets complicated very quickly. The problem can be simplified by approximating ψ as a product of n one-electron wavefunctions φ_i expressed in Equation 2.3.[85]

$$\psi_n(r_1, ...r_n) = \prod_{i=1}^{n} \varphi_i(r_i) \tag{2.3}$$

These one-electron wavefunctions are called atomic orbitals (AOs). They are eigenfunctions of the one-electron Schrödinger equation according to Equation 2.4, where the one-electron Hamiltonian is h_i and the eigenvalues ε_i are the orbital energies.

$$h_i \varphi_i = \varepsilon_i \varphi_i \tag{2.4}$$

The probability density $|\varphi_i|^2$ determines the probability of finding an electron at a given location in a system.[91] In general, the well-established hydrogen-like AOs (s, p, d, ...) define the shapes of any AOs spherically around a given nucleus.[92] The quantum numbers n (principal quantum number), l (azimuthal quantum number), and m_l (magnetic quantum number) determine the shape, size, and orientation of these orbitals. For now, the description excludes the spin quantum number m_s. Since the electron spin is not considered, all orbitals are spatial orbitals and not spin orbitals, which will become relevant in Part II.

A typical way to define the AOs is to use a radial $R_l(r)$ and a spherical harmonic function $Y_{lm_l}(\theta, \phi)$ as given in Equation 2.5, where θ, ϕ, and r are spherical coordinates.[93, 94]

$$\varphi = R_l(r) Y_{lm_l}(\theta, \phi) \tag{2.5}$$

Modeling the AOs is a computational challenge. The most common solution in molecular calculations is to replace the AOs with sets of so-called Gaussian basis functions (basis set).[95] The specifics of these functions depend on the chosen basis set and are not part of the current discussion.

In a molecule, electrons can no longer be assigned to individual atoms. Consequently, they cannot be described by the concept of AOs, but by that of molecular orbitals (MOs) ϕ. MOs are usually defined by a linear combination of atomic orbitals (LCAO), as given in Equation2.6.[96–98]

$$\phi_j = \sum_{i=1}^{n} c_{ij} \varphi_i \tag{2.6}$$

In molecular calculations, the c_{ij} coefficients are optimized,[98]. They determine the contribution of each AO in a given MO. [71, 99] The AOs themselves are also a linear combination of the selected Gaussian basis functions, and in practice their corresponding coefficients are optimized to form an appropriate set of MOs.[92, 94]

The number of MOs in a molecule is equal to the number of AOs in all included atoms of a defined system. AOs can be combined into MOs only if they have the same irreducible representation with respect to their symmetry, overlap spatially, and have a similar energy level. Therefore, MOs can often still be confined to one or a few atoms in the molecule. This can be illustrated by the example of NaCl. Since the system is strongly ionic, the overlap between the AOs of Na and Cl is small because the electrons are localized to either Na^+ or Cl^-. As a result, the HOMO (highest occupied molecular orbital) has a dominant Cl $3p$ character, while the LUMO (lowest unoccupied molecular orbital) has a dominant Na $3s$ character. Figure 2.5 shows the MO diagram representing the electronic structure around the HOMO-LUMO gap of diatomic NaCl.

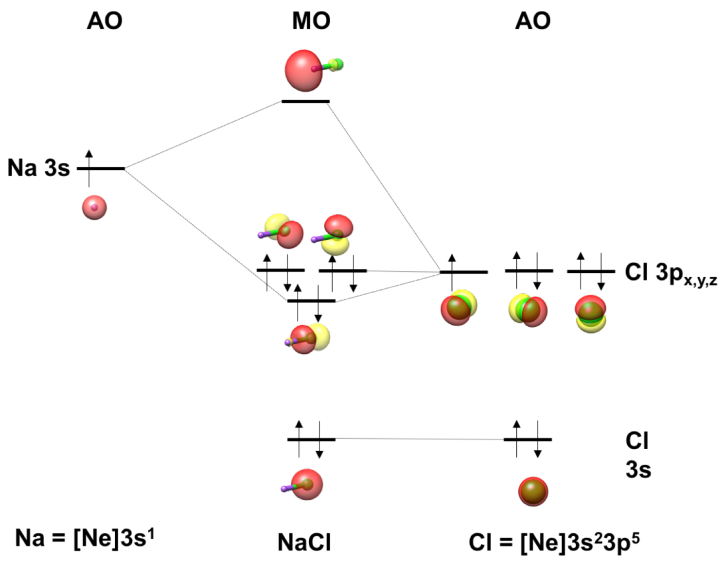

Figure 2.5: MO diagram of a diatomic NaCl molecule.

2.2.2 From Orbitals to Bands

If, instead of a diatomic NaCl molecule, a cluster of two Na and two Cl atoms is considered, additional energy levels appear. The Pauli exclusion principle prohibits electrons from occupying the same quantum state. This leads to a splitting of the energy levels of the MOs of the four atom case around those of the diatomic case, ignoring for simplicity that some energy levels may be degenerate. Figure 2.6a visualizes the process and includes only the orbitals with HOMO - represented by only one arbitray Cl $3p$ orbital instead of Cl $3p_{x,y,z}$ - and LUMO character for simplicity. As the cluster is further enlarged, the resulting orbital energy levels split further and further until they appear as an energy continuum. The result is called a band.[100]

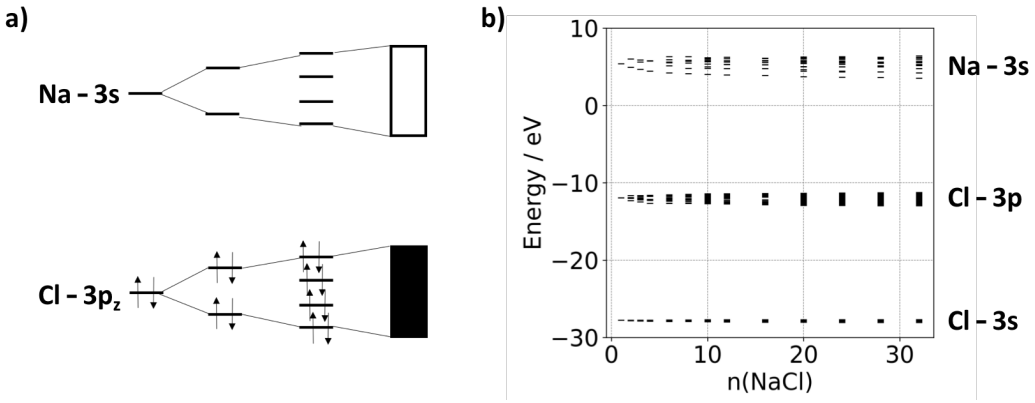

Figure 2.6: **a)** Schematic representation of the valence band formation from the HOMO and the conduction band formation from the LUMO for NaCl. **b)** Orbital picture of NaCl models with increasing cluster sizes. Level of theory: HF/def2-tzvp, clusters modeled with the electrostatic embedded cluster approach.

Figure 2.6b presents calculation results for the MO energy levels for increasing NaCl system sizes modeled with the later introduced electrostatic embedding approach starting from the diatomic system up to a rock salt supercell. The results show the predicted MO energy level splitting with increasing system size. However, the extent of the splitting comes to a halt at relatively small system sizes, resulting in the formation of a distinct band of defined width. Further increases in system size from this point only increase the density of MOs within the bands. The gap between occupied and unoccupied orbitals of these larger clusters is smaller than that of a diatomic system. Nevertheless, the same character can be assigned to the "band of HOMOs" - Cl $3p$ - and to the "band of LUMOS" - Na $3s$. The density of the bands defined by occupied orbitals is significantly different from that of the unoccupied orbitals. The "band of LUMOs" is broader and less dense for all system sizes.

The observed phenomena find their analogues in solid-state theory. The bands in solids are nothing more than an "infinite" number of MOs. The "band of HOMOs" is called the valence band, and the "band of LUMOs" is called the conduction band.[101] The amount of splitting corresponds to the bandwidth (dispersion). The smaller the bandwidth, the more local the orbitals. The number of orbitals within a given energy range corresponds to the concept of density of states (DOS), which is widely used in solid-state theory.[71]

2.2.3 Bands

Although the construction of bands from an increasing number of MOs is valid, it is worth recalling how bands are usually defined.

A crystal is an extended structure composed of unit cells that are arranged in a periodic manner, demonstrating translational symmetry in relation to one another.[84] A unit cell has a specific electronic structure described by a wavefunction ψ. If N identical unit cells are introduced, one would expect the same electronic structure for each. It would be inefficient to define the resulting total wavefunction as a combination of the N identical wavefunctions.[102]

To avoid this problem, the electrons can be expressed by Bloch functions as shown in Equation 2.7. In this representation of the wavefunction, the crystal lattice is not considered in real space, but in reciprocal space. It is defined by [1/length], which is also the unit of the wave vector k, which refers to the spatial frequency of the wave describing the electron.[103]

$$\psi(r + T) = e^{ikT}\psi(r) \tag{2.7}$$

A Bloch function is a periodic eigenfunction. The phase factor e^{ikT} between equivalent positions in the lattice preserves that each electron has the same probability of being found at equal positions. Here, T is any translational operator that preserves translational symmetry. Since the wave vector k is an eigenvalue of the translational operator T in Equation 2.7, it is often considered an additional quantum number or, more precisely, a quantum vector. There are N possible values for k - one value for each of the N unit cells in the crystal and thus, for each translation. However, because of periodicity, the first Brillioun zone, which corresponds to the unit cell in reciprocal space, already represents them all.[101, 103]

As in the case of the molecule, the total wavefunction $\psi(r)$ of a unit cell with n electrons is usually considered as the product of n one-electron wavefunctions. It is possible to model these functions using a periodic analog of the LCAO approach. This approach is called the tight-binding approach because the electrons are confined to specific atoms. In this case, the basis functions are typically expressed using Gaussian basis sets and are usually applied to ionic systems. However, a more common approach in periodic calculations, especially for metallic systems, is to model the one-electron wavefunctions with plane waves. These define the electrons as delocalized particles moving (almost) freely through the crystal, constrained only by a potential function defining the crystal lattice.[103]

Again, the eigenvalue energies $\varepsilon_{i,k}$ of each electron i in the periodic system can be determined from Equation 2.4. However, these eigenvalues depend not only on the electron i, but also on k and accordingly form an energy band of k orbitals. Hence, there are $k \cdot n$ and consequently, $N \cdot n$ one-electron functions defining the crystal.

2.2.4 From Bands to Orbitals

The whole band structure of a crystal is usually visualized as $E(k)$ vs. k and therefore, presented in reciprocal space.[71] Figure 2.7 shows an example band structure for NaCl. Since there is not only one reciprocal space variable, but several, the different directions are indicated here by G, X, W, K, and L. The details about their specific meanings are not relevant at this point. The band structure can be interpreted nonetheless.

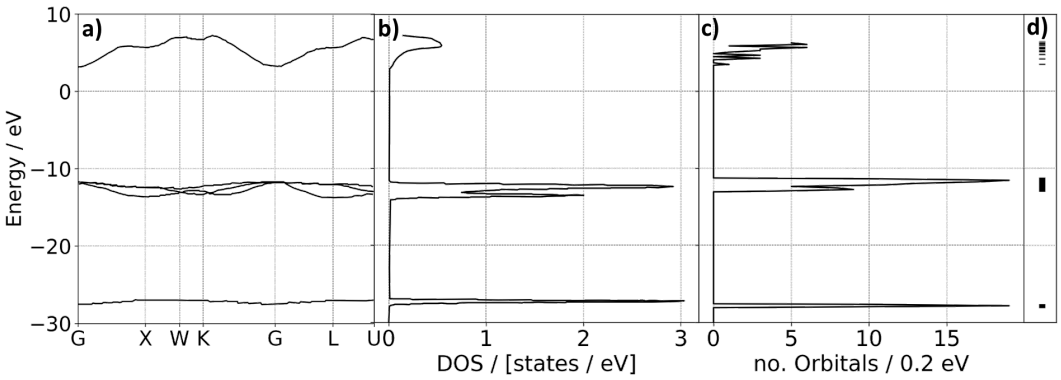

Figure 2.7: a) Band structure and **b)** Density of States (DOS) from a periodic calculation compared to **c)** "Density of States" generated from **d)** the orbitals of a non-periodic calculation of NaCl with system size $[Na_{32}Cl_{32}]^0$. Reduced and modified band structure and density of states data taken from ref. [104].

As in the MO model, each band can be characterized. Here, the lowest energy band has Cl $3s$ character, the three overlapping bands are the three occupied Cl $3p_{x,y,z}$ bands (valence band), and the highest is the unoccupied Na $3s$ band (conduction band).

Not only the position of the bands is important, but also their width. The bandwidth - as mentioned above - is called dispersion. The orbitals described by a band are more delocalized if the bandwidth is broader, such as the Na $3s$ band. They are generally more localized if it is narrow, as for the three Cl $3p$ bands and the lower lying Cl $3s$ band.

The local slope along each band indicates the number of orbitals represented. The flatter the band, the more orbitals it describes and the denser the orbitals are. This property can be brought back to real space by counting the number of orbitals δk in each direction with respect to a given infinitesimal energy interval δE. The resulting diagram is shown in Figure 2.7b and is called the density of states (DOS) because it measures the density of orbitals for a given energy.[71] For example, the

conduction band (Na $3s$) is steeper at lower energies and flatter at higher energies. The corresponding DOS shows a greater density of orbitals at higher energies than at lower energies.

Equivalent to the DOS, the MOs of Figure 2.6b can be summed up in a chosen energy interval ΔE, as shown in Figure 2.7c. Although the density of orbitals is lower than in the periodic case, the qualitative result is the same as the quantitative one with respect to the width and energy position of the bands. Once again, this shows that an increasing number of MOs can approximate the band structure and accurately represent certain features.

2.2.5 A Detour to Many-Electron States

It should be emphasized that atoms, molecules, and solids do not exist in orbitals or bands, and that orbitals and bands are not observables. They are merely one-electron concepts that have proven useful. Therefore, neither the MO diagrams nor the DOS accurately reflect the reality of the system. Atoms, molecules and solids exist in many-electron states.

Based on ligand field theory, a state is determined by its electron spatial distribution (electron configuration), which can be described by orbitals, the overall symmetry in the irreducible representation (Γ) in terms of group theory, the overall spin (S), and the projection of the spin onto the z-axis ($M_S = 2S + 1$, multiplicity). Equation 2.8 characterizes the state of a system.

$$^{2S+1}\Gamma \tag{2.8}$$

Thus, it can be argued that the term "density of states" is misleading because it is the density of orbitals and not of states. States or, more precisely, the difference between states can be measured in spectroscopy.[105, 106]

The electron configuration is a construct resulting from the orbital approximation. Therefore, a state of a system with many electrons cannot be accurately described theoretically and is not represented in the one-electron images of bands or orbitals. Nevertheless, the one-electron perspective is often a valid approximation for strongly ionic materials with low electron correlation, such as NaCl, and the basis for most quantum chemical concepts. However, it can quickly reach its limits for strongly correlated materials, for which the pseudo-independent model of electrons no longer holds.[107] Part II describes concepts and approaches for more accurate wavefunctions and consequently, states, all starting from the orbital perspective.

2.3 Quantum Meets "Classical" Mechanics

The main goal of this chapter is not only to show that crystals and molecules can be explained by the same laws but also to find a model that allows the calculation of crystal properties by viewing it as a "large molecule". Since, in computational chemistry, the properties are usually derived from the orbitals, it is essential that they have the correct energy. While this was taken for granted in the previous section, this section explores how an accurate energy description can be achieved by using the knowledge from Section 2.1 on the electrostatic properties of a crystal.

Equation 2.4 has already introduced the time-independent one-electron Schrödinger equation. Although the orbital energies are ultimately considered critical, it is helpful to consider the crystal as a whole, with a wavefunction Ψ describing the entire system and an associated total energy. Equation 2.9 revisits the time-independent Schrödinger equation for the total electronic energy E, which includes the Born-Oppenheimer approximation.

$$\hat{\mathcal{H}}\psi = (\hat{\mathcal{T}}_e + V)\psi = E\psi \tag{2.9}$$

The Hamiltonian $\hat{H}$, which determines the energy, can be split into two operators, the kinetic $\hat{T}_e$ and the potential V energy operators. Equation 2.10 determines $\hat{\mathcal{T}}_e$, where $\hbar$ is the reduced Planck constant, m_e is the mass of an electron, and ∇_i^2 is the Laplace operator.

$$\hat{\mathcal{T}}_e = -\sum_i \frac{\hbar}{2m_e}\nabla_i^2 \tag{2.10}$$

V can be divided into the potentials of the repulsive electron-electron interaction V_{ee}, the repulsive nucleus-nucleus interaction V_{nn}, and the attractive electron-nucleus interaction V_{en}, as shown in Equation 2.11.

$$V_{ee} = \sum_i \sum_{j,j>i} \frac{e^2}{4\pi\varepsilon_0|r_i - r_j|} \tag{2.11a}$$

$$V_{nn} = \sum_i \sum_{j,j>i} \frac{Z_i Z_j e^2}{4\pi\varepsilon_0|R_i - R_j|} \tag{2.11b}$$

$$V_{en} = \sum_i \sum_j \frac{Z_i e^2}{4\pi\varepsilon_0|R_i - r_j|} \tag{2.11c}$$

Here, R and r are the positions of the nuclei and electrons, respectively, Z is the atomic number, e is the elementary charge, and ε_0 is the permittivity of the vacuum. All potentials are "classical" Coulomb potentials as introduced in Equation 2.1.[90]

Considering that the total electronic energy E is a combination of all the orbital energies ε_i,[85] it becomes evident that each orbital energy depends on the total electrostatic environment created by the other electrons and nuclei. In a primarily ionic system, such as NaCl, where the electrons are predominantly localized, one can assume that an electron explicitly "sees" only the charge of the electrons and nuclei in its immediate vicinity. In a resulting model, the more distant ions act on the electron only as effective charges and can be replaced by corresponding point charges.

This idea is not new and is often referred to as "QM/MM" (Quantum Mechanics/Molecular Mechanics) because a certain part of the computational model is treated at the quantum mechanical level, while the rest is approximated by molecular mechanics using the principles of "classical" mechanics.[108] These methods are primarily well established for biochemical calculations, especially for proteins,[109] but there are also approaches for solid-state systems, here referred to as electrostatic embedding approaches.

Equation 2.12 determines the total energy E^{total} of a QM/MM system.[108]

$$E^{total} = E^{QM} + E^{QM/MM} + E^{MM} \tag{2.12}$$

E^{QM} is the energy of the QM part, $E^{QM/MM}$ is the energy resulting from the interaction between the QM and MM part of the model, and E^{MM} the energy of the MM part, in this case, the point charges.

Since this model aims at a good approximation to the electronic band structure or even more specific properties resulting from the electronic structure of a crystal rather than its total energy, the last term of Equation 2.12 can be neglected. E^{QM} is determined by the Schrödinger equation introduced in Equation 2.9. In contrast, $E^{QM/MM}$ considers only the Coulomb potential resulting from the interaction of the QM part with the point charges. Thus it considers the electrostatic interaction of the point charges with the nuclei V_{nq} and electrons V_{eq} in the QM region as given in Equation 2.13, where q is the charge of the point charges.

$$V_{eq} = -\sum_j \sum_i \frac{e^2 \cdot q_j}{4\pi\varepsilon_0 |r_i - R_j|} \tag{2.13a}$$

$$V_{nq} = -\sum_j \sum_i \frac{e^2 \cdot Z_i \cdot q_j}{4\pi\varepsilon_0 |R_i - R_j|} \tag{2.13b}$$

As a result, the orbitals in the QM region and the resulting band-like structure are determined not only by the interactions within the QM region, but also by those with the point charges. The QM region itself is a discrete molecular-like structure, but acquires crystal-like properties with respect to the electrostatic MM environment. The resulting model is representative of the band structure or a particular property of the electronic structure of the bulk of the crystal only if the following points are satisfied. First, the MM environment contains enough point charges to reproduce the correct Madelung constant acting on the QM region. Second, the QM region is large enough to either approximate the band structure or to represent the property of interest. How to achieve such a model is the subject of the next chapter.

3 How to Model a Crystal with the Electrostatic Embedded Cluster Approach

Based on the concepts introduced in the previous chapter, this chapter introduces a specific electrostatic embedded cluster approach to model crystals. Figure 3.1 visualizes a resulting model of the example NaCl.

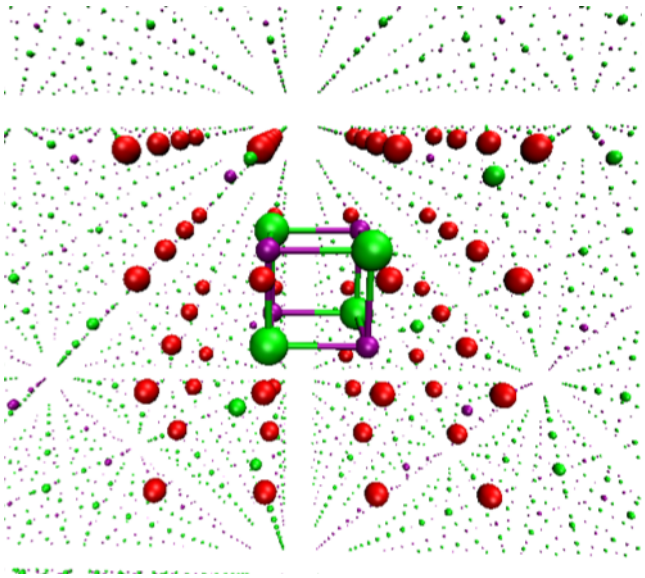

Figure 3.1: Electrostatic embedded cluster model for NaCl with the QC (quantum cluster: atomic structure in the center, green: Cl and purple: Na), the BR (boundary region, red), and the PC (point charge field, small dots) field.

The model consists of a large supercell, representing the crystal, with a defined cluster of atoms at its center. This cluster is treated quantum mechanically and is called a quantum cluster **quantum cluster (QC)** or simply cluster. The calculation of the desired property of the crystal is performed on the QC. Therefore, the main requirement for the QC is that it must be representative of the property under investigation. To achieve this, the QC must be large enough to fully capture the property and may also need to preserve the main features of the crystal structure. Depending on the particular property and the crystal being studied, this could mean that the

QC represents all sites of the crystal and/or preserves a local symmetry feature.

The QC does not involve long-range effects and would be a nanoparticle in itself. The goal of this work is to model the bulk properties of an ideal crystal. Therefore, the long-range electrostatic effects must be considered. As mentioned previously, "classical" mechanics can treat them through a **point charge (PC) field** constructed around the QC. By representing the lattice positions of the crystal's supercell that are not part of the QC, the PCs create the illusion that the QC is located within the bulk of the crystal.To properly account for the fundamental electrostatic properties of an ideal crystal, the PC field must reflect three critical characteristics of the crystal:

1. All bulk atoms in an ideal crystal experience a specific Madelung constant depending on the overall crystal structure.

In the context of the electrostatic embedded cluster model, this means that it is necessary to introduce a sufficient number of PCs around the QC so that all atoms in the QC approach the correct Madelung constant. In addition, the PCs must be positioned according to the crystal lattice so that the correct crystal lattice symmetry is obtained.

2. An ideal crystal has a homogeneous charge distribution.

This second characteristic implies that the charge magnitude of the PCs must be equal to the one of the ion at the particular lattice position where they are placed. Since most bonds in crystals are neither purely ionic nor covalent, the ion-representing charges do not necessarily have to be the formal charge of the ion. The size of the PCs must be optimized to match the charges of the corresponding ions in the QC. The goal of this optimization is to ensure that the charge at each identical lattice position remains consistent throughout the model. This also means that charges representing the same position should not change within the PC field.

3. An ideal crystal is charge-neutral.

This third property dictates that the sum of all charges, including the total charge of the QC and the PCs, must be zero. However, depending on the total number of atoms and charges, and the size of the optimized charge in the model, this condition may not be satisfied automatically. To ensure that the total charge is zero, the PC magnitudes must be adjusted at all or some positions. As a result, the previous requirement of uniform charge distribution has to be compromised to satisfy this condition. As will be discussed in detail later, to balance the second and third requirements, it is best to neutralize the total charge only on the outside of the PC

field, at a sufficient distance from the QC. This is done to minimize the effect of the introduced inhomogeneous character on the QC and the resulting property calculation.

To complete the model, a third component must be considered, the **Boundary Region (BR)**, which lies between the QC and the PCs and consists of **electrostatic core potentials (ECPs)**. The presence of this third component is crucial for the following reasons. Atoms on the surface of the QC may not have all their orbital interactions and resulting bonds saturated due to the absence of orbitals on the neighboring PCs. This can lead to dangling bonds and interface/surface effects, which in turn can lead to an undesirable partial nanoparticle character of the QC. Therefore, the ECPs are responsible for preventing these effects by performing the following task:

1. Placing ECPs at the lattice positions around the QC can minimize surface/interface effects and dampen dangling bonds by addressing the neglected terms between the QC and PCs.

While the PCs positioned on the crystal lattice maintain the overall crystal symmetry, a break in crystal symmetry affecting individual orbitals on the surface of the QC can still occur. This problem is related to the previous point as the PCs do not interact properly with the QC orbitals. By introducing ECPs, specific local orbital symmetries can be preserved, which leads to the second task of ECPs as follows:

2. ECPs placed around the QC can preserve local symmetries.

Another potential problem is the transfer of electrical charge from the QC to the PC field or vice versa, which can cause delocalization of the QC. The ECP task can be formulated accordingly:

3. ECPs can prevent artificial charge flow (spurious electron leakage) between the QC and the PCs and over-delocalization of the QC.

Now that the ground rules for a successful electrostatic embedding model have been established, the remainder of this chapter is divided into two sections. The first section presents general computational protocols for creating an electrostatic embedded cluster model for any inorganic crystal, either manually or using the ORCA_CrystalPrep utility. It then describes how to create appropriate input files for ORCA calculations. A so-called "simple" embedding approach using a typical ORCA input file structure is presented, as well as the "Ionic-Crystal-QM/MM" approach implemented for ORCA 5.0 and later versions using ORCA's QM/MM environment. The second section delves into the physics underlying the introduced protocols and rules for QC, BR, and PCs.

The two sections are loosely based on presentations given at the ORCA user meeting, as well as published work[51, 83] that describes the basics of the protocols revised here. Additional unpublished information is also included.

3.1 General Workflows and Input File Structures

3.1.1 Creating Electrostatic Embedded Cluster Models Manually and with ORCA_CrystalPrep

The electrostatically embedded cluster model of a crystal is constructed from its supercell, which serves as the basis for all three substructures - QC, BR, and PC field - of the resulting model. Therefore, the first step in a generalized electrostatic embedding protocol is to create an appropriate supercell. The information about the experimental structure of a unit cell contained in a CIF (Crystallographic Information File) or an equivalent information file can be converted into a supercell using any available crystallographic or chemical program that can handle this type of task. Three examples of such programs are VESTA[110], MERCURY[111], and CRYSTAL[112]. The QC and BR are cut from the center of the supercell. This process can be accomplished using a program capable of defining and modifying chemical structures, such as AVOGADRO[113],[114], Jmol[115], or CHIMERA[116],[117]. The remaining part of the supercell, which is not defined as QC or BR, is then assigned to the PC field. Figure 3.2 demonstrates the steps from the unit cell defined by the CIF to the final electrostatically embedded cluster model for the example of NaCl.

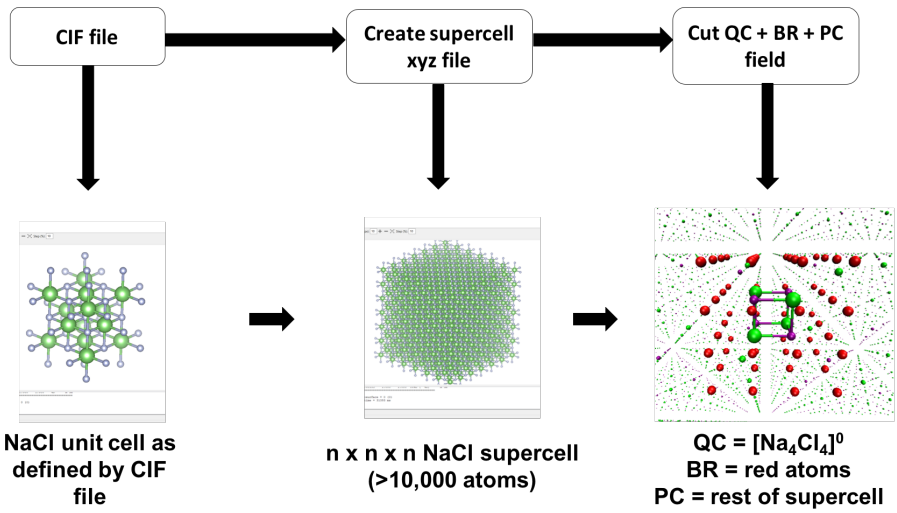

Figure 3.2: Schematic protocol for the creation of an electrostatic embedded cluster model using data from a CIF to create a supercell and the resulting QC, BR, and PC field.

The respective CIF is taken from the crystallographic database[118],[119]. The structure of the QC, the BR, and the PC field can be stored as Cartesian coordinates in an xyz file. The data can be integrated into the ORCA input file structure, as described in the next subsections.

Alternatively, for ORCA 5.0 and more recent versions, it is possible to use the ORCA_CrystalPrep program to prepare a model structure from a CIF or xyz file. The program automatically constructs a supercell, creates QC, BR, and the PC field, and produces the corresponding input files. The following is a brief outline of the basic functions of ORCA_CrystalPrep.

An overview of the possible keywords and functions of ORCA_CrystalPrep can be found by calling the program within the ORCA suite of programs using the command below.

```
ORCA_crystalprep
```

The combination shown in the following box of the keyword "-geninput" with a selected input file name, here "NaCl.inp" generates an ORCA_CrystalPrep input file template.

```
ORCA_crystalprep nacl.inp -geninput
```

As the name of the input file implies, the NaCl model is created. The template suggests several basic keyword options, which can be customized according to the desired model. Section A in the appendix contains the complete default template and a detailed list of possible keywords (see Figure A.1 to Figure A.3 on the pages 310 to 312). The input file combines two steps of the ORCA_CrystalPrep protocol. The left side of Figure 3.3 shows an excerpt from the input file for the NaCl example responsible for generating the supercell of the crystal and specifying how it should be constructed, and the right side of Figure 3.3 shows an excerpt from the same input file specifying the embedding model generated from this supercell.

As shown in the box below, the input file can be run with ORCA_CrystalPrep.

```
ORCA_crystalprep nacl.inp
```

On the left side of Figure 3.3, the template is modified exemplarily to specify that the crystal data is read from a CIF ("DoCIF true"). Alternatively, the data could be taken from an xyz file. The keywords "DoSuperCell true" and "SCDimension "15x15x15"" specify that a supercell of size 15x15x15 is composed. This section of the input file can be run without any additional information and will produce an output file in the form of an xyz file representing the supercell.

Generate supercell from CIF

```
%crystalprep

#*************************
#Read CIF/XYZ
#*************************
DoCIF true

#------------------------
#INPUT CIF/XYZ
#------------------------
InputCIF "nacl.cif"

[...]

#*************************
#Generate SuperCell
#*************************
DoSuperCell true
SCDimension ”15x15x15”

[...]
end
```

Generate input file

```
%crystalprep

[...]

#------------------------
#Set Special Tasks
#------------------------
QCLayers 1
BRLayers 1

[...]

#*************************
#Setup Embedding Approach
#*************************
DoEmbedding true
DoLayers true

#------------------------
#Atom Type Charge Spin
#------------------------
NAtomTypes 8
Na 0  1.0 0.0
Cl 1 -1.0 0.0
[...]

#*************************
#Generate Inputs
#*************************
#------------------------
# Simple/IC-QMMM inputs
#------------------------
#DoSimpleInput true
DoICQMMMInput true

[...]
end
```

Figure 3.3: Sample excerpts from a possible input file for ORCA_CrystalPrep, generated via "geninput" with ORCA_CrystalPrep and modified accordingly.

In order to create an electrostatically embedded cluster model from the created supercell, all atom types - here Na and Cl - as well as their charge and spin must be specified in the ORCA_CrystalPrep input file together with enabling the keyword "DoEmbedding true" (see Figure 3.3 right side). In this example, it was chosen that layers of atoms define the QC and BR. For this purpose, the program determines the center of the generated supercell. The atom in the center or the atoms closest to the center of the supercell based on a distance criterion are usually defined as the first layer. The direct neighbors of the first layer create the second layer, and so on. Here, as an example, the QC and the BR both have one layer. This means that the atoms creating the first layer specify the QC, and the atoms defining the second layer (the layer around the QC) are assigned to the BR. The described case is also the default case defined in the general settings of ORCA_CrystalPrep.

Another option is to select a QC by a volume criterion or by a specified atom selection. For the latter, the program must be run from an xyz file instead of a CIF,

since the atoms are selected by their position within the xyz file. The BR can also be determined in the same way. How to specify an appropriate QC and BR will be part of the discussion in Section 3.2.

The program will assign all atoms not belonging to QC or BR to the PC field. Alternatively, it is possible to assign specific atoms to the PC field as described above for QC and BR. Individual xyz output files of the different regions are automatically generated by running ORCA_CrystalPrep.

Based on these generated coordinates, the ORCA_CrystalPrep utility can create an ORCA input file for the calculation of a "simple" embedding approach or for an Ionic-Crystal-QM/MM calculation by activating the keywords "DoSimpleInput true" and "DoICQMMInput true", respectively. The main aspects of the structure of the two different ORCA input files and their "manual" creation are explained in the next two subsections.

3.1.2 The "Simple" Electrostatic Embedding Approach

As mentioned above, there are two ways to perform calculations on an electrostatically embedded cluster using ORCA. The first method is the "simple" embedding approach using the "standard" ORCA input environment. There is no need to use a special keyword in the input file to identify the system as a crystal or to indicate that the electrostatic embedding approach is being used. Figure 3.4 (left) shows the structure of an example input file for the NaCl model.

The Cartesian coordinates of QC and BR can be entered directly in the input file or in a separate xyz file, as in any other ORCA calculation. The coordinates of the atoms assigned to the QC are included in the coordinates section. The multiplicity and charge are defined for the QC only. In this example the QC is $[Na_4Cl_4]^0$, resulting in a charge of zero and a multiplicity of one. The same coordinate block also contains the atoms associated with the BR. By inserting "NewECP "SDD" end" after each coordinate set, the ECPs of type SDD will replace the respective atoms. Other ECPs can also be selected. To define the atom type and the corresponding ECP charge, the charge value can be inserted after the atomic abbreviation and before the coordinates using ">". In this example Na is replaced by the ECP "Na> 1.0". Since the example is intended to be an initial input file, the formal charge was chosen without further optimization. Formal charges are usually a good starting point for initial calculations, so they are also assigned to the PCs.

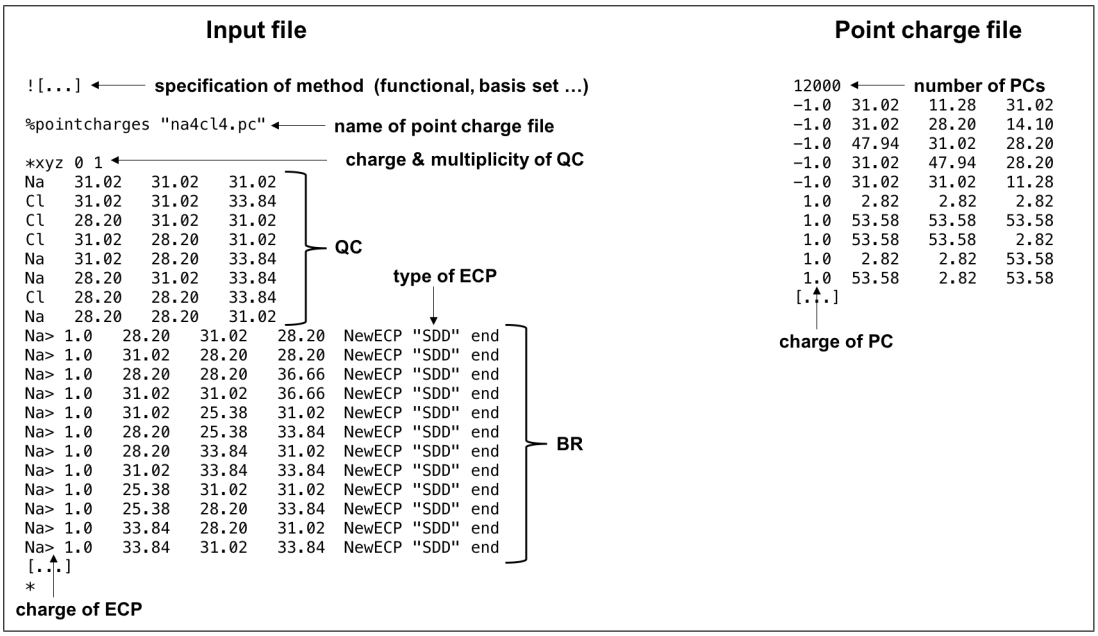

Figure 3.4: Example input file (left) and the corresponding point charge file (right) for a "simple" electrostatic embedded cluster calculation with ORCA for the example of an embedded $[Na_4Cl_4]^0$ cluster.

To avoid increasing the length of the input file, it is more convenient to store the coordinates of the PC field in a separate file. The location of this file must be specified in the input file using the keyword "pointcharges" followed by the chosen file name. To create the PC field, first the charge of the ion to be displayed must be specified, which in this case is 1.0 for Na^+ and -1.0 for Cl^-. Then the coordinates that place the charges on the crystal lattice are specified (see Figure 3.4, right).

The tools and keywords necessary to perform an electrostatic embedding calculation using the "standard" ORCA input file structure have been defined. However, it is crucial to understand the basic principles for optimizing the model in terms of charges and convergence to the desired crystal property. Figure 3.5 shows the iterative multi-step workflow to modify the model parameters until the desired requirements are met.

The first three steps in Figure 3.5 of creating the supercell, cutting and defining the QC, BR, and PC fields, and composing the input file have already been explained. The next step is to run the defined calculation. At this point, it is essential to include a charge analysis in the calculation, preferably the electrostatic charges of type CHELPG (see Section 3.2, page 51 for more information), to ensure that the charge distribution in the model is homogeneous. Section 3.2 gives more information about the choice of charges. The calculated charges of the QC are compared with the selected charges of the ECPs and PCs. If they do not match, the charges

of the PCs and ECPs are swapped accordingly and the calculation is restarted. This process must be repeated until the selected charges of the electrostatic environment (ECPs and PCs) match the charges of the QC.

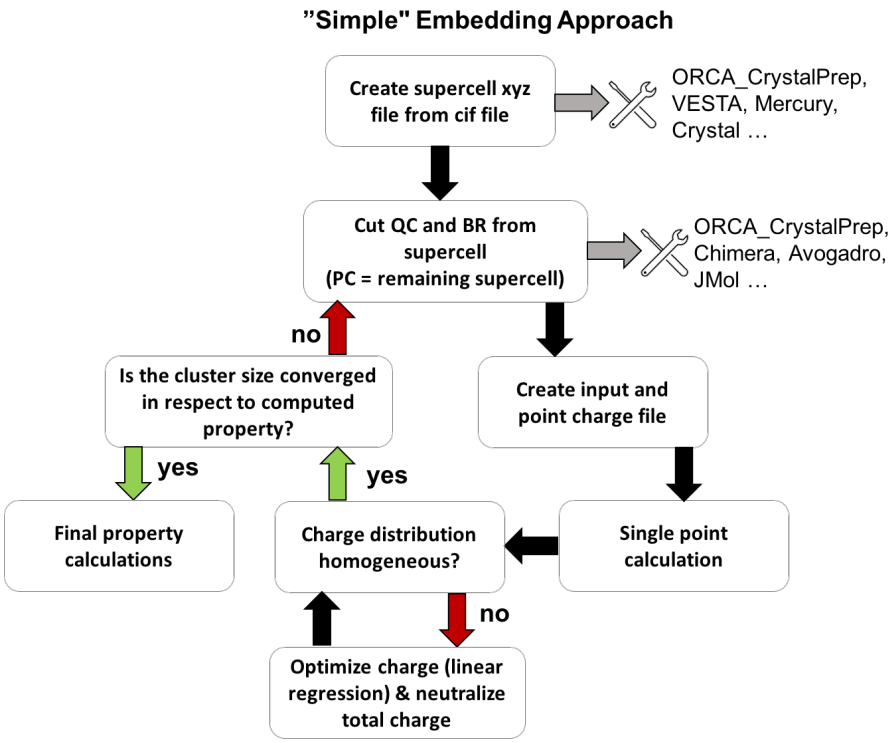

Figure 3.5: Typical workflow for a calculation protocol that follows the "simple" electrostatic embedded cluster approach to model a crystal.

To accelerate the process, two to three initial calculations employing different charge estimates for the PCs and ECPs can be conducted. The correct charge can be determined by plotting the estimated charges against the corresponding calculated charges of the QC and then performing a linear regression of the data. Section 3.2 contains a more detailed description of this method (see Figure 3.19 on page 53). Some good starting points for estimating the charge are the formal charge, the QC charge calculated from the formal charge, and an intermediate charge value.

The total charge must be neutralized manually by artificially changing some or all of the charges until the total charge is neutral. As mentioned earlier, it is reasonable to neutralize the charges on the outer layers of the PC field so that the QC's direct charge environment is homogeneous.

After optimizing the charge of the model, it is necessary to check whether the calculated property converges with respect to the cluster size. By increasing the QC size and repeating the cycle of Figure 3.5, it can be tested if the property is identical for two consecutive QC sizes. If it is, the model can be accepted as converged and

the final calculations can be performed. Otherwise, the cycle must be repeated with increasing QC sizes until convergence is reached.

3.1.3 Ionic-Crystal-QM/MM

Instead of the "simple" embedding approach, electrosatically embedded clusters can be calculated using the Ionic-Crystal-QM/MM utility. It takes advantage of the QM/MM environment in ORCA. The keywords and the calculation protocol for Ionic-Crystal-QM/MM are derived from the workflow of the concepts of the "simple" embedding approach. Figure 3.6 shows the workflow in which the first step of generating the xyz coordinates of the supercell remains as described before.

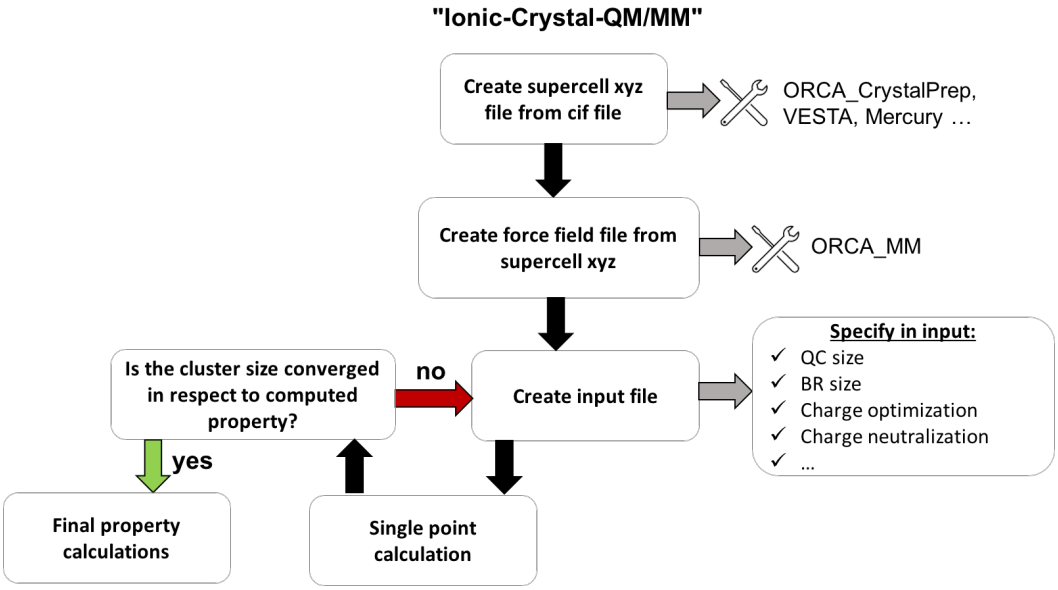

Figure 3.6: Typical workflow for a calculation protocol that uses the Ionic-Crystal-QM/MM environment in ORCA to model a crystal.

Because of the use of QM/MM, a force field must be created for the entire supercell, defining the charges at each lattice point. Therefore, there is no need for a PC file. The utility ORCA_MM creates the force field file using the comment in the box below, specifying the charges of the atoms with "-CEL".

```
ORCA_mm -makeff na4cl4.xyz -CEL Na 1.0 -CEL Cl -1.0
```

ORCA_MM creates a force field file "na4cl4.ORCAFF.prms" for the NaCl example, again with the formal charges. This file contains all necessary information for the further procedure and is generated automatically when ORCA_CrystalPrep is used to create the Ionic-Crystal-QM/MM input file.

Unlike the "simple" approach, explicit selection and definition of QC and BR coordinates is not required. If not predefined by ORCA_CrystalPrep, it is advisable to define QC before the calculations. It is useful to place the corresponding coordinates at the top of the supercell xyz file, as was done for the working example xyz file shown in Figure 3.7 (bottom left). Figure 3.7 also shows the structure of the corresponding force field file (bottom right) and the input file (top).

Input file

```
! Ionic-Crystal-QMMM [...]   ← specification of method (functional, basis set ...)
                            ↖ calling Ionic-Crystal-QM/MM machinery

%qmmm
 QMAtoms {0:7} end          ← specification of QC

 ORCAFFFilename "na4cl4.ORCAFF.prms"   ← name of force field file

 ECPLayerECP "SDD"          ← type of ECPs for BR
 ECPLayers 3                ← number of ECP layers around QC

 CONV_Charges true          ← Automatic iterative optimization of charge
 CONV_CHARGES_MAXNCYCLES 10 ← maximum number of charge optimization cycles
 CONV_CHARGES_CONVTHRESH 0.01 ← charge convergence threshold

 ENFORCETOTALCHARGE true    ← enforce charge of model
 CHARGE_TOTAL 0             ← total charge of model
 OuterPCLayers 1            ← change of charges to enforce total
                              charge only on the outside of PC field
 PrintLevel 4
end

*xyzfile 0 1 na4cl4.xyz     ← name of xyz file
          ↑
  charge & multiplicity of QC
```

xyz file

```
9260

Na   31.02   31.02   31.02
Cl   31.02   31.02   28.20
Cl   28.20   31.02   31.02
Cl   31.02   28.20   31.02   QC
Na   28.20   28.20   31.02   (QMAtoms {0:7})
Cl   28.20   28.20   28.20
Na   28.20   31.02   28.20
Na   31.02   28.20   28.20
Cl   31.02   25.38   33.84
Na   31.02   25.38   31.02
Cl   28.20   25.38   31.02
Na   28.20   25.38   33.84
[...]
```

Force field file

```
$fftype
ORCA
$atoms
9260 1 4
     1   Na     1.000000    -0.030000     2.983000    -0.030000     2.983000
     2   Cl    -1.000000    -0.227000     3.947000    -0.227000     3.947000
     3   Cl    -1.000000    -0.227000     3.947000    -0.227000     3.947000
     4   Cl    -1.000000    -0.227000     3.947000    -0.227000     3.947000
     5   Na     1.000000    -0.030000     2.983000    -0.030000     2.983000
     6   Cl    -1.000000    -0.227000     3.947000    -0.227000     3.947000
     7   Na     1.000000    -0.030000     2.983000    -0.030000     2.983000
     8   Na     1.000000    -0.030000     2.983000    -0.030000     2.983000
     9   Cl    -1.000000    -0.227000     3.947000    -0.227000     3.947000
    10   Na     1.000000    -0.030000     2.983000    -0.030000     2.983000
    11   Cl    -1.000000    -0.227000     3.947000    -0.227000     3.947000
    12   Na     1.000000    -0.030000     2.983000    -0.030000     2.983000
[...]
                   ↑
                 charge
```

Figure 3.7: Example input file (top), corresponding xyz file (bottom left), and force field file (bottom right) for an electrostatically embedded cluster calculation using Ionic-Crystal-QM/MM in ORCA for the example of an $[Na_4Cl_4]^0$ cluster.

In contrast to the "simple" embedding approach, it is necessary to specify in the input file that a crystal is to be calculated by selecting the keyword "Ionic-Crystal-QMMM", which invokes the QM/MM engine. The location of the force field file and the xyz file must be specified in the input file. As with the "simple" embedding approach, the charge and multiplicity must be determined for the QC only and not for the entire system.

The keyword "QMAtoms {...} ..." defines the QC. In the brackets, the atoms to be

treated quantum mechanically, i.e., the QC, can be defined by the numbers representing their positions in the force field and in the xyz file. For the NaCl example, these are selected by "QMAtoms {0:7}", which refers to the first eight atoms of the structure files and defines the QC $[Na_4Cl_4]^0$. It would have been possible to define the same QC if these eight atoms had random positions in the structure files. However, it seems more practical to place them in a sequential order at the beginning of the files.

Another way to define the QC is via layers, using the keyword "QMLayers" followed by an integer number of layers in place of "QMAtoms". In this case, the QC is automatically defined in the center of the model. This is recommended for calculations of larger clusters where geometry is less important, or for initial calculations of a new structure when it is unknown which structure is appropriate for the example. For many calculations, it is more appropriate to use a custom QC that has been explicitly created for the problem under consideration.

Similarly, the BR can be defined by specific atoms using the keyword "ECPLayerAtoms {...}" or by layers defined by a distance criterion to the QC using the keyword "ECPLayers" followed by an appropriate integer. Unlike the QC, it is usually advisable to define the BR by layers, since the structure is not as important as for the QC. The only cases where it is advisable to select the BR region by specific atoms are when the QC is highly asymmetric or when ECPs should replace specific atoms within the QC. The default ECP type is "SDD" but can be redefined with the keyword "ECPLayerECP".

As with the "simple" embedding approach, any atom in the structure files that does not belong to the QC or BR is assigned to the PC field. The PC field does not need to be explicitly defined in the input file, but is automatically selected.

With Ionic-Crystal-QM/MM, the charges of the ECPs and PCs can be automatically optimized in an iterative process based on the CHELPG charges. The procedure is similar to the one performed manually in the "simple" embedding approach and shows one of the advantages of Ionic-Crystal-QM/MM. It removes a lengthy manual optimization process from the calculation record. The sample input in Figure 3.7 shows the keywords "Conv_Charges", "Conv_Charges_Maxncycles", and "Conv_Charges_Convtresh", which specify the charges to optimize, the maximum number of optimization cycles to perform, and the convergence threshold. The convergence threshold is the charge difference accepted for convergence between the last charge optimization cycle and the current one.

The keyword "EnforceTotalCharge" imposes a total charge on the model, defined by the accompanying keyword "Charge_Total" followed by the respective charge value. As mentioned before, a crystal should be neutral overall. Therefore, in most

cases it makes sense to set the total charge to zero. There are certain exceptions where it would be appropriate to assume a different charge. One example is when calculating ionic potentials or electron affinities. In these cases, the total charges should be 1.0 and -1.0, respectively.

Unless otherwise specified, charge neutrality is enforced over the entire point charge field by slightly changing all charges so that the total charge, including the formal charge of the QC, is zero. This affects the homogeneity of the charge distribution. Therefore, often and especially in cases where this change is significant (e.g. when the total number of lattice points is small or when there is a general imbalance between the number of positive and negative charges in the supercell), it is advantageous to neutralize the charge by changing only the charge of the outer PC layers. The keyword "OuterPCLayers" together with an integer number defines these layers. The described automated neutralization process eliminates another step that had to be performed manually in the workflow of the "simple" embedding approach.

The discussion of the Ionic-Crystal-QM/MM input file and the QM/MM block in the input file, as shown in Figure 3.7, may seem rather lengthy and technical. However, this approach is intended to simplify the use of the electrostatic embedding approach and make it more robust in itself and with respect to sources of error, as the explanation of the keywords should have indicated. In practice, the input file in Figure 3.7 can be reduced. All keywords shown are the default settings of Ionic-Crystal-QM/MM and do not need to be specified unless a change is required. The exceptions are the QC definition, which should be defined individually for each calculation, and the keyword "OuterPCLayers", which defaults to zero, neutralizing the charge in the entire PC field. The given default information is valid for ORCA version 5.0 and later versions released up to the date of this document.

A comparison of the overall workflows in Figure 3.4 and Figure 3.7 shows that the use of Ionic-Crystal-QM/MM eliminates the iterative process of charge optimization and manual neutralization of the model. In particular, the automated charge optimization significantly reduces the total number of calculations performed, since only one calculation is required per system size. The only iterative cycle that must be repeated manually with Ionic-Crystal-QM/MM is the convergence of the cluster size with respect to the calculated property.

3.2 Insights into the Quantum Cluster, the Boundary Region, and the Point Charge Field

The QC, BR, and PC field and their purpose have been briefly explained in the introduction to this chapter. The previous section described the technical side of their construction and integration into the general computational protocols and workflows of the electrostatic embedding approach when addressed with the ORCA program package. This subsection takes a step back and re-examines the QC, BR, and PC field, respectively, moving away from a purely technical description and giving them a physical meaning. The goal is to show what constitutes a "reasonable" and robust QC, BR, and PC field, and thus what constitutes a "reasonable" and robust complete electrostatic embedded cluster model. The decision to place the discussion of these matters after the introduction of the general protocols was made because it can be helpful to know the general protocols and keywords before getting into the details behind them.

3.2.1 Different Approaches to a Quantum Cluster (QC)

Before the question of what a good QC should look like can be answered, the question of the purpose of the QC must first be answered. The QC is the part of the model on which the quantum mechanical property calculation is performed. As such, it must be representative of the crystal structure and, more importantly, the desired property of the crystal. This may require the QC to include all the different types of atoms, bonds, and necessary symmetry elements. How important each of these factors is, and how large the QC must be, depends mainly on the property. If it is a relatively local property, a small QC is often sufficient, and a large QC is required if it is a long-range or delocalized property. If the property depends on a local point group of a particular atomic site within the crystal, the symmetric environment of the atom must be preserved. The latter may be influential regardless of the property if the system is generally more covalent. If the system is strongly ionic, it may not be critical.

The purpose of this subsection is not to point out specific QCs for various observable properties, which will be covered in the upcoming chapters on specific properties. At this point, it is only a matter of establishing some basic rules and pointing out some general recipes for creating a QC based on the above statements. Only the HOMO-LUMO gap is considered as a tool for understanding the influence of different QC types. All models presented below consider QCs for the calculation of bulk properties. It is also possible to model a surface using the electrostatic

embedding approach, in which case the QC must include surface-specific structural details. In the bulk of an inorganic crystal, the bonds between different atoms are identical at each equivalent lattice position, but not at the surface of a crystal. Consequently, a QC of a surface model is expected to be larger than for the bulk in order to capture all effects. Surfaces are not the subject of the following investigations and thus, will not be discussed further.

Using the NaCl system discussed above, two main approaches to successful QCs can be identified: the supercell or unit cell approach, abbreviated as "SCe" below, and the spherical cluster or ligand field approach, abbreviated as "SCl". Figure 3.8 shows different cluster sizes for both methods.

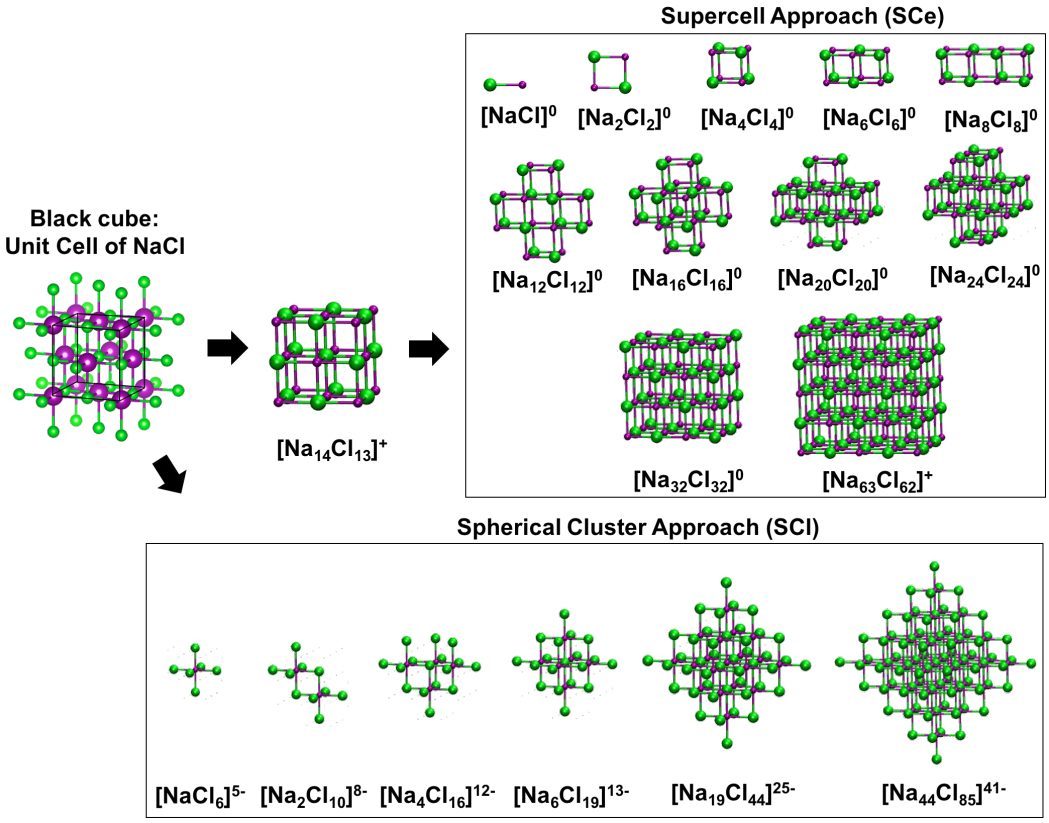

Figure 3.8: Different QC sizes of NaCl (rock salt structure) for the supercell approach (SCe) and spherical cluster approach (SCl).

As the name of the SCe approach implies, this method is derived from the previously introduced representation of crystals in unit cells and supercells. The model is built from an increasing number of, in this case, NaCl building blocks to achieve a complete rock salt unit cell and eventually a supercell. The advantage of this approach is that the overall model is either charge neutral or near neutral. Why this may be of interest in some cases will become clear when the charge model is dis-

cussed. Also, this approach is closely related to the approach often used in periodic boundary calculations. The disadvantage of SCe is that it can break essential bonds of structures with local symmetry elements.

The SCl approach preserves the coordination environment around a particular center and thus, preserves specific symmetry elements of the crystal within the QC. In the example shown, the octahedral environment around Na^+ is conserved. This can be advantageous when the point group of a center is of great importance, as is the case for several spectroscopic properties, or when the influence of the environment and local symmetry is to be studied. This type of structure can give some chemical intuition to the crystal, since many chemical ideas,e.g., ligand field theory, are based on local symmetry elements. The disadvantage is that these clusters are often highly charged. It is possible to make the inverse SCl models of those shown in Figure 3.8. Instead of $[NaCl_6]^{5-}$, the resulting cluster would be $[Na_6Cl]^{5+}$, and so on.

When carefully modeled, the SCe and SCl approaches produce the same results for most properties, but one approach may provide the answer faster than the other. Figure 3.9 shows the convergence of the HOMO-LUMO gap with increasing system size of NaCl for the SCe and SCl approaches.

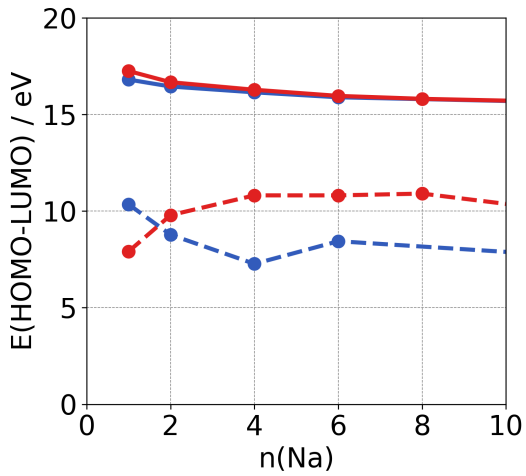

Figure 3.9: Convergence of the energy of the HOMO-LUMO gap for increasing SCe (red) and SCl (blue) NaCl clusters with (solid line) and without (dashed line) electrostatic embedding environment.

The SCe and SCl approaches give the same result for the HOMO-LUMO gap for relatively small system sizes with the same number of Na centers and converge to the same gap. However, in this case the SCe provides the answer for overall smaller cluster sizes because the total number of ions in the QC is lower. In addition, the

HOMO-LUMO gaps are shown for the two QC approaches without embedding. Their results are significantly lower, indicating a nanoparticle rather than bulk crystal character, and do not converge as uniformly as their embedded counterparts.

For various purposes, a "hybrid" QC can be advantageous, where a certain selection of atoms in the QC are computed at a selected level of theory, while Hartree-Fock (HF), a rather small basis set, and core potentials are used for the rest of the cluster and are therefore "cheap" to compute. Such a hybrid QC model can be useful in scenarios where the required QC is very large, or where a high level of theory is needed but only for a smaller set of atoms of interest. In addition, a "QC + HF" model can smooth the transition from the QC to the electrostatic environment by reducing interfacial effects and taking into account bonds on the surface of the QC, which may be of interest for more covalent systems.

Depending on the purpose, the HF cluster may look different and can be defined by selecting specific atoms or, in the case of Ionic-Crystal-QM/MM, also by layers. ORCA_CrystalPrep can predefine the HF structure. Figure 3.10 shows an example for NaCl with the corresponding input file formats for the "simple" and the Ionic-Crystal-QM/MM protocols. The QC has a SCl geometry, while the atoms calculated with HF extend the QC to a SCe structure. The advantage of this concept is that the entire QC (= QC + HF) is approximately charge neutral, while the property is calculated on a structure with a preserved point group.

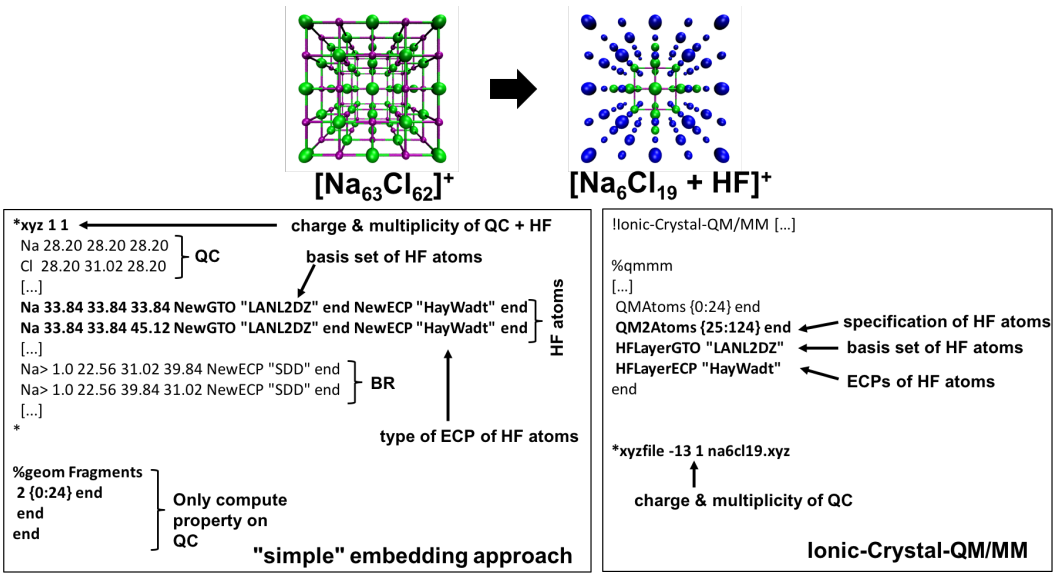

Figure 3.10: Construction of a "QC + HF" cluster model with $[Na_6Cl_{19}]^{13-}$ as the QC, extended to $[Na_{63}Cl_{62}]^+$ with HF layers, and corresponding ORCA input files for the "simple" embedding approach (left) and Ionic-Crystal-QM/MM (right). Color code: Part of QC treated with HF (blue).

Everything that has been and will be discussed for the NaCl example for the QC, Br and PC fields is applicable to other crystal structures. For BR and PC this is very straightforward. This is not necessarily the case for the QC. Therefore, two more examples are presented here.

The first example is the zinc blende structure, presented here for zinc sulfide (ZnS), which will be used frequently throughout this work. Figure 3.11 shows the series of SCe and SCl clusters. Due to the general zinc blende crystal structure, SCe clusters are not necessarily completely charge neutral. Apart from the differences in charge, geometry and cluster growth, they do not differ in handling from the rock salt structure. Therefore, no explanation other than the visual aid of Figure 3.11 is provided here.

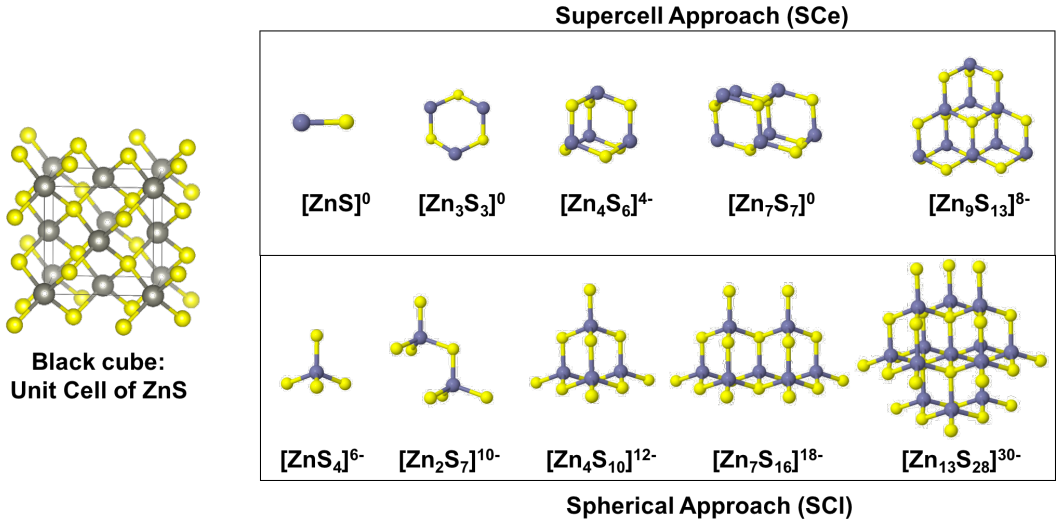

Figure 3.11: Different QC sizes for ZnS (zinc blende structure) for the supercell approach (SCe) and spherical cluster approach (SCl).

The second example is the cobalt oxide Co_3O_4, which crystallizes in the spinel structure. This system presents some new challenges. First, it consists of two different metal centers, Co(II) and Co(III), in a 1:2 ratio. Consequently, both must be present in the correct ratio in a general QC. Second, the QC must represent the two different environments of the two cobalt centers. Co(II) has a tetrahedral (T_d) environment ($[Co(II)O_4]^{6-}$), while Co(III) has a slightly distorted octahedral (D_{3d}) coordination ($[Co(III)O_6]^{9-}$). Third, the Co(II) centers couple antiferromagnetically, which will be a topic of Part IV. For now, it is only important to know that at least two Co(II) centers must be included in the QC model to capture the coupling, and consequently at least four Co(III) centers to maintain the ratio. However, if for some reason a property of the isolated Co(II) or Co(III) sites is of interest, smaller models

can be considered. Therefore, Figure 3.12 also shows smaller clusters in the series. The SCe approach is not considered.

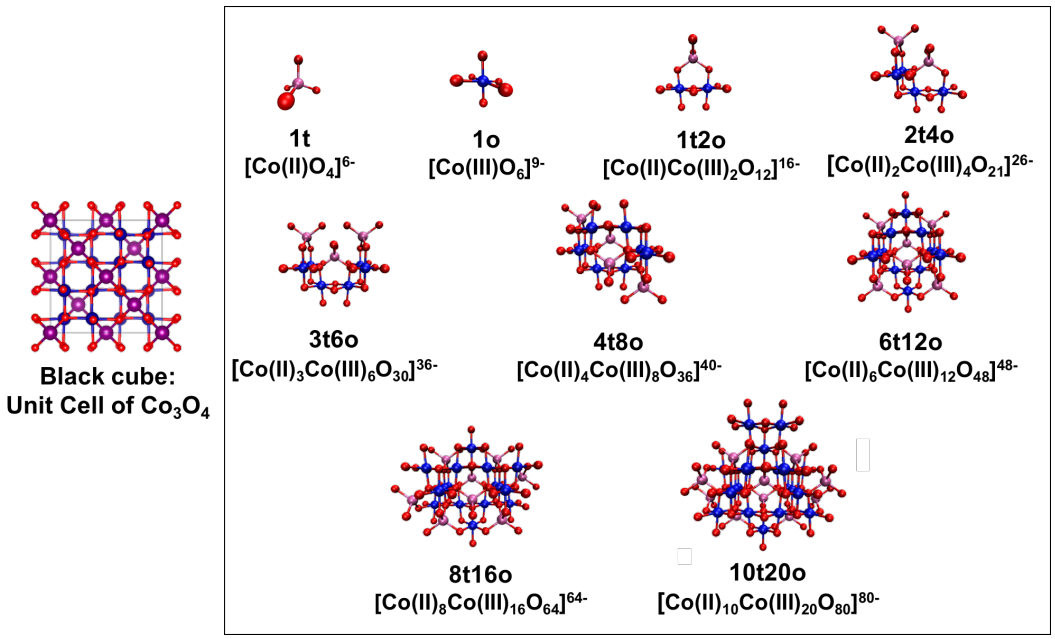

Figure 3.12: Different QC sizes for Co_3O_4 (spinel structure) for the spherical cluster approach (SCl). The abbreviation "t" stands for tetrahedral and represents a tetrahedral unit $[Co(II)O_4]^{6-}$ and the "o" stands for octahedral and represents a distorted octahedral unit $[Co(III)O_6]^{9-}$.

All QC structures presented can be generated either by using the ORCA_CrystalPrep tool or by manually building them from their respective supercells as explained in Section 3.1. The spacing between the atoms is based on experimental crystallographic data, but can be optimized if necessary. The purpose of the studies presented in this paper is to reproduce the experimental data as closely and accurately as possible. Therefore, no optimization is performed. This approach is sometimes used in periodic calculations for the same reason, e.g., in the work of Garza et al.[12].

3.2.2 The Role of the Boundary Region (BR)

In order to achieve a proper and efficient BR, the question of the purpose of the BR must first be addressed. The purpose is to address certain effects that are caused or not covered by the QC and PCs, so that the model achieves a crystalline character. As described, the BR treats neglected terms at the interface between the QC and PCs, such as the damping of dangling bonds. A side effect is the reduction of surface effects of the QC. In addition, the BR maintains the coordination sphere

around the surface ions and prevents artificial charge flow between the QC and PCs.

The BR in this work consists of class "SDD"[120–132], which are sufficient for all types of calculations performed. Table 3.1 gives an overview of all ECPs used for the different elements included in this work.

Table 3.1: Overview of ECPs of class SDD for all elements used in this work.

Element	Type of ECP	References
Li	ECP2SDF	[120, 125]
O, F	ECP2MWB	[129, 130]
Na, Mg	ECP10SDF	[120, 125, 127]
Al, S, Cl, K	ECP10MWB	[120, 123, 125, 129, 130]
Co, Cu, Zn	ECP10MDF	[124–126, 128, 131]
Ge, Se, Br	ECP28MWB	[121, 122, 129, 130, 132]

Any effects that the BR is intended to compensate can usually be considered short range unless the system is significantly delocalized. Thus, a BR of a few ECP layers is usually sufficient. Figure 3.13 shows different numbers of ECP layers automatically created by Ionic-Crystal-QM/MM for SCl and SCe NaCl clusters.

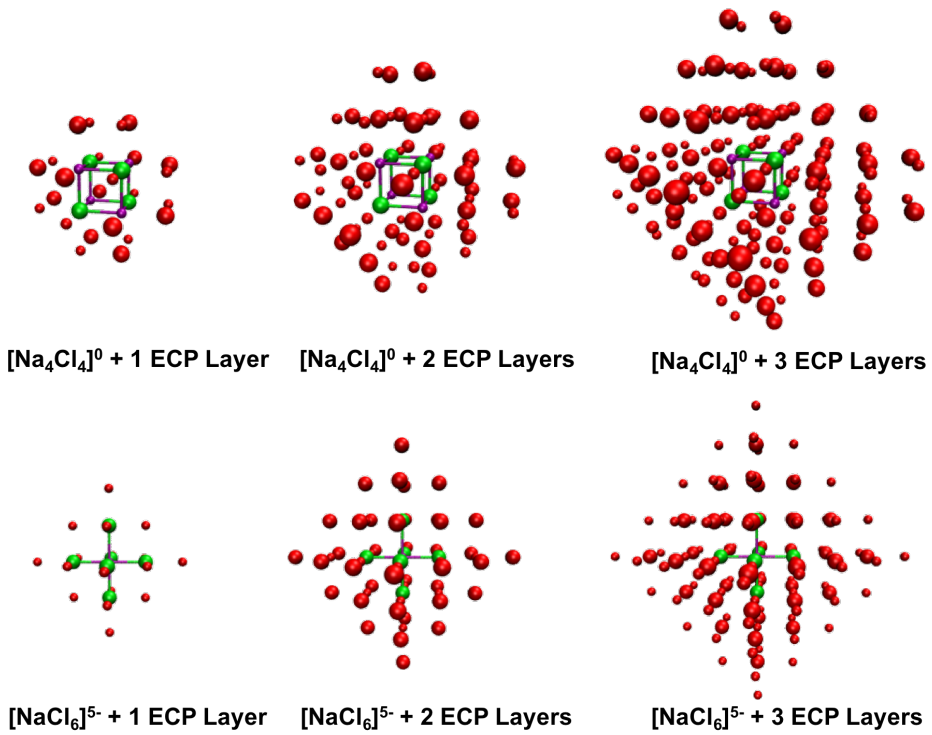

Figure 3.13: Different BR sizes defined by ECP layers around the QC examples $[Na_4Cl_4]^0$ and $[NaCl_6]^{5-}$.

In both approaches, the SCl and SCe approach, the ECPs create a complete set of direct neighbors of the atoms on the surface of the QC, preserving their coordination environment. This approach is equivalent to the construction of the SCl QC models.

Whether the size of the BR is sufficient depends on whether the addition of an extra layer of ECPs changes the properties of the QC. Therefore, if the energy of the QC remains the same when more ECPs are added to the BR, then the BR is considered to be converged. ECPs have only potential energy and no kinetic energy. Hence, the change in the total kinetic energy of the model is a reliable reference point for energy convergence. Also, effects such as charge flow can be observed more clearly in the kinetic energy. Figure 3.14 shows the convergence of the kinetic energy of the QC with increasing number of ECP layers for different cluster models, including the negatively charged $[NaCl_6]^{5-}$, the positively charged inverse $[Na_6Cl]^{5+}$, the larger and more negatively charged $[Na_6Cl_{19}]^{13-}$ system, and two neutral QCs of size $[Na_4Cl_4]^0$ and $[Na_{32}Cl_{32}]^0$.

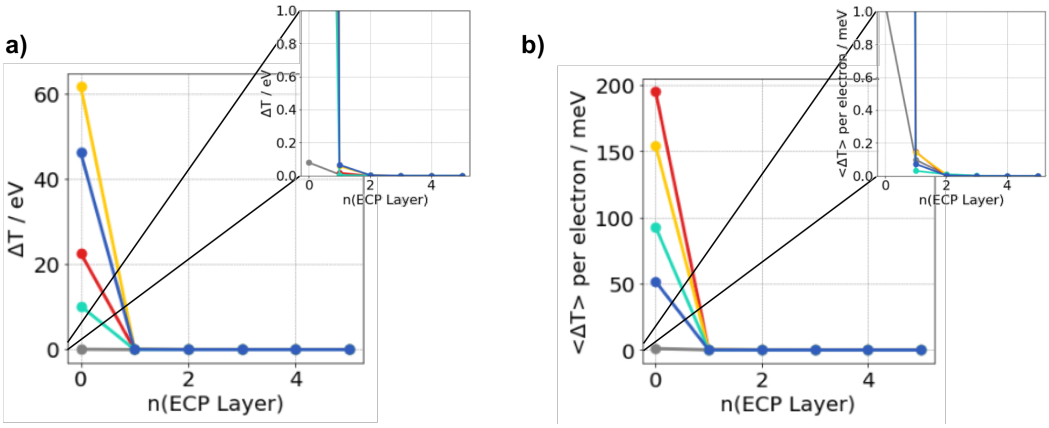

Figure 3.14: Change in kinetic energy T for **a)** the total system and **b)** average per electron with increasing number of ECP layers for the systems $[Na_4Cl_4]^0$ (turquoise), $[Na_{32}Cl_{32}]^0$ (blue), $[Na_6Cl]^{5+}$ (gray), $[NaCl_6]^{5-}$ (red), and $[Na_6Cl_{19}]^{13-}$ (yellow).

The kinetic energies of all tested systems converge after the introduction of two ECP layers. However, there are differences in the way they converge. For the larger QCs, the total change in kinetic energy caused by ECPs is higher than for the smaller ones (see Figure 3.14a), but the average change in kinetic energy per electron is lower (see Figure 3.14b). This is because the larger QCs have more electrons in total, but a smaller surface area to volume ratio, leading to fewer interactions with the electrostatic environment.

The negatively charged $[NaCl_6]^{5-}$ cluster experiences the largest average change in kinetic energy per electron, while its positively charged counterpart $[Na_6Cl]^{5+}$ experiences the smallest. This is explained by the ionic interaction between Na^+

and Cl^- being directed from HOMO Cl $3p$ to LUMO Na $3s$. In $[NaCl_6]^{5-}$ the Cl $3p$ orbitals are in close proximity to the electrostatic environment with the Cl^- localized on the surface of the QC, while in $[Na_6Cl]^{5+}$ they are in the center of the system. Due to the charge donor nature of the Cl $3p$ orbitals, $[Na_6Cl]^{5+}$ is more susceptible to surface effects, charge flow from the QC to the PC field, and thus more dependent on the BR with respect to the total energy of the QC.

This observation may lead to the erroneous conclusion that the ECP layers are more important for negatively charged clusters. However, a similarly large BR is also crucial for positively charged systems, as shown in Figure 3.15. The convergence of the HOMO-LUMO gap, HOMO, and LUMO is shown for the different NaCl clusters, showing that the LUMO undergoes even more significant changes than the HOMO with the introduction of the first and second ECP layers, and still changes slightly up to the third layer. The reason for this is that the LUMO generally has a more delocalized character than the HOMO, which makes it more susceptible to the electrostatic environment when placed in close proximity. The LUMO character can be directly related to the band picture discussed in Section 2 (see also Figure 2.7, page 21). The valence band corresponding to the LUMO was found to be more dispersed than the conduction band corresponding to the HOMO.

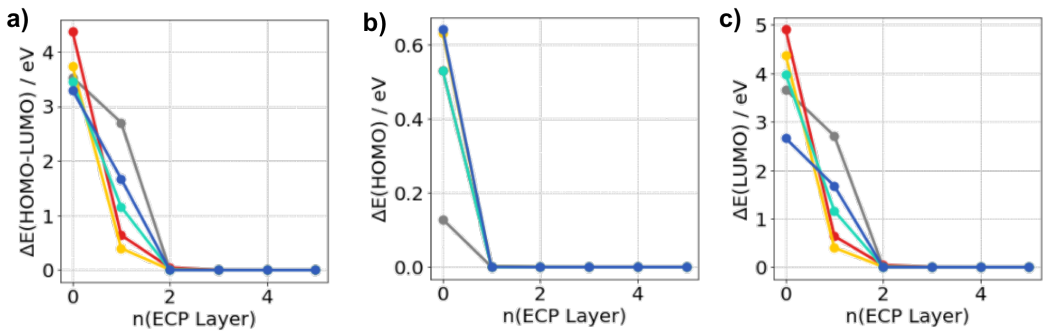

Figure 3.15: Energy change of **a)** the HOMO-LUMO gap, **b)** the HOMO, and **c)** the LUMO with increasing number of ECP layers for systems $[Na_4Cl_4]^0$ (turquoise), $[Na_{32}Cl_{32}]^0$ (blue), $[Na_6Cl]^{5+}$ (gray), $[NaCl_6]^{5-}$ (red), and $[Na_6Cl_{19}]^{13-}$ (yellow).

NaCl is highly ionic. Therefore, its orbitals tend to be localized with the result that the total energy of the QC and that of the orbitals converge after two ECP layers. The default setting for the BR in Ionic-Crystal-QM/MMM, as shown in Figure 3.7 on page 36, is three ECP layers, with the third layer as a safety measure. However, this setting may need to be adjusted for more covalent or even strongly ionic systems to achieve a converged virtual orbital space. Stable virtual orbitals are particularly important for the calculation of excited state properties.

In summary, the optimal size of the BR may depend on the size and charge of

the QC, the specific property being calculated, and the type of crystal.

3.2.3 The Quest for the "Best" Charge Model

In this subsection, the three most important aspects of the PC field are examined in the following order: accounting for long-range electrostatic effects, ensuring homogeneous charge distribution, and neutralizing the charge of the entire model.

a) Electrostatic Long-Range Effects

Section 2.1 stated that each lattice point in a crystal representing a bulk atom must be surrounded by about 7,500 lattice points in order to account for long-range effects by correctly reproducing the Madelung constant. Applying this to the NaCl model, each atom in the QC must be in the center of a volume consisting of at least 7,500 points located in either the QC, the BR, or the PC field. Since the QC has a fixed size and ECPs are much more computationally expensive than PCs, most of these points are assigned to the PC field. To achieve the most efficient model size, the QC should be positioned in the center of the electrostatic embedding model.

The requirement for a certain number of lattice points surrounding each atom in the QC implies that larger QCs require a larger PC field. In Figure 3.16, the QC sizes of $[Na_4Cl_4]^0$ and $[Na_{32}Cl_{32}]^0$ are compared by observing the convergence of the total potential energy of the QC as the number of lattice points increases. The choice of potential energy as the convergence criterion is due to the short-range convergence of kinetic energy within the BR. Long-range electrostatic effects, discussed in Section 2.1, are exclusively characterized by potential energy (Coulomb). The plot starts with more lattice points than the QC and BR to specifically evaluate the effect of an increasing number of PCs.

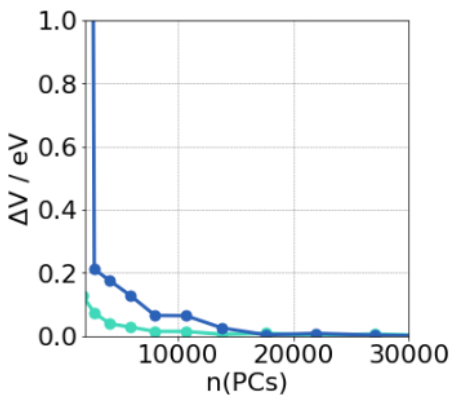

Figure 3.16: Change in potential energy V with increasing number of lattice points for $[Na_4Cl_4]^0$ (turquoise) and $[Na_{32}Cl_{32}]^0$ (blue).

About 10,000 points are sufficient for $[[Na_4Cl_4]^0$, while $[Na_{32}Cl_{32}]^0$ requires approximately 15,000 points to converge the potential energy. As the QC size increases, the total embedding size must increase accordingly. The data show that the long-range effect of the PC field on the total potential energy of the system is less than 1 eV. Nevertheless, a proper model should correctly capture this effect as well.

b) Homogeneous Charge Distribution

Each PC and ECP must represent the charge of the ion it replaces in the crystal lattice. Although the formal charge of these ions can be a reasonable estimate, especially for strongly ionic systems, which include many inorganic crystals, this may not be the best model. An approach to charge optimization and why this may be important is described below.

In the NaCl example, the cations and anions have opposite charges of equal magnitude. Therefore, any electrostatic interaction between neighboring ions is equal, and the charge distribution is homogeneous throughout the bulk of the crystal. Figure 3.17 shows for $[Na_{32}Cl_{32}]^0$ that the charge distribution within the QC is homogeneous only if the ECPs and PCs match the "ideal" charge of the ions in the QC.

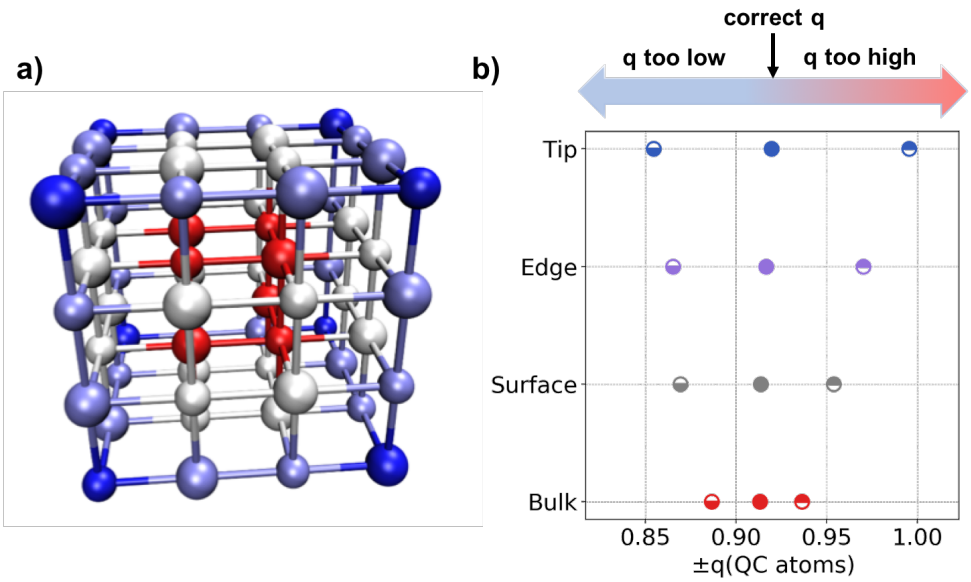

Figure 3.17: a) Color code of the different atomic positions in a QC for the example of $[Na_{32}Cl_{32}]^0$ in the rock salt structure showing the tip (blue), edge (purple), surface (gray), and bulk (red). **b)** Charge distribution within the QC $[Na_{32}Cl_{32}]^0$ when the applied charge of ECPs and PCs is too low (±0.6, circle with filled bottom), matches the charges of the QC (±0.92, filled circle), and is too high (±1.2, circle with filled top). Charges calculated with CHELPG. Level of theory: PBE/def2-tzvp.

If the applied are less than the "ideal" charges, the QC is polarized. Charge is "pulled" out of the QC. The charge in the "bulk" positions of the QC will be higher compared to the deviating positions, resulting in a lower average total charge than desired. Conversely, applying higher charges than the "ideal" ones "pushes" charge into the QC, creating the opposite effect. The electrostatic embedding approach aims to model a QC that has bulk properties at each position within the QC. The "bulk", "surface", "edge", and "tip" positions defined in Figure 3.17a are used only to help distinguish between the different atomic sites. Only the "ideal" case, where all positions have matching charges, is a valid model from an electrostatic perspective. The other cases in Figure 3.17b have nanoparticle or defect characteristics.

The effects of inhomogeneous charge distribution can be minimized by placing the QC in the center of the model, since any charge imbalance within the QC will not polarize the entire model in this way. While this may eliminate or reduce a potential error, it does not completely solve the problem. Therefore, the charges must be optimized, which is a more difficult task since charges are not observable quantities. While different methods define charges differently, e.g., based on the orbitals (e.g. Mulliken[99, 133, 134] and Loewdin[135, 136] charges), the electrostatic potential (e.g. CHELPG[137]), or the density (e.g., Hirshfeld charges[138]), there is no physically correct charge model. Table 3.2 gives the details for the four named charge examples.

All charge models have advantages and disadvantages and are suitable for different tasks. In the electrostatic embedding model, the requirement for the charges is to produce the electrostatic potential of the crystal as accurately as possible. Thus, by definition, the CHELPG charges are the most reasonable charges. In addition, the charges should be robust to changes in the model and the level of theory applied.

Table 3.2: Overview of four different definitions of atomic charges (q) for atom A.

Type of charge	Definition	Explanation
Mulliken charges[99, 133, 134]	$q_A = Z_A - \sum_{\mu \varepsilon A}(PS)_{\mu\mu}$ Z_A: core charge atom A; P: density matrix; S: overlap matrix; μ: atomic basis[139]	Sum of electronic charge of orbitals centered on A; electronic overlap between two atoms divided equally between them[140]
Loewdin charges[135, 136]	$q_A = Z_A - \sum_{\mu \varepsilon A}(S^{1/2}PS^{1/2})_{\mu\mu}$ [139]	As Mulliken charge but with symmetric transformation of orbitals (orthogonal basis): eliminates problem of overlap partition[140]
CHELPG[137] (charges from electrostatic potential using grid-based method)	$V_A = \sum \frac{q_B}{R_{AB}}$ V_A: electrostatic pot. A R_{AB}: distance between A and B[141]	Atomic charges fitted to reproduce electrostatic potential on grid around QC[140]
Hirshfeld charges[138]	$q_A = Z_A - \int \frac{\rho_A^0(r)}{\sum_B \rho_B^0(r)} \rho(r) dr$ $\rho_B^0(r)$: density of atom B; $\rho(r)$: density of QC; r: cartesian coordinates	Charge of A obtained by integrating density over its volume[140]

Figure 3.18a examines the dependence of the different charges on the basis set size for the basis set types def-XVP[142, 143] and cc-pVXZ[144] for the example cluster $[Na_4Cl_4]^0$. CHELPG and Hirshfeld charges converge for triple-ζ basis sets (def2-TZVP and cc-pVTZ), while Loewdin and Mulliken charges show no obvious convergence scheme. The strong basis set dependence of the latter two cases is in agreement with the literature[136, 140, 145, 146].

Figure 3.18b shows the dependence of the charges on the applied method. The charges computed by DFT show increasing magnitude with respect to the Jacobs' ladder of functionals, and DLPNO-CCSD and HF have even higher charges. As for the basis sets, the CHELPG and Hirshfeld charges show the least change with respect to the method.

Overall, the Hirshfeld and CHELPG charges are significantly more robust to the level of theory used than the Loewdin and Mulliken charges. However, the Hirshfeld charges have about half the magnitude of the CHELPG charges. Considering that the studied system NaCl is strongly ionic, the prediction with CHELPG seems to be a better fit. This is also the case for other inorganic crystals. Thus, not only by definition, but also considering the presented factors, CHELPG is the most suit-

able charge model for this electrostatic embedding approach and will be used for the subsequent charge optimization.

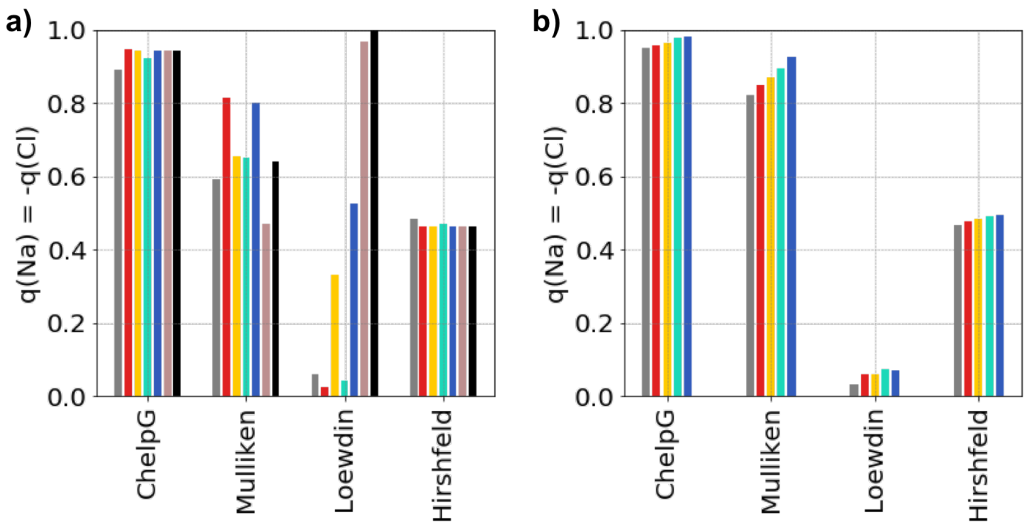

Figure 3.18: Dependence of CHELPG, Mulliken, Loewdin, and Hirshfeld charges on **a)** the basis set size (method: PBE); Color code: def2-SVP (gray), def2-TZVP (red), def2-QZVPP (yellow), cc-pVDZ (turquoise), cc-pVTZ (blue), cc-pVQZ (brown), cc-pV5Z (black) and **b)** the level of theory (basis set: def-TZVP); Color code: average GGA (gray), average hybrid functional (red), double-hybrid functional B2PLYP (yellow), DLPNO-CCSD (turquoise), Hartree-Fock (blue); Cluster example: $[Na_4Cl_4]^0$. The specific GGA and hybrid functionals and there calculated charges can be found in Figure A.4 on page 313 in the appendix.

Section 3.1 introduces the optimization of charges with an iteration by varying the magnitude of the applied charges and calculating the resulting CHELPG charge of the QC until an overall homogeneous charge distribution within the model is achieved. In the Ionic-Crystal-QM/MM method, these iterations are automated. However, for the "simple" embedding approach, the variation process may involve several calculations. Figure 3.19 shows the relationship between the applied charges on the ECP and PCs and the corresponding calculated CHELPG charges of the QC through a linear regression for the example $[Na_{32}Cl_{32}]^0$. By identifying the point of intersection on the linear regression where the predicted charge of the QC matches the applied PCs, the optimal charge for the model can be found. For the present system and level of theory (PBE/def2-TZVP), the optimized charge is about ± 0.92. The result is consistent with Figure 3.17, which shows that the charge distribution in the QC is indeed homogeneous at this point. Ionic-Crystal-QM/MM achieves the same result with the implemented iterative process.

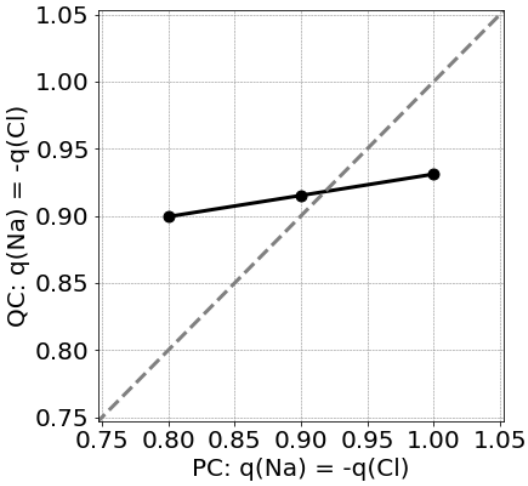

Figure 3.19: Linear regression of the applied charges vs. the average charges in the QC to find the point where the applied and QC charges match for the example $[Na_{32}Cl_{32}]^0$. Level of theory: PBE/def2-TZVP.

The charge depends not only on the level of theory, but also on the size of the QC. Figure 3.20 shows the convergence with system size for the NaCl series of QC type SCe (visualization of the different QC sizes: see Figure 3.8, page 40). For consistency along a cluster series, it may be advisable to optimize the charge for a larger cluster size and apply it to the smaller ones.

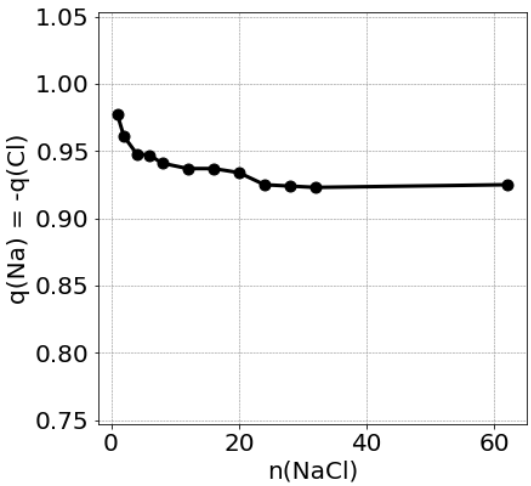

Figure 3.20: Convergence of the optimized charge with cluster size for a series of electrostatically embedded NaCl QCs in the SCe approach. Level of theory: PBE/def2-TZVP.

Up to this point, only neutral SCe clusters have been analyzed. However, charged clusters, such as SCl-type QCs, present an additional challenge. Figure 3.21 illustrates how the QC $[Na_6Cl_{19}]^{13-}$ "traps" its formal charge inside itself, resulting in the conservation of a total formal charge of -13 by assigning unrealistic charges to the atoms. This formal charge problem is common to all charge methods, since the sum of the atomic charges always equals the total formal charge of the QC. In this case, the charge optimization results are inadequate because the calculated charge for Na is much lower than that of Cl, while an equal magnitude was expected for both. One solution to achieve a uniform charge distribution despite a charged cluster is to add an HF layer to completely neutralize the QC. Figure 3.21 shows that this method gives a reasonable charge distribution.

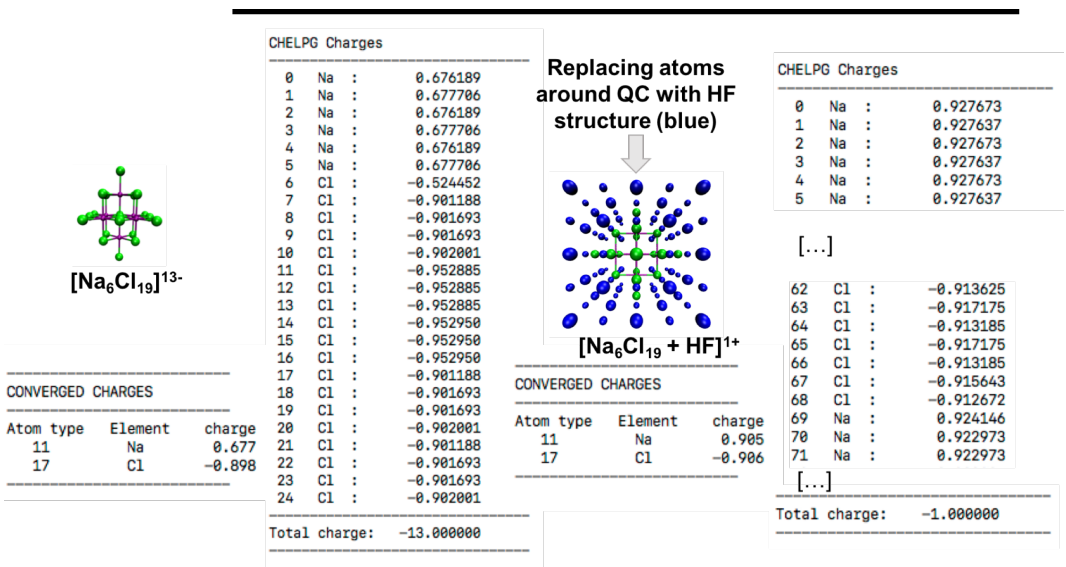

Figure 3.21: Comparison of the optimized charges for the electrostatically embedded QC $[Na_6Cl_{19}]^{13-}$ with and without HF layers. Level of theory: PBE/def2-tzvp + HF/LANL2DZ. Color Code: HF atoms (blue).

In summary, the CHELPG method is the most promising approach for calculating reasonable charges in the electrostatic embedding model because it is based on the definition of the electrostatic potential that the electrostatic embedding approach aims to mimic for the crystal, and because it depends little on the level of theory. The basis set of the charge model should be at least triple-ζ in size. Since Hartree-Fock theory often overestimates the ionic character of a bond and therefore may overestimate the atomic charges, it is reasonable to use DFT for charge prediction. In this case, DFT is preferable to DLPNO-CCSD because the latter yields CHELPG charges similar to Hartree-Fock. To achieve a homogeneous charge distribution, a nearly neutral cluster gives the most reliable optimization result. The calculated charge

depends on the cluster size, so it may be useful to calculate the charge for a larger cluster and apply the result to all cluster sizes in a series for consistency.

Despite the extensive discussion of charge optimization, in many cases the actual charge applied has no significant effect on the property. This is true even when the QC is charged and no HF layer is applied. As an example, Figure 3.22 shows the dependence of the HOMO-LUMO gap of $[Na_{32}Cl_{32}]^0$ on the applied charge. The gap changes by only a few meV when the applied charge varies by a magnitude of 0.2. The influence of charge must be evaluated on a case-by-case basis. It must always be remembered that charges are not observables, and ultimately there is "never a correct charge".

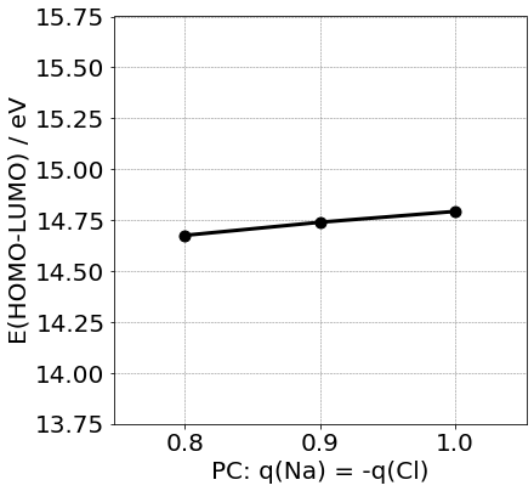

Figure 3.22: Dependence of the HOMO-LUMO gap of $[Na_{32}Cl_{32}]^0$ on different applied charges. Level of theory: HF/def2-tzvp.

c) The Neutralization of the Total Charge

Regardless of the size of the system or the magnitude of the local charges, a crystalline solid-state system is expected to be charge neutral overall. Consequently, the electrostatic embedding approach must fully satisfy the requirement in Equation 3.1.

$$Q_{total} = Q_{QC} + Q_{BR} + Q_{PC} = 0 \tag{3.1}$$

Q_X is the charge of the different regions X (= QC, BR, PC), where Q_{total} is the total charge of the model. It may happen that in a constructed model the total charge is not zero, either because the formal charge of the QC combined with the optimized charges does not add up to zero, or because the total number of cation and anion

lattice points is not equal. The latter is often the case due to the expansion of unit cells into supercells. It is not a good idea to simply delete PCs to balance the total number of positive and negative charges. This creates defects that can cause errors. One approach to balancing the charges is to calculate the total charge Q_{total} of the system and balance it by adding a value $-Q_{total}/n$ to each PC, where n is the total number of PCs. If Q_{total} is large and/or the total model is small, this can significantly disturb the homogeneous character of the PC field and cause another error. A better solution would be to neutralize the charge Q_{total} only in the outer layer(s) of the PC field, so that the effect on the QC is not noticeable. As mentioned in Section 3.1, this is automated in the Ionic-Crystal-QM/MM utility.

4 Limits and Possibilities of the Electrostatic Embedding Approach

While the previous two chapters have introduced the concepts of the electrostatic embedding approach to modeling crystals and outlined specific protocols, the question remains as to why this approach should be used, given the existence of numerous well-established periodic boundary methods for modeling such systems. This final chapter of Part I aims to highlight the advantages, disadvantages, and limitations of the electrostatic embedding approach both in general and in comparison to periodic methods. Various aspects such as band structure, crystal types, basis sets, and computational methods are briefly discussed. An overview of these topics provides insight into when the electrostatic embedding approach is reasonable to use, thereby emphasizing its relevance to the questions addressed in this thesis.

Band Structure

A drawback of the electrostatic embedding approach is that a true continuous band structure is never achieved, only an approximation. While this can be a problem for some property calculations, many properties are already well described based on the approximated band structure. Often the correct position of the bands, as achieved by the electrostatic embedding approach, is more important than their actual energy continuum. Whether this approach is sufficient depends on the crystal and its properties. An example where this approach is sufficient is a localized excited state.

It should be noted that the actual band in a solid state system is not really continuous either. It consists of quantized energy states that are very close together ($\sim 10^{-22} eV$), so it appears to be discontinuous.[71, 82] Also, a band calculated by periodic approaches is not initially continuous. Instead of integrating over the entire k-space with an (impossible) infinite number of k-points, leading to a truly continuous band, it is summed over a discrete number of k-points. Wavefunctions at points close together in k-space are nearly identical and can be represented by a single

point. Each discrete value is multiplied by a weighting factor to "mimic" continuous space. The more k-points used, the smaller the error. The model must be converged with respect to these points. Usually between ten and one hundred k-points are sufficient.[147] This strategy results in a denser but still artificial band than the electrostatic embedding approach, and may be advantageous for certain types of crystals and properties.

Types of Crystals

The explained approach of electrostatic embedding is limited with respect to the different types of crystals. One possible categorization of crystals is into metallic, covalent, ionic, and molecular crystals.

Metals are typically described in terms of the nearly free electron model.[103] The valence electrons are assumed to move freely and delocalized through the crystal. They are determined only by the lattice formed by the nuclei and core electrons.[100] Gaussian basis functions are generally less suitable to describe the electrons for these systems[73], and plane wavefunctions are not available for the electrostatic embedding approach. Furthermore, no reasonable QC size can capture such delocalization. Consequently, the described electrostatic embedding approach cannot model metals.

The spectrum of ionic to covalent crystals ranges from systems such as the rock salt structure discussed (e.g., NaCl) to structures such as diamond, with no system being purely ionic or covalent. As examined, the electrostatic embedding approach is favorable for more ionic systems due to the replication of the electrostatic potential. In ionic systems, the delocalization of the valence electrons is small. Thus, the valence band can be modeled with fewer valence orbitals, allowing for a defined size of the QC. Also, in these systems, breaking ionic bonds at the interface between the QC and the electrostatic environment may not have a critical effect on the property calculations because the electrostatic environment mimics the ionic part of the bond reasonably well. By defining a proper BR, the interfacial effects can be further minimized as discussed in Subsection 3.2.2.

This may be different for more covalent systems, resulting in the need for potentially larger QC sizes to adequately incorporate more bonds and to compensate for the errors that may arise from bond breaking at the interface between the QC and the electrostatic environment. Therefore, the electrostatic embedding approach reaches its limits in strongly covalent systems such as the diamond structure mentioned above. In this example, this is not only due to the bond character, but also because the charges for the ECPs and PCs cannot be unambiguously defined, since carbon is

the only atom type in the crystal. However, for most inorganic crystals containing at least two types of atoms that can be categorized as having a more anionic and a more cationic character, this approach should be sufficient. The previously mentioned examples of zinc blende and spinel structures have a higher covalent fraction than the rock salt structure discussed, but are all still ionic enough to be treated with the electrostatic embedding approach.

The molecular crystal consists of molecules at the lattice points of the crystal held together by relatively weak intermolecular forces. The "Ionic-Crystal-QM/MM" embedding approach is inappropriate for such a system. Since ORCA 5.0, an equivalent approach, "Mol-Crystal-QM/MM", is available for molecular crystals.

Models of Crystal Structures

For bulk properties, periodic calculations are typically limited to unit cell or supercell structures. Electrostatically embedded cluster models provide an alternative view of the crystal by considering the crystal structure not only from the unit cell or supercell perspective, but also with additional flexible cluster approaches. One possibility is to model the crystal structure using the spherical cluster approach (see Section 3.2). This method provides a chemical intuition of the crystal structure by focusing on the point groups and "ligand field" environment of specific (metal) centers within the crystal. This can be useful for studying spectroscopic properties and other applications.

An example of the possibilities offered by the more flexible cluster approach is to select only certain atomic sites of the crystal and study their contribution or influence on the overall electronic structure or its isolated properties. For example, in Section 3.2 the example of Co_3O_4 was mentioned, where this approach allows the study of the isolated distorted octahedral Co(III) or the isolated tetrahedral Co(II) site of the crystal using the appropriate QCs.

Although the electrostatic embedding approach offers more freedom in terms of crystal structure models, it often also requires a better understanding of the crystal structure and a more careful modeling process compared to a simple supercell model with periodic boundary conditions. It is necessary to converge the QC to a property, which can be challenging, and it is important to avoid breaking important symmetries or using QCs that do not accurately represent the crystal or the calculated property in other ways to avoid inaccurate results.

Basis Sets

The choice of basis set plays a vital role in the success of a property calculation. The differences, advantages, and disadvantages of basis sets in periodic and non-periodic calculations are briefly discussed to clarify why the basis sets used for non-periodic calculations are more feasible for the problems studied in this thesis.

The main difference between basis sets in periodic and electrostatic embedding calculations is that the basis functions must satisfy the Bloch theorem for the prior.[103] For periodic calculations, plane wavefunctions are commonly used, but Gaussian basis functions (tight-binding approach) are also feasible.[73, 101, 103, 148, 149] Plane wavefunctions are not applicable to the presented electrostatic embedding approach. Instead, all molecular basis sets can be used, including the most frequently used Gaussian basis sets. This is an advantage of the electrostatic embedding approach because there is a greater variety of basis sets for molecular calculations and several standardized, established basis set libraries that are not generally available for periodic calculations,[73, 150, 151] despite recent attempts.[152–154]

One benefit of standardization is that it makes it easier to approach the basis set limits. Protocols for using basis sets of a particular class with increasing size[144, 155] and for basis set extrapolation schemes[156] are well established for molecules, which is not yet routinely applicable to periodic calculations with Gaussian basis sets. [73] In general, a basis set close to basis set completeness is necessary to achieve chemical accuracy.[156] However, despite extrapolation routines, Gaussian basis sets for polyatomic periodic and non-periodic calculations are always incomplete due to their finite number of basis functions (basis set truncation error)[73, 157]. Furthermore, the approach to the basis set limit is often not systematic. For plane wavefunctions, the basis set limit, and hence, the accuracy, depends only on the kinetic energy cutoff parameter. Thus, the basis set size can be systematically improved and converges smoothly and monotonically.[73, 158–160]

Furthermore, for Gaussian basis sets in (non-)periodic solids and medium to large molecules, a linear dependence for large basis sets and basis set overcompleteness can be a problem, which is not present for plane wavefunctions. [73, 159, 161–163] Plane wavefunctions are computationally simpler and orthonormal in contrast to Gaussian basis functions.[164] In addition, plane wavefunctions are independent of atomic species and positions.[73, 147] The atomic position dependence of Gaussian basis functions can lead to basis set superposition errors (BSSE).[147, 157, 163]

However, plane wavefunctions have disadvantages, especially for the problems studied in the following chapters. For example, the aforementioned independence of plane wavefunctions from atomic positions can be a drawback. Gaussian basis

sets preserve chemical intuition due to their atom-centered view, which can simplify the interpretation of results.[73] On the one hand, this is probably not useful for most metallic crystals since a non-local wavefunction best describes their valence electrons. On the other hand, focusing on inorganic crystals with their predominantly ionic character, Gaussian basis functions may better describe the behavior since the valence electrons are reasonably localized on the respective ions.

Further, core electrons are generally localized and described better and more cost-effectively by Gaussian basis functions. For Gaussian basis sets, the position of the electron within a system has little effect on the number of basis functions needed to describe the electron in question. Plane wavefunctions best describe free valence electrons.[103] Adequately modeling the behavior of core or tightly bound electrons requires a large number of plane wavefunctions.[73, 147] The computational cost increases significantly,[73] which typically leads to the replacement of core electrons with pseudopotentials in plane wave calculations.[147] Thus, most of these calculations are frozen-core calculations, which may be a good approximation for many problems. However, this is not true for many spectroscopic calculations, especially core electron spectroscopy.

Several computational routines and methods for molecular calculations are not available for plane wavefunction basis sets. Many of these techniques can be transferred to periodic calculations with Gaussian basis sets[73] and are directly applicable to the electrostatic embedding approach.

One difficulty that arises when using the molecular basis sets in combination with the electrostatic embedding approach is that the basis sets are not optimized for solid-state systems. When calculating the electronic structure of molecules, the electronic density must exhibit an asymptotic exponential decay at the surface of the molecule.[73] Consequently, by directly transferring the basis sets to the electrostatic embedding approach, the basis functions at the interface between the QC and the electrostatic environment may be incorrectly described and exhibit similar asymptotic behavior. The correct behavior of any supposedly identical position within the QC representative of the bulk would be to exhibit an identical basis set description, which may not be given at different positions within the QC. Although the ECPs mitigate the erroneous behavior at the interface between the QC and the electrostatic embedding, the introduced error is not zero. Periodic boundary calculations combined with Gaussian basis sets do not exhibit the problem because the basis sets are periodic without asymptotic decay at the edge of each unit cell.

The electron density decay in molecules is often described by diffuse basis functions, which are often not considered necessary for non-molecular solids.[73] The inaccurate description of solids can be reduced by not including these functions.

In conclusion, Gaussian basis sets are a better compromise than plane wavefunctions for the problems addressed in this work, because they better describe the valence electrons in inorganic crystals with high ionic tendencies and core electrons in general. The latter is especially important for the upcoming XES and NMR spectroscopy studies. The combination of Gaussian basis sets with the electrostatic embedding approach is more suitable than periodic boundary conditions for this work, as there are more specialized classes of basis sets available for molecular calculations. The Gaussian basis set boundary is also easier and more systematic to approach than in periodic calculations, which is important for the overall accuracy of the results.

Methods

Several state-of-the-art methods for calculating electronic structures and advanced properties, including sophisticated descriptions of spectroscopic properties, are not currently available for periodic boundary codes. The electrostatic embedding approach makes this suite of methods available for solid-state systems that are otherwise only available for molecules.

The methods used in periodic boundary calculations often reach their limits in DFT using LDA and (meta-)GGA functionals. Hybrid functionals are less commonly employed because the inclusion of exact HF exchange leads to a steep increase in computational time.[73] A gain in computational cost for molecular systems, and thus, for embedded cluster models, is also observed, but it is nowhere near as large as for the periodic equivalent.

While DFT is a valuable tool and successfully calculates band structures, especially for metals, its results are generally not chemically accurate. Errors such as the self-interaction error and the inaccuracy introduced by exchange correlation approximations can lead to inaccurate results for both ground and excited state calculations.[165, 166] For many calculations, especially spectroscopic property calculations, a more accurate description of the electron correlation and traceable sources of error are essential.

CCSD(T) is usually considered the gold standard for chemical accuracy.[10, 23] A few coupled-cluster (CC) and generally wavefunction-based methods are available for periodic boundary codes,[24, 26, 27] but, as in the case of DFT, they are generally not as efficient as for molecular calculations. In general, CC methods have a steep scaling factor with increasing system size and are often only suitable for smaller molecules. Therefore, larger QCs are difficult to handle even with these methods. The availability of DLPNO-CCSD(T), which has a linear scaling factor with respect

to system size at an accuracy comparable to CCSD(T),[167, 168] makes the electrostatic embedding approach an attractive candidate for crystal calculations at the CC level.

In addition, the availability of the HF layer implementation provides the opportunity to describe part of the crystal using an expensive method together with a large basis set, while the rest of the system can be modeled at the HF level using a smaller basis set. This, together with active-space methods such as CASSCF,[169–171] provides the opportunity to apply multiconfiguration and multireference methods to electrostatically embedded systems. Recent developments such as ICE-CI[64, 65] can also be applied to these clusters, opening up the possibility of mapping even larger portions of the crystal with high precision.

The availability of multireference methods is particularly important for highly correlated materials, such as many crystals containing transition metal centers.[172] While periodic boundary calculations are commonly used for highly correlated materials by using an external potential (DFT+U) to address the correlated character,[11] this method is known to artificially distort the band structure.[173] The application of multireference methods to such materials can avoid this problem. At the same time, multireference methods can better describe these systems, since the high correlation typically requires a description of ground and excited states beyond single-reference.[172] Thus, these methods open the door to additional perspectives on this class of materials.

The protocols developed in this work for various spectroscopic properties benefit from the wide variety of methods available in molecular codes. Only a few of them are mentioned here. The following Part II provides an overview of the methods used in the subsequent ground state and excited state calculation protocols. This diversity of methods is the main reason why the electrostatic embedding approach is preferred to the periodic boundary approach in this work. While future developments are underway for similarly accurate methods for periodic codes, they are currently limited and insufficient to satisfactorily answer many of the questions addressed in the following chapters.

Part II

Computational Spectroscopy: From Ground to Excited States

Nothing in life is to be feared, it is only to be understood. – Marie Curie

Introduction to Part II

Spectroscopy is a widely used tool for studying various properties of matter. It allows the non-invasive analysis of molecules and solids in different environments and conditions with respect to their structure, properties or dynamics. Different regions of the electromagnetic spectrum are used by various spectroscopic methods to provide a comprehensive picture of the system under investigation. However, the spectra produced are often complex and difficult to understand, and often require extensive computational study.[174]

Computational spectroscopy is a specialized branch of computational chemistry that has become a field in its own right. It uses theoretical models and software tools to predict, analyze, interpret, and understand spectroscopic features, properties, and phenomena. These computational models provide valuable insight into the chemical system under study, particularly in terms of its electronic structure, and complement the information obtained from pure experimental data. The computational spectroscopic models can serve as a bridge between the experiment and the underlying physical properties, providing the theoretical expressions that link the measured observables and the molecular properties.[174, 175]

The combination of experimental data and theoretical models provides a guided understanding of electronic structure and can identify which structural features contribute to specific spectroscopic properties. This knowledge of electronic structure and how it is reflected in experimental spectra can provide insight into entire categories of compounds rather than just individual molecules.

Experimental spectroscopy and computational spectroscopy can serve as benchmarks for each other. Experimental spectroscopy is highly sensitive to the electronic structure of a system, making it an excellent tool for testing the reliability and accuracy of theoretical models and predictions, and for validating quantum chemical calculations and methods.[174]

At the time of this work, many high-accuracy computational protocols are available only in molecular rather than periodic computer codes, and are, therefore, typically applicable only to discrete molecules. As discussed in the previous part, the electrostatic embedding approach offers the possibility to transfer these methods to

solid-state systems.

The purpose of this part is to introduce the theoretical concepts and computational methods used to study the spectroscopic properties presented in this thesis. The information provided is brief and mainly conceptual, as more detailed descriptions can be found elsewhere. The first chapter, starting on page 68, provides an introduction to spectroscopy and its translation into quantum mechanics. Ground state methods form the basis of most computational spectroscopic methods for the calculation of excited states. Therefore, the second chapter, starting on page 72, gives an overview of the ground state methods used. The following two chapters explain the respective spectroscopic methods and concepts relevant for the upcoming studies, with a focus on NMR spectroscopy, starting on page 87, and electronic spectroscopy, starting on page 90. The latter focuses on the determination of (opticalv) band gaps from UV/Vis spectra and on X-ray emission spectroscopy (XES).

5 A Quick Introduction to Spectroscopy

In spectroscopy, the interaction of electromagnetic radiation with matter is studied. The interaction leads to the transition of a system from one state to another and can be explained by the basic principles of quantum mechanics.[176, 177] The first necessary principle is the wave-particle duality, which states that a wave can behave like a particle, and a particle can behave like a wave. It allows viewing the electromagnetic radiation as a wave with perpendicular electric and magnetic fields interacting with the charged particles (electrons and nuclei) in a chemical system. At the same time, the wave can be considered a photon carrying the energy E given in Equation 5.1, where h is Planck's constant and ν is the photon's frequency.[177, 178]

$$E = h \cdot \nu \tag{5.1}$$

The second essential principle is that quantum mechanical systems exist only in discrete energy states. Their energy is quantized. Hence, a system interacts only with photons carrying an amount of energy equivalent to the energy difference between two states of a system. If a photon of a particular frequency and thus, of a specific energy strikes a system in a ground state with energy E_0, and there exists a possible excited state with energy E_1, where the energy difference ΔE between these two states corresponds precisely to the energy of the photon, the system can be promoted into the excited state. In this process, the photon is absorbed. When the system returns to its ground state and possible secondary processes are not considered, a photon with the same frequency can be re-emitted. Figure 5.1 schematically shows these principles of absorption and emission. Depending on the spectroscopic method, the absorbed, transmitted, or emitted frequencies are measured in the experiment.[176–178]

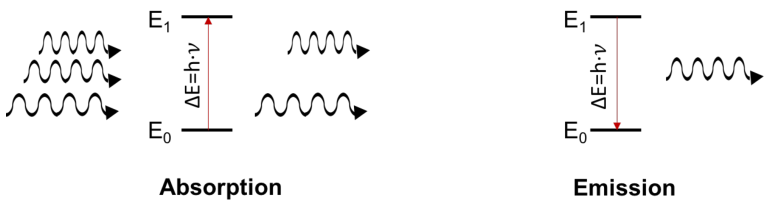

Figure 5.1: Schematic representation of an absorption and emission process.

Different frequencies of electromagnetic waves lead to different interactions with the system and thus, different types of excited states. Figure 5.2 categorizes the electromagnetic spectrum in concerning its relation to the excited states. For example, frequencies from the radiowave range lead to nuclear spin excitations (NMR spectroscopy), the infrared (IR) frequencies to excitations between vibrational states (vibrational spectroscopy), and frequencies in the ultraviolet/ visible (UV/Vis) or X-ray range to electronic excitations (electronic spectroscopy). [176, 178]

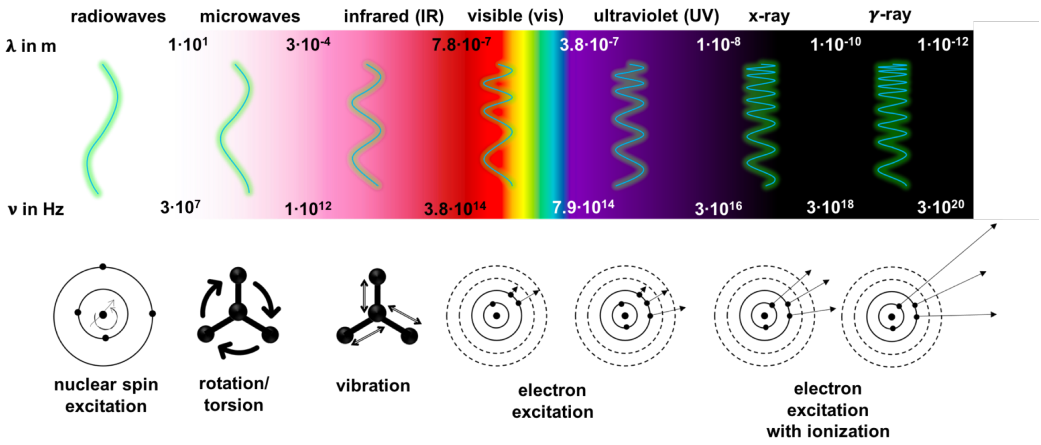

Figure 5.2: The electromagnetic spectrum and the types of excited states caused by electromagnetic waves of different wavelengths λ/ frequencies ν.

The ground and excited states are stationary states described by a wavefunction $\psi(r)$, where r are spatial coordinates. In Chapter 2 it was presented as an eigenfunction in the time-independent Schrödinger equation (see Equation 2.9, page 23) of the energy operator, the Hamiltonian $\hat{H}$. The Hamiltonian was divided into a kinetic and a potential energy operator $\hat{T}$ and $\hat{V}$, respectively. The resulting eigenvalue was the energy of the respective stationary state.

In spectroscopy, the transition between two states is time-dependent. Therefore, the time-dependent Schrödinger equation in Equation 5.2 applies.[106, 177, 179, 180]

$$\hat{H}^{(0)}\Psi_n^{(0)}(r,t) = i\hbar\frac{\delta\Psi_n^{(0)}(r,t)}{\delta t} \tag{5.2}$$

The eigenfunctions $\Psi_n(r,t)$ describing the states are time-dependent as shown in Equation 5.3.[180]

$$\Psi_n^{(0)}(r,t) = \psi_n(r)e^{-iE_n^{(0)}\frac{t}{\hbar}} \tag{5.3}$$

In the previous example, the ground state with energy E_0 would correspond to wavefunction $\Psi_0(r,t)$ and the excited state with E_1 to $\Psi_1(r,t)$. They are eigenfunctions of the time-independent Hamiltonian $\hat{H}^{(0)}$ with the consequence that the resulting energy eigenvalues of the stationary states are also time-independent. A time-dependent term $\hat{H}(t)$ is introduced into the total Hamiltonian $\hat{H}$ to describe the transition between the states, which leads to Equation 5.4 for the total Hamiltonian.[179, 180]

$$\hat{H} = \hat{H}^{(0)} + \hat{H}(t) \tag{5.4}$$

$\hat{H}(t)$ is an external perturbation to the system caused by the electromagnetic wave, either due to its oscillating magnetic or electric field. The oscillating magnetic field causes a change in the kinetic energy because it interacts with the magnetic moment originating from the movement of the electrons. This is the perturbation occurring in, e.g., NMR. The electric field interacts with the electrons directly, leading to a change in the potential energy operator. This is the perturbation occurring in, e.g., IR, UV/Vis, and X-ray spectroscopy.[106, 179–181]

The change in energy ΔE caused by the perturbation is equal to the difference between the ground state (E_0) and the excited state (E_1). It is usually small compared to the total energy E of the system given by Equation 5.5.[180]

$$E = E_0 + \Delta E \tag{5.5}$$

Often, an excited state calculation aims to obtain ΔE accurately. In other cases, a spectroscopic property P may be sought instead, which is usually an experimentally observable quantity. Equation 5.6 expresses ΔE via a Taylor series expansion, where x is, e.g., the internuclear distance or the strength of the electric field $\mathcal{E}$ to which the system might be exposed.[180, 182]

$$\Delta E = \frac{\delta E}{\delta x}x + \frac{1}{2!}\frac{\delta^2 E}{\delta x^2}x^2 + \frac{1}{3!}\frac{\delta^3 E}{\delta x^3}x^3 + ... = \sum_n \frac{1}{n!}(\frac{d^n E}{dx^n})x^n \tag{5.6}$$

The property P can be obtained in most cases as a first- or second-order energy derivative. Equation 5.7 shows the first-order derivative as an example.[182]

$$P = -\frac{\delta E}{\delta x} - \frac{\delta^2 E}{\delta x^2} x - \frac{1}{2!}\frac{\delta^3 E}{\delta x^3} x^2 - ... = -\sum_n \frac{1}{(n-1)!}(\frac{d^n E}{dx^n}) x^{(n-1)} \tag{5.7}$$

It should be kept in mind that quantum mechanical calculations always result in expectation values for any anticipated property P concerning their operator $\hat{P}$ as given in Equation 5.8 if the wavefunction is normalized.

$$\langle P \rangle = \int \psi^* \hat{P} \psi = \langle \psi | \hat{P} | \psi \rangle \tag{5.8}$$

Here, the energy E_0 of a ground state can be a property obtained from the operator $\hat{H}$. In a many-electron system, the ground state is typically calculated via the variational principle given for a (non-normalized) wavefunction in Equation 5.9.

$$E_0 \leq \frac{\langle \psi | \hat{H} | \psi \rangle}{\langle \psi | \psi \rangle} \tag{5.9}$$

The variational principle states that a calculated energy value is always higher than the correct energy. The excited state energy and the derived properties are typically defined as a linear response problem to the previously calculated ground state energy. This approach often includes a non-variational perturbation $\hat{H}(t)$. Thus, the quality of an excited state calculation depends not only on the details of the perturbation method, but also strongly on the quality of the preceding ground state calculation, which is the topic of the next chapter.

6 Ground States

This chapter provides an overview of the methods used in this thesis to calculate the ground state of multi-electron systems. These methods are divided into two types: wavefunction-based methods and density functional theory (DFT) methods. The wavefunction-based methods include Hartree-Fock (HF), configuration interaction (CI), multiconfiguration and -reference (MR), many-body perturbation, and coupled cluster (CC) methods. The description of the DFT distinguishes between different functionals. All descriptions are kept brief and general.

6.1 Wavefunction-Based Methods

6.1.1 Hartree-Fock

The Hartree-Fock (HF) approximation is a well-established concept. It is a wavefunction method for many-electron systems, which is based on the time-independent Schrödinger equation. It is treated here with the Born-Oppenheimer approximation, and thus, the nuclei are considered static.[90]

A wavefunction ψ describing a many-electron system with N electrons can be approximated as a product of N orthonormal one-electron wavefunctions φ_i as introduced in Chapter 2 (see Equation 2.3, page 16). These wavefunctions were introduced as spatial orbitals accommodating two electrons of opposing spin. For generality, spin orbitals χ_i replace them subsequently so that each one-electron wavefunction depends on the electrons' spatial and spin coordinates and implies the need for the wavefunction Ψ_{HF} to be antisymmetric to exchange. The (Slater) determinant in Equation 6.1 now describes the total wavefunction. $N!$ is the normalization factor.[85, 183]

$$|\Psi_{HF}\rangle = \frac{1}{\sqrt{N!}} det|\chi_i \chi_j ... \chi_n| \tag{6.1}$$

The notation in Equation 6.2 abbreviates the wavefunction in Equation 6.1.

$$|\Psi_{HF}\rangle = |i, j...n\rangle \tag{6.2}$$

It is differentiated between restricted closed-shell HF (RHF), in which the spatial components of the spin orbitals are identical for each member of a pair of electrons, its open-shell version ROHF, allowing singly occupied orbitals, and unrestricted HF (UHF), in which an electron pair of opposing spin does not necessarily have to have the same spatial components.[184–186]

The solution of the eigenvalue problem of the HF equation in Equation 6.3 determines the energy ε_i of each orbital i, similar to the general one-electron Schrödinger equation given previously in Equation 2.4 (see page 16).[185, 187, 188]

$$\hat{f}_i\chi_i = [\hat{h}_i + \sum_{j\neq i}(\hat{J}_{ij} - \hat{K}_{ij})]\chi_i = \varepsilon_i\chi_i \tag{6.3}$$

The left-hand side of Figure 6.1 (blue box) visualizes an exemplary resulting orbital energy picture of $|\Psi_{HF}\rangle$ for simplicity with doubly occupied and virtual (unoccupied) spatial orbitals.

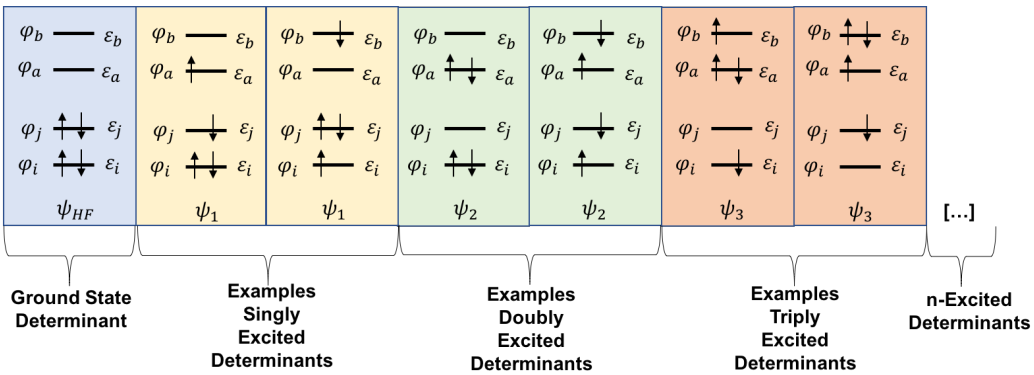

Figure 6.1: Orbital diagram of exemplary selected ground and excited state determinants.

In Equation 6.3, the electronic Hamiltonian from Equation 2.4 is replaced by the Fock operator $\hat{f}_i$. The Fock operator can be divided into two main parts. The first part comprises the one-electron operator $\hat{h}_i$, which contains all terms that depend exclusively on electron i, namely the kinetic energy operators $\hat{t}_i$ of i and the potential energy operators v_{iJ} of the electron-nuclei Coulomb attraction between i and each nucleus J. The nuclei-nuclei Coulomb repulsion can also be included in this operator but is usually introduced as a constant classical Coulomb potential v_{NN}. The second part includes the Coulomb operator $\hat{J}_{ij}$ and the exchange potential operator $\hat{K}_{ij}$. They describe the interactions between electron i and all other electrons j. Table 6.1 contains more detailed explanations of all operators. The total HF energy of a system is not the sum of all orbital energies but the energy from all $\hat{h}_i$ and additionally half of the energy from $\hat{J}_{ij}$ and $\hat{K}_{ij}$ to avoid counting every electron-electron

interaction twice.[183, 185, 187, 188]

Table 6.1: Description of operators in the Hartree-Fock equation shown in the atomic unit notation.[183, 187, 188]

Operator	Equation	Explanation
Kinetic energy operator	$\hat{t}_i = -\frac{1}{2}\nabla^2_{r_i}$	Kinetic energy of electron i with $\nabla^2_{r_i}$ being the Laplacian
Electron-nuclei attraction potential	$v_{iJ} = -\frac{Z_J}{R_{iJ}}$	Coulomb potential of nuclei J acting on electron i with R_{iJ} being the distance between i and J
One-electron operator	$\hat{h}_i = \hat{t}_i + v_{iJ} + v_{NN} = \langle i\|h_{ij}\|j\rangle$	Total one-electron operator with v_{NN} being the potential of the nuclei-nuclei repulsion
Coulomb operator	$\hat{J}_{ij} = \int dr_j \chi^*_j(r_j)\chi_j(r_j)\frac{1}{r_{ij}} = [ii\|jj]$	Coulomb potential of orbital j acting on i with r_{ij} being the distance between i and j
Exchange potential operator	$\hat{K}_j\chi_i = [\int dr_j \chi^*_j(r_j)\chi_i(r_j)\frac{1}{r_{ij}}]\chi_j(r_i) = [ij\|ji]$	Exchange operator gives effect of spin correlation; has to be defined by its action on a specific orbital χ_i

The energy resulting from $\hat{J}_{ij}$ and $\hat{K}_{ij}$ depends not only on the electron i but on all electrons. This has the consequence that the eigenvalue problem in Equation 6.3 is actually a "pseudo" eigenvalue problem, since the eigenvalue problem cannot be solved independently, but must be solved for all electrons simultaneously. Each time it is solved for an electron, its orbital changes, and so do all the other orbitals. HF uses a self-consistent field (SCF) algorithm to solve this problem. In an iterative approach, an estimate for the orbitals is used to solve a "pseudo" eigenvalue function for each electron, resulting in a new and improved set of orbitals for the orbitals, which are reintroduced into the calculation. This process is repeated until the energy with respect to a chosen threshold converges to the actual energy of the system. This is a variational principle, as shown in Equation 5.9.[85, 183, 185]

HF is a mean-field approach. Each electron is calculated in an average field of the other electrons. This means that each electron does not interact explicitly with the other electrons, but with the average of all electrons. Therefore, the correlation between electrons is not considered. Although this approach reflects about 99% of the total energy, the missing 1% is crucial to accurately capture most chemical

phenomena. The exact energy E_{exact} of a system can be expressed as the sum of the HF energy E_{HF} and the correlation energy E_{corr}, as shown in Equation 6.4.[85, 189]

$$E_{exact} = E_{HF} + E_{corr} \tag{6.4}$$

There are several approaches based on the HF formalism to recover the electron correlation to obtain a more accurate description of a many-electron system. They are usually referred to as post-HF methods. The post-HF methods relevant to the studies presented later are briefly described below.

6.1.2 CI - Configuration Interaction

An electron configuration describes the distribution of a given number of electrons among the available spatial orbitals. The distribution can be expressed as a set of numbers with values of zero for VMOs (virtual/unoccupied MOs), one for SOMOs (singly occupied MOs), or two for DOMOs (doubly occupied MOs). A configuration always represents all possible configuration state functions (CSF) for a total spin S. A CSF allows only spin coupling between the singly occupied orbitals leading to S. This implies that each SOMO can have different m_s in a given CSF. Hence, a CSF is a linear combination of Slater determinants. A Slater determinant describes only one particular state where S overall and the m_s of each singly occupied orbital are specified.[64, 65]

In the HF approach, the wavefunction is represented by a single determinant, which means that only one possible arrangement of the electrons in the orbitals is considered, along with a defined total spin S and spin m_s for each electron (as illustrated in the left box of Figure 6.1). To account for electron correlation, the system can be described by a series of determinants that include single, double, and higher excitations with respect to the HF determinant (as indicated by the different boxes in Figure 6.1).

For example, a singly excited determinant with an excitation from orbital j to a is shown in the second box from the left in Figure 6.1, where the total spin S corresponds to the ground state. In this case, one spin-down electron remains in the spatial orbital j, while the spin-up electron moves to orbital a. If the electrons were reversed, the same total spin coupling scheme would still result. Both determinants would be needed to describe the resulting CSF in Equation 6.5.

$$|\Phi_j^a\rangle = |a, i, k, ...n\rangle \tag{6.5}$$

For the example, the given CSF is needed instead of just one of the two determinants to be an eigenstate of S^2. This CSF can be used to account for part of the elec-

tron correlation missing from the ground state HF wavefunction $|\Psi_{HF}\rangle$. Similarly, other CSFs with different excited electrons with respect to $|\Psi_{HF}\rangle$ can be formulated. The total wavefunction is then a linear combination of CSFs as given in Equation 6.6.

$$|\Psi^S\rangle = c_{HF}\,|\Psi_{HF}\rangle + \sum_{\substack{a\\i}} c_i^a\,|\Phi_i^a\rangle + \sum_{\substack{a<b\\i<j}} c_{ij}^{ab}\,|\Phi_{ij}^{ab}\rangle + \sum_{\substack{a<b<c\\i<j<k}} c_{ijk}^{abc}\,|\Phi_{ijk}^{abc}\rangle + ... \tag{6.6}$$

Occupied orbitals are denoted by $i, j, k, ...$ with respect to $|\Psi_{HF}\rangle$, while virtual orbitals are denoted by $a, b, c, ...$ The wavefunction optimization process consists of two steps: First, the SCF optimizes $|\Psi_{HF}\rangle$, and second, the expansion coefficients c are iteratively optimized during the course of the CI. The coefficients determine the contribution of each CSF to the overall ground state wavefunction $|\Psi^S\rangle$.

For convenience, the CI approach presented here is expressed as a linear combination of CSFs. However, it can also be defined as a linear combination of determinants.

The accuracy of the total wavefunction $|\Psi^S\rangle$ depends on the number of excited CSFs included. When all possible CSFs are included, it is called Full CI (FCI), which together with a complete basis set provides the exact solution to the wavefunction.

CI calculations are categorized by the type of excitations included. For instance, CIS involves only single excited CSFs, CISD includes both single and double excitations, and CISDT comprises single, double, and triple excitations. CIS approximates the single excited states to the ground state. However, it does not change the HF ground state energy in the CI process, since the singly excited CSFs cannot mix directly with $|\Psi_{HF}\rangle$ due to symmetry (Brillouin's theorem). However, they can mix with $|\Psi_{HF}\rangle$ through higher excitations. Therefore, the first improvement of the ground state energy in terms of electron correlation is expected by CID (CI with double excitation), followed by CISD.[190, 191]

A disadvantage of the CI approach is that it is not size consistent. A system of subsystems $A + B$ with a large distance between A and B is size consistent if the energy of $A + B$ is equal to the sum of the individual energies of A and B. In CI, an electron in A can be excited to another orbital far from its original orbital in B, which is unlikely and can introduce an error.[190] Restoring size consistency requires complex CI approaches (ECISDT, ECISDTQ) that approximate the full CI solution.[192] However, CI approaches are generally computationally expensive and are currently only applicable to very small systems.

6.1.3 ICE-CI – Iterative-Configuration Expansion Configuration Interaction

Approximate CI methods can provide results close to CI accuracy, but require significantly less computational effort. Recent advances in approximate CI wavefunction methods based on density matrix renormalization group (DMRG),[63] iterative configuration expansion (ICE-CI),[64, 65] or Full Configuration Interaction Quantum Carlo Method (FCIQMC)[66] in the treatment of large active spaces are crucial for the calculation of the magnetic anisotropy or the low-lying valence excitation spectrum of multimetallic centers.[67–70] ICE-CI can handle up to a few dozen electrons and orbitals. ICE-CI defines modern tree-based determinant, configuration, or CSF generation methods that, when used to generate the desired CI problem, provide a compact, efficient, and highly flexible infrastructure that allows one to solve complex and incomplete CI problems of arbitrary chemical spin and symmetry systems.[64, 65]

In a nutshell, assuming that ICE-CI is chosen to be based on the CSFs generation method, the role of ICE-CI is to generate a compact wavefunction representing only the most important CSFs. The complete wavefunction is found in an iterative process where, in the first step, a "generator" set is selected that includes the HF ground state CSF and the single and double excited CSFs that interact most strongly with the HF ground state. In the next step, single and double excited CSFs are generated with respect to the "generator" set of CSFs. From these CSFs, only those that interact most strongly with the "generator" set are selected and added to the set. This process is repeated iteratively until the wavefunction converges.[64, 65]

6.1.4 Multiconfigurational Methods: CASSCF and RASSCF

One way to reduce CI calculation time is to use multiconfigurational self-consistent field (MCSCF) methods such as CASSCF (CAS = complete active space).[169–171] In this method, the orbitals from an initial single-configuration calculation, e.g., RHF/ROHF calculation, are divided into three categories. The first category contains frozen DOMOs described by the initial RHF/ROHF result. The second category consists of active orbitals, which may include DOMOs, SOMOs, and virtual orbitals treated with the CI approach. The third category contains frozen virtual orbitals analogous to the frozen DOMOs. Figure 6.2 shows an example of the scheme.

In CASSCF, the orbitals in the active space entering the CI process are iteratively optimized in an SCF fashion. Alternatively, the orbitals entering the CI process can be selected without further SCF optimization (CASCI). Similarly, RASSCF or RASCI (restricted active space) methods can be specified (see Figure 6.2, right).[193] These

methods differ from the corresponding CASSCF/CASCI methods in that they include additional particle/hole excitation spaces that can be used to restrict the number of excitations in the selected orbital windows.

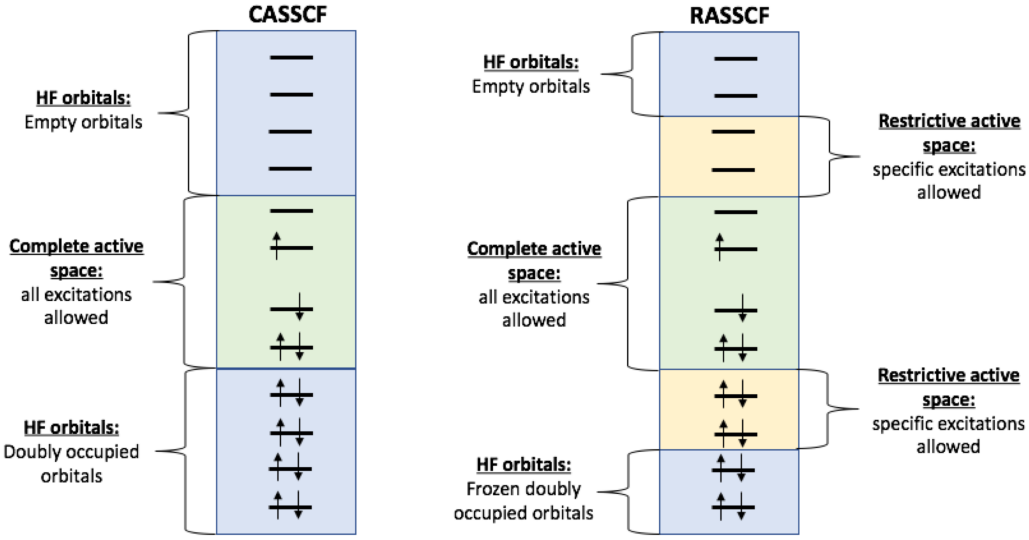

Figure 6.2: Schematic representation of the construction of the orbital space for CASSCF/CASCI (left) and RASSCF/RASCI (right) calculations.

Methods such as CASSCF/CASCI and RASSCF/RASCI provide the ability to calculate and study specific energy windows in a selected system with the precise tool of CI while "freezing" the rest of the system with respect to the single-configuration result. This allows the selected calculation window to be studied in detail. Moreover, the total energy of a system can be calculated more accurately by including orbitals in the active space that are known to be strongly affected by electron correlation, such as valence orbitals, and describing those that are less affected, such as core electrons, by the single-configuration wavefunction.

6.1.5 Many-Body Perturbation Methods: MP2, NEVPT2, CASPT2

While the focus of the methods presented so far has been on enhancing the wavefunction to recover the correlation energy of the electrons, the perturbation methods rely on changing the Hamiltonian operator acting on the wavefunction to achieve the same goal. The approach is similar to that used to calculate the properties of excited states in Chapter 5.

Any of the previously described methods can obtain a zeroth-order wavefunction $|\Psi^{(0)}\rangle$. Thus, it can be either a single-determinant as in HF or a linear combination of determinants or CSFs as, e.g., in ICE-CI or a multiconfigurational method.

Equation 6.7 gives the general form of $|\Psi^{(0)}\rangle$ with c_l being the respective CI expansion coefficients.

$$|\Psi^{(0)}\rangle = \sum_l c_l \, |\Phi_l\rangle \tag{6.7}$$

In this concept, various single- or multireference perturbation methods add to the relevant zeroth-order Hamiltonian $\hat{H}^{(0)}$ a perturbation operator $\hat{H}_V^{(\lambda)} = \lambda V$, as shown in Equation 6.8.[194]

$$\hat{H} = \hat{H}^{(0)} + \lambda V \tag{6.8}$$

Here, λ is a parameter between zero and one. If it is zero, the resulting Hamiltonian is equivalent to the zeroth order operator $\hat{H}^{(0)}$, and if it is one, it is the anticipated correct Hamiltonian $\hat{H}$. This updated operator can be introduced into the Schrödinger equation with the goal that the added perturbation recovers the missing electron correlation. Opposing the previously described methods, this approach is size extensive but not variational. Due to the latter, it does not necessarily give higher energy than the exact energy and thus, is not subject to the variational theorem.[186]

It follows that the first-order wavefunction can be calculated from Equation 6.9, where $E_0 = H_0 \, |\Psi^{(0)}\rangle$ is the zeroth-order energy.[194]

$$(E_0 - H_0) \, |\Psi^{(1)}\rangle = (H_V - E_1) \, |\Psi^{(0)}\rangle \tag{6.9}$$

This first-order wavefunction can be expanded in a set of determinants or CSFs, as given in Equation 6.10, constituting the first-order interaction space (FOIS).

$$|\Psi^{(1)}\rangle = \sum_l c_l^{(1)} \, |\Psi_l\rangle \tag{6.10}$$

Equation 6.11 follows, such that the problem reduces to a relevant to the known eigenvalue problem.[194, 195]

$$\sum_l \langle \Psi_K | E_0 - H_0 | \Psi_l \rangle \, c_l^{(1)} = \langle \Psi_K | H_V | \Psi^{(0)} \rangle \tag{6.11}$$

One of the most frequently used methods utilizing this ansatz is the many-body perturbation method MPPT (Møller-Plesset Perturbation Theory). The zeroth-order Hamiltonian $\hat{H}^{(0)}$ is, in this case, the sum of all one-electron Fock operators. Hereby, the electron-electron repulsion is counted twice (see Hartree-Fock explanation, page 72). The perturbation operator V corrects this error by reducing the electron repulsion by eliminating half of the repulsion energy in terms of the Fock operator. Then it adds the proper electron-electron repulsion as described in the "actual"

many-electron Hamiltonian (see Equation 2.11a, page 23), which results in Equation 6.12.[196, 197]

$$V = \sum_i \sum_{i>j} \frac{1}{r_{ij}} - \sum_i \sum_j (J_{ij} - \frac{1}{2} K_{ij}) \tag{6.12}$$

The zeroth-order perturbation result is just the energy of all non-interacting orbitals – the HF energy yields by adding the first-order perturbation, including V, per definition. The second-order perturbation gives the first energy correction regarding the electron correlation. The resulting method is MP2 (Møller-Plesset second order perturbation). It is possible to include higher order perturbations (MP3, MP4, ...) which are significantly more expensive to compute.[197]

The wavefunction used as a basis for the MP2 approach is the single-configurational HF ground state wavefunction. A similar perturbation operator can also be applied to a multiconfigurational wavefunction. In most cases, this is a CASSCF wavefunction. Three methods of doing so are NEVPT2 (n-electron valence state perturbation theory of second order),[198–200] CASPT2 (complete active space perturbation theory of second order),[201, 202] or DCD-CAS(2) (dynamic correlation dressed CAS(2)).[203] MP2 is a single-reference method because only a single-configurational wavefunction is used as a reference for the perturbation. NEVPT2 and CASPT2 are multireference methods because multiconfigurational wavefunctions are utilized.

One might ask why it makes sense to add perturbation theory to approaches such as CASSCF since they are already aiming to recover the electron correlation. It has to be differentiated between static and dynamic electron correlation to answer this question. The static correlation is associated with a ground state consisting of a superposition of two or more CSFs, each of which significantly contributes to the resulting wavefunction. Comparing the energy of each of these CSFs individually, they are usually nearly degenerated. Systems with large static correlations are typically those in which a single determinant cannot appropriately approximate their ground state.[172]

Roughly spoken, the dynamic correlation is associated with the movement of the electrons. It expresses itself primarily due to mixing higher-order excited CSFs with smaller contributions to the ground state.[172] CASSCF recovers both types of electron correlation but primarily static correlation. This is especially the case if higher excitations in the CI are not allowed (no FCI). Perturbation methods are known to recover primarily the dynamic electron correlation and can account for the missing correlation towards FCI. Therefore, a combination of both may be useful depending on the system and the goal of the model.

6.1.6 Coupled Cluster (CC) Methods: CCSD, DLPNO-CCSD, and MR-CC

The final category of wavefunction-based methods described at this point is the coupled cluster (CC) method. Like CI, CC is an iterative process concerning the correlation of electrons by referring to higher determinants. Unlike CI, CC methods are size extensive. CI has a linear approach to improve the HF result by accounting for the explicit interaction of one electron with all other electrons. CC theory is based on the idea that the interaction of an electron with more than one other single electron at once is unlikely to be significant. Consequently, CC refers to the many-electron interactions through simultaneous electron pair interactions, which are called "clusters". CC involves the excited determinants in an exponential ansatz via an excitation operator $\hat{T}$ with single, double, and higher excitations, as defined in Equation 6.13.

$$\hat{T} = t_a^i \hat{c}_i^a + \frac{1}{2} t_{ab}^{ij} \hat{c}_i^a \hat{c}_j^b + ... = t^\lambda \hat{c}_\lambda \tag{6.13}$$

Here t is an amplitude, $\hat{c}$ are annihilation and creation operators of the excitations, i and j stand for occupied and a and b for virtual orbitals. The full CC wavefunction $|\Psi_{CC}\rangle$ can be determined by applying the excitation operator to the HF wavefunction $|\Psi_{HF}\rangle$ and eventually approaching it with a Taylor expansion series, as defined in Equation 6.14.

$$|\Psi_{CC}\rangle = e^{\hat{T}} |\Psi_{HF}\rangle = (1 + \hat{T} + \frac{\hat{T}^2}{2!} + \frac{\hat{T}^3}{3!} + ...) |\Psi_{HF}\rangle \tag{6.14}$$

The repeated application of $\hat{T}$ on $|\Psi_{HF}\rangle$ - implied in the Taylor extension series - generates the "clusters".[204]

As in the case of CI, different CC methods exist depending on the included excitations. Examples are CCD (Coupled Cluster Doubles), CCSD (Coupled Cluster Singles Doubles), CCSDT (Coupled Cluster Singles Doubles Triples), or CCSD(T). In the latter, the triple contribution is included non-iteratively but perturbatively.[186] In general, CCSD(T) is considered the gold standard of computational chemistry and is applicable to significantly larger systems than its CI equivalent. However, calculations are still demanding and get exponentially more expensive as system size increases.

DLPNO-CCSD and -CCSD(T) methods reduce computation time and make CCSD and CCSD(T) applicable to large systems. They show linear scaling with system size and recover 99.99% of the "original" CC energy. DLPNO stands for "domain-based local pair natural orbital". Equation 6.15 symbolizes the transformation of the MO

basis to the DLPNO basis with a, b,... representing the MO, μ, ν,... the AO and $\overline{\mu}, \overline{\nu}$,... the PAO basis.

$$T_{ab}^{ij} \Rightarrow C_{a\mu}^{ij} T_{\mu\nu}^{ij} C_{\nu b}^{ij} \Rightarrow L_{\mu\overline{\mu}}^{ij} T_{\mu\overline{\nu}}^{ij} L_{\nu\overline{\nu}}^{ij} \Rightarrow d_{\overline{\mu}a\overline{a}_{ij}}^{ij} T_{\overline{a}_{ij}\overline{b}_{ij}}^{ij} d_{\overline{b}_{ij}\overline{\mu}}^{ij} \tag{6.15a}$$

$$MO \Rightarrow AO \Rightarrow PAO \Rightarrow PNO \tag{6.15b}$$

With this type of orbital definition, described in detail elsewhere,[167, 168, 205–207] the electron pair correlation can be restricted only to a certain domain in space for each pair. This makes the calculation significantly more efficient.

So far, all CC methods mentioned are single-reference because they are based on the HF wavefunction. It is also possible to perform CC calculations based on a multiconfigurational wavefunction, such as those generated by CASSCF. The resulting CC approach is therefore multireference and is abbreviated as MR-CC.

6.2 Density Functional Theory

Besides the calculation of ground states with wavefunction-based methods, it is possible to use size-extensive charge-density-based methods within the Born-Oppenheimer approximation.[165] It is namely the density functional theory (DFT) based on the Hohenberg-Kohn theorems.[208] The first theorem states that the electron density of a system determines its external potential, which is the Coulomb attraction between electrons and nuclei. If this statement is true, it follows that the electron density ρ determines the Hamiltonian operator and consequently, the total ground state energy E and resulting properties of the system. This makes the total energy E a functional E[ρ] of the electron density ρ. The electron density, in turn, is a function $\rho(r)$ of the three spatial coordinates summarized in r. This reduces a problem with N electrons from a previously $3N$-dimensional problem to one that depends only on the three spatial coordinates. The second theorem is the variational theorem. It states that the energy of an approximated density is always higher than the actual energy. This makes DFT - as HF - a SCF method.[165, 166]

The total energy can be divided - like the energy in the previously discussed theories - into the kinetic energy contributions $T[\rho]$ of the electrons, the nuclei-electron attraction $V_{ne}[\rho]$, and the electron-electron repulsion $V_{ee}[\rho]$. The latter can be divided into the classical Coulomb term $J[\rho]$ and the exchange term $K[\rho]$. As known from previous descriptions, accurate treatment of the kinetic energy requires differentiation of a wavefunction. The charge density of a system with a wavefunction ψ can be defined by the probability distribution function $|\psi|^2$. For that reason, in the Kohn-Sham method, a fictitious set of N non-interacting electrons - similar to an electron

gas - is introduced. The density is expressed in terms of the resulting orbitals ϕ_i, as given in Equation 6.16. These are called Kohn-Sham orbitals and are non-interacting orbitals capable of determining the true ground state density.[165, 166, 209]

$$\rho = \sum_i |\phi_i|^2 \tag{6.16}$$

Analogous to HF, the kinetic energy can be determined via Equation 6.17.[165]

$$T_s = \sum_i \langle \phi_i | -\frac{1}{2}\nabla^2 | \phi_i \rangle \tag{6.17}$$

The suffix s indicates that this is not the true kinetic energy but that of non-interacting electrons.[166]

The classical Coulomb expression define $V_{ne}[\rho]$ and $J[\rho]$. Each electron interacts with the potential generated by the nuclei and the potential generated by the electron density, respectively. The consequence of the latter is that each electron interacts with all other electrons, including itself, since all electrons define the density at each step. The resulting error is called the self-interaction error.[165, 166]

The Coulomb interaction includes only the classical description of the electron-electron interaction, but not the exchange potential and the electron correlation. In DFT, the missing exchange potential, the missing electron correlation, as well as the self-interaction error and the kinetic energy error are combined in the so-called exchange-correlation functional $E_{xc}[\rho]$, as shown in Equation 6.18.[165, 210]

$$E_{xc}[\rho] = E_x[\rho] + E_c[\rho] = T[\rho] + V_{ee}[\rho] - (T_s[\rho] + J[\rho]) \tag{6.18}$$

The total energy functional is given by Equation 6.19.[166]

$$E[\rho] = T_s[\rho] + E_{ne}[\rho] + J[\rho] + E_{xc}[\rho] \tag{6.19}$$

While the first three terms can be computed accurately, the correct $E_{xc}[\rho]$ is currently unknown and can be approximated in several ways. Since it is an approximation, the variational theorem does not have to be correct, and the resulting energy is not necessarily higher than the true energy.[165]

The functionals that approximate $E_{xc}[\rho]$ in different ways are classified into LDA, GGA, meta-GGA, hybrid, and double-hybrid functionals. It is assumed that the accuracy increases in this order. This classification is often called the "Jacob's ladder of DFT functionals".[211] Each category includes a variety of different functionals, many of which are specialized for calculating different properties.

6.2.1 LDA Functionals

A first approach to the $E_{xc}[\rho]$ is the local density approximation (LDA). It assumes that the density behaves locally like a homogeneous electron gas whose exchange-correlation energy can be determined. Equation 6.20 provides the resulting approximation, which presumes the uniform electron gas exchange-correlation energy per electron as a function of the density $\varepsilon_{xc}(\rho)$.[166]

$$E_{xc}[\rho] \approx \int [\rho(r)\varepsilon_{xc}(\rho(r))]dr \tag{6.20}$$

6.2.2 (Meta-)GGA Functionals

The error in the LDA is significant. The generalized gradient approximation (GGA) attempts to compensate for this by creating an exchange-correlation functional dependent on the charge density $\rho(r)$ and its gradient $\nabla\rho(r)$ according to Equation 6.21 with ε_{xc} being ones more the exchange-correlation energy of the homogeneous electron gas.[165, 166, 210]

$$E_{xc}[\rho] \approx \int [\rho(r)\varepsilon_{xc}(\rho(r), \nabla\rho(r))]dr \tag{6.21}$$

Moreover, the $E_{xc}[\rho]$ term in a meta-GGA functional in Equation 6.22 depends explicitly on the semi-local information of the density gradient $\nabla^2\rho(r)$ or on the local kinetic energy density $\tau(r)$.[166, 210]

$$E_{xc}[\rho] \approx \int [\rho(r)\varepsilon_{xc}(\rho(r), \nabla\rho(r), \nabla^2\rho(r), \tau(r)]dr \tag{6.22}$$

The functionals in Equation 6.21 and Equation 6.22 represent the general form of the two approaches. There are a variety of different GGA and meta-GGA functionals that differ from each other in one way or another. To name a few: PBE,[212] BLYP,[213, 214] and BP86[213, 215] are examples of GGA functionals, and TPSS[216] and M06L[217] are examples of meta-GGA functionals.

6.2.3 Hybrid Functionals

Hybrid functionals mix the $E_{xc}[\rho]$ of one of the previously described DFT functional types with the exact exchange energy determined by HF. The various hybrid functionals differ in the percentage of HF exchange energy they contain and on which DFT functional or combination of functionals they are based. Equation 6.23 displays the typical functional form, where a is a constant between zero and one.[166, 211]

$$E_{xc}[\rho] \approx E_{XC}^{DFT} + (1-a)E_X^{HF} - aE_X^{DFT} \tag{6.23}$$

Examples of hybrid functionals are B1LYP and B3LYP. Both are based on the GGA functional BLYP, but B1LYP has 25%, while B3LYP has 20% HF exchange energy contributions.[213, 214, 218] Other examples for hybrid functionals are PBE0,[212, 219] TPSSh,[220–222] B3PW91,[218, 222] and M06.[217]

6.2.4 Double-Hybrid Functionals

Simply put, double-hybrid functionals are a combination of hybrid functionals and MP2. Thus, the exchange-correlation functional $E_{xc}[\rho]$ contains terms that depend on a chosen (meta-)GGA functional, the exact Hartree-Fock exchange, and perturbation theory in terms of MP2 to restore some electron correlation. Equation 6.24 shows a typical structure of the functional, where a, b, c are values between zero and one.[223]

$$E_{xc}[\rho] \approx (1-a)E_X^{DFT} + aE_X^{HF} + bE_C^{DFT} + cE_C^{MP2} \tag{6.24}$$

Often the amount of exact HF exchange is much larger for these functionals than for the hybrid functionals. This is because the correlation recovered by MP2 can correct for HF deficiencies not accounted for in hybrid functionals and at the same time improve the self-interaction error. Examples of double-hybrid functionals are B2PLYP,[223] DSD-BLYP,[224, 225] or DSD-PBEP86.[226]

6.3 Remarks to the Ground State Methods

When choosing a method for a particular calculation, one must consider the advantages and disadvantages of the available methods. Although DFT methods are less expensive, wavefunction-based methods generally offer higher accuracy. The choice of method should be tailored to the problem at hand. This depends not only on the desired accuracy and computational affordability but also on the property to be calculated and the material. For example, systems containing transition metal atoms often require multireference methods due to the presence of partially filled d orbitals.[172] In contrast, single-reference methods are usually sufficient for most main group elements. A combination of methods is also possible. In the embedding approach, the HF layer option allows most of the crystal to be treated at the HF level, while a selected part of the crystal can be calculated with a more accurate method.

Although all the methods discussed so far are based on a non-relativistic Hamiltonian, a relativistic energy correction is necessary for most spectroscopic properties,

especially for heavy elements. This correction includes two types of relativistic effects, spin-orbit coupling (SOC) and scalar relativistic effects. SOC arises from the coupling between the intrinsic electron spin and the electron orbital spin[227], while scalar relativistic effects are all other relativistic effects besides SOC. Both types of effects can be included in the Hamiltonian. The scalar relativistic Hamiltonian used in most of the calculations presented in this work is the DKH2 (Douglas-Kroll-Hess second order Hamiltonian).[228, 229] A detailed discussion of relativistic corrections is beyond the scope of this work.

An additional consideration of relativistic effects can be accomplished with relativistic basis sets. In general, besides the choice of the method, the choice of the basis set is essential for an accurate calculation. As mentioned in the context of CI, a result can only be correct if the basis set is complete. While this is never achievable in practice, the larger the basis set, the more accurate the result. A basis set should be chosen depending on the desired accuracy, the applied method, the type of system, and the property being calculated. For example, cc-pVXZ basis sets are specialized for correlation methods such as CC approaches.[144] However, they can also be used successfully for DFT calculations. Although, for DFT, e.g., def2-XVP[142, 143] basis sets may provide a better overall cost/accuracy ratio. An example of basis sets customized for a specific property is pcSseg-X, designed explicitly for NMR calculations.

The majority of the ground state methods discussed can be used in combination with perturbation methods or other modifications to calculate excited states or related spectroscopic properties. The next two chapters discuss these approaches in the context of NMR and electronically excited states.

7 Nuclear Magnetic Resonance Spectroscopy

Nuclear Magnetic Resonance (NMR) is one of the most widely used spectroscopic techniques to investigate structures of a variety of systems. The basic principles and how to calculate one of the NMR observables – the nuclear shielding – will be shortly summarized in the following.

When a magnetic field with magnetic induction B_0 is applied to a nucleus with an odd number of protons or neutrons, the spin states of the nucleus split into different states. Figure 7.1 symbolizes this for a nucleus with a spin quantum number $l = \frac{1}{2}$ splitting into its α ($m_l = \frac{1}{2}$) and β ($m_l = -\frac{1}{2}$) states.[230]

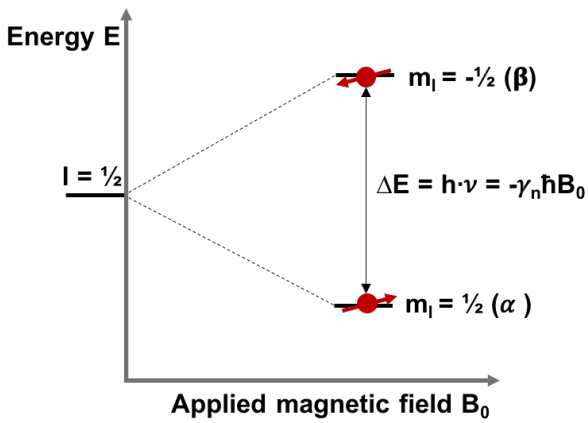

Figure 7.1: Schematic representation of the excitation process between spin states in NMR spectroscopy.

The frequency ν of an electromagnetic wave required to excite the spin depends on the gyromagnetic ratio γ_n specific to each type of nucleus and the local magnetic field induction B_{loc} at the nucleus, which is different from the applied B_0. The difference is caused by B_0 itself, which induces a circulation of electrons through the system analogous to an electric current, which consequently generates an additional magnetic field δB around the nucleus of interest. Since the additional field δB de-

pends on the magnitude of the applied field B_0, they are proportional to each other, as given in Equation 7.1.[181, 230]

$$\delta B = -\sigma B_0 \tag{7.1}$$

Here σ is a dimensionless quantity called the nuclear shielding constant. The frequency which excites the considered spin exposed to B_{loc} is defined by Equation 7.2 and is called Lamour frequency ν_L.

$$\nu_L = \frac{\gamma_n B_{loc}}{2\pi} = \frac{\gamma_n (B_0 + \delta B)}{2\pi} = \frac{\gamma_n B_0}{2\pi}(1 - \sigma) \tag{7.2}$$

The desired frequency is in the radiowave region of the electromagnetic spectrum (see Figure 5.2) and is measured in an NMR experiment. In order to make the results autonomous of B_0, an observable independent of the applied field, called the chemical shift δ, is used as given in Equation 7.3.

$$\delta = \frac{\nu - \nu_0}{\nu_{spect}} \cdot 10^6 \approx (\sigma^0 - \sigma) \cdot 10^6 \tag{7.3}$$

Here, ν_{spect} is the operating frequency of the spectrometer, and ν_0 is the resonance frequency of a standard used as a reference to the system of interest, while σ^0 is its shielding. Thus, the observed chemical shift is relative. Nuclei with a positive chemical shift are less shielded than their reference, and nuclei with a negative shift are more shielded.

The higher the electron density around a nucleus, the more shielded a nucleus is, and the larger σ. Therefore, an element with many core electrons has greater shielding than one with fewer, which makes NMR element-specific. In addition, if an electronegative or electropositive atom is near the nucleus of interest, its shielding will decrease or increase, respectively. This makes NMR environment specific.[230]

The magnetic field has to be defined to approach the nuclear shielding constant computationally. The magnetic field induction can be expressed by Equation 7.4, where A is a vector potential.[181]

$$B = \nabla \times A \tag{7.4}$$

NMR properties are derivatives of the kinetic energy operator since the magnetic moments of the electrons are generated by the movement of charged particles. The kinetic energy is defined depending on the momentum p. By applying a magnetic field, this momentum changes regarding the potential of the magnetic field expressed by A so that the new momentum is $p + A$. The resulting Hamiltonian $\hat{H}$ with zeroth-, first- and second-order perturbation concerning a magnetic field is given in Equation 7.5 with p being $-i\hbar\nabla$.

$$\hat{H} = \hat{H}^{(0)} + \hat{H}^{(1)} + \hat{H}^{(2)} = [\frac{p^2}{2m_e} + V] + \frac{e}{m_e} \cdot A \cdot p + \frac{e^2}{2m_e} \cdot A^2 \tag{7.5}$$

The vector potential A fully determines the perturbation. Equation 7.4 follows that A is defined by Equation 7.6.[181]

$$A = \frac{1}{2} B \times r \tag{7.6}$$

The vector potential is, by definition, not unique because the direction r is arbitrary. Thus, it can be written as $r - R_0$. Here, R_0 defines the so-called gauge origin of the field. The coordination system of the calculation has to be specified in this respect. If the correct wavefunction is used, this would not be a problem because it would be independent of the gauge origin. Since this is usually impossible, the computational protocol can introduce GIAOs (gauge-including atomic orbitals).[181, 231] These orbitals incorporate the gauge origin into the basis functions, so the resulting model is gauge-independent. An analogous for periodic basis sets are GIPAW (gauge-including projector augmented wavefunctions).[232]

In general, the choice of the basis sets in NMR calculations is of utter importance because the shielding originates primarily from the core electrons, which are often not well described by the standard basis sets. There are specialized basis sets such as pcSseg-X to compensate for these deficiencies.[233]

The nuclear shielding constant can be defined and computed via Equation 7.7.[181]

$$\sigma = \frac{\delta^2 E}{\delta B_0 \delta \mu_l} \tag{7.7}$$

Here, B_0 is the external magnetic field induction, and μ_l is the magnetic dipole moment of the respective nucleus. For molecules and thus, for crystals modeled with the embedded cluster approach, the nuclear shielding constant can be calculated using most available DFT methods as well as MP2 and CC methods by employing the perturbed Hamiltonian and deriving the nuclear shielding constant from the resulting energy.

8 Electronic Spectroscopy: UV/Vis and X-ray Spectroscopy

Typically spectroscopic methods utilizing electromagnetic waves from the visible to the X-ray spectrum range are considered electronic spectroscopy. The process of the spectroscopic methods can be understood as a displacement of a charge in a system caused by a perturbation induced by an oscillating electric field that interacts with the dipole of the system. In the orbital picture, the interaction provokes transitions of electrons between different orbitals. While visible and UV light only excites the valence orbitals in many systems, X-ray waves can excite core electrons (see Figure 5.2, page 69). Despite this difference, both methods underly the same selection rules for absorption and emission processes, determining if a transition between initial and final electronical states $|I\rangle$ and $|F\rangle$ is allowed. The first selection rule is the orbital or dipole selection rule, as given in Equation 8.1.[234]

$$\langle I_{el}|\hat{\mu}_{el}|F_{el}\rangle \neq 0 \tag{8.1}$$

The suffix el indicates that only the electronic part of the wavefunction excluding the spin is considered and $\hat{\mu}_{el}$ is the electric dipole operator given by Equation 8.2.

$$\hat{\mu}_{el} = \sum_A e \cdot Z_A \cdot R_A - \sum_i e \cdot r_i = -\frac{\delta E}{\delta \mathcal{E}} - \frac{\delta^2 E}{\delta \mathcal{E}^2}\mathcal{E} - \frac{1}{2}\frac{\delta^3 E}{\delta \mathcal{E}^3}\mathcal{E}^2 - ... \tag{8.2}$$

The electric dipole originates from the charge e of electrons i at their position r and the nuclei A with charges $e \cdot Z_A$ at positions R. In an alternative description, it is the first-order derivation of the energy regarding the oscillating electric field $\mathcal{E}$ of the electromagnetic wave, which perturbs and interacts with the system in the spectroscopic process.[182, 234, 235]

Equation 8.1 is non-zero and thus, the transition dipole-allowed if the dipole changes between$|I\rangle$ and $|F\rangle$. This is the case if the triple direct product $\Gamma(I) \times \Gamma(\hat{\mu}_{el}) \times \Gamma(F)$ contains the total symmetric irreducible representation (Γ) of the point group of the system. In other words: for an initial state $|I\rangle$, only transitions to final states $|F\rangle$ are allowed, which have the symmetry of at least one component of the

dipole moment operator $\hat{\mu}_{el}$.[234]

The second selection rule is the spin selection rule shown in Equation 8.3.

$$\langle I^S | F^S \rangle \neq 0 \tag{8.3}$$

The rule is directly derived from the orthogonality requirement of the spin-wavefunction, which demands that the $|I\rangle$ and $|F\rangle$ states involved must have the same spin multiplicity. $|I\rangle$ and $|F\rangle$ must be eigenfunctions $|I^S\rangle$ and $|F^S\rangle$ of the total spin S and M_S. Nevertheless, several transitions with different multiplicities are possible in a spectrum, which can mix via SOC (multiplet effect).[234, 235]

If a transition is dipole- and spin-allowed, it is called "fully allowed". Nevertheless, states contradicting one or even both rules can still exist in a spectrum. The rules merely determine the probability of a transition happening. This probability or strength of the transition can be expressed in terms of the oscillator strength f_{IF}, which takes the form of Equation 8.4 within the electric dipole approximation (ED) and upon isotropic orientational average.[234, 236, 237]

$$f_{IF}^{ED} = \frac{2m_e}{3e^2\hbar} E_{IF} | \langle I | \mu_{el} | F \rangle |^2 \tag{8.4}$$

In practice, the oscillator strength is proportional to the area of the absorption band, as Equation 8.5 shows.[234]

$$f_{IF} = 4.33 \cdot 10^{-9} \int_0^\infty \epsilon^{(F)}(\overline{\nu}) d\overline{\nu} \tag{8.5}$$

ϵ is the extinction coefficient, and $\overline{\nu}$ is the transition frequency. Table 8.1 indicates what kind of oscillator strength can be expected for the forbidden, partly allowed, or fully allowed transitions.

Table 8.1: Approximated oscillator strengths of allowed, partly allowed, and forbidden states.[234]

Condition	Approximate range of ϵ values in $M^{-1}cm^{-1}$
spin-forbidden	$10^{-5} - 10^0$
spin-allowed, dipole-forbidden	$10^0 - 10^3$
spin- and dipole-allowed	$10^3 - 10^5$

Further modulation of the transition probability and consequently of the intensity can be expected from the quadrupole moments, magnetic dipole moments and vibronic excitations (vibronic selection rule). The latter can modulate the oscillator

strength if the geometry changes due to the excitation and hence, electronic and vibronic excitations are present. In the following, only purely electronic excitations are considered. This approach is called the sudden approximation, in which the excitations occur under the assumption that no structural or orbital relaxation takes place.[238]

For absorption type spectroscopies (e.g., UV/Vis, XAS) as well as induced emission spectroscopies (e.g., XES), the absorption cross-section $\sigma_{ABS/XAS/XES}$ is given by Equation 8.6.[235, 237]

$$\sigma_{ABS/XAS/XES} = \frac{4\pi}{3c} E_{ex} \sum_{F} \sum_{\rho=x,y,z} |\langle F|\mu_{el}|I\rangle|^2 \delta(E_{FI} \pm E_{ex}) \tag{8.6}$$

E_{ex} are the excitation or emission photon energies, while E_{FI} are the energies between the initial and final states in the absorption or the photoluminescent processes. δ refers to the line-broadening mechanism arising from the lifetimes of the relevant final states, and c is the speed of light.

8.1 Band Gaps

Band gaps (BGs) are essential for the characterization of solid-state systems and are extensively studied properties. There are two main types of band gaps: the transport (trans.) and the optical (opt.) band gap. In the context of molecules, transport gaps are called fundamental band gaps.[239]

This section will first briefly introduce the different types of band gaps and how the width of the band gap plays a role in classifying materials. There are many difficulties in modeling and predicting the band gap of a material. To this end, the calculation of the different band gaps by DFT using HOMO-LUMO gaps, $\Delta-$SCF/DFT, and TD-DFT (TD = time-dependent) are discussed and distinguished. Then an approach to the band gaps with an EOM-CC (equation-of-motion CC) approach, namely bt-PNO-STEOM-CCSD, is explained. The section concludes with an overview of other ways to approach the band gaps. The different calculation methods are discussed in more detail than the concepts in the previous section of this part, as they are an integral component of a publication[51] that forms the basis for this work.

The transport gap is defined by the energy difference between the valence band and the conduction band. It quantifies the energy required to generate unbound free carriers, as it represents the difference between a system with an electron in the valence band and the same system with that electron transferred to the conduction band. In the conduction band, the electron is unbound and can move freely,

contributing to the electric current as a free carrier.

The energy separation between the valence and conduction bands in a system can be defined as the difference between the vertical ionization potential (IP) and the electron affinity (EA), as given by Equation 8.7.

$$\Delta E^{IP-EA}trans = IP - EA = [EN - 1 - E_N] - [E_N - E_{N+1}] \tag{8.7}$$

Where E_N is the ground state energy of a system with N electrons, and E_{N-1} and E_{N+1} are the corresponding energies with $N \pm 1$ electrons. IP is the minimum energy required to create a positive carrier (hole) in the valence band, or in other words, to remove an electron from the system. It is typically measured by ultraviolet photoelectron spectroscopy (UPS). EA is the minimum energy required to create a negative charge carrier (electron) in the valence band, or in other words, to add an electron to the system. It is typically measured by inverse photoemission spectroscopy (IPES). The transport gap is calculated from the two individual results.[239]

Figure 8.1 visualizes the concept of transport gap in terms of IP and EA along with the optical band gap.[239]

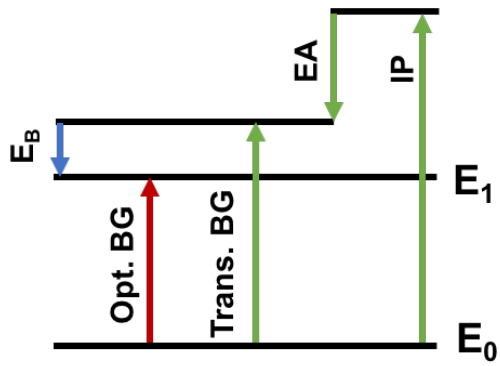

Figure 8.1: Schematic representation of the optical (opt.) and transport (trans.) band gaps (BG) in a solid-state system. Nomenclature: IP = ionic potential, EA = electron affinity, E_B = exciton binding energy, E_0 = ground state energy, E_1 = first excited state energy. Figure inspired by ref. [239].

The optical band gap refers to the energy difference between the ground state energy E_0 and the first excited state energy E_1. It is the minimum energy required for an electron to undergo an (allowed) optical excitation from the valence band to the conduction band. In this case, the excited electron remains electrostatically bound to the hole in the valence band it leaves behind.

The optical band gap is often determined by UV/Vis spectrophotometry and

can be derived from the resulting spectrum using methods such as the Tauc plot relation. It estimates the first excited state by linearizing the onset of the spectrum. The Tauc plot distinguishes between dipole-allowed and forbidden, and direct and indirect gaps. The difference between direct and indirect allowed optical band gaps is that for direct band gaps the crystal momentum does not change upon excitation as it does for indirect band gaps.[239–241] In the following, only direct optical band gaps are considered.

The key difference between the transport and optical band gaps is the behavior of the excited electron. In the optical band gap, the excited electron in the valence band remains attached to the hole it has created in the conduction band, whereas in the transport gap an electron moves from a bound state in the valence band to an unbound state in the conduction band. The electron-hole pair is considered a quasiparticle called an exciton. The energetic difference between the two band gaps is the electron-hole pair or exciton binding energy E_B (see Figure 8.1). In single molecules, E_B can be quite large (> 0.5 eV), while in molecular crystals it is usually smaller (about a few tenths of eV). For inorganic solids, which are the focus of this work, E_B decreases to a few meV. This can have the consequence that the optical excitation leads directly to a free carrier, and it can be assumed that opt. BG $\approx$ trans.BG.[239]

Due to their different definitions, the transport and optical band gaps provide complementary information about the electronic and optical properties of a material. The transport gap provides insight into charge transport behavior and the availability of free carriers, which is critical for electronic and electrical applications. In contrast, the optical band gap is relevant for understanding the absorption of light and the generation of optical excitations within the material, which is essential for optical and photonic applications. By considering both gaps, a more complete understanding of the material's behavior can be achieved.

Band gaps can be used to classify materials as conductors, semiconductors, or insulators. Conductors, such as metals, have a large number of free electrons that can easily move through the material and generate an electric current when an electric field is applied. In these materials, there is no energy gap between the valence and conduction bands, and therefore, no band gap.[100] In contrast, insulators have very few free electrons and high resistance to the flow of electric charge, preventing the movement of electrons and exhibiting low conductivity. Therefore, they have a large energy gap between the valence and conduction bands. Semiconductors are materials that exhibit electrical conductivity between conductors and insulators. Unlike conductors, semiconductors have a band gap in an energy range that allows optical excitations, thereby allowing the flow of electrons and contributing to the

intermediate conductivity of the semiconductor.[242] When exposed to photons or other forms of electromagnetic radiation, semiconductors can undergo electronic transitions across the band gap that promote electrons from the valence band to the conduction band.

While the definition of conductors in terms of the band gap is clear due to its absence (0 eV), the exact definition of the boundary between semiconductors and insulators is not universally agreed upon. Semiconductors have a band gap greater than 0 eV and depending on the reference less than 3 eV or 4 eV,[242, 243] since the interface between the UV and Vis spectral regions is approximately 3.2 eV. However, other sources report the boundary between the two material types to be around 5eV,[244, 245] or even higher. The insulators have band gaps of correspondingly higher energy. Some references define semiconductors not by a fixed band gap width, but simply as a substance with an electrical conductivity that increases with temperature.[100] At low temperatures, semiconductors behave more like insulators, while under certain conditions they conduct electricity. Either way, knowing the precise band gap of a material under certain conditions can provide valuable insight into its properties and potential applications. Therefore, methods for calculating band gaps are discussed below.

In computational protocols, the optical band gap is often approximated as the transport gap for solid-state systems. In turn, the transport gap is often approximated by the HOMO-LUMO gap. It is well known that MOs such as HOMO and LUMO correspond to one-electron wavefunction energies. IP and EA, or for that matter the excitation energy, are not one-electron problems but N and $N \pm 1$ electron problems. The Δ self-consistent field DFT ($\Delta-$SCF/DFT) approach can give a more accurate description. $\Delta-$SCF/DFT treats the transport gap by determining the three different ground state energies and concluding the transport gap via the previously introduced Equation 8.7. Koopmans' theorem states that in Hartree-Fock theory the negative energy ε_{i_N} of the HOMO of an N-electron system is equal to IP. Although Koopmans' theorem is less accurate for DFT, it is still qualitatively valuable. In this context, EA is often related to the LUMO with energy ε_{a_N}. Consequently, Equation 8.8 can serve as a first approximation to the energy of the transport gap across the hOMO-LUMO gap.[14, 15, 165, 246–248]

$$\Delta E_{trans}^{IP-EA} \approx \varepsilon_{a_N} - \varepsilon_{i_N} = \Delta\varepsilon_{i \to a} \tag{8.8}$$

The uppercase labels refer to many electron quantities, while the lowercase labels refer to one-electron quantities. In the ground state, i, j, k,... are doubly occupied and a, b, c,... virtual orbitals. Only closed-shell ground states are concerned for now. In practice, the given approximation has been proven to be an acceptable

approximation to calculate transport gaps.

At this point, the question arises of how the transport energy gap relates to the optical energy gap. In a first approach, it can be considered that the ground state E_0, as well as the first excited state E_1, are singlet states (S) so that E^{S_0} and E^{S_1} abbreviate the two energies of the states. $\Delta E_{opt}^{S_0 \rightarrow S_1}$ shortens their energy difference, the optical band gap energy. In DFT, this excitation process can also be approached with $\Delta-$SCF/DFT. The purification formula in Equation 8.9 determines the first excited state energy E^{S_1}.

$$E^{S_1} = 2E^{BS} - E^{T_0} \tag{8.9}$$

Here, T_0 is the zeroth triplet state, and BS is the broken-symmetry state, as defined in Equation 8.10.[249]

$$|\psi_{S_1}\rangle \, \alpha \, |i^\alpha i^\beta ... m^\alpha n^\beta\rangle - |i^\alpha i^\beta ... m^\beta n^\alpha\rangle \tag{8.10a}$$

$$|\psi_{T_0}\rangle \, \alpha \, |i^\alpha i^\beta ... m^\alpha n^\beta\rangle + |i^\alpha i^\beta ... m^\beta n^\alpha\rangle \tag{8.10b}$$

$$|\psi_{BS}\rangle \, \alpha \, |i^\alpha i^\beta ... m^\alpha n^\beta\rangle \, \alpha \, |\psi_{S_1}\rangle + |\psi_{T_0}\rangle \tag{8.10c}$$

The spin of each orbital is indicated by α and β, respectively. A more common approach to the first excited state with DFT is by utilizing TD-DFT. There are multiple TD-DFT approaches, which are all typical linear response approaches via perturbation of the ground state density. One of the phrasings used for the TD-DFT problem is Casida's Equation, which is a non-Hermitian eigenvalue problem given in Equation 8.11.[250]

$$\begin{bmatrix} A & B \\ B^* & A^* \end{bmatrix} = \Omega \begin{bmatrix} 1 & 0 \\ 0 & -1 \end{bmatrix} \begin{bmatrix} X \\ Y \end{bmatrix} \tag{8.11}$$

In this context, Ω represents the excitation energy, X and Y vectors of the occupied-virtual and virtual-occupied blocks of the first-order density response matrix, and A and B orbital rotation matrices defined in Equation 8.12.

$$A_{ia\sigma,jb\eta} = \delta_{ij}\delta_{ab}\delta_{\sigma\eta}(\varepsilon_{a_\sigma} - \varepsilon_{i_\eta}) + (a_\sigma i_\sigma | j_\eta b_\eta) - c_x \delta_{\sigma\eta}(j_\sigma i_\sigma | a_\sigma b_\sigma) + (a_\sigma i_\sigma | f_{\sigma\eta}^{xx} | j_\eta b_\eta) \tag{8.12a}$$

$$B_{ia\sigma,jb\eta} = (a_\sigma i_\sigma | b_\eta j_\eta) - c_x \delta_{\sigma\eta}(a_\sigma j_\sigma | b_\sigma i_\sigma) + (a_\sigma i_\sigma | f_{\sigma\eta}^{xx} | j_\eta b_\eta) \tag{8.12b}$$

$(...|...)$ are the two-electron repulsion integrals in the Mulliken notation, and $(...|f_{xc}|...)$ is the matrix of the exchange-correlation kernel in the adiabatic approximation of the orbitals with σ and η being spin variables. δ is the Kronecker delta, and c_x is a coefficient between zero and one. The third term in Equation 8.12a and

the second term in Equation 8.12b describe the contribution of the Hartree-Fock exchange part of the Kohn-Sham operator. If c_x is 0, this describes the limiting TD-DFT case in which pure DFT functionals are employed (e.g., (meta)-GGA or LDA), and if c_x is 1, it is TD-HF.

It can be shown that the optical energy gap $\Delta E_{opt}^{S_0 \to S_1}$ involving $i \to a$ long-range charge transfer (CT), core or Rydberg excitations in the presence of a hybrid functional ($0 < c_x < 1$) the excitation energy is given as Equation 8.13.[251, 252]

$$\Delta E_{opt}^{S_0 \to S_1} = \Delta \varepsilon_{i \to a} - c_x (ii|aa) \tag{8.13}$$

This is because, in practice, all the exchange integrals in Equation 8.12 vanish. The $(ii|aa)$ integrals, which represent the Coulomb integrals, are not small and can have values of several electron volts. Hence, the orbital energy difference $\Delta \varepsilon_{i \to a}$ (HOMO-LUMO gap) in Equation 8.13 does not approximate the state energy difference accurately. By inserting Equation 8.8 in Equation 8.13 the energy of the first excited singlet state can be approximated by Equation 8.14.

$$\Delta E_{opt}^{S_0 \to S_1} = \Delta E_{trans}^{IP-EA} - c_x (ii|aa) \tag{8.14}$$

This approximation shows that the energy of the first excited state and thus, the optical band gap does not approximate the energy difference between IP and EA and hence, the transport gap – unless a non-hybrid functional is considered.

In the $\Delta-$SCF/DFT approach, different sets of orbitals are used for each state of interest. Separate calculations optimize them. Hence, they can be orthonormal. This is not the case in TD-DFT. Only one set of orbitals is used; consequently, the computed states are orthonormal.

As an alternative to the shown DFT approaches, post-Hartree-Fock methods as Equation-of-Motion (EOM) coupled cluster (CC)[253–255] can be used to calculate band gaps. More specifically, the bt-PNO-STEOM-CCSD (back transformed-pair natural orbital-similarity transformed equation of motion-coupled cluster single double)[48–50, 256] method will be described since it will be the primary method besides TD-DFT used in Chapter 11.

Any EOM-CC approach includes a ground state calculation of a chosen CC level and the subsequent calculation of excited states with EOM. The EOM approach obtains excited states operating a linear excitation operator $\hat{R}_k$ as given in Equation 8.15.)[48, 49]

$$\hat{H} \hat{R}_k |\Phi_0\rangle = E_0 \hat{R}_k |\Phi_0\rangle \tag{8.15}$$

The linear excitation operator is defined for the excited state energy EE, IP, and

EA, respectively, as shown in Equation 8.16 with r being the excitation operator in respect to a specific virtual orbital indicated by its subscript and an occupied orbital indicated by the superscript.

$$\hat{R}_k^{EE} = r_0 + \sum_{i,a} r_a^i a^\dagger i + \sum_{i<j,a<b} r_{ab}^{ij} a^\dagger i b^\dagger j \tag{8.16a}$$

$$\hat{R}_k^{IP} = \sum_{i} r^i i + \sum_{b,j>i} r_b^{ij} b^\dagger j i \tag{8.16b}$$

$$\hat{R}_k^{EA} = \sum_{a} r_a a^\dagger + \sum_{j,a>b} r_{ba}^{j} b^\dagger j a^\dagger \tag{8.16c}$$

In bt-PNO-STEOM-CCSD, the ground state calculation is performed at the level of DLPNO-CCSD, as briefly described in Section 6.1. It replaces the Hamiltonian $\hat{H}$ with the similarity transformed Hamiltonian $\overline{H}$ in Equation 8.15. A second similarity transformation given in Equation 8.17 reduces the canonical expansion space of the excited states.[48, 49, 256]

$$G = \{e^{\hat{S}}\}^{-1}\overline{H}\{e^{\hat{S}}\} \tag{8.17}$$

$\hat{S}$ is a transformation operator for singles and doubles truncations parameterized in terms of IP and EA. This is the concept of STEOM-CC.

When bt-PNO-STEOM-CCSD was developed and at the time of the study in Chapter III, it was not feasible to transfer the DLPNO quantities to the excited states yet. Hence, before calculating the excited states via STEOM-CC, the DLPNO-CCSD ground state is back-transformed to the canonical basis (bt-PNO). Equation 8.18 summarizes the scheme.[48, 49]

$$d_{\overline{\mu}a\overline{a}_{ij}}^{ij} T_{\overline{a}_{ij}\overline{b}_{ij}}^{ij} d_{\overline{b}_{ij}\overline{\mu}}^{ij} \Rightarrow L_{\mu\overline{\mu}}^{ij} T_{\mu\overline{\nu}}^{ij} L_{\nu\overline{\nu}}^{ij} \Rightarrow C_{a\mu}^{ij} T_{\mu\nu}^{ij} C_{\nu b}^{ij} \Rightarrow T_{ab}^{ij} \tag{8.18a}$$

$$PNO \Rightarrow PAO \Rightarrow AO \Rightarrow MO \tag{8.18b}$$

The nomenclature in Equation 8.18 is identical to the one of Equation 6.15 on page 82.

By now, STEOM-DLPNO-CCSD[257] has been developed. In this case, the PNOs do not have to be back-transformed and can be used for the excited states, which makes the computational approach even more affordable and applicable to even larger systems.

Figure 8.2 symbolizes the expected accuracy of the introduced methods for calculating optical and fundamental band gaps. For the discussed methods, the EOM-CC methods have the potential to give the most accurate results due to their ex-

plicit treatment of electron correlation and because they do not suffer from the self-interaction error as the DFT-based methods do. This error leads to an anticipated underestimation of the band gaps. The use of hybrid or double-hybrid functionals might reduce this error. In general, all types of DFT functionals are applicable to TD-DFT. Figure 8.2 shows CIS additionally. As introduced in Section 6.1, CIS gives an approximation to the excited states but overestimates them systematically due to the lack of electron correlation. The results are comparable to the previously mentioned TD-HF.

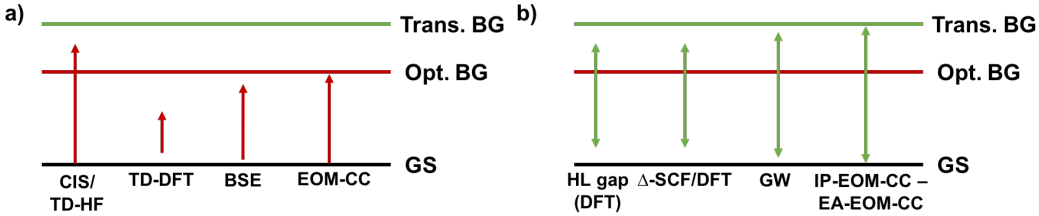

Figure 8.2: Schematic representation of the expected errors symbolized by arrows of different sizes in comparison for different single-reference methods for the calculation of **a)** optical (opt.) and **b)** transport (trans.) band gaps (BG). Nomenclature: GS = ground state, HL gap = HOMO-LUMO gap.

In periodic calculations, it is typical to approach the transport gaps either via the HOMO-LUMO gap or via $\Delta-$SCF/DFT. Another possibility is the GW approach, which uses the one-particle Green function (G) to describe the removal or addition of an electron to a system while accounting for the electron correlation with a dynamically screened Coulomb potential (W). There are GW approaches in combination with DFT (e.g., G0W0).[258] The optical band gap can be calculated using the Bethe-Salpeter equation (BSE). Using a result from a GW approach as a basis, in BSE the binding between the removed and added electron and thus, the exciton binding energy is included using Casida's equation similar to TD-DFT.[259] The GW and BSE approaches are not applied in this work, but respective results from the literature will be used later as a reference.

All methods, compared in Figure 8.2, are single-reference methods. If a system with a multiconfigurational ground state is approached, multireference methods are a better choice to obtain the excited states and hence, the optical band gap. A multiconfigurational method, as CASSCF introduced in Section 6.1, not only results in ground states but can generate in the same way excited states by mixing, instead of the ground state CSFs, the excited CSFs with higher excited determinants. CASSCF is likely to overestimate the optical band gap due to an incomplete description of the dynamic electron correlation, which is very important for the excited state de-

scription. By including perturbation via CASPT2,[201, 202] DCD-CAS(2),[203] or NEVPT2,[198–200] the CASSCF excited state energies could be improved. Another applicable method is MR-EOM-CC which is similar to the single-reference EOM-CC but based on the MR-CC approach mentioned in Section 6.1.[260] ICE-CI allows for the calculation of higher excited states, similar to CASSCF.[64, 65]

8.2 X-ray Emission Spectroscopy

X-ray emission spectroscopy (XES) is a relatively local and element-specific tool for structural analysis. Emission is a secondary process to an X-ray absorption process in which an electron is excited from the ground state $|G\rangle$ with N electrons into the energy continuum far above the absorption edge, resulting in a core-ionized state $|I\rangle$ with $N-1$ electrons. This state is the initial state of an X-ray emission process in which the hole created by the excited electron closes immediately ($\sim 10^{-15}s$) after its creation by an electron of a higher lying orbital.[261] This process emits a photon whose frequency is measured. The resulting state is called the final state $|F\rangle$.

Within the concept of sudden approximation (also known as the Koopman's theorem for inner shell ionization),[262] under core electron ionization conditions, the core-ionized initial state $|I_{N-1}\rangle$ of an $N-1$ electron system can be approximated by the ground state of the respective N electron system upon removing a core electron ($|I_{N-1}\rangle \approx |G^{+}_{N-1}\rangle$). The approach assumes a sudden single-photon ionization process so that no orbital relaxation can occur. As described above, the emission cross section σ_{XES} can be determined by Equation 8.6 (see page 92).

The so-called one-electron approach based on the DFT orbital energies provides a simplified computational approach to XES (and also to XAS and RXES) intensities. This approach's nature is based on the fact that in terms of TD-DFT, the orbital energies deliver a well-defined approximation to the state energies if no Hartree-Fock exchange is present in the DFT potential (see Section 8.1, Equation 8.13, page 97). This approach has the obvious drawback of not properly treating the multiplet structure of the final state manifold. In a nutshell, the ground $|G\rangle$, core-ionized initial $|I\rangle$, and final $|F\rangle$ states can be expressed in a single determinantal form as given in Equation 8.19.

$$|G\rangle = |i...j...n\rangle \tag{8.19a}$$

$$|I\rangle = |a...j...n\rangle \tag{8.19b}$$

$$|F\rangle = |a...i...n\rangle \tag{8.19c}$$

Here, i, j, k,... label occupied orbitals, and a, b, c,... label unoccupied orbitals. The difference between each $|I\rangle$ and $|F\rangle$ is the occupation of orbitals i and j so that the state energy difference ΔE is the DFT orbital differences $\Delta\varepsilon$ between i and j. Hence, Equation 8.20 follows, where ω_{IF}^{σ} is the transition frequency.

$$\Delta E_{IF} = \hbar\omega_{IF}^{\sigma} = \varepsilon_j^{\sigma} - \varepsilon_i^{\sigma} \tag{8.20}$$

In relevance to Equation 8.6, the absorption cross section for XES within the on-electron approach is provided by Equation 8.21.

$$\sigma_{XES}^{one-electron} = \frac{4\pi}{3c} E_{ex} \sum_{j_\sigma i_\sigma} \sum_{\rho=x,y,z} |\langle a_\sigma|\hat{\mu}_{el}|j_\sigma\rangle|^2 \delta(\varepsilon_j^{\sigma} - \varepsilon_i^{\sigma} \pm E_{ex}) \tag{8.21}$$

The nomenclature is in accordance to Equation 8.6. The index σ indicates the spin α or β. Further reasoning in regard to this approach is well documented elsewhere.[263]

Figure 8.3a shows the XES process schematically. The depicted case is a first-row transition metal complex or solid in which the $1s$ core orbital is ionized (K-edge XAS). This is the only case that will be considered exemplarily in the following. The orbital i describes the metal $1s$ core orbital, and j is either a semi-core metal orbital or a valence orbital.

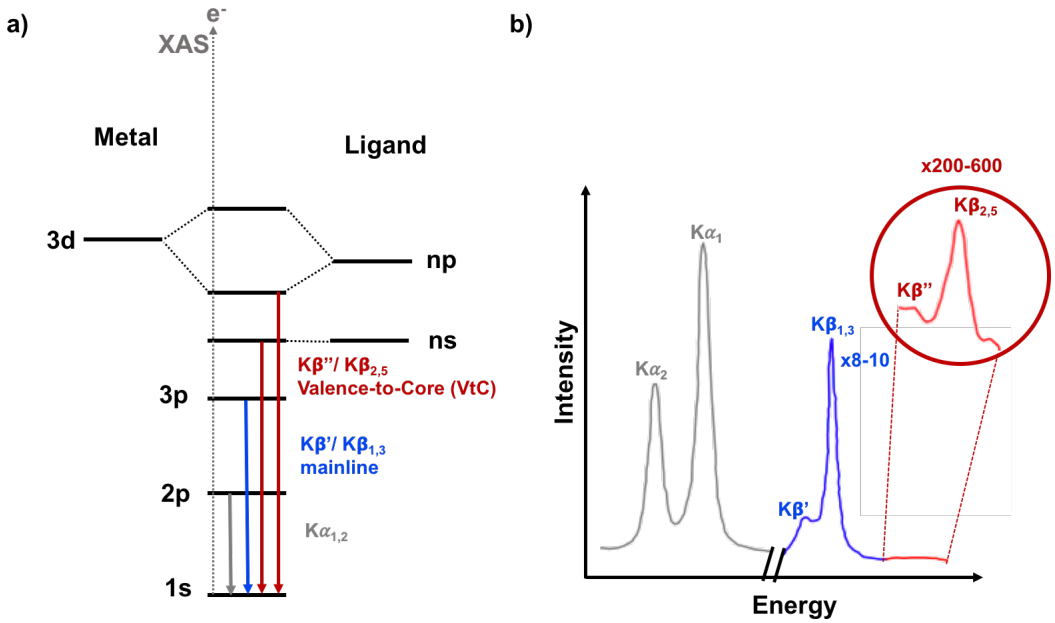

Figure 8.3: a) Schematic representation of the XES process resulting as a secondary process from a K-edge XAS and **b)** the corresponding XES spectra. Figure inspired by ref. [62].

In principle, three types of XES spectra can originate depending on the character of the orbital j. For j being a $2p$ metal orbital, the resulting spectrum is a $K_{\alpha_{1,2}}$ XES. For j being a $3p$ metal orbital, the resulting spectrum is a $K_{\beta_{1,3}}/K'_{\beta}$ XES, which is also called $K_{\beta_{1,3}}/K'_{\beta}$ mainline XES. And for j being a valence orbital (metal $3d$ or ligand valence orbital/ bonding orbital) the resulting spectrum is called $K_{\beta_{2,5}}/K''_{\beta}$ or valence-to-core (VtC) XES. Which transitions $i \rightarrow j$ are allowed specifically depends on the selection rules concerning the point group of the system introduced at the beginning of this section (see page 90 ff.). The transitions must be dipole-allowed, which is not the case for metal ns to metal $1s$ orbitals transitions for almost all point groups. This is why the presented emission scheme does not include these transitions.[62, 261]

Without going into further details concerning the origin of the different XES features, which will be discussed in detail in Chapter IV, it is important to note that SOC and multiplet effects play an essential role in XES. SOC can be regarded in the DFT calculations by incorporating the SOC operator in the computational protocol.[264] The multiplet effects cannot be described correctly.

A more rigorous approach to XES spectra computation is provided in the concept of wavefuction-based multiconfigurational approaches. In particular, it has been shown that even entry-level RASCI calculation, described in Section 6.1 (see also Figure 6.2 on page 78), can provide access to mainline XES spectra of small molecules with satisfactory performance.[53] In this framework, the emission process is only described precisely for the active space. For this type of protocol, typically, only the mainline is computed by including the singly occupied core $1s$ orbital as well as the $3p$ orbitals of the metal in the active space and allowing all possible CSFs describing the transitions from the $3p$ to the $1s$ orbital, while the metal $3d$ orbitals are included in the restricted active space. Alternatively, this can directly be transferred to CASCI, which allows including larger active spaces and approaching the VtC XES. In this case, all CSFs describing all desired final states and the core-ionized initial state are included in the active space. The resulting CSFs with different multiplicities can be mixed via SOC so that the multiplet effect is regarded. A detailed description of the computational protocol and how larger active spaces in the context of crystals in the electrostatic embedding approach can be addressed will be shown in Chapter IV.

Part III

Benchmark Studies of Spectroscopic Properties in Solid-State Systems

[. . .] If it disagrees with experiment, it's wrong. In that simple statement is the key to science. It doesn't make any difference how beautiful your guess is, how smart you are, who made the guess, or what his name is. If it disagrees with experiment, it's wrong. That's all there is to it. - Richard Feynman[265]

Introduction to Part III

This part is based on "Computation of NMR Shielding Constants for Solids Using an Embedded Cluster Approach with DFT, Double-Hybrid DFT, and MP2"[83] and "Accurate Band Gap Predictions of Semiconductors in the Framework of the Similarity Transformed Equation of Motion Coupled Cluster Theory"[51]. These projects aimed to develop computational protocols for calculating the observables of two standard experimental spectroscopic techniques used in solid-state analysis: solid-state nuclear magnetic resonance (NMR) for measuring chemical shifts, and optical spectroscopy for determining optical band gaps

The NMR study focuses on the calculation of the chemical shielding constants for nuclei in solid-state systems, followed by the determination of the corresponding chemical shifts. The optical band gap study concerns the calculation of the first optical excited state in solid-state systems, which directly determines the optical band gap.

The main goal of both studies was to establish predictive computational protocols that could accurately calculate these properties for crystalline solid-state systems in a straightforward manner. To this end, various theoretical levels, ranging from GGA DFT to post-Hartree-Fock methods, were combined with the electrostatic embedding approach to model these properties for a series of inorganic solid-state systems. This series served as a benchmark set to evaluate the performance of the electrostatic embedding approach for the calculation of these properties and in particular, to evaluate the performance of the different theoretical methods. Their performance was compared with each other and with experimental data, analyzing specifically their mean absolute errors. This comparative analysis allowed a comprehensive evaluation of the methods in terms of their accuracy and relative performance.

As described in the Part II, NMR shielding and band gap energies are chemical problems of different nature. The first is an electronic ground state property that requires an explicit treatment of nuclear-nuclear and nuclear-electron interactions. The second is an electronic excited state property that requires a precise treatment of electron-electron interactions, especially in the valence region. As a first step

in the development of the protocols, the general possibility of applying molecular methods in combination with the electrostatic embedding approach to crystalline solid-state systems must be explored. In this context, it is of interest to investigate whether these parameters can be determined with an accuracy threshold similar to that achieved in equivalent calculations on molecular chemical systems. In parallel, it is useful to investigate whether the results obtained with the embedded cluster approach converge with those obtained using periodic boundary conditions. The latter point will be investigated in the following only for the band gaps.

These two studies join and complement a larger group of several other studies showing that the results of different embedded cluster approaches can converge against their periodic counterparts[38, 40–43, 75, 81] and studies calculating NMR parameters using embedded cluster approaches[76–79]. The respective chapters below provide further details on the context of the two studies in terms of prior publications and developments specific to these two cases.

This section is organized as follows. The introductory chapter gives an overview of the selected benchmark study sets, which begins on page 107. Next, the NMR study is presented, starting on page 113. This is followed by the chapter on the band gap study, which is found on page 142. The final chapter, beginning on page 158, draws comparative conclusions from both studies and highlights key findings.

9 Introduction to the Solid-State Benchmark Study Set

The benchmark investigations in the NMR and band gap studies were performed on a selected set of crystalline inorganic solid-state systems. This set consists of inorganic semiconductors and insulators, mainly belonging to the rock salt and zinc blende space group, together with one orthorhombic system. Figure 9.1 shows all the systems included in the benchmark set. As an additional reference, a set of organic oligoacene semiconductors were included in the band gap study and are also visualized.

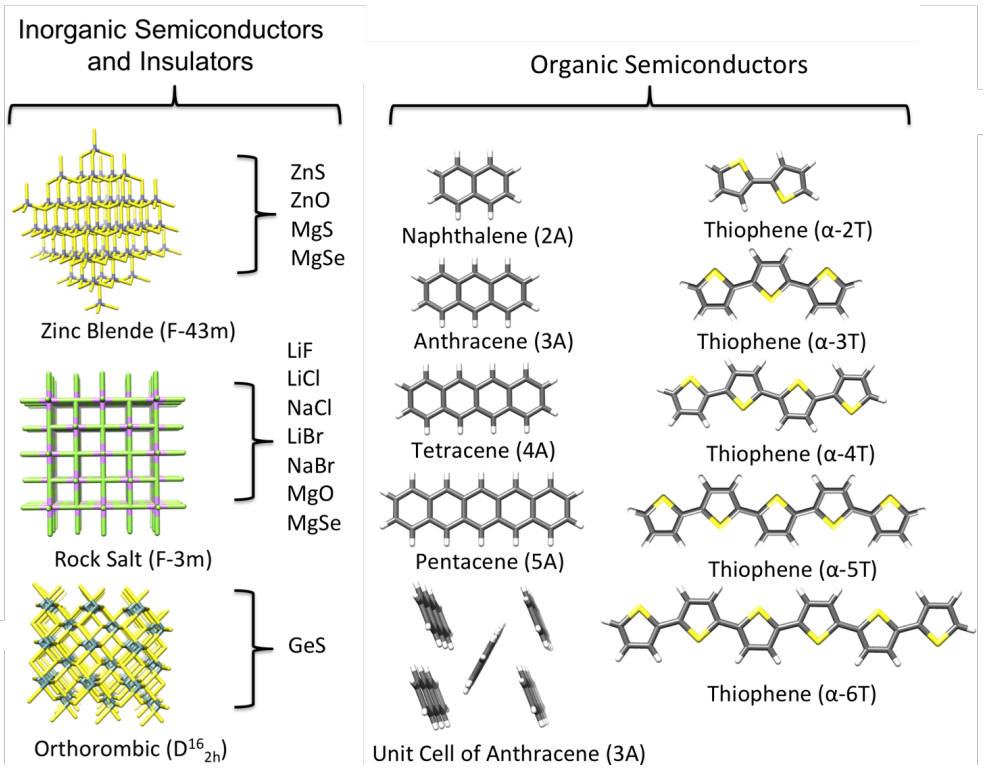

Figure 9.1: Benchmark set of inorganic and organic semiconductors and insulators.

Since the solid-state systems are modeled using the electrostatic embedded clus-

ter approach, QCs must be defined for each of these inorganic systems. Chapter 3 presented the QC series for the rock salt and zinc blende structures applicable to the respective systems in the present studies. These QC series were derived from the crystal structures shown in Figure 3.8 on page 40 and Figure 3.11 on page 43, respectively. In addition, Figure B.1 on page 314 in the appendix shows the QC series for the orthorhombic structure. These different QC series will play a crucial role in achieving convergence of the desired spectroscopic properties with respect to the corresponding system size. In the following chapters on NMR and band gap calculations, the convergence of the QC sizes with respect to the different properties will be discussed.

The next two chapters will also discuss the influence and optimization of the electrostatic environment in the electrostatic embedded cluster model for each of the two spectroscopic properties studied. Nonetheless, Table 9.1 already provides a comprehensive overview of the calculated charges used in the electrostatic embedded cluster models for each benchmark system. It also includes information on the space groups of their crystal structures and the corresponding bond lengths incorporated into the models. These data have been taken from CIF files containing experimentally determined structures and serve as the basis for the derived atomic coordinates of all systems. The CIF files are obtained from reliable sources such as the American Mineralogist Crystal Structure Database [266] or the Crystallography Open Database[118, 119]. Table 9.1 additionally indicates whether a particular system is part of the NMR or the band gap study. Also, Table B.1 on page 314 in the appendix compares the experimental bond lengths[118, 119, 266] used in the electrostatic embedded cluster calculations with the bond lengths optimized in periodic calculations from literature[267] for selected systems.

The development of the general embedding protocol for the "simple" embedded cluster approach[23, 268, 269] and the later development of the more elaborate Ionic-Crystal-QM/MM approach were primarily driven by the upcoming benchmark studies. Therefore, the models presented in the studies are modeled using the "simple" embedded cluster approach. However, some adjustments to the generalized protocols as presented in Chapter 3 have been made based on later insights and developments after the publication of these studies. As a result, the protocols used in the benchmark studies may differ in some respects from the generalized protocols. The studies presented may have benefited from the later findings and developments in the embedded cluster models. However, as each step has been carefully optimized and calibrated, the results remain robust and of general validity.

Table 9.1: Overview of all systems of the benchmark set, their space groups abbreviated with RS for Rock Salt (Fm-3m), ZB for Zinc Blende (F-43m) and OR for Orthorhombic, bond lengths in Å, information about participation in studies, calculated charges and experimental (exp.) parameters. NMR shift (δ) in ppm[270–273] and optical band gap (opt. BG) in eV (value in brackets: chosen reference).

System	Space Group	Bond Length	Charge	NMR	Exp. δ(Metal)	Exp. δ(Halide)	BG	Exp. opt. BG	Ref. exp. opt. BG
LiF	RS	2.022	±1.23	✓	-0.30 vs. $LiCl_{(aq)}$	-74.00 vs. $KF_{(s)}$	✓	11.60-14.20 (11.60)	[274–279]
LiCl	RS	2.586	±0.95	✓	-1.19 vs. $LiCl_{(aq)}$	1.31 vs. $KCl_{s)}$	✓	9.40	[278, 280]
LiBr	RS	2.745	±0.79	✓	-2.04 vs. $LiCl_{(aq)}$	64.74 vs. $KBr_{(s)}$	✓	7.60	[278]
NaF	RS	2.310	±1.10	✓	7.13 vs. $NaCl_{(aq)}$	-91.00 vs. $KF_{(s)}$	✗	-	
NaCl	RS	2.820	±0.93	✓	7.21 vs. $NaCl_{(aq)}$	-49.73 vs. $KCl_{(s)}$	✓	8.50-9.00 (8.97)	[276, 278, 281–283]
NaBr	RS	2.954	±0.86	✓	5.04 vs. $NaCl_{(aq)}$	-52.89 vs. $KBr_{(s)}$	✓	7.00-7.50 (7.50)	[276, 278, 284]
KF	RS	2.660	±1.05	✓	22.60 vs. $KCl_{(aq)}$	0.00 vs. $KF_{(s)}$	✗	-	-
KCl	RS	3.116	±0.90	✓	47.80 vs. $KCl_{(aq)}$	0.00 vs. $KC_{(s)}$	✗	-	-
KBr	RS	3.299	±0.78	✓	55.10 vs. $KCl_{(aq)}$	0.00 vs. $KBr_{(s)}$	✗	-	-
MgO	RS	2.109	±1.70	✓	26±1 vs. $MgSO_{(4)(aq)}$ 26.26±0.05 vs. $Mg(NO_3)_{2(aq)}$	-	✓	5.40-7.90 (6.21)	[285–289]
MgS	RS	2.830	±1.51	✓	-3±1 vs. $MgSO_{(4)(aq)}$ -1.11±0.02 vs. $Mg(NO_3)_{2(aq)}$	-	✗	-	
MgS	ZB	2.830	±0.80	✗	-	-	✓	4.50-5.50 (4.78)	[290–292]
MgSe	RS	2.073	±1.51	✗	-	-	✓	3.90	[293]
MgSe	ZB	2.937	±0.68	✗	-	-	✓	3.59-4.10 (3.81)	[293–299]
ZnO	ZB	2.315	±0.76	✗	-	-	✓	3.10-3.44 (3.44)	[300]
ZnS	ZB	2.673	±0.55	✓	-378 or -380.5 vs. $ZnSO_{4(aq)}$	-	✓	3.66-3.78 (3.78)	[296, 301, 302]
ZnSe	ZB	2.871	±0.50	✓	-273 or -276.3 vs. $ZnSO_{4(aq)}$)	-	✓	2.68-2.82 (2.82)	[295, 303–305]
GeS	OR	1.820/ 2.150	±0.47	✗	-	-	✓	1.54-1.74 (1.55)	[306–308]

The organic oligoacene semiconductors used in the band gap benchmark study are approximated as molecules without any electrostatic embedding, rather than actual molecular crystals. Due to the rigid nature of the oligoacene semiconductors,

the experimental and calculated energy gaps of the respective molecules are directly related to the band gap energies of the actual semiconductor.[309] At the time of the study, the molecular equivalent of Ionic-Crystal-QM/MM, namely Mol-Crystal-QM/MM, which could be applied to these types of organic semiconductors, had not yet been developed. Table 9.2 lists the experimental data of the organic semiconductors.

Table 9.2: Overview of organic semiconductor benchmark set including their crystal structure and optical (opt.) and fundamental (fund.) band gaps (BG) in eV.

System	Name	Crystal Structure	Opt. BG	Fund. BG
		Oligoacenes[310–312]		
2A	Naphtalene	P21 / α	4.14	8.19
3A	Anthracene	P21 / α	3.20	6.87
4A	Tetracene	P-1	2.54	5.51
5A	Pentacene	P-1	1.84	4.80
		α-Oligothiophenes[313]		
α-2T	Thiophene	P21 / α or P21 / c	4.11	7.70
α-3T	Thiophene	P21 /α or P21 / c	3.49	6.44
α-4T	Thiophene	P21 / α or P21 / c	3.18	5.76
α-5T	Thiophene	P21 / α or P21 / c	2.98	5.40
α-6T	Thiophene	P21 / α or P21 / c	2.87	3.20

The benchmark set of inorganic solid-state systems includes well-defined and closed-shell chemical systems consisting of main group and first-row transition metal elements with filled $3d$-shells. This selection ensures a diverse and reliable set of systems for evaluating the performance of computational protocols. In order to provide a comprehensive assessment, the benchmark set includes challenging elements, such as the highly electronegative fluorine,[314, 315], allowing for a deeper understanding of the design process of the electrostatic embedded cluster approach and the effectiveness of the protocol.

The bonding character within the benchmark set exhibits a range from strongly ionic, as observed in alkali metal halides and rock salt structures in general, to more covalent bonding, as observed in metal sulfides and zinc blende structures overall. The choice to include primarily rock salt and zinc blende structures is justified by their characteristic local point groups, namely octahedral and tetrahedral, respectively. These point groups are commonly found in a wide variety of crystal structures. In addition, systems such as MgS and MgSe, which can occur in both crystal structure types, provide insight into the influence of geometries and bond types on

the performance of computational protocols.

For the NMR study in particular, the benchmark set of inorganic crystals provides nuclei ranging from very light, e.g. Li, to rather heavy, e.g. Br, nuclei. Consequently, the associated nuclear shielding constants cover a range of values from small to large. The influence of the total number of electrons and possible consequences can be studied.

The nuclear shielding constant is not an experimentally observable quantity, but the chemical shielding - the difference between two shielding constants - is. The selected benchmark set allows to test the accuracy and sensitivity of the calculation protocol, since it contains significantly small shifts close to 0 ppm and large shifts up to about 100 ppm. The halides have a wider overall range with typically larger shifts that differ significantly within a group of halides (F, Cl, Br). They tend to be highly shielded and should be less sensitive to small environmental changes. As such, they provide a solid foundation for the overall functionality of the calculation protocol.

The alkali metal cation groups (Li, Na, K) are the opposite of the halides due to their strongly cationic nature, making them highly deshielded. Their shielding is expected to be sensitive to small environmental changes, and their shifts are typically close to zero and not significantly different from each other. Therefore, these cations are computationally challenging and may indicate shortcomings in the calculation protocols.

Error compensation within the shift calculation can be an issue and may mask potential problems. In cases where the bonding character differs between two reference systems of a shift, as is the case with MgS and MgO, further information can be obtained in this regard.

For the band gap study, the benchmark set of inorganic crystals covers a wide range of band gap magnitudes from about 1.5 eV to 11.6 eV. The rock salt structures generally have band gaps greater than 6 eV, while the zinc blende and orthorhombic structures have band gaps less than 6 eV. In particular, wide band gap semiconductors and insulators can be computationally challenging.[11, 12, 316] This is especially true for LiF, which not only has the largest band gap of the benchmark set, but also contains the problematic element fluorine.

All inorganic crystals are expected to have a dipole-allowed and direct first excited state. In this respect, the optical band gap is easy to identify, allowing one to focus on the model and methods rather than the band gap itself. Figure 9.2 shows the excitation diagrams in the one-electron picture for LiCl and ZnS, representing all rock salt and zinc blende systems, respectively. The models assume O_h ligand field coordination around the centers in the rock salt crystals and T_d coordination around

the centers in the zinc blende crystals. The first excited state, which is the optical band gap, has a ligand-to-metal charge transfer (LMCT) character in both cases.

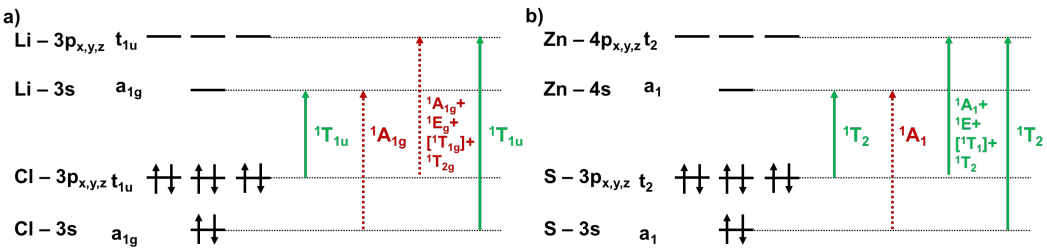

Figure 9.2: Excitation scheme of **a)** LiCl and **b)** ZnS adopted in a one-electron picture assuming an O_h ligand field coordination environment around Li or Cl centers and a T_d one around the Zn or S centers. Color-coded arrows: dipole-allowed transitions (green solid arrows), dipole-forbidden transitions (red dashed arrows).

The additional set of organic semiconductors can further distinguish the selected methods for the computation of band gaps concerning different materials and can potentially indicate deficiencies in the embedded cluster benchmark set as they are not embedded.

10 Benchmarking NMR Shielding Constants for Solid-State Systems: A Comparative Study Using DFT, Double-Hybrid DFT, and MP2

10.1 The Context and Aim of the NMR Study

As mentioned in the previous chapters, multiple high-precision methods applicable to molecules are not directly transferable to periodic boundary calculations and consequently, to solid-state property calculations. That is no different for the NMR nuclear shielding constants shortened with NSC in the following. NSCs are primarily computed at the DFT level of theory in the framework of periodic boundary conditions.[232, 317, 318] That approach became widely popular for computing NSCs only after developing the gauge-including projector augmented wave (GIPAW) scheme.[319] GIPAW NSC calculations are performed conventionally by employing GGA functionals. Hybrid density functionals offer improved accuracy for NSCs predictions but at computational costs that are orders of magnitude larger than the respective GGA calculations utilizing plane wave basis sets and limiting the method's applicability.[76, 232, 320–322] Plane wave post-HF methods are currently under development,[24, 26, 27, 323, 324] and periodic boundary condition methods employing Gaussian basis sets have been devised and are currently applied with growing success.[325–327] Nevertheless, they are not yet applicable to the broader calculations of NSCs.

On the contrary, for molecular systems, a large variety of electronic structure methods are employed to compute NSCs, which range from Hartree-Fock (HF)[231, 328, 329] and Density Functional Theory (DFT)[330–332] to post-HF wavefunction-based methods like the Møller-Plesset second-order perturbation theory MP2[332–335] and Coupled Cluster theory (CC).[336–339] Although conventional CCSD and CCSD(T) methods are presently only applicable to small molecules due to the steep

scaling of the canonical methods with system size, they have been used to construct reference data sets and evaluate the performance of HF, DFT and MP2 based methods in computing NSCs.[332, 340–342] These studies have shown that for NMR applications which require a computational approach with predictive power, post-HF methods like the CC-hierarchy are recommended because they are robust and systematically improvable. MP2 provides the best balance between accuracy and computational cost, performing best compared against reference CCSD(T) concerning a variety of common GGA, meta-GGA, and hybrid DFT functionals.[332, 340] At the MP2 level and in the framework of the local correlation approaches and the use of the resolution of identity approximation RI[342, 343] access to NSC computations for systems with a few hundred atoms has been achieved. In combination with linear and sublinear scaling techniques, even larger systems can be treated.[344–346]

Focusing on DFT, it has been demonstrated that NMR-specialized functionals like KT2[347] have satisfactory performance for computing NSCs although not for their separate dia- and paramagnetic components, due to its flawed description of the density.[348] Recently, it has been shown that NSCs can be efficiently computed by employing double-hybrid functionals in the framework of gauge-including atomic orbitals (GIAOs).[314, 332] In particular, it has been found that in benchmark calculations, the dispersion corrected spin-component-scaled DSD-PBEP86 functional yields chemical shifts with an accuracy superior to MP2.[332]

For NMR NSCs, various cluster approaches have been adopted.[76–79] However, up to the point of this study and similar to the solid-state studies utilizing periodic boundary conditions, these approaches were carried out exclusively at the DFT level of theory employing GGA and hybrid density functionals. Recalling the importance of the NMR experimental studies in the field of solid-state materials and heterogeneous catalysis,[349, 350] there is an urgent need for improving and extending the employed computational protocols for NMR properties, and this is where the study at hand aims to contribute.

In this work, the performance of bare and embedded cluster computational protocols, performed at the MP2 level and with a variety of DFT methods, will be evaluated for their efficiency and ability to compute NMR nuclear shielding constants on a study benchmark set of inorganic crystalline solid-state systems.

In particular, it will be shown that by employing carefully designed embedded clusters that can afford large quantum mechanical regions ingrained in point charge fields, the cluster size converges for the studied systems at all levels of theory. The influence of the employed basis sets on the computed NSCs on bare and embedded clusters is investigated using specialized NMR basis sets at different levels of theory. Based on the cluster size and basis set convergence, the best-performing calculation

protocol is employed to investigate the performance of MP2 and various DFT methods to compute NSCs across the study set of inorganic solids. For a series of small clusters, DFT and MP2 results are compared to CCSD(T) computed NSCs. Please note that the NCSs are absolute values as they can be computed via electronic structure methods, while chemical shifts are relative values w.r.t. a standard. In a final step, results obtained using these protocols are compared to experimental chemical shifts, and a detailed error analysis is performed. It will be revealed that, provided sufficiently large clusters are employed, the results can be considered insensitive to the chosen embedding scheme such that the residual error of the method, namely basis set and level of theory, dominate the residual error of the calculation.

10.2 General Computational Details

Non-relativistic calculations were performed with the ORCA 4.2 suite of programs[351] on a chosen study set with and without the electrostatic embedding approach. The NSCs were evaluated at the RI-MP2 and DFT levels of theory using the pcSseg-X (X = 1–4) basis sets[233] optimized for NMR shieldings. Additionally, basis sets of type def2-XVP (X = S, TZ, QZ)[142] and cc-pVXZ (X = D, T, Q)[144] were tested. The ORCA calculations were accelerated by using the RI approximation for the Coulomb integrals (RI-J),[352] while the exchange terms were computed using the "chain-of-spheres" (COSX) approximation.[353, 354] Hence, auxiliary basis sets had to be included. The def2/JK[355] and def2-XVP/C (X=S,T,Q)[356, 357] auxiliary basis sets were used for RI-J and RI-MP2, respectively. All NMR DFT computations were carried out in the framework of standard, established, uncoupled approximation for DFT.[358–362]

Various DFT functionals were employed, ranging from (meta) generalized gradient approximation (GGA) to hybrid functionals and double-hybrid functionals. The GGA functionals were KT2,[347] BLYP,[213, 214, 222] PBE,[212] and the meta-GGA functionals TPSS[222] and M06L.[213, 363] The test set of hybrid functionals included M06,[217] B3LYP,[213, 214, 218] PBE0,[212, 364] and TPSSH,[220–222], and the double-hybrid functionals B2PLYP,[223] DSD-PBEP86[225, 226] and DSD-BLYP.[224] As mentioned above, besides DFT, MP2 calculations were performed. For evaluation, HF calculations were also included.

Comparison calculations employing HF, MP2, and CCSD, as well as CCSD(T), were performed with the CFOUR package[365] and pcSseg-X (X = 1–3) basis sets[233] without the electrostatic embedding.

NSCs, including scalar relativistic effects and spin-orbit coupling (SOC) on prototype non-embedded systems, were computed using the DIRAC19 computational

package.88 A two-component Barysz-Sadlej-Snijders (BSS)[366–369] Hamiltonian for relativistic Kohn–Sham density functional theory was used. This includes non-collinear spin magnetization and involves London atomic orbitals to ensure gauge-origin independent results. The DIRAC calculations were obtained with the PBE0[212, 364] functional, and the triple-zeta basis set dyall.ae3z.[370, 371] These computations capture the essential effects of the presence of heavy atoms and the NMR chemical shielding constants of adjacent light atoms. In order to obtain the relativistic corrections, the shieldings are computed with BSS, including two-electron spin-orbit corrections by default and with the spin-free[372] version of BSS, excluding the spin-orbit corrections only giving the scalar relativistic influence. The results are compared to the non-relativistic shieldings computed with the same method by changing the speed of light to 2000 a.u..[373]

Further details and example input files for NSC calculations with ORCA, CFOUR, and DIRAC19 can be found in the appendix in Section B starting on page 314.

10.3 Dependence of the Nuclear Shielding Constants on Different Model Parameters

Section 3.2 introduced a basic approach toward a proper electrostatic embedding protocol for a model with stable energy and orbital descriptions approaching solid-state character. Thereby, two strategies for quantum clusters (QC) were introduced. One strategy is the "supercell" (SCe) approach, in which the resulting clusters contain building units that correspond to the crystallographic unit cell. The other one is the spherical cluster" (SCl) approach, whereby the cluster expands spherically around a chosen center with complete coordination (i.e., octahedral O_h or tetrahedral T_d in the rock salt or zinc blende systems, respectively). Both approaches are expected to ultimately lead to the same results for a given property if they are appropriately embedded, as demonstrated previously for the HOMO-LUMO gap of NaCl (see Figure 3.9, page 41).

This section will first address the general influence of the electrostatic environment on the computation of NSCs, and second, the influence of the different QC types and sizes on named property. These investigations will be discussed based on the established model of NaCl. Both points will ultimately answer whether the electrostatic embedding approach, as applied here, leads to stable NSCs corresponding to the bulk of a crystal.

10.3.1 Influence of the Electrostatic Embedding Environment

The general influence of the embedding environment (BR, PC) on the NSCs computed for the QC is tested for small system sizes of SCe ($[Na_4Cl_4]^0$) and SCl ($[NaCl_6]^{5-}$). Table 10.1 shows the results. Introducing one layer of ECPs around the QC significantly influences the NSCs. One of the tasks of the ECPs is to dampen the dangling bonds on the surface of the QC. By that, it already balances the charge inside the QC towards a more homogeneous distribution. The results reflect this behavior.

In the charged $[NaCl_6]^{5-}$ and the neutral $[Na_4Cl_4]^0$, the NSC of Cl rises from the bare QC to the embedded one. This increase can be ascribed to the overall higher charge density in the cluster due to the embedding and the lower delocalization of the Cl electrons. The same effect can also be seen in Na in $[Na_4Cl_4]^0$. An additional reason contributing to this gain could originate from the change from a more covalent bond between Na and Cl due to the surface effect of the bare cluster towards a more ionic character in the embedded cluster. In contrast, the NSC of Na decreases in $[NaCl_6]^{5-}$ by introducing the electrostatic embedding. In the bare cluster of $[NaCl_6]^{5-}$, Cl shields Na more since Na is at the cluster's center and has a higher charge excess. The charge is "pulled out" of the center and distributed more homogeneously by introducing the embedding.

Table 10.1: Computed NSCs in ppm of Na and Cl in $[NaCl_6]^{5-}$ and $[Na_4Cl_4]^0$ with different electrostatic environments. Level of theory: PBE/pcSseg-2.

$[NaCl_6]^{5-}$	no embedding	1 ECP layer	1 ECP and 1 PC layer	1 ECPs and 2 PC layer	1 ECP layer, 10,000 PCs
NSC(Na)	558.74	546.90	550.76	549.82	550.21
NSC(Cl)	1042.21	1086.66	1091.62	1090.86	1091.18
$[Na_4Cl_4]^0$	no embedding	1 ECP layer	1 ECP and 1 PC layer	1 ECPs and 2 PC layer	1 ECP layer, 10,000 PCs
NSC(Na)	570.76	583.77	583.61	583.63	583.63
NSC(Cl)	1059.61	1085.50	1085.12	1085.17	1085.16

The number of necessary PC layers for a stable result of NSCs for the charged cluster, and the neutral cluster differs significantly. While for $[Na_4Cl_4]^0$, one PC layer appears to be enough to get a stable result, its charged counterpart needs at least three PC layers. For consistency, in all cases, the QC is embedded in about 10,000 PCs in the following. For the charged QC, a more significant number of PCs

is necessary to balance out the charges due to the high formal charge of the QC. While this is more of a technicality, the small number of PCs needed for the neutral cluster indicates that the long-range electrostatic effects effectively seem not to have a strong influence on the shielding of the atoms. From this perspective, only the local effects of the charges on their direct neighbor have a dominant impact.

In the next step, exemplarily, the influence of the electrostatic embedding on the different Na sites in the larger neutral QC $[Na_{32}Cl_{32}]^0$ is investigated. Previously, Figure 3.17 (see page 49) introduced the nomenclature of the different sites (top, edge surface, and bulk) concerning this model. Figure 10.1 reintroduces it in addition to visualizing the nomenclature transferred to the SCl example $[Na_{19}Cl_{44}]^{25-}$. Figure 10.2 shows the NSCs of different Na sites in the QC and their electrostatic charges (CHELPG) for the electrostatically embedded and bare QC.

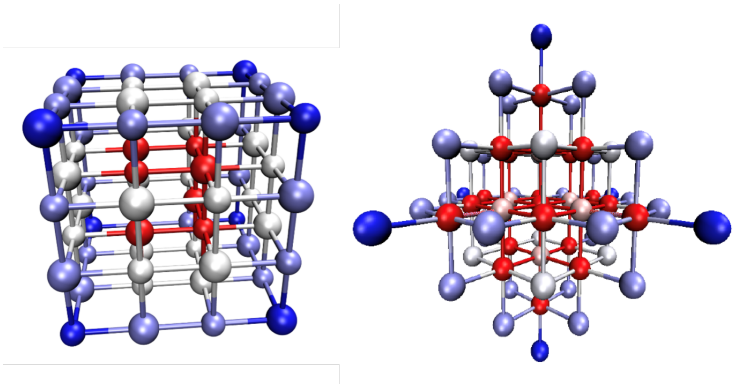

Figure 10.1: Nomenclature for the example of the quantum clusters $[Na_{32}Cl_{32}]^0$ and $[Na_{19}Cl_{44}]^{25-}$. Centers with different chemical environments are denoted with color code: tip (blue), edge (purple), surface (grey), and bulk (red). Small spheres: Na, large spheres: Cl.

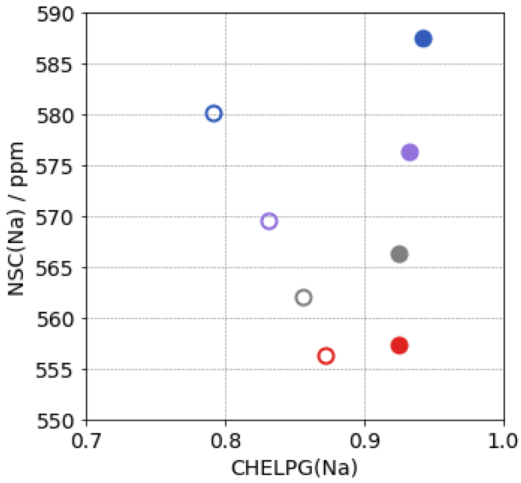

Figure 10.2: NSCs vs. electrostatic charges (CHELPG) for the different Na sites in the quantum cluster ($[Na_{32}Cl_{32}]^0$) treated within the electrostatic embedded cluster approach (full circles) or as a bare neutral cluster (non-embedded, empty circles). Color code: tip (blue), edge (purple), surface (grey), and bulk (red).

The influence of the electrostatic embedding environment on the charge distribution within the QC was already a topic of Section 3.2 and also visualized in the previously mentioned Figure 3.17. The results in Figure 10.2 are in agreement with the prior. As expected, the electrostatic embedding distributes the charge homogeneously and is approaching typical solid-state behavior. The bare QC indicates the behavior of nanoparticles. It has lower charges overall, decreasing from the bulk to the tip.

However, the NSCs show the same trend in the bare and electrostatic embedded clusters. In both cases, the shielding increases with decreasing coordination number (CN) from the bulk (CN = 6) to the tip (CN = 3) position. Due to the higher charge in the embedded cluster model, the shielding is higher than in the bare cluster. The difference between the NSCs in the two models decreases with increasing CN. In the bulk position, they only defer by less than 1.2 ppm for the embedded and non-embedded clusters by absolute NSCs in the range of 555 ppm to 590 ppm.

The charges applied are the optimized charges ±0.93. By varying the charge by 0.1, the NSC of Na changes by less than 0.06 ppm. Hence, the applied charge magnitude seems not to have a significant influence. For Cl, a similar picture is obtainable.

It should be noted that this study aims to compute the NSC as a bulk property of the crystals. Among the different sites, the bulk position of the QC represents the correct chemical environment for the calculations. Based on the previous results, this makes the size of the QC regarding shift convergence more crucial than the

charge balance itself. Despite this, the electrostatic embedding environment is still essential for the correct convergence of the clusters. For highly charged QCs, this is especially critical, as discussed in Section 3.2.

10.3.2 Convergence of the Cluster Size

The following discusses the convergence and choice of the size of QC. For this purpose, different system sizes are studied for the SCe, and SCl approaches. A sequence of SCe type of clusters $[Na_nCl_n]^0$ with $n = 1 - 50$, as well as Na-centered $[NaCl_6]^{5-}$, $[Na_2Cl_{10}]^{8-}$, $[Na_4Cl_{16}]^{12-}$, $[Na_6Cl_{19}]^{13-}$, $[Na_{19}Cl_{44}]^{25-}$, and $[Na_{44}Cl_{19}]^{25+}$ as well as Cl-centered $[Na_6Cl]^{5+}$, $[Na_{10}Cl_2]^{8+}$, $[Na_{16}Cl_4]^{12+}$, $[Na_{19}Cl_6]^{13+}$, $[Na_{44}Cl_{19}]^{25+}$, and $[Na_{19}Cl_{44}]^{25-}$ SCl type of clusters were studied. Section 3.2 introduced and visualized this series of the rock salt structure in Figure 3.8 (see page 40) already. The series of the zinc blende clusters, also included in this study, is visualized in Figure 3.11 (see page 43).

Figure 10.3 shows the convergence schemes of the different sites of Na and Cl in SCe and SCl clusters. For SCe, the embedded and non-embedded cases are shown, while for SCl, only the embedded one is presented. Due to the high formal charge of the SCl clusters, the non-embedded models were excluded from the study.

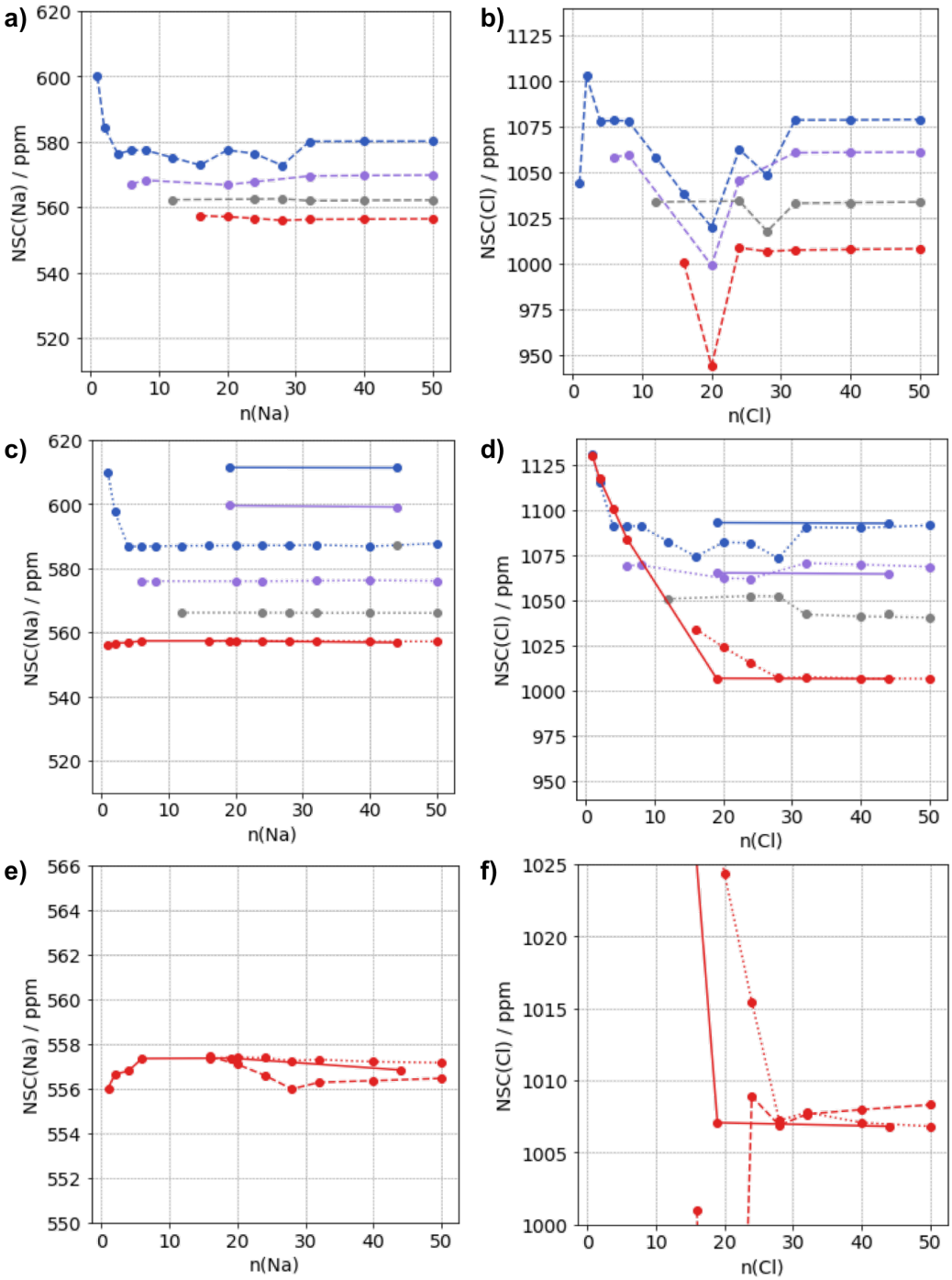

Figure 10.3: NSCs of Na (left) and Cl (right) in NaCl for a sequence of **a)** and **b)** bare SCe clusters (dashed line) and **c)** and **d)** embedded SCe (dotted line) and SCl clusters (solid line). **e)** and **f)** Comparison of NSCs of bare (dashed line) and embedded SCe (dotted line) and embedded SCl clusters (solid line) at the bulk cluster position. Color code: tip (blue), edge (purple), surface (gray), and bulk (red). Level of theory: PBE/pcSseg-2.

The observation that the NSCs of the bulk position in cluster size $[Na_{32}Cl_{32}]^0$ is approximately independent of the electrostatic embedding holds for the other neutral SCe model sizes with the premise that the shielding of the atoms on the bulk is converged (see Figure 10.3 and for just the bulk convergence see Figure 10.3c). Nonetheless, the already mentioned effects of the electrostatic embedding lead to more consistent results and faster convergence than the bare clusters. This is primarily true for positions differing from the bulk position. The effect is more pronounced for Cl than for Na. The statements above are transferable to the other tested systems. In all cases, the effect is less pronounced for the metal. The importance of the electrostatic embedding for a smooth and consistent convergence can especially be seen for cluster size $[Na_{20}Cl_{20}]^0$. For the non-embedded system, the effects of the positions that are different from the bulk influence the shielding of the bulk position significantly. Not surprisingly, such an effect is not present in the embedded cluster equivalent.

Besides the general difference in importance of the embedding environment, the convergence schemes of the computed NSCs differ for Na and Cl. In the SCe approach, the NSCs of the Na bulk positions converge for the smallest cluster size possessing a bulk position, the QC $[Na_{16}Cl_{16}]^0$. In the SCl approach, the NSC of Na can be accepted as converged for the smallest cluster size $[NaCl_6]^{5-}$. In $[NaCl_6]^{5-}$, Na holds bulk position immediately due to the six coordinating Cl's. The computed NMR NSC only differs by about 1 ppm from the larger $[Na_6Cl_{19}]^{13-}$. For Cl, the bulk position in the SCe approach converges for cluster size $[Na_{32}Cl_{32}]^0$ and in the SCl approach for size $[Na_6Cl_{19}]^{13-}$. The results imply that Na only needs one sphere of surrounding Cl. However, Cl needs not only one sphere of Na but also the next adjacent Cls. An indication for the latter is the build-up of the QC structure around a Cl at a bulk position. This shows the series from $[[Na_6Cl]^{5+}$ to $[Na_6Cl_{19}]^{13-}$ as well as from $[Na_{16}Cl_{16}]^0$ to $[Na_{32}Cl_{32}]^0$. The change of the NMR NSC of Cl appears to be linear for both cases in the bulk and converges at the end point of the two series quite abruptly as it reaches a full set of next Cl neighbors (see Figure 10.3b and Figure 10.3c).

If the system size is converged, the two approaches, SCe and SCl, lead to the same results for the bulk positions. That validates both approaches and the embedding approach in general for the computation of these NMR properties. As the NSC convergence is conditioned by a complete set of neighbors and neighbors-neighbors but not by the total size of the cluster, it is recommendable to choose the SCl approach over the SCe approach. The converged SCl cluster sizes have, in total, a smaller number of atoms due to the higher bulk-to-surface ratio. Hence, this approach is computationally more affordable.

The convergence scheme appears transferable from NaCl to the other rock salt structures tested and transfers similarly to the zinc blende structures. For comparison, Figure B.2 in the appendix visualizes the convergence procedure for the example of the less ionic system MgS.

As a general approach for the rock salt structures, the results suggest that it is recommendable to apply for the computation of the NSCs of the more negatively charged halides Y cluster sizes $[M_6Y_{19}]^{13-}$. It is advisable to employ the identical cluster size for the metals M. For the zinc blende series it is recommendable to use cluster size $[Zn_4Y_{10}]^{12-}$. Table 10.2 presents the converged, largest, and smallest cluster size of the different tested systems.

Table 10.2: Cluster sizes that were employed to compute the DFT and MP2 NMR parameters.

System	Smallest Cluster Tested SCl/SCe	Largest Cluster Tested SCl/SCe	Converged Cluster Metal SCl/SCe	Converged Cluster Halide/Chalcogenide SCl/SCe
LiBr	$[LiBr_6]^{5-}$/ $[LiBr]^0$	$[Li_{19}Br_{44}]^{25-}$/ $[Li_{62}Br_{62}]^0$	$[Li_6Br_{19}]^{13-}$/ $[Li_{16}Br_{16}]^0$	$[Li_6Br_{19}]^{13-}$/ $[Li_{32}Br_{32}]^0$
LiCl	$[LiCl_6]^{5-}$/ $[LiCl]^0$	$[Li_{19}Cl_{44}]^{25-}$/ $[Li_{62}Cl_{62}]^0$	$[Li_6Cl_{19}]^{13-}$/ $[Li_{16}Cl_{16}]^0$	$[Li_6Cl_{19}]^{13-}$/ $[Li_{32}Cl_{32}]^0$
LiF	$[LiF_6]^{5-}$/ $[LiF]^0$	$[Li_{19}F_{44}]^{25-}$/ $[Li_{62}F_{62}]^0$	$[Li_6F_{19}]^{13-}$/ $[Li_{16}F_{16}]^0$	$[Li_6F_{19}]^{13-}$/ $[Li_{32}F_{32}]^0$
NaBr	$[NaBr_6]^{5-}$/ $[NaBr]^0$	$[Na_{19}Br_{44}]^{25-}$/ $[Na_{62}Br_{62}]^0$	$[Na_6Br_{19}]^{13-}$/ $[Na_{16}Br_{16}]^0$	$[Na_6Br_{19}]^{13-}$/ $[Na_{32}Br_{32}]^0$
NaCl	$[NaCl_6]^{5-}$/ $[NaCl]^0$	$[Na_{19}Cl_{44}]^{25-}$/ $[Na_{62}Cl_{62}]^0$	$[Na_6Cl_{19}]^{13-}$/ $[Na_{16}Cl_{16}]^0$	$[Na_6Cl_{19}]^{13-}$/ $[Na_{32}Cl_{32}]^0$
NaF	$[NaF_6]^{5-}$/ $[NaF]^0$	$[Na_{19}F_{44}]^{25-}$/ $[Na_{62}F_{62}]^0$	$[Na_6F_{19}]^{13-}$/ $[Na_{16}F_{16}]^0$	$[Na_6F_{19}]^{13-}$/ $[Na_{32}F_{32}]^0$
KBr	$[KBr_6]^{5-}$/ $[KBr]^0$	$[K_{19}Br_{44}]^{25-}$/ $[K_{62}Br_{62}]^0$	$[K_6Br_{19}]^{13-}$/ $[K_{16}Br_{16}]^0$	$[K_6Br_{19}]^{13-}$/ $[K_{32}Br_{32}]^0$
KCl	$[KCl_6]^{5-}$/ $[KCl]^0$	$[K_{19}Cl_{44}]^{25-}$/ $[K_{62}Cl_{62}]^0$	$[K_6Cl_{19}]^{13-}$/ $[K_{16}Cl_{16}]^0$	$[K_6Cl_{19}]^{13-}$/ $[K_{32}Cl_{32}]^0$
KF	$[KF_6]^{5-}$/ $[KF]^0$	$[K_{19}F_{44}]^{25-}$/ $[K_{62}F_{62}]^0$	$[K_6F_{19}]^{13-}$/ $[K_{16}F_{16}]^0$	$[K_6F_{19}]^{13-}$/ $[K_{32}F_{32}]^0$
MgO	$[MgO_6]^{10-}$/ $[MgO]^0$	$[Mg_{19044}]^{50-}$/ $[Mg_{62062}]^0$	$[Mg_6O_{19}]^{26-}$/ $[Mg_{16}O_{16}]^0$	$[Mg_6O_{19}]^{26-}$/ $[Mg_{32032}]^0$
MgS	$[MgS_6]^{10-}$/ $[MgS]^0$	$[Mg_{19}S_{44}]^{50-}$/ $[Mg_{62}S_{62}]^0$	$[Mg_6S_{19}]^{26-}$/ $[Mg_{16}S_{16}]^0$	$[Mg_6S_{19}]^{26-}$/ $[Mg_{32}S_{32}]^0$
ZnS	$[ZnS_4]^{6-}$	$[Zn_8S_{19}]^{22-}$	$[Zn_4S_{10}]^{12-}$	-
ZnSe	$[ZnSe_4]^{6-}$	$[Zn_8Se_{19}]^{22-}$	$[Zn_4Se_{10}]^{12-}$	-

Since the difference in the computed NSCs between $[M_6Y_{19}]^{13-}$ or $[M_6Y_{19}]^{26-}$ and $[MY_6]^{5-}$ or $[MY_6]^{10-}$ is not significant for the more ionic systems, it is also possible to use them for the computation. Table 10.3 shows that this difference is more significant for more covalent systems such as MgS. The smaller system sizes enable the use of a higher level of theory and therefore, more accurate and computationally expensive methods. In line with recent studies,[374] it is possible to compute the size effect between the smaller and larger system size with a less expensive method and correct the result of the higher method on a smaller cluster in this regard. However,

such corrections are empirical and hence, not used in the following. As indicated in Table 10.3, such a correction might be method dependent and thus, could introduce an additional source of error.

Table 10.3: Difference of NSCs of M in ppm computed with pcSseg-2 between $[MY_6]^{5-}$ and $[M_6Y_{19}]^{13-}$. Bolt values are significant errors.

	Li			Na			K		Mg		
	Br	Cl	F	Br	Cl	F	Br	Cl	F	O	S
HF	0.28	0.60	0.52	0.58	0.32	0.72	-0.62	**-1.03**	**-3.96**	**1.16**	**-13.10**
KT2	0.18	0.50	0.57	**1.46**	**1.31**	0.61	**1.52**	-0.88	**-7.15**	**-4.94**	**-3.61**
M06L	0.38	0.78	0.8	0.19	-0.35	-0.72	-0.13	**-1.10**	**-6.99**	**2.36**	**-17.04**
BLYP	0.20	0.50	0.41	**1.11**	0.95	0.36	0.80	**-1.33**	**-7.50**	**3.98**	**-3.41**
PBE	0.19	0.49	0.41	**1.18**	**1.00**	0.20	0.82	**-1.48**	**-7.44**	**4.41**	**-4.08**
TPSS	0.24	0.59	0.52	**1.01**	0.82	-0.05	0.34	**-1.70**	**-5.89**	**4.27**	**-5.87**
M06	0.12	0.46	0.58	0.47	0.20	0.84	0.51	-0.70	**-6.86**	**3.47**	**-18.61**
B3LYP	0.20	0.51	0.43	**1.02**	0.84	0.47	0.49	**-1.17**	**-6.41**	**3.34**	**-6.31**
PBE0	0.20	0.51	0.44	**1.00**	0.80	0.31	0.32	**-1.35**	**-6.05**	**3.47**	**-7.57**
TPSSH	0.24	0.59	0.51	0.95	0.75	0.03	0.21	**-1.61**	**-5.56**	**3.9**	**-6.96**
MP2	0.29	0.66	0.60	0.81	0.63	0.54	-0.34	**-1.32**	**-5.66**	**1.65**	**-10.77**
DSD-PBEP86	0.30	0.62	0.67	0.56	0.38	0.04	**-1.01**	**-2.03**	**-6.55**	**2.05**	**-9.51**
DSD-BLYP	0.26	0.58	0.58	**1.67**	0.33	0.09	**-1.05**	**-2.06**	**-6.61**	**1.85**	**-9.36**
B2PLYP	0.14	0.58	0.57	0.61	0.42	-0.07	**-1.18**	**-2.08**	**-6.96**	**2.27**	**-7.91**

Although the absolute difference between two cluster sizes might differ for two different methods, their convergence scheme is identical, as a comparison of Figure 10.3 and Figure B.2 reveals. They show the NaCl cluster size convergence computed with PBE and MP2, respectively. Hence, it is possible to converge the NSCs of different systems with a computationally less demanding method (e.g., PBE) and subsequently apply more demanding methods (e.g., MP2).

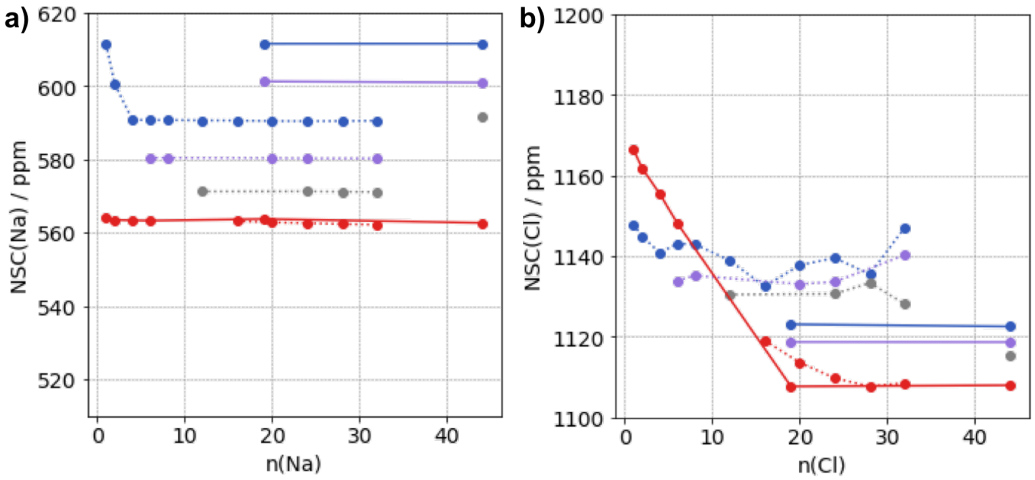

Figure 10.4: NSCs of **a)** Na and **b)** Cl for NaCl for a sequence of embedded SCe (dotted line) and SCl (solid line) clusters. Color code: tip (blue), edge (purple), surface (grey), and bulk (red). Level of theory: MP2/pcSseg-1.

10.4 Influence of the Level of Theory on Nuclear Shielding Constants

This section examines the influence of different parameters, such as the basis set size and the influence of relativistic effects concerning the different methods and nuclei types. Additionally, the different methods are compared to CCSD and CCSD(T).

10.4.1 Basis Set Size

To investigate how far the results obtained using a given basis set are from the complete basis set limit for different methods, increasing basis set sizes are employed for (meta-)GGA, hybrid, and double-hybrid functionals, and MP2. Figure 10.5 visualizes the results of the examples Na and Cl in the clusters $[NaCl_6]^{5-}$ and $[[Na_6Cl]^{5+}$, respectively, for the basis set type pcSseg-X with X = 1-4. The NSCs are computed with the representatively chosen functionals PBE, PBE0, and DSD-PBEP86, as well as MP2. For Na, the data indicates that the basis set can be considered converged for pcSseg-2 concerning all methods. For Cl, this is likewise true for PBE and PBE0. For DSD-PBEP86 and MP2, the larger basis set pcSseg-3 is necessary.

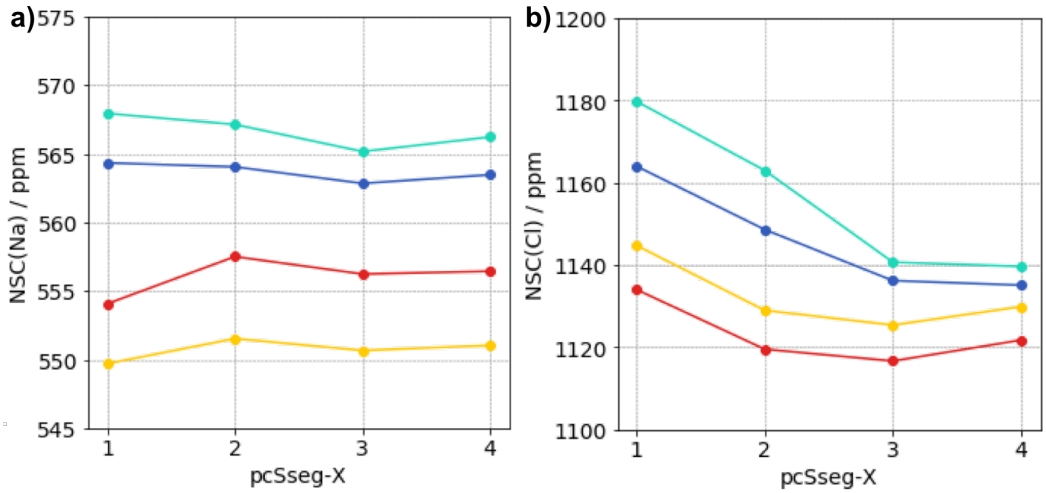

Figure 10.5: NSCs of **a)** Na in embedded $[NaCl_6]^{5-}$ and **b)** Cl in embedded $[Na_6Cl]^{5+}$ clusters for increasing pcSseg-X basis set size calculated with PBE (yellow), PBE0 (red), DSD-PBEP86 (blue), and MP2 (turquoise).

The visualized results are representative of most systems of the benchmark set. For the majority of metals, the basis set pcSseg-2 is sufficient for all types of functionals and MP2. An exception is zinc which needs at least the basis set pcSseg-3. For most halides, pcSseg-2 is sufficiently close to the basis set limit for (meta-)GGA and hybrid functionals, while double-hybrid functionals and MP2 need at least pcSseg-3. The behavior of the double-hybrid functionals is generally in between the hybrid functionals and MP2. For NaCl in Figure 10.5, the NSC of Cl decreases from pcSseg-2 to pcSseg-3 by 12.40 ppm for DSD-PBEP86. For the same step, it decreases by 3.59 ppm for PBE and by 22.30 ppm for MP2. In the appendix, Table B.2 (see 322) shows the difference between the results obtained with pcSseg-2 and pcSseg-3 for all methods and systems. It reveals that M06 and M06L give the most inconsistent results in this regard.

Besides pcSseg-X, the basis set types cc-pVXZ and def2-XVPP were tested. Especially for the halides and zinc, both do not show clear convergence. Figure 10.6 shows that the convergence improves with decontraction of the basis sets, but it increases the total number of basis functions significantly and hence, the computational demand. The pcSseg-X basis sets are optimized for NMR, and their results with contracted basis sets do not differ significantly from the decontracted ones. In the appendix, Table B.3 (see page 323) gives the difference between NSCs computed with contracted and decontracted pcSseg-2 for all methods and systems. Again, the results show that the outcomes of M06 and M06L are most inconsistent. For the basis set type of pcSseg-X, a higher basis set is more beneficial than a decontracted one

(compare Table B.2 and Table B.3). That is why the contracted basis set pcSseg-3 is used in the following.

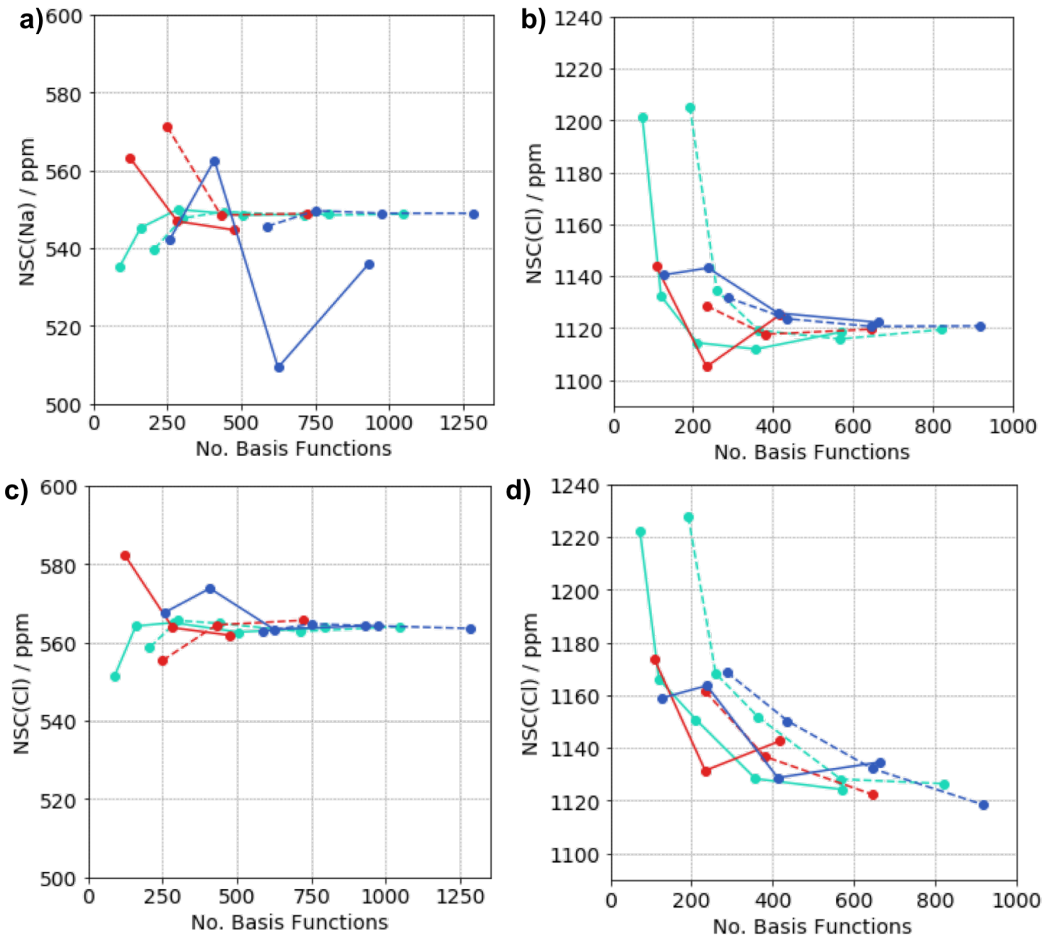

Figure 10.6: NSCs of Na in embedded $[NaCl_6]^{5-}$ computed with **a)** PBE and **b)** MP2 and Cl in embedded $[Na_6Cl]^{5+}$ computed with **c)** PBE and **d)** MP2 calculated with contracted (solid line) and decontracted (dashed line) basis sets: pcSseg-X (turquoise), def2-XVPP (red), and cc-pVXZ (blue).

10.4.2 Residual Error of MP2 and Double-Hybrid DFT with Respect to CCSD(T)

In this study, the highest level of theory applied to compute NSCs is MP2, followed by double-hybrid functionals. Since MP2 is not the "gold standard" for the description of electron correlation, it is uncertain how far the NSC results are converged concerning this description. To investigate the residual error in this regard, the NSCs computed with MP2 are compared to NSCs computed with CCSD and CCSD(T). At the time of the presented study, CCSD and CCSD(T) calculations for

NMR parameters were unavailable with the ORCA suite of programs. Thus, the calculations were carried out with the CFOUR package without the electrostatic embedding environment. This kind of evaluation is eligible on the one hand because the results computed with ORCA 4.2 are in good agreement with the results computed with CFOUR with the same methods, and on the other hand, because the investigated NSCs are the ones of the atoms in the center of the QCs. As demonstrated above, the electrostatic embedding is more crucial for the atoms in positions differing from the bulk of the QC region.

Figure 10.7 illustrates the results for HF, MP2, CCSD, and CCSD(T) computed with basis set pcSseg-2 for the central atoms Na and Cl in the small clusters $[NaCl_6]^{5-}$ and $[[Na_6Cl]^{5+}$, respectively. Additionally, it shows the results of the GGA functional PBE, the hybrid functional PBE0, and the double-hyrbid functional DSD-PBEP86 to compare the convergence in the definition of Perdew's "Jacob's Ladder". These results embody all pcSseg-X basis set sizes since the overall trend appears independent of the size (see Figure B.3 on page 318 in the appendix). It is also representative of the trend in the different alkali metal halides. Table B.4a to Table B.4f in the appendix (see page 324) show the results for the systems $[MX_6]^{5-}$ and $[M_6X]^{5+}$ computed with the different methods and basis set sizes and with and without embedding

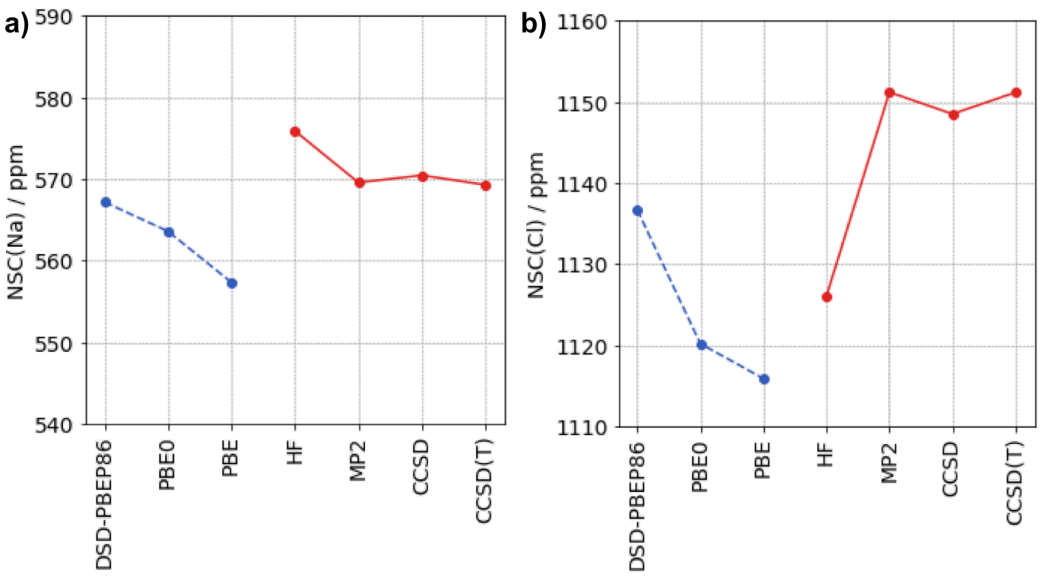

Figure 10.7: NSCs of **a)** Na in non-embedded $[NaCl_6]^{5-}$ and **b)** Cl in non-embedded $[[Na_6Cl]^{5+}$ for different methods. Dashed blue line: PBE, PBE0, DSD-PBEP86, and solid red line: HF, MP2, CCSD, CCSD(T). Basis set: pcSseg-2.

The behavior visualized in Figure 10.7 shows the importance of the correct treat-

ment of electron correlation for the computation of NSCs and demonstrates at the same time that MP2 reproduces significant good results in comparison to CCSD(T). This is in agreement with earlier studies.[332, 375] Although this can partly be accounted to error compensation at this level, it indicates that the MP2 calculations have predictive power.

The chosen set of DFT functionals demonstrates from the GGA to the double-hybrid functional more monotonous convergence towards CCSD(T). Only the double-hybrid functional yields results approaching the range of post-HF methods qualitatively. As mentioned in the context of Figure 10.5, the double-hybrid functionals deliver NSCs between the hybrid functionals and MP2 quantitatively.

10.4.3 Relativistic Effects

Besides the already discussed effects that could influence the computed NSCs, relativistic effects can also be a source of error. That is especially the case for heavier elements.[376] At the point of the study, NMR parameter calculations, including relativistic effects, were not available with the ORCA suite of programs. Hence, the computational protocol has to neglect them. A calculation series of non-embedded clusters studies and assesses the possible relativistic effects using the DIRAC19 computational package. The clusters are $[MX_6]^{5-}$ for the alkali metals and $[M_6X]^{5+}$ for the halides (where M= Li, Na, K, and X= F, Cl, Br) and $[MgO_6]^{10-}$, $[MgS_6]^{10-}$, $[ZnS_4]^{6-}$ and $[ZnSe_4]^{6-}$ for Mg and Zn. Table 10.4a and Table 10.4b give the outcomes for the halides and metals, respectively. The results are obtained by applying a two-component BSS Kohn-Sham Hamiltonian, including SOC, together with the PBE0 hybrid functional and the basis set dyall.ae3z. The respective non-relativistic calculations are carried out by changing the speed of light accordingly. Table B.5 on page 326 in the appendix portrays that the influence of the basis set size on the relativistic effects is small.

As expected, the relativistic effects increase for the alkali metals from Li to K and for the halides from F to Br. The heaviest elements (Se and Br) have sizeable effects of two kinds. The first one is the effect of heavy atoms shielding heavy atoms (HAHA effect), and the second is the one of heavy atoms shielding light atoms (HALA effect).[377–381] For example, the NSC series of Br in LiBr, NaBr, and KBr show the HAHA effect. The scalar relativistic effects excluding SOC (NSCs increase between 579 ppm and 586 ppm) and total relativistic effects including SOC (NSCs increases between 584 ppm and 580 ppm) are of similar magnitude in all cases. Consequently, the expectation is that the order of the NSCs from LiBr to KBr and therefore, the order of resulting chemical shifts will not change if the relativistic effects are disregarded.

Table 10.4: Non-relativistic computed NCSs and two-component Hamiltonian BSS relativistic correction for a series of non-embedded model systems for **a)** metals and **b)** halides without embedding. Level of Theory: PBE0/dyall.ae3z.

a)	Non-relativistic in ppm	Scalar Relativistic in ppm	Relativistic with SOC in ppm	ΔNon-relativistic: Scalar relativistic in %	ΔNon-relativistic: Relativistic with SOC in %
$[LiF_6]^{5-}$	121.2	121.6	121.6	0.33	0.41
$[LiCl_6]^{5-}$	97.5	97.9	98	0.41	0.51
$[LiBr_6]^{5-}$	95.7	96.2	97	0.42	1.36
$[NaF_6]^{5-}$	628.5	646	646	2.78	2.78
$[NaCl_6]^{5-}$	573	590.7	588	3.09	2.62
$[NaBr_6]^{5-}$	566.5	584.6	579.4	3.18	2.26
$[KF_6]^{5-}$	1298.3	1387.5	1387.5	6.87	6.87
$[KCl_6]^{5-}$	1281.2	1370.3	1369.1	6.95	6.86
$[KBr_6]^{5-}$	1238.5	1331.8	1317.6	7.53	6.39
$[MgO_6]^{10-}$	560.7	581.6	584.4	3.71	4.21
$[MgS_6]^{10-}$	590.5	612.6	599.2	3.74	1.47
$[ZnS_4]^{6-}$	1560.2	1891.4	1910.8	21.23	22.54
$[ZnSe_4]^{6-}$	1582.9	1923	2054.8	21.49	29.81
b)	Non-relativistic in ppm	Scalar Relativistic in ppm	Relativistic with SOC in ppm	ΔNon-relativistic: Scalar relativistic in %	ΔNon-relativistic: Relativistic with SOC in %
$[[Li_6F]^{5+}$	423.4	432.9	433	2.24	2.27
$[[Na_6F]^{5+}$	441.2	453.7	453.5	2.83	2.79
$[[K_6F]^{5+}$	307.9	321.7	321	4.48	4.25
$[[Li_6Cl]^{5+}$	1095	1160.3	1160.5	5.96	5.98
$[[Na_6Cl]^{5+}$	1121.7	1189	1188.5	6.00	5.96
$[[K_6Cl]^{5+}$	985.8	1055.5	1054.4	7.07	6.96
$[[Li_6Br]^{5+}$	3025.3	3607	3609	19.23	19.29
$[[Na_6Br]^{5+}$	3081.9	3667.7	3669.1	19.01	19.05
$[[K_6Br]^{5+}$	2847.2	3426.2	3427.1	20.34	20.37

The Na series of NaF, NaCl, and NaBr is an example that displays the HALA effect. The NSCs increase in all cases between 17.5 and 18.0 ppm by only including the scalar relativistic correction. If SOC is included, the NSCs decrease concerning the scalar relativistic results from 0.0 ppm for the lightest halide (NaF) to 5.2 ppm for the heaviest one (NaBr). Since the overall NSCs are lower for Na than for the heavier elements, as notable in the discussed results of the Br series and the values

of NSCs, in particular of NaCl and NaBr, are in direct proximity to each other, the influence of the SOC effect could be significant. This could change the order of the shieldings and consequently, the order of the chemical shifts. Equivalently, this could happen in the Li series regarding LiCl and LiBr. ZnS, in comparison to ZnSe, depicts a similar effect.

The numbers above suggest that the relativistic effects, if they become large enough, can significantly affect the computed NSCs. These effects are similar within a group of systems. The most significant change is due to the SOC effect on lighter atoms interacting with heavier ones. However, the numbers can only be used as an indicator but not as a final relativistic correction for three reasons. First, further calculations indicate that the relativistic effects are somewhat size-dependent, although they appear converged after introducing one whole sphere of neighbors around the center in question (see Figure B.4 on page 319 in the appendix). Nevertheless, the numbers could still change with increasing system size. Second, the models are not embedded. Although the atom in question is usually in the model's center and accordingly, is not significantly influenced by the embedding effects, this could still fine-tune the numbers. Third and most important, the computed relativistic effects are method-dependent.

The results above are based on a two-component BSS Hamiltonian. Table B.6 to Table B.9 in the appendix (see pages 327 to 330) summarize the results of further calculations obtained with the exact two-component (X2C) Hamiltonian,[382, 383] the four-component Hamiltonian LVCORR,[384] and the unrestricted kinetically balanced four-component Hamiltonian URKBAL.[385] They include additionally non-relativistic results computed with the four-component Hamiltonian LEVY-LEBLOND[386] for comparison. These calculations all indicate the same trend as discussed above, but the magnitudes of the effects differ significantly. For example, using the two-component Hamiltonian X2C instead of BSS would change the shifts from NaF to NaBr from the range of 17.5 ppm to 12.8 ppm to the range of 2.9 ppm to 5.4 ppm. The scalar relativistic effect of X2C is only between 2.9 ppm and 3.4 ppm, and the SOC effect increases from NaF to NaBr by 0.0 ppm to 2.0 ppm. For BSS, the SOC effect changes from 0.0 ppm for NaF to -5.2 ppm for NaBr.

On the one hand, this example shows that the scalar relativistic effect for X2C and BSS shifts the NSCs for NaF, NaCl, and NaBr. On the other hand, it shows that the magnitude of the scalar relativistic effect is significantly different for the two methods. This is similar for the SOC effect. NaBr has the highest SOC effect and NaF the lowest for both methods. However, the two methods differ in magnitude and regarding the sign.

10.5 Method dependence of the Computed Nuclear Shielding Constants and Comparison to Experiment

After discussing multiple effects that could influence the outcome of the calculations, in this section, the defined set of DFT functionals and MP2 are tested concerning their performance in computing NSCs and chemical shifts of the complete benchmark set of solids and compared to experiments. The computed NSCs are absolute values, while the experimental shifts are relative to a particular standard. A relative shift can be computed from the NSCs using another NSC as a standard. Doing this without prior evaluation of the absolute values could eliminate essential aspects from the calculation results or introduce error compensation without being able to reflect on its origin. For satisfactory agreement with experiments, the computation requires either accurate and robust NSCs or good error compensations reflected by large deviations of NSCs, but minor deviations by their difference. In general, better methods should converge to consistent NSC values and accurate chemical shifts as a consequence. A comparison of the NSCs allows approaching this statement.

Therefore, in a first step, the relative positions and order of the computed NSCs are compared to each other and the experimental shifts. The results will be discussed separately for the group of halides (F, Cl, and Br) and for the group of alkali metals (Li, Na, and K) in the alkali metal halides as well as for Mg and Zn in their respective systems to differentiate between the different challenges of these groups. Based on the discussions above, the NSC calculations are carried out on the cluster sizes $[M_6Y_{19}]^{13-}$ for the alkali metal halides, $[Mg_6Y_{19}]^{26-}$ for the magnesium systems, and $[Zn_4Y_{10}]^{12-}$ for the zinc systems. The basis set is going to be pcSseg-3. The chemical shifts computed from the NSCs are compared to the experimental values in a second step.

10.5.1 Method Dependence of Halide Nuclear Shielding Constants

The analysis starts with the halides series. The shielding is high in halides. Hence, they are rather insensitive to small changes in the immediate environment than other systems. Consequently, they can be a good indicator of general problems and characteristics of the different methods. Figure 10.8 illustrates the computed NSCs of the three halides using various methods. The primary y-axis (left) gives the computed NSCs, while the experimental relative values are on the secondary y-axis (right). For the hybrid functionals and (meta-)GGA functionals, M06 and M06L are the most significant outliers. That can likely be accounted to errors in the de-

scription of the core region and is consistent with recent discussions.[332, 387–389] Even by excluding these two outliers, MP2 and double-hybrid functionals give more consistent results than the other functionals. Their range of computed NSCs is the lowest. This is especially the case for the potassium halides, which are highly inconsistent in the range of the DFT functionals. Overall, the hybrid functionals give more consistent results than the (meta-)GGA functionals.

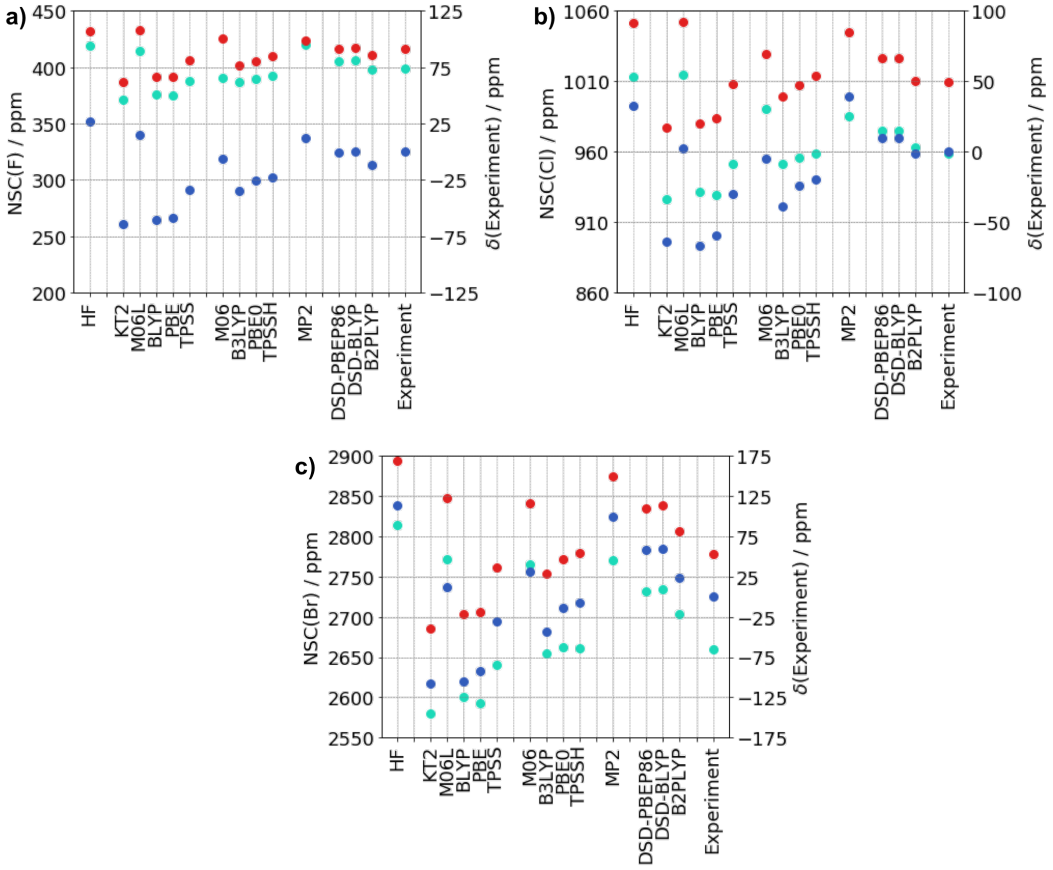

Figure 10.8: NSCs (left, primary y-axis) of the halides Y in $[M_6Y_{19}]^{13-}$ for **a)** $[M_6F_{19}]^{13-}$, **b)** $[M_6Cl_{19}]^{13-}$, and **c)** $[M_6Br_{19}]^{13-}$ vs. experimental chemical shifts δ (right, secondary y-axis). Basis set: pcSseg-3.

For the double-hyrbids, NaCl and LiCl have a similar range as KCl, making a better error compensation possible. The ranges differ in the cases of hybrid functionals and (meta-)GGAs leading to more inconsistent results, which also shows for F and Br. The range of computed NSCs of KCl with (meta-)GGA – excluding M06L – has a magnitude of about 40.3 ppm; for hybrid functionals – excluding M06 – it is 21.3 ppm, and for double-hyrbid functionals, it is only 11.3 ppm.

The order of the NSCs concerning the experimental shifts is predicted correctly for all cases and methods with two exceptions. The first exceptions are M06 and

M06L, which predict the order of KBr and LiBr wrong. The second exception is HF, which predicts the order of LiCl and KCl incorrectly. The error carries on in all DFT functionals. Only MP2 is able to predict the order adequately. Although the incorrect order is reflected in the double-hybrid functionals as well, the distance between the NSCs of LiCl and KCl is significantly decreasing compared to the other DFT functionals due to the influence of MP2. The prediction of the correct order of LiCl and KCl is tricky since the experimental shifts of LiCl and KCl are very close. The experimental shift of LiCl is -1.3 ppm regarding the standard KCl (0.0 ppm), and their computed NSC magnitudes range between 900 ppm and 1060 ppm. Hence, a difference of 1.3 ppm is relatively small.

10.5.2 Method Dependence of Alkali Metal Nuclear Shielding Constants

In contrast to the halides, alkali metals are highly deshielded and hence, significantly more sensitive to small environmental changes. Also, the experimental shifts do not differ significantly, as visible in the listed experimental shifts in Table 9.1 on page 109. As mentioned regarding the shift of LiCl relative to KCl, a small appearing error in the NSC can have relatively large consequences in the resulting shielding, especially if the shift itself is tiny. This issue is apparent in the Na and Li series. In both cases, the range of chemical shifts amounts to less than 2 ppm. Li's computed average shielding constant is about 92 ppm, and Na's about 560 ppm. Based on these averaged values, an NSC error of 1% for Li would lead to a chemical shift error of about 46%. An NSC error of 1% for Na would amount to a chemical shift error of about 280%.

Figure 10.9 shows that no method accurately predicts the relative positions and order of the NSCs concerning the experimental chemical shifts. In the case of Li, within a method, all calculated NSCs are within 1 ppm relative to each other and differ from the respective experimental chemical shifts by less than 2 ppm. A similar picture presents the case of Na. The absolute values of the computed NSCs lie within 4 ppm to 5 ppm by employing (meta-)GGA functionals, within 3 ppm for hybrid functionals, and below 2 ppm for MP2 and double-hyrbid functionals. In both cases, none of the methods employed has the sensitivity to predict such slight chemical shift differences precisely. Besides the residual error of the electron correlation that could be crucial for this level of detail, the relativistic effects could also play a critical role. The discussion in Section 10.4 showed that the HALA effect could cause a substantial influence due to SOC. For LiBr, this could be particularly pronounced. The relative positions of the respective NSCs are significantly off.

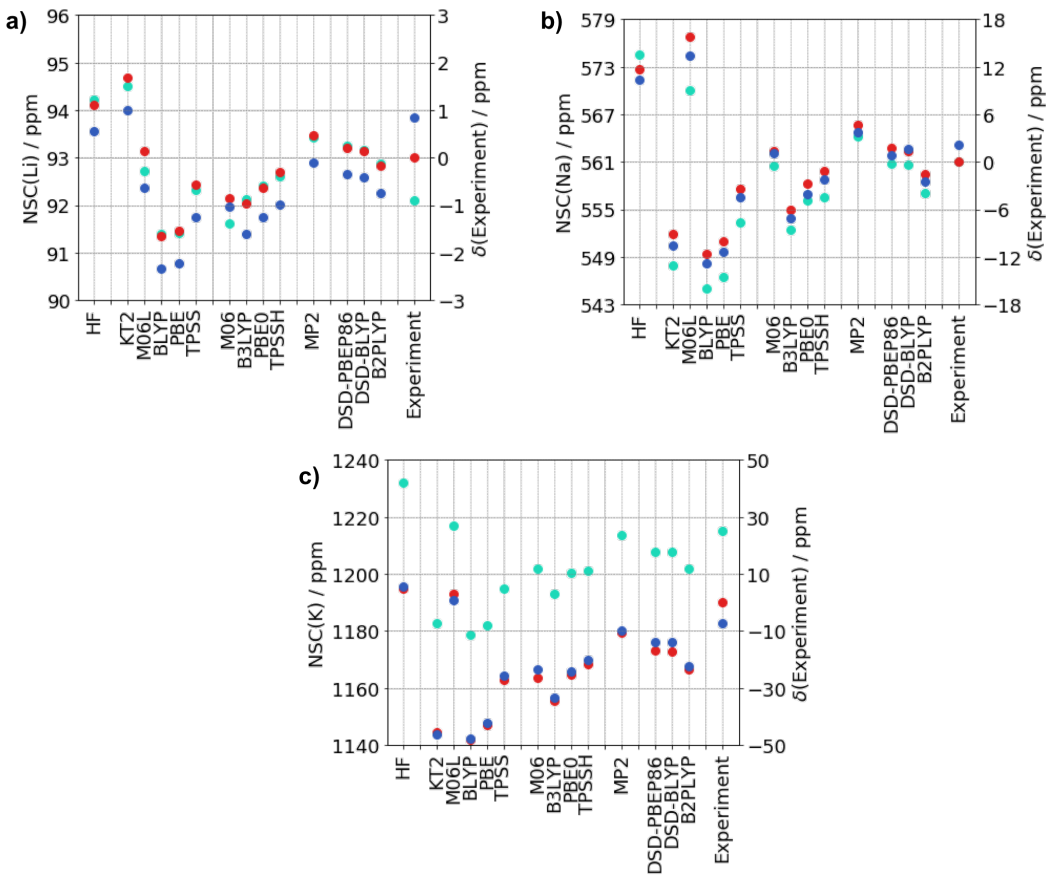

Figure 10.9: NSCs (left, primary y-axis) of the alkali metals M in $[M_6Y_{19}]^{13-}$ for **a)** $[Li_6Y_{19}]^{13-}$, **b)** $[Na_6Y_{19}]^{13-}$, and **c)** $[K_6Y_{19}]^{13-}$ vs. experimental chemical shifts δ (right, secondary y-axis). Basis set: pcSseg-3.

The exclusion of the relativistic effects could also be eminent for the potassium series. In this case, the range of the experimental chemical shifts is significantly larger than for Na and Li, reaching from -7.0 ppm to 33.0 ppm. Regardless, once again, no method can predict the correct order of KCl and KBr, possibly due to the exclusion of the relativistic effects. The possibility can be investigated by considering the relativistic corrections in Table 10.4 on page 130. Although it was stated that the values should not be taken as a final and accurate relativistic correction, applying them could still give a qualitative indication if the relativistic effects could change the order of the NSCs. In the non-relativistic limit, the PBE0 computed NSC values amount to 1202 ppm, 1166 ppm, and 1168 ppm for KF, KCl, and KBr, respectively. Inclusion of the relativistic corrections for the model systems $[KF_6]^{5-}$ (89.2 ppm), $[KCl_6]^{5-}$ (87.9 ppm), and $[KBr_6]^{5-}$ (79.1 ppm) results in 1291 ppm, 1254 ppm, and 1247 ppm for KF, KCl, and KBr respectively. At this level of theory, the inclusion of the relativistic effects is changing the order of the NSCs, and it indicates that an

even higher level of theory is necessary to get an accurate result. That goes about the reach of the current study.

10.5.3 Method Dependence of Magnesium and Zinc Nuclear Shielding Constants

The examples of magnesium and zinc, shown in Figure 10.10, introduce the bonding character as a further difficulty in the problem at hand. While the alkali metal halides are strongly ionic, ZnS and ZnSe are much more covalent. In the case of magnesium, the bonding character is different between the more ionic MgO and the more covalent MgS. Regardless, all methods predict the correct order of NSC concerning their experiment.

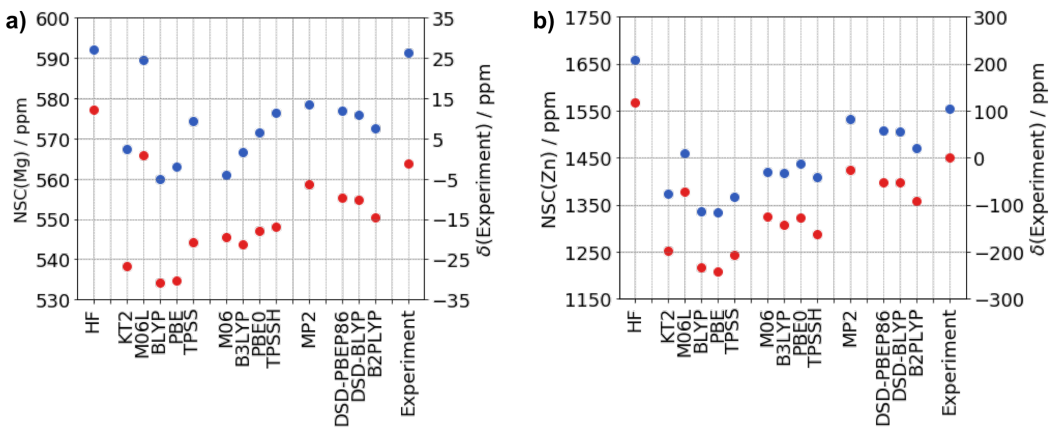

Figure 10.10: NSCs (left, primary y-axis) of the metals in **a)** $[Mg_6Y_{19}]^{26-}$ and **b)** $[Zn_4Y_{10}]^{12-}$ vs. experimental chemical shifts δ (right, secondary y-axis). Basis set: pcSseg-3.

In the case of magnesium, the experimental shift of MgS with MgO as a standard is 27.4 ppm. HF underestimates this value by about 13 ppm. However, this does not continue systematically in the DFT functionals. Although the (meta-)GGA results are not systematic, the difference between the NSCs of MgO and MgS is generally 2 to 3 ppm larger than the experimental shift. All relative positions of NSC computed with hybrid functionals, except with TPSSH, underestimate the chemical shift. TPSSH has the best agreement and overestimates the shift by only 0.9 ppm. The NSCs of MgO are similar for all hybrid functionals, whereas they are far apart for MgS. One possible reason for this discrepancy could be the difference in bonding character. The relative positions of NSCs calculated with MP2 and the double-hyrbid functionals underestimate the chemical shift by about 5.0 ppm to 6.0 ppm.

The experimental shift of ZnSe with ZnS as a standard is 104.2 ppm. The difference between the NSCs overestimates this value by 40 ppm on average for most (meta-)GGA functionals. For hybrid functionals, it is 30 ppm, and for MP2 and double-hyrbid functions between 20 ppm and 22 ppm. Nevertheless, HF, M06L, and M06 agree well with the experiment. The lack of relativistic effects could also cause these unsatisfactory results.

Summarizing the results of the halides, alkali metals, zinc, and magnesium, the comparison of the calculated NSC with different methods and for different groups of systems shows a trend concerning the chosen methods. The different classes of methods show significantly different performances. While the NSCs calculated with (meta-)GGAs strongly depend on the functional, this effect is generally less pronounced for the hybrid functions and even less for the double-hyrbid functions. The performance differences are significant for (meta-)GGAs, hybrid functionals, and HF. Figure 10.8 to Figure 10.10 show that the GGA PBE, the meta-GGA TPSS, and the hybrid functionals PBE0 and TPSSH perform well in several cases. Overall, MP2 and the double-hyrbid functionals are the most robust for all systems. The results between the different double-hyrbid functionals are generally similar. This allows the interpretation that the double-hybrids selected in this set are all good candidates for the computation of NSC.

10.5.4 Chemical Shifts: Comparison to Experiment

The next step is to determine the chemical shifts from the NSCs. As mentioned earlier, a chemical shift is the difference between an NSC of a reference standard and a target compound. Each system can be a reference for another, as long as both have the element of the investigated shift. The chemical shift calculation can decrease or increase the error depending on the reference and compound chosen. Therefore, the choice of a reference introduces some bias in the results.

By keeping the inevitable bias in mind, for all halides, the sodium halides are chosen as a reference for the shifts, and for all alkali metals, the alkali metal fluorides are the references. Since there are only two zinc and magnesium systems each, only one choice of reference is possible. Figure 10.11a to Figure 10.11c show the absolute errors regarding the experiments. Table 10.5a and Table 10.5b list each element's mean absolute errors and mean absolute deviations, respectively. Additionally, the tables demonstrate the approximated range of the shifts and NSCs for comparison. At the beginning of the chapter, Table 9.1 on page 109 documents the actual experimental values. In the appendix on page 320, Figure B.5 and Figure B.6 give the results for the other potential combinations of reference standards for the alkali metal nuclei and halide nuclei, respectively.

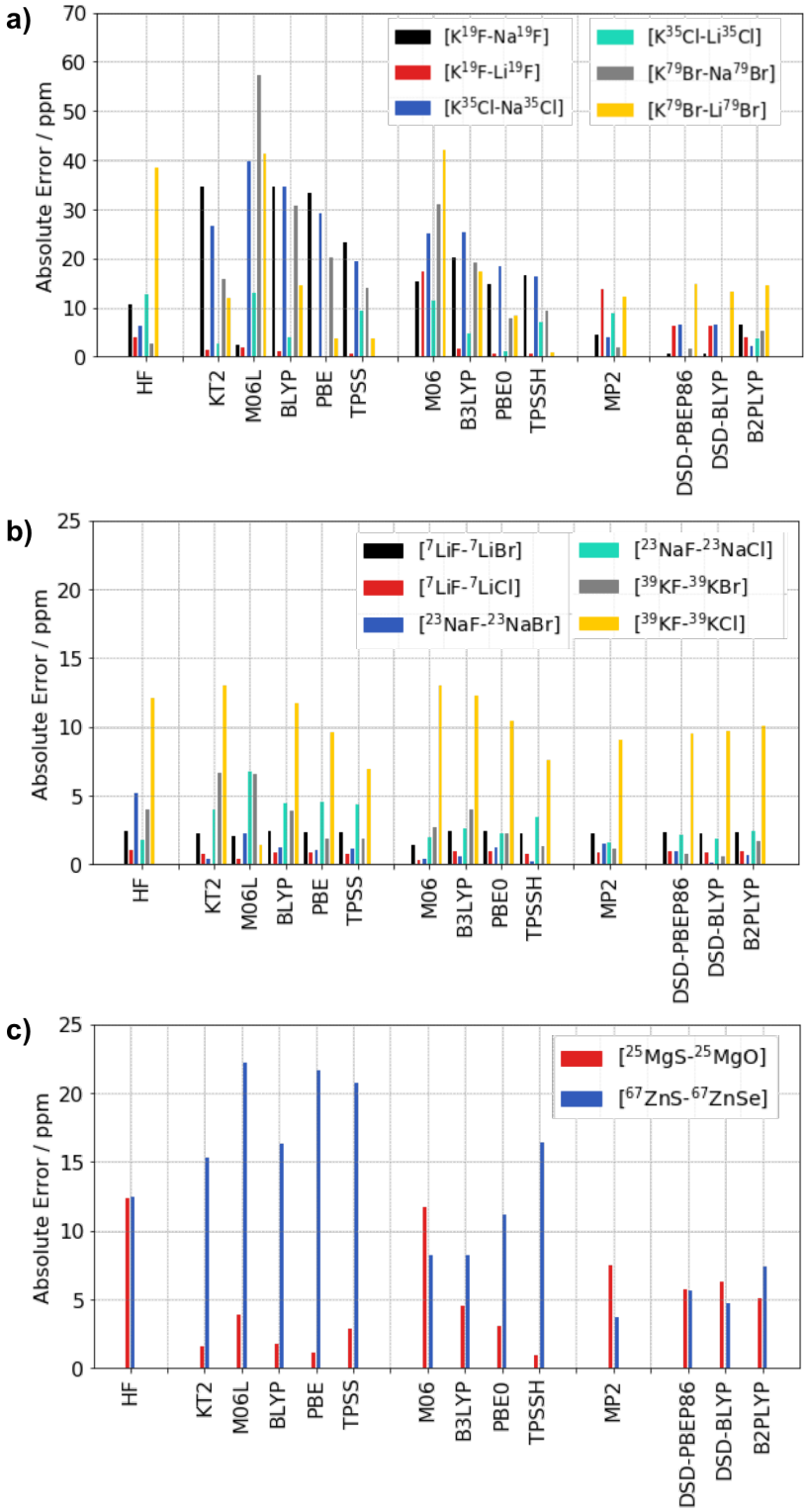

Figure 10.11: Absolute errors of calculated vs. experimental chemical shifts δ computed with different methods for **a)** halides, **b)** alkali metals, and **c)** magnesium and zinc. Basis set: pcSseg-3.

Figure 10.11b displays KCl with KF as a reference standard as the only significant outlier in the chemical systems, giving significantly worse results for all methods used. However, this is not the case for KBr with KF as a standard. By consulting the other reference combinations, as shown in Figure B.5, it is evident that the issue originates from KCl, as it gives significantly worse potassium shifts than the other counterparts. Besides this example, most differences in the errors seem to originate from the methods. The performance of the methods is first discussed in general terms, and then the individual element groups are examined.

Overall, MP2 and the double-hybrid functionals perform best. The mean absolute error is generally lower for the double-hybrid functionals, while the mean absolute deviation is lower for MP2. The double-hybrid functionals provide consistent performance, are comparable, and agree with each other. In comparison, the hybrid functions deliver very inconsistent performance. TPSSH appears to provide the best overall performance in this class, followed by PBE0. M06 shows the most inconsistent performance in this group and has the largest mean absolute errors and deviations. The errors of the results and their mean absolute deviations calculated with (meta-)GGA functionals are the largest of all method groups tested. Their performance is the most inconsistent. TPSS has the best performance in this group, followed by PBE. M06L is the most uneven functional, sometimes yielding very small and sometimes very large errors. One can conclude that it delivers the right results for the wrong reasons in the cases in which it outperforms.

In Section 10.5b, it was observed that the order of the NSCs regarding the experiments is never correct for all alkali metals. Nevertheless, the (mean) absolute errors and mean deviations are small compared to the calculated absolute NSCs - except for the mentioned case with KCl. As noted earlier, the magnitudes range around 90 ppm and 500 ppm for Li and Na, respectively, while the range of the relative chemical shift is 2 ppm in both cases. Therefore, the errors in Figures 10.11 and Table 10.5 are significant regarding the shift.

In general, all groups of methods give very similar results for the alkali metals. Nevertheless, the group of double-hybrid functionals and MP2 and the hybrid functional TPSSH seem to perform slightly better, followed by PBE0. In the group of (meta-)GGAs, TPSS and PBE provide the best results. The performances of M06 and M06L deliver the most inconsistent outcomes but outperform the other methods for Li. Given the discussed circumstances of the small Li shifts, this may be a coincidence.

Table 10.5: a) Mean absolute error and **b)** mean deviation for the different methods and nuclei. Color code: worst two values (red) and best two values (blue) for each nucleus. Basis set: pcSseg-3. Range of chemical shift for each nucleus is $\Delta\delta$ and approximate magnitude computed nuclear shielding constants ~NSC. All values in ppm.

a)	HF	KT2	M06L	BLYP	PBE	TPSS	M06	B3LYP	PBE0	TPSSH	MP2	DSD-PBEP86	DDSD-BLYP	B2PLYP	$\Delta\delta_{Experiment}$	~$NSC_{Computed}$
^{7}Li	1.7	1.5	1.3	1.7	1.6	1.5	0.9	1.7	1.7	1.6	1.6	1.6	1.6	1.6	2	90
^{23}Na	3.5	2.2	4.5	2.8	2.8	2.7	1.2	1.6	1.7	1.8	1.5	1.5	0.9	1.6	2	500
^{39}K	8.0	9.9	4.0	7.9	5.8	4.4	7.9	8.1	6.3	4.4	5.1	5.1	5.1	5.9	32	1100
^{19}F	7.7	18.1	2.2	18.2	16.9	12.3	16.5	11.2	7.9	8.8	9.3	3.5	3.5	5.3	91	400
^{35}Cl	9.7	14.8	26.5	19.4	14.7	14.5	18.5	15.3	9.9	11.7	6.5	3.4	3.6	3.0	55	1000
^{79}Br	20.7	14.0	49.7	22.7	12.2	8.9	36.8	18.5	8.3	5.3	7.4	8.4	6.8	10.2	120	2800
^{25}Mg	12.5	1.6	3.8	1.7	1.0	2.8	11.8	4.5	3.0	0.9	7.5	5.7	6.3	5.1	28	500
^{67}Zn	12.6	15.3	22.3	16.2	21.8	20.7	8.2	8.3	11.2	16.4	3.8	5.7	4.7	7.3	104	1300

b)	HF	KT2	M06L	BLYP	PBE	TPSS	M06	B3LYP	PBE0	TPSSH	MP2	DSD-PBEP86	DDSD-BLYP	B2PLYP	$\Delta\delta_{Experiment}$	~$NSC_{Computed}$
^{7}Li	0.7	0.8	0.8	0.8	0.8	0.8	0.5	0.7	0.7	0.8	0.7	0.7	0.7	0.7	2	90
^{23}Na	2.6	2.0	3.4	2.2	2.3	2.2	1.0	1.3	1.1	1.7	0.8	1.1	0.9	1.2	2	500
^{39}K	7.1	8.0	3.4	5.6	3.5	2.2	6.9	6.8	5.2	2.7	4.3	4.0	4.2	4.7	32	1100
^{19}F	4.1	8.2	2.6	10.4	11.2	7.9	8.6	4.2	4.1	4.4	4.0	4.4	4.6	4.2	91	400
^{35}Cl	10.7	15.6	26.5	19.5	17.9	17.2	18.5	15.7	11.0	14.4	5.4	8.2	8.4	10.3	55	1000
^{79}Br	14.5	13.2	47.8	21.8	11.7	7.5	30.9	16.3	6.8	4.8	3.7	5.6	3.6	7.6	120	2800

The mean absolute errors and deviations for the halide group are generally higher than for the alkali metals. This is not surprising since the halides have a wider range of chemical shifts. The error must be viewed in the context of the range of chemical shifts and the absolute values of the calculated NSCs, as listed in the last two columns of Table 10.5.

The halides appear to be more dependent on the methods. The double-hybrid functionals have the smallest mean absolute error, followed by MP2, which has the smallest mean absolute deviation. Outliers are the results of Br concerning double-hybrid functionals and MP2 since the mean absolute error of Br is more extensive than of Cl and F. This could be due to relativistic effects and can be largely ascribed to the contributions of LiBr, which has a much larger error than KBr and NaBr (see

the yellow bar in Figure 10.11a and Figure B.6).

This general increase in the mean absolute error for Br compared to Cl and F is not visible for (meta-)GGA and hybrid functionals. On average, the errors for Br are lower with TPSSH, PBE, and TPSS than for the other halides. There seems to be error compensation. For the halides generally, the hybrid functionals give more inconsistent results than MP2 and double-hybrid functionals. TPSSH and PBE0 give the best performance in this group and M06 the worst. The (meta-)GGA results are even more inconsistent than those of the hybrid functionals, and the overall errors are even more pronounced. TPSS and PBE provide the best and M06 the most inconsistent results in this group.

No mean deviation is available for the Mg and Zn systems due to the lack of data points. For Mg, the error is most consistent across the different double-hybrids and similar for MP2, but hybrid functionals and (meta-)GGAs seem to perform better. The error trend for Zn is similar to that for halides, with MP2 and double-hybrid functionals outperforming the other methods. But in this case MP2 performs slightly better than the double-hybrid functionals.

This chapter showed that the results of double-hybrid functionals outperform other DFT functionals using GIAOs to compute NMR parameters, which agrees with molecule results for molecules.[332] This shows that the presented methods developed for molecular systems can be applied to solid-state systems with comparable accuracy using the electrostatic embedding approach. If methods including post-HF electron correlation are applied, the residual errors are only a few percent, and other effects become more important, such as relativistic and zero-point vibration corrections (ZPEVC). These effects have been omitted as they go beyond the scope of the present study. However, this study demonstrated that relativistic effects might become important in the case of chemical systems containing, e.g., Br and Se atoms. That alters the results of the heavy nuclei and can also affect the shieldings of light nuclei.

11 Shedding Light on Band Gap Predictions for Solid-State Systems: A Comparative Study Using TD-DFT and bt-PNO-STEOM-CCSD

11.1 The Context and Aim of the Band Gap Study

Over the last decades, DFT has been widely applied in periodic or non-periodic embedded cluster calculations for electronic band structure studies to predict the fundamental property of the transport or fundamental and optical BG.[11–15] As introduced in Section 8.1, a variety of DFT approaches (one-electron energies or Δ-SCF), linear response DFT approaches like TD-DFT, many-body Green's function approximation, and the Bethe-Salpeter equation provide access to the transport and optical BG energy with an accuracy that is strongly DFT functional dependent.[11–13, 16–18] Periodic DFT calculations showed that the local as well as the semilocal and the generalized gradient approximation (GGA or meta-GGA) density functionals, the most affordable functionals for solids, strongly underestimate the magnitude of the band gap energies in the semiconductor class of chemical systems by more than 1 eV on average.[12, 13, 15] Global or screened hybrid functionals demonstrated generally better performance. Global hybrid functionals like B3LYP, B3PW91, and PBE0 or screened hybrid functionals (in plane wave DFT) like HSE can lower the mean absolute errors in the band gap calculations to about 0.4 eV.[11, 12] These errors are very similar to the errors of the many-body perturbation GW approach.[11, 12] Meanwhile, a wide variety of specialized functionals are designed to minimize the self-interaction, like the SCAN meta-GGA functional, and improve the efficiency of the band gap calculations for solids towards the accuracy of hybrid functionals and GW methods.[14, 15] Similarly, the range separated quantum theory project (CAM-QTP) family of functionals has been proven successful in calculating band gaps and charge transfer excitation energies on benchmark studies,

provided that the occupied DFT orbitals approximate the principal ionization potentials (IPs).[246, 390] Diagrammatically derived functionals based on the random phase approximation (RPA) employed to calculate band gaps are limited to small solid-system sizes due to the high computational cost.[20]

In contrast, until recently, ab initio wavefunction-based reference calculations have been either infeasible for the large system sizes arising from surface problems or too demanding to be routinely applied.[21–28, 324] However, there are several important applications for the ground and excited states at the level of periodic Monte Carlo coupled cluster (CC) and full configuration interaction (Full-CI).[24, 25, 28, 324] Recently, band structure calculations of several semiconductors have been performed at the level of the periodic equation of motion-based coupled cluster (EOM-CC) theory.[29, 30]

Local correlation techniques that exploit the relatively short-range nature of dynamical correlation have been shown to overcome the severe limitations imposed by the steep scaling of wavefunction-based methods with system size.[31] This has enabled the treatment of several surface problems in second-order periodic local Møller-Plesset perturbation theory (MP2).[32, 37] Similarly, for non-metallic systems, employing an embedded cluster approach can reduce the system size that must be treated quantum mechanically by treating long-range electrostatics and polarization at the molecular mechanical level.[38–43] The combination of these two approaches has proven to be the "gold standard" for surface systems when performing CCSD(T) level calculations.[10, 23] By describing the quantum cluster at the level of the domain-based local pair natural orbital version of the CCSD(T) approach (DLPNO-CCSD(T)),[44] the adsorption energies for a range of small molecules on the rutile TiO2(110) surface can be calculated with errors of < 0.04 eV (1 kcal/mol) with respect to the available experimental values.[23]

Local correlation methods are less explored in combination with excited state methods. Excited state PNOs can be generated from correlated methods for excited states based on either configuration interaction or couple cluster schemes like CIS(D), CC2, ADC2,[45–47] and thus, leading to state-specific PNO-CI and PNO-CC based methods. More recently, a ground state PNO scheme was used in combination with the original equation-of-motion based techniques like EOM-CC and STEOM-CC ones[253–255] resulting in the back-transformed (bt) bt-PNO-EOM-CCSD and bt-PNO-STEOM-CCSD methods (also referred to as EOM-CC and STEOM-CC), which provide a balanced description for valence, charge transfer (CT) and Rydberg states in optical spectroscopy.[48, 49] In particular, bt-PNO-STEOM-CCSD has been able to describe the excited states of various chemical systems delivering errors below $\sim$0.1 eV for valence, Rydberg, and CT states.[48–50]

In this chapter, the performance of the bt-PNO-STEOM-CCSD method to calculate a variety of energy gaps in organic and inorganic solid-state systems will be evaluated for the test set of systems as given in Table 9.1 and Table 9.2 with band gap energies ranging between 1-14 eV. In particular, this chapter reveals that bt-PNO-STEOM-CCSD alone or combined with the embedded cluster approach delivers an efficient computational protocol with strong predictive ability for band gap energies. The performance of bt-PNO-STEOM-CCSD will be evaluated against available experimental data and various TD-DFT methods and for the organic semiconductors against Δ-SCF/DFT.

11.2 General Computational Details

All calculations were performed with the ORCA 4.1 suite of programs.[351] For the inorganic solid-state systems, the electrostatic embedding approach was used at all times. Optical ($\Delta E_O^{S_0 \rightarrow S_1}$) and fundamental ($\Delta E_F^{IP-EA}$) energy gaps were evaluated at the TD-DFT, Δ-SCF/DFT, and bt-PNO-STEOM-CCSD levels of theory. For the ground and excited state energetics, various DFT functionals were employed. This included the generalized gradients approximation (GGA) functionals: BP86,[213, 363] BLYP,[213, 214, 222] and PBE,[212] as well as the hybrid functionals: B3LYP,[213, 214, 218] B1LYP,[213, 214, 218] PBE0,[212, 364] and B3PW91[222]. Additionally, the double-hybrid functional B2PLYP[223] was used. All the calculations were performed using the second-order Douglas-Kroll-Hess correction (DKH2)[228, 229] to account for the scalar relativistic effects, which employs the finite nucleus model.[384] Spin-orbit coupling effects (SOC) were computed in the framework of quasi-degenerate perturbation theory (QDPT).[391–393] Deconstructed versions of the correlation-consistent triple and quadrupole-zeta quality (cc-pVXZ, X=T,Q) one-electron basis sets[394] were applied. The calculations were accelerated by employing the resolution of identity approximation (RI)[395] for the Coulomb integrals. At the same time, the exchange terms were efficiently computed using the "chain-of-spheres" (COSX)[354, 396] approximation by utilizing the def2/J and the cc-pV(T/Q)Z/C auxiliary basis sets. For bt-PNO-STEOM-CCSD, extrapolation to the basis set limit was carried out based on the two-point coupled-electron pair extrapolation scheme with the all-electron cc-pVTZ/cc-pVQZ basis sets.[156] Within this scheme, only the correlation energy of the ground and excited states are regarded for the energy extrapolation of the excited states. By contrast, DFT/cc-pVQZ calculations are considered to be at the basis set limit. Example input file structures are provided in the appendix starting from page 331.

11.3 Influence of the Model Parameters on the Optical Band Gap

The influence of the electrostatic embedding environment and the model size on the optical band gap is tested for LiCl in the following. LiCl will be the primary working example for the inorganic crystals throughout this section. The long-range effects mimicked by the PCs are essential for the convergence of the optical band gap. For system size $[Li_6Cl_6]^0$ in combination with bt-PNO-STEOM-CCSD, without embedding, the BG amounts to 6.27 eV. With an increasing number of PCs and an introduced BR layer, the band gap converges towards 9.35 eV. The band gap changes not significantly after the introduction of 1,000 PCs. For consistency and the correct reproduction of the Madelung constant, the PC field contains about 10,000 PCs.

The charges of the PCs and ECPs are optimized via linear regression, as introduced in Section 3.2 on page 53. For LiCl, the optimized charges are 0.95 and -0.95 for Li and Cl, respectively. Figure 11.1 demonstrates that the best agreement with the experiment is achieved in this case with bt-PNO-STEOM-CCSD. The influence of the computed charges on the computed optical band gap is similar for TD-DFT and bt-PNO-STEOM-CCSD and decreases with increasing system size.

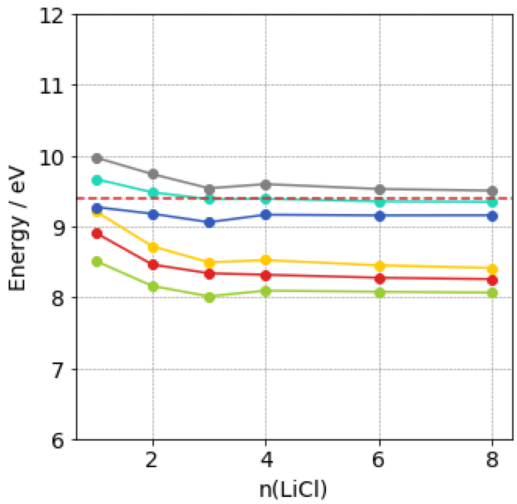

Figure 11.1: Calculation results of the first excited states of $[Li_nCl_n]^0$ (n=1-4, 6 and 8) with bt-PNO-STEOM-CCSD for charges equal to 1.05 (gray), 0.95 (turquoise) and 0.85 (blue) and with B3PW91 for charges equal to 1.05 (yellow), 0.95 (red) and 0.85 (green). Red dashed line: experiment.

Figure 11.2 shows that the convergence scheme is identical for DFT and bt-PNO-STEOM-CCSD, which makes it a valid choice to identify the converged cluster sizes

at the DFT level, and that the SCe and SCl cluster types converge towards the same result. For SCl, the optical band gap converges for $[Li_4Cl_{16}]^{12-}$ towards the same value as SCe, which shows convergence for $[Li_4Cl_4]^0$. Here, the converged cluster size of the SCe model has fewer atoms overall than SCl. Thus, it is more convenient to use this approach to calculate the optical band gap for all rock salt structures. A similar convergence scheme for the charges and cluster sizes is present for the orthorhombic and the zinc blende crystals. For the latter, the SCl approach is used as the SCe approach gave inconsistent results for this crystal structure.

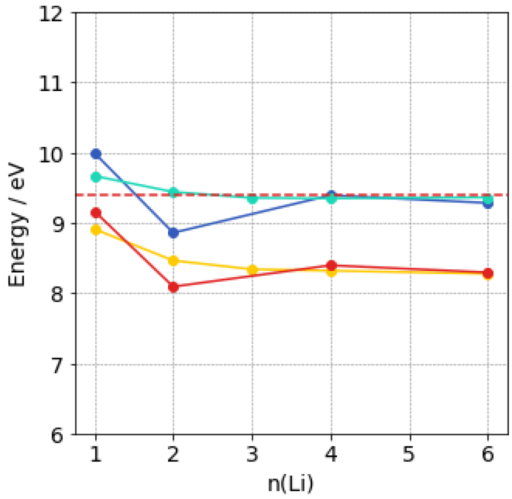

Figure 11.2: Calculations of the first excited states of LiCl with the SCe approach ($[Li_nCl_n]^0$, n=1-4, 6, 8) with bt-PNO-STEOM-CCSD (turquoise) and B3PW91 (yellow) and with the SCl approach ($[LiCl_6]^{5-}$, $[Li_2Cl_{10}]^{8-}$, $[Li_4Cl_{16}]^{12-}$ and $[Li_6Cl_{19}]^{13-}$) with bt-PNO-STEOM-CCSD (blue) and B3PW91 (red). Red dashed line: experiment.

Table 11.1 lists the converged cluster sizes for all tested systems. The converged clusters contain less than ten building units in all studied cases. This relatively fast cluster size convergence relates directly to the band gap representing the minimum of the band excitation energies in the solid-state context. Although this might not directly relate to a stationary character, it seems to do so in this case due to the high ionic character, which makes the bands less dispersed (see also Figure 2.6 and Figure 2.7 on page 19 and 21]) and the first excitations more local. As Figure B.7 on page 333 in the appendix visualizes, in the case of LiCl, the first ten bt-PNO-STEOM-CC calculated excitation energies are essentially converged at the $[Li_8Cl_8]^0$ cluster size, while the convergence of higher excitation energies ($>$ 20 states) require much larger cluster sizes.

Table 11.1: Cluster sizes employed to compute the optical band gaps of the different inorganic crystals.

System	Smallest System Tested SCl/SCe	Largest System Tested SCl/SCe	Converged Size SCl/SCe
LiF	$[LiF_6]^{5-}/[LiF]^0$	$[Li_6F_{19}]^{13-}/[Li_{20}F_{20}]^0$	$[Li_4F_{16}]^{12-}/[Li_4F_4]^0$
LiCl	$[LiCl_6]^5-/[LiCl]^0$	$[Li_6Cl_{19}]^{13-}/[Li_{20}Cl_{20}]^0$	$[Li_4Cl_{16}]^{12-}/[Li_4Cl_4]^0$
LiBr	$[LiBr_6]^5-/[LiBr]^0$	$[Li_6Br_{19}]^{13-}/[Li_{20}Br_{20}]^0$	$[Li_4Br_{16}]^{12-}/[Li_4Br_4]^0$
NaCl	$[NaCl_6]^5-/[NaCl]^0$	$[Na_6Cl_{19}]^{13-}/[Na_{20}Cl_{20}]^0$	$[Na_4Cl_{16}]^{12-}/[Na_4Cl_4]^0$
NaBr	$[NaBr_6]^5-/[NaBr]^0$	$[Na_6Br_{19}]^{13-}/[Na_{20}Br_{20}]^0$	$[Na_4Br_{16}]^{12-}/[Na_4Br_4]^0$
MgO	$[MgO_6]^{10-}/[MgO]^0$	$[Mg_6O_{19}]^{26-}/[Mg_{20}O_{20}]^0$	$[Mg_6O_{19}]^{26}/[Mg_6O_6]^0$
MgS	$[MgS_6]^{10-}/[MgS]^0$	$[Mg_6S_{19}]^{26-}/[Mg_{20}S_{20}]^0$	$[Mg_6S_{19}]^{26}/[Mg_6S_6]^0$
MgSe (RS)	$[MgSe_6]^{10-}/[MgSe]^0$	$[Mg_6Se_{19}]^{26-}/[Mg_{20}Se_{20}]^0$	$[Mg_6Se_{19}]^{26}/[Mg_6Se_6]^0$
MgSe (ZB)	$[MgSe_4]^{6-}$/-	$[Mg_8Se_{19}]^{22-}$/-	$[Mg_4Se_{10}]^{12-}$/-
ZnO	$[ZnO_4]^{6-}$/-	$[Zn_8O_{19}]^{22-}$/-	$[Zn_4O_{10}]^{12-}$/-
ZnS	$[ZnS_4]^{6-}$/-	$[Zn_8S_{19}]^{22-}$/-	$[Zn_4S_{10}]^{12-}$/-
ZnSe	$[ZnSe_4]^{6-}$/-	$[Zn_8Se_{19}]^{22-}$/-	$[Zn_4Se_{10}]^{12-}$/-
GeS	-/$[GeS]^0$	-/$[Ge_{16}Cl_{16}]^0$	-/$[Ge_8Cl_8]^0$

11.4 Influence of the Basis Set Size on the Optical Band Gap

Figure 11.3 shows the results for LiCl with system size $[Li_8Cl_8]^0$ with increasing basis set sizes of the basis set family cc-pVXZ on the one hand, for bt-PNO-STEOM-CCSD, and on the other hand, for the Jacob's ladder of DFT functionals BLYP, B3LYP, and B2PLYP. With cc-pVXZ, the basis set converges for bt-PNO-STEOM-CCSD relatively fast and monotonous. The difference between cc-pVDZ and cc-pVTZ is only 0.034 eV, and between cc-pVTZ and cc-pVQZ 0.007 eV. The extrapolated basis set cc-pV(T,Q)Z differs by 0.005 eV from cc-pVQZ. For all DFT functionals, cc-pVXZ shows much slower convergence.

The basis set family def2-XVP was also tested, and Figure B.8 in the appendix on page 333 compares the results to cc-pVXZ. The basis sets def2-XVP are cheaper than cc-pVXZ, and def2-QZVPP and cc-pVQZ yield equivalent values. Nevertheless, the basis set family cc-pVXZ is chosen over def2-XVP because the extrapolated cc-pV(T,Q)Z is more reliable than def2-(T,Q)ZVPP for bt-PNO-STEOM-CCSD due to a smoother convergence of increasing basis set sizes of the cc-pVXZ family. Also, cc-pVXZ are explicitly designed for correlation consistent calculation. Although DFT calculations are not such, the basis set class can apply without a loss in accuracy. Thus, in the following, cc-pVQZ applies for the DFT calculations and the extrapo-

lated basis set cc-pV(T,Q)Z for bt-PNO-STEOM-CCSD.

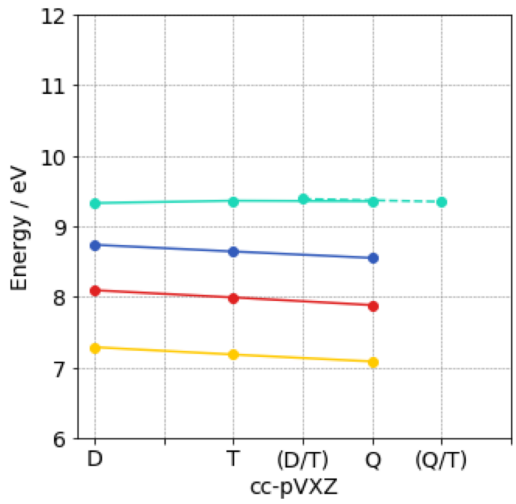

Figure 11.3: Comparison of cc-pVXZ basis set sizes with different methods BLYP (yellow), B3LYP (red), B2PLYP (blue), and bt-PNO-STEOM-CCSD (turquoise) for $([Li_8Cl_8]^0$. Dashed line: extrapolated basis functions for bt-PNO-STEOM-CCSD.

Similar behavior to the one of LiCl also shows for the other tested systems. The rock salt structures, the one orthorhombic crystal, and the organic semiconductors are closer to the basis set limit for cc-pVTZ already than the tested zinc blende structures.

11.5 Organic Semiconductors: The Case of Anthracene

Before going into the details of the inorganic semiconductor results, this section discusses the example of the organic semiconductor 3A set to demonstrate different approaches to the BGs. Table 11.2 shows the results for the HOMO-LUMO gap computed with DFT, the first singlet excitation and the first singlet-triplet excitation computed with TD-DFT and bt-PNO-STEOM-CC, the fundamental band gap computed with Δ-SCF/DFT and the IP/EA calculations in the framework of bt-PNO-STEOM-CC in comparison to the experimental values. The experimental values of the singlet (3.20 eV) and triplet (1.84 eV) excitations differ by 1.36 eV. Hence, the SOC effect is respectively influential. In turn, the fundamental band gap (6.87 eV) is significantly larger than the two excitations. Therefore, the expectation is that this organic semiconductor is a good example to demonstrate the differences in the results regarding the BG approaches described in Section 8.1.

Table 11.2: Performance of various DFT functionals in the framework of Δ-SCF/DFT and TD-DFT vs. bt-PNO-STEOM-CC for calculating the optical and fundamental band gap energies in eV of Anthracene (3A) with LR meaning linear response (TD-DFT or STEOM-CC) and HL is HOMO-LUMO gap.

	$\Delta\epsilon^{HL}$	$\Delta E_{LR}^{S_0\rightarrow S_1}$ ($\Delta E_{\Delta-SCF}^{S_0\rightarrow T_0}$)	$\Delta E_{LR}^{S_0\rightarrow T_0}$ ($\Delta E_{\Delta-SCF}^{S_0\rightarrow T_0}$)	average $\Delta E_{\Delta-SCF}^{S_0\rightarrow S_1/S_0\rightarrow T_0}$	$\Delta E_{\Delta-SCF}^{IP-EA}$ or $\Delta E_{STEOM-CC}^{IP-EA}$
BP86	2.34	3.10 (2.41)	1.97 (1.98)	2.19	6.51
BLYP	2.34	3.11 (2.40)	1.99 (2.00)	2.19	7.5
PBE	2.33	3.09 (2.39)	2.00 (2.01)	2.19	6.97
B1LYP	3.82	3.46 (2.91)	2.03 (2.07)	2.49	6.74
B3LYP	3.53	3.39 (2.79)	2.05 (2.06)	2.43	6.67
B3PW91	3.52	3.39 (2.80)	2.06 (2.09)	2.43	6.65
PBE0	3.81	3.44 (2.89)	2.05 (2.09)	2.49	6.67
B2PLYP	5.5	3.54 (3.56)	2.02 (2.08)	2.81	6.95
STEOM-CC		3.28	1.84		6.85
Exp.		3.2	1.84		6.87

The triplet excitations, computed with TD-DFT and Δ-SCF/DFT are in reasonably good agreement with each other for all functionals. For the singlet excitations, the results with TD-DFT are on average 0.7 eV higher than the one of Δ-SCF/DFT for the GGA functionals and on average 0.5 eV higher for the hybrid functionals, while they match for the double-hybrid functional. For bt-PNO-STEOM-CC and DFT, the singlet and triplet excitations and the fundamental band gap agree sufficiently with the experiment. In all three cases, bt-PNO-STEOM-CC has the best agreement with the experiment. For TD-DFT, the excitation energies increase in the sequence of GGA, hybrid and double-hybrid functionals, while the results are all fairly similar for the triplet excitations. The results of the DFT functionals for the fundamental band gap do not follow a specific order. Overall, the hybrid functionals are more consistent than the GGA functionals and deliver a better agreement with the experiment. This is also consistent with previous studies on organic and inorganic semiconductors.[16, 313] The results of bt-PNO-STEOM-CC do not have a specific position with respect to the functionals in all three discussed cases.

The orbital energy difference between the HOMO and the LUMO is neither in good agreement with the optical nor the fundamental band gap, which is in accordance with the discussion in Section 8.1. The HOMO-LUMO gap approximates the average excitation energy between singlet and triplet states $\Delta E_{\Delta-SCF}^{S_0\rightarrow S_1/S_0\rightarrow T_0}$ well only if there is no Hartree-Fock exchange in the functional (BP86, BLYP, PBE). This is because, in the presence of hybrid or double-hybrid functionals, the orbital en-

ergy difference $\Delta\epsilon^{HL}$ drastically overestimates the singlet excitation energies and approaches the value of the fundamental energy gap ΔE_F^{IP-EA} as the fraction of the Hartree-Fock exchange in the functional increases. In pure Hartree-Fock calculations, $\Delta\epsilon^{HL}$ becomes higher than 8 eV.

11.6 Inorganic Semiconductors: The Cases of LiCl and ZnS

The distinction between the fundamental and optical band gap and differentiation regarding the HOMO-LUMO gap translates to the inorganic crystals. The available data for most of them is limited to absorption experiments and the computational protocol at the time of the study prohibited the calculation of the transport BG with Δ-SCF/DFT or bt-PNO-STEOM-CC. For most inorganic crystals, the fundamental and optical band gaps only differ by a few meV;[239] thus, approaching only the optical BG is justified. This section compares the first excited state computed with bt-PNO-STEOM-CC and TD-DFT and the DFT HOMO-LUMO gap to each other, to experiment, and to periodic calculations from literature.[11, 12] The objects of discussion are ZnS and LiCl, which are representative examples for most cases of the benchmark set. They differ in geometry – tetrahedral vs. octahedral –, bond character – more covalent vs. highly ionic –, optical band gap wide – 3.78 eV vs. 9.40 eV - and QC model type - SCl vs. SCe, respectively.

The difference between the singlet and triplet states and accordingly, the SOC effects of the whole set of studied inorganic solids are rather small compared to the organic semiconductors. It attributes to the LMCT character of the optical band gap. All inorganic systems have either entirely filled or empty d orbitals; thus, they are not contributing, which reduces the SOC effect.

Figure 11.4 shows the energy difference between the first singlet $\Delta E_{LR}^{S_0\rightarrow S_1}$ and first triplet $\Delta E_{LR}^{S_0\rightarrow T_0}$ excited state and between $\Delta E_{LR}^{S_0\rightarrow S_1}$ and the first excited state, including SOC $\Delta E_{LR}^{SOC_0\rightarrow SOC_1}$ for the different methods. B2PLYP is excluded because, at the time of the study, the SOC effect was not available for double-hybrid functionals. For ZnS and LiCl, the SOC effects are the lowest for GGA. For LiCl, the effect is quite similar in bt-PNO-STEOM-CC and hybrid functionals, while for ZnS, it is somewhat smaller for bt-PNO-STEOM-CC than for the hybrid functionals. For LiCl, the average energy lowering of the first excited state due to SOC regarding the first singlet state is 0.08 eV; for ZnS, it is only 0.05 eV.

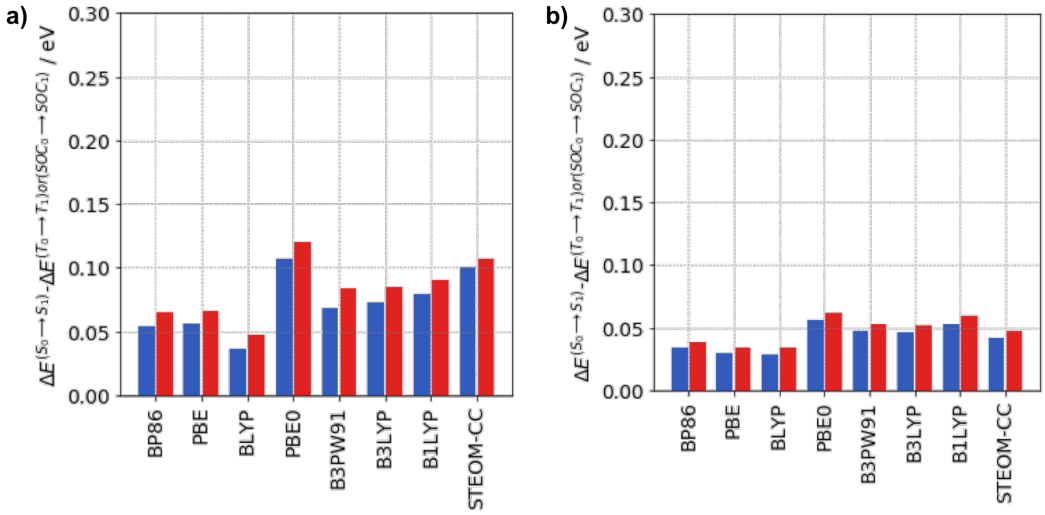

Figure 11.4: Difference between first singlet and triplet excited states (blue) and between first singlet excited state and first excited state including SOC (red) for **a)** $[Li_8Cl_8]^0$ and for **b)** $[Zn_4S_{10}]^{12-}$.

For the example of the organic semiconductor, the HOMO-LUMO gap amounts to the average between the triplet and singlet first excited state if there is no HF exchange in the functional and is by no means a good approximation of the optical or fundamental band gap. Since there is no significant difference between the singlet and triplet state in the examples of the inorganic solids, it is expectable that as long as there is no HF exchange in the functional, the orbital energy difference between HOMO and LUMO is almost identical to the energy of the first excited state ($\Delta E^{S_0 \rightarrow S_1}_{TD-DFT} \sim \Delta\epsilon^{HL}$). Figure 11.5 shows the energy difference between the HOMO-LUMO gap and the first excited state for all tested methods for ZnS and LiCl. In fact, for the GGA functionals, the difference is, as expected, close to zero for both systems. By introducing HF exchange via applying hybrid functionals, the HOMO-LUMO gap is larger by 0.5 eV to 1.0 eV than the first excited state. This difference is increasing even more for the tested double-hybrid functional.

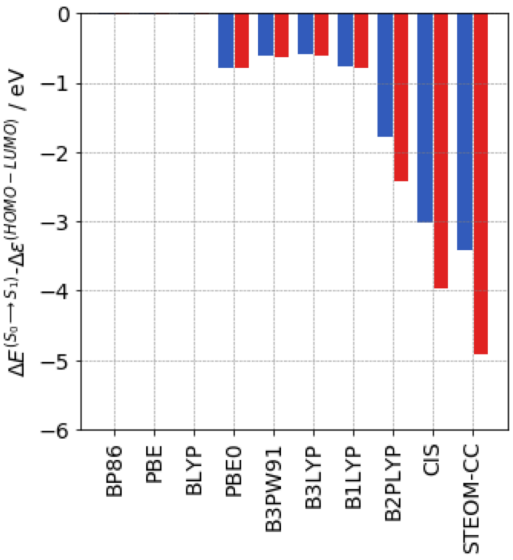

Figure 11.5: CIS, TD-DFT, and bt-PNO-STEOM-CCSSD (STEOM-CC) calculated energy difference between first excited state and HOMO-LUMO gap ($\Delta E_{LR}^{S_0 \rightarrow S_1} - \Delta\epsilon^{HL}$) for the case of $[Li_8Cl_8]^0$ (blue) and $[Zn_4S_{10}]^{12-}$ (red) clusters.

Figure 11.6 shows for the exemplarily chosen GGA functional PBE and hybrid functional B3PW91 that the difference between the HOMO-LUMO gap and the first excited state is size consistent. Further, it shows that for the two examples, ZnS and LiCl, the HOMO-LUMO gaps, rather than the first excited states, are converging towards periodic results[11, 12] obtained with B3PW91. This is because periodic calculations usually use the difference between valence and conduction bands to describe the band gap, which is synonymous with the HOMO-LUMO gap in the one-electron picture. Since the first excited state is equivalent to the HOMO-LUMO gap for PBE, both appear in fair agreement with the periodically obtained band gaps.

PBE underestimates the experimental optical band gaps by more than 1 eV and 2 eV for ZnS and LiCl, respectively. These errors can decrease effectively using hybrid functionals, which agrees with the literature.[11, 12] In the case of LiCl, the B3PW91 calculated orbital energy differences (obtained by periodic or embedded cluster calculations) range between 0.8 eV and 0.6 eV from the experimental values. The B3PW91 TD-DFT results (obtained by embedded cluster calculations) underestimate the experimental value by about 1.1 eV. For ZnS, the calculated orbital energy differences obtained with B3PW91 are in fair agreement with the experiment deviating by 0.2 eV or less, while TD-DFT underestimates the experiment by about 0.5 eV. The results of bt-PNO-STEOM-CC differ by less than 0.2 eV for ZnS and LiCl and show the best agreement with the experiment.

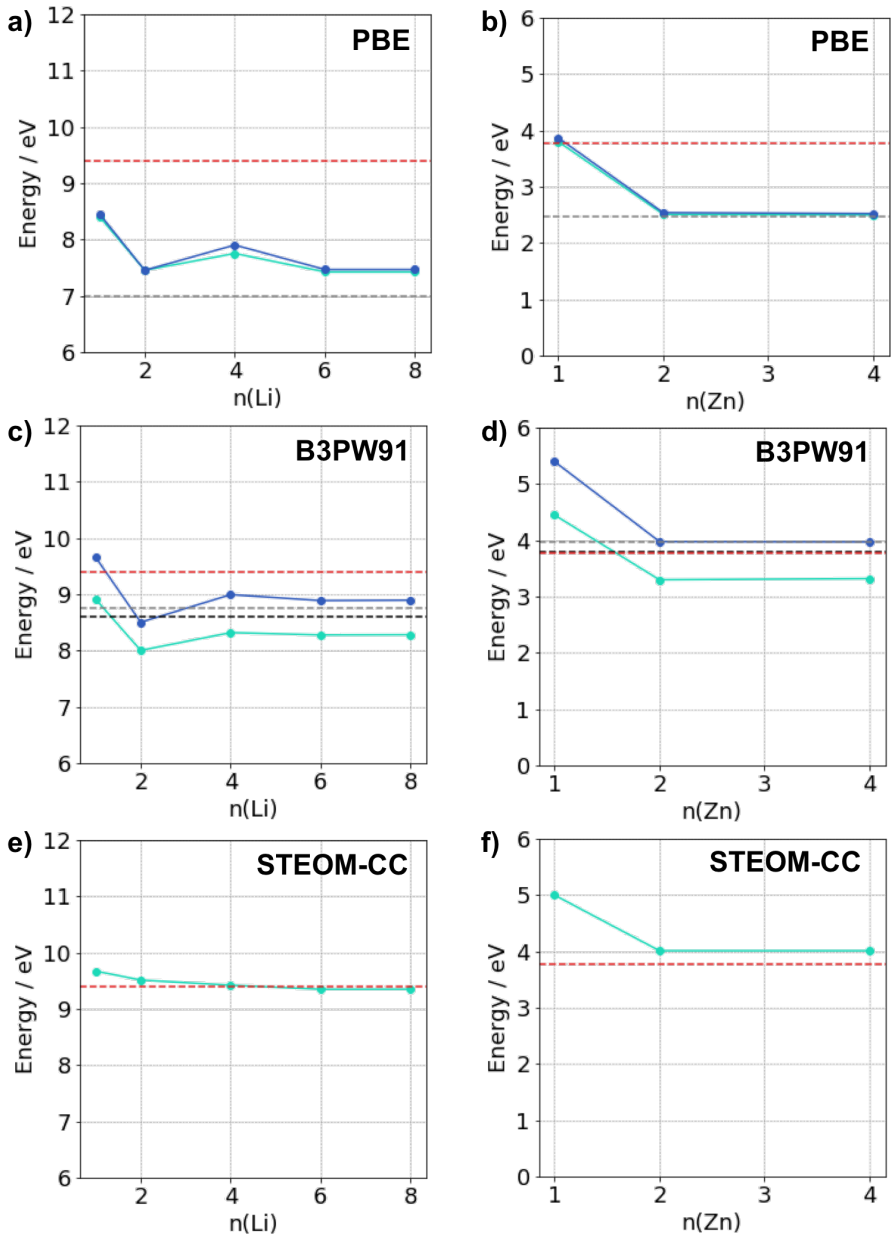

Figure 11.6: Experimental versus calculated band gap energies with **a)** and **b)** PBE, **c)** and **d)** B3PW91, and **e)** and **f)** bt-PNO-STEOM-CCSD (STEOM-CC) for LiCl (left) for cluster sizes $[Li_nCl_n]^0$ with n=1-4, 6 and 8 and for ZnS (right) for cluster sizes $[ZnS_4]^{6-}$, $[Zn_2S_7]^{10-}$ and $[Zn_4S_{10}]^{12-}$. Color code: experiment (dashed red line), first excited state (turquoise line), HOMO-LUMO gap (solid blue line), periodic DFT results (dashed black[12] and gray[11] line).

11.7 Performance Evaluation of TD-DFT and bt-PNO-STEOM-CCSD

In the following analysis, the calculated optical band gaps of the selected set of organic and inorganic systems are compared with their respective experimental values, as shown in Table 9.1 and Table 9.2. To provide a visual representation of the energy discrepancies between the experimental and calculated results, Figure 11.7 has been included, showing the respective absolute errors. Additionally, for a comprehensive reference, the calculated values of the optical band gaps are listed in Table B.10, while Table B.11 focuses specifically on the calculated fundamental band gaps of the organic semiconductors. The tables can be found in the appendix starting on page 335. They also show the Mean Absolute Errors (MAEs) as well as the Maximum Absolute Errors (MaxAE) of the different calculation methods.

The MAE for the entire benchmark set decreases consistently across the different TD-DFT methods, following a pattern from (meta-)GGA (1.18 eV) to hybrid (0.67 eV) to double-hybrid (0.56 eV), which is consistent with Jacob's ladder of DFT functionals. An even lower MAE of 0.16 eV yields bt-PNO-STEOM-CCSD. Significant differences exist within the groups, allowing a comprehensive comparison between inorganic and organic materials and within the two groups.

On average, TD-DFT shows lower errors when applied to organic compounds. Specifically, the MAE decreases from GGA (0.30 eV) to hybrid (0.25 eV) to double-hybrid (0.24 eV) for the organic semiconductors. The MAE of bt-PNO-STEOM-CCSD is 0.22 eV. Within the group of organic semiconductors, however, there is a notable difference between oligoacenes and α-oligothiophenes. The α-oligothiophenes follow the expected trend of decreasing MAE from GGA (0.49 eV) to hybrid (0.26 eV) to double-hybrid (0.17 eV), while bt-PNO-STEOM-CCSD achieves an even lower MAE of 0.06 eV. In contrast, oligoacenes show an opposite trend with an increasing MAE from GGA (0.10 eV) to hybrid (0.24 eV) to double-hybrid (0.31 eV), and bt-PNO-STEOM-CCSD achieves a higher MAE of 0.38 eV.

In comparison, the fundamental band gaps, summarized in Figure B.9 on page 334 of the appendix, remain consistent for oligoacenes and α-oligothiophenes. In terms of fundamental band gaps, GGA functionals produce the most inconsistent results within the group of functionals, while other methods generally show consistency. The group of GGA functionals gives an MAE of 0.94 eV, the group of hybrid functionals 0.23 eV, the tested double-hybrid functional 0.53 eV (deviating from Jacob's ladder trend), and bt-PNO-STEOM-CCSD 0.19 eV. Within this group of organic semiconductors, the MAEs for the fundamental band gaps calculated by DFT are consistently higher than for the optical band gaps, but similar for both band

gaps calculated by bt-PNO-STEOM-CCSD.

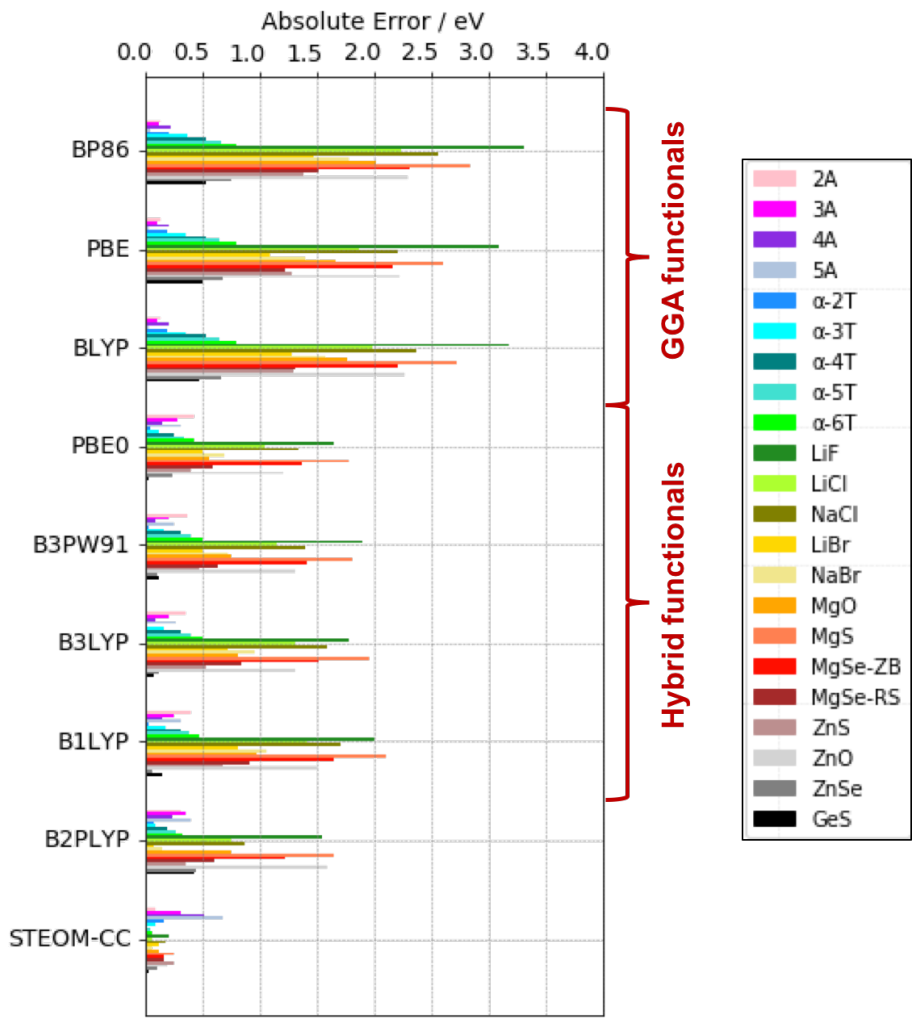

Figure 11.7: Absolute errors in eV of the experimental vs. TD-DFT and bt-PNO-STEOM-CCSD (STEOM-CC) computed optical band gap.

Returning to the optical band gaps and the comparison between inorganic and organic materials, TD-DFT consistently performs worse for inorganic solid-state systems compared to organic semiconductors. However, bt-PNO-STEOM-CCSD achieves comparable performance with an MAE of 0.14 eV for inorganic semiconductors and insulators compared to 0.22 eV for the organic semiconductors. Thus, the method not only performs equally well on two different types of materials, but also on two different models - the free molecular model approximating the organic semiconductors and the electrostatic embedded cluster model for the inorganic semiconductors and insulators. This indicates that the electrostatic embedded cluster model seems to have little influence on the overall result in terms of MAE.

The bt-PNO-STEOM-CCSD method is considered to be less biased than TD-DFT. Since bt-PNO-STEOM-CCSD does not indicate a significant influence of the electrostatic embedded cluster approach on the MAE, the higher error for TD-DFT concerning the inorganic solid state systems compared to the organic ones is probably due to TD-DFT itself rather than to the electrostatic embedding approach.

This statement finds support when comparing to studies[11, 12] using (meta-)GGA and hybrid functionals to calculate band gaps of inorganic solid-state systems with periodic calculations. They report similar errors for the GGA functionals. However, the errors obtained for the hybrid functionals in this report (MAE of 1.07 eV for inorganic solid-state systems) are consistently and systematically higher than in the previously reported results. As discussed, this difference seems to lie in the general approach, as here the first excited state calculated by TD-DFT is used to calculate the optical band gap, while the other studies used the orbital difference. As shown in Figure 11.5 for example examples of LiCl and ZnS, satisfactory agreement between the periodic results and the HOMO-LUMO gap, rather than the first excited state, can be achieved.

Within the group of inorganic solid state systems, a comparison can be made especially between zinc blende and rock salt structures. In general, both structures follow the Jacob's ladder trend. However, there is an unexpected trend in the double-hybrid functionals for zinc blende systems, where the MAE for hybrid and double-hybrid functionals are similar, with values of 1.06 eV and 1.04 eV, respectively. In contrast, there is a clear difference for rock salt structures, with MAE values of 1.07 eV for hybrid functionals and 0.66 eV for double-hybrid functionals.

Surprisingly, for the only orthorhombic system tested, GeS, the MAE is 0.08 eV for hybrid functionals and 0.42 eV for double-hybrid functionals. The post-Hartree-Fock method bt-PNO-STEOM-CC achieves an MAE of 0.02 eV for GeS. Notably, GeS has the smallest experimental optical band gap of the entire inorganic benchmark set with a value of 1.55 eV.

The post-Hartree-Fock method bt-PNO-STEOM-CC shows slightly higher MAE for zinc blende structures compared to rock salt structures, with values of 0.18 eV and 0.11 eV, respectively. However, the rock salt structures generally have higher band gaps, typically above 6 eV, except for the rock salt MgSe, which has a band gap of 3.81 eV. In contrast, the zinc blende structures have smaller band gaps, typically below 5 eV. This suggests that the performance of bt-PNO-STEOM-CC does not significantly depend on the size of the band gap as TD-DFT tends to show worse performance for larger band gaps, as previous studies[11, 12] have shown.

Consistent with these studies[11, 12], the absolute errors of the GGA functionals for these large band gap rock salt structures remain consistently high, with an MAE

of 1.93 eV. Thus, bt-PNO-STEOM-CC shows the potential to significantly reduce the error even within this group. Even for the largest band gaps, such as LiF with an optical band gap of 13.6 eV, bt-PNO-STEOM-CC achieves an error of only 0.19 eV. LiF, which not only has the largest band gap but also contains the challenging element fluorine, does not seem to pose significant problems for bt-PNO-STEOM-CCSD.

In contrast, the TD-DFT results have the largest absolute errors overall for this system, with GGAs having an MAE of 3.18 eV and hybrid functionals of 1.82 eV, and double-hybrid functionals of 1.53 eV, indicating the worst performance of TD-DFT among the last two groups of functionals. Only MgS, which has the largest band gap among the zinc blende structures, shows a similar performance for hybrid and double-hybrid functionals. However, this material has varying experimental results ranging from 4.50 eV to 5.50 eV,[293–299] which introduces uncertainty in the experimental data against which the calculation results are compared. Therefore, the larger error in this case can also be attributed to the experimental uncertainty rather than to the model and method.

MgSe is included in the benchmark set as both a rock salt and a zinc blende structure. While comparable errors are observed for bt-PNO-STEOM-CC, the error is consistently higher for TD-DFT in the zinc blende structure. However, this is not the case for the other zinc blende systems compared to the rock salt systems, indicating that this is an outlier and does not provide further insight into the influence of the crystal structure on the methods and the model as anticipated.

In conclusion, molecular methods can be used to calculate optical band gaps for embedded cluster inorganic solid-state systems, as their errors are comparable to periodic calculations using the same methods. The post-Hartree-Fock method bt-PNO-STEOM-CCSD gives similar results when applied to organic, treated as separate molecules, and inorganic semiconductors and insulators, independent of the elements in the systems and the band gap size. The MAE of bt-PNO-STEOM-CCSD was 0.16 eV across systems. This is comparable to the previously reported error of the method of less than 0.2 eV.[48, 49] Therefore, it shows comparable performance for molecules and solid-state systems.

12 Conclusions of the NMR and Band Gap Benchmark Studies: Key Insights and Findings

This part has demonstrated the possibility of transferring molecular theory methods to solid-state systems for two fundamentally different spectroscopic properties: the nuclear shielding constants together with the resulting chemical shifts and the (optical) band gaps.

It was shown that carefully embedding the atomic clusters of inorganic solid-state systems in an electrostatic environment leads to a model with accuracy independent of the specific electrostatic embedded cluster model itself. This approach allows for predictive power comparable to discrete models for molecules or periodic models for solid state systems, depending on the level of theory. This observation is equally supported by the results of the NMR and band gap benchmark studies.

The NMR benchmark study shows similar accuracy trends as observed in molecular systems with increasing accuracy with respect to the Jacob's ladder of DFT functionals, with the double-hybrid functionals giving comparable accuracy to MP2.[332] Similarly, for the calculation of the optical band gap, the errors compared to experimentally calculated values using bt-PNO-STEOM-CCSD for the inorganic benchmark set were comparable to the organic benchmark set without electrostatic embedding. As importantly, they were also consistent with previous studies[48, 49] on molecules, which also predict an error smaller than 0.2 eV, as do the current studies.

However, there is a discrepancy in the TD-DFT results of the optical band gaps between the organic and inorganic benchmark systems. The inorganic systems show larger average absolute errors, which are likely influenced by the methods and materials themselves rather than by the molecular theory approach or the electrostatic embedded cluster model. This conclusion is drawn from the agreement between the calculated optical band gaps and the expected errors from previous benchmark studies[11, 12] of periodic clusters at the DFT level.

During the development of an effective electrostatic embedded cluster model for

the two benchmark studies, it was found that the design of the cluster model had a minimal influence on the nuclear shielding constants when a sufficiently large QC was used. However, the embedding environment played a critical role in achieving convergence, especially for QCs with significant formal charges that required neutralization and balanced charge distribution. Cluster size convergence was particularly important for the NMR shielding of the innermost atoms, since these atoms exhibited the properties closest to bulk behavior and were used to predict the NMR shielding constants of the various materials. The decision to focus on the innermost atoms of the QC was driven by the inaccuracy observed in the calculations with the outermost atoms, which were directly affected by the electrostatic environment. Even with a homogeneous charge distribution, relying only on the outermost atoms led to incorrect shielding constants. This highlighted the importance of including "real" atomic neighbors to capture all relevant effects in nuclear shielding calculations.

In contrast, the band gap study showed that the transition between the QC and the electrostatic environment was satisfactory when a uniform charge distribution was established across the QC, BR, and PC regions. This allowed the valence orbitals of all atoms within the predominantly ionic QCs to effectively capture the correct energetic positions of the overall band structure necessary for the calculation of the band gap. In addition, the study demonstrated a rapid convergence of cluster size with respect to calculated band gaps.

Although the electrostatically embedded cluster protocol was successful for both studies in terms of designing and optimizing the QC, BR, and PC regions, the QCs themselves converged for different sizes specific to each property and material type due to their different nature. Thus, while this shows that the general electrostatic embedded cluster protocol appears to be applicable to spectroscopic properties of various types, for efficient computation it is essential to tailor the cluster size according to the specific requirements of each property. In other words, there is no universal cluster configuration that fits all cases. However, in both cases, the cluster convergence scheme concerning the property was identical for all methods. This transferability allows at least for the employed study set and indication to a wider generality to define the converged cluster size on a lower level of theory and recompute the property with a more accurate one.

In addition to the general findings regarding the suitability of the electrostatic embedded cluster model in combination with molecular theory methods for solid-state spectroscopy, specific insights can be gained regarding the performance of the tested methods in the calculation of properties. These are summarized first for NMR and then for the band gap benchmark study.

For the nulcear shielding constants a good balance between efficiency and accuracy is achieved by using Jensen's pcSseg-3 basis set for MP2 and double-hybrid DFT, while the smaller pcSseg-2 basis set could be used in conjunction with GGA and hybrid DFT functionals. A study of small cluster structures without embedding shows that for the benchmark systems chosen in this study, MP2 results are quite close to values obtained at the CCSD(T) level of theory.

The calculated chemical shifts were compared with experiments at several levels of theory, including standard (meta-)GGA (KT2, M06L, BLYP, PBE, and TPSS), hybrid (M06, B3LYP, PBE0, and TPSSH), and double-hybrid (DSD-PBEP86, DSD-BLYP, and B2PLYP) functionals and MP2. The results confirm the trend found by comparing nuclear shielding constants values obtained at different levels of theory. The (meta-)GGA functionals give results with acceptable accuracy but somewhat larger deviations, while TPSS shows the best performance. Hybrid functionals give results with slightly improved robustness (lower standard deviations) in many cases, but still some outliers can be found. MP2 and double-hybrid functionals significantly improve the results over standard DFT. They give more consistent results for all nuclei, while most DFT functionals perform significantly differently for different nuclei. A prominent example of inconsistent performance for different nuclei is M06L. When using MP2 and double-hybrid functionals, the maximum deviations are reduced and low or lowest average deviations are observed for almost all nuclei in the study.

In assessing the overall performance, certain key considerations were outlined in the introduction to the benchmark set in Chapter 9. One aspect mentioned was the influence of bonding character, focusing specifically on MgO and MgS, which represent systems with different covalent and ionic characteristics. The study showed that the overall approach is independent of bonding character, although certain methods, such as hybrid functionals, show more inconsistent results when dealing with this change.

Another point raised was the effect of geometry on the approach used. It was found that there was no significant influence attributable to geometry, suggesting that the approach remains robust regardless of the crystal structure as long as the protocol is followed.

The comparison between highly unshielded alkali metal ions and shielded nuclei in halides showed that the predicted order of nuclear shielding constants is generally accurate compared to experiment, with a few exceptions. However, the accuracy of the comparison with experiment is reduced for unshielded nuclei because their shifts are often close to zero, resulting in relatively less accurate results. The highly deshielded nuclei are more sensitive to methodological and environmental

changes.

The study highlighted the importance of accounting for relativistic effects by examining nuclei with a high or low number of electrons. Especially for heavy elements, it was shown that they require the inclusion of relativistic effects. It should be considered that even zero point vibrational corrections may need to be included to improve accuracy and further reduce deviations from experiments. Especially if elements beyond the late fourth period are included, in terms of scalar relativistic effects, and spin-orbit coupling becomes increasingly important.

For the band gap, a variety of DFT functionals - GGA (BP86, PBE, BLYP), hybrid (PBE0, B3PW91, B3LYP, B1LYP) and double-hybrid (B2PLYP) - and bt-PNO-STEOM-CCSD were tested. Among the different methods applied to organic and inorganic systems, bt-PNO-STEOM-CC provides the best agreement with the available experimental values, resulting in absolute errors that are on average less than 0.2 eV. Relative to bt-PNO-STEOM-CC and the experimental values, TD-DFT and Δ-SCF/DFT results are of varying accuracy, showing a tendency that roughly follows the expectations from Jacob's ladder and is consistent with the periodic DFT results. In this context, the double-hybrid functionals perform best in the GGA, hybrid, and double-hybrid functional series.

The introduction to the benchmark set in Chapter 9 highlighted important factors for the inclusion of certain systems. One factor was the potential comparison of two crystal structures: zinc blende and rock salt. Consistent results were found only for SCl models in zinc blende structures, while both SCce and SCl were viable for rock salt, with SCl being more efficient. The inconsistency may be due to the role of symmetry breaking and bond breaking in accurately describing the band structures of the more covalent zinc blende structure within the QC, while these factors are less important in the more ionic rock salt structure. More research is needed to fully understand this phenomenon. The results for the two crystal structures were comparable.

In addition, the wide range of band gaps played an important role in the selection of the band gap benchmark set. The approach demonstrated its applicability across different band gap sizes, with bt-PNO-STEOM-CCSD consistently providing reliable results. This was evident even for challenging materials such as LiF, indicating that the performance of the model remains consistent regardless of the specific band gap size.

The individual and collective results of the benchmark studies pave the way for obtaining accurate results by applying high-level molecular methods within the electrostatic embedded cluster model. This result was the overall goal of the benchmark study: quantitative results comparable to experimental values were obtained

as long as post-Hartree-Fock methods with a sufficiently large basis set were applied. However, this approach also promises to provide valuable insights into solid-state properties. This research direction will be further pursued in the upcoming part.

Part IV

Unraveling the Spectroscopic Response of Multimetallic Oxide Solid-State Systems

It is nice to know that the computer understands the problem. But I would like to understand it, too. - Eugene Wigner[397]

Introduction to Part IV

In recent years, heterogeneous oxidation catalysis has played a crucial role in the functionalization of hydrocarbon oil and biomass feedstock, leading to the production of a range of fine chemicals.[398–400] The use of multimetallic oxide surfaces, in particular, has demonstrated high selectivity based on established principles of oxidation catalysis.[401, 402] Compared to their monometallic heterogeneous and homogeneous catalysts counterparts, multimetallic oxide surfaces offer advantages in separation, recovery, recycling, and amenability under continuous processing.[403] While noble metals such as gold, platinum, or palladium are often employed to create highly active oxidation catalysts, their high cost, low thermal stability, and tendency to sinter and poison pose significant challenges.[404] In contrast, transition metal oxide catalysts, such as cobalt-based spinel oxides like Co_3O_4, offer cost-effective alternatives with higher thermal stability and greater resistance to poisoning.[405] Co_3O_4 based catalysts have been successfully used in various oxidation reactions, including selective CO oxidation,[406–412] combustion of volatile organic compounds (VOC),[404, 412, 413] alcohol oxidation[414–417] , and hydrogen evolution reactions (HER).[418–420]

The crystalline solid-state system Co_3O_4, also known as $Co(II,III)_3O_4$, adopts the spinel structure with tetrahedral Co(II) centers and distorted octahedral Co(III) centers in a 1:2 ratio, making it a multimetallic system. The Co(III) sites are low spin and diamagnetic, while the Co(II) sites are locally high spin and couple antiferromagnetically (AF), giving Co_3O_4 an overall antiferromagnetic character. Unraveling the electronic structure of Co_3O_4 and its role in catalysis is essential to design targeted chemical products with desired properties. To this end, extensive synthetic, spectroscopic, and computational efforts have been undertaken to investigate the local coordination environments of the Co(II) and Co(III) centers of these cobalt-based oxide catalysts. Recent spectroscopic studies of the alkaline oxygen evolution reaction (OER) have linked the increase in catalytic activity to an increase in occupancy of Co(II) at tetrahedral defect sites induced by laser[421]. In contrast, in thermally catalyzed oxidation of 2-propanol, the formation of unsaturated five-coordinated Co(III) centers appears to be a crucial factor in the catalytic activity[416].

These findings highlight the importance of establishing unambiguous correlations between geometric and electronic structures to spectroscopic response. However, this task is complicated even for Co_3O_4 because of the antiferromagnetic coupling between interacting Co centers, which extends beyond direct Co(II)-Co(II) exchange interactions[422, 423].

Based on the Co_3O_4 spinel catalyst, the synthetic derivatives $Co(III)_2ZnO_4$ and $Al_2Co(II)O_4$ that aim to isolate the different cobalt centers (octahedral Co(III) and tetrahedral Co(II), respectively) have been synthesized.[424, 425] In these systems a large variety of spectroscopic and mechanistic studies have been reported.[426–439] These experimental observations have been often combined with a range of computational studies to establish electronic structure relations with the experimentally observed spectroscopic response of these catalysts as precursors or under reaction conditions.[80, 173, 427–429, 439–441] These studies have offered significant insight regarding the role of Co(III) and Co(II) sites in oxidation reactions when acting in a synergic fashion like in spinel Co_3O_4 or as isolated sites in Co_2ZnO_4 and Al_2CoO_4. Despite this progress probing the degree of the antiferromagnetic coupling in Co_3O_4 spinel catalyst and its synthetic derivatives Co_2ZnO_4 and Al_2CoO_4 through correlation to spectroscopic observables remains a fundamentally challenging task.[416, 423, 426, 434, 442]

Several synthetic derivatives of the Co_3O_4 spinel catalyst have been synthesized, such as $Co(III)_2ZnO_4$ and $Al_2Co(II)O_4$, to isolate the different cobalt centers - the octahedral Co(III) and tetrahedral Co(II), respectively.[424, 425] Numerous spectroscopic and mechanistic studies have been conducted on these systems,[426–439] combined with a range of computational studies to establish electronic structure relations with the experimentally observed spectroscopic response of these catalysts as precursors or under reaction conditions.[80, 173, 427–429, 439–441] These studies have provided valuable insight into the role of Co(III) and Co(II) sites in oxidation reactions when acting in a synergic fashion like in spinel Co_3O_4 or as isolated sites in Co_2ZnO_4 and Al_2CoO_4. However, despite this progress, probing the degree of the antiferromagnetic coupling in Co_3O_4 spinel catalyst and its synthetic derivatives through correlation to spectroscopic observables remains a fundamentally challenging task.[416, 423, 426, 434, 442]

The following chapters of this work utilize the established electrostatic embedding approach to model the electronic structure of Co_3O_4 and its derivatives Co_2ZnO_4 and Al_2CoO_4. This will involve a combination of density functional theory (DFT) and wavefunction-based protocols. The first part of the study aims to examine the optical band gaps of Co_3O_4 while emphasizing the separate influences of the Co(II) and Co(III) sites, which will be evaluated using Co_2ZnO_4 and Al_2CoO_4, respectively.

Additionally, this work intends to acquire knowledge regarding the cobalt oxides by recalculating the experimental X-ray emission (XES) spectra of the three cobalt oxide derivatives and analyzing the impact of the geometric and electronic structures. Furthermore, this will include a focus on the role played by antiferromagnetic coupling in these systems.

The organization of this part is as follows. Chapter 13 starting on page 168 introduces the crystal and electronic structure of the three cobalt oxides, as well as the concept of antiferromagnetic coupling. This chapter also explains the general considerations concerning the theoretical methods used in the study. Chapter 14, which begins on page 181, investigates the optical band gaps of Co_3O_4 and explores the role of the different Co sites and antiferromagnetic coupling in this property with methods ranging from (broken-symmetry) TD-DFT up to multireference methods including MR-EOM-CC. Chapter 15 and Chapter 16, starting on page 226 and 261, respectively, focus on the $K\beta_{1,3}/K\beta'$ mainline and $K\beta_{2,5}/K\beta''$ Valence-to-Core (VtC) XES spectra of the three cobalt derivatives Co_3O_4, Al_2CoO_4, and Co_2ZnO_4. These chapters aim to decipher the intensity mechanism of the different XES spectra by examining the contributions of the Co sites, their local environment, and antiferromagnetic coupling with one-electron DFT protocols as well as CASCI. Further details on the structure of the chapters and an introduction to the different problems and their significance are provided in the appropriate places within the chapters. Contrary to the previous part, no general conclusion will be drawn at the end, as individual conclusions are already made in the respective chapters of the individual studies, since it was found more comprehensible for this part.

13 Introduction to Co_3O_4 and Its Derivatives

The primary goal of this chapter is to introduce the three cobalt oxide derivatives, namely Co_3O_4, Al_2CoO_4, and Co_2ZnO_4. In addition, the phenomenon of antiferromagnetic coupling, which is pertinent to the description of Co_3O_4 and Al_2CoO_4, is also covered in detail.

The chapter is organized into two main parts:

First, the crystal structures of the three cobalt oxide derivatives are thoroughly described, and their respective electrostatic embedding models are discussed. The synthesis of these crystals, which serves as the foundation for building the models, is summarized in the appendix, in Section C on page 337.

Second, the chapter introduces antiferromagnetic coupling through the use of a toy model, Al_2CuO_4, and discusses different approaches for addressing this phenomenon. The discussion then shifts to the cobalt oxides, where potential challenges associated with applying the concept of antiferromagnetic coupling are also explored.

Overall, this chapter aims to provide a thorough understanding of the crystal structures, electrostatic embedding models, and antiferromagnetic coupling of the cobalt oxide derivatives, which are crucial to understanding their properties in the context of the subsequent spectroscopic studies.

13.1 The Crystal Structures and Models of the Cobalt Oxides

13.1.1 The Crystal Structures of the Cobalt Oxide Derivatives

The crystal structure of $Co(II,III)_3O_4$, visualized in Figure 13.1a, is in a cubic space group (F-43m) known as the spinel group.[443] It is a mixed-valence compound where Co(II) and Co(III) centers are present in a 1:2 stoichiometry. Hence, it is also known as $Co(II)[Co(III)_2O_4]$. The Co(II) and Co(III) centers form corner-sharing $[Co(II)O_4]^{6-}$ and $[Co(III)O_6]^{9-}$ units termed A and B sites, respectively. The

high spin Co(II) ions occupy the tetrahedral A sites, which exhibit a local magnetic moment of 3.02 μB detected by SQUID magnetometry. The Co(III) ions occupying the octahedral B sites are low spin.[444]

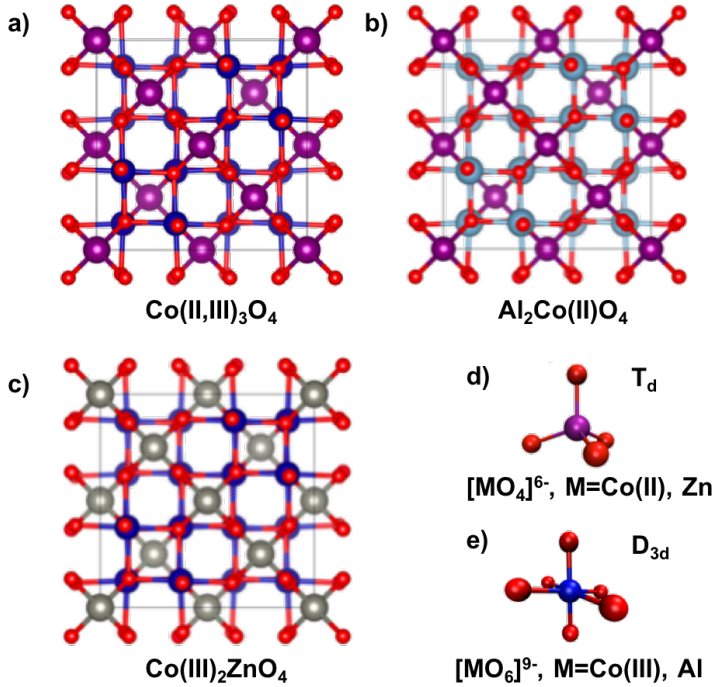

Figure 13.1: Crystal structures of the spinel cobalt oxides: **a)** Co_3O_4, **b)** $Co(III)_2ZnO_4$, and **c)** $Al_2Co(II)O_4$. Local view of the **d)** T_d symmetric $[MO_4]^{6-}$ (M=Co(II) or Zn) and **e)** D_{3d} symmetric $[MO_6]^{9-}$ (M=Co(III) or Al) building units. Color code: Co(III) (blue), Co(II) (purple), Al (turquoise), Zn (gray).

The spinel structure of $Co(II,III)_3O_4$ arises from the difference in local spin-pairing between the A and B sites. Despite differences in oxidation and spin states, the Co-O bond lengths are similar, with values of 1.955 Å for Co(III) and 2.025 Å for Co(II). The tetrahedral Co(II) centers are antiferromagnetically coupled, leading to an open singlet state. The octahedral sites undergo a distortion that lowers the symmetry from O_h to D_{3d}, while the tetrahedral sites retain an "ideal" T_d symmetry, as depicted in Figure 13.1d and Figure 13.1e.

Both $Co(III)_2ZnO_4$ (also known as Co_2ZnO_4, see Figure 13.1b) and $Al_2Co(II)O_4$ (also known as Al_2CoO_4, see Figure 13.1c) can be considered as derivatives of Co_3O_4 in which the tetrahedral Co(II) sites and the octahedral Co(III) sites are substituted with Zn(II) and Al(III), respectively. The M-O bond lengths in $Al_2Co(II)O_4$ are 1.932 Å for Al and 1.974 Å for Co(II). Similarly, the M-O bond lengths in $Co(III)_2ZnO_4$ are 1.931 Å for Co(III) and 1.925 Å for Zn; thus, they are not significantly different from those in Co_3O_4 in either case.

13.1.2 The Electrostatic Embedding Models of the Cobalt Oxide Derivatives

The crystals in the subsequent studies are simulated using the electrostatic embedding approach within the Ionic-Crystal-QM/MM framework discussed in Chapter 3. The local point groups of the tetrahedral Co(II) and distorted octahedral Co(III) sites are critical factors in the studies, and thus, the spherical cluster approach (described on page 39) is used for the QC design. Each QC includes a specific number of metals along with a complete oxygen sphere around each center to capture the impact of the local geometry (in this case, T_d and D_{3d}) on the calculated spectroscopic properties. Figure 13.2 illustrates QC 3t6o, which is representative of all three cobalt oxide derivatives. The "t" abbreviation stands for the building units of the tetrahedral sites, $[MO_4]^{6-}$, where M is Co(II) or Zn, and "o" represents the distorted octahedral sites, $[MO_6]^{9-}$, where M is Co(III) or Al. Therefore, the depicted QC example contains three tetrahedral and six octahedral sites.

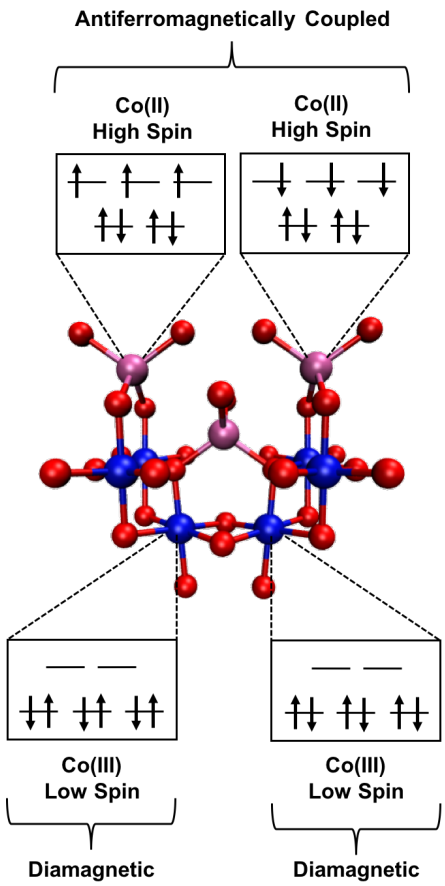

Figure 13.2: Cluster model size 3t6o of Co_3O_4 with the respective electronic structure of the $3d$ orbitals of the Co(II) and Co(III) centers.

The complete sequence of Co_3O_4 QCs, which has been illustrated in Figure 3.12 and presented in Subsection 3.2.1, is also representative for Co_2ZnO_4 and Al_2CoO_4. The series encompasses the isolated tetrahedral and distorted octahedral sites, namely 1t and 1o, respectively, and proceeds up to the 10t20o structure. With the exception of the isolated sites, each QC sustains the stoichiometric ratio of 1:2 in relation to the tetrahedral and distorted octahedral sites.

Following the guidelines presented in Chapter 3 on constructing electrostatically embedded cluster models, the QCs are embedded in approximately 30,000 PCs, accounting for the long-range Coulomb effects of the crystal. The embedding enviroment also includes three layers of ECPs as the BR. Table 13.1 provides a comprehensive list of all QC models used in the study, along with the corresponding number of ECPs and PCs for each.

Table 13.1: Detailed description of the employed cobalt oxide models within the embedded cluster approach in terms of the QC compositions, the number of ECPs in the BR and the number of point charges in the PC region.

QC type	Co_3O_4	Al_2CoO_4	Co_2ZnO_4	n(ECP)	n(PC)	n(QC+ ECP+ PC)
1t	$[Co(II)O_4]^{6-}$	$[Co(II)O_4]^{6-}$	-	92	29391	29488
1o	$[Co(III)O_6]^{9-}$	-	$[Co(III)O_6]^{9-}$	88	29393	29488
1t2o	$[Co(III)_2Co(II)O_{12}]^{16-}$	$[Al_2Co(II)O_{12}]^{16-}$	$[Co(III)_2ZnO_{12}]^{16-}$	141	29332	29488
2t4o	$[Co(III)_4Co(II)_2O_{21}]^{26-}$	$[Al_4Co(II)_2O_{21}]^{26-}$	$[Co(III)_4Zn_2O_{21}]^{26-}$	181	29280	29488
3t6o	$[Co(III)_6Co(II)_3O_{30}]^{36-}$	$[Al_6Co(II)_3O_{30}]^{36-}$	$[Co(III)_6Zn_3O_{30}]^{36-}$	220	29229	29488
4t8o	$[Co(III)_8Co(II)_4O_{36}]^{40-}$	$[Al_8Co(II)_4O_{36}]^{40-}$	$[Co(III)_8Zn_4O_{36}]^{40-}$	248	29192	29488
6t12o	$[Co(III)_{12}Co(II)_6O_{48}]^{48-}$	$[Al_{12}Co(II)_6O_{48}]^{48-}$	$[Co(III)_{12}Zn_6O_{48}]^{48-}$	292	29130	29488
8t16o	$[Co(III)_{16}Co(II)_8O_{64}]^{64-}$	$[Al_{16}Co(II)_8O_{64}]^{64-}$	$[Co(III)_{16}Zn_8O_{64}]^{64-}$	540	28860	29488
10t20o	$[Co(III)_{20}Co(II)_{10}O_{80}]^{80-}$	$[Al_{20}Co(II)_{10}O_{80}]^{80-}$	$[Co(III)_{20}Zn_{10}O_{80}]^{80-}$	596	28782	29488

In the context of the Ionic-Crystal-QM/MM framework, the electrostatic embedding environment was constructed and refined. Specifically, for the 2t4o model of the Co_3O_4 series, the charges were automatically optimized applying the keyword "CONV_CHARGES true" at the BP86/DKH-def2-tzvp level of theory. The resulting charges for the distorted octahedral Co(III)/Al site and the tetrahedral Co(II)/Zn site were 2.49 and 1.66, respectively, while the oxygen charge was -1.66. To maintain uniformity, these charges were utilized for all cluster sizes and calculation types. Furthermore, the same charges were employed for Co_3O_4, Co_2ZnO_4, and Al_2CoO_4. The total charge of all models was neutralized with "ENFORCETOTALCHARGE true" and "CHARGE_TOTAL 0" for all calculations.

Notably, the magnitude of the charges had an insignificant effect on the calculated XES spectra and band gaps, provided that the charges remained within a phys-

ically reasonable range. Although all QCs in Table 13.1 are formally strongly negatively charged, initial results demonstrated that the excess charge in the clusters did not impact the quality of the computed results. This suggests that the electronic structure of the systems was accurately represented and that no additional measurements towards the design of neutralized QCs have to be taken, such as introducing a Hartree-Fock layer between the QC and the BR+PC regions or employing the supercell QC design scheme (see also page 42).

13.2 A brief Introduction to Antiferromagnetically Coupled Metal Centers

13.2.1 An Antiferromagnetic Coupling Model

Throughout this work, only closed-shell systems have been taken into account. However, in the case of Co_3O_4, this situation changes, as Figure 13.2 demonstrates. The Co(III) centers that are locally octahedrally coordinated possess a $3d^6$ electron configuration with low spin and therefore, behave as closed-shell systems in the initial consideration. In contrast, the tetrahedrally coordinated Co(II) sites have a high spin $3d^7$ electron configuration with three unpaired electrons. Therefore, they are regarded as open-shell centers. Moreover, the Co(II) sites couple antiferromagnetically, which makes Co_3O_4 and Al_2CoO_4 antiferromagnetic overall. Co_2ZnO_4 contains only low spin Co(III) sites; thus it is regarded as diamagnetic.

The partially filled $3d$ orbitals, open-shell character, and antiferromagnetic coupling present new challenges in applying accurate computational models and methods. This section briefly discusses the key points to consider when dealing with an antiferromagnetic system. The specific effects that antiferromagnetism has on the band gap and XES problems are discussed in greater detail in the relevant chapters.

To explain antiferromagnetism, a simplified model is constructed by replacing the $3d^7$ Co(II) centers in Al_2CoO_4 with $3d^9$ Cu(II) centers. This model is advantageous as each Cu(II) center has only one unpaired electron as opposed to three unpaired electrons in Co(II) centers. Figure 13.3 visualizes the corresponding QC example 3t6o

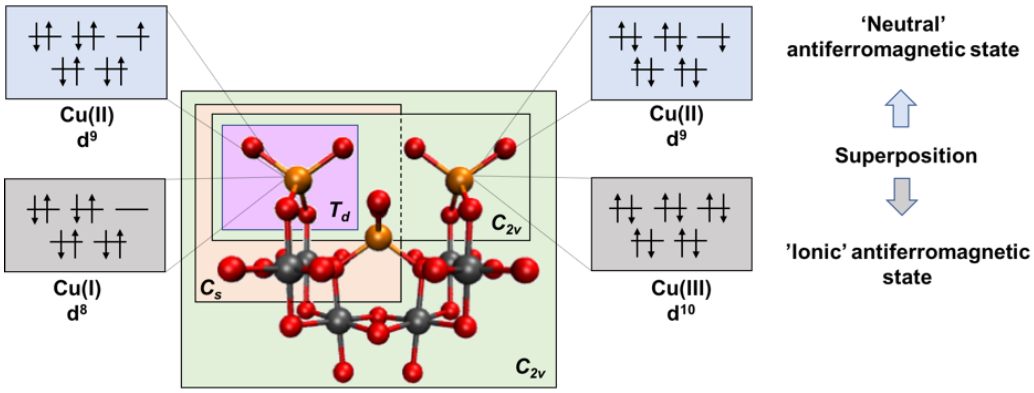

Figure 13.3: Cluster model the "toy" model 3t6o-$Al_2Cu(II)O_4$ with three tetrahedral Cu(II) centers with the respective electronic structures of the centers' $3d$ orbitals regarding the "neutral" and "ionic" antiferromagnetic states. The symmetries of the centers locally and with respect to each other are indicated (T_d, C_s, or C_{2v}).

In general terms, antiferromagnetic coupling between metal centers occurs when the unpaired electrons in each center have spins that align antiparallel with those of the neighboring centers. This is depicted in Figure 13.3 for the Cu(II) example (blue boxes), where the left box has an electron with an up spin and the right box one with a down spin. Figure 13.2 shows the same for the Co(II) sites in Co_3O_4. The antiferromagnetically coupled centers in both cases form an open singlet. Nonetheless, this is not the end of the story. The open singlet, as described, is referred to as the "neutral" antiferromagnetic state. In superposition to this state, there exists the "ionic" antiferromagnetic state in which the two coupled electrons share one orbital localized on one of the two Cu centers (gray boxes in Figure 13.3). While in the "neutral" antiferromagnetic state, both centers are formally Cu(II), in the "ionic" antiferromagnetic state, the Cu centers have effective charges of Cu(I) and Cu(III), respectively. It has been demonstrated that the interaction with the "ionic" antiferromagnetic states stabilizes the "neutral" antiferromagnetic states, which forms the basis of antiferromagnetic coupling.[56].

It is essential to investigate the symmetry elements of the Cu(II) centers in the extended $Al_2Cu(II)O_4$ structure to achieve a more comprehensive picture of antiferromagnetic coupling as a multicenter interaction. Moreover, it is worth noting that understanding the symmetry of multicenter systems is also relevant to other types of interactions and processes in spectroscopy.

As the system size increases from a single tetrahedral Cu(II) center to multiple centers, symmetries beyond the local T_d structure become significant. For two centers, the symmetry can either be C_s or C_{2v}. In the case of the 3t6o model, the overall symmetry of the three Cu(II) centers is C_{2v}. Figure 13.3 illustrates the different sym-

metry elements. As the size of the structure increases further, such as in the 6t12o model, the symmetry turns to C_{2h}. It is assumed that for interactions between a specific number of centers, only the local symmetry involving the centers and their direct ligands are relevant, but not the global symmetry of the whole spinel structure. Additionally, it is presumed that a process forbidden in the smallest symmetric unit representing the process, e.g., electron excitations or decays, is not allowed in larger system sizes, even if the symmetry of these would allow it.[445] For now, only the interactions between two Cu(II) centers will be evaluated, with a focus on centers with the C_{2v} symmetry since it is the same symmetry as for three Cu(II) centers. The latter will play a vital role in the subsequent chapters.

In the first step of combining the concepts of symmetry and antiferromagnetism, Figure 13.4a visualizes the interacting canonical MOs of two Cu(II) centers in C_{2v} symmetry.

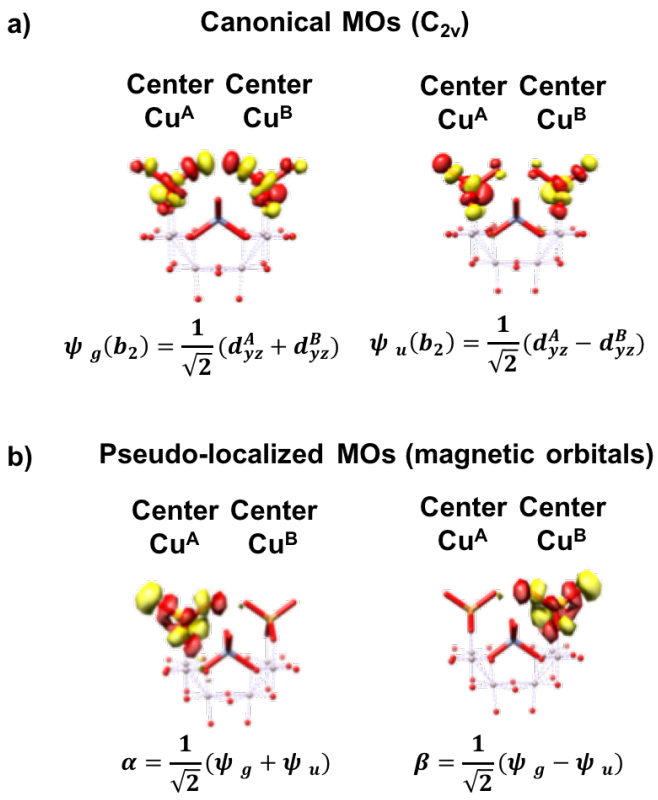

Figure 13.4: Visualization of **a)** the canonical singly occupied MOs of the Cu(II)-Cu(II) interacting centers in 3t6o type of clusters in C_{2v} symmetry referring to the symmetric as $\psi_g(b_2) = \frac{1}{\sqrt{2}}(d^A_{yz} + d^B_{yz})$ and the antisymmetric as $\psi_u(b_2) = \frac{1}{\sqrt{2}}(d^A_{yz} - d^B_{yz})$ and **b)** the pseudo-localized broken-symmetry magnetic orbitals of C_{2v} symmetry referring to as $\alpha = \frac{1}{\sqrt{2}}(\psi_g + \psi_u)$ and $\beta = \frac{1}{\sqrt{2}}(\psi_g - \psi_u)$.

The two unpaired electrons occupy symmetric and antisymmetric MOs, $\psi_g(b_2) = \frac{1}{\sqrt{2}}(d^A_{yz}+d^B_{yz})$ and $\psi_u(b_2) = \frac{1}{\sqrt{2}}(d^A_{yz}-d^B_{yz})$, respectively.[446] When a pair of unpaired electrons is distributed between two interacting centers, it gives rise to three singlet and one triplet configuration state functions (CSFs) with M_S=0, as previously demonstrated.[56] The resulting CSFs can lead to different states based on the localized "magnetic orbitals" of the two centers (Cu^A and Cu^B), $\alpha = \frac{1}{\sqrt{2}}(\psi_g + \psi_u)$ and $\beta = \frac{1}{\sqrt{2}}(\psi_g - \psi_u)$, which are visualized in Figure 13.4b.

Figure 13.5a shows the "ferromagnetic" state $|^3F\rangle$ with $^3A_1$ symmetry, in which the two unpaired electrons localized in the two separate orbitals are aligned with parallel spins. Alternatively, the previously introduced "neutral" antiferromagnetic state $|^1N\rangle$ in Figure 13.5b with $^1A_1$ symmetry can occur, where the two unpaired electrons are located in separate orbitals but with antiparallel spins, coupling to an open singlet. Similarly, the antiferromagnetic coupling can lead to two interchangeable "ionic" antiferromagnetic singlet states $|^1I\rangle$ with symmetry $^1A_1$, where the interacting electrons are localized in one or the other copper center of the interacting pair. Figure 13.5c visualizes one of the two potential "ionic" antiferromagnetic states. It is important to note that all these states are proper spin-adapted CSFs of $^{1,3}A_1$ symmetries. The two types of antiferromagnetic states can mix since they have the same symmetry and as mentioned above are usually thought of as a superposition.[56, 447, 448]

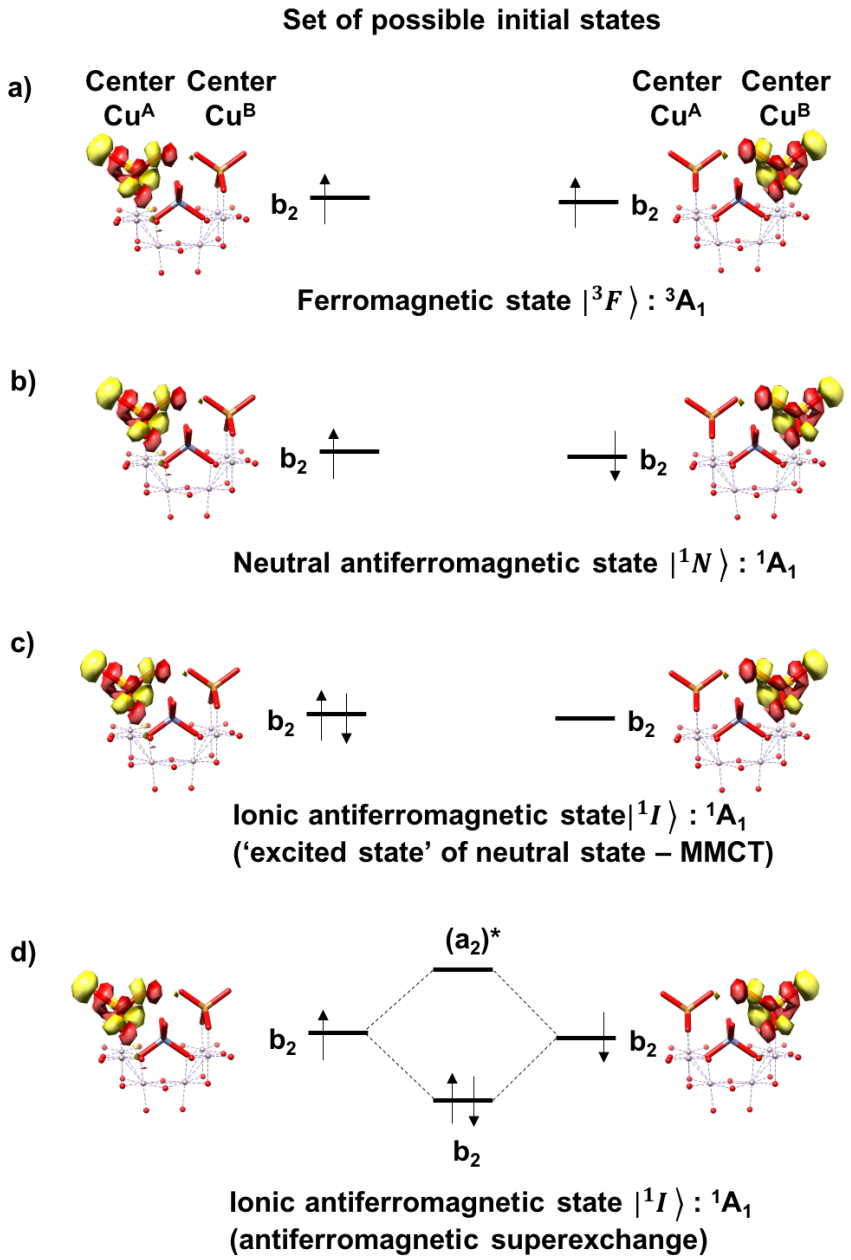

Figure 13.5: MO diagrams of **a)** the ferromagnetic, **b)** the antiferromagnetic "neutral", and **c-d)** the antiferromagnetic "ionic" states of symmetries $^{1,3}A_1$.

Obtaining the "ionic" state from the "neutral" antiferromagnetic state can be understood in two different ways. One way is to view the "ionic" state as a metal-to-metal charge transfer (MMCT) state of the "neutral" state, or vice versa, which would be the transition between the states in Figure 13.5b and Figure 13.5d. Another way, and the more common representation, is to describe the "ionic" state resulting

from an antiferromagnetic superexchange coupling interaction, which is a covalent metal-ligand interaction. In this case, the two localized MOs of the "neutral" state can combine to form a doubly occupied MO with metal character (Cu $3d_{yz}$; b_2) and an unoccupied MO with ligand character (O $2p$; a_2^*), as illustrated in Figure 13.5d. In this picture, the "ionic" states can be connected to the "neutral" states via MLCT-LMCT (metal-to-ligand/ligand-to-metal charge transfer) transitions.[447, 449].

Whether the "ionic" and "neutral" antiferromagnetic states are connected via MMCT or superexchange is irrelevant to the forthcoming spectroscopic studies. Both models lead to the same result with states of identical symmetry. Subsequently, it is only crucial that the electrons are localized at the same center for the "ionic" state and different centers for the "neutral" state and that these states are expected to be in a superposition.

13.2.2 Methods to Address Antiferromagnetic Coupling

The superposition of "ionic" and "neutral" antiferromagnetic states is a multireference problem. It can be addressed by finding a multiconfigurational description of the antiferromagnetic states. Thus, methods such as CASSCF, described in Chapter 6.1, can be used as a starting point. In the following chapters, mainly CAS-based protocols will be applied. A qualitatively correct picture of the electronic structure can be achieved by including electron configurations in the active space that describe "ionic" and "neutral" antiferromagnetic states. By running the CASSCF calculation with the respective singlet multiplicity, the set of resulting CSFs can describe the antiferromagnetic states. This can provide a reasonable zeroth-order wavefunction to handle the static correlation between the two types of states.[172] Furthermore, the ferromagnetic state can also be included in the representation by accounting for the same set of electron configurations as used for the "neutral" antiferromagnetic states and by treating the desired multiplicity of the ferromagnetic state (triplet for the Al_2CuO_4 example) enabled by SOC within one CASSCF calculation.

Describing the magnetic coupling and energetics of the "ionic" and "neutral" antiferromagnetic states accurately is a challenging task. The notion of "superposition" used to describe the mixing of the two isolated types of states imposes genuine degeneracy of the states. However, the CASSCF protocol may not correctly account for this mixing, and as a result, the "ionic" and "neutral" antiferromagnetic states may differ significantly in energy so that they appear as "actual" excited states of each other. This discrepancy is especially apparent for weak antiferromagnetical coupling, possibly due to large distances between the coupling centers. The extent of mixing between the "ionic" and "neutral" antiferromagnetic states is greater

when the coupling centers are closer in distance, which leads to a larger potential for overlap of the interacting orbitals. In such cases, either the two states can actually mix within the CASSCF framework, or their calculated energies are at least close. For example, in the case of Co(II) or Cu(II) centers with C_{2v} symmetry in Co_3O_4 or Al_2CuO_4, the distance between the centers is relatively large at 5.78 Å. Therefore, it is less likely that the CASSCF approach accurately describes the phenomenon of antiferromagnetic coupling in this system.

The CASSCF approach is limited by the lack of dynamic correlation, which results in an overestimation of the energetic difference between the two antiferromagnetic states. To accurately describe both states simultaneously, perturbation methods like NEVPT2, CASPT2, or DCD-CAS(2) can be employed to handle dynamic correlation. Additionally, recent advancements in CI wavefunction-based methods, such as density matrix renormalization group (DMRG),[63] iterative configuration expansion (ICE-CI),[64, 65] and full configuration interaction quantum Monte Carlo (FCIQMC),[66] which are critical for calculating magnetic anisotropy or the low-lying valence excitation spectrum of multimetallic centers, are promising alternatives for addressing antiferromagnetic problems.[67–70]

The broken-symmetry (BS) DFT method is an alternative approach to treating antiferromagnetic coupling. This method has previously been discussed in Chapter 8.1 in relation to band gaps. It involves treating a system using specific spin-unconstrained Slater determinants. BS-DFT calculations involve two SCF steps. First, the system is calculated as a high-spin state with all spins aligned. Second, the spin on half of the centers is flipped (= the spin vector is rotated), resulting in a total spin S of zero, indicating an antiferromagnetically coupled state.

Thus, for antiferromagnetic systems, one presently only has three choices based on the introduced methods: The first choice is to use an elaborate multireference wavefunction-based method. The second choice is to disregard the antiferromagnetic coupling and align the local spins in parallel. The third choice is to break the spin symmetry and run calculations off a broken-symmetry (BS) determinant. The multireference option is rigorous but quickly gets out of hand regarding its computational complexity. Presently, treatments incorporating dynamic electron correlation can treat two centers at most.[450] It should be emphasized that ignoring the antiferromagnetic coupling or using the BS approach are not entirely satisfactory solutions either. Thus, there is a pressing need for wavefunction-based protocols which can treat conventional properties of antiferromagnetically coupled solids such as band gaps and X-ray emission spectra.

13.2.3 Antiferromagnetic Coupling, Multiplet Effects, and More in the Cobalt Oxides

The previous model for the copper system aimed to capture the different magnetic states of "neutral" and "ionic" antiferromagnetism and ferromagnetism, characterized by singlet and triplet multiplicity, respectively. However, the presence of antiferromagnetically coupled Co(II) centers in the Co_3O_4 and Al_2CoO_4 systems introduces a higher level of complexity. These Co(II) centers possess three unpaired electrons instead of the previously encountered single unpaired electron, leading to an increased complexity in the description. Nevertheless, the principles of symmetry and state mixing remain applicable to both systems.

In Co_3O_4 and Al_2CoO_4, each of the two Co(II) centers has three unpaired electrons, resulting in a potential ferromagnetic state with septet multiplicity, as shown in Figure 13.6a. The "neutral" antiferromagnetic state, characterized by an open singlet state, is retained, with one center having three up-spin electrons and the other having three down-spin electrons, as shown in Figure 13.6b. Both centers retain a locally high spin state.

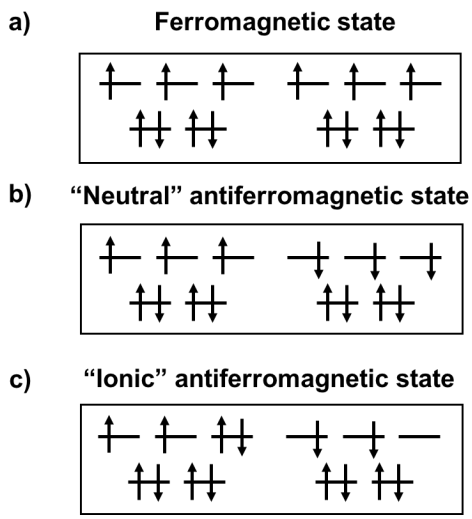

Figure 13.6: Possible **a)** ferromagnetic and **b)** "neutral" or **c)** "ionic" antiferromagnetic states concerning the $3d$ orbitals of two tetrahedral Co(II) sites.

The "ionic" antiferromagnetic state involves the exchange of an electron between the two centers, as shown in Figure 13.6c. However, this representation depicts only one possible scenario, since all three electrons of each center can be subject to superexchange, resulting in a more complicated description of the "ionic" antiferromagnetic state. Therefore, the "ionic" antiferromagnetic state is represented by a linear combination of wavefunctions corresponding to each potential exchange.

While the above cases are likely to be representative of the antiferromagnetic structure of the materials, it is possible that alternative combinations of spin states exist. For example, it is conceivable that more than one electron to "ionic" antiferromagnetic states participate in the superexchange mechanism, leading to the localization of two electrons from one Co center to the other. In addition, intermediate spin multiplicities, namely triplet and quintet states, could arise. However, these states imply a deviation from the ideal antiferromagnetic ground state, where at least one center undergoes spin flip excitation and is not in a high spin state with locally aligned unpaired electrons. Therefore, these cases are only partially considered in the following analysis.

Since the following descriptions of the antiferromagnetic states rely primarily on CAS-based protocols, the issue of spin flips in one or both centers also presents a challenge for the open singlet state. CAS-based approaches typically include the full set of configuration state functions (CSFs) for a given electron configuration and multiplicity. Consequently, besides the "neutral" antiferromagnetic state shown in Figure 13.6b, other CSFs with singlet multiplicity and different spin coupling schemes can contribute to a CAS-based description of the Co(II) centers. These states may not exhibit exclusively antiferromagnetic behavior, but they could be relevant for a comprehensive system characterization or potentially introduce errors.

In conclusion, the magnetic interactions and multiplet effects of the antiferromagnetically coupled Co(II) centers in Co_3O_4 and Al_2CoO_4 are more complex than in the Cu(II) toy model. The description becomes even messier when the model size is increased to more than two Co centers. Furthermore, in the case of the Co(III) centers in Co_3O_4 and Co_2ZnO_4, which are technically low spin, a multiconfiguration approach may be more appropriate. However, further exploration of these issues will not be pursued at this time. The explicit treatments and protocols will be reviewed separately for the band gap and XES studies in their respective chapters.

14 The Quest for the Band Gap(s) of Co_3O_4

14.1 The Context and Structure of the Band Gap Study

The cobalt oxide Co_3O_4 is not only a promising candidate for catalysis, as described in the introduction to this part, but also for solar cell endeavors. Alloys containing Co_3O_4 have been the subject of various investigations for photovoltaic applications.[451–455] Of particular interest is that the semiconducting Co_3O_4 has different optical excitations covering a large part of the solar spectrum.[451, 456] The optical band gap of a material, which is its first non-dark excited state,[239] is usually the associated critical fundamental property.

Based on current experimental and theoretical studies, it is widely accepted that Co_3O_4 possesses not one but at least two direct band gaps. The first direct band gap is located at approximately 1.5 eV, while the second is more intense at approximately 2.1 eV.[437, 457–477] Some experimental studies suggest an even higher number of band gaps[460, 461, 472, 475] or at least lower-lying absorption bands that could be directed toward another band gap.[471, 472, 474–484] Furthermore, there are still ambiguities regarding the actual origin and character of these band gaps.[475]

The optical band gaps of Co_3O_4 are critical to understanding its photochemical behavior and broader electronic structure, which in turn can shed light on the physical, chemical, and catalytic behavior of this material for various applications.[475] It is therefore of interest to investigate the role of the different cobalt sites in the system in determining the band gap character, as Co_3O_4 consists of tetrahedral Co(II) sites and distorted octahedral Co(III) sites in a 1:2 ratio. Additionally, it is worth noting that the Co(II) sites with locally high spin exhibit antiferromagnetic coupling. In contrast, the Co(III) sites with locally low spin are typically considered diamagnetic, as discussed in Chapter 13.[444, 475] However, the study of the influence of the different cobalt sites and antiferromagnetic coupling on the band gap is still an active area of research.

In addition to the experimental studies,[437, 457–477] several computational in-

vestigations[173, 475, 485–496] were performed to accurately determine the band gaps of Co_3O_4 and explain their origin. Most recent studies combine DFT methods employing GGA-level functionals with periodic boundary conditions.[173, 485, 490–496] While this protocol is considered a successful standard for calculating many properties of solid-state systems, it is also known that pure DFT functionals, in particular, tend to underestimate band gaps, mainly due to the self-interaction error.[12, 13, 15, 19] An improvement can be expected by using hybrid functionals or determining the band gap utilizing Green function methods,[14, 15] as has been done for Co_3O_4.[173, 485, 487, 490, 493, 496] However, post-Hartree-Fock methods are more promising candidates for accurate calculations of optical excitations,[51, 341] as also Chapter 11 demonstrated. As noted throughout this work, these methods are often limited or unavailable for periodic boundary protocols.

Another hurdle in the computational description of Co_3O_4 is that it is argued to be a highly correlated material among others because of the antiferromagnetic coupling.[173, 475] Single-reference methods such as DFT are restricted in their capacity to describe such phenomena.[172, 497, 498] One solution to this shortcoming is to treat these materials with a DFT+U approach in periodic boundary calculations.[11] This approach is applied to Co_3O_4 in multiple studies.[173, 485, 488, 489, 491–496] The procedure is reported to distort the materials' electronic structure,[173] which might lead to correct band gap magnitudes but limits the prospect of an accurate analysis of its character. For transition metal complexes and other molecular systems, post-Hartree-Fock methods such as SA-CASSCF[169–171] can handle highly correlated materials alone or in combination with perturbation methods such as NEVPT2.[198–200] These methods were introduced and briefly described in Chapter 6.

The band gap study using the electrostatic embedding approach together with TD-DFT and an EOM-CC method in Chapter 11 introduced the possibility of accurate optical band gap calculations on different cluster sizes of inorganic crystals. In this study, this approach is taken up and extended to open-shell systems and various post-Hartree-Fock methods to reinvestigate the possible optical band gaps of the cobalt oxide Co_3O_4 in several steps.

First, the available literature on experimental studies of the absorption bands and band gaps of Co_3O_4 is summarized and discussed, followed by the available literature on theoretical studies and characterization of the band gaps. The second part presents theoretical considerations regarding the character of potential band gaps. Third, a first approach to the band gap is made via broken-symmetry (BS) TD-DFT to capture the antiferromagnetic behavior. The systems Co_2ZnO_4 and Al_2CoO_4 are presented as auxiliary systems to understand better the different roles of the

Co(III) and Co(II) sites. Since the benchmark study in Chapter 11 showed that the TD-DFT results converge identically with cluster size for all tested DFT functionals as well as for the applied EOM-CC method, the convergence of the band gap is first calculated using only one hybrid DFT functional (PBE0). The converged result is then recalculated using a variety of DFT functionals as well as EOM-CC.

The fourth objective of this study is to extend and reevaluate the TD-DFT results using multireference wavefunction-based post-Hartree-Fock methods, such as CASSCF in combination with NEVPT2 and CASPT2, MR-EOM-CC, and CAS-ICE. In particular, the potential effect of antiferromagnetic coupling, which multireference methods may better describe compared to the previously used single-reference methods TD-DFT and EOM-CC, will be investigated, and how the results correlate with the results obtained using broken-symmetry TD-DFT.

14.2 Literature Overview

14.2.1 Experiments

During the last decades many measurements of the absorption spectra of Co_3O_4 and the corresponding optical band gaps have been published. Figure 14.1a shows a selection of experimental absorption bands of Co_3O_4.[467, 471–484, 499, 500] Figure 14.1b illustrates the respective experimental (optical) band gaps[437, 457–477] In the appendix, Table C.1 to Table C.6 (see pages 341 to 346) document details of the experimental results, measurement techniques, materials, and more. This section outlines the main results with the aim of providing reference values for subsequent band gap calculations and to give a first insight into their possible origins.

How Many Band Gaps Can Be Observed Experimentally?

Two to five absorption bands were measured depending on the applied spectroscopic wavelength range. If the experiment included the NIR (near infrared) spectrum in addition to the UV/Vis one, typically, one absorption band or two overlapping absorption bands (indicated with black in Figure 14.1a) were identified at average values of 0.82 eV $\pm$ 0.03 eV and 0.94 eV $\pm$ 0.01 eV, respectively. Thota et al.[474] mention an even lower band at 0.56 eV, which other references[460] indicate as well, e.g., due to Tauc plot relations, but they do not claim it in particular. In all cases, two prominent bands – in Figure 14.1a marked in red and blue – can be found at average values of 1.70 eV $\pm$ 0.07 eV and 2.93 eV $\pm$ 0.28 eV. The intensity is rising, and the peaks are broadening with increasing energy so that the peaks at 0.82 eV and 0.94 eV are significantly less intense and broad than the one at 1.70 eV, which in

turn is less intense and broad than the one at 2.93 eV.

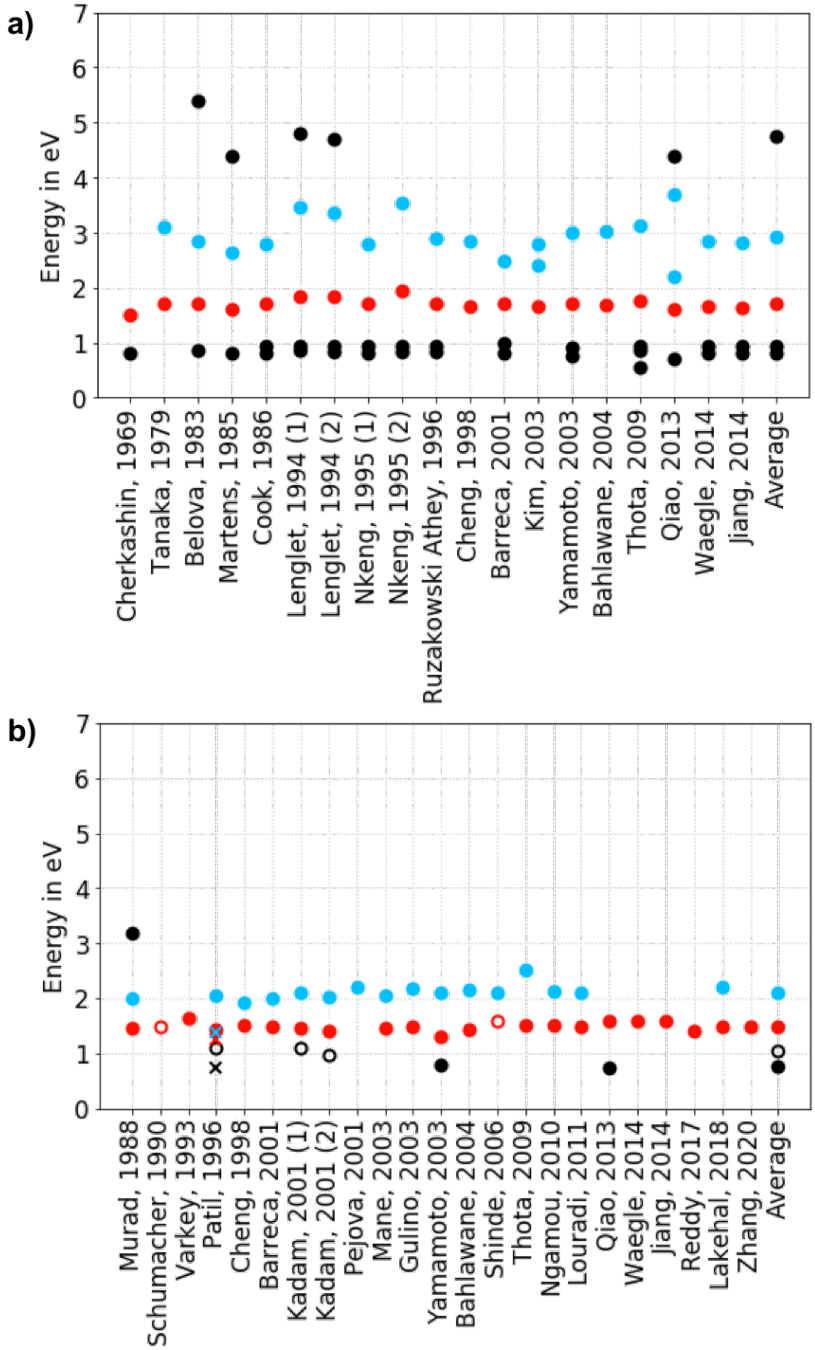

Figure 14.1: Overview of experimental **a)** absorption bands[467, 471–484, 499, 500] and **b)** band gaps[437, 457–477] found in literature. Empty circles: indirect band gaps. Filled circles: direct band gaps. Cross: forbidden gaps. Colors indicate different energy ranges of the absorption bands and the corresponding band gaps.

The optical band gap is usually the first so-called "non-dark" excited state. This

refers to the first dipole-allowed transition state. Although the first band of the absorption spectrum can often be identified at about 0.82 eV, many references have not assigned an optical band gap in this energy range.[471, 474, 476, 477] This is the case, for example, in the work reported by Waegle et al.[476], in which only one band gap is determined at 1.60 eV based on an electrochemical measurement method. However, they measured features at 0.81 eV and 0.93 eV in the absorption spectrum, and the electrochemical method showed an onset at about 0.70 eV. However, the alleged gap at 0.70 eV was not claimed as a band gap but was once referred to as a "midgap". By including the "midgap" in the other references[472, 475], which consider a band gap for the lower lying absorption bands, a band gap at an average value of 0.75 eV $\pm$ 0.04 eV is obtained, and by excluding it, the average value is 0.78 eV $\pm$ 0.05 eV.

Despite the definition of the optical band gap as the first dipole-allowed excited state, most of the references listed in Figure 14.1b agree that Co_3O_4 has at least two optical band gaps related to the two higher absorption bands at 1.70 eV and 2.93 eV. They have average values of 1.50 eV $\pm$ 0.06 eV and 2.12 eV $\pm$ 0.09 eV, respectively.

In summary, based on the above studies, it is likely that three band gap energies can be identified for Co_3O_4. A first estimate suggests average values of 0.78 eV $\pm$ 0.05 eV, 1.50 eV $\pm$ 0.06 eV, and 2.12 eV $\pm$ 0.09 eV. The latter two are the more prominent.

At Which Energies Can the Band Gaps Be Observed?

Analysis of the available data in Figure 14.1 indicates that if the absorption band maximum shifts to higher energies at an average value of 1.70 eV, the band at 2.93 eV shifts to even higher energies. The peak of the first band varies between 1.50 eV[482] and 1. 95 eV,[480] and the second band is between 2.20 eV[475] and 3.55 eV[480]. As the absorption bands change, so do the band gaps. Thus, the first band gap is between 1.30 eV[472] and 1.65 eV[459] and the second is between 1. 92 eV[467] and 2.53 eV[474]. The band gap energy variation is not as substantial as for the absorption bands themselves, which may be due to the fact that the band gap depends only on the onset of the absorption bands. Nevertheless, it is important to recognize the possible reasons for the differences in the obtained band gaps in order to better understand which band gap values are the best references for the subsequent band gap calculations.

It appears that the primary factors influencing the position of the band gap energy are the crystallization and finite size effects. Its origin seems to be ascribed mainly to the experimental preparation method of the material. Most references used thin films for their measurement,[437, 457–473, 475–481, 483, 499] but some

used (polycrystalline) ceramics,[482, 484, 500] or even powder samples.[474] The thin films were usually prepared by sintering,[479, 500] spray pyrolysis,[480, 481] sol-gel method,[474, 479, 499] physical vapor deposition (PVD: sputtering/ magnetron sputtering),[472, 476–478, 480, 483] or chemical vapor deposition (CVD).[467, 471, 473] The results seem to be more consistent for the thin films. Thereby, thin films prepared with spray pyrolysis appear to have the least consistent results. Further, the film thickness also influences the absorption bands and band gaps. Typically, thin films prepared with PVD are significantly thinner than other preparations resulting, on average, in higher band gap energies. It should be noted that Nkeng et al.[480] claimed that measurements on films thinner than 0.1 μm lead to less accurate measurements. Plots relating the spectroscopic values to the different influential factors as the film thickness and the film preparation can be found in the appendix on page 356 in Figure C.1. The substrate of the thin film is another factor influencing the optical properties, as shown by Ruzakowski Athey et al.[481], who prepared Co_3O_4 thin films by spray pyrolysis on different substrates. The preparation of the films on glass leads to higher roughness than on silica, which in turn leads to higher peak positions of the absorption band shown in Figure 14.1a in blue color (2.82 eV for two measurements on silica, 2.95 eV, and 3.10 eV for two measurements on glass).

Based on the above, the data set is limited to measurements reportedly obtained on thin films thicker than or equal to 0.1 μm, not prepared by spray pyrolysis, and further excludes values with a maximum error significantly different from the mean absolute error (MAE). Despite the above, the substrate is not included in the considerations due to a lack of conclusive data. The first prominent absorption band now varies between 1.65 eV and 1.70 eV, with a mean of 1.67 eV $\pm$ 0.02 eV and a median of 1.65 eV. The corresponding band gap ranges from 1.50 eV to 1.52 eV with a mean of 1.51 (1.505) eV $\pm$ 0.01 (0.007) eV and a median of 1.50 eV. The next higher absorption band varies between 2.75 eV and 2.85 eV. The average value is 2.81 eV $\pm$ 0.04 eV with a median of 2.83 eV. The associated band gap ranges from 2.00 eV to 2.20 eV with a mean of 2.14 (2.135) eV $\pm$ 0.07 (0.068) eV and a median of 2.17 eV.

In the literature selection process, only a limited amount of data exists for the first two low-lying absorption bands[471, 472, 474–484] and the lowest band gap.[472, 475, 476] Therefore, the average values at 0.82 eV $\pm$ 0.03 eV and 0.94 eV $\pm$ 0.01 eV and the corresponding band gap at 0.78 eV $\pm$ 0.05 eV are considered without further consideration of material or film thickness. This is a valid approximation based on the available data, since these lower absorption bands seem to be less affected by the material overall. While there is also evidence for (indirect) band gaps related to the absorption band at 0.94 eV, this is not considered further due to lack of conclusive data.

What Are the Character and Origin of the Different Experimental Band Gaps?

Most of the band gaps listed in Figure 14.1b are derived from transmission data using the Tauc plot, making them optical band gaps. Optical band gaps can be classified as direct or indirect, depending on whether the experimentally studied excitation process involves vertical (non-adiabatic) or adiabatic excitations.[241] The three band gaps discussed are often claimed in the literature to be direct. Only in two cases,[458, 465] the band gap at about 1.51 eV was identified as indirect. In addition, Kadam et al.[461], and Patil et al.[460] reported an indirect band gap at an average value of 1.06 eV $\pm$ 0.05 eV. Patil et al.[460] found an indirect forbidden gap at 0.75 eV and two direct forbidden gaps at 1.26 eV and 1.38 eV. These band gaps were not discussed above and will not be considered further as only direct optical band gaps are pursued in the following. Qiao et al.[475] claimed their band gap of 0.76 eV as a fundamental rather than an optical band gap.

In addition to the discussion of direct and indirect band gaps, there is also the question of why there appear to be multiple direct optical band gaps. In several references,[457, 460, 461, 465, 469, 471, 474] the band gaps at 1.51 eV and 2.14 eV are explained by the band structure. It is found that the conduction band is mainly dominated by Co(II) t_2 ($3d$) orbitals, while O $2p$ dominates the valence band. The resulting interband transition gives rise to the often called "true"[471] band gap at about 2.14 eV. Thus, the band gap at 2.14 eV is identified as LMCT O $2p$ $\rightarrow$Co(II) e_g. Due to the presence of Co(III) ($3d$ orbitals), a "subband" [471] is formed in the energy gap leading to the optical band gap at 1.51 eV. It is often identified as MMCT Co(III) t_{2g} $\rightarrow$Co(II) t_2[467, 472, 473] or Co(II) t_2 $\rightarrow$Co(III) e_g[474] or as LMCT O $2p$ $\rightarrow$Co(III) e_g[466, 469, 471]. The characterizations in these experiments were mainly based on the computational work of Miedzinska et al. from 1987[501], which will be discussed in more detail in the next section.

Although many experimental studies agree with the picture drawn by Miedzinska et al.[501], there is little evidence for the origin of the band gap from the experimental studies themselves. Martens et al.[484] observed that the absorption features in their measurement at 0.8 eV, 1.6 eV, and 2.6 eV are increased by replacing the octahedral Fe sites in the ferrimagnetic $CoFe_2O_4$ with Co(III). The substitution shifts the Co(II) centers, which previously occupied the octahedral sites in the pure $CoFe_2O_4$, to the tetrahedral sites. Thus, the system changes from $CoFe_2O_4$ to Co_3O_4. While Martens et al.[484] concluded that the octahedral Co(III) sites are, therefore, a primary cause of the three absorption features, it would also be possible to interpret these features as originating from the newly introduced tetrahedral Co(II) sites or both. However, the observation led Schumacher et al.[458] to identify the band gap

at 1.50 eV as the ligand field transition of the octahedral Co(III) site.

Kim et al.[499] similarly investigated the substitution of the tetrahedral Co(II) sites by Zn for the transition from Co_3O_4 to Co_2ZnO_4, which precluded the measurement of the pure Co_2ZnO_4 system. They observed a gradual decrease in the absorption bands in their measurement at 1.65 eV and 2.4 eV, demonstrating the importance of the Co(II) sites for the respective features. They found that the higher and broader band associated with the band gap at 2.14 eV actually contains two peaks at 2.4 eV and 2.8 eV for Co_3O_4. Substitution of the Co(II) sites with Zn shifted the feature to the higher peak. Although this conclusion was not drawn in Kim et al.[499], the observation may suggest that this absorption band is an overlap of at least two different transitions and that its upper part is related to Co(III) and the lower part to Co(II) sites.

Jiang et al.[477] related the band at 2.81 eV to Co(III) based on oxidation state-sensitive measurements with XUV and claimed it to be LMCT based on Miedzinska et al.[501].

Concluding the Experimental Studies

Based on the above discussion, three potential band gaps occur at 0.78 eV, 1.51 eV, and 2.14 eV. The first band gap may originate from the lower of two overlapping absorption bands with peaks at 0.82 eV and 0.94 eV, respectively. The band gap at 2.14 eV originates from a broad absorption band caused by at least two overlapping features. The general origin of these band gaps is not fully understood based on experimental data, and their origin is primarily based on a theoretical study[501] in the experimental literature. In the following section, results from several theoretical studies will be presented, which have been used to shed light on the origin of these band gaps and give additional perspectives to the one discussed.

14.2.2 Calculations

Apart from the referenced experimental studies, several published computational studies have investigated the magnitude and nature of the various candidate band gaps in Co_3O_4. Figure 14.2,[173, 485, 490–496] Figure 14.3,[485–489] and Table 5. 2[475, 483, 486, 487, 501] summarize a selection of these studies. Table C.7 to Table C.14 in the appendix (see pages 347 to 354) provide further details on all references. A summary of the notable results of all these studies is given below.

Summary of Computational Studies Targeting a Selected Band Gap with Different Methods

Figure 14.2 summarizes the literature references where one selected band gap is targeted with periodic boundary conditions using different DFT methods. Most of these calculations[485, 490–495] target the experimental band gap at 1. 51 eV, mainly referring to the experiments of Shinde et al.[465] and Kim et al.[499], but some[496] aim for the one at 2.14 eV. A few cases[173, 487, 493] consider the experiment of Qiao et al.[475], which obtained a band gap at 0.74 eV.

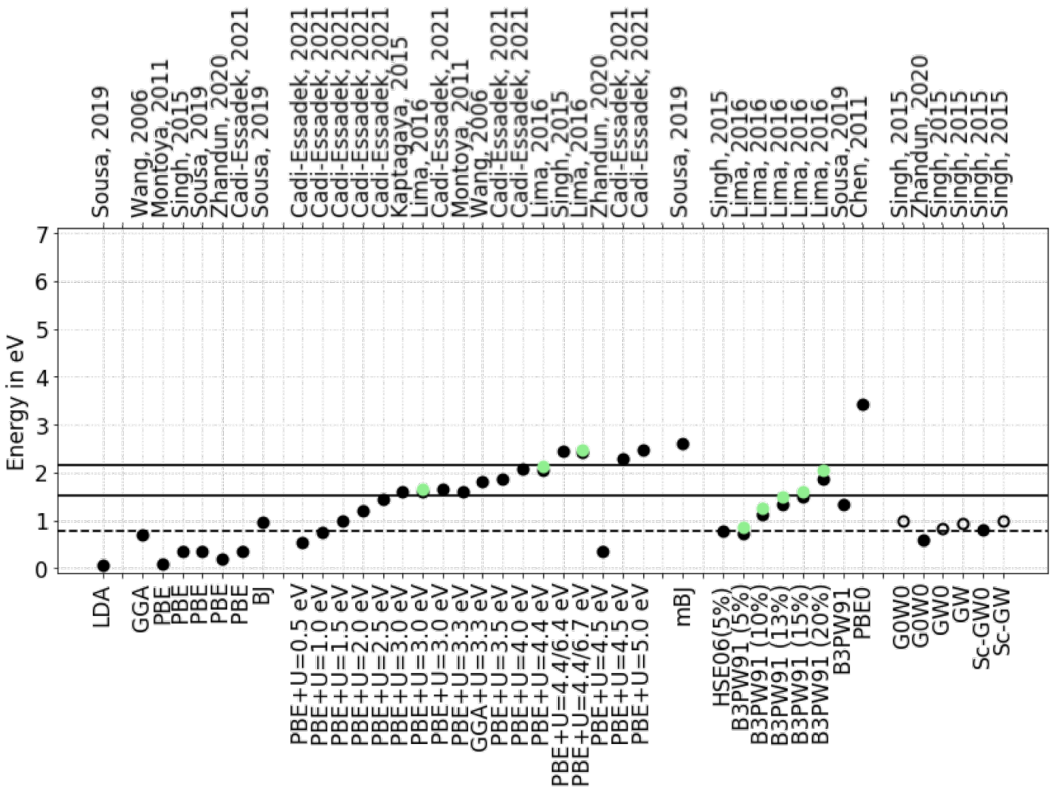

Figure 14.2: Overview on calculated band gaps found in literature.[173, 485, 490–496] Unfilled circles: indirect band gaps. Filled circles: direct band gaps. Green circles: band gaps including SOC.

These studies most commonly use GGA functionals, especially PBE.[173, 490, 492–496] It has been found that GGA or LDA DFT functionals often underestimate the experimental band gap.[19] LDA and GGA results confirm this for Co_3O_4. In many cases the calculated band gap is close to zero.[173, 490, 492–494] In order to keep the band gap "open", it is a common practice to apply an effective on-side potential U (DFT+U), which can adjust the calculated band gap energies towards the experimental value. In general, this practice has been followed primarily for

strongly correlated materials.[11] Even though the recent study by Qiao et al. [475] states differently, Co_3O_4 is often claimed to be a strongly correlated material,[173] as it is typical for materials with magnetic effects such as antiferromagnetism[497, 502] or generally for transition metal chemical systems with partially filled $3d$ shells.[498]

Studies such as Cadi-Essadek et al.[494] show that the band gap increases linearly with increasing U. Similar results were obtained by Lima et al.[496] by targeting the band gap at 2.14 eV. Among other approaches, the study uses a combination of different values of U for Co(II) and Co(III) instead of the same value for both Co sites. Other works, such as Singh et al.[173], stated that applying two different U values might be the best approach to address the band gap problem of Co_3O_4 in the case of a GGA+U protocol. The respective U values, as shown in Figure 14.2, have been established in Chen et al.[485], and others. Although this practice seems to be quite efficient in obtaining the desired band gap value, it is reported, e.g., by Singh et al.[173] that the application of an effective potential U leads to an undesired modification of the electronic structure of the system (e.g., leading to incorrect DOS (Density of States) results).

In the same direction, Lima et al.[496] showed a linear dependence of the band gap calculated with hybrid functionals - in their case B3PW91 - on the percentage of Hartree-Fock exchange, comparable to GGA+U. Unlike GGA+U, this does not appear to artificially alter the electronic structure. The same study shows a slight band gap increase after including spin-orbit coupling (SOC).

Singh et al.[173] investigated the band gap using different Green Function methods. The results are close to or in agreement with the direct band gap of 0.78 eV and/or the indirect band gap of 1.06 eV. While for all DFT methods shown in Figure 14.2 the predicted band gaps had a direct character, their nature seems ambiguous in the concept of Green Function approaches. In Singh et al.[173], Sc-GW_0 predicts the band gap to be direct, while it is indirect for Sc-GW, GW_0, and G_0W_0. In contrast, in Zhandun et al.[493] G_0W_0 results in a direct band gap.

Most of the references in Figure 14.2 derive the band gap and its character from DOS calculations. In this context, the band gap magnitude is defined as the difference between the valence band maximum and the conduction band minimum. The character is called direct if the two points have the same crystal momentum, and indirect if they do not.[241] As discussed in Chapter 8 and Chapter 11, the difference between the valence and conduction bands without consideration of exciton binding leads to the fundamental band gap rather than the optical one. The approach is still valid for (meta-)GGA functionals due to the absence of XC energy, which leads to the same result of fundamental and optical band gap as discussed before (see also page 97).

Summary of Computational Studies Targeting Multiple Band Gaps with Different Methods

The studies[485–489] summarized in Figure 14.3 have identified more than one band gap by periodic calculations aimed in particular at the experimental band gaps at 1. 51 eV and 2.14 eV.

In all cases two direct band gaps have been calculated. In addition, one or two indirect band gaps were identified between the two direct band gaps. The lower direct band gap has the character $X \rightarrow X$, while the higher one has the character $\Gamma \rightarrow \Gamma$, where X and Γ describe different high symmetry points in the Brillouin zone. The indirect band gaps have $X \rightarrow \Gamma$ and $\Gamma \rightarrow X$ characters. As with the previously discussed results involving only one band gap, there is no general consistency in the resulting band gap values.

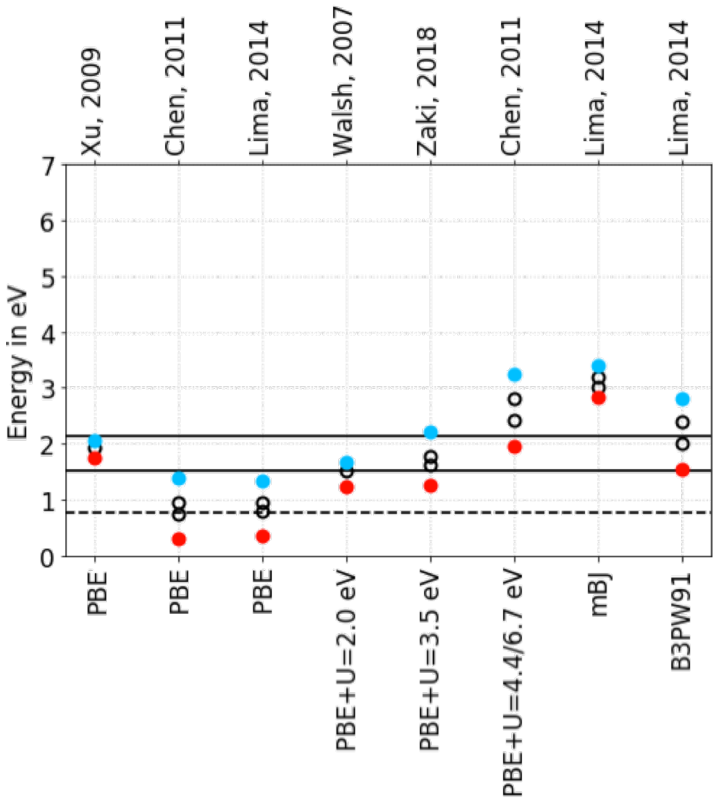

Figure 14.3: Overview on calculated band gaps found in literature including more than one band gap.[485–489]

Summary of Computational Studies Characterizing Absorption Bands and Band Gaps

Several studies have discussed the transition character of the absorption bands and band gaps in the orbital picture. Table 14.1 summarizes a selection of these studies.[475, 483, 486, 487, 501]

Table 14.1: Transition character of specific excited states and their energy based on calculation results from literature[475, 483, 486, 487, 501]. Transition energy in eV.

	Belova, 1983[483]	Belova, 1983[483]	Miedzinska, 1987[501]	Xu, 2009[486]	Qiao, 2013[475]	Lima, 2014[487]
Method	SCF-XαSW, spin restricted	Data re-considered with spin	Semi-empirical MO (VS1E)	PBE/DNP, spin polarized	DFT (GGA)	B3PW91/FP-LAPW, dielectric function
Model	$[CoO_4]^{6-}$ & $[CoO_6]^{9-}$ cluster in electrostatic model (external field)		Unit Cell	Periodic	Periodic	Periodic
Co(II) $e \rightarrow t_2$	0.80	-	0.8	-	0.83 (↓)	1.86/2.4/2.9
Co(III) $t_{2g} \rightarrow e_g$	2.61	0.87	-	-	1.84	1.86/2.4/2.9
Co(III) $e_g \rightarrow e_g$	-	2.61	-	-	-	-
Co(II) t_2 →Co(III) e_g	-	-	1.0	-	0.95 (↓)/1.04 (↑)	-
Co(III) t_{2g} →Co(II) t_2	-	-	1.3	(2.06 (↑)/)3.3 (↓)	1.64	-
O $2p$ →Co(II) t_2	-	-	2.1	(1.75 (↑)/)2.2 (↓)	2.62 (↓)/4.69 (↑)	-
O $2p$ →Co(III) e_g	-	-	-	2.9 (↓)	3.66/5.80	-
Co(II) $e \rightarrow 4s$	2.18	1.38	-	-	-	-
O $2p$ →Co(II) $4s$	5.67	5.67	-	-	-	-
O $2p$ →Co(III) $4s$	6.39	-	-	-	-	-

Xu et al.[486] have assigned the $X \rightarrow X$ transition to the LMCT orbital transition, O $2p$ →Co(II) t_{2g}, and $\Gamma \rightarrow \Gamma$ to Co(III) t_{2g} →Co(II) t_2, resulting in band gaps of 1.75 eV and 2.06 eV, respectively.

On the other hand, Miedzinska et al.[501], whose results were briefly discussed in the experimental section, identified the lower transition in their case at 1.30 eV as MMCT Co(III) t_{2g} →Co(II) t_2. The next higher transition at 2.10 eV was assigned to LMCT O $2p$ →Co(II) t_{2g}. Two additional transitions were identified at 1.0 eV as MMCT Co(II) t_2 →Co(III) e_g, and at 0.8 eV as a ligand field transition Co(II)

$e \rightarrow t_2$. It is important to note that the results presented in Miedzinska et al.[501] were obtained using a semiempirical MO method with a unit-cell model and not with periodic boundary conditions, unlike the more recent studies.

Belova et al.[483] also observed the ligand field transition Co(II) $e \rightarrow t_2$ at an energy of 0.80 eV. They used an SCF-XαSW approach with isolated $[CoO_4]^{6-}$ and $[CoO_6]^{9-}$ clusters in an external electrostatic field. A more recent study by Qiao et al.[475] utilizing DFT (GGA) with periodic boundary conditions also located the same transition at a similar energy of 0.83 eV and assigned it as the band gap.

The sequence of transitions presented in the periodic DFT study by Qiao et al.[475] agreed reasonably well with the earlier study of Miedzinska et al.[501]. Qiao et al.[475] predicted an MMCT Co(II) t_2 →Co(III) e_g transition at 0.95 eV, followed by Co(III) t_{2g} →Co(II) t_2 at 1.64 eV, the ligand field transition of Co(III) at 1.84 eV, and finally the LMCT O $2p$ →Co transitions of Co(II) and Co(III) at 2.62 eV and 3.66 eV, respectively. The intensity of the transitions increased with increasing excitation energy, except for the ligand field transition of Co(II), which had a higher intensity than the MMCT Co(II) t_2 →Co(III) e_g.

The established transition characters have been challenged by Lima et al.[487]. They argue that the MMCT transitions are unlikely to occur at energies as low as the band gap values. They also made a similar claim for the LMCT transitions. Their absorption spectrum was calculated using the dielectric function based on DOS results obtained with the hybrid functional B3PW91 and periodic boundary conditions. They identified the resulting absorption bands at 1.86 eV, 2.4 eV, and 2.9 eV as a superposition of the ligand field transitions Co(II) $e \rightarrow t_2$ and Co(III) $t_{2g} \rightarrow e_g$, which is, therefore, also the expected character for the two respective band gaps.

Concluding the Computational Studies

Most of the presented computational studies obtained possible band gaps with periodic boundary conditions and DFT. Pure GGA or LDA DFT functionals underestimated the band gaps. Hybrid functionals seemed to give better results, and Green Function methods agreed reasonably well with the first possible experimental band gap (0.78 eV).

Regarding the character of the band gaps, most studies suggest that MMCT and LMCT transitions dominate the 1.51 eV and 2.14 eV band gaps, while the first one at about 0.78 eV could be attributed to Co(II) ligand field transitions. Lima et al.[487] suggest Co(II) and Co(III) ligand field transitions for the band gaps of 1.51 eV and 2.14 eV.

Overall, there are still uncertainties. All the calculation methods used were

single-reference, excluding the possibility of a multireference character of the band gaps, e.g. due to multiplet effects of the antiferromagnetic nature of the solid. On this basis, further investigations are justified in the framework of a systematic and carefully calibrated computational protocol such as the one presented below.

14.3 Computational Details

The calculations were performed using the ORCA 5.01 suite of programs.[351, 503] The present calculation protocol consists of several steps.

The first step involves the convergence of excited states with TD-DFT using multimetallic clusters of increasing size representing the cobalt oxides Al_2CoO_4, Co_2ZnO_4, and Co_3O_4 in the framework of the electrostatic embedding approach treated with Ionic-Crystal-QM/MM as described in Section 13.1. Since the goal is to study the band gaps of Co_3O_4, the atomic positions used for the Al_2CoO_4 and Co_2ZnO_4 models are equivalent to Co_3O_4. The functional PBE0[212, 219] is used together with the basis set DKH-def2-TZVP. Depending on the system, the calculations include spin-orbit coupling (SOC) effects, spin flip, and/or broken-symmetry. In all calculations, scalar relativistic corrections are applied using the second-order Douglas Kroll Hess (DKH2)[228, 367] scheme.

In addition, the excited states will be recomputed on the converged models with CIS, EOM-CCSD (shortened in the following with EOM-CC),[253–255] and multiple TD-DFT methods, including a variety of DFT functionals, namely (meta-)GGA functionals (BP86,[213, 215] PBE,[212] TPSS,[216] B97-3c,[504] BLYP,[213, 214] r2Scan-3c[505]), hybrid functionals (PBE0,[212, 219] B3PW91,[218, 222] B3LYP,[213, 214, 218] B1LYP,[213, 214, 218] TPSSH[220–222]) as well as double-hybrid functionals (DSD-BLYP[224, 225], DSD-PBEP86,[226] ωPBEPP86,[506] SCS-ωPBEPP86,[506] B2PLYP,[223] ωB2PLYP,[507]). To accelerate the EOM-CC calculations, selected atoms in the cluster were included as HF layers within the Ionic-Crystal-QM/MM scheme for speeding up the embedded cluster calculations, as described in Section 3.2. Comparison calculations showed that the inclusion of the HF layer does not change the excitation energy of the excitations studied in the respective context.

The second step revises the excited states by developing a protocol beyond the single-reference methods based on a series of multireference post-Hartree-Fock methods. The various employed methods of increasing accuracy are CASSCF,[169–171] CASSCF/ DCD-CAS(2),[203] CASSCF/ CASPT2,[201, 202] and CASSCF/ NEVPT2, [198–200] as well as MR-EOM-CCSD [260](shortened in the following with MR-EOM-CC). Further, ICE-CI and CAS-ICE[64, 65] were employed.

A series of DKH-def2-XVP[142, 143] and cc-pVXZ-DK[144] basis sets were tested

for all methods. For the DFT calculations, the performance of DKH-def2-XVP appeared satisfactory, and the sequence of DKH-def2-SVP, DKH-def2-TZVP, and DKH-def2-QZVPP basis sets indicated that DKH-def2-TZVP was sufficient. These were used for the TD-DFT convergence scheme, while DKH-def2-QZVPP was used for the final results. The DKH-def2-XVP basis sets were used together with the auxiliary basis sets def2-XVP/C and def2/J.

For the post-Hartree-Fock methods, cc-pVXZ-DK outperformed DKH-def2-XVP in terms of convergence in the respective sequences. In the post-Hartree-Fock calculations that yield the final results, cc-pVQZ-DK and its auxiliary basis sets are used. Table C.15 in the appendix (see page 355) shows the results for the different methods and basis sets, which will not be discussed further in this paper. Examples of input files are also given in the appendix in Section C starting on page 338.

Based on the concept of the relationship between the intensity of states and their oscillator strength introduced in Chapter 8 (see page 91), the calculated oscillator strength will be used as a criterion to determine whether a state is dark or non-dark. A state is classified as non-dark if the oscillator strength is greater than 0.001 a.u.. The state is classified as dark or dipole-forbidden if it is smaller than 0.0001 a.u.. The states with oscillator strengths in between are referred to as "potentially" non-dark states. The inclusion of the latter distinction avoids the false exclusion of states that are not dark in the experiment but have low intensity in the computational model used, since many methods do not provide fully reliable oscillator strengths, which in some cases also depend on the system size.

14.4 Theoretical Considerations on the Excited States

14.4.1 Single-Center Co Models

Figure 14.4a and Figure 14.4b show the excitation models adopted within the one-electron approach of the two isolated cobalt sites. As discussed in the previous chapter, the isolated octahedral (O_h) $[Co(III)O_6]^{9-}$ site (1o) is distorted and hence, has (D_{3d}) symmetry obtaining a low spin $3d^6$ electron configuration. Regardless of whether it is referred to as D_{3d} or O_h, the excitation scheme of transitions concerning possible optical band gaps has the same result. In both cases, the ligand field transitions Co(III) $3d_{xy,xz,yz} \rightarrow 3d_{x2y2,z2}$ ($t_{2g} \rightarrow e_g$; $^1(T_{1g} + T_{2g})$ or $e_g \rightarrow e_g/a_{1g}$; $^1(A_{1g} + [A_{2g}] + E_g)/\ ^1E_g$) are dipole-forbidden. Thus, the resulting states are expected to have no or little intensity and hence, will likely result in dark states. For simplicity, the distorted octahedral sites will be treated as octahedral sites in the following.

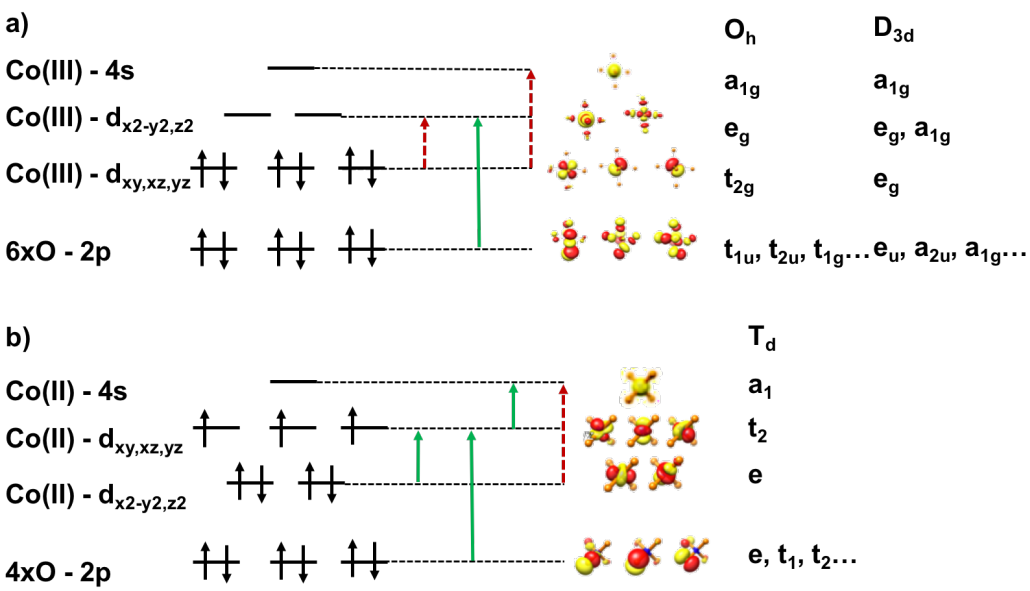

Figure 14.4: Schematic representation of excited states in the one electron picture for **a)** $[Co(III)O_6]^{9-}$ (O_h/ D_{3d}) and **b)** $[Co(II)O_4]^{6-}$ (T_d). Dashed red lines: dipole-forbidden transitions, solid green lines: dipole-allowed transitions.

The first dipole-allowed excited state in the octahedral site 1o is LMCT transition of O $2p \rightarrow$ Co(III) $3d_{x2y2,z2}$ ($t_{1u}, [\ldots] \rightarrow e_g$; $^1(T_{1u} + T_{2u})$ or $e_u, [\ldots] \rightarrow e_g, a_{1g}$; $^1(A_{1u} + A_{2u} + E_u)/^1E_u$) electron excitations. Consequently, it could be expected that the optical band gap in the isolated octahedral site has LMCT character. It could be possible that dipole-forbidden states are non-dark due to, e.g., an intensity borrowing mechanism[508–510] or simply because the singlet excitations are spin-allowed. Therefore, these types of transitions cannot be excluded altogether from the optical band gap considerations.

In the single tetrahedral site $[Co(II)O_4]^{6-}$ (1t) in the high spin $3d^7$ electron configuration, the Co(II) ligand field transitions $3d_{x2y2,z2} \rightarrow 3d_{xy,xz,yz}$ ($e \rightarrow t_2$; $^4(T_1 + T_2)$) are dipole-allowed, in contrast to the Co(III) ligand field transitions. Thus, they are a possible source of the band gap. The LMCT states resulting from the O $2p \rightarrow$ Co(III) $3d_{xy,xz,yz}$ ($e, [...] \rightarrow t_2$ $^4(T_1 + T_2)$) transitions are also dipole-allowed.

14.4.2 Multicenter Co Models

Although the consideration of single cobalt sites gives a first idea of possible excitations and band gaps, in the whole system of Co_3O_4 it is also necessary to consider interactions between the cobalt sites and thus to include MMCT excitations in a theoretical model. Cluster sizes beyond one center can represent such interactions. By increasing the system size, the symmetry changes from the local tetrahedral or octa-

hedral symmetries to a single symmetry, including the respective centers involved in the respective excitation, as discussed in Section 13.2.

The smallest substructure defining the prospect of an MMCT transition encloses any two adjacent Co centers. For MMCT between two Co(II) centers, these two Co(II)'s can form C_s or C_{2v} symmetry. Figure 13.3 on page 173 illustrates this for the tetrahedral Cu(II) centers in $Al_2Cu(II)O_4$ and is directly applicable to the Co(II) centers in Co_3O_4 and $Al_2Co(II)O_4$. Similarly, two adjacent distorted octahedral Co(III) sites, representative of Co(III)→Co(III) MMCT, can maintain C_s or C_{2v} symmetry. Two closest centers involved in Co(III)→Co(II) or Co(II)→Co(III) MMCT can only have C_s symmetry. Table 14.2 summarizes these transitions and declares them all dipole-allowed. Therefore, they could all be a potential source of optical band gaps.

Table 14.2: Orbital symmetries of $3d$ orbitals and whether the transition between the $3d$ orbitals of the nearest tetrahedral and octahedral cobalt centers is a dipole-allowed transition, considering that they have either C_s or C_{2v} symmetry to each other.

		C_{2v}	C_s
Orbital	d_{xy}, d_{xz}, d_{yz}	a_2, b_1, b_2	a', a''
Symmetry	d_{x2y2}, d_{z2}	a_1	a'
	Dipole Operator	$A_1 + B_1 + B_2$	$2A' + A''$
	Co(II)→Co(II)	dipole-allowed	dipole-allowed
MMCT	Co(III)→Co(III)	dipole-allowed	dipole-allowed
transitions	Co(III)→Co(II)	-	dipole-allowed
	Co(II)→Co(III)	-	dipole-allowed

Recalling Section 13.2, the antiferromagnetic coupling between two Co(II) sites involves a superposition of "neutral" and "ionic" states. The "ionic" antiferromagnetic state can be understood either as a superexchange involving the oxygen orbitals or as a result of an MMCT transition.[56, 447–449] It is therefore necessary to distinguish between actual MMCT transitions and "ionic" antiferromagnetic states.

Furthermore, different possible descriptions of Co(II) centers, e.g. concerning magnetism or multiplet effects, as introduced in Figure 13.6 (see Section 13.2, page 179), might play a role in the excitation process concerning local Co(II) sites and multicenter processes. In particular, the antiferromagnetic description can be considered either via broken-symmetry DFT[511, 512] or wavefunction-based approaches

like CASSCF. Only "ionic" antiferromagnetic states with one electron exchanged between two antiferromagnetically coupled centers are considered. For the sake of simplicity, the possibility of multiple electron exchange will not be discussed for the time being.

The diamagnetic Co(III) sites could have definitions beyond the low spin $3d$ electron configuration. This idea is not pursued further, since test calculations have shown that for the present problem it is sufficient to describe the Co(III) sites by singlet and triplet states formed from ground states with low spin and closed $3d^6$ electron configurations.

14.5 Convergence and Characterization of Excited States with TD-DFT

The following section discusses the convergence scheme of different excited states for Co_2ZnO_4, Al_2CoO_4, and Co_3O_4 with increasing cluster sizes calculated by TD-DFT using the PBE0 hybrid functional. Since the overall goal is to find the optical band gaps, not the convergence scheme of all excited states is relevant, but the convergence of each first excited (non-dark) state of each distinct absorption band and excitation type. Thus, while all states are calculated, only the first excited states of the different absorption bands are usually observed and discussed. The results of the different cobalt oxides are presented from Figure 14.5 to Figure 14.7 in the relevant energy range 0 eV to 6.5 eV by showing all excited states with respect to their energy and oscillator strength for system size 2t4o on the left side of the figures. The right side shows only the convergence of the first or first non-dark excited state of each absorption band with respect to cluster size, which varies from the single cobalt site (1o or 1t) up to the largest cluster size of 10t20o (see cluster models in Figure 3.12 on page 44). The line style represents the different types of excitations, with dotted lines symbolizing dark, dashed lines symbolizing "potentially" non-dark, and solid lines symbolizing non-dark states. At the end of the section, the results of the convergence schemes are recomputed with different single-reference methods and compared to the experiment and literature.

14.5.1 Co_2ZnO_4

The system Co_2ZnO_4 represents the octahedral Co(III) sites. Figure 14.5 shows the four different types of excitations found for this system, which are split into several absorption bands. The first four distinct absorption bands have ligand field transition character $3d\ t_{2g} \rightarrow e_g$ local to the Co(III) centers, with the first two narrow

bands inheriting triplet character (1.0 eV and 1.3 eV) and the other two even narrower bands have singlet character (1.9 eV and 3.0 eV). Although the calculations include SOC, it is still valid to distinguish between the singlet and triplet excitations, since the initial singlet and triplet states do not mix after SOC for the $3d\ t_{2g} \rightarrow e_g$ transitions (see Figure C.2 on page 357 in the appendix). Nevertheless, the inclusion of SOC increases the energy position of the bands by a few meV. This observation is in agreement with the work of Lima et al.[496].

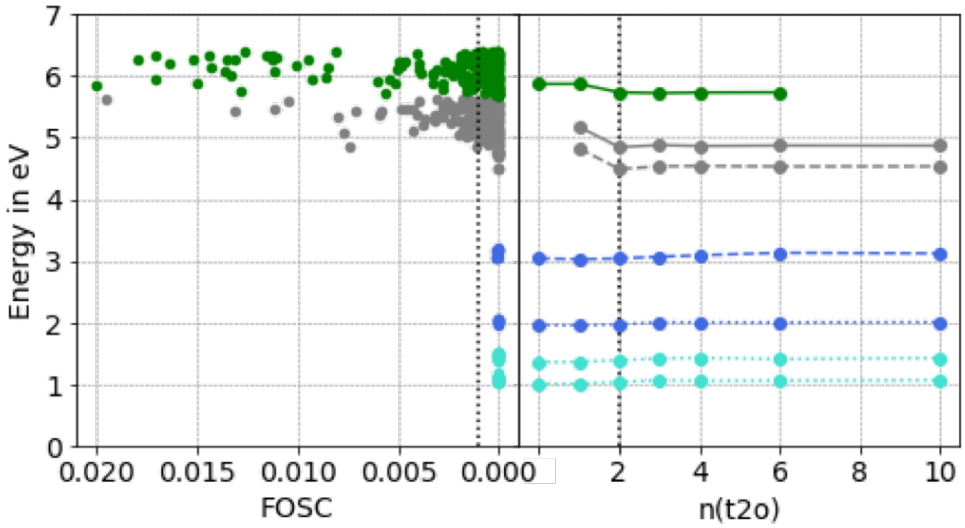

Figure 14.5: TD-DFT convergence scheme of Co_2ZnO_4 with PBE0/DKH-def2-tzvp. The left side of the figure shows all excited states for model size 2t4o, while the right side shows the convergence of only the first excited state of each absorption band with cluster size. Color code: Co(III) $3d\ t_{2g} \rightarrow e_g$ triplet (turquoise) and singlet (blue) excitations, Co(III) $3d \rightarrow 3d$ Co(III) MMCT (gray), O $2p$ →Co(III) $3d$ LMCT (green); dark states (dotted line), "potentially" non-dark states (dashed line), non-dark states (solid line).

The oscillator strengths of the ligand field transitions are all close to zero, and thus, all excited states of this type are considered to be dark states. This is in agreement with the electronic structure analysis of the "ideal" one-center models in Section 14.4, where all involved transitions are shown to be dipole-forbidden. Only states belonging to the second singlet band originating at 3.0 eV have oscillator strengths of about 0.0001 a.u. and could be declared "potentially" non-dark. A possible reason could be an intensity borrowing mechanism, e.g. from dipole-allowed LMCT excitations.[508–510]

The right side of Figure 14.5 shows that the ligand field transitions appear independent of the system size and can be considered as converged already for the sin-

gle Co(III) site 1o (in Figure 14.5 n(t2o)=0). All ligand field transitions lead to dark states, regardless of the cluster size used. This indicates that they can be considered local to the Co(III) sites even after the introduction of multiple Co(III) centers. The degeneration of the $3d$ orbitals does not seem to lower the energy of the orbitals. Thus, they are very local and the resulting band is therefore narrow. The result also shows that the electrostatic environment around the cluster mimics the crystal environment well enough that the introduction or deletion of additional centers does not change the local result.

The first LMCT state consisting of O $2p$ →Co(III) $3d$ electron excitations converges to 5.8 eV for system size 2t4o. Similarly, the MMCT transitions of Co(III) $3d$ →Co(III) $3d$ converge for system size 2t4o. The respective first excited state is a dark or "potentially" non-dark state at 4.6 eV and consists of triplet excitations in the absence of SOC interactions. The first non-dark excited state is at 4.9 eV (see left side of Figure 14.5). The oscillator strengths of the LMCT and MMCT states are significantly larger than those of the ligand field transitions because they are dipole-allowed. The absorption bands of the LMCT and MMCT states are broader than those of the ligand field transitions and overlap.

14.5.2 Al_2CoO_4

Analogous to Co_2ZnO_4, the excitations in Al_2CoO_4 are approached to represent the Co(II) sites. Figure 14.6a models Al_2CoO_4 as a high spin system, so that the multiplicity of each cluster with n Co(II) results in [3n+1]. Figure 14.6b describes all systems with multiplicity 2S+1=1 via broken-symmetry TD-DFT, taking into account the antiferromagnetic nature of the Al_2CoO_4 solid. It should be noted that the 2t4o is the smallest cluster suitable for this approach.

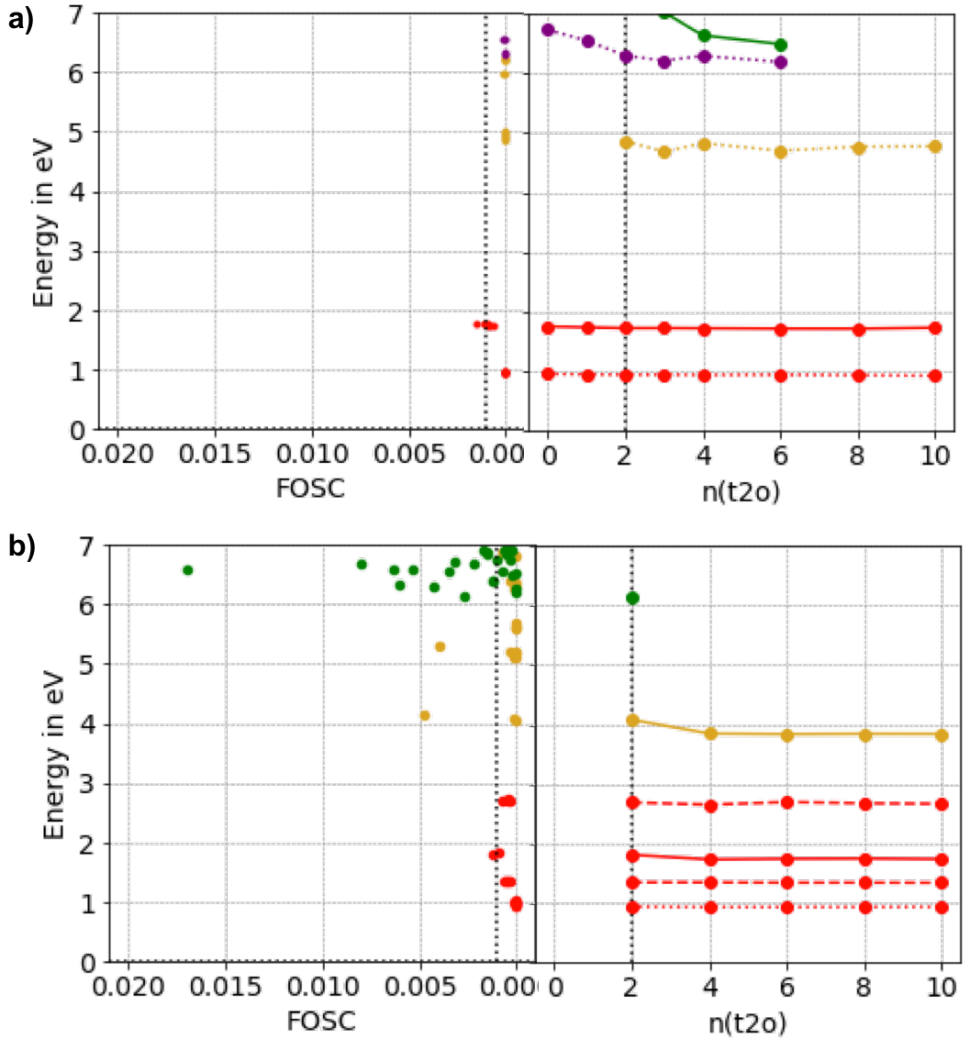

Figure 14.6: a) Standard TD-DFT and **b)** broken-symmetry TD-DFT convergence scheme of Al_2CoO_4 with PBE0/DKH-def2-tzvp. The left side of the figures shows all excited states for model size 2t4o, while the right side shows the convergence of only the first excited state of each absorption band with cluster size. Color code: Co(II) $3d$ $e \rightarrow t_2$ excitations (red), Co(II)→Co(II) MMCT (yellow), O $2p$ →Co(II) $3d$ LMCT (green); dark states (dotted line), "potentially" non-dark states (dashed line), non-dark states (solid line).

As in the case of Co_2ZnO_4, the first distinct absorption bands of Al_2CoO_4 describe the ligand field transitions $3d$ $e \rightarrow t_2$, which are local to the Co(II) centers and converge for the smallest system size. For the high spin case, bands of this character appear at 0.9 eV, consisting of dark states, and at 1.7 eV, which can be regarded as non-dark. The broken-symmetry model seems to encounter two bands with the same intensity and a similar position, slightly differing from the high spin case. The

broken-symmetry case has three more bands of $3d\ e \rightarrow t_2$ character than the high spin one. The first, located at 1.0 eV, overlaps the states originating at 0.9 eV. It has a slightly higher oscillator strength but is still close to zero. Because of the substantial overlap, the two bands are shown as one in this convergence scheme but will be discussed separately later.

The other additional absorption bands originate at 1.3 eV and 2.7 eV and can be considered "potentially" non-dark according to their oscillator strengths. If the high spin and broken-symmetry descriptions include spin-flip transitions, more bands of $3d\ e \rightarrow t_2$ signs appear, ranging between 0.5 eV and 3.8 eV. They all lead to dark states since they are spin-forbidden and are therefore not considered further at this point. The results can be found in the appendix in Figure C.3 on page 358.

In the assessed energy range, the MMCT states Co(II) $3d$ →Co(II) $3d$ converge with system size 4t8o to a first excited state located at 3.9 eV in the broken-symmetry model. As for Co_2ZnO_4, these states hold significantly higher oscillator strength than the ligand field transitions. The LMCT states will not be contemplated for Al_2CoO_4 since they originate at even higher energies; thus, they are no reasonable optical band gap candidates.

14.5.3 Co_3O_4

Since the difference between "standard" high spin and broken-symmetry TD-DFT was already examined for Al_2CoO_4 and is equivalent for Co_3O_4 to address the antiferromagnetic character, Figure 14.7a shows its convergence scheme only concerning broken-symmetry TD-DFT. The previous discussions about Co_2ZnO_4 and Al_2CoO_4 have revealed that ligand field transitions local to the Co(III) and Co(II) centers dominate the energy range of about 0.0 eV to 3.5 eV. For system size 2t4o, Figure 14.7b compares in the respective range the excited states for Co_3O_4 with the sum of the ones in Co_2ZnO_4 and Al_2CoO_4.

It gets apparent that the same set of Co ligand field transitions is evident in Co_3O_4 as in the two combined systems. The energies of the states are identical, and the oscillator strengths are comparable, although the Co(II) $3d\ t_{2g} \rightarrow e_g$ oscillator strengths appear to be slightly enhanced. This can either be due to the method or due to enhancement of the Co(II) excitations due to the present of Co(III). No additional states appear in Co_3O_4 in this regard. Therefore, it is justified to describe the local Co ligand field transitions in the system Co_3O_4 as a sum of Al_2CoO_4 and Co_2ZnO_4. Since the Co(III) ligand field transitions are all dark states, except the "potentially" non-dark transitions at about 3.0 eV, the lower non-dark or "potentially" non-dark states can all be accounted solely to the Co(II) centers.

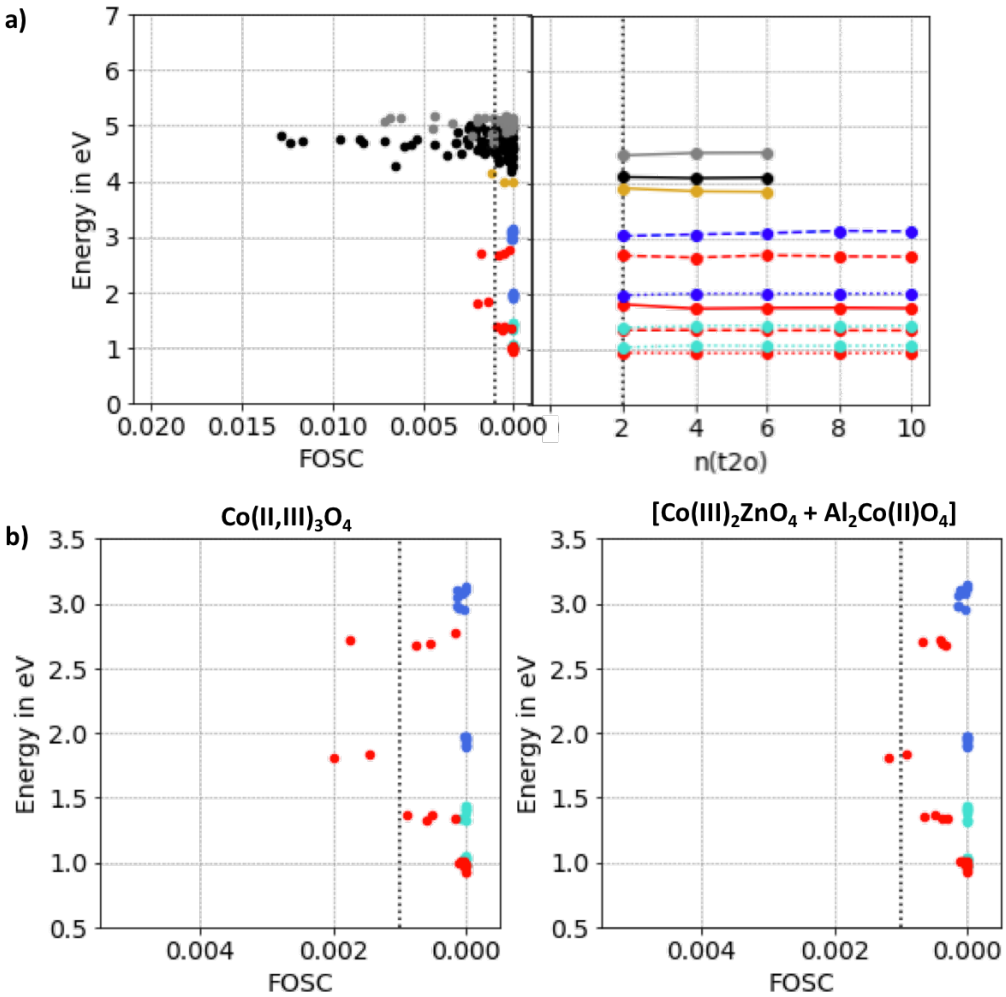

Figure 14.7: a) Broken-symmetry TD-DFT convergence scheme of Co_3O_4. The left side of the figure shows all excited states for model size 2t4o, while the right side shows the convergence of only the first excited state of each absorption band with cluster size. **b)** Co ligand field excitations of Co_3O_4 (left) vs. [Co_2ZnO_4 + Al_2CoO_4] (right). Color code: Co(II) $3d$ $e \rightarrow t_2$ (red), Co(III) $3d$ $t_{2g} \rightarrow e_g$ triplet (turquoise) & singlet (blue) excitations, Co(III)→Co(III) MMCT (gray), Co(II)→Co(II) MMCT (yellow), Co(II)→Co(III) MMCT (black); dark states (dotted line), "potentially" non-dark states (dashed line), non-dark states (solid line). Level of theory: PBE0/DKH-def2-tzvp

The energetically higher MMCT states Co(II) $3d$ →Co(II) $3d$ form at 3.9 eV as in Al_2CoO_4 and Co(III) $3d$ →Co(III) $3d$ at 4.6 eV as in Co_2ZnO_4. An additional excited state group, identified as MMCT Co(II) $3d$ →Co(III) $3d$, overlaps the other MMCT states in the given energy range. The first transition is at about 4.1 eV. The counterpart Co(III) $3d$ →Co(II) $3d$ seems outside the computed number of excited states

and is not included due to computational limitations. The exclusion of these states is justified since the states exceed the potential energy range of the optical band gaps. Again, the MMCT states retain a significantly higher oscillator strength than the local ligand field transitions.

14.5.4 Comparison of Single-Reference Methods (DFT, CIS, EOM-CC) and Literature

Based on the previous convergence model that showed that the energy range of the three band gaps in Co_3O_4, which are at 0.78 eV, 1.51 eV, and 2.14 eV experimentally, can be approached as the sum of the equivalent Al_2CoO_4 and Co_2ZnO_4 models, this section will reinvestigate the energy space of the two latter models with different DFT functionals as well as with CIS and EOM-CC to find a first explanation for the three band gaps. The approach is justified by the band gap study in Chapter 11, which showed that the band gap converges for the DFT and EOM-CC models in identical ways.

As test calculations with reduced basis sets show, the current systems also converge equivalently for the different methods. Exceptions are the (meta-)GGA functionals. These functionals do not predict distinct bands between 0 eV and 3.5 eV. As the system size increases, the excited states build a continuum. Figure C.4 in the appendix (see page 359) demonstrates this exemplarily for the PBE functional for Co_3O_4, Al_2CoO_4, and Co_2ZnO_4. Although this indicates that this class of functionals cannot predict the excitation energies with the chosen approach, likely because of the missing XC functional crucial for TD-DFT excitation calculations, some features nevertheless converge with system size. Therefore, an interpretation of the converged potential band gaps is still possible, and the potential states will be considered in the following discussion of the results.

The discussed PBE0 model, representative of all methods except (meta-)GGA, showed immediate convergence of the ligand field transitions in Co(II) and Co(III) at the smallest system sizes tested. However, the MMCT transitions in broken-symmetry Al_2CoO_4 models and all states in the (meta-)GGA models only converge for 4t8o. Therefore, for consistency, Figure 14.8 shows the first excited states of each absorption band representing the ligand field transitions and MMCT for QC size 4t8o. An exception is the EOM-CC result, calculated only for the isolated Co sites due to computational limitations and represents only the ligand field transitions. Since there is no option to calculate EOM-CC as broken-symmetry, the given EOM-CC Al_2CoO_4 result is high spin.

The empty circles in Figure 14.8 symbolize dark states with oscillator strengths between 0 and 0.0001, the half-filled circles represent states with oscillator strength

between 0.0001 and 0.001, and the filled circles are non-dark states. The oscillator strength varies somewhat with the functionals. Nevertheless, all methods show a consistent picture regarding the type of excitations and their visibility.

In Figure 14.6b, the band calculated with PBE0 at 0.9 eV, which is visible in the high spin case, and at 1.0 eV, which occurs in the broken-symmetry model, were initially combined into one band for simplicity. However, they are shown as two bands in Figure 14.8b. While they overlap strongly for all hybrid functionals, they are distinguishable for double-hybrid functionals and CIS. In addition, Figure C.5 on page 360 in the appendix shows the results for CIS for the high spin case (2S+1=7) and the broken-symmetry cases (2S+1=5), (2+1=3), and (2+1=1), showing that all bands in the broken-symmetry model are original to the method and have slightly different energies than those in the high spin case. The intermediate spin states provide a combined picture that includes all states. However, since the affected bands still overlap significantly in all methods, Figure 14.8b shows only the lowest states in each case, as they are only relevant for the determination of the band gap.

In order to identify the source of the optical band gaps at 0.78 eV, 1.51 eV, and 2.14 eV, it is necessary to consider the calculated energy range from 0 eV to 3 eV. This range only includes the ligand field transitions in the tetrahedral Co(II) and distorted octahedral Co(III) centers for all hybrid functionals, double-hybrid functionals, CIS, and EOM-CC, indicating that they are likely to be the origin of the band gaps. The MMCT transitions typically occur at energies higher than 3 eV. Based on the oscillator strength, the ligand field transitions in Co(II) sites are (potentially) non-dark states and are dipole-allowed. In contrast, the Co(III) ligand field transitions in the same energy range are all dipole-forbidden dark states. However, the Co(III) ligand field transitions may contribute to or generate the band gaps by means of intensity borrowing mechanisms or by enhancing the Co(II) ligand field transitions, as indicated in Figure 14.7b.

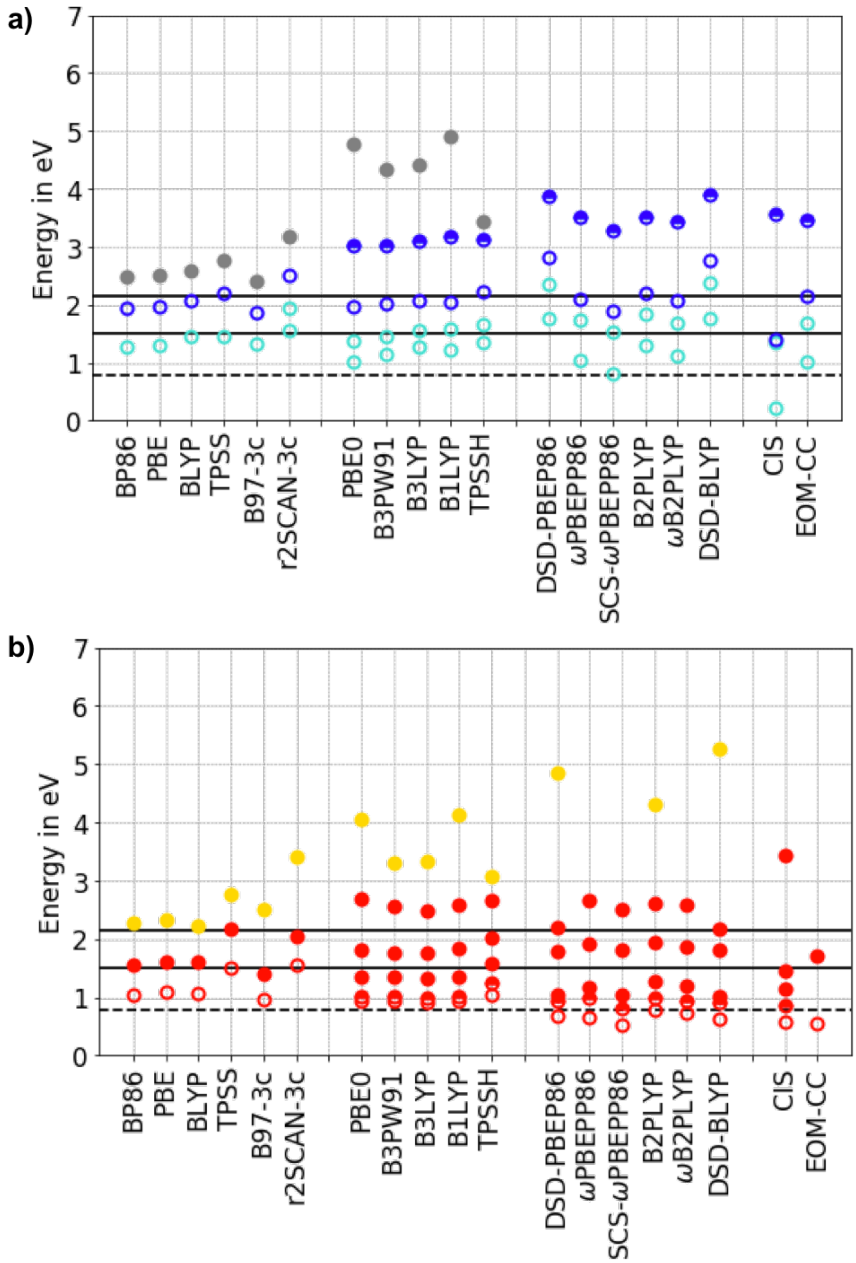

Figure 14.8: Results of first excited states belonging to different absorption bands for TD-DFT for **a)** Co_2ZnO_4 and b) Al_2CoO_4 for cluster size 4t8o (Exception: EOM-CC, cluster sizes are 1o and 1t, respectively). Basis sets: def2-QZVPP for TD-DFT and CIS, cc-pVQZ for EOM-CC. Color code: Co(II) $3d$ $e \rightarrow t_2$ (red), Co(III) $3d$ $t_{2g} \rightarrow e_g$ triplet (turquoise) & singlet excitations (blue), Co(III)→Co(III) MMCT (gray), Co(II)→Co(II) MMCT (yellow). Dark states (empty circle), "potentially" non-dark states (half-filled circles), non-dark states (filled circles).

All (meta-)GGA functionals agree with the other methods that the band gaps at

0.78 eV and 1.51 eV originate from ligand field transitions. However, for the band gap at 2.14 eV, these functionals suggest the possibility that it may originate from a combination of Co(II)→Co(II) MMCT and dark singlet ligand field transitions of Co(III).

The experimental results do not exclude either perspective, the (meta-)GGA functionals or the other methods. Martens et al.[484] observed absorption bands at 0.8 eV, 1.6 eV, and 2.6 eV, which can be related to Co(II) or Co(III) or both. Kim et al.[499] observed that the features at 1.65 eV and 2.4 eV are essential for Co(II) sites, which could be due to the ligand field transition of Co(II) or the MMCT Co(II)→Co(II), among other possibilities.

Lima et al.[487] found that the band gaps at 1.51 eV and 2.14 eV computed with the hybrid functional B3PW91 originate from a superposition of ligand field transitions local to the Co(II) and Co(III) centers, which supports the current hybrid and double-hybrid functional results. In contrast, Xu et al.[486] applied PBE and suggested Co(III)→Co(II) MMCT for the band gap at 2.14 eV, in agreement with the (meta-)GGA functionals used in this study.

All computational studies that analyzed the first excited state in the energy range of the band gap at 0.78 eV, such as Belova et al.[483], Miedzinska et al.[501], and Qiao et al.[475], agree that it can be characterized as a Co(II) ligand field transition. This agrees with all the methods used in the present study, as the first Co(II) ligand field transition always has a lower energy than the first Co(III) ligand field transition. Therefore, this transition can be considered the first excited state of Co_3O_4.

The transition types generally agree among the different methods, except for a few exceptions. However, their quantitative results are inconsistent and therefore, inconclusive overall. None of the methods satisfactorily agrees with the experiments, and ambiguities remain concerning the assignment of states to specific band gaps.

For example, different methods predict inconsistent values for the first excited state, with (meta-)GGA (average: 1.20 eV) and hybrid functionals (average: 0.95 eV) overestimating it and double-hybrid functionals (average: 0.67 eV) and EOM-CC (average: 0.56 eV) underestimating it, it is reasonable to assume that the predicted state is within the expected error range, given the known error of 0.2 eV of EOM-CC established in Chapter 11. However, the EOM-CC result is at the border of the known error range and is a dark state, making it unlikely to be the optical band gap. Experimental evidence suggests a low absorption feature at about 0.5 eV, which better agrees with the calculated first excited state. However, it is not reported as a band gap in any experimental study.[460, 474]

Therefore, the next Co(II) ligand field transition (hybrid functionals: 1.05 eV,

double-hybrid functionals: 0.92 eV), which only occurs via broken-symmetry DFT, on its own or in combination with the triplet ligand field transitions of Co(III) (average value (meta-)GGA: 1.38 eV, hybrid functionals: 1.20 eV, double-hybrid functionals: 1.21 eV, EOM-CC: 1.01 eV), may be a suitable candidate for the band gap. The overlapping states of various intensities demonstrated by calculations and the close energies of the experimental absorption bands at 0.82 eV and 0.94 eV suggest that one or a combination of the discussed states may be responsible for the second absorption band.

It is uncertain which states contribute to the band gaps at 1.51 eV and 2.14 eV. Two possible cases are related to the ligand field transitions of Co(II). In one case, average state energies calculated for hybrid and double-hybrid functionals at 1.39 eV/1.12 eV cause the band gap at 1.51 eV, while states at 1.84 eV/1.87 eV cause the band gap at 2.14 eV. In the other case, states at 1.84 eV/1.87 eV cause the band gap at 1.51 eV, while states at 2.59 eV/2.51 eV cause the band gap at 2.14 eV. The distinction is important for understanding the role of antiferromagnetic coupling, as the states 1.39 eV/1.12 eV and 2.59 eV/2.51 eV states only originate in the broken-symmetry model.

Sousa et al.[490] calculated an energy with B3PW91 of 1.33 eV for the experimental band gap of 1.51 eV. This agrees with the B3PW91 calculated value of 1.35 eV in the current study and suggests that the first case of the two possible assignments of the experimental band gap may be more reasonable. It is also consistent with the knowledge that DFT generally underestimates band gaps.[19] However, the calculation of the band gap of 0.78 eV does not agree with this assignment because the Co(II) ligand field transitions calculated with DFT functionals overestimate the band gap in most cases. For the (meta-)GGA functionals, the high spin Co(II) ligand field transition has an average value of 1.54 eV, excluding TPSS and r2Scan-3c, which agrees well with the band gap of 1.51 eV. However, this result is inconclusive due to the shortcomings of the (meta-)GGA functionals, which may give the right numbers for the wrong reasons, and their disagreement with all other results regarding the band gap at 2.14 eV.

EOM-CC predicts a Co(II) ligand field transition at 1.72 eV, between the experimental band gaps of 1.51 eV and 2.14 eV. The result is therefore inconclusive. The Co(III) ligand field transitions show better agreement, with the second triplet state at 1.68 eV in fair agreement with the experimental band gap of 1.51 eV, and the first singlet state at 2.14 eV in perfect agreement with the other band gap. The corresponding hybrid functional results also agree with average states at 1.52 eV and 2.06 eV, respectively. However, these are all dark states with zero or near-zero oscillator strength.

To summarize, additional research is needed to determine the band gaps of Co_3O_4. The complex nature of Co_3O_4 may necessitate the use of a multireference method for accurate calculation, as all the methods used so far have been single reference methods. Additionally, the broken-symmetry DFT method only provides an approximation of the antiferromagnetic coupling and can be better modeled using multireference methods. As a result, the next section will delve into such models based on the findings thus far.

14.6 Towards a Multireference Model

Based on the results of the single-reference methods, ligand field transitions are most likely to cause the band gaps in question. With this assumption in mind, multiconfigurational and multireference models have been constructed to further investigate the three potential band gaps. These models mainly focus exclusively on the $3d$ orbitals of the different Co centers. The TD-DFT analysis showed that the band gap energy range of Co_3O_4 can be accurately described as the sum of the Co_2ZnO_4 and Al_2CoO_4 models. Therefore, in this section, Co_2ZnO_4 will be studied first, followed by Al_2CoO_4, representing the Co(III) and Co(II) sites, respectively. The results of these models are combined and compared with Co_3O_4 to confirm the accuracy of the individual results for the multireference models. Finally, an overview of the results obtained with different methods is given.

14.6.1 Co_2ZnO_4

It was mentioned earlier that distorted octahedral Co(III) sites, such as those in Co_2ZnO_4, are typically considered to be low-spin and single-configurational in the ground state. However, this view does not necessarily hold for excited states, which may be better described by multiconfigurational methods beyond the one-electron picture. The TD-DFT model showed that the dipole-forbidden $3d$ $t_{2g} \rightarrow e_g$ ligand field transitions for the entire Co_2ZnO_4 system can be accurately represented by a single Co(III) site (1o). Therefore, Figure 14.9 shows the multiconfigurational SA-CASSCF results for the single Co(III) site 1o, with and without perturbation by NEVPT2. In addition, the MR-EOM-CC and ICE-CI results are shown, as are the single-reference results represented by PBE0, EOM-CC, and CIS.

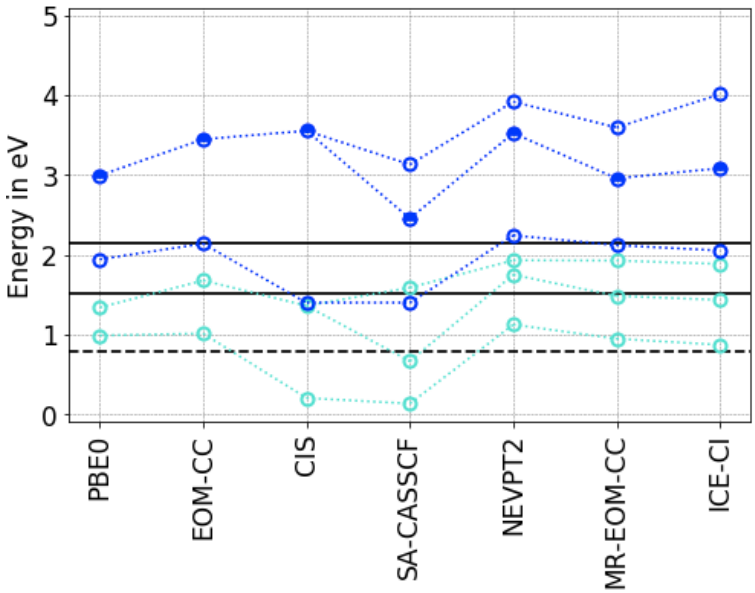

Figure 14.9: Calculation results of the first excited triplet (turquoise) and singlet (blue) states of absorption bands originating from ligand field transitions in the isolated Co(III) site 1o in terms of single configurational methods (PBE0, EOM-CC, CIS) and with multiconfigurational/-reference methods (SA-CASSCF, NEVPT2, MR-EOM-CC, ICE-CI). Dark states (empty circle), "potentially" non-dark states (half-filled circles), non-dark states (filled circles).

The multiconfiguration description of Co(III) leads to a splitting of the previous two bands of triplet and singlet ligand field excitations into three bands each. Figure 14.9 shows this by switching from CIS to SA-CASSCF. In the single configuration description, all excitations are single excitations. In the multiconfiguration description, the first two bands (singlet and triplet) are still dominated by single excitations, so their energies calculated with CIS and SA-CASSCF agree well. However, in the second triplet and singlet band, about 90% of the character comes from CSFs representing single excitations mixed with about 10% representing double excitations. In the third bands, double excitations dominate, with only about 10% single excitation character. The 10% double excitation character in the second triplet and singlet bands can be interpreted as an electron correlation correction to the state energy. However, the dominant double excitations of the third bands are unlikely to contribute significantly to the spectrum since double excitations are unlikely. Therefore, they will be excluded from the final discussion, and the focus will be on the dominantly single excitations.

CIS and SA-CASSCF approaches are inaccurate for calculating band gaps due to their lack of dynamic correlation. To compensate for this, NEVPT2 and MR-EOM-

CC are used in addition to SA-CASSCF. The first excited states of both the triplet and singlet descriptions agree for MR-EOM-CC and EOM-CC, which is consistent with the results obtained from SA-CASSCF and CIS. Therefore, the first singlet state of the MR-EOM-CC result still agrees with the third band gap at 2.14 eV. The second and third singlet and triplet bands split around the second bands in EOM-CC. The second triplet excitation now agrees with the second band gap. The NEVPT2 bands have a slightly higher energy than the corresponding MR-EOM-CC results.

The methods described based on SA-CASSCF treat only the $3d$ orbitals of Co(III) with active-space methods. ICE-CI, however, allows most of the O $2p$ orbitals to be included in the CI-treated space. The result is shown on the right side of Figure 14.9 and is similar to the NEVPT2 and MR-EOM-CC results. This indicates that oxygen orbitals are important for ligand field transitions in the Co(III) site, and those dynamic correlation methods can account for these missing contributions.

The ligand field excited states local to the Co(III) site and in the energy region of the band gaps are dark, just as in the single reference approaches. Therefore, the good agreement with the experiment does not necessarily imply that these excitations are the primary cause of the band gaps.

According to the TD-DFT model, the energy range of the experimental band gaps for Co_2ZnO_4 can be fully described by an isolated distorted octahedral Co(III) site 1o. To determine whether additional excitations for multiple Co(III) sites are present in this range in the multireference model, Figure 14.10 shows the increase in QC size from 1o to 1t2o. To handle the complete set of necessary excitations in the $3d$ space of the two Co(III) centers, ICE-CI is used in the first step. It explicitly treats only the $3d$ space of 1o and 1t2o; therefore, the ICE-CI result of 1o agrees with the SA-CASSCF result shown in Figure 14.9.

Several additional excitations occur for 1t2o. However, all of them can be categorized as double or higher excitations occurring locally at the Co(III) sites or simultaneously at both sites. Currently, ICE-CI cannot compute the oscillator strengths. To obtain them, the states are recalculated with SA-CASSCF, and the results demonstrate that they have zero oscillator strength. Therefore, they do not appear to be MMCT transitions and are unlikely to contribute to the band gaps due to their double and higher excitation nature. By removing the corresponding CSFs, the SA-CASSCF and NEVPT2 results agree with the 1o result. Consequently, the energy range of the band gaps for Co_2ZnO_4 is again entirely described by the single Co(III) site.

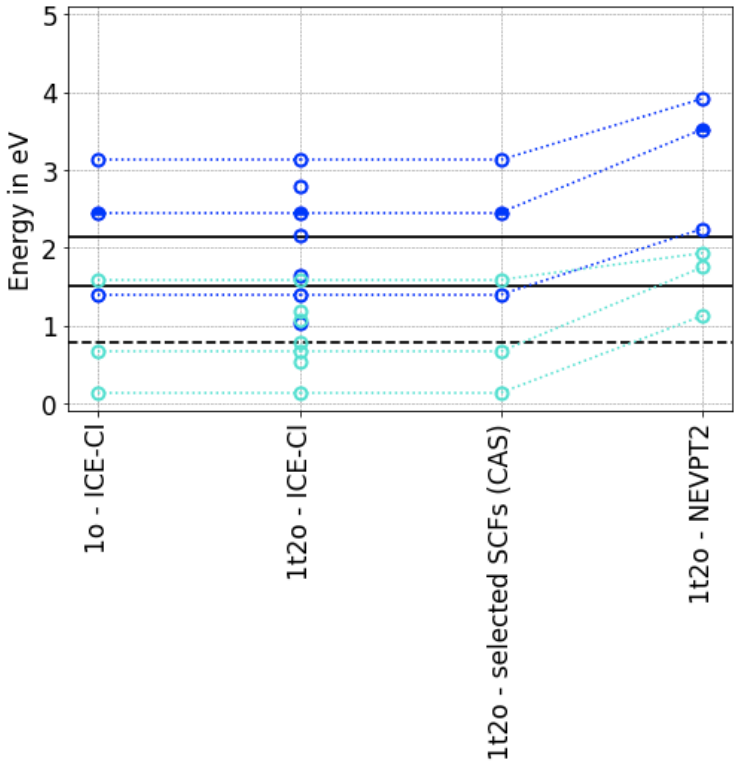

Figure 14.10: Calculation results of the first excited triplet (turquoise) and singlet (blue) states of absorption bands originating from ligand field transitions in cluster sizes 1o and 1t2o of Co_2ZnO_4 computed with ICE-CI, SA-CASSCF, and NEVPT2. Dark states (empty circle), "potentially" non-dark states (half-filled circles), non-dark states (filled circles).

14.6.2 Al_2CoO_4

Moving on to Al_2CoO_4, Figure 14.11 shows the ligand field transitions of the tetrahedral high spin Co(II) site (1t) for both the single- and multireference methods, similar to the Co(III) case. As mentioned above, the single-reference Co(II) results differ from the experimental observations.

Similar to Co(III), when the Co(II) $3d$ orbital space of a high spin single Co(II) site (1t) is treated with SA-CASSCF, the two absorption bands of ligand field excited states split into three. A possible interpretation is that the first band contains singly excited states, the second band contains 85% doubly excited and 15% singly excited states, and the states of the third absorption band have an opposite character to those of the second.

The oscillator strength increases from the first to the third group of states, and all three have non-zero oscillator strength. Nevertheless, the states of the first absorption band can still be considered dark according to the selected criteria. The

states of the second band are "potentially" non-dark, while those of the third band are non-dark. However, since the states in the second absorption band have a predominantly double excitation character, they are unlikely to contribute significantly to the observed absorption spectrum. Nonetheless, moving forward, they will be discussed in contrast to the Co(III) case since they show some oscillator strength.

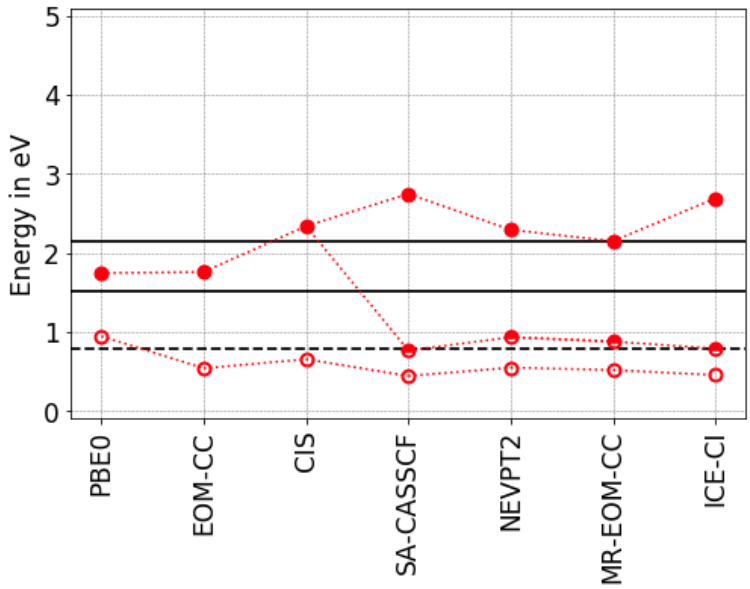

Figure 14.11: Calculation results of the first excited states of absorption bands originating from ligand field transitions in the single Co(II) site 1t in terms of single-reference methods (PBE0, EOM-CC, CIS), and with multiconfigurational/-reference methods (SA-CASSCF, NEVPT2, MR-EOM, ICE-CI). Dark states (empty circle), "potentially" non-dark states (half-filled circles), non-dark states (filled circles).

Equivalent to the Co(III) site, the first excited state of the EOM-CC method agrees with that of the MR-EOM-CC method, indicating the validity and consistency of the model, as both states have a pure single excitation character. The first excited state of the second absorption band, which has an energy of 0.83 eV, agrees well with the first band gap energy of 0.78 eV. The first excited state of the third absorption band is in perfect agreement with the experimental band gap value of 2.14 eV.

The ICE-CI result on the right side of Figure 14.11 explicitly includes all Co(II) $3d$ and O $2p$ orbitals of the 1t site. The result is consistent with SA-CASSCF and indicates that an active space comprising only the $3d$ orbitals is sufficient to assess band gaps but that further dynamic correlation, such as those provided by MR-EOM-CC or NEVPT2, is necessary.

The results for the isolated Co(II) site compared to the Co(III) site suggest that the ligand field excited states of Co(III) are much more dependent on dynamic corre-

lation. The results show significant changes from methods such as CIS to EOM-CC or from SA-CASSCF to MR-EOM-CC for Co(III) but much less for the Co(II) equivalent.

As mentioned above, for the TD-DFT model, the isolated Co(II) site only partially represents the potential excited states of Al_2CoO_4 in the band gap energy region because the antiferromagnetic coupling can only be considered when there are at least two Co(II) sites, as in the 2t4o model. Figure 14.12 shows the SA-CASSCF result of the 1t and 2t4o models. In contrast to the two-center model of Co(III), the entire $3d$ active space can be adequately described by SA-CASSCF, making ICE-CI redundant at this stage.

In addition to the states found for the isolated Co(II) site, several other states emerge. Although they resemble states in the TD-DFT and CIS broken-symmetry models and have similar energies to the CIS states (see Figure 14.8), their origins are not identical. In the broken-symmetry method, the states were attributed to antiferromagnetic coupling and exhibited oscillator strength. In SA-CASSCF, as in the two-center Co(III) model, they can be characterized as double and higher Co ligand field excitations occurring simultaneously in the two Co(II) centers. Due to their multiple electron excitation nature, they possess zero oscillator strength, unlike the other Co(II) ligand field transitions, and therefore, can be excluded from further discussion.

The broken-symmetry model is designed to achieve antiferromagnetic behavior by inducing an (open) singlet state between the two Co(II) centers. However, in the SA-CASSCF result for 2t4o shown in Figure 14.12, where 2S+1=1, the same states are observed as for the isolated high spin Co(II) site, indicating that this approach does not adequately describe the antiferromagnetic coupling. Figure C.6 in the appendix (see page 360) shows the results of further calculations using SA-CASSCF for 2t4o with 2S+1=1, 3, 5, and 7. In this energy space, the results are similar for all three multiplicities since all states originate from the "neutral" antiferromagnetic ground state. In contrast, the broken-symmetry approach formally includes the "ionic" antiferromagnetic state.

In the results of the 2t4o SA-CASSCF model in Figure 14.12, the "ionic" antiferromagnetic states (indicated in purple) are observed at energies higher than 19 eV. The introduction of dynamic electron correlation via NEVPT2 significantly lowers their energy, causing them to overlap with the "neutral" antiferromagnetic states, as predicted by antiferromagnetic theory. The superposition of "ionic" and "neutral" antiferromagnetic ground states is usually explained by LMCT-MLCT superexchange mechanisms. This superposition stabilizes the "neutral" state with the "ionic" state, which may be close to or even lower in energy than the "neutral" state.

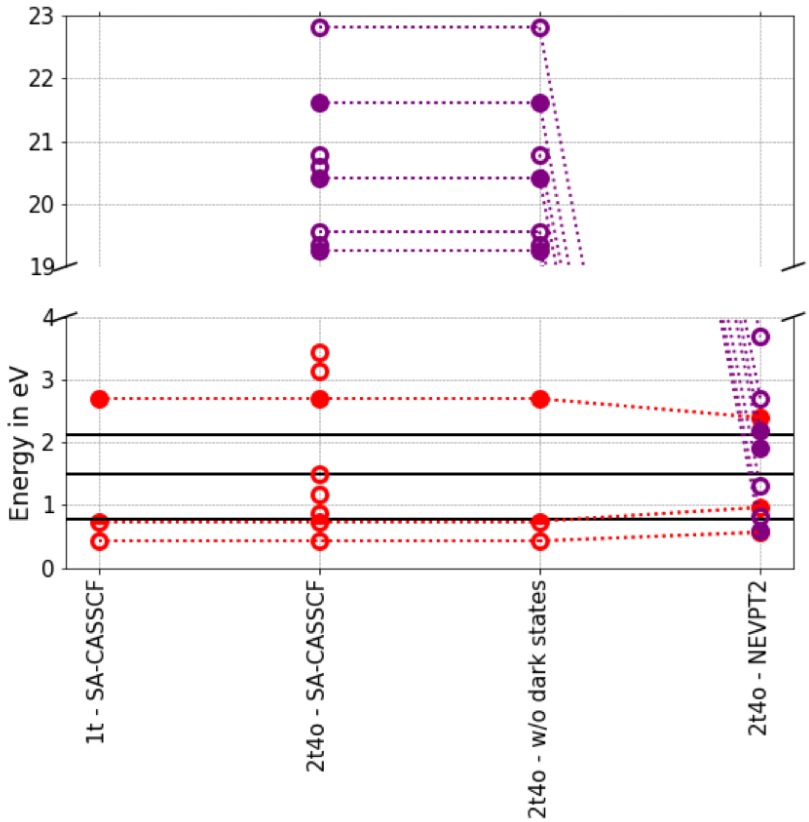

Figure 14.12: Calculated first excited states of absorption bands orginating from ligand field transitions in Al_2CoO_4 with system size 1t as high spin (2S+1=4) and 2t4o computed for "neutral" (red) and "ionic" (purple) antiferromagnetic states (2S+1=1) with SA-CASSCF and NEVPT2. Dark states (empty circle), “potentially” non-dark states (half-filled circles), non-dark states (filled circles).

In the NEVPT2 result in Figure 14.12, the "ionic" antiferromagnetic "ground state" is found to be about 0.60 eV higher in energy than the "neutral" antiferromagnetic state. However, this energy difference may not be reliable due to several factors. First, the active space used in the model does not include oxygen orbitals, which would exceed the available computational power. Second, NEVPT2 may not recover all necessary dynamic correlations. Third, the applied basis set (cc-pVQZ) may not be large enough. The convergence of the "ionic" and "neutral" states with respect to the basis set is shown in Figure C.7 in the appendix. Therefore, the energy difference between the two antiferromagnetic "ground states" should be considered only as an indicator that there is a superposition of "ionic" and "neutral" antiferromagnetic states in the multireference model, but not as a reliable energy difference. The two states are subsequently treated as being in an "ideal" superposition.

Figure 14.13 examines the "neutral" and "ionic" antiferromagnetic ground states

and their resulting excited states separately, using the NEVPT2 results for 2t4o. For clarity, states with zero or near-zero oscillator strength, which are not relevant to the problem, are excluded in both cases. However, dark states with low but non-zero oscillator strength that coincide with relevant energy positions are shown. The "neutral" antiferromagnetic states of the two-center system are well represented by the single high spin Co(II) site, as shown in Figure 14.13a. Based on the previously discussed MR-EOM-CC results, it is suggested that the ligand field transition of the tetrahedral Co(II) site could cause the first band gap at 0.78 eV and the third at 2.14 eV. However, the ligand field excitation that correlates with the band gap at 0.78 eV may not be the accurate description since it is claimed to be a double excitation as described above.

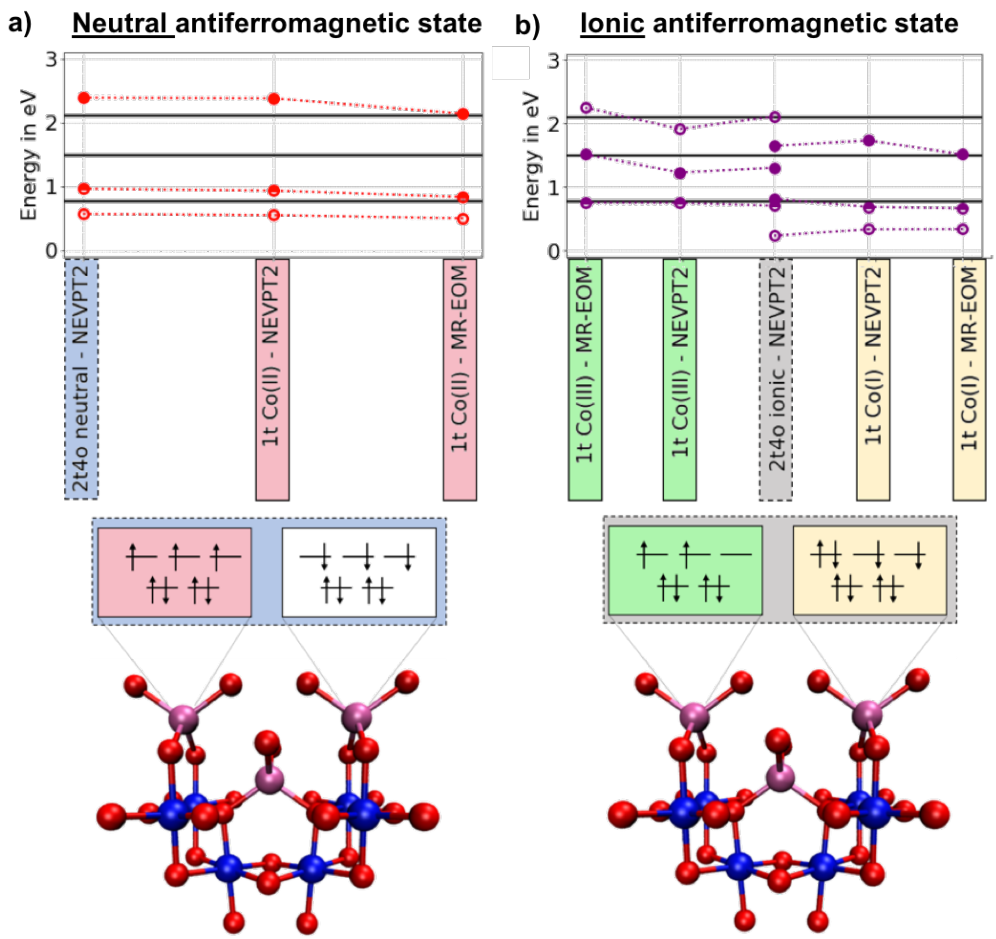

Figure 14.13: Calculated first excited states of absorption bands originating from ligand field transitions in Al_2CoO_4 for cluster size 2t4o with **a)** "neutral" and **b)** "ionic" antiferromagnetic description and 1t with Co centers that are formally Co(I), Co(II), and Co(III) with NEVPT2 and MR-EOM-CC. Dark states (empty circle), "potentially" non-dark states (half-filled circles), non-dark states (filled circles).

In the NEVPT2 model, which has an explicit "ionic" antiferromagnetic ground state and corresponding excited states, two bands of non-dark states appear at 1.31 eV and 1.65 eV. These states arise from ligand field transitions (see Figure 14.13b). There is also a ligand field state at 1.59 eV with very low oscillator strength (dark state), which is not discussed further but is localized to the Co(III) site. In addition, there are "potentially" overlapping non-dark states between 0.71 eV and 0.82 eV. The excited states occur at overall lower intensities than in the "neutral" description.

In the "ionic" antiferromagnetic ground state, the two Co centers, which are tetrahedrally coordinated and in the "neutral" state Co(II), are formally considered to be Co(I) and Co(III). Figure 14.13b shows that the absorption spectra of isolated tetrahedral Co(I) centers ($[Co(I)O_4]^{7-}$) and Co(III) centers ($[Co(III)O_4]^{5-}$) models are subspectra of the total spectrum of the "ionic" antiferromagnetic 2t4o model and represent all occurring non-dark states with comparable oscillator strength. By utilizing these models, it is possible to associate the state at 1.65 eV and 0.82 eV with a ligand field transition occurring in the local tetrahedral Co(I) site. Furthermore, the state at 1.31 eV and 0.71 eV can be attributed to the local tetrahedral Co(III) site.

When the isolated Co(I) sites are subjected to MR-EOM-CC, the state at 1.65 eV undergoes a reduction to 1.51 eV, which is in excellent agreement with the experimental second band gap. In addition, the excited state at 1.31 eV calculated with MR-EOM-CC for the Co(III) site also undergoes an increase to 1.51 eV. The states at 0.82 eV and 0.71 eV result in 0.67 eV and 0.76 eV, respectively.

Combining the separate "ionic" and "neutral" antiferromagnetic models gives a good description of all three band gaps. The lowest band gap can be explained by either the "neutral" or the "ionic" antiferromagnetic model since both have states close to 0.78 eV, with the ligand field excitation local to the tetrahedral Co(III) site in the "ionic" state giving the best agreement (MR-EOM-CC: 0.76 eV). It is more likely that states described by the "ionic" antiferromagnetic model cause this band gap, in particular, the Co(III) site. The Co(II) site in the "neutral" antiferromagnetic model and the Co(I) site in the "ionic" antiferromagnetic model have predominantly double excitations in this energy range. In contrast, the Co(III) site in the "ionic" antiferromagnetic model has single excitations. In addition, the broken-symmetry DFT model suggests that "ionic" antiferromagnetic states cause these states since an excitation with "potentially" non-dark oscillator strength in this energy range occurs only with the introduction of broken-symmetry and not in the high spin model.

The Co(I) site in the "ionic" and the Co(II) site in the "neutral" antiferromagnetic model show the first single excitation, albeit with insignificant oscillator strength, at about 0.5 eV. This is consistent with experimental findings of low absorption bands observed by Thota et al.[474] and briefly noted in Patil et al.[460] (see also Figure

14.1a), as already discussed in the context of EOM-CC. However, it has never been called a band gap.

The band gap at 1.51 eV is in perfect agreement with the ligand field transitions local to the tetrahedral Co(I) and Co(III) sites in the "ionic" model, which are non-dark states. The band gap at 2.14 eV perfectly agrees with the ligand field excitation local to the tetrahedral Co(II) site in the "neutral" non-dark state model. The tetrahedral Co(III) site in the antiferromagnetic model exhibits a low-intensity state in reach of the band gap at 2.14 eV and could contribute to it.

It should be noted that this is only one possible model. Competing representations exist when the isolated Co sites are described with different local multiplicities. In the applied models, the Co(II) site is high spin (2S+1=4), and the Co(I) and Co(III) sites are both triplets (2S+1=3), which are the multiplicities with the lowest energy for the cases and match the subspectra of the two-center model best.

14.6.3 Co_3O_4

Figure 14.14 compares the ICE-CI results of a Co_3O_4 model with the Co_2ZnO_4 and Al_2CoO_4 results to confirm that the sum of the Co_2ZnO_4 and Al_2CoO_4 results represents the band gap energy range for Co_3O_4 in the multiconfiguration description. The calculations were performed for a system size of 2t4o, where only two octahedral sites are occupied by Co(III) and two by Al(III) in the Co_3O_4 model for efficiency. The active space of the calculation includes the $3d$ orbital space of two tetrahedral Co(II) and two octahedral Co(III) centers. The results exclude the excitations associated with the Co(II) centers with zero oscillator strength and those associated with the Co(III) centers with double or higher excitation character for clarity. The oscillator strengths used to classify the darkness of the results are based on SA-CASSCF calculations with selected CSFs. An additional comparison of ICE-CI calculations of the described Co_3O_4, Co_2ZnO_4, and Al_2CoO_4 models can be found in Figure C.8 on page 362 in the appendix.

The ICE-CI approach used for Co_3O_4 has limitations in reaching the "ionic" antiferromagnetic states because it must consider both Co(III) and Co(II) $3d$ orbitals, resulting in a larger number of states to be accounted for before reaching the "ionic" antiferromagnetic states than in the Al_2CoO_4 case. As in the Al_2CoO_4 model, the "ionic" antiferromagnetic states are energetically much higher than the "neutral" states without any additional dynamic correlation. The result shows that for states originating only from the "neutral" antiferromagnetic ground state, the sum of the Al_2CoO_4 and Co_2ZnO_4 models can reproduce the Co_3O_4 band gap region without additional states. However, whether this is true for the "ionic" states is unclear. SA-CASSCF test calculations using only selected CSFs show that the separation of the

two models is also justified for the "ionic" antiferromagnetic states. The results are not presented because the calculated values are unreliable. Nevertheless, it is assumed that the statement is still true, based on the results of the other models and the test calculations in the remainder of the discussion.

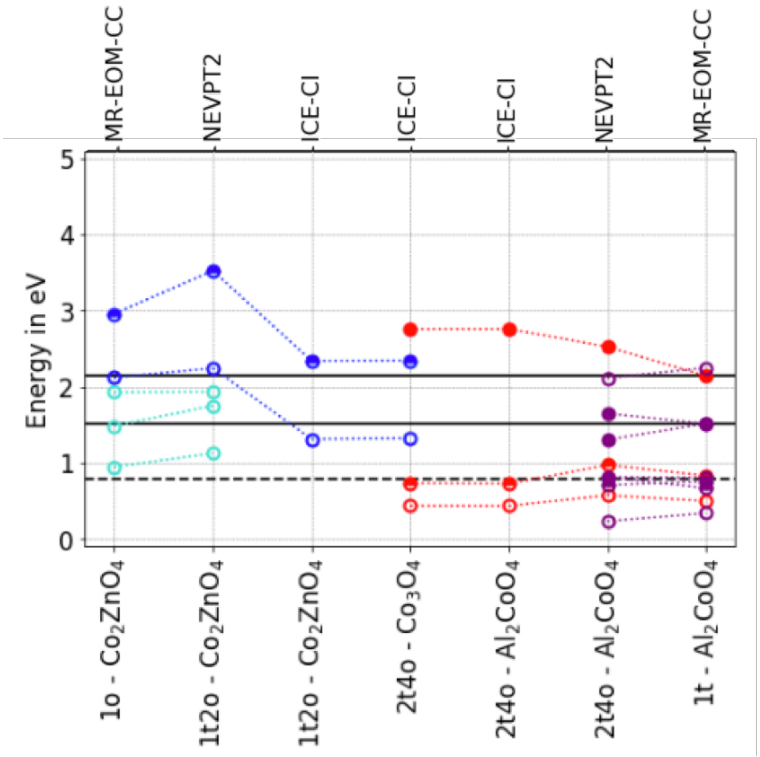

Figure 14.14: Comparison of calculated first excited states of overlapping absorption bands originating from ligand field transitions in multiconfigurational models of Co_3O_4, Al_2CoO_4, and Co_2ZnO_4. Dark states (empty circle), "potentially" non-dark states (half-filled circles), non-dark states (filled circles). Color code: tetrahedral Co $3d$ $e \rightarrow t_2$ excitation for "neutral" (red) and for "ionic" (purple) antiferromagnetic states, octahedral Co $3d$ $t_{2g} \rightarrow e_g$ triplet (turquoise) and singlet (blue) excitations.

Figure 14.14 shows, besides the singlet ICE-CI results, the previously developed models for the local representations of the distorted octahedral Co(III) with its spin-orbit coupled singlet and triplet states and the tetrahedral Co site, which is formally either Co(I), Co(II) or Co(III). Comparing the submodels calculated with MR-EOM-CC indicates that all three band gaps likely originate from the ligand field transitions of the tetrahedral Co sites, as they contribute significant oscillator strength. In this model, as discussed above for the representative Al_2CoO_4 model, the ligand field transitions of tetrahedral coordinated Co(II) in "neutral" antiferromagnetic states give rise to the band gap at 2.14 eV. Tetrahedral Co(I) and Co(III) sites in "anti-

ferromagnetic" states contribute to the band gap at 1.51 eV and may also play a role in the band gap at 0.78 eV.

Furthermore, there are ligand field transitions of the distorted octahedral Co(III) site with similar energies, especially in the region of the two higher band gaps (1.49 eV (triplet) and 2.12 eV (singlet)). Therefore, they could contribute directly to the band gaps despite being dipole-forbidden.

14.6.4 Comparison of Different Multireference Methods

The MR-EOM-CC method has provided promising results in explaining the electronic properties of the different tetrahedral Co sites in the "ionic" and "neutral" antiferromagnetic model combined with the single octahedral Co(III) site. The calculated band gaps are in good agreement with experimental data, suggesting the validity of this approach. However, other multireference methods and their performance are worth considering, especially since the MR-EOM-CC method can only handle one tetrahedral Co site at a time. Other methods, such as SA-CASSCF/ NEVPT2, as shown in the comparison above, or SA-CASSCF/ CASPT2 can handle two Co sites simultaneously, making them potentially more representative of the actual antiferromagnetic states. Therefore, a comparison between MR-EOM-CC and other multireference methods could provide further insight into the electronic properties of these systems.

Figure 14.15 shows the multireference results for Co_2ZnO_4 and Al_2CoO_4, where Co_2ZnO_4 represents the octahedral and Al_2CoO_4 represents the tetrahedral Co sites in Co_3O_4. It should be noted that the results for Co_2ZnO_4 are obtained for only one Co(III) site, which has been demonstrated to be sufficient for all the methods thus far. However, for Al_2CoO_4, SA-CASSCF calculations are performed independently and with perturbation via NEVPT2, CASPT2, and DCD-CAS(2) for a two-center model. The "ionic" antiferromagnetic states are adjusted towards an optimal ideal superposition to the "neutral" state. The ICE-CI and MR-EOM-CC results are obtained for only one tetrahedral Co site at a time, with MR-EOM-CC being computationally limited. In contrast, ICE-CI is limited because it includes most valence oxygen orbitals. This is done to study the influence of orbitals other than the $3d$ orbitals, which are only included in the active space in the other cases. The same applies to the ICE-CI result of Co_2ZnO_4.

To ensure clarity in the results presented in Figure 14.15, all excitations with double excitation characters in the octahedral Co(III) site have been excluded. Similarly, only the excitations relevant to the band gap are shown for the tetrahedral sites, along with the lowest dark state of the "neutral" antiferromagnetic case for reference.

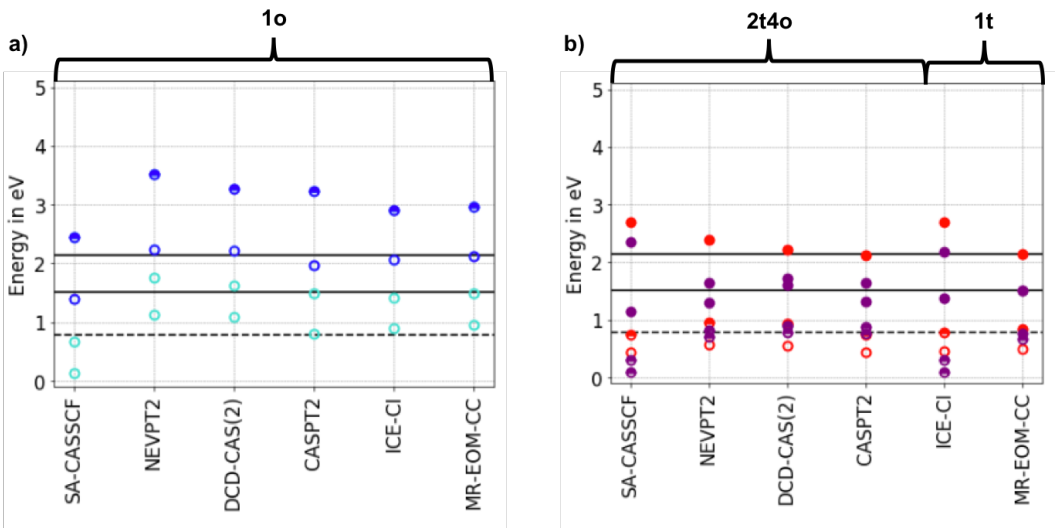

Figure 14.15: Results of first excited states of absorption bands originating from ligand field transitions for mulifconfiguration/-reference methods for **a)** Co_2ZnO_4 and **b)** Al_2CoO_4. Color code: tetrahedral Co $3d$ $e \rightarrow t_2$ excitation for "neutral" (red) and for "ionic" (purple) antiferromagnetic states, octahedral Co $3d$ $t_{2g} \rightarrow e_g$ triplet (turquoise) and singlet (blue) excitations.

Qualitatively, the results describing the band gaps with tetrahedral sites are consistent for the "neutral" antiferromagnetic states. However, SA-CASSCF and ICE-CI do not accurately capture the behavior of the "ionic" antiferromagnetic states, leading to an inaccurate representation of the band gaps in these models. For quantitative agreement with experimental results, methods that account for dynamic correlation are significantly more accurate than SA-CASSCF and ICE-CI. Among these methods, MR-EOM-CC provides the best agreement with experimental results in predicting the band gaps of systems with tetrahedral sites. This is due to its ability to accurately describe the excited states of the system by taking into account electron correlation, resulting in reliable predictions.

In the previous discussion of the MR-EOM-CC results, it was discovered that the first band gap observed experimentally at about 0.78 eV originates from the tetrahedral Co sites, particularly the one formally charged Co(III) in the "ionic" antiferromagnetic state. Although there are other excitations in this energy range, this specific excitation will be discussed for simplicity. MR-EOM-CC predicts a band gap of 0.76 eV. Excluding the ICE-CI and SA-CASSCF methods, which predict a band gap of about 0.31 eV, the multireference methods range from 0.71 eV for SA-CASSCF/ NEVPT2 to 0.89 eV for SA-CASSCF/ DCD-CAS(2), with SA-CASSCF/ CASPT2 providing the best result of 0.77 eV. It is important to note that two absorption bands are predicted in the vicinity of this band gap in the experiment. Therefore, the other

competing excitations of differently charged tetrahedral Co centers may also contribute to the other absorption band.

MR-EOM-CC explained the experimental band gap at 1.51 eV by the presence of formally Co(I) and Co(III) tetrahedral sites in the "ionic" antiferromagnetic model, resulting in a calculated band gap of 1.51 eV from both sites. As already described and visualized in Figure 14.13, the two corresponding ligand field excitations have different energies when NEVPT2 is applied. This is also the case for all other methods tested. SA-CASSCF and ICE-CI again give ambiguous results due to the lack of dynamic correlation. According to the SA-CASSCF/ NEVPT2 and SA-CASSCF/ CASPT2 methods, the excited state of Co(III) is predicted to be at 1.31 eV and 1.32 eV, respectively, and the corresponding excited state of Co(I) is predicted to be at 1.65 eV. However, the DCD-CAS(2) method overestimates the band gap, placing the state originating from Co(III) state at 1.60 eV and the one from Co(I) at 1.73 eV.

The experimental band gap of 2.14 eV was in excellent agreement with the ligand field transition of high spin tetrahedral Co(II) calculated by MR-EOM-CC. The other multireference methods - again excluding SA-CASSCF and ICE-CI - vary from 2.12 eV for SA-CASSF/ CASPT2 to 2.40 eV for SA-CASSCF/ NEVPT2, with SA-CASSCF/ DCD-CAS(2) placing the corresponding state at 2.22 eV.

As described above, the second triplet and first singlet ligand field excited states of the octahedral Co(III) sites represented by Co_2ZnO_4 states calucalted with EOM-CC show reasonable agreement with the band gaps at 1.51 eV and 2.14 eV, respectively. Switching to MR-EOM-CC improves the agreement, with calculated values of 1.49 eV and 2.12 eV. The results shown in Figure 14.15 support these findings, as SA-CASSCF/ NEVPT2 (1.75 eV/ 2.24 eV) and SA-CASSCF/ CASPT2 (1.62 eV/ 2.22 eV) slightly overestimate the two band gaps, while SA-CASSCF/ CASPT2 (1.49 eV/ 1.97 eV) and ICE-CI (1.42 eV/ 2.06 eV) slightly underestimate them. This suggests that although the ligand field transition states of the octahedral site are formally considered dipole-forbidden "dark states" and thus, have zero or near-zero oscillator strength, they may still contribute to the two band gaps in conjunction with the ligand field transitions of the tetrahedral sites. This could happen either by gaining intensity themselves or by enhancing the intensity of the tetrahedral ligand field excitations.

The idea of a superposition of the octahedral and tetrahedral ligand field excitations has already been entertained in the TD-DFT discussion and is also based on Lima et al.[487]. The contribution of the octahedral ligand field excitations may also explain the experimental evidence for Co(III) sites, such as in the higher absorption peak associated with the second band gap. Kim et al.[499] showed that this feature in Co_3O_4 shifted from 2.40 eV to 2.80 eV for Co_2ZnO_4. In all tested computa-

tional methods, the second band of singlet states in Co_2ZnO_4 gains more oscillator strength. These states appear at 2.96 eV in the MR-EOM CC calculations and may explain this observation.

Notably, the first bands of the triplet states of the octahedral ligand field excitations are close to the first band gap of 0.78 eV. Although overestimation occurs in all methods, including dynamic correlation, except SA-CASSCF/ CASPT2, which agrees well with the band gap, this finding suggests that the octahedral sites may also play a role in this case or, more likely, contribute to the higher absorption band found experimentally in this energy range (peak at about 0.94 eV).

While the multireference description may provide an overall more satisfactory description of the cobalt oxides that is in better agreement with the experiments than TD-DFT, the drawback is that certain states, such as the MMCT states, are not included in the final model due to computational limitations. In addition, the approach is restricted to smaller cluster sizes. Thus, the combination of the two approaches provides not only competing but also concordant explanations, leading to a more rounded overall explanation. In general, the two protocols provide a valuable complementary approach.

14.7 Conclusions

The presented investigation followed numerous experimental and computational studies that have explored the band gap of Co_3O_4. To provide context, a brief review of the relevant literature was conducted, which revealed that previous experiments had mainly identified three different band gaps for Co_3O_4: 0.78 eV, 1.51 eV, and 2.14 eV. The last two values were the most frequently observed. These three values were used as reference points in the current investigation.

Based on point group analysis of the tetrahedral and octahedral cobalt sites in Co_3O_4, it has been determined that the first excited state for the tetrahedral Co(II) site is likely to be its dipole-allowed ligand field transition. In contrast, for the distorted octahedral Co(III) case, the ligand field transition is dipole-forbidden. For models with multiple Co centers, all potential LMCT and MMCT transitions are dipole-allowed and are expected to occur at higher energies than the ligand field transitions.

Follow-up TD-DFT calculations were performed on an electrostatically embedded cluster model of the cobalt oxide to validate the predictions. The model size was progressively increased to converge the calculated excited states with respect to model size. Two auxiliary models, $Al_2Co(II)O_4$ and $Co(III)_2ZnO_4$, were introduced to represent the tetrahedral Co(II) and octahedral Co(III) sites in Co_3O_4. The TD-DFT

results of these two models were then compared with the TD-DFT results of Co_3O_4. This comparison showed that the two auxiliary models accurately represented the local ligand field transitions specific to the Co(II) and Co(III) sites in Co_3O_4 and were likely the source of the band gaps since they were the only excitations present in the relevant energy range for most of the DFT functionals tested. The TD-DFT results also confirmed that the Co(III) ligand field transitions were likely to be dark states, which meant that they were less likely to be the source of the band gaps. It was therefore concluded that the ligand field transition of the tetrahedral Co(II) sites is probably the primary source of the band gaps. However, non of the DFT functionals delivered satisfactory quantitative agreement with the experiment.

Multiconfiguration and -reference methods were used to understand the band gaps better. The methods used varied from SA-CASSCF to SA-CASSCF with perturbation methods like NEVPT2, DCD-CAS(2), and CASPT2, as well as MR-EOM-CC and ICE-CI. MR-EOM-CC showed the best agreement with the experiment. These methods confirmed that the tetrahedral ligand field transitions were the most likely explanation for all three band gaps. In this context, two antiferromagnetic models were introduced: the "neutral" model, which includes only tetrahedral Co(II) sites, and the "ionic" model, which combines tetrahedral Co(I) and Co(III) sites to account for the antiferromagnetic superexchange. The band gaps at 0.78 eV and 1.51 eV are better explained by the ligand field transitions local to the tetrahedral Co(I) and/or Co(III) site in the "ionic" antiferromagnetic state. The band gap at 2.14 eV probably originates from the tetrahedral Co(II) site in the "neutral" antiferromagnetic state. These Co(II) sites may also contribute to the lowest band gap at 0.78 eV.

Similar to the TD-DFT model, the results of this method indicated that the second and third band gaps may not originate solely from the tetrahedral sites. Instead, a combination of ligand field transitions from both the tetrahedral and octahedral Co sites may be a competing explanation, as both transitions overlap energetically for these two band gaps. Depending on the method, the distorted octahedral Co(III) sites have zero or near-zero oscillator strength. However, they may receive some intensity from the Co(II) sites or contribute intensity by other mechanisms, especially for the higher energy states.

Although the multireference model can provide a more comprehensive and accurate description of cobalt oxides that better agrees with experimental results than TD-DFT, it has limitations. For example, due to computational constraints, certain states are excluded from the final model and only the ligand field transitions are explicitly considered. In addition, the multireference approach is limited to smaller cluster sizes. Therefore, combining both approaches provides consistent explanations, resulting in a more complete overall understanding.

Finally, it is worth noting that it may not be appropriate to consider all three optical band gaps as actual band gaps, assuming the presented model is correct. In previous literature, the different optical band gaps have been attributed to subbands and different types of transitions within Co_3O_4. However, according to the proposed model, all three band gaps can be attributed to ligand field transitions primarily localized at the tetrahedral Co sites. This suggests that only the first optical band gap can be considered the "true" band gap. However, this determination could be subjective and depend on the observer's interpretation.

15 Uncovering the Spectral Features of Secret Final States in the $K\beta_{1,3}/K\beta'$ Mainline X-ray Emission Spectra of Co_3O_4, Co_2ZnO_4, and Al_2CoO_4

15.1 The Context and Structure of the Study

X-ray-based techniques, and, in particular, core-level X-ray emission spectroscopy (XES), play an important role in advancing the understanding of electronic structure. These techniques work in an element-specific manner and allow to examine the electronic structure in the vicinity of the core hole. XES spectroscopies have been extensively used to investigate the oxidation and spin states, local environments, and electronic structures of transition metal complexes, biological systems, and solids.[58, 513–531] X-ray emission spectroscopies have been successfully applied in various studies to uncover important information. For example, they have been used to determine the identity of the central carbide atom in nitrogenase enzymes,[5, 532] to investigate the cobalt catalytic activity of CoNiO catalysts in dry methane reforming reactions,[533] and to study the activity of the electrochemically probed oxygen evolving reaction in cobalt-iron nanowires[430] and graphene.[534] X-ray emission spectroscopies have also been applied to various other fields, such as sulfur speciation in biochars[535] and probing defects in InP fluorescent materials (quantum dots).[536] With recent advances in instrumentation development, it is now possible to construct laboratory-based XES spectrometers in-house, [537, 538] making these techniques even more accessible for solving complex problems in heterogeneous catalysis.

Interpreting XES spectra can be difficult due to the intricate multiplet structures that arise from the various electron decay channels in the experiment. In addition to accounting for the multiplet structure of the final state, a successful computational approach must take into consideration spin-orbit coupling effects and the extent of

metal-ligand covalency, as these factors have a significant impact on the intensity distribution and the energy positions of the computed spectral features.

The success of using one-electron approaches based on differences in orbital energies obtained from DFT calculations has been demonstrated in various chemical systems for computing $K\beta_{2,5}/K\beta''$ Valence-to-Core (VtC) XES spectra.[519, 521, 522, 539, 540] These spectra observe the transitions of valence electrons to the core hole (see also Figure 8.3 on page 101). The $K\beta_{1,3}/K\beta'$ mainline XES spectrum observes metal $3p$ to $1s$ transitions. This property makes the $K\beta_{1,3}/K\beta'$ mainline XES spectrum valuable for obtaining local information in multimetallic systems, such as Co_3O_4. In these systems, the $K\beta_{1,3}/K\beta'$ mainline XES spectra are anticipated to provide insights into specific metal sites. For instance, for the example of Co_3O_4, the $K\beta_{1,3}/K\beta'$ mainline XES spectra are expected to offer information about the two different cobalt sites ($[Co(III)O_6]^{9-}$ and $[Co(II)O_4]^{6-}$), which have been proven of being of importance for understanding the band gaps of Co_3O_4 in the previous chapter. This information from the $K\beta_{1,3}/K\beta'$ mainline XES spectrum is expected to be specific to one Co site at a time and thus, independent of the effect of the other cobalt sites and of the magnetic effects.

The key feature of the $K\beta_{1,3}/K\beta'$ mainline XES spectra is the energy splitting between the $K\beta_{1,3}$ and $K\beta'$ peaks, which cannot be accurately reproduced using one-electron approaches. Previous studies[53, 541] have shown that this splitting is proportional to the $3p - 3d$ exchange interactions in the context of ligand field theory (LFT) based models. Thus, the accurate computation of $K\beta_{1,3}/K\beta'$ mainline XES spectra can only be achieved using wavefunction-based methods, such as restricted active space configuration interaction (RASCI)[53] and restricted open-shell configuration interaction (ROCIS).[542, 543]

Previous studies have only focused on mononuclear transition metal chemical systems in $K\beta_{2,5}/K\beta''$ VtC and $K\beta_{1,3}/K\beta'$ mainline XES spectra analysis. Currently, there is limited understanding of how one-electron or wavefunction-based methods perform in treating XES problems in multimetallic chemical systems. In this work, the existing restricted active space configuration interaction (RASCI) XES protocol[521] will be expanded to include a complete active space configuration interaction approach, resulting in the formation of the CASCI XES method. The CASCI XES method combines the RASCI XES protocol with the efficient CAS module of the ORCA computational package[351, 503]. This framework allows the treatment of large active spaces, different spin states, and a specific selection of electron configurations representative of the CSFs of different core-ionized initial and final states. Thus, it provides the ability to compute $K\beta_{1,3}/K\beta'$ mainline XES spectra in chemical systems with complex electronic structures such as those discussed in this

work.

This chapter presents a comprehensive study of the Co $K\beta_{1,3}/K\beta'$ mainline X-ray emission spectra of three spinel systems: Co_3O_4, Co_2ZnO_4, and Al_2CoO_4. As introduced in the previous chapter, $Co(III)_2ZnO_4$ and $Al_2Co(II)O_4$ are expected to be representative of the distorted octahedral Co(III) and tetrahedral Co(II) sites, respectively, in Co_3O_4. The study combines experimental analysis and computational protocols and focuses on analyzing the information in the spectra to understand the role of local symmetry and electronic states in the $K\beta_{1,3}/K\beta'$ mainline XES spectra.

The study begins with a description of the computational protocol using the electrostatic embedded cluster approach to predict and analyze the information contained in the spectra. A first analysis of the experimental spectra will be presented. The convergence scheme for increasing model sizes of the three spinel systems will be shown for the one-electron and CASCI approaches to demonstrate the expected locality of the $K\beta_{1,3}/K\beta'$ mainline XES spectra. The limitations of the one-electron approach in calculating the spectra will be explored, and the need for the CASCI approach will be established.

Before discussing the results of the CASCI computed $K\beta_{1,3}/K\beta'$ mainline XES spectra of the three cobalt oxide derivatives, an explanation of the underlying theory will be provided, and the expected splitting between $K\beta'$ and $K\beta_{1,3}$ for the different spectra explored. The analysis of the cobalt oxide spectra emphasizes the relationship between the selected core-ionized initial state and the manifold of final states. The aim of the study is to determine how the transitions between them gain intensity, allowing the reproduction of the experimental observations. This study will demonstrate the importance of the CASCI method in accurately calculating $K\beta_{1,3}/K\beta'$ mainline XES spectra and offer deeper insights into the local electronic structures of these complex multicenter systems.

15.2 Computational Details

All calculations were performed with the ORCA 5.0.1 suite of programs.[351, 503] Throughout, DKH-def2-TZVP[142, 544] basis sets were employed together with automatically generated auxiliary basis sets (AutoAux protocol)[545] and the keyword NoFrozenCore. All calculations considered scalar relativistic effects using the second-order Douglas-Kroll-Hess (DKH2) correction.[228, 229, 546–548] The cobalt oxide solids were modeled as a series of clusters with increasing system size in the framework of the embedded cluster approach in the Ionic-Crystal-QM/MM scheme. Further details in regard to the models were already established in Section 13.1 (see also Table 13.1 on page 171 and Figure 3.12 on page 44). The $K\beta_{1,3}/K\beta'$

mainline XES calculations based one-electron DFT orbital energy differences as described previously[263] and as introduced in Section 8.2, including spin-orbit coupling, effects[264] were carried out employing the BP86 functional.[213, 363] All the one-electron XES computed spectra were shifted by 126.4 eV to match the experiment better visually. The orbital contributions and conrtibutions of the different Co centers to the underlying states in the one-electron spectra were explored. An algorithm determined the character of each orbital based on Loewdin Population analysis.

In addition, the $K\beta_{1,3}/K\beta'$ mainline spectra were computed in the complete active space configuration interaction CASCI XES framework. Quasi-restricted orbitals (QROs)[549] were generated by DFT calculations employing the BP86 functional to adequately describe the covalent mixing between the metal and oxygen centers and used as a base for the subsequent CASCI calculations. When necessary, especially for the larger system sizes of the Co_2ZnO_4 system, the orbitals were localized using ORCA_LOC. The mainline XES calculations were performed by rotating the Co $1s$ and Co $3p$ MOs in the active space, whcih also includes the Co $3d$ MOs. The selection of configurations describing the emission process includes multiple steps. First, for small cluster sizes (1o or 1t), including a choice of configurations involving the Co $3d$ orbital space chosen based on preliminary RASCI calculations performed according to the established protocol[521] saturates the space of all relevant configurations. The relevant configuration space for larger system sizes evolves by extending the defined configuration space of the small-sized cluster. The initial states of the emission process with an ionized $1s^1$ orbital in the Co "emissive" center were chosen based on the initial state rule.[550] Besides configurations describing the initial states, configurations representing the corresponding emissive final states with singly occupied $3p$ orbitals are defined accordingly. The selection of the emissive final state manifold will be discussed for the particular cases in detail below.

The CASCI calculations were performed for the full set of states in chosen multiplicities to explicitly treat the relevant final state multiplet structure, assuming sudden approximation conditions for the core-ionized initial and the emissive final states. The computed transition densities of the relativistically corrected spectra were considered up to first order in the multiple expansion to include electric dipole, magnetic dipole, and electric quadrupole, as well as spin-orbit-coupling contributions. All the CASCI XES computed spectra have been shifted by -49.8 eV to obtain a better visual agreement with respective experimental spectra.

In the appendix, Section C provides representative inputs for one-electron and CASCI calculations starting on page 363.

15.3 Experimental Spectra

Figure 15.2 presents the experimental Co $K\beta_{1,3}/K\beta'$ mainline XES spectrum of the $Co(III)_2ZnO_4$, $Al_2Co(II)O_4$, and Co_3O_4 spinel solids. The details on the the experimental measurement can be found in the appendix in Section C on page 362.

A broad and asymmetric $K\beta_{1,3}$ spectral feature is evident in Co_2ZnO_4 and Co_3O_4, with the maximum intensity at 7650.2 eV. However, in the case of Al_2CoO_4, the maximum intensity is at 7650.6 eV with a shoulder at 7647.0 eV. The $K\beta'$ spectral feature is more pronounced in Al_2CoO_4, appearing at 7638.0 eV with a higher intensity relative to the total intensity compared to the other two systems. In contrast, the $K\beta'$ spectral feature appears at 7640.0 eV in both Co_2ZnO_4 and Co_3O_4. To sum up, the Co $K\beta_{1,3}/K\beta'$ mainline XES spectra of Co_2ZnO_4 and Co_3O_4 are similar, while Al_2CoO_4 shows differences.

In light of the above observations, it is proposed that the shift in the mainline to higher energies for Al_2CoO_4 compared to Co_2ZnO_4, along with the increase in the energy difference and the higher intensity of $K\beta'$, is due to the decreased $3p - 3d$ exchange integral and increased effective charge Z_{eff} from Co(II) to Co(III). This is based on the assumption that the tetrahedral Co(II) sites are in a high spin configuration and the distorted octahedral Co(III) sites are in a low spin configuration.

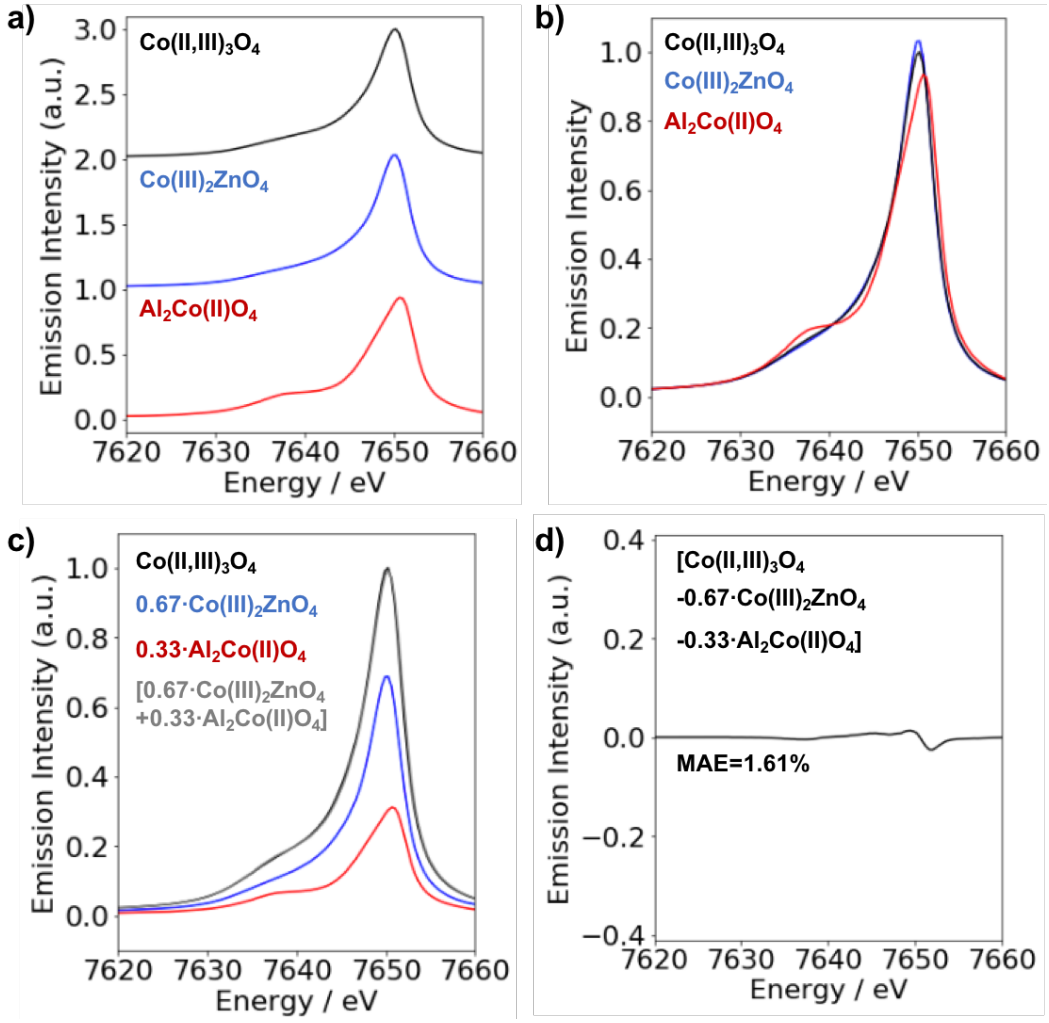

Figure 15.1: Experimental Co $K\beta_{1,3}/K\beta'$ mainline XES spectra of Co_3O_4 (black), $Co(III)_2ZnO_4$ (blue), and $Al_2Co(II)O_4$ (red) for **a)** normalized to themselves; **b)** compared to each other; **c)** $Co(III)_2ZnO_4$ and $Al_2Co(II)O_4$ shown with prefactors representing the Co(III):Co(II) site ratio in Co_3O_4 compared to the combined spectrum (gray) and Co_3O_4. **d)** Difference spectrum between Co_3O_4 and the combined $Co(III)_2ZnO_4$ and $Al_2Co(II)O_4$ $K\beta_{1,3}/K\beta'$ mainline XES spectrum.

Figure 15.2: a) – c) Experimental Co $K\beta_{1,3}/K\beta'$ mainline XES spectrum of Co_3O_4 (black), $Co(III)_2ZnO_4$ (blue), and $Al_2Co(II)O_4$ (red) spinel solids with different prefactors regarding the intensity of the cobalt oxide derivatives and the respective sum of $Co(III)_2ZnO_4$ and $Al_2Co(II)O_4$ (dotted gray line). **d) & e)** Difference spectra between Co_3O_4 and the summed-up spectra $Co(III)_2ZnO_4$ and $Al_2Co(II)O_4$ with respective prefactors.

The main idea of including Al_2CoO_4 and Co_2ZnO_4 in the analysis is to represent

the Co(II) and Co(III) sites in Co_3O_4. The combination of the spectra of Al_2CoO_4 and Co_2ZnO_4 in stoichiometric portions, which represents the Co(II):Co(III) ratio in Co_3O_4 of 1:2, is shown in Figure 15.2c. The difference spectrum between this summed spectrum and the one of Co_3O_4 is shown in Figure 15.2d and results in an MAE of 1.61%. The MAE is calculated by integrating the difference spectrum.

To summarize, the comparison of the combined spectra of Co_2ZnO_4 and Al_2CoO_4 with the one of Co_3O_4 suggests that the Co(III) sites are the main source of the Co $K\beta_{1,3}/K\beta'$ mainline XES spectrum of Co_3O_4. The following sections will investigate the intensity mechanisms in more detail.

15.4 Cluster Size Convergence

Figure 15.3 depicts the results of the cluster size convergence for the Co $K\beta_{1,3}/K\beta'$ mainline XES spectrum of the three cobalt oxide derivatives. Both the one-electron (see Figure 15.3a-c) and the CASCI (see Figure 15.3d-f) protocols were used in the computation. The results show that the calculated spectra converge for the smallest system size with both protocols, indicating the localized nature of the $K\beta_{1,3}/K\beta'$ mainline XES spectrum.

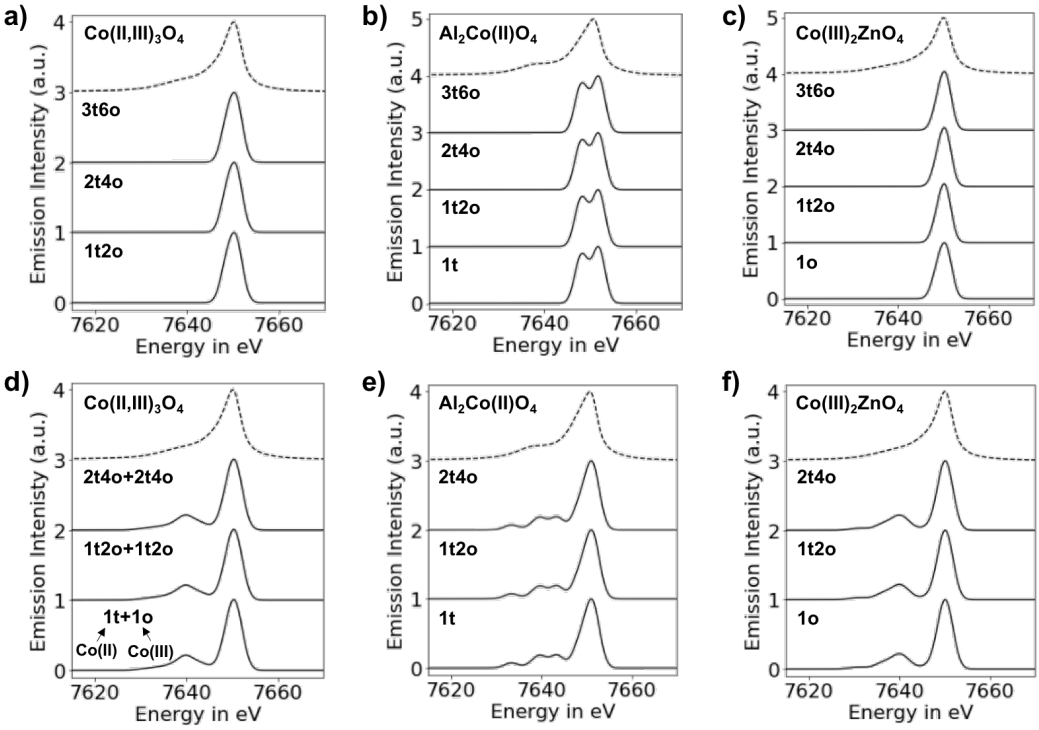

Figure 15.3: Convergence of the computed one-electron (top) and CASCI (bottom) $K\beta_{1,3}/K\beta'$ mainline XES spectrum employing increasing cluster sizes of **a)** and **d)** Co_3O_4, **b)** and **e)** Al_2CoO_4 as well as **c)** and **f)** Co_2ZnO_4. Dashed line: experiment.

Since the CASCI $K\beta_{1,3}/K\beta'$ mainline XES spectra converge for the smallest system size, the calculated Co_2ZnO_4 and Al_2CoO_4 CASCI $K\beta_{1,3}/K\beta'$ mainline XES spectra are represented by the isolated distorted octahedral Co(III) site (1o) and the tetrahedral Co(II) site (1t), respectively. This convergence allows the reconstruction of the Co_3O_4 mainline XES spectrum as the sum of the spectra of the Co(II) and Co(III) centers represented by the Co_2ZnO_4 and Al_2CoO_4 spectra in stoichiometric amounts. The smallest resulting Co_3O_4 model is the combination of 1t and two times 1o (1t+2o). The spectra of increasing cluster sizes 1t2o and 2t4o are represented by the sums 1t2o-$Al_2Co(II)O_4$ and 1t2o-$Co(III)_2ZnO_4$ or the sums of the respective 2t4o clusters.

The results in Figure 15.3 demonstrate that the one-electron approach is not able to reproduce the full $K\beta_{1,3}/K\beta'$ mainline XES spectrum as it only calculates the $K\beta_{1,3}$ components. On the other hand, the CASCI XES results show good agreement with the experimental results for both the $K\beta'$ and $K\beta_{1,3}$ components of the mainline XES spectrum.

15.5 One-Electron $K\beta_{1,3}/K\beta'$ Mainline XES Spectra Results

The spin-orbit coupling and scalar relativistically corrected one-electron results are used to obtain an initial understanding of the mainline XES spectra of the cobalt oxides before applying the CASCI approach. Figure 15.4 displays the computed one-electron mainline XES spectra of Co_3O_4, $Al_2Co(II)O_4$, and $Co(III)_2ZnO_4$ for a cluster size of 2t4o, considering the high-spin ionized state (2S+1=8) for Co_3O_4 and Al_2CoO_4 and the low-spin ionized state (2S+1=2) for Co_2ZnO_4. The use of the cluster size 2t4o in the computation of the mainline XES spectra, despite being aware that the spectra converge for the isolated sites, serves multiple purposes discussed below.

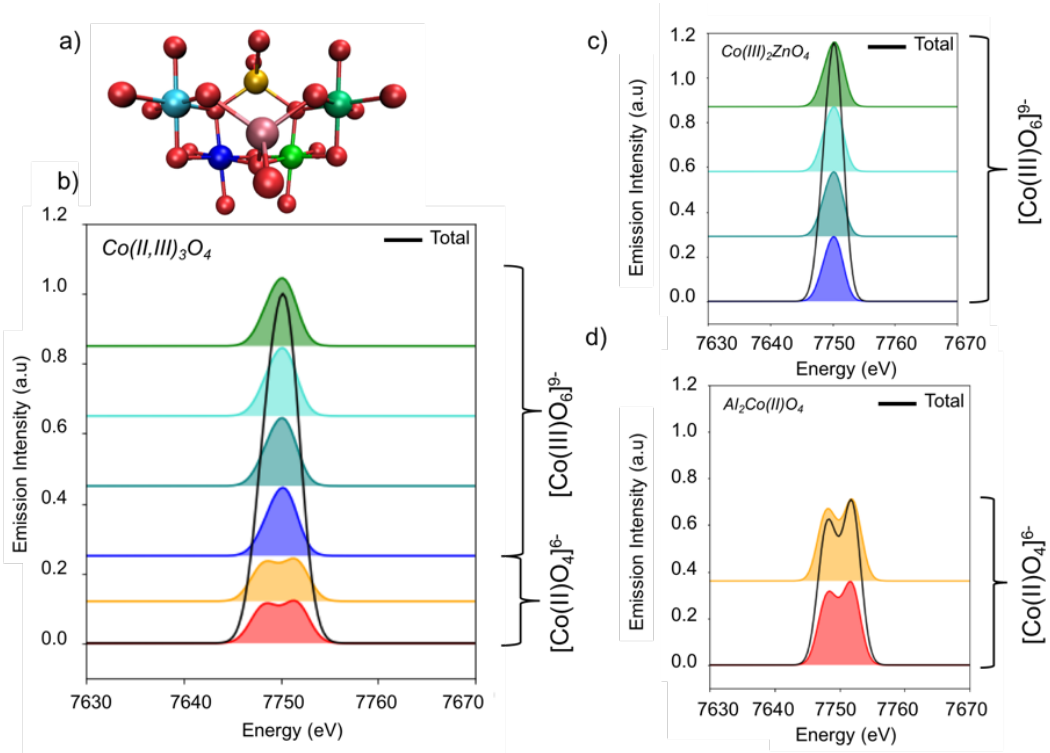

Figure 15.4: Calculated $K\beta_{1,3}/K\beta'$ mainline XES spectra using the one-electron approach for the 2t4o type cluster model of **b)** Co_3O_4, **c)** $Co(III)_2ZnO_4$, and **d)** $Al_2Co(II)O_4$ shown in **a)**. The color coded subspectra correspond to the contributions of the individual Co centers as emission centers according to the color code given by the 2t4o model in **a)**. Color code: subspectra corresponding to tetrahedral Co(II) (red and orange) and distorted octahedral Co(III) sites (blue, cyan, turquoise, and green). Black line: total spectrum. The spectra are normalized with respect to the maximum intensity of the spectrum of Co_3O_4 as shown in **b)**.

The use of the larger cluster size 2t4o in the calculation of the mainline XES

spectra not only confirms the convergence of the computed spectra for the smaller system sizes but also strengthens the confidence in the results obtained from those smaller systems. The calculation of the total spectrum takes into account the $1s$ orbitals of all cobalt centers as potential core-ionized centers. The color-coded subspectra in Figure 15.4 present the spectra calculated with only one cobalt center as the core-ionized center at a time. The subspectra of the tetrahedral Co(II) sites in Co_3O_4 are identical to each other, as are the subspectra of the distorted octahedral Co(III) sites. This supports the requirement of an ideal homogeneous solid-state system, in which equivalent sites in the bulk must have identical properties. The consistency of this behavior across other cluster sizes supports the validity of the electrostatic embedded cluster protocol for calculating mainline XES spectra in solid-state systems.

These results also confirm that the total spectrum of Co_3O_4 can be considered a sum of the subspectra of its different cobalt sites. The subspectra of the tetrahedral Co(II) sites in Al_2CoO_4 match those of the corresponding sites in Co_3O_4, while the subspectra of the octahedral Co(III) sites in Co_2ZnO_4 are equivalent to those of the corresponding sites in Co_3O_4. This demonstrates that using the one-electron approach, the Co(II) and Co(III) sites in Co_3O_4 are accurately represented by Al_2CoO_4 and Co_2ZnO_4 models, respectively.

A closer examination of the different subspectra shows that the one-electron approach solely captures part of the $K\beta_{1,3}$ mainline feature, and the corresponding $K\beta'$ is entirely absent as expected for the one-electron approach. The tetrahedral Co(II) centers contribute a double peak in all cases, while the distorted octahedral Co(III) centers contribute a single broad and unresolved band. The double peak is believed to be due to a stronger SOC effect in the $3p$ MOs of the tetrahedral Co(II) centers compared to the distorted octahedral Co(III) centers. The dominant single electron decays were found to originate from the expected Co(II/III)$3p \rightarrow 1s$ electron transitions local to the respective sites, as described in the XES model in Section 8.2 and shown in Figure 8.3 on page 101.

Overall, the mainline XES spectrum contains predominantly contributions from the Co(III) centers of Co_3O_4, not only because there are twice as many Co(III) centers as Co(II) centers but also because their individual subspectra are about twice as intense as those of Co(II). Thus, the overall calculated Co_3O_4 one-electron mainline XES spectrum appears like that of Co_2ZnO_4.

In conclusion, although the one-electron can give a first indication towards the $K\beta_{1,3}$ mainline XES spectral feature and describe the corresponding underlined intensity mechanism, the method cannot capture the $K\beta'$ mainline XES spectrum adequately. Therefore, a direct comparison with the experiments is impossible, im-

plying that a thorough investigation of the intensity mechanism beyond the one-electron picture is required.

15.6 An Introduction to the $K\beta_{1,3}/K\beta'$ Mainline XES Intensity Mechanism

Before entering into the discussion of the CASCI $K\beta_{1,3}/K\beta'$ mainline XES spectrum computation, this section briefly summarizes the basic aspects of the intensity mechanism involved that could not be captured by the one-electron approach. This highlights the complexity of the $K\beta_{1,3}/K\beta'$ mainline XES mechanism and the need for a many-electron protocol such as the CASCI approach applied below.

15.6.1 Radiative and Non-Radiative XES Cross Sections

The discussion of the basics of XES spectroscopy in Section 8.2 and the one-electron mainline XES approach presented so far have focused only on the radiative process of XES, which involves the transition from the core-ionized initial state to analogous final states without changing the electron configuration or spin state of the $3d$ orbitals between the initial and final states. However, in addition to the radiative process, a secondary non-radiative process can occur, known as the optical Auger process, in which the $3d$ electrons from the initial "original" final state are excited to different $3d$ excited final states. They are also called "shake-up" states[551] and can cause satellite features in the $K\beta_{1,3}/K\beta'$ mainline XES spectrum. Figure 15.5 shows a schematic representation of the radiative and non-radiative XES emission processes assumed for the $K\beta_{1,3}/K\beta'$ mainline XES emission process.

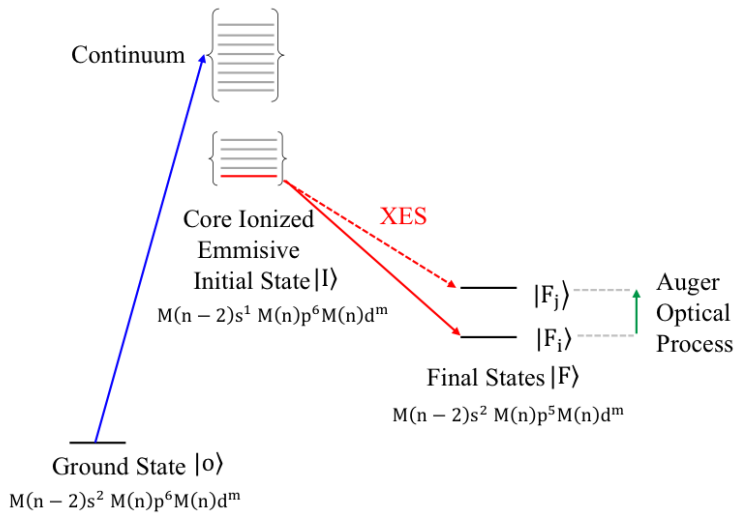

Figure 15.5: Schematic representation of the $K\beta_{1,3}/K\beta'$ mainline XES emission process as a secondary independent process of the core-ionization of the $1s$ metal orbital by XAS. The XES process includes radiative spontaneous emission from the $1s$ core-ionized initial state to the $3p$ core-ionized final states and non-radiative optical Auger processes.

Assuming that the optical Auger photons do not interact with the emission process, the emission intensity I_{XES} can be determined within the electric dipole approximation using Equation 15.1.

$$I_{XES} \sim \frac{4\pi\omega_{em}}{3c\hbar} \sum_{\rho=x,y,z} \sum_{F_i,F_j} |\langle I| \mu_\rho |F\rangle|^2 f(E_{FI} - \omega_{em}, \Gamma_F) \tag{15.1}$$

Here, $\langle \Psi_I| \mu_\rho \rho |\Psi_F\rangle$ is the transition probability, E_{FI} is the emission energy between the core-ionized initial $|I\rangle$ and final $|F\rangle$ states, and μ_ρ defines the electric dipole operator. ω_{em} is the emission photon energy, f is the line broadening resulting from the lifetimes of the respective final states, c is the speed of light, and $\hbar$ is the Planck constant.

To account for the non-radiative optical Auger processes presented in Figure 15.5, the two-photon Kramers-Heisenberg-Dirac (KHD) scattering expression can be used.[552] This expression is established for RXES (Resonant XES) mechanisms and has a resonant and a non-resonant term. The focus is on the non-resonant XES (NXES) KHD term as XES is studied, where emission precedes absorption.[553] As a first approximation, it is assumed that all final states $|F_i\rangle$ directly reached by the core-ionized initial emissive state $|I\rangle$ act as "intermediate" states $|V\rangle$, while the final states $|F_j\rangle$ excited by the Auger photon serve as the corresponding "final" states.

Within this framework, the KHD expression is given by Equation 15.2.

$$I_{NXES} \sim \frac{8\pi^2\omega_{ex}^3\omega_{em}}{9c^4\hbar^4}|\alpha_{\rho,\lambda}(\omega_{em},\omega_{ex})|^2 \tag{15.2a}$$

$$I_{NXES} \sim \frac{8\pi^2\omega_{ex}^3\omega_{em}}{9c^4\hbar^4}\sum_{\rho,\lambda=x,y,z}\sum_{F=F_j}|\sum_{V=F_i}\frac{\langle F|\,\mu_\rho\,|V\rangle\,\langle V|\,\mu_\lambda\,|I\rangle}{f(E_{FI}+\omega_{ex},\Gamma_F)}|^2 f(E_{FV}-\omega_{ex}+\omega_{em},\Gamma_F) \tag{15.2b}$$

Equation 15.2a includes the polarizability tensor $\alpha_{\rho,\lambda}$ for inelastic scattering, specifically considering only the non-resonance term defined in Equation 15.2b. Together with the emission photon energy ω_{em} defined in Equation 15.1, ω_{ex} represents the energy of the Auger excited photons. As in Equation 15.1, E_{FI} refers to the emission process between the core-ionized initial state $|I\rangle$ and the final state $|F\rangle$, with the corresponding transition energies between the final states $|F_i\rangle$ and $|F_j\rangle$. All other quantities are defined as in Equation 15.1.

Provided that the photon emission energy ω_{em} is tuned to the emission energy E_{FI} and the induced Auger photon energy ω_{ex} is tuned to the final state transition energy such that $\omega_{ex} = E_{FV} = E_{F_jF_i}$, Equation 15.2b can be simplified to its "direct" one-photon non-resonant XES form as given in Equation 15.3.

$$I_{NXES} \sim \frac{8\pi^2\omega_{ex}^3\omega_{em}}{9c^4\hbar^4}\sum_{\rho,\lambda=x,y,z}\sum_{F=F_i,F_j}E_{F_jF_i}^3|\langle F_j|\,\mu_\lambda\,|F_i\rangle|^2|\langle F_i|\,\mu_\lambda\,|I\rangle|^2 f(E_{FI},\omega_{em},\Gamma_F) \tag{15.3}$$

Two cases are now possible:

1. No induced optical photons are considered along the emission process. Equation 15.3 then simply reduces to Equation 15.1 as given in Equation 15.4.

$$I_{NXES} \sim I_{XES}, |F_i\rangle \equiv |F_j\rangle \tag{15.4}$$

2. The XES process is followed by a valence excitation. The Equation 15.3 then reduces to Equation 15.1 scaled by the factor $C_{F_jF_i}$ as given in Equation 15.5.

$$I_{NXES} \sim C_{F_jF_i}I_{XES}, |F_i\rangle \neq |F_j\rangle \tag{15.5}$$

The scaling factor $C_{F_jF_i}$ is given by Equation 15.6.

$$C_{F_jF_i} = \frac{2\pi}{3c^3\hbar^4}\sum_{\lambda=x,y,z}\sum_{F_j}\frac{E_{F_jF_i}^3}{E_{F_iI}+E_{F_iF_j}}|\langle F_j|\,\mu_\lambda\,|F_i\rangle|^2 \tag{15.6}$$

Equation 15.4 to Equation 15.6 provide an intrinsic intensity balance between the optically excited final states following the primary emission XES process and the final states of the primary emission XES process itself. The extent to which this affects the $K\beta_{1,3}/K\beta'$ mainline XES spectra of the cobalt centers studied will be investigated below.

15.6.2 $K\beta_{1,3}/K\beta'$ Mainline Emission Pathways

One of the key features of the $K\beta_{1,3}/K\beta'$ mainline XES spectra is the energy splitting between the peaks of $K\beta_{1,3}$ and $K\beta'$, which could not be reproduced using the one-electron approach. Previous studies[53, 541] have shown that this splitting is proportional to the $3p - 3d$ exchange interactions in the context of ligand field theory (LFT)-based models. In this regard, for a series of octahedrally coordinated metals with d-electron counts between d^0 and d^{10}, the energy difference ΔE was found to be represented by the Equation 15.7.[53]

$$\Delta E(K\beta_{1,3} - K\beta') \sim \alpha^2(4G^1_{pd} + 42G^3_{pd}) \tag{15.7}$$

The terms G^1_{pd} and G^3_{pd} refer to the Slater-Condon integral for the $3p - 3d$ exchange interaction. The coefficient α^2 represents the dilution of covalency in the atomic $3d$ orbitals and is dependent on the metal's $3d$ electron count and the covalency reduction factors within the $3d$ shell from the atomic limit. This means that α^2 can take on values that are combinations of t^2 and e^2, which are related to the energies of the $3d_{e_g}$ and $3d_{t_{2g}}$ orbitals in octahedral systems.

The model described can be applied not only to octahedral transition metal systems but also to tetrahedral complexes, as has been established previously.[53] This means that it can be used to analyze both distorted octahedral Co(III) sites, which are discussed in the limits of ideal octahedral symmetry subsequently, as well as tetrahedral Co(II) sites in the cobalt oxide derivatives.

It is important to emphasize that the presented model considers the system in a state-pair model. This model considers only final state pairs with the same dominant electron configuration but opposite electron spins in the single occupied $3p$ orbitals for the system in question. As a result, the model excludes the electron-electron interaction in the $3d$ shell from any mixture of many-electron excitations and spin-orbit couplings between different potential final states and obeys the initial state rule. This means that only the transitions from the lowest core-ionized initial states to the corresponding final states contribute to the intensity of the resulting spectrum.[550] To illustrate the state-pair model and the resulting CASCI mainline XES spectrum, a brief example is given using the Cu(II) system, $[Cu(II)O_4]^{6-}$,

which was previously introduced in Section 13.2. The mainline XES processes for $[Cu(II)O_4]^{6-}$ are a $2e2o$ (two electrons and two orbitals) problem, making it a simple and straightforward illustration.

The ground state of Cu(II) in $[Cu(II)O_4]^{6-}$ has a $1s^2 3p^6 3d_e^4 3d_{t_2}^5$ electron configuration and the symmetry $^2T_2$. After core ionization, the electron configuration of the core-ionized initial states $|I\rangle$ is $1s^1 3p^6 3d_e^4 3d_{t_2}^5$, while that of the final states $|F\rangle$ is $1s^2 3p^5 3d_e^4 3d_{t_2}^5$. The states have the symmetries $^{1,3}T_2$ and $^{1,3}[A_2, E, T_1, T_2]$. The final states are DOMO-SOMO states, since the transition is between doubly occupied MOs (DOMOs, $3p$) and singly occupied MOs (SOMOs, $1s$). Based on the state-pair model, these are the only states that contribute to the resulting $K\beta_{1,3}/K\beta'$ mainline XES spectrum.

The initial and final states of both the singlet and triplet multiplicity differ in the direction of the electron spin in the $1s$ and $3p$ orbitals relative to the unpaired electron in the $3d$ shell. The singlet state has antiparallel spins (β), while the triplet state has aligned spins (α). The initial states of the singlet and triplet multiplicity, $^1T_2$ and $^3T_2$, have the same energy due to the symmetry of the $1s$ orbital. However, this changes for the final states with a single electron in one of the $3p$ orbitals. The final triplet states result in the appearance of the $K\beta_{1,3}$ feature in the spectrum. This process will be referred to as the α emission pathway since it is associated with an unpaired electron with an α spin in the $3p$ orbitals. The final singlet states give rise to the $K\beta'$ feature. This process will be referred to as the β emission pathway since it is associated with an unpaired electron with a β spin in the $3p$ orbitals. The energy difference between the $K\beta_{1,3}$ and $K\beta'$ features is $t^2(4G_{pd}^1 + 42G_{pd}^3)$ based on Equation 15.7. Figure 15.6 provides a visual representation of the splitting by a CASCI calculation that follows these rules to illustrate the concepts described.

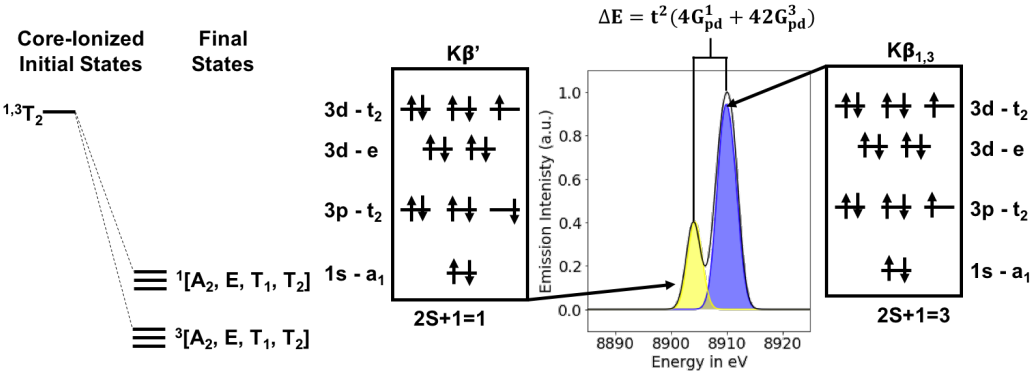

Figure 15.6: CASCI XES calculated $K\beta_{1,3}/K\beta'$ mainline XES spectrum for the toy model $[Cu(II)O_4]^{6-}$. Color code of multiplets: yellow (2S+1=1), blue (2S+1=3).

The presented model is going to be used to explain the CASCI mainline XES

spectra calculated for Al_2CoO_4 and Co_2ZnO_4. Based on the convergence scheme and the discussed one-electron calculations, these are represented by the isolated tetrahedral Co(II) site $[Co(II)O_4]^{6-}$ and the isolated octahedral Co(III) site $[Co(III)O_6]^{9-}$. Although the application may seem straightforward, there are obstacles to the direct transfer of the concepts. These difficulties are briefly addressed here and further explored in the relevant subsections.

The state pair model provides a well defined and understandable mainline XES spectrum with separated $K\beta_{1,3}$ and $K\beta'$ peaks for the Cu(II) toy system. However, this is not the case for the octahedral Co(III) site $[Co(III)O_6]^{9-}$, which has no unpaired electrons in its $3d$ shell and therefore, exhibits low spin. Because of this, the final states do not depend on the electron spin in the singly occupied $3p$ orbital as the $3p - 3d$ exchange integral is zero. Thus, the final states are the same regardless of the spin. This leads to no expected splitting in the spectrum and a single mainline XES feature. At the same time, the experimental Co_2ZnO_4 mainline XES spectrum features both a $K\beta_{1,3}$ and a $K\beta'$, which cannot be explained by the state pair model as it stands. To resolve this discrepancy, the model must be combined with the concept of non-radiative and radiative final states introduced in Subsection 15.6.1.

By introducing the concept of optical Auger excitation, the low spin final states with $1s^2 3p^5 3d^6_{t_{2g}} 3d^0_{e_g}$ electron configurations can be excited to $1s^2 3p^5 3d^5_{t_{2g}} 3d^1_{e_g}$ via single $t_{2g} \rightarrow e_g$ excitation. These are called DOMO-VMO (doubly occupied MO to virtual MO) excited states. If these final states show the characteristic of splitting into $K\beta_{1,3}$ and $K\beta''$ with respect to the $3p - 3d$ exchange integral of the state will be investigated below.

Similarly, for $[Co(II)O_4]^{6-}$, besides the splitting analogous to $[Cu(II)O_4]^{6-}$ with final states of electron configuration $1s^2 3p^5 3d^4_{t_g} 3d^3_{t_{2g}}$, additional splittings can be expected for different final states reached by Auger electron excitations within the $3d$ shell. Table 15.1 shows the expected splitting values with respect to the $3p - 3d$ exchange integral for the different potential electron configurations according to LFT for $[Co(II)O_4]^{6-}$ and $[Co(III)O_6]^{9-}$. The corresponding subsections will examine the role of these different states in shaping the final spectrum.

Table 15.1: Calculated $\Delta E(K\beta_{1,3} - K\beta')/(4G^1_{pd} + 42G^3_{pd})$ splittings for a variety of $K\beta_{1,3}/K\beta'$ mainline XES final state electron configurations in tetrahedral (T_d) Co(II) and octahedral O_h Co(III) centers as a function of the e^2 and t^2 covalency reduction factors.

Center	Electron Configuration	Spin State	$E(K\beta_{1,3} - K\beta'')/(4G^1_{pd} + 42G^3_{pd})$
T_d Co(II)	$1s^2 3p^5 3d^4_e 3d^3_{t_2}$	HS	$2t^2$
	$1s^2 3p^5 3d^3_e 3d^4_{t_2}$	HS	$\frac{3}{4}(2t^2 + e^2)$
	$1s^2 s3p^5 3d^3_e 3d^4_{t_2}$	HS	$\frac{2}{3}(2t^2 + e^2)$
	$1s^2 3p^5 3d^4_e 3d^3_{t_2}$	IS	t^2
O_h Co(III)	$1s^2 3p^5 3d^6_{t_{2g}} 3d^0_{e_g}$	LS	0
	$1s^2 3p^5 3d^5_{t_{2g}} 3d^1_{e_g}$	IS	$\frac{3}{4}(t^2 + e^2)$
	$1s^2 3p^5 3d^4_{t_{2g}} 3d^2_{e_g}$	HS	$\frac{5}{4}(t^2 + e^2)$

15.7 CASCI $K\beta_{1,3}/K\beta'$ Mainline XES Spectra Results

15.7.1 Co_2ZnO_4

a) A First Co_2ZnO_4 CASCI $K\beta_{1,3}/K\beta'$ Mainline XES Spectrum

Co_2ZnO_4 can be represented by a single octahedral Co(III) site as shown by the convergence scheme in Figure 15.3. The Co(III) center has a low spin ground state ($S = 0$) and no unpaired electrons in the $3d$ shell. The state has symmetry $^1A_{1g}$ and electron configuration $1s^2 3p^6 3d^6_{t_{2g}} 3d^0_{e_g}$. Core ionization of the $1s$ orbital produces a doublet core-ionized initial state $|I\rangle$ with symmetry $^2A_{1g}$ and electron configuration $1s^1 3p^6 3d^6_{t_{2g}} 3d^0_{e_g}$. In non-resonant XES there is no preference for ionization. Therefore, the unpaired electron in the $1s$ orbital has either a α or a β spin. From these core-ionized initial states, final states of electron configuration $1s^2 3p^5 3d^6_{t_{2g}} 3d^0_{e_g}$ and symmetry $^2T_{2u}$, hereafter referred to as $|A^{1s}_{3p}\rangle$, are produced via $3p \rightarrow 1s$ DOMO-SOMO electron decays. The process is symbolized in Figure 15.7, and the equations representing the initial and final states are given in Equation C.1 and Equation C.5 in the appendix on page 366.

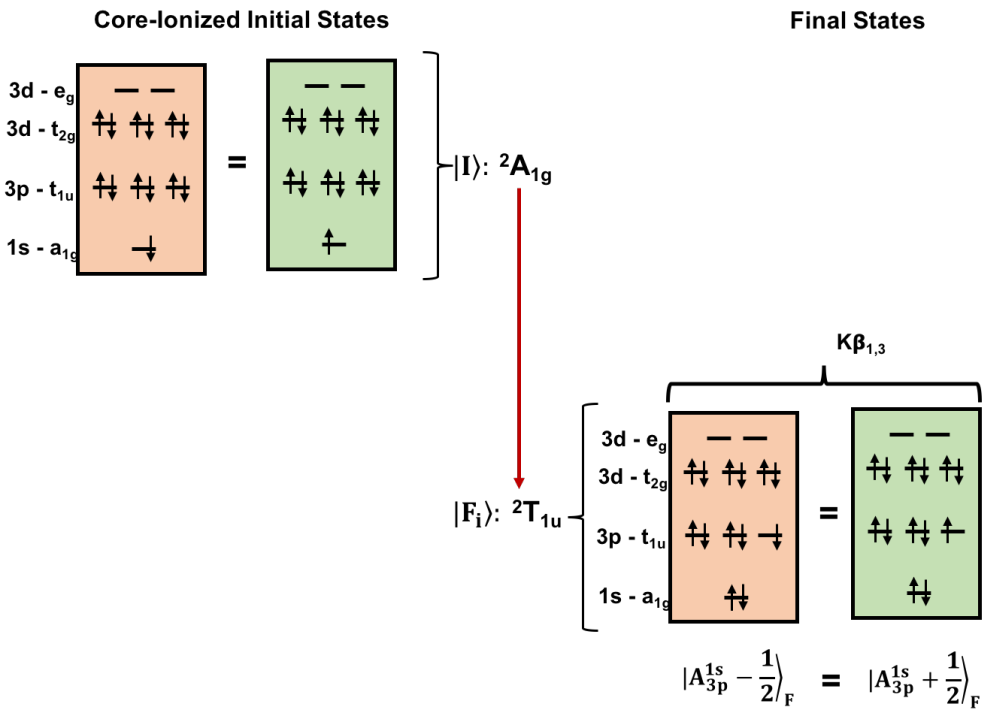

Figure 15.7: Predominant electron configurations and term symbols of the core-ionized initial and final states reached by the $K\beta_{1,3}/K\beta'$ mainline XES in the case of the low spin octahedral Co(III) sites in Co_2ZnO_4.

Figure 15.7 implies that the two core-ionized initial doublet states $|I\rangle$ are degenerate. As mentioned above, this is due to the symmetry of the $1s$ orbital, which always leads to degenerate core-ionized initial states as long as they have the same $3d$ state. In this case the final states $|A^{1s}_{3p} + \frac{1}{2}\rangle_F$ and $|A^{1s}_{3p} - \frac{1}{2}\rangle_F$ are also degenerate, since there are no unpaired electrons in the $3d$ shell, as explained in Section 15.6. Consequently, no splitting between $K\beta_{1,3}$ and $K\beta'$ occurs as it depends on the $3p - 3d$ exchange integral (see also Table 15.1). Therefore, this case has no distinct α and β emission pathways, and only the $K\beta_{1,3}$ XES mainline feature is expected. This is confirmed by the corresponding CASCI calculation, as shown in Figure 15.8.

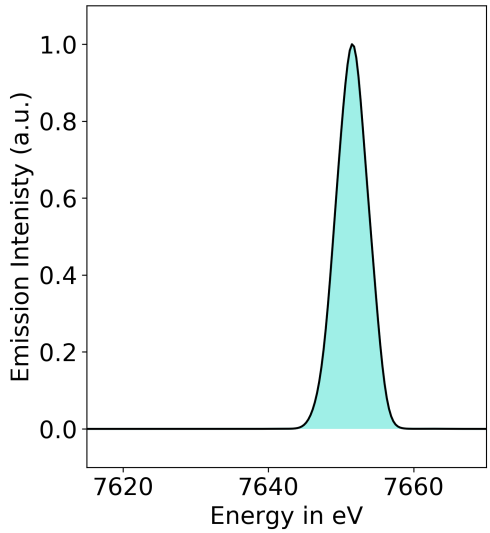

Figure 15.8: CASCI computed $K\beta_{1,3}/K\beta'$ mainline XES spectra considering final states with $1s^s3p^53d^6_{t_{2g}}3d^0_{e_g}$ electron configuration of symmetry $^2T_{1u}$ originating from the low spin octahedral Co(III) sites. Color code of multiplets: turquoise (2S+1=2).

b) Investigation of an Intermediate Spin State Co_2ZnO_4 Model

The $K\beta'$ feature cannot be explained by low spin states. Based on Subsection 15.6 the idea can be proposed that it is introduced as a satellite feature resulting from multielectron shake-up excitations within the final states.[541, 551] As an example, the ligand field single-electron excitation $3d\ t_{2g} \rightarrow e_g$ has been mentioned, resulting in a final electron configuration of $1s^23p^53d^5_{t_{2g}}3d^1_{e_g}$. While these are potential final states, the corresponding core-ionized initial state does not exist because the initial state rule limits the core-ionized initial states to the low spin state $^2A_{1g}$. However, to better understand these excited final states and their potential impact on the Co(III) spectrum, a thought experiment involving Co(III) with an assumed core-ionized initial state of $1s^13p^63d^5_{t_{2g}}3d^1_{e_g}$ is explored.

The configurations of core-ionized initial and final states for Co(III) with three unpaired electrons in three orbitals ($3e3o$) lead to excited CSFs describing either one type of quartet ($M_S \pm \frac{3}{2}$) or three types of doublet ($M_S \pm \frac{1}{2}$) states. The quartet $|Q^{e_g}_{t2g}\rangle$ is defined by all parallel spins, while the three triplets differ in the way the spins couple in their $3d$ electrons. Quartet $|Q^{e_g}_{t2g}\rangle$ and the so-called "trip-doublet" $|D^{e_g}_{t2g}\rangle$ states are core-ionized initial states which are degenerate since they have the same $3d$ state representing a triplet locally. They differ in their electron spin the $1s$ orbital. The "sing-doublet" states are spin flip excited states of the other two

with local singlet states in their $3d$ shell and are summarized in $|C^{e_g}_{t2g}\rangle$. Due to the initial state rule, only quartet $|Q^{e_g}_{t2g}\rangle$ and trip-doublet $|D^{e_g}_{t2g}\rangle$ states are valid core-ionized initial states ($^{2,4}[T_{1g}, T_{2g}]$), while sing-doublet $|C^{e_g}_{t2g}\rangle$ states do not contribute. However, all have admissible final states ($^{2,4}[A_{1u}, A_{2u}, T_{1u}, T_{2u}]$). Figure 15.9 shows the different states schematically. The description of the different states and their M_S-components can be found in the appendix in Equation C.2 to Equation C.4 and Equation C.6 to Equation C.8 (see pages 366 to 367).

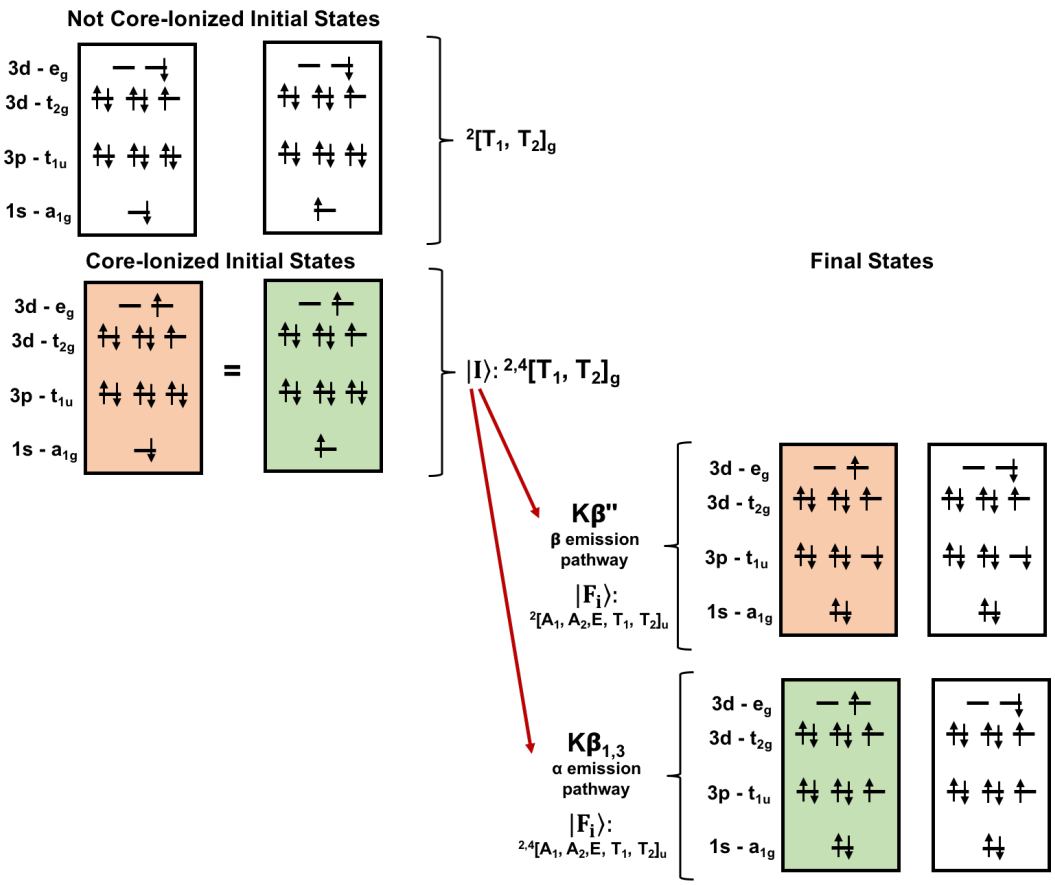

Figure 15.9: Predominant electron configurations and term symbols of the core-ionized initial and final states reached by the $K\beta_{1,3}/K\beta'$ mainline XES in the case of hypothetical intermediate spin state octahedral Co(III) sites in Co_2ZnO_4.

CASCI provides a mixing mechanism between the "C" and "D" types of CSFs, described by Equation 15.8. When $\Delta E(D^{e_g}_{t2g} \pm \frac{1}{2} - C^{e_g}_{t2g} \mp \frac{1}{2}) > 0$, the corresponding $|A_+\rangle$ and $|A_-\rangle$ states are mainly composed of "C" and "D" types of CSFs, respectively.

$$|A_+\rangle = cos\theta\, |C^{e_g}_{t_{2g}} \pm \frac{1}{2}\rangle_F + sin\theta\, |D^{e_g}_{t_{2g}} \mp \frac{1}{2}\rangle_F \tag{15.8a}$$

$$|A_-\rangle = cos\theta\,|C^{e_g}_{t_{2g}} \pm \frac{1}{2}\rangle_F - sin\theta\,|D^{e_g}_{t_{2g}} \mp \frac{1}{2}\rangle_F \tag{15.8b}$$

Although core-ionized sing-doublet initial states are not part of the XES process, they are still created in the CASCI algorithm and mixed via the CI with the other states as described. Thus, they contribute to the $K\beta_{1,3}/K\beta'$ mainline XES spectrum. To illustrate this effect, Figure 15.10a shows the $K\beta_{1,3}/K\beta'$ mainline XES spectrum calculated with CASCI. Figure 15.10b shows a manually corrected CASCI computed $K\beta_{1,3}/K\beta'$ mainline XES spectrum, which only includes core-ionized initial doub-triplet and quartet state contributions.

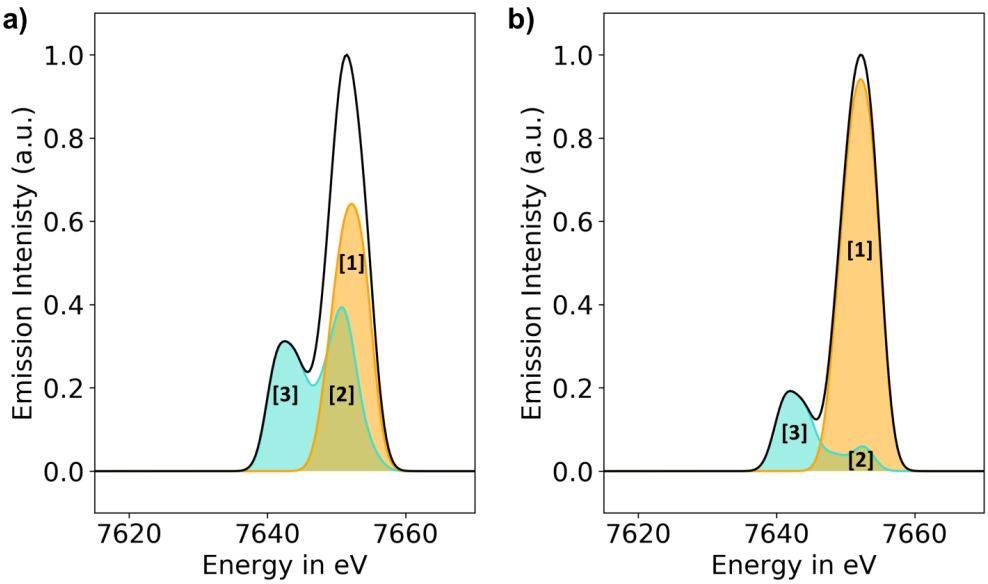

Figure 15.10: $K\beta_{1,3}/K\beta'$ mainline XES spectra considering final states with electron configuration $1s^s3p^53d^5_{t_{2g}}3d^1_{e_g}$ originating from hypothetical octahedral Co(III) sites with an intermediate spin state with **a)** being the uncorrected CASCI and **b)** being the core-ionized initial state corrected spectrum. Color code of multiplets: turquoise (2S+1=2), orange (2S+1=4).

The $K\beta_{1,3}$ feature in the CASCI calculated spectrum is mainly composed of quartet final states $|Q^{e_g}_{t2g}\rangle_F$ (band [1]) and doublet final states $|A_+\rangle$, dominated by sing-doublet states $|C^{e_g}_{t2g}\rangle_F$, contribute lower intensity (band [2]). These two bands gain intensity via the α emission pathway. The $K\beta'$ region (band [3]) originates from final states $|A_-\rangle$, corresponding primarily to trip-doublet $|D^{e_g}_{t2g}\rangle_F$ states. This part of the spectrum gains intensity via the β emission pathway. The result aligns with the theory introduced in Subsection 15.6. Thus, the LFT model, which relates the $\Delta E = K\beta 1,3 - K\beta'$ splitting to the $3p - 3d$ exchange integral, can be applied. For

the final state pair $|Q^{e_g}_{t2g}\rangle_F$ and $|D^{e_g}_{t2g}\rangle_F$, Table 15.1 predicts the $\Delta E = K\beta_{1,3} - K\beta'$ splitting to be $\Delta E \sim \frac{3}{4}(t^2 + e^2) \cdot (4G^1pd + 42G^3_{pd})$. In the corresponding core-ionized initial state corrected CASCI model in Figure 15.10a, the splitting amounts to 10.8 eV.

c) A First Approach to the Correct Final State Description in the Co_2ZnO_4 CASCI $K\beta_{1,3}/K\beta'$ Mainline XES Spectrum

The mainline XES spectrum in Figure 15.10 of Co(III) cannot exist because the initial state rule does not allow the ligand field excited $3d$ core-ionized initial state. However, the $3d$ final states can still contribute as shake-up states to the spectrum originating from the "true" core-ionized initial state, the low spin $3d$ state $^2A_{1g}$. This is possible as the excited states are dipole-allowed transitions from $^2A_{1g}$ as they have $^{2,4}[A_{1u}, A_{2u}, T_{1u}, T_{2u}]$ symmetries. Figure 15.11 shows the expected emission scheme resulting from this process.

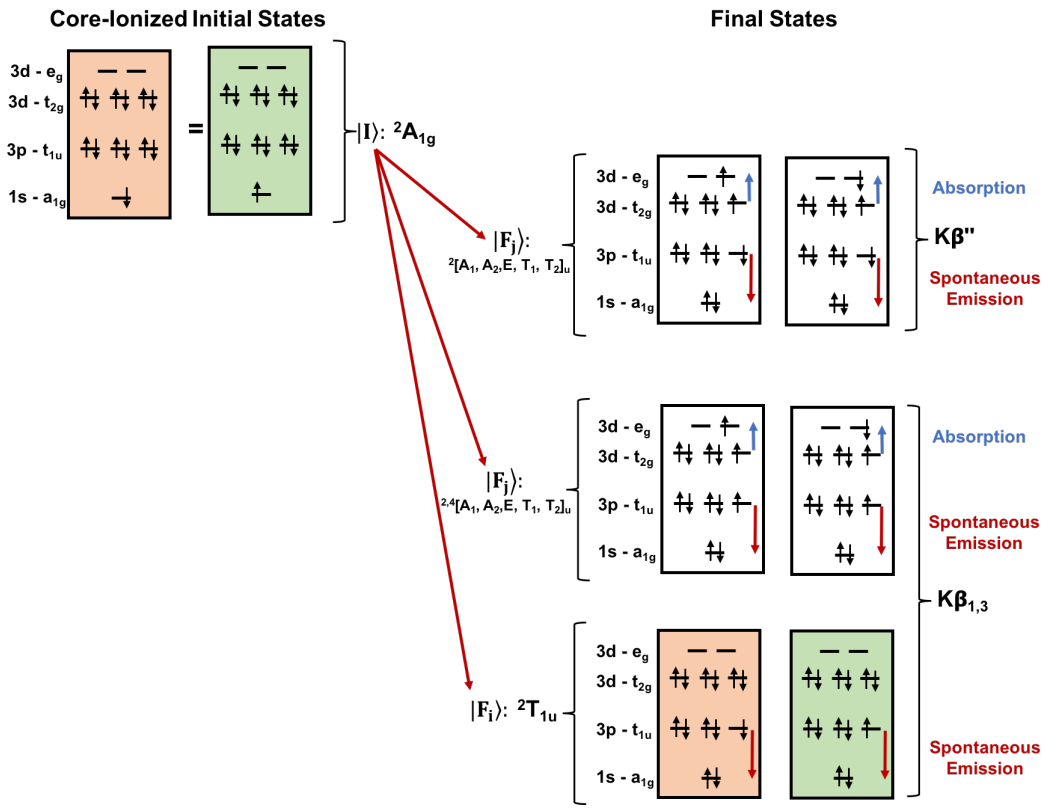

Figure 15.11: Predominant electron configurations and term symbols of the core-ionized initial and final states reached by the $K\beta_{1,3}/K\beta'$ mainline XES in the case of the low spin core-ionized initial and low and intermediate spin final states originating from octahedral Co(III) sites in Co_2ZnO_4.

Subsection 15.6.1 presented two different perspectives on how the additional

$3d$ excited final states gain intensity. The first perspective, described by a one-photon process in Equation 15.1, can be directly accounted for by the CASCI protocol by including electron configurations beyond the $3d$ low spin ones in the calculation. For the current example, the active space includes electron configurations $1s^2 3p^5 3d^5_{t_{2g}} 3d^1_{e_g}$ and $1s^2 3p^5 3d^6_{t_{2g}} 3d^0_{e_g}$ corresponding to final states, but only the $1s^1 3p^6 3d^6_{t_{2g}} 3d^0_{e_g}$ electron configuration for the core-ionized initial state. Figure 15.12a illustrates the result.

The second perspective involves a two-photon process described by Equation 15.4. The corresponding emission spectrum can be calculated in two steps. First, the CASCI $K\beta_{1,3}/K\beta'$ mainline XES spectrum is calculated for the "pure" low spin case, as shown in Figure 15.8 Second, the CASCI absorption spectrum is calculated monitoring excitations from states with electron configurations $1s^2 3p^5 3d^6_{t_{2g}} 3d^0_{e_g}$ to $1s^2 3p^5 3d^5_{t_{2g}} 3d^1_{e_g}$ to account for the optical Auger excitations between the final states. The final emission spectrum can then be obtained by combining the mainline XES spectrum of the "pure" low spin case with the CASCI absorption spectrum. The energy of the $3d$ excited shake-up emission states is determined by subtracting the excitation energy from the absorption process of the different shake-up states from the emission energy of the low spin final states. The intensity of the shake-up states can be calculated by scaling the intensity of the $1s^2 3p^5 3d^6_{t_{2g}} 3d^0_{e_g}$ final states with that of the corresponding absorption processes, as described by Equation 15.5. The resulting spectrum is shown in Figure 15.12b.

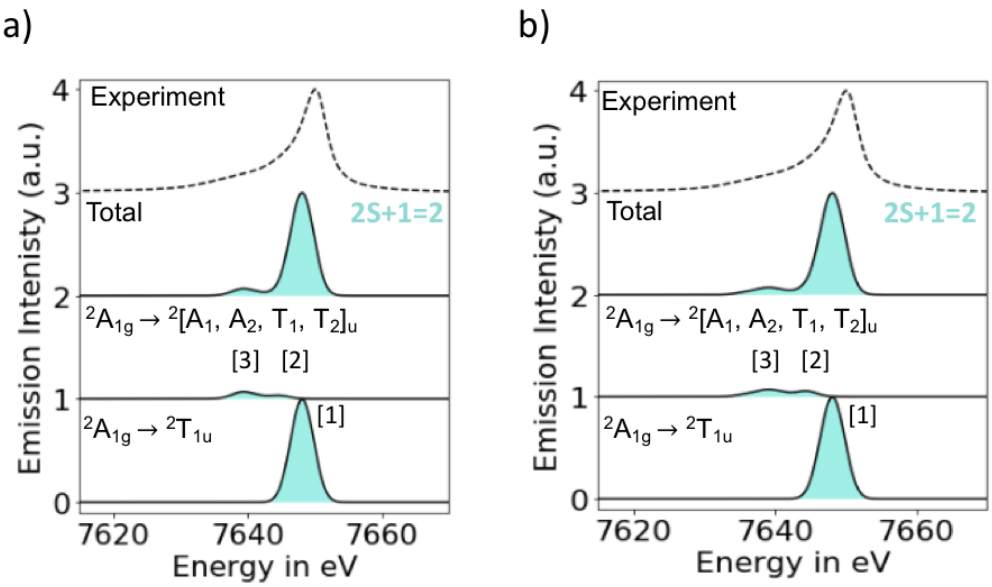

Figure 15.12: Experimental (dashed line) vs. total CASCI calculated $K\beta_{1,3}/K\beta'$ mainline XES spectra employing a) one-photon relation of Equation 15.1 and b) two-photon relation of Equation 15.5. The spectra are analyzed in terms of parent non-relativistic final states, belonging to low spin $1s^2 3p^5 3d^6_{t2g} 3d^0_{eg}$ electron configuration of symmetry $^2T_{1u}$ as well as intermediate spin $1s^2 3p^5 3d^5_{t2g} 3d^1_{eg}$ electron configurations of symmetry $^{2,4}[A_{1u}, A_{2u}, T_{1u}, T_{2u}]$. Color code of multiplets: $2S + 1 = 2$ (turquoise).

Interestingly, the two spectra in Figure 15.12 are essentially identical, implying that in practice there are no interactions between the optical Auger photons and the $K\beta_{1,3}/K\beta'$ mainline XES emission process.

The XES spectra shown in Figure 15.12 can be interpreted as follows. The main contribution to the $K\beta_{1,3}$ mainline XES feature comes from the low spin final states with the same $3d$ electron configuration as the core-ionized initial state. The corresponding subspectrum is shown in the bottom panels of Figure 15.12. In addition, the intensity arises from final states with ligand field Auger excited $3d$ electrons. The corresponding subspectra of the resulting satellite features are shown in the middle panels of Figure 15.12. The subspectrum of the ligand field excited final states is similar to the doublet subspectrum shown in Figure 15.10, but it is shifted in energy with respect to the excitation energy of these states from the low spin final states, and the subspectrum intensity is scaled as described above. The quartet states of the ligand field excited final states do not contribute significantly because they are spin-forbidden transitions with respect to the low spin final states.

The doublet ligand field excited final states contribute to the $K\beta_{1,3}$ and $K\beta'$ fea-

tures since the "α" and "β" emission channels are now present as described above. The splitting between the two features is related to the $3p - 3d$ exchange integral, which is in this case approximately $\frac{3}{4}(t^2 + e^2) \cdot (4G^1_{pd} + 42G^3_{pd})$, as explained earlier. However, the splitting is somewhat smaller ([to-do]) than in the case shown in 15.10, because the quartet state is not present and the splitting is between the "sing-doublet" and "trip-doublet" final states.

The Total Co_2ZnO_4 $K\beta_{1,3}/K\beta'$ Mainline XES Spectrum

In the final step, all relevant configuration types are considered simultaneously, and the resulting spectrum is shown in Figure 15.13a. Overall, the agreement with the experimental data is satisfactory, including the shape of the $K\beta'$ region and the energy distribution of $\Delta E = K\beta_{1,3} - K\beta'$, as well as the $K\beta_{1,3}/K\beta'$ ratio. As shown in Figure 15.13b, the relevant LFT parameters can be extracted using ORCA's multiplet simulation program ORCA_LFT, and the CASCI $K\beta_{1,3}/K\beta'$ XES spectra can be accurately reproduced by scaling down the $G^{1,3}_{3p3d}$ Slater-Condon integrals by 80%-60% from their initial values of about 15.6 and 9.5 eV, respectively. Appropriate scaling of the corresponding coulomb $F^{0,2}_{3d3d}$ does not affect the results.

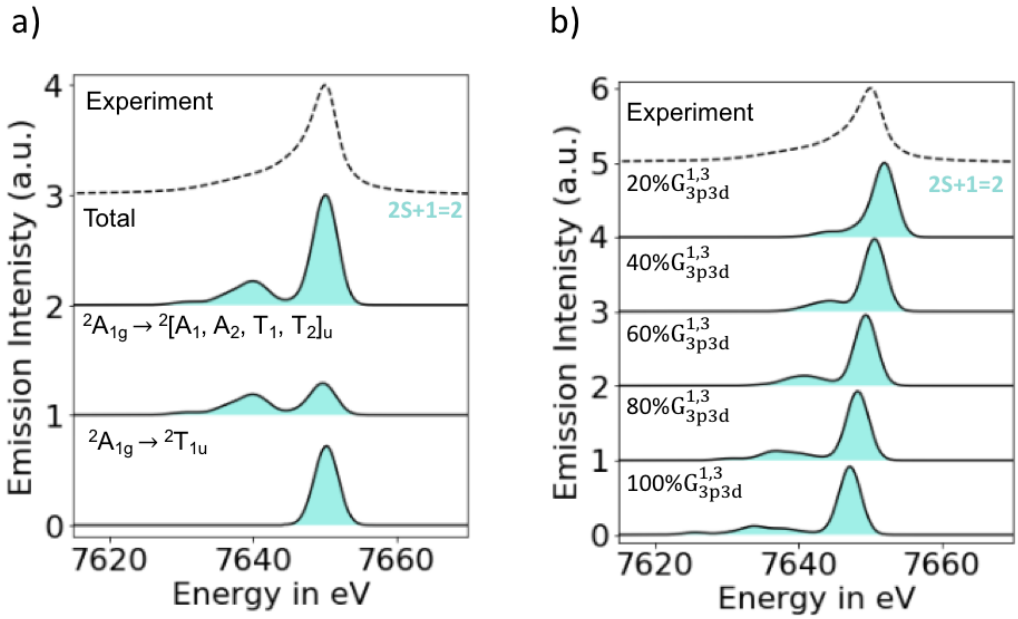

Figure 15.13: Experimental (dotted line) vs. CASCI calculated $K\beta_{1,3}/K\beta'$ mainline XES spectra of the octahedral Co(III) site representing Co_2ZnO_4 for **a)** considering all possible final states with no excited electrons in the $3d$ orbitals (bottom panel) and with excited electrons within the $3d$ orbitals (second panel from bottom) and for **b)** with scaling of the LFT parameters $1s3d$ and $3p3d$ in the total CASCI spectrum calculated using AILFT for different scalings of the exchange $G^{1,3}_{3p3d}$ Slater-Condon integrals from their initial values (∼15.6 and 9.5 eV).

15.7.2 Al_2CoO_4

a) A First Al_2CoO_4 CASCI $K\beta_{1,3}/K\beta'$ Mainline XES Spectrum

The $K\beta_{1,3}/K\beta'$ mainline XES spectrum of Al_2CoO_4 can be approximated using a single tetrahedral Co(II) site $[Co(II)O_4]^{6-}$, based on the convergence scheme in Figure 15.3. The system has three unpaired electrons in the $3d^3_{t_2}$ orbitals, with an electron configuration of $1s^2 3p^6 3d^4 e_2 3d^3 t_2$ and a ground state symmetry of $^4A_2$. After core ionization, two degenerate initial states of multiplicity $2S+1 = 3$ ($|Trip_0\rangle_I$) and $2S+1 = 5$ ($|Quint\rangle_I$) are formed with electron configuration $1s^1 3p^6 3d^4 e_2 3d^3 t_2$ and symmetry $^{3,5}A_2$, making it a $4e4o$ problem. The quintet and triplet states have a local quadruplet in the $3d$ shell but differ in their spin in the $1s$ orbital, with the quintet having an aligned and the triplet an antiparallel spin with respect to the unpaired $3d$ electrons.

As explained for the intermediate spin case of the Co(III) site, the CASCI protocol forms the full set of CSFs from the given configurations. Thus, in the first approach,

two additional triplet states ($|Trip_1\rangle_I$ and $|Trip_2\rangle_I$) are automatically formed, which differ from $|Trip_0\rangle_I$ in the spin coupling scheme in the $3d$ shell because they form local doublets. Therefore, $|Trip_1\rangle_I$ and $|Trip_2\rangle_I$ are referred to as "doub-triplets" and $|Trip_0\rangle_I$ as "quart-triplets". All core-ionized initial states are shown in Figure 15.14, and the branching diagrams[554, 555] of the respective CSFs are shown in Figure C.9 in the appendix on page 369.

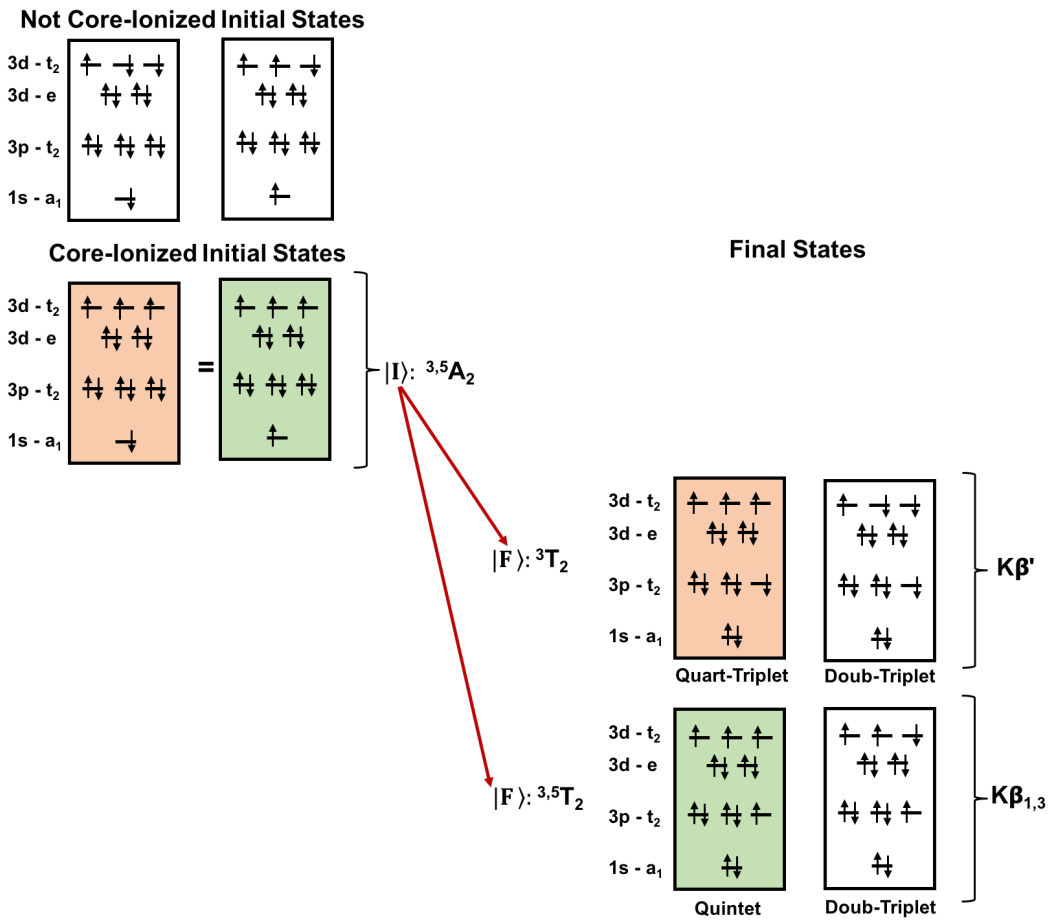

Figure 15.14: Predominant electron configurations and term symbols of the core-ionized initial and final states reached by the $K\beta_{1,3}/K\beta'$ mainline XES in the case of high spin tetrahedral Co(II) sites in Al_2CoO_4.

The doublet-triplet states are not allowed as initial states, but the related final states of the electron configuration $1s^2 3p^6 3d^4_{e_2} 3d^3_{t_2}$ along with the quintet and quart-triplet cases are possible. The resulting final state manifold has a symmetry of $^{3,5}[A_1, A_2, T_1, T_2]$. It can be accessed via $3p \rightarrow 1s$ DOMO-SOMO electron decays in the mainline XES process from the quintet and quart-triplet core-ionized initial states. The schematic representation of the final states is shown in Figure 15.14.

The CI mixes the quart-triplet and doub-triplet $4e4o$ CSFs, resulting in a set of $|A'\pm\rangle$ states. This mixing is exemplified by the mixing of $|Trip_0\rangle_I$ and $|Trip_1\rangle_I$ in Equation 15.9.

$$|A'_+\rangle = cos\theta' \, |Trip_0 \pm 1\rangle_F + sin\theta' \, |Trip_1 \mp 1\rangle_F \tag{15.9a}$$

$$|A'_-\rangle = cos\theta' \, |Trip_0 \pm 1\rangle_F - sin\theta' \, |Trip_1 \mp 1\rangle_F \tag{15.9b}$$

Here, θ is the respective mixing coefficient.[556] It is essential to note that the three-state mixing mechanism above is more complex because the $|Trip_{0-2}\rangle_I$ mix simultaneously within the CI process. However, this complexity will not be addressed further at this point. The equations for the M_S components of the CSFs can be found in the appendix on page 367 for all states.

As for the CASCI approach to the intermediate Co(III) model in Figure 15.10, Figure 15.15a and Figure 15.15b show for the tetrahedral Co(II) site the "standard" CASCI computed mainline XES spectrum and the manually modified one excluding the doub-triplet initial states, respectively. The computed CASCI spectrum agrees well with the theory, with the α emission path dominating $K\beta_{1,3}$ and main contributions coming from quintet final states (band [1]), as well as some smaller contributions from doub-triplet final states (band [3]). On the other hand, the β emission path dominates $K\beta''$ and is dominated by triplet final states. The splitting between the quintet and quart-triplet final states is expected to be $\Delta E_1 \sim 2t^2 \cdot (4G^1_{pd} + 42G^3_{pd})$, corresponding to X eV in the calculation.

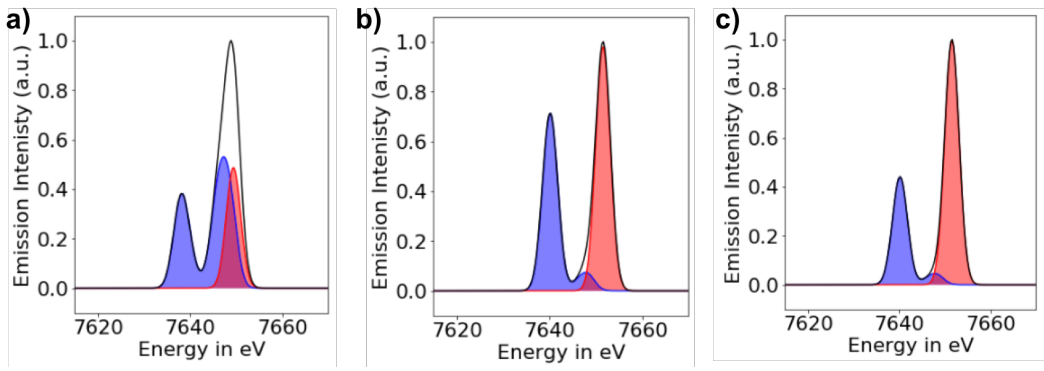

Figure 15.15: CASCI calculated $K\beta_{1,3}/K\beta'$ mainline XES spectra considering final states with $1s^s3p^53d^4_e3d^3_{t_2}$ electron configuration of symmetry $^{3,5}T_2$ belonging to high spin tetrahedral Co(II) sites in Al_2CoO_4. **a)** Uncorrected calculation result, **b)** calculation result without the doub-triplet initial states, and **c)** calculation result without the doub-triplet initial states and the incorrect contributions from the α emission pathway. Color code for multiplets: blue (2S+1=3), red (2S+1=5).

The ratio between $K\beta''$ and $K\beta_{1,3}$ is significantly overestimated compared to the experiment in Figure 15.15b. The expectation is that $K\beta''$ is dominated by the β emission pathway, which consists mainly of direct transitions from the quart-triplet core-ionized initial state to the corresponding quart-triplet final state, with some contribution from doub-triplets belonging to the β emission pathway. However, CI mixing overemphasizes the contribution of doub-triplets of the α emission pathway to $K\beta''$. Figure C.10 on page 370 in the appendix shows an example of this artificial mixing. The corrected spectrum in Figure 15.15c eliminates the contributions from the α emission pathway, resulting in a better match between the ratio in the computed $K\beta_{1,3}/K\beta''$ mainline XES and the experimental data.

b) The Total Al_2CoO_4 CASCI $K\beta_{1,3}/K\beta'$ Mainline XES Spectrum

To obtain the full $K\beta_{1,3}/K\beta'$ mainline XES spectrum for the tetrahedral Co(II) site, similar to the Co(III) site, additional sets of excited final states must be considered. However, this will be demonstrated in less detail than for Co(III) since the process is essentially the same. The overall $K\beta_{1,3}/K\beta'$ mainline XES scheme for Co(II) shown in Figure 15.16 includes ligand field excitations of the type $e \rightarrow t_2$ leading to triplet and quintet final states of the $1s^s 3p^5 3d_e^3 3d_{t_2}^4$ electron configuration and $^{3,5}[A_1, A_2, T_1, T_2]$ symmetries.

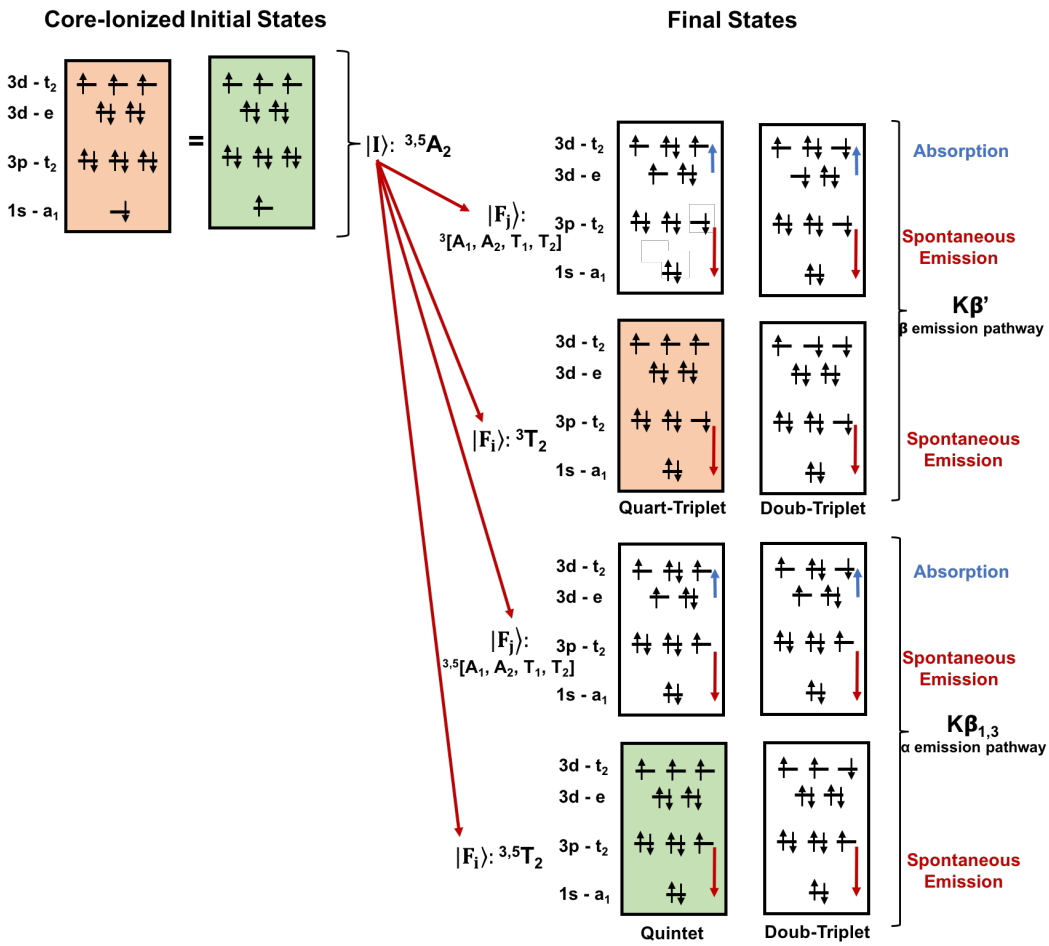

Figure 15.16: Predominant electron configurations and term symbols of the core-ionized initial and final states reached by the $K\beta_{1,3}/K\beta'$ mainline XES process in the case of high spin tetrahedral Co(II) sites in Al_2CoO_4 including final states with ligand field excitations.

The CASCI results shown in Figure 15.17 approach the full $3d$ CI picture of the final states, allowing the mixing of higher excitations in the $3d$ shell. Similar to Figure 15.15, Figure 15.17a to Figure 15.17c show the path from the triplet initial and final states automatically generated by CASCI to the manually corrected results, with the final corrected spectrum in Figure 15.17c being the correct spectrum.

The $K\beta_{1,3}/K\beta'$ mainline XES spectrum of the tetrahedral Co(II) site exhibits shake-up satellite features due to final state excitations, consistent with the Co(III) case. These additional features in the spectrum primarily arise from single electron ligand field excitations. The middle panels of Figure 15.17 show the subspectrum created by the satellite features, where band [4] is mainly due to shake-up states belonging to the α emission pathway, which mostly contributes quintet states. Band

[5] corresponds to states of the β emission pathway, contributing triplet states.

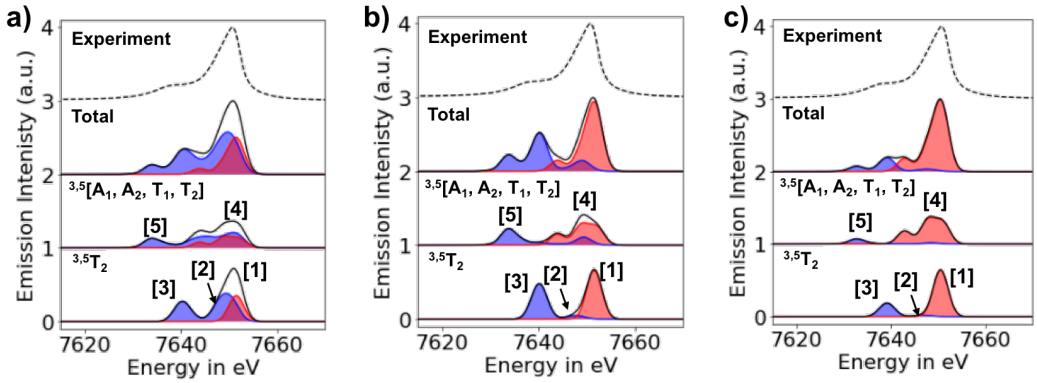

Figure 15.17: Experimental (dashed line) vs. total CASCI computed $K\beta_{1,3}/K\beta'$ mainline XES spectra considering all possible final states originating from high spin tetrahedral Co(II) sites in Al_2CoO_4. **a)** Uncorrected calculation result, **b)** calculation result without the doub-triplet initial states, and **c)** calculation result without the doub-triplet initial states and the incorrect contributions from the α emission pathway. Color code for multiplets: blue (2S+1=3), red (2S+1=5).

Similar to the Co(III) case, the subset of final states can be explained as being shifted with respect to the high spin spectrum of the $^{3,5}T_2$ final states concerning their excitation energy from $^{3,5}T_2$. The satellite features are found at lower energies than band [1] if they are an excited state of the "α" $^{3,5}T_2$ final state, and band [3] if they are an excited state of the "β" $^{3}T_2$ final state. The intensity of these features can be explained by scaling the absorption intensity of these excitations with respect to the intensity of the $^{3,5}T_2$ final states. The ligand field splittings predicted in Table 15.1 enable the identification of the underlying splitting of the $1s^s3p^53d_e^33d_{t_2}^4$ state pair final states between band [4] and band [5].

The CASCI calculations have yielded satisfactory results both qualitatively and quantitatively. However, a better agreement with the experimental data can be achieved by scaling the relevant LFT parameters extracted by ORCA's multiplet simulation program, ORCA_LFT. Figure 15.18 shows that the results improve when the $G_{3p3d}^{1,3}$ Slater-Condon integrals are scaled down from their initial values of about ~16.9 and 9.8 eV by 80% to 60%. Changing the corresponding $F_{3d3d}^{2,4}$ Coulomb integral does not affect the results. Note that ORCA_LFT operates within the RASCI framework rather than the CASCI framework, which still results in some artificial states contributing to the final spectra.

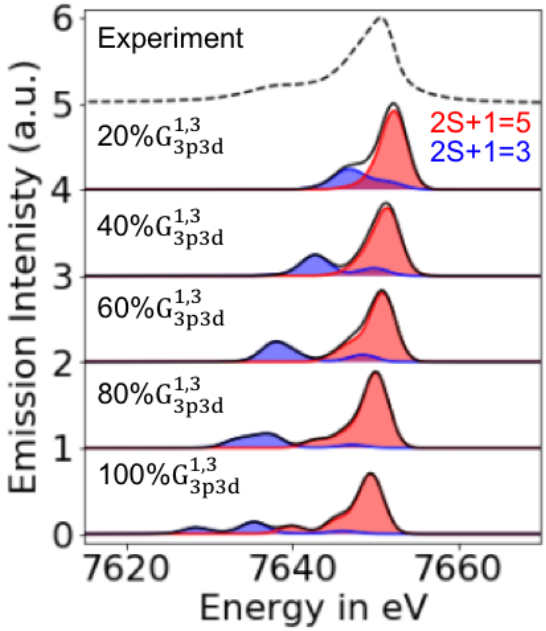

Figure 15.18: Experimental (dashed line) vs. total CASCI computed $K\beta_{1,3}/K\beta'$ mainline XES spectrum of high spin tetrahedral Co(II) sites in Al_2CoO_4 based of LFT parameters from $1s3d$ and $3p3d$ AILFT calculations computed for different scalings of the exchange $G^{1,3}_{3p3d}$ Slater-Condon integrals from their initial values (∼16.9 and 9.8 eV).

15.7.3 Co_3O_4

This section discusses the mainline XES spectral features of Co_3O_4 in the $K\beta_{1,3}/K\beta'$ regions. As mentioned earlier, if the Co(II)-Co(III) interactions can be neglected, the total mainline XES spectrum of Co_3O_4 can be approximated by adding the individual spectra of $Al_2Co(II)O_4$ and $Co(III)_2ZnO_4$, representing the tetrahedral Co(II) sites and distorted octahedral Co(III) sites in Co_3O_4, respectively. This agrees with the one-electron approach, which revealed that the intensity contributions arising from the individual Co(II) and Co(III) centers in the Co_3O_4 models resemble the shape and spectral features of the $Al_2Co(II)O_4$ and $Co(III)_2ZnO_4$ models, respectively.

Figure 15.19 shows the complete spectrum of Co_3O_4 by adding the spectra of individual Co(II) and Co(III) sites, represented by the Al_2CoO_4 and Co_2ZnO_4 models in a 1:2 stoichiometric ratio. The Co(III) sites not only dominate the spectrum due to their stoichiometry but also by the total intensity of the individual subspectrum compared to Co(II). The intensity of the individual Co(II) subspectrum is about 0.4 times that of the individual Co(III) subspectrum, resulting in a 1:5 intensity ratio of the summed-up spectrum. This confirms the expectations set in Section 15.3 as

the overall shape of the calculated and experimental spectra of Co_3O_4 is practically identical to that of Co_2ZnO_4.

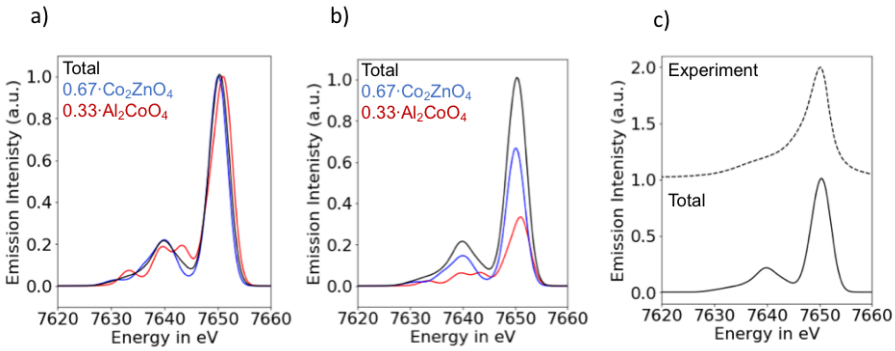

Figure 15.19: Experimental (dotted line) versus CASCI calculated $K\beta_{1,3}/K\beta'$ mainline XES spectra (solid black line) for the 2t4o type of clusters for Co3O4. The computed spectra are analyzed in terms of dominating subspectra arising Co(III)-D_{3d} and Co(II)-T_d centers in 1:2 ratio, as well as dominating 2S+1=2 (turquoise), 2S+1=4 (orange) and 2S+1=3 (blue), 2S+1=5 (red) multiplicities respectively.

Figure 15.19 shows the multiplet effects for individual sites but they become less significant in the total spectrum as they are a local phenomenon. However, it should be noted that the concept of multiplets can be transferred to multiple centers. This will become of importance in the upcoming chapter discussing the VtC XES spectra. However, for simplicity, the current CASCI discussion will stop for single centers as given here.

15.8 Conclusions

In this chapter, the $K\beta_{1,3}/K\beta'$ mainline XES spectra of Co_3O_4, as well as its zinc Co_2ZnO_4 and aluminum Al_2CoO_4 derivatives, were studied using the one-electron approach and CASCI within the LFT framework based on experimental data. The results reveal that the total spectrum of Co_3O_4 can be explained by individual subspectra from isolated octahedral Co(III) and tetrahedral Co(II) metal centers, which are identical to the spectra of the Co_2ZnO_4 and aluminum Al_2CoO_4 derivatives, respectively.

To unravel the complex intensity mechanism of the $K\beta_{1,3}/K\beta'$ mainline XES spectra, the established RASCI XES protocol for high spin mononuclear complexes was extended to work in a CASCI formalism. This allowed for formulation of a CASCI XES protocol that can handle extended active spaces and be applied to multimetallic XES problems. For qualitative reasons, preliminary one-electron XES cal-

culations were also performed, which were used in the construction of the cluster models and as a starting point for the CASCI XES calculations.

The previously applied cluster models of the band gap study in the framework of the electrostatic embedding approach were applied up to a cluster size with nine cobalt centers (3t6o). In all cases, the convergence schemes showed that cluster sizes containing isolated Co(II) (1t) and Co(III) (1o) centers provide converged results. These clusters are chosen to elucidate the intensity mechanism of the $K\beta_{1,3}/K\beta'$ mainline XES of Al_2CoO_4 and Co_2ZnO_4.

To begin the discussion of cobalt solids, the one-electron approach was used to calculate the corresponding XES spectra. As expected, the one-electron approach does not correctly reproduce the experimental spectra. Nevertheless, this protocol showed, on the one hand, that the embedding approach is a suitable tool to approach the problem at hand since each supposedly identical Co site produces an identical subspectrum in all aspects. On the other hand, it was shown that the Co(II)-Co(III) interactions are negligible. Thus, the Co(II) and Co(III) subspectra in Co_3O_4 sites can be approximated by the Al_2CoO_4 and Co_2ZnO_4 spectra, respectively.

Therefore, in the next step, the CASCI XES protocol was used to investigate the intensity mechanism of these cobalt systems in a stepwise approach. This involved a multi-step analysis. First, the individual spectra were calculated over a selection of individual sets of core-ionized and final states belonging to specific groups of electron configurations, followed by a thorough electronic structure analysis of the calculated bands. In the final step, all significant contributions were treated simultaneously to produce the final computed spectra. The resulting spectra were discussed in terms of their ability to reproduce the experimental spectral shape, the $\Delta E = K\beta_{1,3} - K\beta'$ energy splitting, and the $K\beta_{1,3}/K\beta'$ ratio of the experimental $K\beta_{1,3}/K\beta'$ mainline XES spectra. In all cases studied, it was shown that core-ionized states beyond Kasha's rule must be considered.

In particular, in the case of Al_2CoO_4 isolated tetrahedral Co(II) centers, core-ionized final states belonging to the high spin electron configurations $1s^s3p^53d_e^43d_{t_2}^3$ and $1s^s3p^53d^3e3d_{t_2}^4$ must be taken into account before the $K\beta_{1,3}/K\beta'$ mainline XES spectra can be successfully calculated. The $K\beta_{1,3}$ region consists of the parent doub-triplet and quintet states, while the $K\beta'$ region consists of the corresponding quart-triplet states. Similarly, in the case of Co_2ZnO_4, the experimental $K\beta_{1,3}/K\beta'$ mainline XES spectra of the isolated octahedral Co(III) centers can only be reproduced by considering core-ionized final states belonging to intermediate spin electron configurations $1s^s3p^53d_{t_{2g}}^53d_{e_2}^1$ besides the low spin one $1s^s3p^53d_{t_{2g}}^63d_{e_2}^0$. Like the tetrahedral Co(II) centers, the $K\beta_{1,3}$ region consists of the parent doublet and quartet states, while the $K\beta'$ region originates from the corresponding trip-doublet states.

Along with the above analysis, the ability of a previously developed LFT protocol to predict the $\Delta E = K\beta_{1,3} - K\beta'$ energy splitting as a function of the $3p3d$ exchange integrals and the metal-ligand covalency was evaluated. It was shown that, provided that representative states of the electron configurations involved, as dictated by the CASCI calculations, are taken into account, the predicted $\Delta E = K\beta_{1,3} - K\beta'$ energy differences follow the experimental observations.

In the case of Co_3O_4, it was shown that octahedral Co(III) centers primarily dominate the spectral intensity. Indeed, it has been shown that, in agreement with experimental observations, the stoichiometric parts of the calculated CASCI $K\beta_{1,3}/K\beta'$ mainline XES spectra of Al_2CoO_4 and Co_2ZnO_4 are in good agreement with the experiment. Thus, these results fully support that the Co_3O_4 $K\beta_{1,3}/K\beta'$ mainline XES spectra resemble the shape of the Co_2ZnO_4 solid.

16 Decoding the Hidden Spectra Behind the $K\beta_{2,5}/K\beta''$ Valence-to-Core X-ray Emission Processes of Co_3O_4, Co_2ZnO_4, and Al_2CoO_4

16.1 The Context and Structure of the Study

The main goal of Chapter 15 was to develop an approach that integrates experimental and computational methods to interpret the $K\beta_{1,3}/K\beta'$ mainline XES spectra of the cobalt oxides Co_3O_4, Co_2ZnO_4, and Al_2CoO_4. Emphasis has been placed on the analysis of the electronic structure of the octahedral Co(III) and tetrahedral Co(II) sites locally within these solids. The results provided insights into the probed spin and oxidation states in relation to the local symmetry of the centers. The mainline XES spectrum of Co_3O_4 has been demonstrated to be primarily determined by the intensity generated by the octahedral Co(III) centers, with a lower-intensity subspectrum produced by the tetrahedral Co(II) centers. The significance of considering a manifold of final states, including the corresponding multiplet effects, was highlighted. In this process, the state-pair model as well as excited final states leading to satellite features were considered to accurately replicate the experimental spectra using a CASCI protocol. Furthermore, the study demonstrated the possibility of using the developed CASCI mainline XES protocol for multicenter systems within the convergence scheme of the mainline XES spectrum with respect to the embedded cluster size. However, the multicenter CASCI results were not examined in detail.

Inspired by the previous results, in this chapter, the developed CASCI protocol is applied to $K\beta_{2,5}/K\beta''$ Valence-to-Core (VtC) XES spectra of the spinel structured solids Co_3O_4, Co_2ZnO_4, and Al_2CoO_4. While one-electron (DFT) approaches based on orbital energy differences have been successful in computing $K\beta_{2,5}/K\beta''$ VtC XES spectra for various chemical systems,[53, 263, 519] it will be shown that this is not the case for the chosen study set. Therefore, the first main goal is to develop a

CASCI protocol that can investigate the role of oxygen ligands in the VtC intensity mechanism in these solids.

The second main goal of this study is to investigate the influence of the octahedral Co(III) and tetrahedral Co(II) centers on the $K\beta_{2,5}/K\beta''$ VtC XES intensity mechanism. Unlike the $K\beta_{1,3}/K\beta'$ mainline XES spectrum, which probes the electronic states of isolated centers, the $K\beta_{2,5}/K\beta''$ VtC XES spectrum examines the valence region of the core-ionized center. Thus, multicenter interactions might become critical, which includes antiferromagnetic coupling between the Co(II) centers. In Chapter 14, the importance of accurate treatment of antiferromagnetic states was highlighted in investigating the band gap of Co_3O_4. The study in the current chapter aims to combine those findings with the $K\beta_{1,3}/K\beta'$ mainline XES analysis and develop a comprehensive CASCI protocol that models the antiferromagnetic coupling and its effect on the spectra. This approach will provide a deeper understanding of the correlation between the electronic and geometric structure and spectroscopic response, ultimately leading to a better understanding of the materials.

The study follows a structure similar to the $K\beta_{1,3}/K\beta'$ mainline XES study and comprises multiple steps. Firstly, the experimental spectra are briefly analyzed. Next, the one-electron $K\beta_{2,5}/K\beta''$ VtC XES spectra of the different cobalt oxides are presented and discussed. Then, the general rules and concepts for the simplified Cu model, already used for the $K\beta_{1,3}/K\beta'$ mainline XES study, are established with regard to the antiferromagnetic coupling and its implications for the $K\beta_{2,5}/K\beta''$ VtC XES spectrum and the applied CASCI model. Finally, the concepts are transferred to the respective cobalt models, and the computed $K\beta_{2,5}/K\beta''$ VtC XES spectra using CASCI are presented and discussed for the three cobalt oxide derivatives Co_3O_4, Co_2ZnO_4, and Al_2CoO_4.

16.2 Computational Details

In principle, the same computational models, protocols, and details as described in Section 15.2 on page 228 for the $K\beta_{1,3}/K\beta'$ mainline XES study are applicable. This includes the use of the same set of clusters for the electrostatic embedding approach (see Table 13.1 on page 171 and Figure 3.12 on page 44), as well as the application of the one-electron DFT approach (BP86/DKH-def2-TZVP) and the extended (multicenter) CASCI. However, there is a significant difference in the construction of the active space for the CASCI calculations in the $K\beta_{2,5}/K\beta''$ VtC CASCI XES calculations.

In contrast to the $K\beta_{1,3}/K\beta'$ mainline XES calculations, the active space in the $K\beta_{2,5}/K\beta''$ VtC CASCI XES calculations includes the $1s$ and $3d$ orbitals of the Co

centers and the $2s$ and $2p$ orbitals of the oxygen atoms. This makes the required active space significantly larger than for the $K\beta_{1,3}/K\beta'$ mainline XES calculations. For cluster sizes with more than one Co center and the corresponding oxygen environment (larger than 1t or 1o models), the active space had to be split into several subspaces to avoid unmanageably large active spaces. Therefore, different calculations with different oxygen $2s$ and $2p$ orbital space segments were performed and the results of each calculation were combined to obtain the total spectra. Initial calculations dividing the active space into partitions of different sizes show that this approximation is valid to obtain a comparable result to a calculation including the full required active space.

The active space included the core-ionized initial states and the corresponding manifold of final states as introduced in Chapter 15. The configurations with alternating occupation of orbitals of the Co $1s$, Co $3d$, O $2s$, and O $2p$ MOs were used to represent the core-ionized initial and final states. However, due to the increasing importance of multicenter interactions, and in particular Co(II)-Co(II) antiferromagnetic interactions, different configurations of the Co $3d$ orbital space, representing the different "neutral" and "ionic" antiferromagnetic states as introduced earlier, were selected for the core-ionized initial and final states based on preliminary CASICE calculations. These additional states will be discussed in more detail later.

16.3 Experimental Spectra

The experimental $K\beta_{2,5}/K\beta''$ VtC XES spectra of the spinel solids $Co(III)_2ZnO_4$, $Al_2Co(II)O_4$, and Co_3O_4 are shown in Figure 16.1. Information on the experimental measurement procedures is given in Section C on page 362 in the appendix.

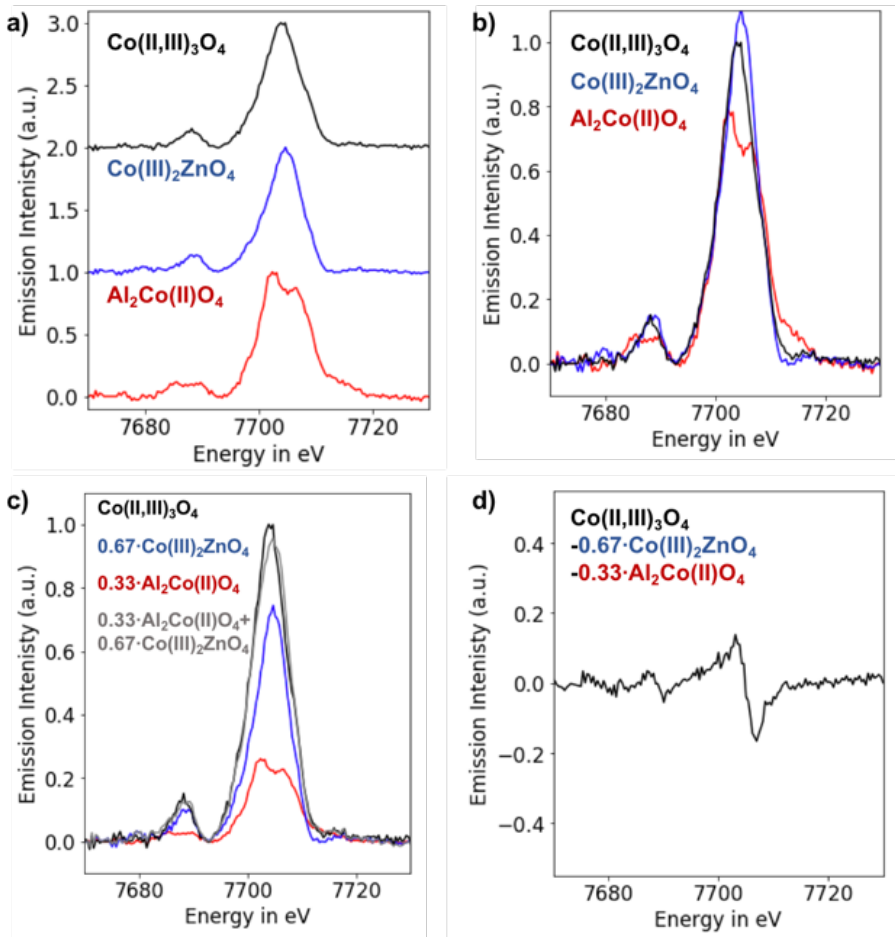

Figure 16.1: Experimental Co $K\beta_{2,5}/K\beta''$ VtC XES spectra of Co_3O_4 (black), $Co(III)_2ZnO_4$ (blue), and $Al_2Co(II)O_4$ (red) for **a)** normalized to themselves; **b)** compared to each other; **c)** $Co(III)_2ZnO_4$ and $Al_2Co(II)O_4$ shown with prefactors representing the Co(III):Co(II) site ratio in Co_3O_4 compared to the combined spectrum (gray) and Co_3O_4. **d)** Difference spectrum between Co_3O_4 and the combined $Co(III)_2ZnO_4$ and $Al_2Co(II)O_4$ $K\beta_{2,5}/K\beta''$ VtC XES spectrum.

Analogous to the mainline XES case, the Co-VtC XES regions of Co_2ZnO_4 and Co_3O_4 have similar spectral features, but Al_2CoO_4 differs. The Co_2ZnO_4 and Co_3O_4 spectra have a broad, asymmetric $K\beta_{2,5}$ spectral feature with a maximum intensity at 7704.5 eV and 7705.0 eV, respectively. The Al_2CoO_4 $K\beta_{2,5}$ spectral feature is split into two components located at 7702.5 eV and 7706.5 eV with another less pronounced feature at 7698.0 eV. In the same way, the $K\beta''$ VtC XES spectral feature of Co_2ZnO_4 and Co_3O_4 is also asymmetric with a maximum intensity at 7689.0 eV, while Al_2CoO_4 has two similarly intense spectral features at 7685.2 eV and 7689.8 eV.

The primary intent for the inclusion of Co_2ZnO_4 and Al_2CoO_4 in the study is

the assumption that their XES spectra represent the XES subspectra of the Co(III) and Co(II) sites, respectively, in Co_3O_4. By combining the two spectra in a 1:2 ratio (representing the Co(II):Co(III) ratio), the resulting XES spectrum is expected to resemble that of Co_3O_4. Figure 16.1c demonstrates the approach, and Figure 16.1d shows the respective difference spectrum when comparing the summed spectrum of Co_2ZnO_4 and Al_2CoO_4 with that of Co_3O_4. The difference VtC XES spectrum has a mean absolute error (MAE) of 3.91%.

The high energy region (about 7705 eV - 7710eV) of the $K\beta_{2,5}$ VtC XES spectrum shows the main difference between the Co_3O_4 and the summed VtC XES spectrum (see Figure 16.1c). The negative difference spectrum in Figure 16.1d in this region suggests that the MAE is due to an impurity in one of the cobalt oxide derivatives, whereas an actual additional feature in Co_3O_4 would more likely contribute to a positive difference. The VtC XES spectrum of Al_2CoO_4 has a significant peak in the region in question, which could also appear as a smaller subspectrum in Co_2ZnO_4 in the case of an impurity caused by Co centers replacing the Zn sites, leading to the error. In the absence of further data, this hypothesis is not investigated further.

As for the mainline XES spectrum, a comparison of the summed VtC XES spectrum of Co_2ZnO_4 and Al_2CoO_4 with that of Co_3O_4 indicates that the subspectrum originating from the Co(III) sites dominates the Co_3O_4 VtC XES spectrum. This results in an overall similarity between the Co_2ZnO_4 and Co_3O_4 VtC XES spectra. The Gaussian fit components of the experiment shown in Figure 16.2 also indicate the prevalence of the similarity between these two spectra. The primary Gaussian features of $Co(III)_2ZnO_4$ (A-D) are also present in Co_3O_4 (A-D), with the latter having additional smaller features (E and F) in the high energy region. These can probably be related to contributions of the Co(II) centers as the Al_2CoO_4 VtC XES spectra show features in this region as well and will be explored in the calculations below.

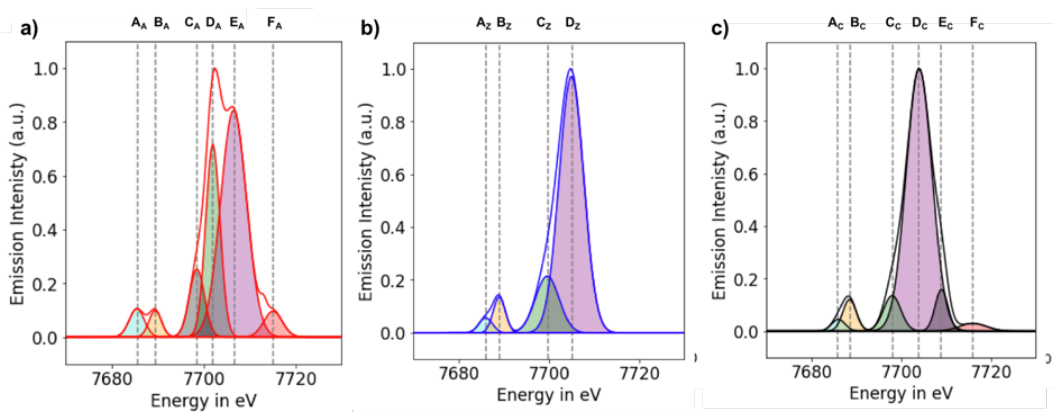

Figure 16.2: Gaussian fit of experimental Co $K\beta_{2,5}/K\beta''$ VtC XES spectra of **a)** $Al_2Co(II)O_4$, **b)** $Co(III)_2ZnO_4$, and **c)** Co_3O_4 spinel solids.

Based on the experimental observations and assuming that the tetrahedral Co(II) sites exist in a high spin state while the octahedral Co(III) sites are low spin, some notations can be made for the VtC XES spectra. The shift to higher energies of the Al_2CoO_4 $K\beta_{2,5}$ VtC XES feature compared to Co_2ZnO_4 could be due to the decreasing Co-O bond lengths in the series and the reduction of the CoO_n unit from $n = 6$ to 4. However, the trends in the respective $K\beta''$ region cannot be extracted with certainty due to an unexpected double spectral feature in the case of Al_2CoO_4. Surprisingly, the Al_2CoO_4 spectrum has lower Co $K\beta_{2,5}/K\beta''$ VtC intensities than $Co(III)_2ZnO_4$ (see Figure 16.1b), which does not follow the general trend expected from the decrease in Co-O bond lengths across the series.

16.4 Cluster Size Convergence

Figure 16.3 displays the convergence of the Co $K\beta_{2,5}/K\beta''$ VtC XES with cluster size, calculated using both the one-electron (see Figure 16.3a-c) and CASCI (see Figure 16.3d-f) protocols, for all three cobalt oxide derivatives.

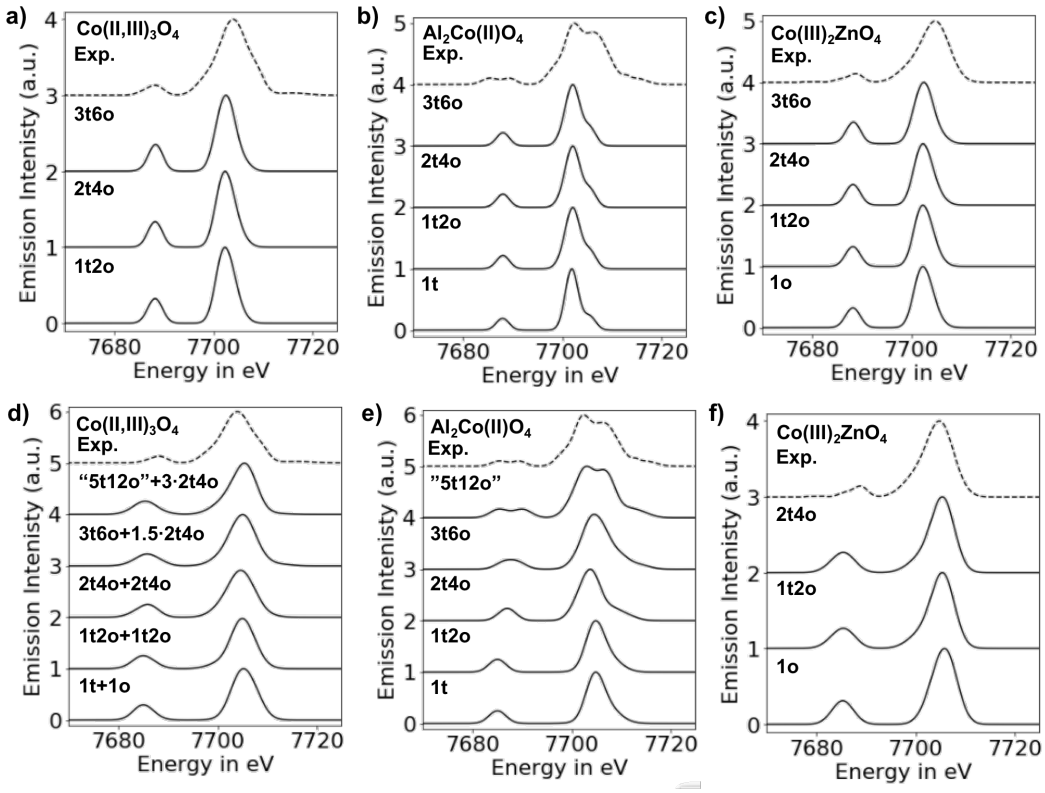

Figure 16.3: Convergence of computed one-electron DFT (top) and CASCI (bottom) $K\beta_{2,5}/K\beta''$ VtC XES spectra with increasing cluster sizes for: **a)** and **d)** Co_3O_4, **b)** and **e)** Al_2CoO_4, and **c)** and **f)** Co_2ZnO_4. Dashed line: experimental spectrum.

The one-electron computed $K\beta_{2,5}/K\beta''$ VtC XES spectra converge for the smallest tested system sizes for all three cobalt oxides, similar to the mainline XES. However, the 2t4o system sizes are still considered in all cases when discussing the one-electron calculations since this is the smallest size to reveal potential underlying interactions of the different cobalt sites, despite the convergence scheme not exhibiting any influence from the different cobalt sites.

The CASCI calculated $K\beta_{2,5}/K\beta''$ VtC XES spectra were generated for each cobalt oxide derivative for different cluster sizes. For Co_2ZnO_4 cluster sizes of 1o, 1t2o, and 2t4o were used, while for Al_2CoO_4 cluster sizes ranging from 1t to 3t6o were used and additionally a model labeled "5t12o" was applied, which is a combination of several 3t6o models and will be explained in detail in Subsection 16.7.2.

The smallest system size of 1o was found to produce a VtC XES spectrum showing the main features for Co_2ZnO_4. The spectrum becomes broader as the system size increases. For Al_2CoO_4 the first three system sizes are almost identical, while for a system size of 3t6o additional features become apparent, and only the "5t12o" model is comparable to the experiment, showing all expected features. Due to computational limitations, further convergence of this spectrum was not investigated.

The convergence scheme for Co_3O_4 is shown in Figure 16.3d. The CASCI calculated VtC XES spectra of Co_3O_4 were obtained by combining the relevant Co(III) and Co(II) site subspectra from the Co_2ZnO_4 and Al_2CoO_4 systems, as for the $K\beta_{1,3}/K\beta'$ mainline XES spectra. Since the Co_2ZnO_4 spectrum is computed only up to system size 2t4o, while Al_2CoO_4 requires larger system sizes, the convergence scheme combines many of the 2t4o-Co_2ZnO_4 $K\beta_{2,5}/K\beta''$ VtC XES spectra with those of Al_2CoO_4 exceeding 2t4o to achieve spectrum convergence with the correct Co(III):Co(II) ratio of 2:1. Co(II) ratio of 2:1. For example, the spectrum of system size 3t6o for Co_3O_4 is represented by 1.5·2t4o-Co_2ZnO_4 and 3t6o-Al_2CoO_4. The spectrum appears to converge at the same point as the Co_2ZnO_4 $K\beta_{2,5}/K\beta''$ VtC XES spectrum, since it dominates the Co_3O_4 spectrum. The converged spectrum is in agreement with the experiment.

16.5 One-Electron $K\beta_{2,5}/K\beta''$ VtC XES Results

The preliminary results of the one-electron VtC XES spectra are presented before analyzing the CASCI VtC XES results. The one-electron approach reproduces the $K\beta_{2,5}$ and $K\beta''$ VtC components for all three cobalt oxide derivatives for system size 2t4o by approximating Co_3O_4 and Al_2CoO_4 as high spin (2S+1=7) and treating Co_2ZnO_4 as low spin (2S+1=2). Figure 16.4 visualizes the results. As for the one-electron mainline XES, the subspectra of the Co(II) and Co(III) sites, respectively, are

identical within one system. The VtC XES spectra of Co_2ZnO_4 and Al_2CoO_4 reflect the VtC XES subspecta of the Co(II) and Co(III) centers in Co_3O_4. In the case of Co_3O_4, the four Co(III) sites dominate the spectrum contributing about 80% to the intensity, while the Co(II) ones contribute 20%. Thus, each Co(II) site contributes half of the intensity of a Co(III) site.

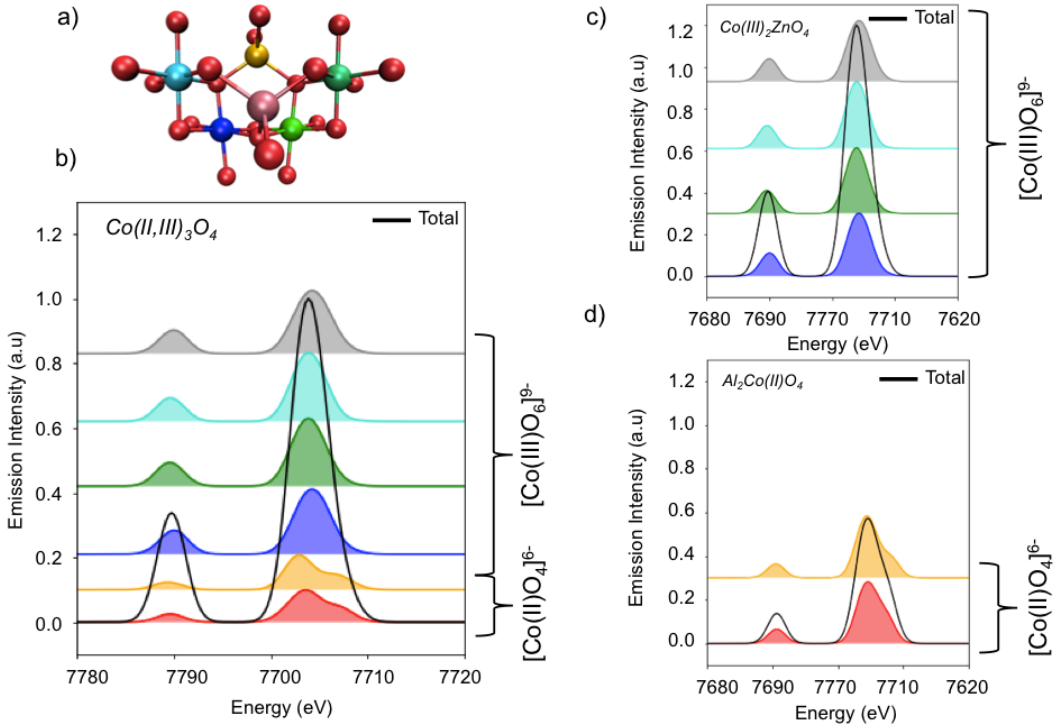

Figure 16.4: One-electron DFT calculated $K\beta_{2,5}/K\beta''$ VtC XES spectra for cluster size 2t4o shown in **a)** of **b)** Co_3O_4, **c)** $Co(III)_2ZnO_4$, and **d)** $Al_2Co(II)O_4$. Subspectra represent contributions from individual Co centers in the 2t4o structure, indicated by the color code shown in **a)**. Color code: subspectra of tetrahedral Co(II) (red and orange) and octahedral Co(III) (gray, turquoise, green, and blue) sites and total spectrum (black). Spectra are normalized to the total spectrum of Co_3O_4 in **b)**.

Further analysis of the individual site contributions reveals that the Co(II) sites contribute a broad asymmetric band in the $K\beta_{2,5}$ region and a single symmetric band in the $K\beta''$ region. On the contrary, the respective Co(III) sites produce a spectrum with a single symmetric and unresolved band in both the $K\beta_{2,5}$ and $K\beta''$ regions.

Figure 16.5 provides a breakdown of the one-electron VtC XES of Co_3O_4 by showing the quantitative contributions of individual single electron decays. The $K\beta''$ feature oiriginates due to LMCT transitions, with 69% of the intensity coming from O $2p$ $\rightarrow$ Co $1s$ decays, 21% from Co $3d$-O $2p$ $\rightarrow$Co $1s$ decays, and 1% from

O $2p$-Co $3s/p$ →Co $1s$ decays. Similarly, the $K\beta_{2,5}$ feature is dominated by LMCT electron decays, with 69% of the intensity coming from O $2p$ →Co $1s$ decays, 22% from O $2p$-Co $3d$ →Co $1s$ decays, and 9% from O $2p$-Co $3s/p$ →Co $1s$ decays. The high-energy region of the spectrum has contributions from intra-metal Co $3d$ →Co $1s$ single electron decays of the tetrahedral Co(II) site. This area provides 9% of the total $K\beta_{2,5}$ intensity. However, there are also some insignificant contributions from Co(II)-Co(II) MMCT that may be present due to the artificial orbital mixing of the method. This breakdown of electron decays is consistent with the XES scheme presented in Figure 8.3 in Section 8.2 on page 101.

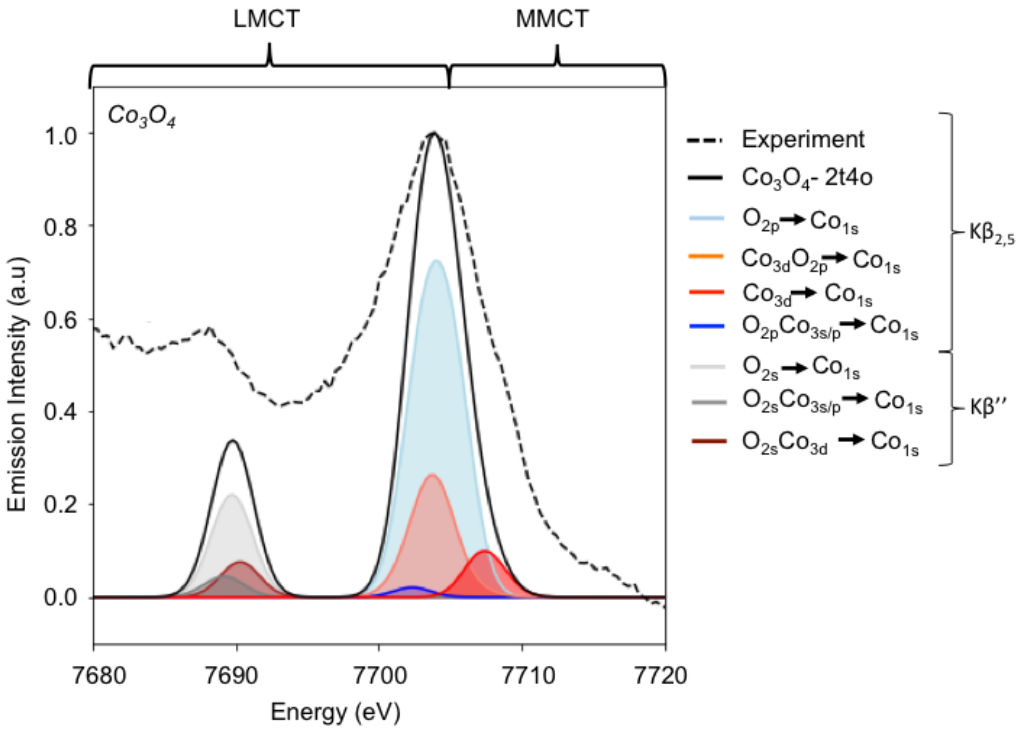

Figure 16.5: One-electron DFT calculated $K\beta_{2,5}/K\beta''$ VtC XES spectrum for cluster size 2t4o of Co_3O_4 (solid black line) compared to experiment (dashed line). Colored spectra indicate the dominant contributions in terms of single electron decays as shown in figure.

Figure 16.6 compares the distorted octahedral Co(III) and tetrahedral Co(II) sites of Co_3O_4 and their counterparts in Co_2ZnO_4 and Al_2CoO_4. It shows that the contributions of the sites in Co_3O_4 are similar to their analogs in the two derivatives.

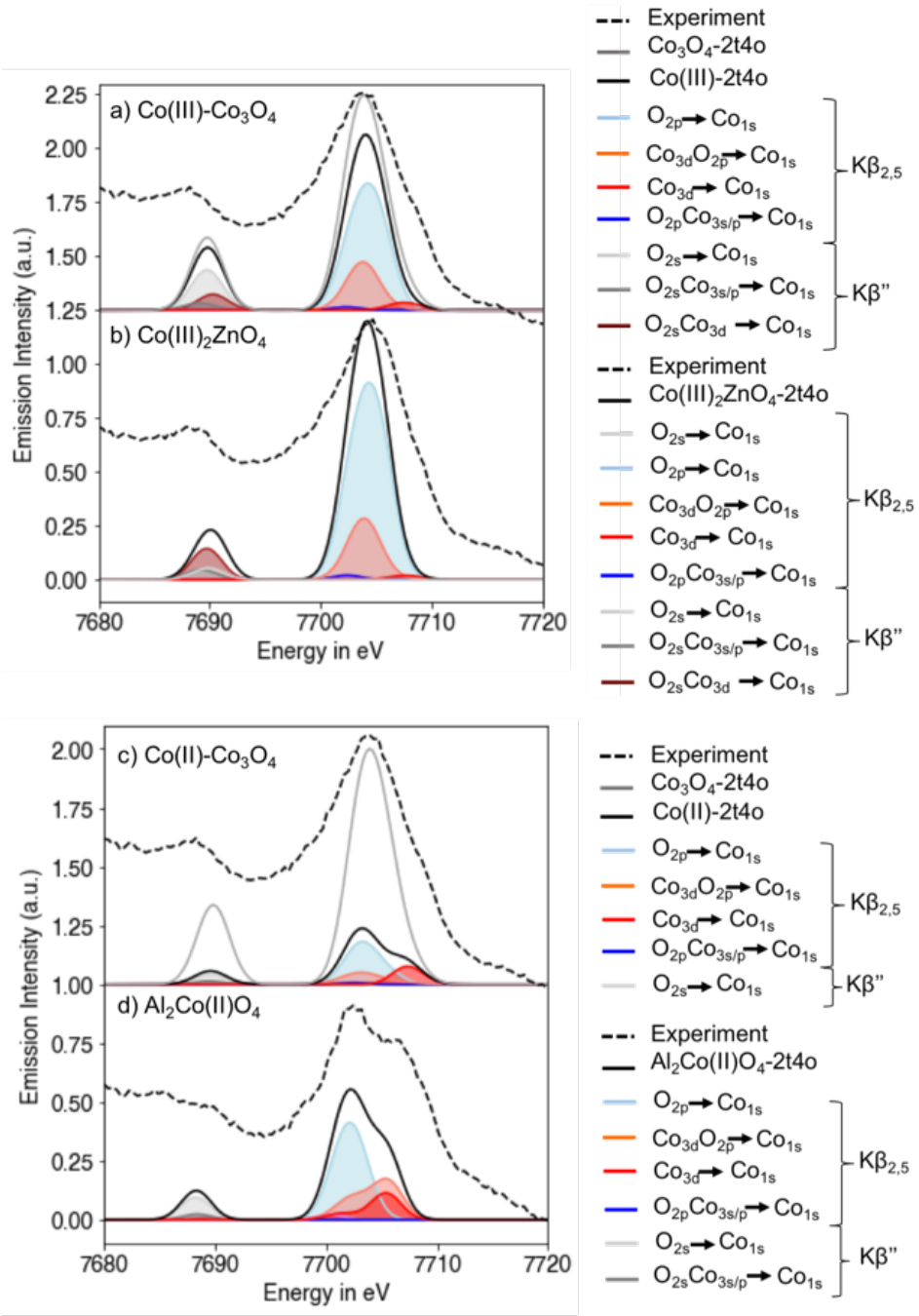

Figure 16.6: The one-electron DFT calculated $K\beta_{2,5}/K\beta''$ VtC XES spectra (black solid line) for cluster size 2t4o for different cobalt sites compared to experiment (dashed line). Contributions from tetrahedral Co(II) sites from **a)** Co_3O_4 and **b)** $Al_2Co(II)O_4$. Contributions from distorted octahedral Co(III) sites in **c)** Co_3O_4 and **d)** $Co(III)_2ZnO_4$. All spectra are normalized to the total calculated $K\beta_{2,5}/K\beta''$ VtC XES spectrum of Co_3O_4 (solid gray line). Colored spectra indicate the dominant contributions in terms of single electron decays as indicated in the figure.

The $K\beta_{2,5}$ feature in Al_2CoO_4 has an asymmetric shape due to Co(II) $3d \rightarrow 1s$ decays, while no pure Co(III) $3d \rightarrow 1s$ decays are detected for the Co(III) sites in Co_2ZnO_4 and Co_3O_4. This is consistent with group theory, which predicts that the Co $3d \rightarrow 1s$ decay in the tetrahedral Co(II) sites is dipole-allowed but for the distorted octahedral Co(III) sites, it is dipole-forbidden.

To summarize, this section concludes that the one-electron calculated $K\beta_{2,5}/K\beta''$ VtC XES spectra of Co_3O_4 can be approximated by combining the $K\beta_{2,5}/K\beta''$ VtC XES spectra of $Al_2Co(II)O_4$ and $Co(III)_2ZnO_4$. The computed spectra agree with most of the experimental features, except, e.g., for the double peak nature of the Al_2CoO_4 $K\beta''$ feature, which is not reproduced in the calculation. This raises the question of whether the calculated asymmetric feature of the $K\beta_{2,5}$ originating mainly from intra-metal Co(II) $3d$ to $1s$ transitions in the one-electron computed Al_2CoO_4 VtC XES spectrum is the end to the story of the double peak feature in the $K\beta_{2,5}$ spectral feature of Al_2CoO_4 since it has a similar splitting pattern as the $K\beta''$ feature in experiment. Additionally, the one-electron protocol shows further limitations, as the shapes of the $K\beta_{2,5}$ and $K\beta''$ features of Co_3O_4 and Co_2ZnO_4 are asymmetric in the experiments but symmetric in the calculation results. Therefore, further investigation is necessary and will be addressed in the upcoming sections with CASCI.

16.6 Analysis of the Intensity Mechanism of the $K\beta_{2,5}/K\beta''$ VtC XES Spectra for Multicenter Systems

This section provides an overview of the principles underlying the $K\beta_{2,5}/K\beta''$ VtC XES spectrum of antiferromagnetically coupled multimetallic centers. The focus is on a "simplified" multicenter structure that serves as a basis for understanding the more complex cobalt derivatives discussed in the next section. The structures analyzed are copper models introduced in Section 13.2, constructed from $Al_2Co(II)O_4$ models of different cluster sizes (1t, 2t4o, and 3t6o). The 1t-Cu(II) model has already been used to explain the underlying mechanisms for the $K\beta_{1,3}/K\beta'$ mainline XES spectrum in Section 15.6. The substitution of Co(II) centers by Cu(II) ($Al_2Cu(II)O_4$) reduces the problem of three unpaired $3d$ electrons per Co(II) to one per Cu(II) center. Figure 13.3 on page 173 illustrates the electron configuration and structure for the example of the 3t6o cluster for the Cu(II) model.

The investigation is divided into four steps. First, it focuses on the $K\beta_{2,5}/K\beta''$ VtC XES spectrum of the isolated Cu(II) site (1t), developing a basic CASCI protocol and comparing it with that of the $K\beta_{1,3}/K\beta'$ mainline XES study to highlight the differences in approach to these two problems. In the second step, multicenter Cu(II) systems are analyzed, with particular emphasis on possible core-

ionized initial states. The third step involves the first approximation of a multicenter $K\beta_{2,5}/K\beta''$ VtC XES spectrum for these multicenter Cu(II) systems. The second and third steps emphasize the importance of treating multiple centers, especially the antiferromagnetic coupling between them. This inclusion is essential for an accurate description of the valence region, which plays a significant role in the processes underlying the $K\beta_{2,5}/K\beta''$ VtC XES spectra. Finally, the principles derived from this analysis are applied to discuss possible core-ionized initial states of the cobalt derivatives.

16.6.1 The Valence-to-Core X-Ray Emission Spectrum of an isolated tetrahedral Cu(II) site

Figure 16.7a schematically shows the transitions allowed locally in the $K\beta_{2,5}/K\beta''$ VtC XES process of an isolated tetrahedral $[Cu(II)O_4]^{6-}$ site. Figure 16.7b depicts their contributions to the CASCI $K\beta_{2,5}/K\beta''$ VtC XES. The $K\beta_{2,5}$ spectral feature consists of O $2p$ →Cu(II) $1s$, and Cu(II) $3d$ →Cu(II) $1s$ electron decays. The O $2p$ and Co $3d$ orbitals are only separated by about 2 eV, which is within the lifetime broadening of the core hole relaxation. Hence, both electron decays contribute intensity to the $K\beta_{2,5}$ spectral feature. On the contrary, the $K\beta''$ is solely dominated by O $2s$ →Cu(II) $1s$ transitions. All these transitions are formally dipole-allowed and agree with the theoretical XES scheme in Section 8.2, Figure 8.3 (see page 101). It is assumed that all processes allowed within the isolated Cu(II) site are also allowed in the larger system sizes.

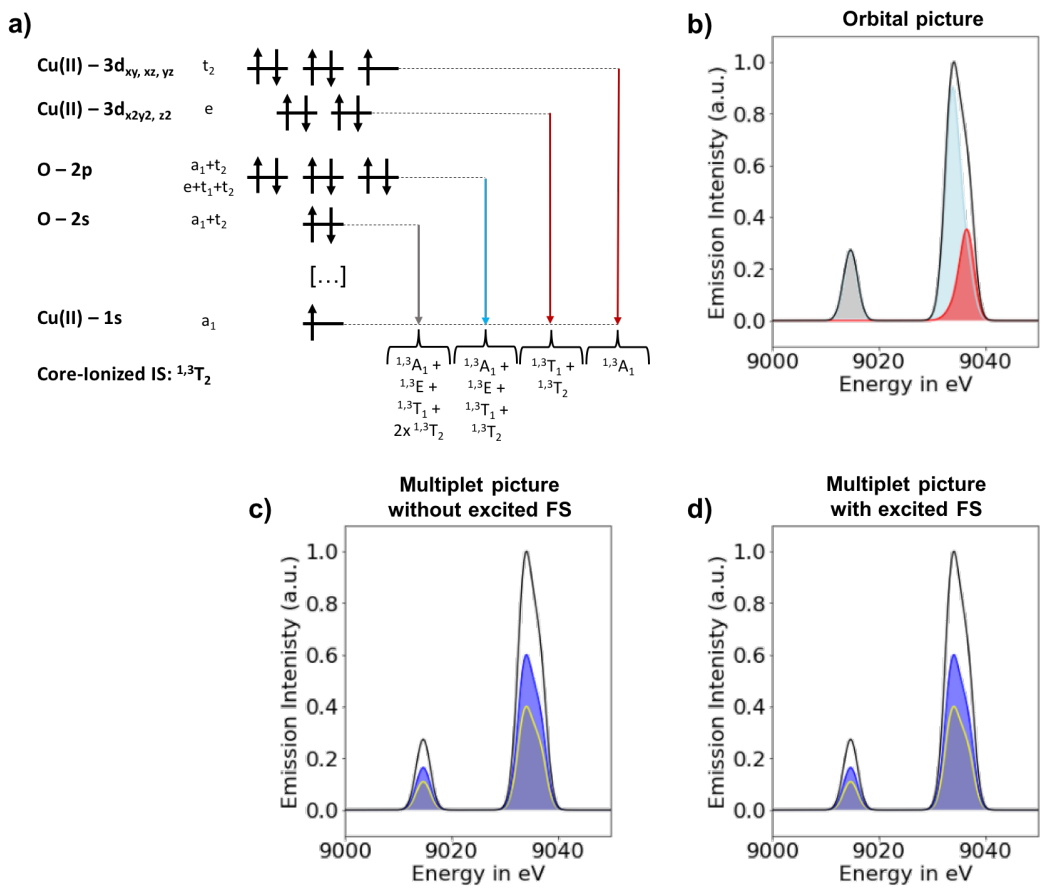

Figure 16.7: a) Diagram of the electron decays with the symmetries of the states contributing to the $K\beta_{2,5}/K\beta''$ VtC XES of the tetrahedral site $[Cu(II)O_4]^{6-}$. **b)** Corresponding CASCI spectrum, highlighting the one-electron decays. Color code: O $2s \rightarrow$ Cu(II) $1s$ (gray), O $2p \rightarrow$ Cu(II) $1s$ light blue, Cu(II) $3d \rightarrow 1s$ (red). Underlying multiplets, singlet (yellow) and triplets (blue), of the CASCI calculated spectrum for final states **c)** without and **d)** with $3d$ excited electrons.

The scheme in Figure 16.7a, like all subsequent XES processes, is constructed under the assumption of the sudden approximation,[238] in which no structural or orbital relaxation occurs upon core ionization. In this model, the symmetry of the system is determined by the coordination environment of the Cu(II) centers, which carry the unpaired electrons in the ground state geometry. In the case of the 1t cluster, this leads from a doublet $^2T_2$ ground state to a core-ionized initial state $^{1,3}T_2$. There is no preference for α or β ionization. Thus, the core-ionized initial state, and therefore, all final states, can be either singlet or triplet.

In the corresponding $K\beta_{1,3}/K\beta'$ mainline XES spectrum (see Figure 15.6 on page 240), the singlet and triplet states produce distinct features. However, in the $K\beta_{2,5}/K\beta''$ VtC XES spectrum, both the singlet and triplet features have identical

shapes, albeit with different intensities (see Figure 16.7c). For the $K\beta_{1,3}/K\beta'$ mainline XES spectrum, not only the different multiplets play a significant role, but also the manifold of final states with exictations in the $3d$ orbitals. These do not seem to affect the $K\beta_{2,5}/K\beta''$ VtC XES spectrum either (compare Figure 16.7c and Figure 16.7d). These observations indicate that the orbital picture obtained from the DFT approach remains valid. Previous studies[53, 263, 519] also support this notion and state that the one-electron DFT approach adequately represents the $K\beta_{2,5}/K\beta''$ VtC XES processes.

When considering larger system sizes beyond the one-center cluster for both Cu(II) and Co models, the multiplet effect and the excited final state manifold still appear to have a negligible impact and do not affect the overall shape and features of the $K\beta_{2,5}/K\beta''$ VtC XES spectrum. Therefore, for the sake of simplicity, the multiplet effect will not be discussed in detail and the excited final states will be neglected. Only the orbital picture derived from the CASCI results will be visualized, as shown for the 1t-Cu(II) model in Figure 16.7b.

16.6.2 Nature of Core-Ionized Initial States in Cu(II) Multicenter Model Systems

The effect of Cu(II) center interactions on the core-ionized initial states for the $K\beta_{2,5}/K\beta''$ VtC XES spectrum is investigated using two and three Cu(II) center models, namely 2t4o and 3t6o. In order to understand the potential influence on the core-ionized states and the underlying spectral mechanism, it is necessary to review the existing knowledge of these interactions, with particular emphasis on the antiferromagnetic coupling between them.

In Section 13.2, the generation of either a ferromagnetic state $|^3F\rangle$ or a "neutral" antiferromagnetic state $|^1N\rangle$ by two Cu(II) centers was demonstrated and visualized in Figure 13.5 (page 176). Each Cu(II) center has an unpaired electron in both states, resulting in either a triplet state with parallel electron spin alignment or an open singlet state with antiparallel electron spin alignment. The resulting spectra are expected to have the same overall shape and features, since multiplicity does not play a role in the VtC XES spectra, as discussed for the one-center CASCI model. The corresponding preliminary CASCI calculations for larger model sizes further support this expectation.

Furthermore, these Cu(II) centers can exist in two interchangeable "ionic" antiferromagnetic states $|^1I\rangle$, where one center localizes the two electrons in one orbital, while the corresponding orbital in the other center remains vacant. Typically, the "ionic" and "neutral" antiferromagnetic states are considered to be superpositions, which already played a major role in the band gap study in Chapter 14. However,

it is also possible that either the "neutral" or the "ionic" antiferromagnetic state has a lower energy, which will be relevant in future considerations. For the time being, the simplified Cu(II) model assumes that these states exist in a superposition.

Section 13.2 also discussed that a single Cu(II) center has T_d symmetry locally. However, the symmetry of two interacting Cu(II) centers is C_{2v} or C_s, while the symmetry of three interacting Cu(II) centers is C_{2v}. For simplicity, only the C_{2v} symmetry will be considered. These symmetries have been distinguished for the ground state cases, but also apply to the core-ionized initial and final states, since the models are constructed under the assumption of sudden approximation.

When two or more metal centers are involved in the emission process, only one center is core-ionized at a time. This means that the experimental spectrum can be viewed as multiple individual spectra, each corresponding to the core ionization and subsequent emission process of a particular metal center. In this study, in models with multiple centers, the metal centers are classified as either "emissive" or "spectator" centers. An "emissive" metal center has a core-ionized metal $1s$ orbital where the XES process occurs, while "spectator" metal centers have fully occupied metal $1s$ orbitals and only "observe" the emission process occurring in the "emissive" center.

The core-ionization of one of two (or more) interacting centers has specific consequences, especially for "ionic" antiferromagnetic systems. When the core of one center is ionized, it causes a symmetry breaking between the centers, resulting in distinct "ionic" antiferromagnetic core-ionized states of the previously exchangeable ground states.

Moreover, the effective local charges of the two centers differ in the "ionic" compared to the "neutral" antiferromagnetic ground, and hence, in the core-ionized initial state. In the "neutral" antiferromagnetic states, both copper centers (Cu^A and Cu^B) have a $3d^9$ electron configuration. However, in the "ionic" antiferromagnetic state, one center has a $3d^8$ electron configuration and an effective charge of Cu^{3+}, while the other center has a $3d^{10}$ electron configuration and an effective charge of Cu^{1+}.

This difference in effective charges poses a problem for the off-resonance XES process, which does not change the valence electron number of the "emissive" center. As a result, the XES process specifically probes "emissive" Cu(II) centers with a $3d^9$ electron configuration, which corresponds to the "neutral" antiferromagnetic states. A workaround is introduced to overcome this limitation and to consider the "ionic" antiferromagnetic state.

The workaround involves the introduction of an "emissive" center Cu^C, which is always locally in a high spin Cu(II) state with one unpaired electron and a $3d^9$ elec-

tron configuration. This center is surrounded by two "spectator" centers, Cu^A and Cu^B, which observe the emission process in Cu^C. Together they create a "neutral" or "ionic" antiferromagnetic environment for Cu^C, representing either a Cu^{2+}-Cu^{2+} "neutral" pair or a Cu^{1+}-Cu^{3+} "ionic" pair.

Therefore, to accurately capture the magnetic behavior of $Al_2Cu(II)O_4$, a minimum cluster size of 3t6o is required in the model. This cluster size accounts for the presence of the "emissive" center and the two "spectator" centers, allowing the representation of both "neutral" and "ionic" antiferromagnetic states and their effects on the XES process.

The three-center model is studied to understand the transition from ground to core-ionized initial states in a Cu(II) system. Figure 16.8 shows the arrangement of the Cu centers: Cu^A, Cu^B, and Cu^C. Different pairings of "neutral" and "ionic" states are shown in an antiferromagnetic fashion.

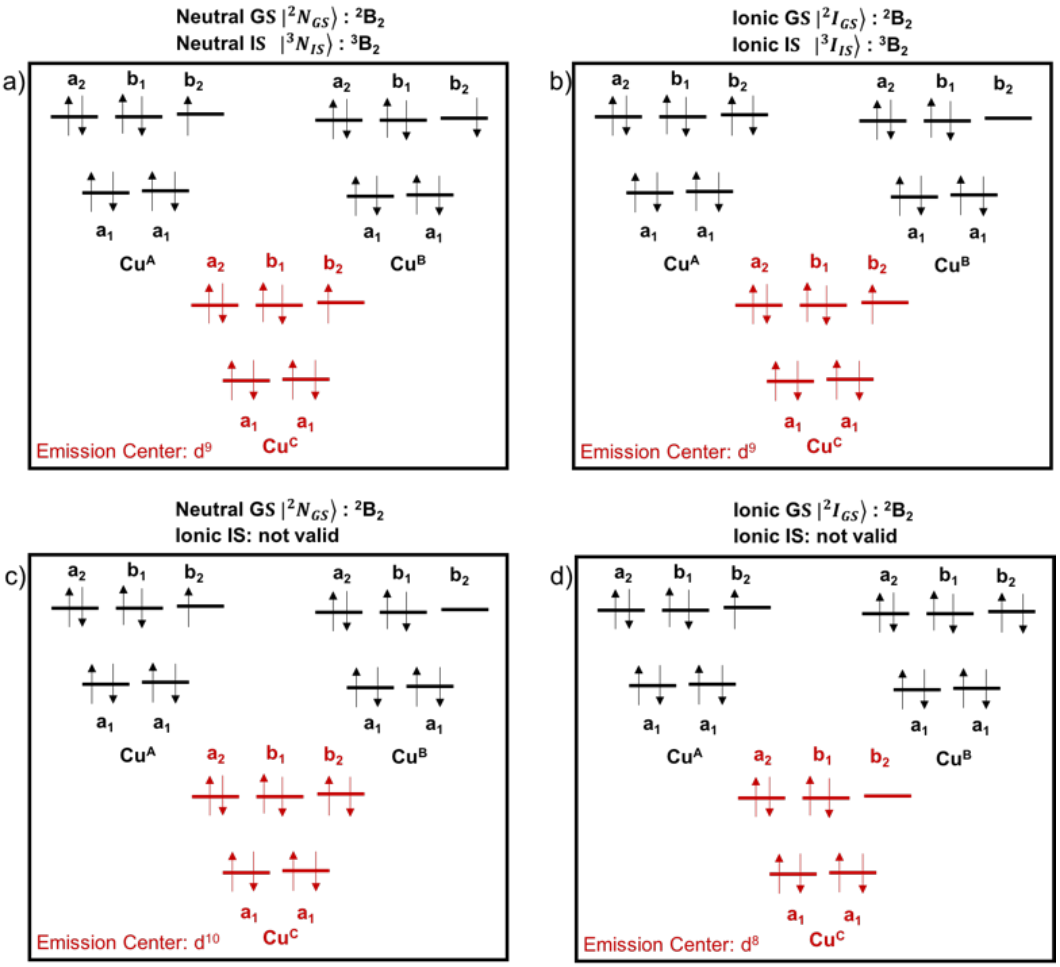

Figure 16.8: Possible "neutral" and "ionic" antiferromagnetic states of three interacting Cu centers (cluster size 3t6o). Color code: "spectator" centers (black), "emissive" center (red) after core-ionization.

Before core ionization, the system consisted of antiferromagnetically coupled centers, with the third center having a high spin configuration. The model includes two "neutral" ground states, here represented by one example (see Figure 16.8a), denoted as $|^2N_{GS}\rangle$, and six "ionic" states, denoted as $|^2I_{GS}\rangle$, here represented by three examples (see Figure 16.8b through Figure 16.8d). Both "neutral" and "ionic" antiferromagnetic ground states have $^2B_2$ symmetry, maintaining the interchangeability between the three Cu(II) centers.

After core ionization, one Cu^C center becomes "emissive", while Cu^A and Cu^B become "spectator" centers. Only Figure 16.8a and Figure 16.8b represent the valid core-ionized initial states. Figures 16.8c and 16.8d are not applicable because the claimed "emissive" center Cu^C does not have the correct $3d^9$ electron configuration.

Considering a core-ionized initial state of $^{1,3}B_2$ symmetry, there are now "neu-

tral" $|^{1,3}N_{IS}\rangle$ and "ionic" $|^{1,3}I_{IS}\rangle$ singlet or triplet core-ionized initial states of $^{1,3}B_2$ symmetry. The "emissive" center can be in either a triplet or a singlet state, depending on the alignment of the electrons in the core and the $3d$ orbitals. The antiferromagnetic coupling of the electrons in the spectator centers leads to a singlet state, preserving the overall multiplicity.

The CASCI approach can demonstrate the interchangeability and differentiation of "ionic" antiferromagnetic states in the ground and core-ionized ionic states. Figure 16.9 shows the ordering and mixing of these calculated states. In the ground state there is significant mixing between the states (Figure 16.9a). However, upon core ionization, the symmetry breaking effect causes the "ionic" states to separate, resulting in distinct core-ionized initial "ionic" antiferromagnetic states (Figure 16.9b). States with a $3d^9$ "emissive" center (shown in gray) are the only valid core-ionized initial "ionic" antiferromagnetic states for the emissive process.

The separation of the different "ionic" states in the calculation by moving from the ground to the core-ionized initial states highlights the validity of treating them independently, which allows to exclude "emissive" center states with different $3d$ electron numbers from the model.

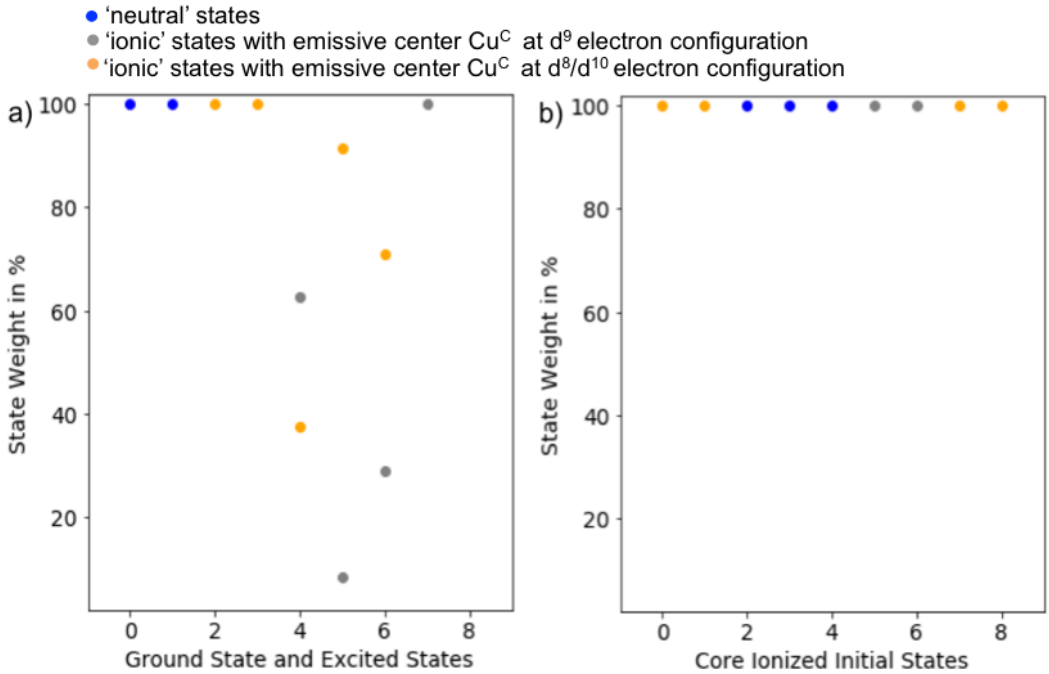

Figure 16.9: Energetic ordering and state mixing of **a)** ground states and **b)** core-ionized initial states in different antiferromagnetic states. Color code: "neutral" antiferromagnetic states (blue), "ionic" antiferromagnetic states with the "emissive" center in a $3d^9$ electron configuration (orange), "ionic" antiferromagnetic states with the "emissive" center in a $3d^8$ or $3d^{10}$ electron configuration (gray).

Figure 16.9 also shows that the "neutral" states have lower energy compared to the valid "ionic" antiferromagnetic states in both the ground and core-ionized initial states. The weak antiferromagnetic coupling between the Cu(II) centers, characterized by a Cu-Cu distance of 5.78 Å, contributes to the separate and non-mixing nature of the "ionic" and "neutral" antiferromagnetic states in this model.

It is worth noting that without additional perturbations to account for dynamic correlation, the CASCI model may not accurately capture the superposition of "ionic" and "neutral" states, as demonstrated in the band gap study in Chapter 14. However, since the NEVPT2 calculations in the band gap study demonstrated the superposition for the antiferromagnetic model, it can be assumed that it also exists for the Cu(II) model in the following.

16.6.3 Nature of the $K\beta_{2,5}/K\beta''$ VtC XES Spectra Final States in Cu(II) Multicenter Model Systems

The core-ionized initial states for the three-center Cu system 3t6o discussed earlier give rise to a corresponding set of final states. It is important to emphasize that

the processes occurring within the core-ionized "emissive" Cu(II) center and involving the oxygens are the major contributors to the spectrum. The active participation of the other two centers is not expected since their primary function in this model is to create two different antiferromagnetic environments for the "emissive" center. Figure 16.10 shows the expected emission scheme for the two scenarios.

The final states can have symmetries such as A_1, A_2, B_1, or B_2. Due to the recurring symmetries in the two different antiferromagnetic scenarios, the two different antiferromagnetic cases are allowed to mix and thus, can exist simultaneously.

The emission pathways connecting the core-ionized initial and final states are predominantly dipole-allowed and are expected to contribute significantly to the overall spectrum. These pathways include electron decays from Cu(II) $3d$ to Cu(II) $1s$, O $2p$ to Cu(II) $1s$, and O $2p$ to Cu(II) $1s$ transitions.

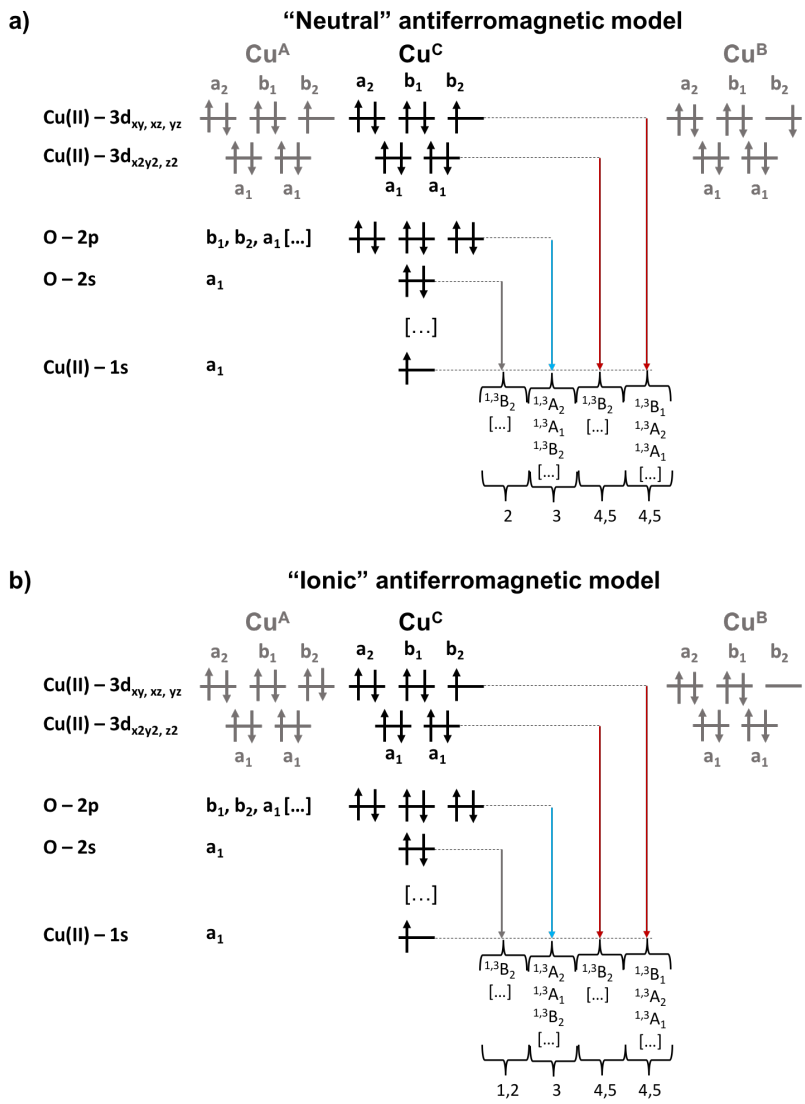

Figure 16.10: Diagram of the electron decays and symmetries of the final states contributing to the $K\beta_{2,5}/K\beta''$ VtC XES spectra involving the $3d$ orbitals of the "emissive" center and the $3d$ orbitals involved in the antiferromagnetic coupling between the "spectator" centers Cu^A/Cu^B, originating from a **a)** "neutral" and **b)** "ionic" antiferromagnetic core-ionized state. Color-coded arrows: O $2s$ →Cu(II) $1s$ (gray), O $2p$ →Cu(II) $1s$ (light blue), Cu(II) $3d \rightarrow 1s$ (red) electron decays.

The schemes shown in Figure 16.10 can be translated into CASCI calculations, and the results are shown in Figure 16.11. The two antiferromagnetic cases are calculated separately, as shown in the bottom two panels of Figure 16.11a, and together, as shown in the top panel of Figure 16.11a. This first approximation assumes that the "neutral" and "ionic" antiferromagnetic states contribute in the same ratios to the total spectrum.

The overall processes agree with the one-center Cu(II) case visualized in Figure 16.7. In particular, the $K\beta''$ feature originates primarily from O $2s$ →Cu(II) $1s$ electron decays. The lower energy region of the $K\beta_{2,5}$ feature originates from O $2p$ →Cu(II) $1s$ decays, and the higher energy region originates from Cu(II) $3d$ →Cu(II) $1s$ electron decays.

Furthermore, in the "neutral" antiferromagnetic state, the subspectrum exhibits a similar shape to the total spectrum in the one-center case, but with broader features (compare Figure 16.10a and Figure 16.7, bottom panel). This phenomenon will be further investigated in the context of relevant cobalt oxides.

The subspectrum originating from "ionic" states displays an additional band splitting in the $K\beta_{2,5}$ and $K\beta''$ spectral features. This splitting is attributed to the difference in effective charge between the two "spectator" centers, Cu^A and Cu^B, compared to the "emissive" center, Cu^C. Cu^A has an effective charge of Cu^{3+} while Cu^B has an effective charge of Cu^{1+}. These distinct charges alter the local electrostatic environment of the emissive Cu(II) center and impact the local oxygen coordination environment of the Cu centers in the $K\beta_{2,5}/K\beta''$ VtC XES. The strength of the band splitting is in relation to the strength of the tetrahedral field splitting. This phenomenon will be further investigated in the context of relevant cobalt oxides.

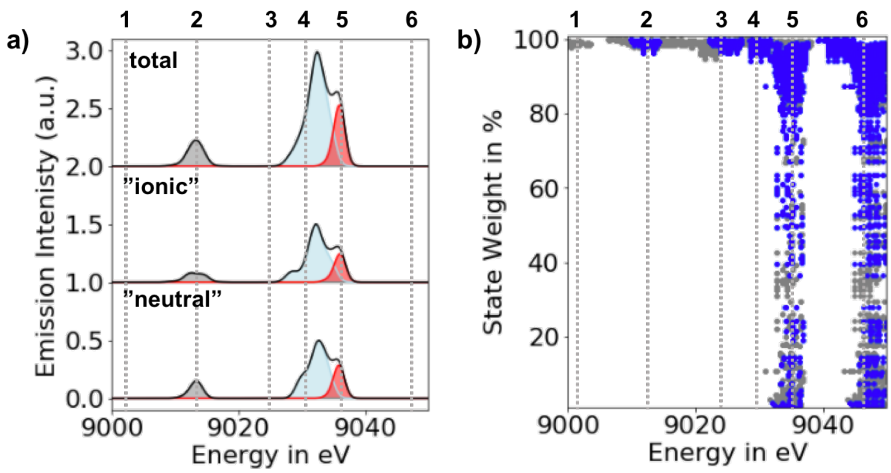

Figure 16.11: a) Total (top panel) CASCI calculated $K\beta_{2,5}/K\beta''$ VtC XES for cluster size 3t6o of $Al_2Cu(II)O_4$ with subspectra originating from "neutral" (bottom panel) and "ionic" (middle panel) antiferromagnetic final states. Contributing one-electron decays are highlighted in different colors. Color code: O $2s$ →Cu(II) $1s$ (gray), O $2p$ →Cu(II) $1s$ (light blue), Cu(II) $3d$ →Cu(II) $1s$ (red) electron decays. **b)** State weights of the contributing "neutral" and "ionic" antiferromagnetic states to the total spectrum in **a)**. Color code: "neutral" (blue) and "ionic" (gray) antiferromagnetic states. Numbers 1 to 6 denote the six energy groups.

Figure 16.11b illustrates the complete set of final states, taking into account the mixing between the "neutral" and "ionic" states during the XES emission process from the core-ionized initial antiferromagnetic states. The spectra show significant mixing, especially in the $K\beta_{2,5}$ region dominated by Cu(II) $3d$ →Cu(II) $1s$ electron decays. While the mixing is important to confirm the coexistence of the two spectra from a symmetry point of view, the intensity gained from the mixing is relatively small. Therefore, the total spectrum shown in the top panel of Figure 16.11 can also be effectively reproduced by adding the subspectra of the "ionic" and "neutral" states without significant loss of spectral features. This allows a simplified CASCI protocol that treats different antiferromagnetic states separately.

16.6.4 Nature of Initial States and Electronic Structure of Co(II) and Co(III) Centers in Al_2CoO_4 and Co_2ZnO_4, and a Hypothetical Larger Multicenter Model - "5t12o"

This subsection applies the principles established for the copper model to investigate the emission schemes of Al_2CoO_4 and Co_2ZnO_4 solids. This aims to gain a preliminary understanding of the core-ionized initial states and subsequent final states in these systems. Also, the subsection addresses the limitations of the previous 3t6o model and explores an additional model called "5t12o" as a potential workaround.

Similar to the Cu(II) model system, Al_2CoO_4 contains multiple tetrahedral Co(II) sites with locally high spin $3d^7$ configurations. Figure 16.12 illustrates the core-ionized initial states and corresponding VtC XES one-electron schemes for the single Co(II) center model (1t) and the three Co(II) center model (3t6o). In the 1t model (see Figure 16.12a), all the transitions shown are dipole-allowed, similar to the Cu(II) model, indicating their contribution to the intensity of the $K\beta_{2,5}/K\beta''$ VtC XES spectra also in multicenter models.

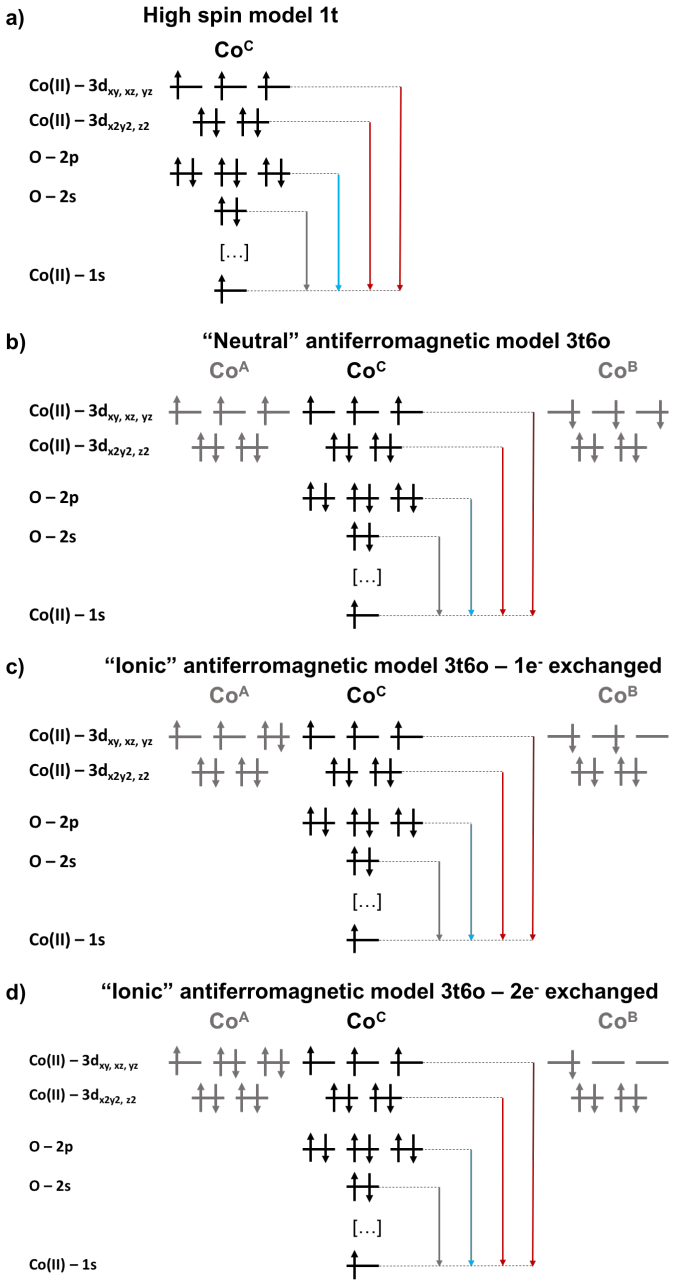

Figure 16.12: Core-ionized initial states and possible electron decays in Al_2CoO_4 relevant to the $K\beta_{2,5}/K\beta''$ VtC XES process for different cluster sizes: **a)** high spin single-center case (1t) and **b)** to **d)** antiferromagnetic three-center cases (3t6o). For the three-center case, the "spectator" centers are in **b)** a "neutral" antiferromagnetic state, **c)** an "ionic" antiferromagnetic state with one electron exchanged by superexchange, and **d)** an "ionic" antiferromagnetic state with two electrons exchanged by superexchange. Color-coded arrows: O $2s$ →Co(II) $1s$ (gray), O $2p$ →Co(II) $1s$ (light blue), Co(II) $3d \rightarrow 1s$ (red) electron decays.

For the 3t6o model, Figures 16.12b and Figure 16.12c depict the "neutral" and "ionic" antiferromagnetic states, respectively, analogous to the Cu(II) model. In these states, the "spectator" Co sites ($Co^{A/B}$) exhibit antiferromagnetic coupling, while the "emissive" site (Co^{C}) maintains a high spin state. The "ionic" antiferromagnetic states involve electron exchange between the coupled sites via superexchange.

However, unlike the simplified Cu(II) model, there are multiple possibilities to consider due to the presence of three unpaired electrons in each of the two coupled centers. This opens up the potential for various exchange mechanisms. Figure 16.12c only shows one potential scenario. The different scenarios do not only include the exchange of one of the three unpaired electrons per center at a time but also two or even three.

Currently, two points argue against considering the exchange of two or three electrons between the centers. First, the consulted literature and the experiment do not show any evidence for a superexchange mechanism involving more than one electron between two antiferromagnetically coupled centers. Second, when one electron is exchanged, the effective charge of the "spectator" center pairs is Co^{1+}-Co^{2+}. Exchanging two electrons results in a pair of Co^{0}-Co^{3+}, and exchanging three electrons leads to Co^{1-}-Co^{4+}, both of which seem unreasonable.

Nevertheless, Figure 16.12d represents a scenario where two electrons are involved in the exchange process, resulting in two "spectator" centers, each with one unpaired electron. This model becomes relevant for further exploration.

One particular shortcoming of the 3t6o model, which has yet to be discussed, is that it only captures a partial aspect of the larger picture. While it effectively creates an antiferromagnetic environment with two neighboring Co centers for the "emissive" Co center in the emission process, it neglects the surrounding environment.

In the framework of an extended $Al_2Co(II)O_4$ system representing solid-state bulk properties, each tetrahedral Co(II) center is surrounded by four neighboring tetrahedral Co(II) centers. The smallest cluster representing this is a 5t12o model shown in Figure 16.13. By considering the central Co(II) site as the " emissive" center surrounded by the four outer Co(II) sites, the antiferromagnetic environment becomes more complex.

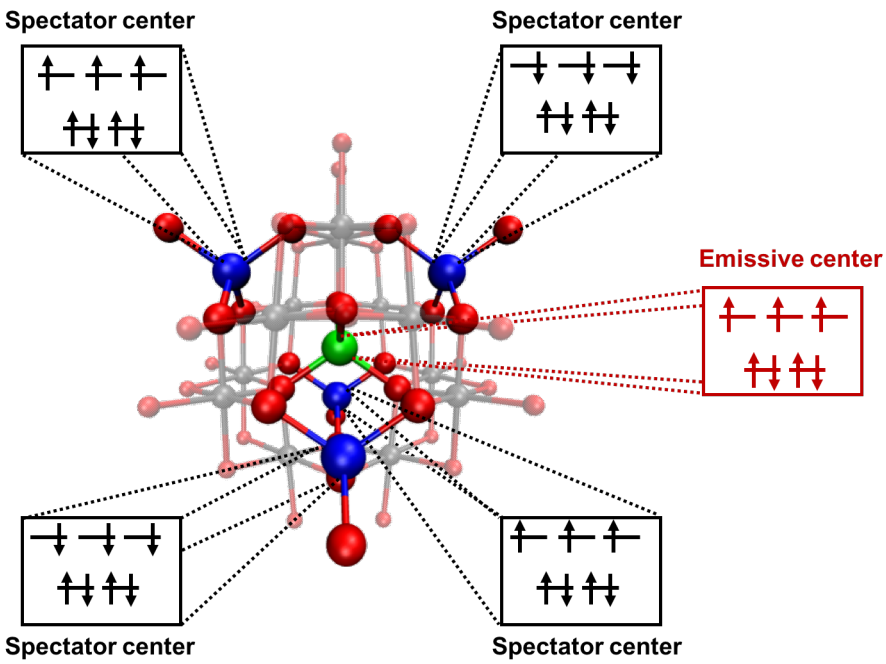

Figure 16.13: Cluster size 5t12o, representing a "neutral" antiferromagnetic system with four Co(II) "spectator" centers (blue) forming a "cage" around the "emissive" Co(II) center (green).

To simplify the problem, is is assumed that the four "spectator" Co sites always form two antiferromagnetically coupled sites. Each pair can exist in either a "neutral" or an "ionic" antiferromagnetic state. The two pairs of antiferromagnetically coupled "spectator" sites can be in both "neutral" states, both "ionic" states, or in different states simultaneously.

When both coupled Co(II) pairs are in a "neutral" state, no electron is relocalized through superexchange, whereas if one pair is in a "neutral" state and the other is in an "ionic" state, one electron undergoes relocalization. However, if both coupled Co(II) pairs are in an "ionic" antiferromagnetic state, the superexchange results in the relocalization of two electrons within the Co(II) pairs. This leads to a greater degree of charge relocalization, altering the effective environment of the "emissive" Co(II) center.

As observed in the case of the 3t6o $Al_2Cu(II)O_4$ toy model, the change in effective charge leads to a splitting of the spectral feature based on the tetrahedral field splitting. Consequently, a more pronounced splitting can be expected, proportional to the number of exchanged electrons.

Due to its size and complexity, it is currently impossible to directly apply CASCI to the 5t12o model for cobalt oxides or the discussed $Al_2Cu(II)O_4$ toy models. Instead, the model is approximated using multiple 3t6o models, where each 3t6o

model represents possible couplings between the "spectator" center pairs and the central site acting as the "emissive" center, as shown in Figure 16.14. The 3t6o model accurately captures all potential pairs due to their shared symmetry and structure. This approximation method, called "5t12o", will be used for the case of $Al_2Co(II)O_4$.

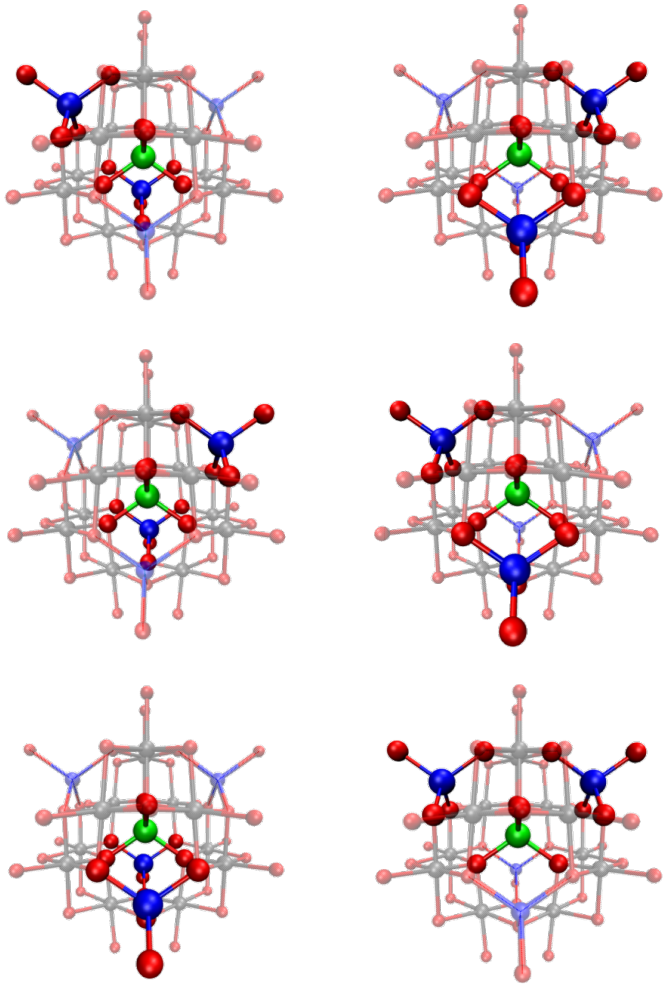

Figure 16.14: Potential 3t6o subsystems with a central "emissive" Co(II) center (green) and two neighboring "spectator" Co(II) centers (blue) in cluster 5t12o.

The scheme shown in Figure 16.12d serves as a surrogate model for the "5t12o" system, representing the scenario where both pairs are in "ionic" antiferromagnetic states, resulting in the objection of two electrons to the superexchange mechanism. The schemes in Figure 16.12b and Figure 16.12c are applicable to the 3t6o case itself and serve as approximations for the "5t12o" system when both pairs are in "neutral" or a combination of "neutral" and "ionic" antiferromagnetic states, respectively.

The Co(III) centers in Co_2ZnO_4 are distorted octahedrally coordinated and possess D_{3d} symmetry. These centers are low spin and exhibit diamagnetic behavior,

indicating that interactions with neighboring Co(III) centers are expected to be negligible. Nonetheless, for completeness, Figure 16.15 shows the one-electron XES schemes for both the isolated octahedral site 1o ($[Co(III)O_6]^{9-}$) and the two Co(III) centers system 1t2o. The latter can also be seen as approximating more Co(III) "spectator" sizes as in the 2t4o model.

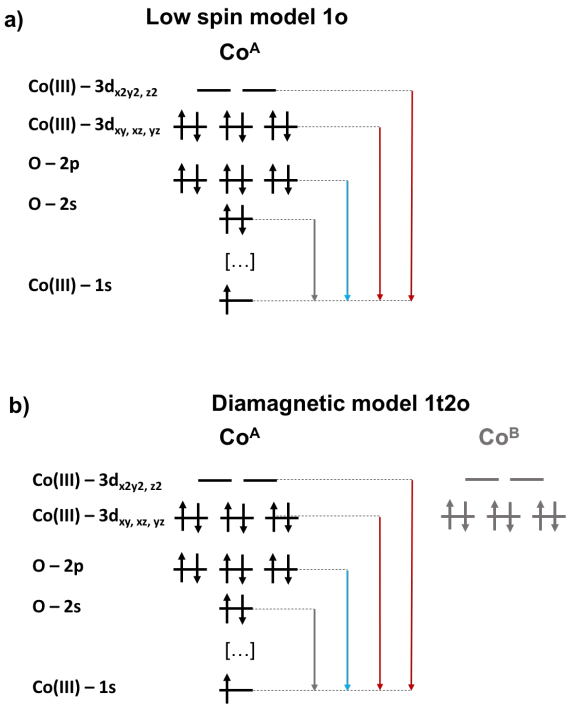

Figure 16.15: Core-ionized initial states and possible electron decays in Co_2ZnO_4 relevant to the $K\beta_{2,5}/K\beta''$ VtC XES process for different cluster sizes: **a)** low spin single-center case (1o) and **b)** diamagnetic two-center case (1t2o). Color-coded arrows: O $2s$ →Co(III) $1s$ (gray), O $2p$ →Co(III) $1s$ (light blue), Co(III) $3d \rightarrow 1s$ (red) electron decays.

The electron decays from the O $2p$ and O $2s$ orbitals to the Co(III) $1s$ during the $K\beta_{2,5}/K\beta''$ VtC XES process are dipole-allowed, indicating their potential contribution to the spectrum. However, the electron decays from the Co(III) $3d$ orbitals to Co(III) $1s$ during the same process are dipole-forbidden. Therefore, it is unlikely that the latter contribute significantly, if at all, to the observed spectrum, as already suggested by the one-electron study.

The schemes of core-ionized initial and resulting final states considered above will be used to investigate the intensity mechanism of the $K\beta_{2,5}/K\beta''$ VtC XES spectra of Co_2ZnO_4, Al_2CoO_4, and Co_3O_4 solids with CASCI in the next section.

16.7 CASCI $K\beta_{2,5}/K\beta''$ VtC XES results

Analogous to the $K\beta_{1,3}/K\beta'$ mainline XES study, the CASCI analysis of the $K\beta_{2,5}/K\beta''$ VtC XES spectra is divided into Co(III)$_2$ZnO$_4$, Al$_2$Co(II)O$_4$, and Co$_3$O$_4$ sections.

16.7.1 Co_2ZnO_4

In the previous study of the $K\beta_{1,3}/K\beta'$ mainline XES spectrum in Chapter 15, it was shown that the octahedral Co(III) sites in Co_2ZnO_4 give rise to core-ionized initial and final states with electron configuration ($3d^6_{t2}3d^0_{eg}$) and final states with singly excited $3d$ electron configuration ($3d^5_{t2}3d^1_{eg}$), which contribute significantly to the spectrum. However, as noted for the Cu(II) example, these excited final states do not appear to play a role in the $K\beta_{2,5}/K\beta''$ VtC XES mechanisms. The one-electron analysis presented in Section 16.5 provided satisfactory agreement with the experimental results for Co_2ZnO_4, suggesting that the one-electron picture is generally applicable to this problem.

However, it is advantageous to recalculate the spectrum using the CASCI method. This is done not least to show that the CASCI protocol gives comparable results to the one-electron approach, thus justifying its use in the calculation of $K\beta_{2,5}/K\beta''$ VtC XES spectra.

Figure 16.16 presents the CASCI results showing the electron decay paths for the Co_2ZnO_4 models with cluster sizes 1o and 2t4o. It also includes a comparison between the 2t4o model and the Gaussian fit of the experimental data.

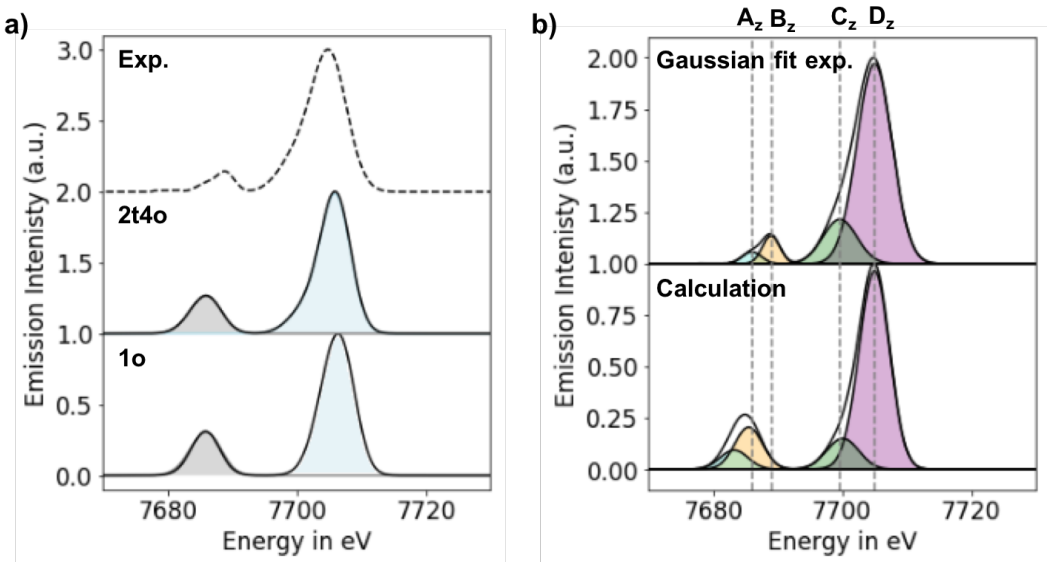

Figure 16.16: CASCI calculated spectra of Co_2ZnO_4: **a)** electron decay contributions for cluster sizes 1o (bottom panel) and 2t4o (middle panel) compared to the experimental spectrum (top panel, dashed line). Color code: O $2s$ →Co(III) $1s$ (gray), O $2p$ →Co(III) $1s$ (light blue) electron decays. **b)** Comparison of the Gaussian fit of the CASCI calculated spectrum for cluster size 2t4o (bottom panel) with the experimental Gaussian fit (top panel).

The CASCI results provide two important insights:

First, the observed electron decays are consistent with the expected scheme shown in Figure 16.15. The $K\beta''$ and $K\beta_{2,5}$ features arise from O $2s$ →Co(III) $1s$ and O $2p$ →Co(III) $1s$ transitions, respectively. Although Co(III) $3d \rightarrow 1s$ transitions are quadrupole allowed, they are dipole-forbidden and have an insignificant effect on the spectrum. This overall scheme is consistent with the results of the one-electron calculations shown in Figure 16.6.

Second, while the 2t4o cluster does not introduce any new contributions to the spectrum compared to 1o, the larger cluster shows slightly better agreement with the experimental data. A possible explanation for this observation is that the increased number of oxygen orbitals in the 2t4o cluster contributes to the spectrum and results in broader features. Figure 16.17 supports this statement by showing the calculated bandwidth as a function of model size. The plot shows that the bandwidth of the O 2s and O 2p bands converge for system sizes of 2t4o.

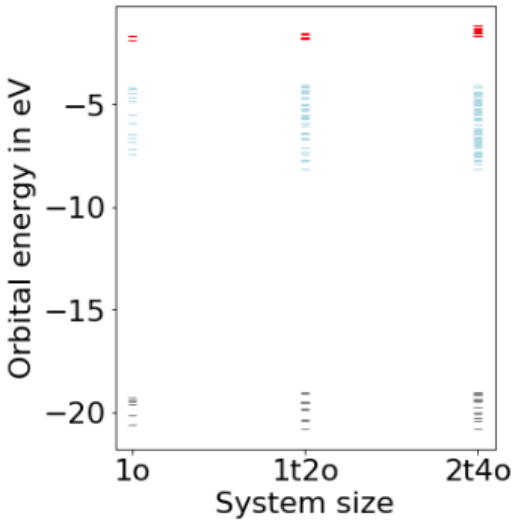

Figure 16.17: CASCI calculated orbital bands for cluster sizes 1o, 1t2o, and 2t4o. Color code: O $2s$ (gray), O $2p$ (light blue), Co(III) $3d$ (red) orbitals.

Since no new contributions appear that can be related to the influence of more than one Co(III) center, it can be concluded that the "spectator" Co(III) centers do not influence the spectrum generated by the "emissive" center, supporting the expectation of a diamagnetic system. The spectrum remains local.

The VtC XES features calculated by CASCI, especially the $K\beta_{2,5}$ feature, show a slight asymmetry. This asymmetry is particularly visible in the Gaussian fit of the CASCI result compared to the experimental result in Figure 16.16b. However, this asymmetry is less pronounced in the CASCI results compared to the experimental data. The one-electron calculation shows no obvious asymmetry.

The $K\beta''$ is overestimated in the calculation. Here, the ratio between $K\beta''$ and $K\beta_{2,5}$ is about 1:3, which represents the ratio of O 2s to O 2p orbitals. In the experiment the ratio is about 1:5. Despite the differences, the overall agreement between the CASCI calculation and the experimental results is considered satisfactory.

In conclusion, the CASCI result gives an equivalent orbital picture to the one-electron results and agrees well with the expected underlying transitions for the $K\beta_{2,5}/K\beta''$ Vtc XES spectrum. At the same time, it reveals even more details, such as the asymmetric shape for the case of Co_2ZnO_4, giving even better agreement with the experiment than the one-electron protocol.

16.7.2 Al_2CoO_4

For the $K\beta_{2,5}/K\beta''$ VtC XES analysis of $Al_2Co(II)O_4$, the model copper system $Al_2Cu(II)O_4$ can be used as a template. Similar to Cu(II), the isolated tetrahedral

site (1t) is inadequate for XES analysis as it cannot reproduce significant features of the $K\beta_{2,5}$ and $K\beta''$ spectral features as shown in the bottom panel of Figure 16.18. The spectrum shows a symmetric $K\beta''$ VtC XES feature resulting exclusively from O $2s$ →Co(II)$1s$ electron decays. The $K\beta_{2,5}$ VtC XES feature consists of a symmetric feature due to O $2p$ →Co(II)$1s$ electron decays and an overlapping smaller feature at higher energies due to Co(II)$3d \rightarrow 1s$ transitions, resulting in an overall asymmetric $K\beta_{2,5}$ feature. These results are in agreement with the one-electron calculations in Figure 16.6.

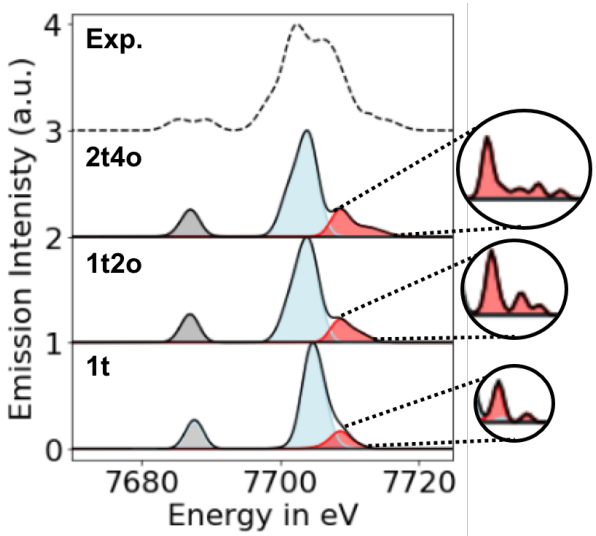

Figure 16.18: CASCI calculated spectra of Al_2CoO_4 compared to the experimental spectrum (top panel) for increasing cluster sizes 1t (bottom panel), 2t4o (second from bottom panel), and 3t6o (second from top panel, dashed line), where all Co(II) centers are in a local high spin $3d^7$ electron configuration. Spectra cutouts in circles: spectral region visualized with lower Gaussian broadening of the plotted spectrum (weighting is 1.0 instead of 3.5). Color code: O $2s$ →Co(II) $1s$ (gray), O $2p$ →Co(II) $1s$ (light blue), Co(II) $3d \rightarrow 1s$ (red) electron decays.

The spectra obtained from the 2t4o and 3t6o models, when for the latter only the "neutral" antiferromagnetic environment created by the "spectator" centers is considered, are for the most part equivalent to those of the 1t model. The spectra are shown in the middle panels of Figure 16.18. There are two notable differences. First, the $K\beta_{2,5}$ VtC XES feature in particular becomes asymmetric with increasing system size. As with the Co_2ZnO_4, this can be related to the broadening of the O 2p band as the cluster size converges.

Second, the feature originating from the Co(II)$3d \rightarrow 1s$ transitions becomes a distinct shape with an increasing number of several smaller underlying peaks broad-

ening the feature, which can be related to the increasing number of unpaired $3d$ electrons in the model from cluster size 1t to 3t6o.

As expected from the $Al_2Cu(II)O_4$ toy model, none of the models in Figure 16.18 show satisfactory agreement with the experimental data. These spectra represent only the "neutral" antiferromagnetic component of the spectrum. To accurately capture the effect of antiferromagnetic coupling on the $K\beta_{2,5}/K\beta''$ VtC XES spectrum, similar to the Cu(II) model, it is essential to include the "ionic" antiferromagnetic component as well.

As discussed in Subsection 16.6.4, any given "emissive" tetrahedral high spin Co(II) center in the bulk of $Al_2Co(II)O_4$ is surrounded by four nearest neighboring tetrahedral "spectator" Co centers. These "spectator" centers create an effective antiferromagnetic environment of pairs of "neutral" and "ionic" antiferromagnetic states that act on the emission process occurring in the "emissive" center. This is represented by the previously introduced "5t12o" approximation, which captures these environmental effects by combining several 3t6o models.

A summary of the results of the emission process occurring within this given central "emissive" Co(II) center is shown in Figure 16.19. The bottom panel represents the case where the four "spectator" centers are coupled only in pairs in "neutral" antiferromagnetic states. Therefore, no electron is exposed to the antiferromagnetic superexchange. The middle panel represents the case where one potential pair is in the "neutral" and the other in the "ionic" antiferromagnetic state, resulting in one electron being relocalized via the superexchange mechanism. Finally, the top panel represents the case where all pairs of "spectator" Co centers are in the "ionic" state, resulting in two electrons being relocalized via superexchange.

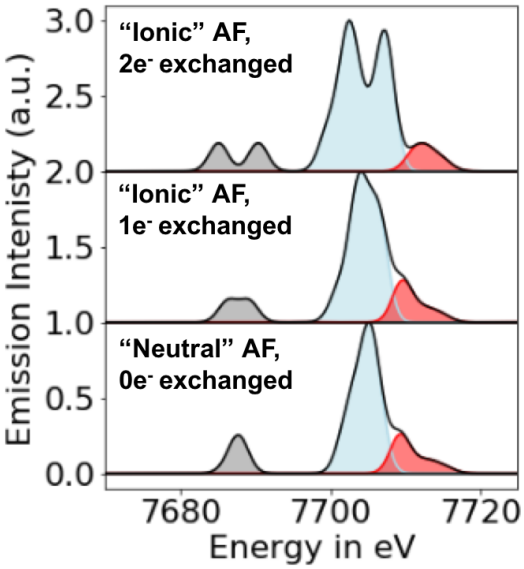

Figure 16.19: CASCI calculated spectra of Al_2CoO_4 showing the electron decay contributions for cluster size 3t6o representing model size "5t12o". The "spectator" centers generate pairs of "neutral" (bottom panel) and "ionic" antiferromagnetic states with one (middle panel) or two (top panel) electrons exchanged via superexchange. Color code: O $2s$ →Co(II) $1s$ (gray), O $2p$ →Co(II) $1s$ (light blue), Co(II) $3d \rightarrow 1s$ (red) electron decays.

The results presented in Figure 16.19 show corrected spectra that specifically show the effects of zero to two electrons being exchanged between the "spectator" Co centers. To better understand these results and the corrections made, Figure 16.20 shows the components of the $K\beta''$ feature from the 3t6o model, which represents the "5t12o" model with a total of two electrons exchanged, so that all potential antiferromagnetic state pairs are in the "ionic" antiferromagnetic state.

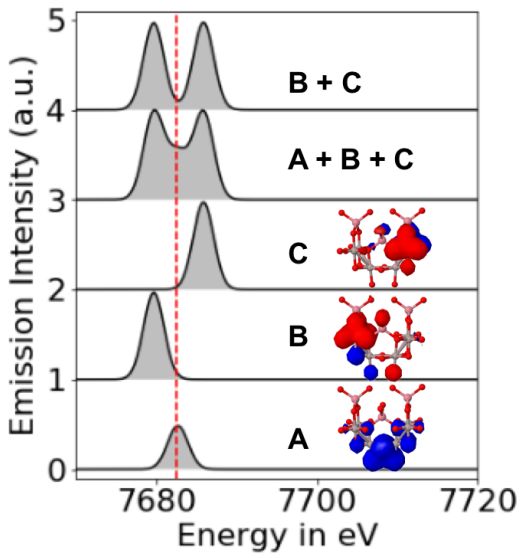

Figure 16.20: Components of the $K\beta''$ feature originating from O $2s$ →Co(II) $1s$ electron decays (gray) and their relevance in the antiferromagnetic scenarios in the "5t12o" model with two exchanged electrons. Panel A shows features originating from O $2s$ orbitals not associated with the "spectator" centers, panel B associated with the "spectator" center with reduced and panel C increased effective charge. The top two panels show the respective summed-up features.

The underlying features are associated with the O $2s$ →Co(II)$1s$ transitions. In panel A of Figure 16.20, the O 2s orbitals involved in this transition are not located at an oxygen bridging one of the two "ionic" antiferromagnetic spectator centers and the "emissive" center. As a result, the corresponding feature appears in the center of the overall spectrum, shown in panel A+B+C (second from the top). This case represents the "neutral" antiferromagnetic scenario, since no oxygen associated with a "spectator" center in an "ionic" state is involved, and is therefore irrelevant to the spectrum of a purely "ionic" antiferromagnetic scenario.

Moving to panel B of Figure 16.20, it represents a situation where the orbital with O 2s character is localized at the oxygen bridge between the "spectator" Co center and the "emissive" Co center. In this case the "spectator" Co center has a reduced effective charge compared to the "emissive" Co^{2+} center. It is Co^0 that represents two Co^{1+} ions in the "5t12o" model.

Similarly, panel C of Figure 16.20 shows the orbital with O 2s character localized at the oxygen bridge between the "spectator" and "emissive" Co centers, but with an increased effective charge of the "spectator" center compared to Co^{2+}. Here the "spectator" Co^{4+} center represents two Co^{3+} ions in the "5t12o" model.

To clearly distinguish the effect of "neutral" and "ionic" antiferromagnetic envi-

ronments, panel A+B in Figure 16.19 is used for the described case instead of panel A+B+C in Figure 16.20. The same adjustment applies to the case with one electron exchanged in the "ionic" antiferromagnetic case in Figure 16.19.

The orbital representation shown in Figure 16.20 not only provides a clear understanding of the structure of the model, but also strongly supports the thesis presented in Section 16.6 regarding $Al_2Cu(II)O_4$. It was found that the splitting observed in the $K\beta''$ feature, originating from the O $2s$ →Co(II)$1s$ transition, results from the altered effective charge of the "spectator" centers in the "ionic" antiferromagnetic states.

These modified effective charges directly influence the bond order of the corresponding oxygen orbitals contributing to the emission process in the "emissive" center via LMCT, leading to a splitting of the spectrum based on the modified tetrahedral crystal field of the "spectator" centers. The splitting is symmetric, i.e. whenever a feature associated with a reduced effective charge of a "spectator" center appears, a mirrored feature associated with a correspondingly increased charge of a "spectator" center also appears, since these centers always form pairs of "ionic" antiferromagnetically coupled centers. This symmetry applies not only to the O $2s$ →Co(II)$1s$ transition, but also to the part of the $K\beta_{2,5}$ feature that comes from the O $2p$ →Co(II)$1s$ transition.

The overall spectrum is a combination of the three subspectra representing different numbers of electrons exchanged (zero to two). However, determining the exact contributions of each subspectrum to the total spectrum is challenging due to several factors. One crucial factor is the energy of the core-ionized initial states, which is difficult to determine accurately with CASCI without taking into account the dynamic electron correlation as discussed above. So far, an ideal superposition of "neutral" and "ionic" antiferromagnetic initial states is assumed, implying that all subspectra contribute equally. This assumption does not lead to a satisfactory agreement with the experimental spectrum.

A comparison of the calculation and the experiment shows that the splitting of the double peak features is most consistent with the pure "ionic" antiferromagnetic case in the "5t12o" model, where all "spectator" center pairs adopt an "ionic" antiferromagnetic state, resulting in the exchange of two electrons. This suggests that the "ionic" antiferromagnetic states play a dominant role in shaping the overall spectrum. The final overall spectrum shown in Figure 16.21a is an approximation that balances the contributions of each subspectrum to match the experimental data. For the broadening and methodology used, this approximation assigns equal contributions of 12.5% each to the "neutral" and mixed "neutral" and "ionic" antiferromagnetic states with one exchanged electron, while the remaining 75% contribution

comes from the pure "ionic" antiferromagnetic state with two exchanged electrons.

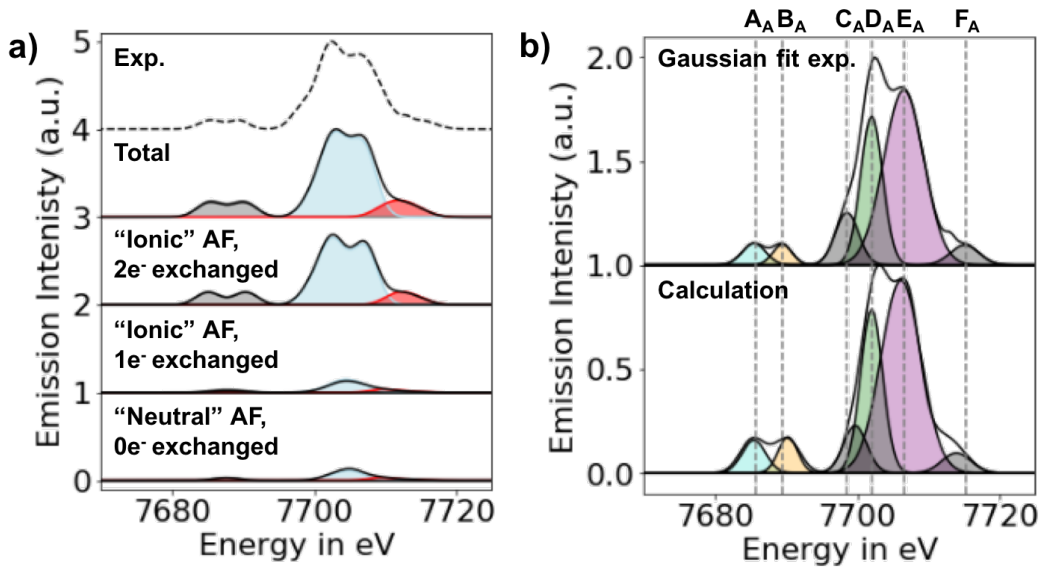

Figure 16.21: CASCI calculated spectra of Al_2CoO_4 in the "5t12o" model. **a)** Weighted contributions of subspectra with final states including "spectator" centers in "neutral" (0 electrons exchanged, bottom panel) and "ionic" antiferromagnetic states with one (second from bottom) and two (middle panel) electrons exchanged via superexchange, along with the total spectrum (second from top) and the experimental spectrum (top panel, dashed line), highlighting the underlying electron decays. Color code: O $2s$ →Co(II) $1s$ (gray), O $2p$ →Co(II) $1s$ (light blue), Co(II) $3d \rightarrow 1s$ (red) electron decays. **b)** Comparison of the Gaussian fit of the total CASCI spectrum (bottom panel) with the experimental Gaussian fit (top panel).

Figure 16.21b shows a Gaussian fit of the experimental data compared to a CASCI calculated spectrum with the same Gaussian fit structure. Features A through F in the Gaussian fit can be assigned to specific transitions.

Features A through E can be assigned primarily to LMCT and can be attributed primarily to the pure "ionic" antiferromagnetic case. A and B create the $K\beta''$ feature and originate from O $2s$ →Co$1s$ transitions. Feature A represents transitions of O $2s$ orbitals bridging the "emissive" center and the "spectator" centers with reduced effective charge. Feature B represents transitions of O $2s$ orbitals bridging the "emissive" center and the "spectator" centers with increased effective charge.

Features C through E are associated with O $2p$ →Co(II) $1s$ transitions and correspond to the lower energy region of the $K\beta_{2,5}$ feature. Features D and E are analogous to features A and B, respectively. Feature C arises from the broadening caused by the O $2p$ band, resulting in an asymmetric feature similar to that observed and

discussed for Co_2ZnO_4. Therefore, C corresponds to the asymmetric broadening of feature D. The corresponding asymmetry of feature E leads to an additional contribution to D, resulting in a higher intensity for feature D compared to E.

F represents intrametallic transitions Co(II) $3d \rightarrow 1s$. These intrametallic transitions also contribute slightly to feature D. No double peak feature splitting is observed here, leading to the conclusion that the intrametallic transitions are not affected by the antiferromegnatic environment in the way that the LMCT transitions are. This is in agreement with the results of the $K\beta_{1,3}/K\beta'$ mainline XES study, which also suggested that the intrametallic transitions Co(II) $3p \rightarrow 1s$ are independent of the antiferromagnetic effects. However, as noted above, the number of unpaired electrons included in the model affects the underlying structure in feature F. This effect is largely lost in the broadening of the model shown. A similar structure associated with feature F is also present in the experiment. This suggests that the correlation between the unpaired $3d$ electrons in the "emissive" and " spectator" centers may play a role in the outcome of the feature.

While the presented model agrees with the experiment and explains it well, a complementary thought experiment can also lead to a reasonable agreement with the observed total $K\beta_{2,5}/K\beta''$ VtC XES spectrum. If one takes the calculated 1t or better 2t4o spectrum, since it already contains the more pronounced asymmetry of the $K\beta_{2,5}$ features, and shifts it twice along the energy axis, once to lower energy and once in the opposite direction to achieve the double peak splitting, a reasonable agreement with the experimental data can be obtained. Consequently, the whole spectrum can also be interpreted as a combination of the local spectra unaffected by the environment, shifted to represent the changes in the environment caused by the "ionic" antiferromagnetic coupling. Figure 16.22 compares this approach with the "5t12o" model and experiment. The result of the "5t12o" model is still in better agreement with the experiment, since it takes into account that Co(II) $3d \rightarrow 1s$ is not affected by the change in the environment.

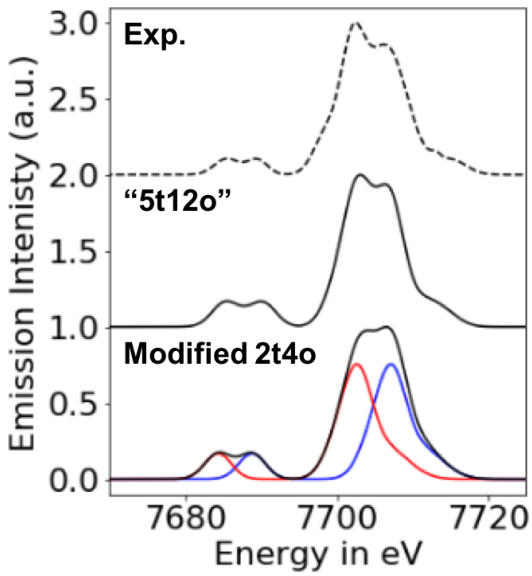

Figure 16.22: Comparison of CASCI $K\beta_{2,5}/K\beta''$ VtC XES spectra generated from the thought experiment (lower panel), where two 2t4o spectra were shifted along the axis to fit the upper (blue) and lower (red) energy double-peak features, the "5t12o" model (middle panel), and the experimental spectrum (upper panel, dashed line).

16.7.3 Co_3O_4

The calculated $K\beta_{2,5}/K\beta''$ VtC XES spectrum of Co_3O_4 using CASCI can be understood as the combination of the spectra of $Al_2Co(II)O_4$ and $Co(III)_2ZnO_4$, representing the tetrahedral Co(II) and octahedral Co(III) sites, respectively, as supported by the mainline XES study of $K\beta_{1,3}/K\beta'$ and preliminary one-electron results. In Figure 16.23, the composite CASCI $K\beta_{2,5}/K\beta''$ VtC XES spectrum of Co_3O_4 is obtained by normalizing the calculated spectra of the "5t12o" model for $Al_2Co(II)O_4$ and the 2t4o model for $Co(III)_2ZnO_4$. These spectra are then adjusted to obtain a Co(II):Co(III) ratio of 1:2, which represents the composition of Co_3O_4. Thus, the final spectrum of Co_3O_4 consists of a 1:2 ratio of the combined normalized spectra. Although the intensity of the calculated $K\beta''$ feature is again overestimated, the resulting overall spectrum agrees well with the experiment, as shown by the comparison with the Gaussian fit of the experiment in Figure 16.23.

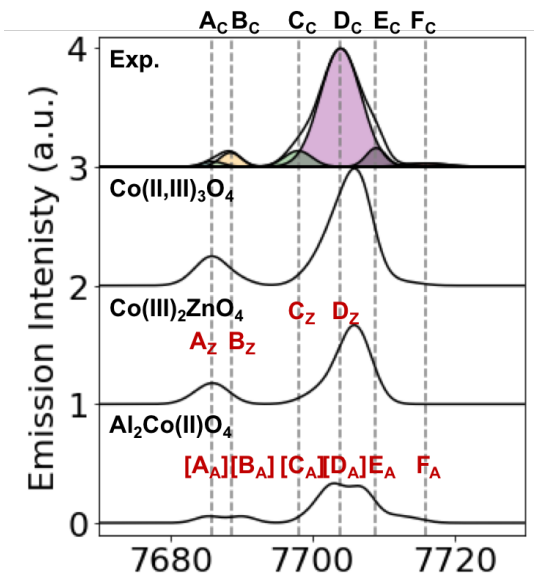

Figure 16.23: Comparison of the Gaussian fit of the experiment (top panel) with the computed $K\beta_{2,5}/K\beta''$ VtC XES spectrum of Co_3O_4 (second from top), which was generated as the sum of the ratio 2: 1 ratio representing the Co(III):Co(II) ratio in Co_3O_4 from the normalized CASCI calculated $K\beta_{2,5}/K\beta''$ VtC XES spectra of Co_2ZnO_4 (second from bottom) and Al_2CoO_4 (bottom panel).

The results in Figure 16.23 confirm that the Co(III) sites dominate the total spectrum due to their higher availability. Accordingly, the A-D features of the Co_2ZnO_4 and Co_3O_4 experimental Gaussian fits are equivalent and dominated by LMCT O $2s$ and O $3p$ to Co(III) $1s$ as described for Co_2ZnO_4.

The features E and F in the Gaussian fit of the experimental Co_3O_4 spectrum can be explained by the broader Co(II) subspectrum. In particular, feature E can be attributed partly to the LMCT of O $2p \rightarrow$ Co(II)$1s$ and partly to the higher energy region of the $K\beta_{2,5}$ feature in the $Al_2Co(II)O_4$ VtC XES spectrum caused by intrametallic Co(II) $3d \rightarrow 1s$ transitions. The intrametallic transition can also explain the F feature in the Gaussian fit of the Co_3O_4 $K\beta_{2,5}/K\beta''$ VtC XES spectrum.

16.8 Conclusions

In this chapter, a combined computational and experimental approach has been used to study the $K\beta_{2,5}/K\beta''$ valence-to-core X-ray emission (VtC XES) spectra of three cobalt oxide derivatives: Co_3O_4, $Co(III)_2ZnO_4$, and $Al_2Co(II)O_4$. The main idea was to analyze the spectra of $Co(III)_2ZnO_4$ and $Al_2Co(II)O_4$ as representative subspectra of the Co(III) and Co(II) sites in Co_3O_4. Both single-electron and CASCI (Complete Active Space Configuration Interaction) protocols with electrostatic em-

bedding were used. The computational models included both single-center and multicenter approaches. The investigations have provided a comprehensive understanding of the electronic structures of the cobalt oxide derivatives and how they are mirrored in the $K\beta_{2,5}/K\beta''$ VtC XES spectra.

The study started with an analysis of the experimental $K\beta_{2,5}/K\beta''$ VtC XES spectra, which showed that, as in the $K\beta_{1,3}/K\beta'$ mainline XES spectra, the Co_3O_4 spectra were dominated by intensity mechanisms originating from the Co(III) centers, as the overall spectrum of Co_3O_4 was found to be similar to that of Co_2ZnO_4. In this regard, the Gaussian fit of the experiment supported this first indication by also highlighting that the upper energy region of the $K\beta_{2,5}$ region did not coincide between Co_3O_4 and Co_2ZnO_4.

The convergence scheme for the one-electron and CASCI calculations was investigated, showing that the one-electron spectrum for all three cobalt oxide derivatives appeared to converge immediately, while this was not true for the CASCI calculated spectra.

The one-electron results showed good agreement with the assumed XES scheme as presented in Section 8.2 in Figure 8.3 on page 101, but did not show satisfactory agreement with the experiment. Furthermore, the one-electron calculated subspectra of the Co(II) and Co(III) sites in Co_3O_4 were found to be identical to those in Al_2CoO_4 and Co_2ZnO_4, as already known from the $K\beta_{1,3}/K\beta'$ mainline XES study. This justifies summing the CASCI spectra of Al_2CoO_4 and Co_2ZnO_4 to obtain the spectrum of Co_3O_4.

To investigate the influence of antiferromagnetic coupling on the $K\beta_{2,5}/K\beta''$ VtC XES spectra and its implications for the CASCI models of cobalt oxide derivatives, in particular Al_2CoO_4, a Cu(II) toy model was used as a preliminary investigation. The Cu(II) toy model showed that both "ionic" and "neutral" antiferromagnetic states must be considered to fully account for the total antiferromagnetic effect. However, it was observed that these "ionic" states can only be present in the spectator centers, since they change the effective charge of the centers. The metal center of interest must maintain an unchanged effective charge. To solve this problem, the concept of "spectator" centers was introduced, creating an antiferromagnetic environment for the "emissive" center where the emission process takes place. The "ionic" antiferromagnetic states in the "spectator" centers alter the electrostatic environment of the "emissive" center and influence the character of the oxygen orbitals that bridge the "spectator" and "emissive" centers and participate in the emission process.

The Cu model showed that this change in the electrostatic environment and bond order of the oxygen orbitals leads to the observed splitting in the $K\beta_{2,5}$ and

$K\beta''$ regions of the VtC XES spectra. These results highlight the importance of considering the interplay between "ionic" and "neutral" antiferromagnetic states and their influence on the spectroscopic features.

The results from the Cu(II) model and the $K\beta_{1,3}/K\beta'$ mainline XES study served as the basis for applying the CASCI protocol to study Co_2ZnO_4 and Al_2CoO_4. In the case of the diamagnetic Co_2ZnO_4, magnetic effects did not play a role. However, in order to accurately reproduce the asymmetric features observed in the experimental $K\beta_{2,5}/K\beta''$ VtC XES spectra, it was necessary to consider system sizes beyond the one-center model. The asymmetry became pronounced and the spectrum broadened as the oxygen orbital bands converged, indicating the importance of including larger cluster sizes.

The preliminary $K\beta_{1,3}/K\beta'$ mainline XES study indicated that the inclusion of excited $3d$ states in the "emissive" Co(III) center, in addition to the low-spin $3d$ states, was necessary. However, for the $K\beta_{2,5}/K\beta''$ VtC XES spectrum, this additional inclusion was not necessary. Therefore, the orbital picture for the $K\beta_{2,5}/K\beta''$ VtC XES spectrum is retained.

The model used for Al_2CoO_4, called "5t12o", consisted of an "emissive" center and pairs of "ionic" and "neutral" antiferromagnetically coupled "spectator" centers. This model gave good agreement with the experimental $K\beta_{2,5}/K\beta''$ VtC XES spectrum, explaining all the observed features. The splitting observed in the $K\beta_{2,5}$ and $K\beta''$ spectral features can be attributed to the presence of "ionic" states leading to changes in the electrostatic environment around the "emissive" center. The magnitude of the splitting depends on both the tetrahedral field splitting and the number of exchanged electrons. In particular, the best agreement with the experimental data was obtained when the system was predominantly in an "ionic" antiferromagnetic state.

While the splitting mainly affected the LMCT processes dominating the $K\beta''$ feature and the lower energy region of the $K\beta_{2,5}$ feature, the intrametallic Co $3d \rightarrow 1s$ transitions dominating the higher region of the $K\beta_{2,5}$ feature were largely unaffected by the antiferromagnetic environment. However, the number of unpaired $3d$ electrons in the model, and thus, the correlation between the unpaired $3d$ electrons of the different centers, seemed to play a role in the underlying structure and broadening of the associated feature.

The CASCI spectrum of Co_3O_4 was obtained by combining the CASCI results of Co_2ZnO_4 and Al_2CoO_4. In agreement with the analysis of the experimental VtC XES spectra, the dominant processes in the Co_3O_4 spectrum are related to the emissive centers in the Co(III) centers. The Co(II)-related processes are only visible in the high energy region of the $K\beta_{2,5}$ spectral feature.

In conclusion, the present study demonstrates the importance of combining experimental and theoretical approaches for a detailed understanding of the electronic structure of complex materials. The use of multi-step protocols combining different computational methods, including one-electron and CASCI approaches, provides a comprehensive picture of the electronic transitions and spectral features. Furthermore, the agreement between the computational and experimental results highlights the importance of an accurate computational protocol that can accurately model the electronic structure and predict the observed spectroscopic features. The insights gained from such studies are not only valuable for explaining and understanding the properties of complex materials, but can also guide the design and optimization of new materials for various applications.

17 Conclusions

The present work explored the possibilities of computational protocols that combine an electrostatic embedded cluster approach to model inorganic crystalline solid-state systems with molecular theoretical methods for accurate calculation of spectroscopic bulk properties.

First, a generalized protocol for modeling the bulk properties of solid state systems with an electrostatic embedded cluster approach using ORCA was presented. This includes the ability to treat these systems using the "classical" ORCA input environment and the newly developed Ionic-Crystal-QM/MM. The electrostatic embedding models consist of three domains. The first is the quantum cluster (QC), where the properties are calculated quantum mechanically. The second instance, the boundary region (BR), consists of electrostatic core potentials (ECPs) that separate the QC from the third instance, the point charge (PC) field. The ECPs account for missing terms at the interface of the QC and PC fields. The PCs introduce electrostatic effects into the model to mimic the long-range Coulomb behavior in the bulk.

It is then shown that, at the same level of theory, the accuracy of the calculated bulk properties is comparable to that of molecular and periodic calculations for solid-state systems. This is achieved by carefully designing the electrostatic environment and ensuring convergence of the QC size with respect to the selected property. Specifically, benchmark sets of systems were used to demonstrate this accuracy in terms of NMR nuclear shielding constants and resulting chemical shifts, as well as optical band gaps.

The NMR study included a range of ionic crystalline solid-state systems, including zinc blende and rock salt structures. The nuclei selected included halides, alkali and alkaline earth metals, and closed shell transition metals. The variety of nuclei, with all their different challenges, allowed a balanced analysis of the influence of the embedding and the different methods used. In particular, it was found that highly deshielded nuclei, such as alkali metals, are more sensitive to environmental changes. A number of DFT functionals were tested, including (meta-)GGA, hybrid and double-hybrid functionals, as well as MP2. The study showed an increasing

consistency of the nuclear shielding constants when moving from (meta-)GGA to hybrid to double-hybrid functionals. The latter gave results similar to MP2, while the first two groups showed a stronger functional dependence. A comparison of the calculated chemical shifts from the nuclear shielding constants with the experiments showed increasing accuracy in the same order of functional groups. The double-hybrid functional showed similar accuracy to MP2.

Similarly, the optical band gap benchmark study investigated various GGA, hybrid, and double-hybrid DFT functionals using both TD-DFT and the post-Hartree-Fock method bt-PNO-STEOM-CCSD for the determination of this property. The study focused on a variety of inorganic crystalline solid-state systems, mainly zinc blende and rock salt structures, along with organic semiconductors. For the latter, the fundamental band gaps were also calculated. The selection of materials covered a wide range of optical band gaps, from about 1 eV to 14 eV, allowing a comprehensive study of the different methods employed. The calculated optical band gaps showed increasing accuracy, starting from GGA with the largest MAE above 1.0 eV, through hybrid and double-hybrid functionals, to bt-PNO-STEOM-CCSD with the smallest MAE below 0.2 eV. Notably, the study showed that the accuracy achieved with bt-PNO-STEOM-CCSD was consistent across different band gap widths and materials analyzed.

In addition to the individual results of the studies, the two benchmark studies demonstrated the feasibility of computational protocols that combine the electrostatic embedded cluster approaches with a selection of computational methods from the molecular theory repertoire to calculate inherently different bulk properties of inorganic crystalline solid-state systems. While the two approaches converged at different QC sizes, highlighting the need to design the QCs for each property individually to obtain the most efficient protocol, both showed the advantage that the tested properties converged at the same point for all DFT functionals and the post-Hartree-Fock methods. Thus, they pointed out the potential of converging a model at a lower level of theory within the electrostatic embedded cluster approach and then recalculating this property at a higher level.

The developed approach was used to study the character and magnitudes of the band gaps of Co_3O_4. Since Co_3O_4 is a strongly correlated material with antiferromagnetic coupling, the previously developed protocol for converging the optical band gap with TD-DFT and recalculating it with an EOM-CC method had to be revised to accommodate its multireference character. Thus, the excited states were first calculated with (broken-symmetry) TD-DFT. Subsequently, the states were recalculated not only with EOM-CC, but also with SA-CASSCF and then with NEVPT2 and MR-EOM-CC, among others.

The local and global structures of Co_3O_4 added another layer to the problem. The material consists of antiferromagnetically coupled tetrahedral Co(II) sites, which locally exhibit high spin, and diamagnetically distorted octahedral Co(III) sites, which locally exhibit low spin. In the study of the band gap of Co_3O_4, the general, symmetric, and magnetic influences of the two distinct cobalt sites in the material were investigated using cobalt oxide derivatives: $Al_2Co(II)O_4$, representing the Co(II) sites, and $Co(III)_2ZnO_4$, representing the Co(III) sites. The results indicate that Co_3O_4 can be effectively modeled as the sum of the individual contributions of these two materials.

Experimental data from previous studies provided three potential optical band gaps of Co_3O_4 in the NIR and UV/Vis spectral regions. The computational protocol revealed that the energy range is primarily dominated by ligand field transitions local to the tetrahedrally coordinated Co(II) sites. The results emphasize the need to explicitly treat the antiferromagnetic coupling and to consider both "neutral" and "ionic" antiferromagnetic states, since the potential band gaps were dominated by Co centers involved in "ionic" and "neutral" antiferromagnetic states. The distorted octahedral Co(III) centers also exhibited ligand field transitions in the same energy range; however, these transitions were dipole-forbidden and predicted to be dark states. Nevertheless, they could potentially contribute to the overall band gaps.

The knowledge gained from the band gap study of Co_3O_4 was used to study the X-ray emission spectra of Co_3O_4 and its two derivatives, the antiferromagnetic $Al_2Co(II)O_4$ and the diamagnetic $Co(III)_2ZnO_4$.

A computational protocol has been developed by combining an established one-electron DFT method with an XES CASCI approach, extending the previously developed XES RASCI protocol to multiple centers with the more efficient CASCI machinery. The $K\beta_{1,3}/K\beta'$ mainline and $K\beta_{2,5}/K\beta''$ VtC XES spectra were first calculated using the DFT approach. The results showed that the Co_3O_4 spectra could be considered as the sum of the spectra of $Al_2Co(II)O_4$ and $Co(III)_2ZnO_4$ representing their tetrahedral Co(II) and distorted octahedral Co(III) sites, respectively, as in the case of the band gap study. The XES of Co_3O_4 was explained as the sum of Al_2CoO_4 and Co_2ZnO_4. This was justified by the preliminary one-electron calculations, which suggested that the Co(II) and Co(III) spectra arise independently. However, the one-electron approach was not sufficient to accurately reproduce either the $K\beta_{1,3}/K\beta'$ mainline or, especially for $Al_2Co(II)O_4$, the $K\beta_{2,5}/K\beta''$VtC XES spectra.

By applying the CASCI protocol, all experimental XES spectra could be reproduced. The results showed for the $K\beta_{1,3}/K\beta'$ mainline and the $K\beta_{2,5}/K\beta''$ VtC XES spectra that the Co_3O_4 spectra are dominated by the intensity contributed by the distorted octahedral Co(III) centers. While the $K\beta_{1,3}/K\beta'$ mainline spectra were

effectively calculated by applying only one center at a time, or for Co_3O_4 the sum of single center Co(II) and Co(III) calculations in the correct ratio, larger system sizes were required to calculate the $K\beta_{2,5}/K\beta''$ VtC XES spectra.

The study of the $K\beta_{1,3}/K\beta'$ mainline XES spectra was motivated by the intriguing observations made in the corresponding experimental spectrum of $Co(III)_2ZnO_4$. Despite the low spin nature of the material, it was expected on the basis of widely accepted theory that only a $K\beta_{1,3}$ spectral feature would be present, while the $K\beta'$ spectral feature would be absent. However, the experimental results revealed a distinct $K\beta'$ spectral feature. Using the CASCI protocol, it was determined that this feature can be accounted for by a series of excited final states involving electron excitations within the $3d$ shell. Furthermore, it was observed that these types of excited final states also contribute significantly to the $Al_2Co(II)O_4$ $K\beta_{1,3}/K\beta'$ mainline XES spectrum, suggesting a general intensity contribution from these states. The appearance of these states was explained by the Kramers-Heisenberg-Dirac expression.

The study of the $K\beta_{2,5}/K\beta''$ VtC XES spectra went beyond the conventional one-electron approach with CASCI, driven by intriguing observations in the experimental spectrum of $Al_2Co(II)O_4$. While the one-electron calculations successfully captured the general features of the $Co(III)_2ZnO_4$ and Co_3O_4 $K\beta_{2,5}/K\beta''$ VtC XES, they failed to predict and explain the presence of double peak features in both the $K\beta_{2,5}$ and $K\beta''$ spectral regions of the experimental $Al_2Co(II)O_4$ spectrum. For this purpose, the CASCI approach was applied, explicitly taking into account the "ionic" and "neutral" antiferromagnetic states, which were already found to be important in the band gap study.

The observed double peak splitting in the $K\beta_{2,5}/K\beta''$ VtC XES spectral features can be attributed to the presence of these different antiferromagnetic states, in particular the "ionic" antiferromagnetic states which were found to dominate the spectrum. These "ionic" antiferromagnetic states arise from the superexchange interaction between "ionic" antiferromagnetically coupled Co centers, which redistributes an unpaired electron between them. As a result, pairs of Co centers are formed, with one Co center having an increased formal charge and the other having a decreased formal charge. In the context of the XES process, a model has been developed in which these Co center pairs create an antiferromagnetic environment for the Co(II) center undergoing the XES process.

The presence of the antiferromagnetic environment influences both the electrostatic environment in general and the character of the oxygen orbitals located between the Co(II) center involved in the XES process and the neighboring Co centers participating in an "ionic" antiferromagnetic pair. These oxygen orbitals primar-

ily contribute to the intensity of the $K\beta_{2,5}/K\beta''$ features via LMCT processes and cause their observed splitting. Specifically, increasing the charge of a tetrahedral Co center bonded to said oxygen shifts the resulting spectral contribution to higher energy, while decreasing the charge shifts it to lower energy, ultimately resulting in the double peak feature. These results emphasize the importance of considering the interplay between "ionic" and "neutral" antiferromagnetic states and their influence on the spectroscopic properties, as well as the need to apply protocols beyond a one-electron description for this case.

In conclusion, the extensive studies conducted in this thesis have revealed the remarkable potential of molecular theory methods when applied to solid state problems. The solid-state field, typically viewed through the lens of physicists, can benefit from incorporating the perspectives and methods of chemists in addition to the established approaches. Adopting, in addition to conventional approaches, the localized viewpoint inherent in chemistry, focusing on individual atomic centers or local structures, as demonstrated in the cobalt oxide studies by focusing on local cobalt sites, enables a deeper and more complementary understanding of the properties of extended solid-state structures. Bridging the languages of physics and chemistry for solid-state systems, as emphasized in the first part of this thesis, reveals a significant overlap in the fields.

Moreover, while the primary focus of this work has been on the application of wavefunction-based methods beyond Hartree-Fock, and it has been shown several times throughout this work that the application of these methods leads to more accurate results, it is important to note that the successes achieved in this research extend beyond these methods alone. The use of multi-step protocols that combine wavefunction-based methods with DFT techniques has proven to be highly advantageous. Rather than taking an "either/or" approach, the results from the interplay of different techniques can lead to more accurate and insightful results as well as more efficient protocols. For example, in the benchmark studies presented, convergence of a property at a lower level of theory followed by recalculation at a higher level leads to fruitful results. Similarly, in the context of the cobalt oxide studies, the preliminary insights provided by DFT methods not only form the basis for subsequent wavefunction-based calculations, but also are complementary to their results.

Appendices

A Additional Information Part I

ORCA_CrystalPrep Keywords and Input File Structure

```
*****************************************************************************************************
Generate initial ORCA CrystalPrep Input
*****************************************************************************************************

=====================================================================================================
Usage: orca_crystalprep [Basename Input] [options]
=====================================================================================================

-----------------------------------------------------------------------------------------------------
[Options]:
-----------------------------------------------------------------------------------------------------
-geninput                    Generate Initial Input
-----------------------------------------------------------------------------------------------------
```

```
*****************************************************************************************************
Generate ORCA Embedding Cluster Inputs using the CrystalPrep Utility
*****************************************************************************************************

=====================================================================================================
Usage: orca_crystalprep [CrystalPrep Input]
=====================================================================================================

-----------------------------------------------------------------------------------------------------
[CrystalPrep Input Options]:
-----------------------------------------------------------------------------------------------------
General Definitions
-----------------------------------------------------------------------------------------------------
DoCIF                       true                    This will process a .cif file
DoXYZ                       true                    This will process a .xyz file
InputCIF                    "CIFFileName"           Set the name of the CIFFileName
InputXYZ                    "XYZFileName"           Set the name of the XYZFileName
-----------------------------------------------------------------------------------------------------
SuperCell Construction Definitions
-----------------------------------------------------------------------------------------------------
DoSuperCell                 true                    Flag to generate a SuperCell
SCDimension                 "axbxc"                 The Dimension of the SuperCell (e.g. "1x1x1")
InputCIF                    "CIFFileName"           Set the name of the CIFFileName
InputXYZ                    "XYZFileName"           Set the name of the XYZFileName
-----------------------------------------------------------------------------------------------------
Special Tasks on SuperCells
-----------------------------------------------------------------------------------------------------
DoFractional                 true                   Flag to Transform Cartesian to Fractional coordinates
DoSymmetryOperations         true                   Flag to enforce using built in Symmetry Operations
```

Figure A.1: Keyword list for ORCA_CrystalPrep (1).

```
-----------------------------------------------------------------------------------------------------
Embedding Cluster Definitions
-----------------------------------------------------------------------------------------------------
DoEmbedding                  true                    Flag to generate the files for the embedding approach
UseVolumeCriterion           true                    Volume Criterion to generate layers
UseDistanceCriterion         true                    Distance Criterion to generate layers
CellVolumeFraction           value                   Cell(UniCell/SuperCell) fraction (default 1.0)
DoMolecularFragments         value                   Define Molecular Fragments during the build
DoSimpleInput                true                    Flag to generate a conventional Embedding Cluster input
DoICQMMMInput                true                    Flag to generate a Ionic-Crystal-QMMM input
DoMCQMMMInput                true                    Flag to generate a Mol-Crystal-QMMM input
WritePDB                     true                    Flag to run a Ionic-Crystal-QMMM input from a PDF file
QCCharge                     Charge Number           Specify the total QC Charge
QCMult                       Multiplicity Number     Specify the total Multiplicity
-----------------------------------------------------------------------------------------------------
Special Tasks on Embedding Cluster Construction/Definition
-----------------------------------------------------------------------------------------------------
DoLayers                     true                    Request Layers Definition
1) Layers Definition. There are 2 Options:
            a) The Differnt regions are build in layers as multipoles of the UnitCell
            b) The Differnt regions are build in layers around a predefined QC cluster via a QCAtom List
QCLayers                     QC Layers Number        Specify the number of the QC Layers
ECPLayers                    ECP Layers Number       Specify the number of the ECP Layers
PCLayers                     PC Layers Number        Specify the number of the PC Layers
HFLayers                     HF Layers Number        Specify the number of the HF Layers
Example Input
QCLayers 1
2) Atoms Definition. This is alternative to Layers Definition (e.g. DoLayers false)
NQCAtoms                     QC Atoms  Number        Specify the number of the QC Atoms
NHFAtoms                     HF Atoms  Number        Specify the number of the HF Atoms
NECPAtoms                    ECP Atoms  Number       Specify the number of the ECP Atoms
NPCAtoms                     PC Atoms  Number        Specify the number of the PC Atoms
QCAtoms                      QC Atoms  List          Specify the List   of the QC Atoms (e.g. 0,1,4,10...
HFAtoms                      HF Atoms  List          Specify the List   of the HF Atoms (e.g. 0,1,4,10...
ECPAtoms                     ECP Atoms  List         Specify the List   of the ECP Atoms (e.g. 0,1,4,10...
PCAtoms                      PC Atoms  List          Specify the List   of the PC Atoms (e.g. 0,1,4,10...
Example Input
NQAtoms= 4
QCAtoms 0,1,4,10
SetHFAtoms                    true                    Set explicitely the HF Atoms
SetECPAtoms                   true                    Set explicitely the ECP Atoms
SetPCAtoms                    true                    Set explicitely the PC Atoms
SetPC2Atoms                   true                    Set explicitely the PC2 Atoms
-----------------------------------------------------------------------------------------------------
Redefine SuperCell Origin. This is for shifting the center origin to a desired atom during the SC Construction
This Helps to automatically construct desired Cluster structures using the Layers Definition
-----------------------------------------------------------------------------------------------------
ShiftOrigin                   true                    Request Origin Shift  to a particular Atom
ChosenAtom                    an Atom Number          The Number of the Chosen atom (e.g. 2)
-----------------------------------------------------------------------------------------------------
Neutralize the Embedded Cluster in the Simple Input
Note that in the Ionic-Crustal QMMM Input this step is taken care on demand during the QM/MM run
-----------------------------------------------------------------------------------------------------
ChargePoints                 the charge points       Specify the number of the charge points (default 1000)
ChargeStep                   the charge points       Define the step during the iterations (default 0.01)
ChargeThres                  the threshold           Define the neutralization threshold (default 0.01)
Neutralization Schemes:
NeutralizingScheme1          true                 ->  Neutralization is based on All Charges
NeutralizingScheme2          true                 ->  Neutralization is based on different charges
                                                      Equiping the ECP and PC regions
NeutralizingScheme3          true                 ->  Neutralization is based on PC2 Region
-----------------------------------------------------------------------------------------------------
Special Definitions for the .metainfo File in the Ionic-Crustal QMMM
This helps Setting Charge/Spin in a specific atom type
It can also aid the neutralization step of the Embedded Cluster in the Simple Input
-----------------------------------------------------------------------------------------------------
NAtomTypes                   Number of Atom Types    Specify The Atom types that will be defined
Example Input
#-------------------------
#Atom Type Charge Spin
#-------------------------
AtomTypes 2
Co    1    2.0   1.5
Co    2    3.0   0
end
This specifies the local Spin and Charge of a Td HS Co2+ center (Type 1) and a OH Co3+ center (Type 2)
During the Embedding cluster construction
-----------------------------------------------------------------------------------------------------

*************** ORCA CRYSTALPREP TOOL TERMINATED SUCCESFULLY ************
```

Figure A.2: Keyword list for ORCA_CrystalPrep (2).

```
%crystalprep

#************************
#Read CIF/XYZ
#************************
DoCIF true

#------------------------
#INPUT CIF/XYZ
#------------------------
#InputCIF "CIFName.cif"
#------------------------
#Set Special Tasks
#------------------------
#SpaceGroupNumber 200

#************************
#Generate SuperCell
#************************
DoSuperCell true
SCDimension "1x1x1"

#************************
#Setup Embedding Approach
#************************
DoEmbedding true
DoLayers true

#------------------------
#Call the Mol-QMMM
#------------------------
#DoMolecularFragments true

#------------------------
#------------------------
#Atom Type Charge Spin
#------------------------
#NAtomTypes 2
#Co 1 2.0|  1.5
#Co 2 3.0|  0.0

#************************
#Generate Inputs
#************************
#------------------------
# Simple/IC-QMMM inputs
#------------------------
#DoSimpleInput true
#DoICQMMMInput true

#Neutralize true
#------------------------
#Mol-QMMM inputs
#------------------------
#DoMCQMMMInput true

#------------------------
#QCCharge 0
#QCMult 1
#------------------------
end
```

Figure A.3: Template input file for ORCA_CrystalPrep.

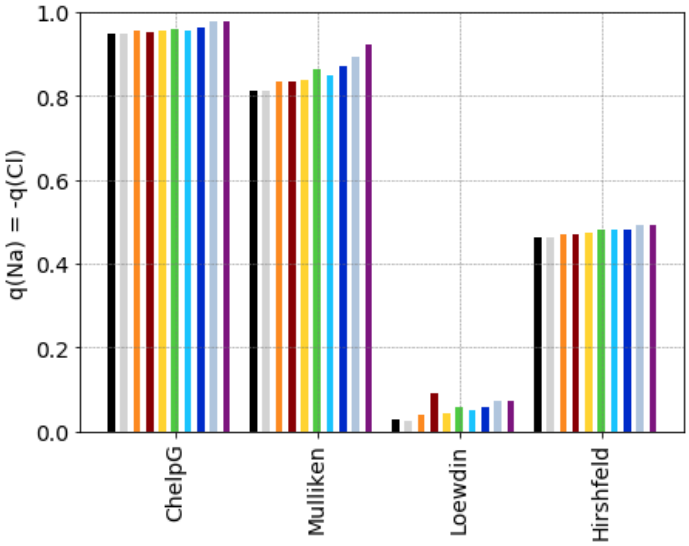

Figure A.4: Dependence of CHELPG, Mulliken, Loewdin, and Hirshfeld charges on the level of theory (basis set: def-TZVP). Color code: GGA functionals: BLYP (black), PBE (lightgray), BP86 (darkorange); hybrid functionals: B3LYP (darkred), B1LYP (gold), PBE0 (deepskyblue), double-hybrid functionals: B2PLYP (medium-blue); wavefunction-based method: DLPNO-CCSD (lightsteelblue), HF (purple); Cluster example: $[Na_4Cl_4]^0$.

B Additional Information Part III

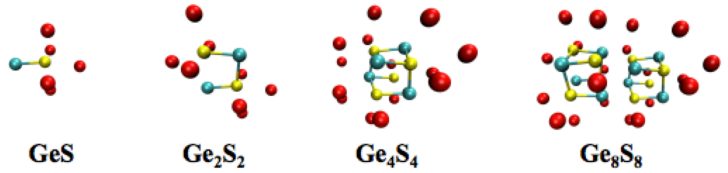

Figure B.1: Different QC sizes for GeS (orthorhombic structure) for the supercell approach (SCe) in the electrostatic embedded cluster model.

Table B.1: Comparison of experimental[118, 119, 266] and periodic[267] bond lengths in Å for different crystals.

Bond length	LiCl	NaCl	LiF	NaF	MgO	MgS
Experiment	2.56	2.82	2.02	2.31	2.10	2.56
PBE	2.58	2.86	2.04	2.35	2.13	2.62
TPSS	2.58	2.86	2.02	2.35	2.12	2.62

Example Input Files NMR

Example Input File ORCA

```
! NMR

! RI-DSD-BLYP/2013 D3BJ
! NoFrozenCore
%mp2 density relaxed end

! Grid4 NoFinalGrid

! VeryTightSCF
%eprnmr tol 1e-8 end
%method z_tol 1e-8 end

! pcSseg-3 decontract
! def2-qzvpp/C

! RIJK def2/JK
! RITrafo

%pointcharges "example.pc"

*xyz -5 1
[...]
*
```

Example Input Files DIRAC19

Non-relativistic:

```
**DIRAC
.PROPERTIES
**GENERAL
.CVALUE
2000.0
**MOLECULE
*CHARGE[...]
*BASIS
.DEFAULT
dyall.ae3z
**INTEGRALS
*READIN
UNCONTRACT
**HAMILTONIAN
.BSS
109
.SPINFREE
.DFT
PBE0
**WAVE FUNCTION
.SCF
**PROPERTIES
.SHIELDING
*NMR
.LONDON
**END OF
```

Scalar relativistic:

```
**DIRAC
.PROPERTIES
**MOLECULE
*CHARGE[...]
*BASIS
.DEFAULT
dyall.ae3z
**INTEGRALS
*READIN
.UNCONTRACT
**HAMILTONIAN
.BSS
109
.SPINFREE
.DFT
PBE0
**WAVE FUNCTION
.SCF
**PROPERTIES
.SHIELDING
*NMR
.LONDON
**END OF
```

Relativistic with SOC:

```
**DIRAC
.PROPERTIES
**MOLECULE
*CHARGE[...]
*BASIS
.DEFAULT
dyall.ae3z
**INTEGRALS
*READIN
.UNCONTRACT
**HAMILTONIAN
.BSS
099
.DFT
PBE0
**WAVE FUNCTION
.SCF
**PROPERTIES
.SHIELDING
*NMR
.LONDON
**END OF
```

Additional Information NMR Study

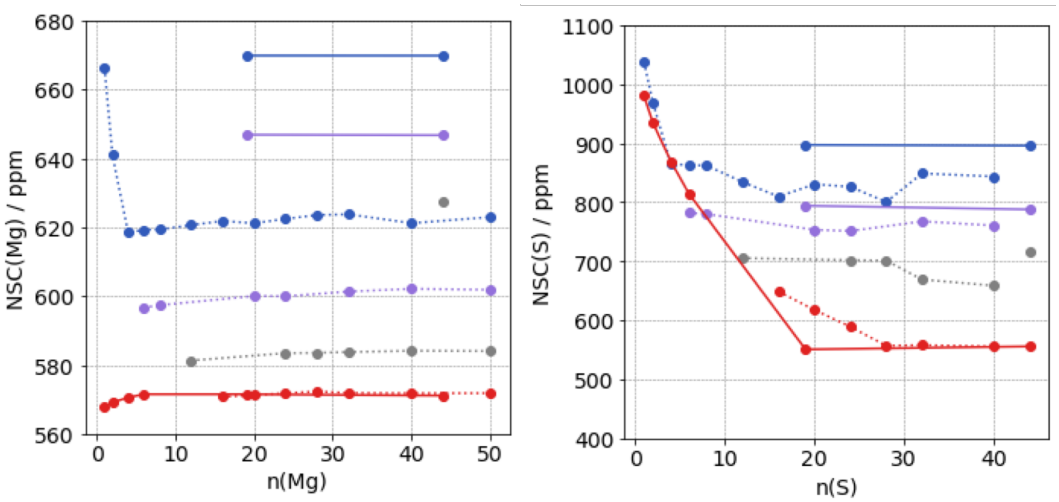

Figure B.2: PBE/pcSseg-2 computed NMR NSCs of Mg (left) and S (right) for MgS by employing a sequence of embedded SCe (dotted line) and SCl (solid line) type clusters for the different atom positions in the cluster. Color code: tip (blue), edge (purple), surface (grey), and bulk (red).

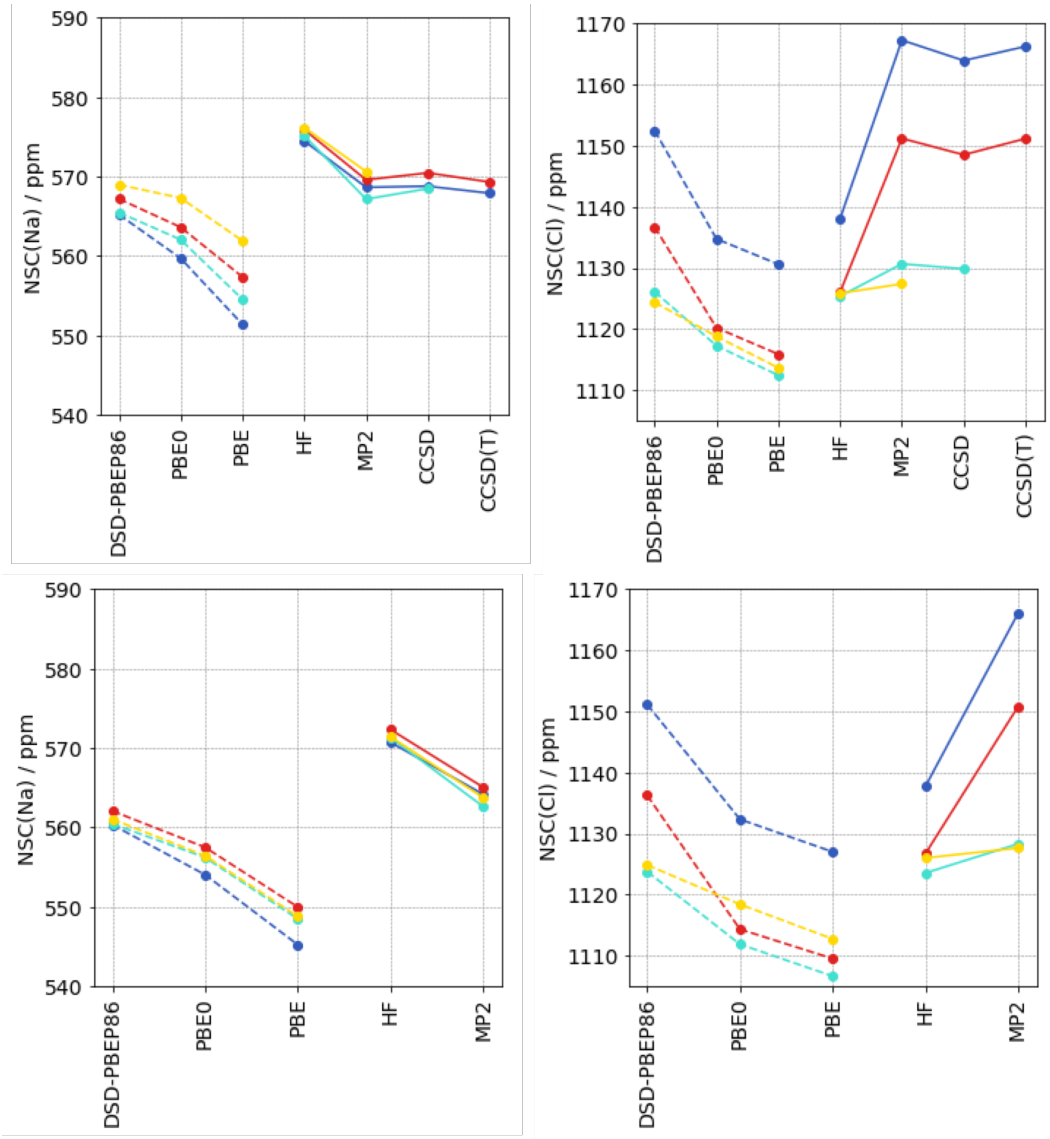

Figure B.3: Computed NMR NSCs of Na in $[NaCl_6]^{5-}$ (left) and Cl $[Na_6Cl]^{5+}$ (right) with respect to method and dependent on the basis set size of pcSseg-X for non-embedded (top) and embedded (bottom) clusters. Dashed line: PBE, PBE0, HF, DSD-PBEP86, solid line: HF, MP2, CCSD, CCSD(T). Color code: X=1 (blue), X=2 (red), X=3 (turquoise), X=4 (yellow)

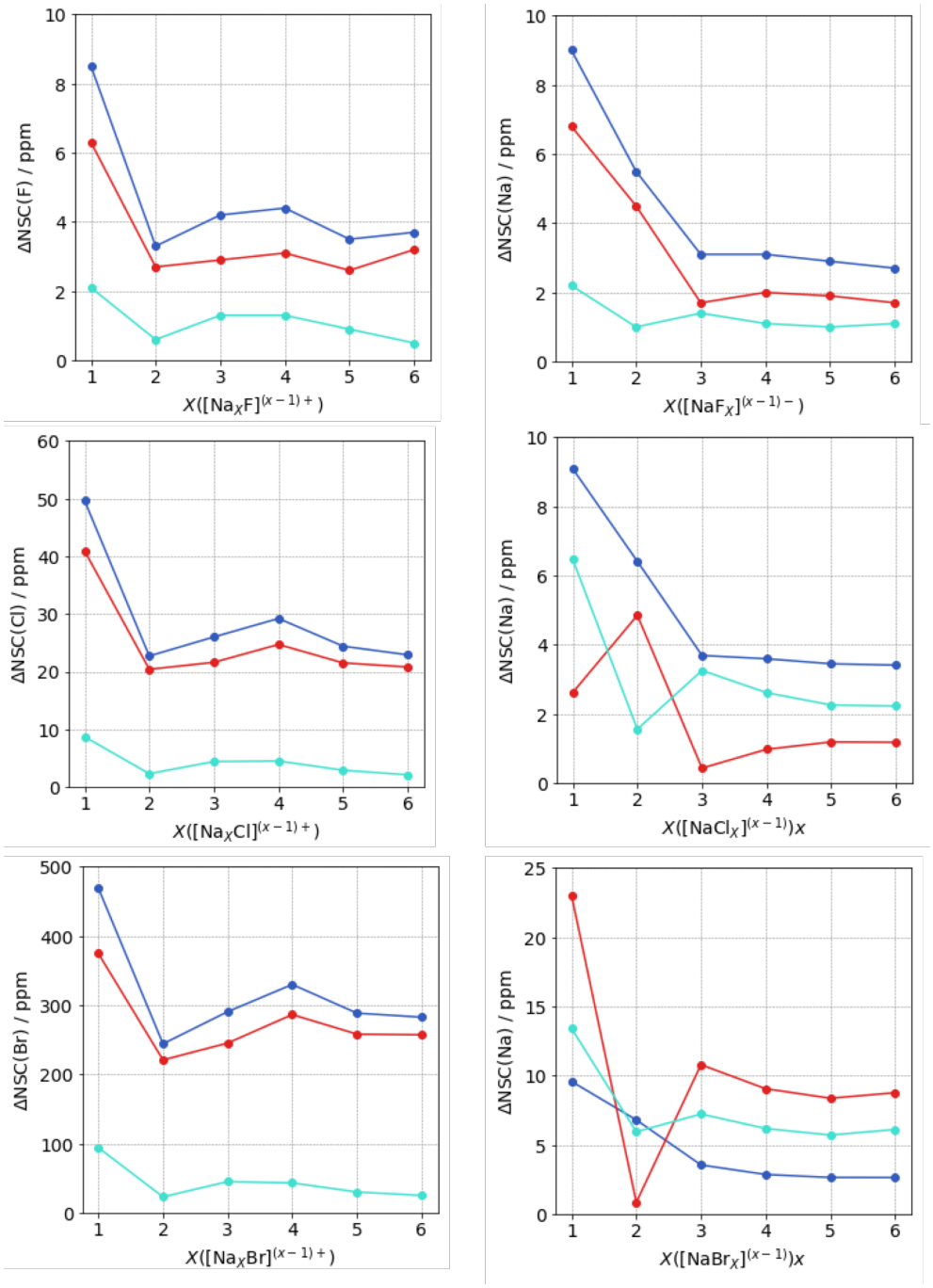

Figure B.4: Influence of the model size (non-embedded) on the relativistic effects for F, Cl, Br, (left) and Na (right) in NaF (top), NaCl (center), and NaBr (bottom). Color code: difference between non-relativistic NSC and scalar relativistic NSC (scalar relativistic effect) (blue), difference between non-relativistic NSC and total relativistic NSC (total relativistic effect = scalar relativistic effect + SOC) (red), difference between scalar relativistic NSC and total relativistic NSC (spin-orbit coupling effect) (turquoise). Level of theory: two-component Hamiltonian: X2C with PBE0/dyall.ae2z. Computed with DIRAC19.

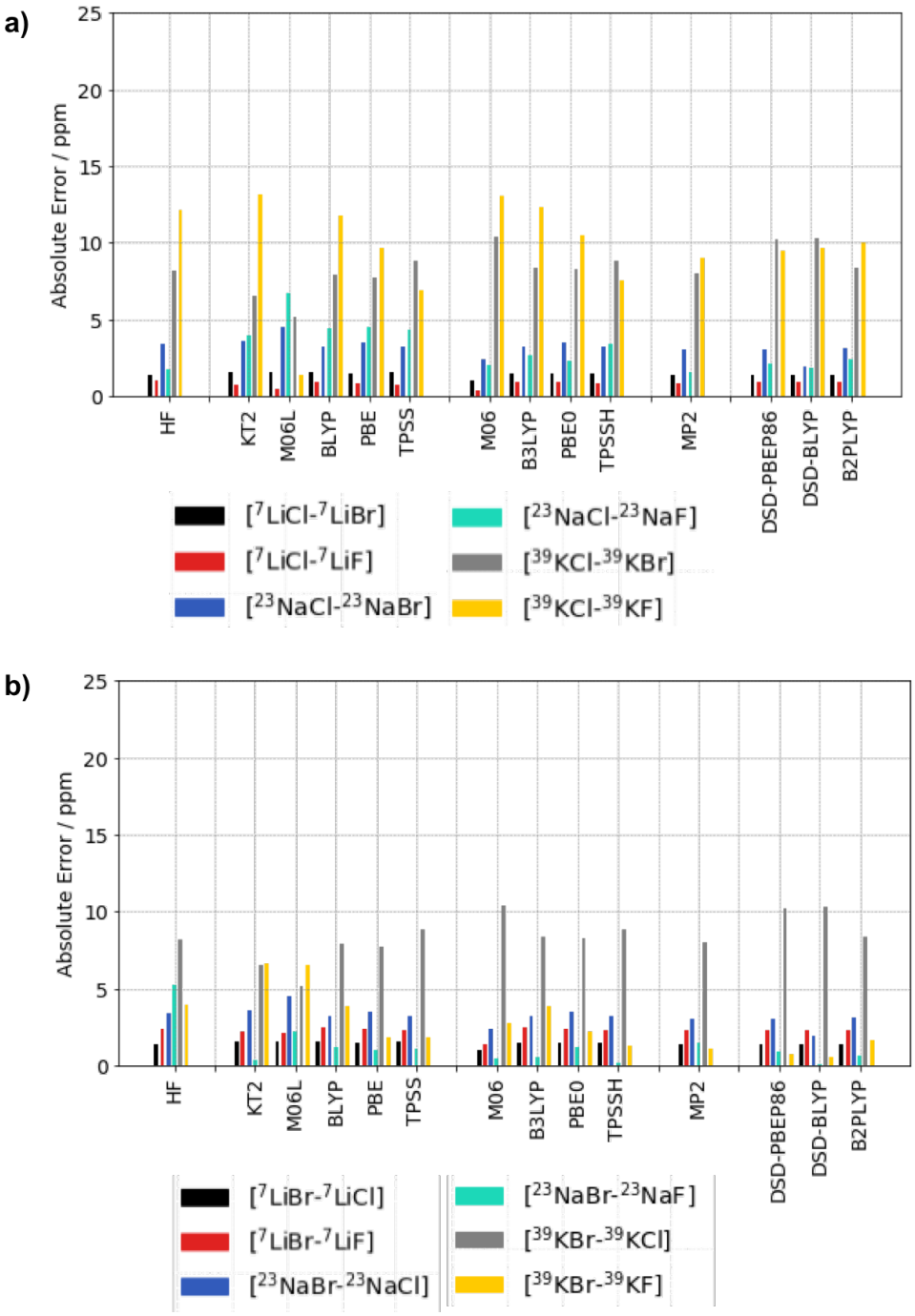

Figure B.5: Absolute errors in ppm of calculated vs. experimental chemical shifts with different methods for alkali metals with **a)** alkali metal chlorides and **b)** alkali metal bromides being the standard reference. Basis set: pcSseg-3.

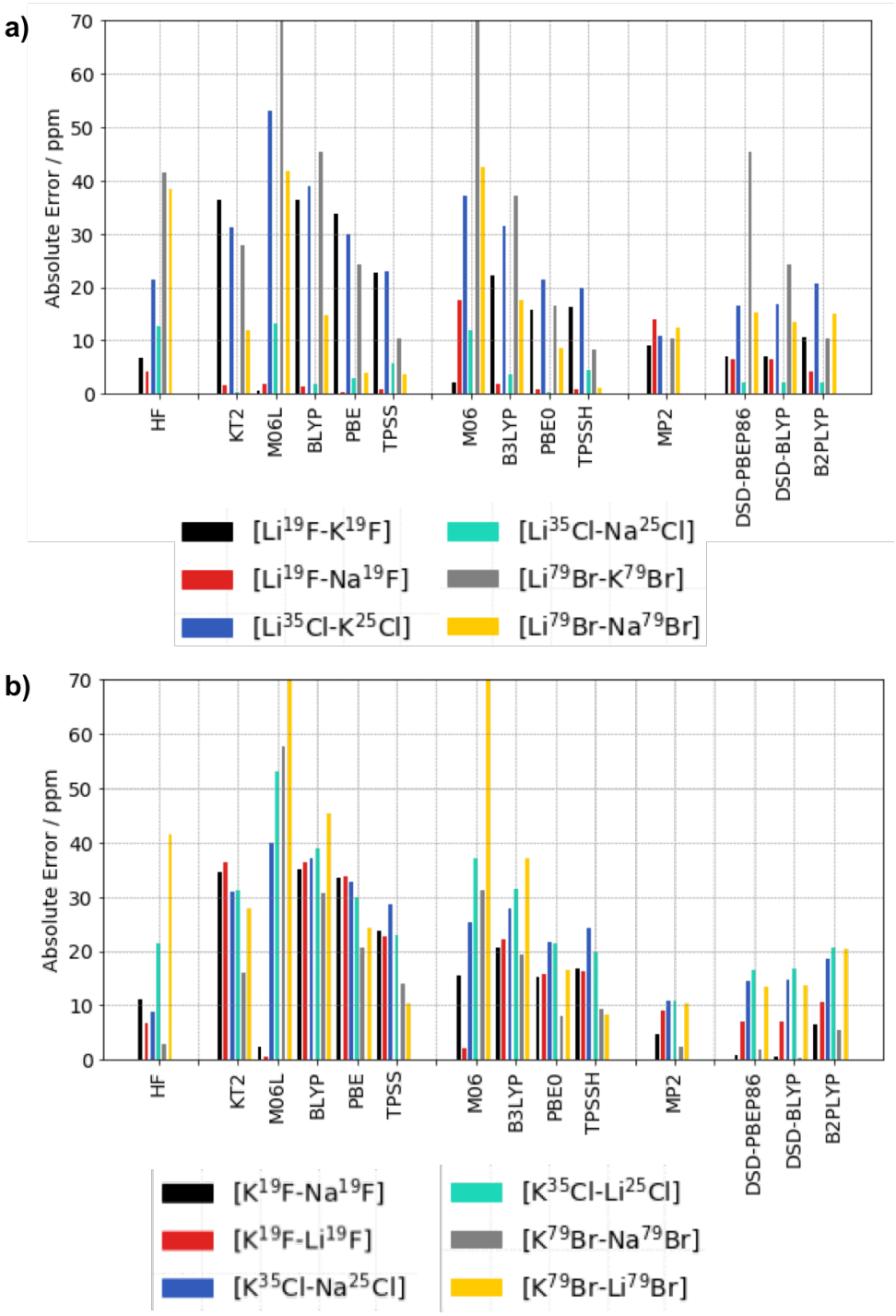

Figure B.6: Absolute errors in ppm of calculated vs. experimental chemical shifts with different methods for halides with **a)** lithium halides and **b)** potassium halides being the standard reference. Basis set: pcSseg-3.

Table B.2: Difference between NSC in ppm calculated with contracted pcSseg-2 and pcSseg-3 basis sets for different methods and all systems of the benchmark set of the size $[X_6Y_{19}]^{13-/26-}$ or $[X_4Y_{10}]^{12-}$.

		HF	KT2	M06L	BLYP	PBE	TPSS	M06	B3LYP	PBE0	TPSSH	MP2	DSD-PBEP86	DSD-BLYP	B2PLYP
Li	Br	0.59	0.52	0.40	0.45	0.51	0.57	0.31	0.50	0.56	0.58	0.70	0.72	0.68	-0.10
	Cl	0.92	0.82	0.91	0.73	0.78	0.87	0.81	0.80	0.85	0.89	0.98	0.95	0.95	-0.46
	F	0.71	0.75	1.17	0.67	0.72	0.87	0.81	0.70	0.74	0.86	0.79	0.12	0.75	0.08
Na	Br	0.42	0.86	0.80	0.90	0.86	0.60	-0.68	0.74	0.70	0.57	2.10	2.05	2.59	1.49
	Cl	0.77	1.11	1.17	1.12	1.09	0.73	0.02	0.99	0.95	0.72	2.11	1.43	1.52	1.17
	F	0.28	1.29	0.54	1.24	1.20	0.82	0.05	0.90	0.83	0.73	2.25	-1.87	-2.44	-5.90
K	Br	-1.93	-1.14	-0.47	-1.53	-1.29	-1.76	-0.13	-1.67	-1.39	-1.72	2.13	0.78	0.49	0.62
	Cl	-1.67	-0.33	1.32	-0.76	-0.54	-1.02	1.74	-1.10	-0.92	-1.12	-1.35	-1.45	-1.23	-0.63
	F	-0.46	2.46	1.54	2.08	2.14	1.29	3.61	1.20	1.03	0.97	3.55	2.32	1.86	1.93
Mg	O	0.99	1.34	2.88	1.49	1.28	0.91	-0.09	1.44	1.24	0.94	1.99	2.41	2.11	2.35
	S	1.17	2.15	1.22	1.93	2.28	2.85	-3.28	1.88	2.16	2.73	2.40	2.50	2.42	0.03
Zn	S	11.20	29.01	25.25	34.16	32.13	29.49	16.57	24.80	20.89	24.66	24.12	22.46	23.47	24.41
	Se	-0.92	8.70	10.47	10.11	8.02	6.29	4.54	5.99	3.24	4.30	5.76	8.07	8.33	9.34
F	K	0.64	3.29	31.90	4.82	5.29	5.96	69.54	4.26	4.15	5.65	6.19	10.33	5.33	9.64
	Li	2.59	-0.79	24.38	1.68	1.75	9.24	-11.1	2.11	2.16	7.75	7.91	7.56	4.41	6.21
	Na	1.70	-3.26	10.08	0.08	0.29	4.89	5.50	0.66	0.88	4.33	11.39	10.45	11.97	6.13
Cl	K	0.14	3.47	47.60	4.37	4.27	0.19	66.88	2.95	2.63	0.59	10.18	7.92	8.63	0.65
	Li	2.14	5.06	37.85	4.47	5.21	13.13	-4.66	3.91	4.30	10.96	33.98	17.55	18.95	15.31
	Na	2.44	7.57	32.66	6.56	7.84	9.46	44.36	5.29	5.89	8.45	25.22	15.52	16.40	16.99
Br	K	0.26	4.21	187.7	6.09	5.69	1.48	71.59	4.49	3.86	2.03	19.32	8.03	8.82	3.54
	Li	5.71	4.43	62.82	3.79	4.66	10.42	-12.80	4.66	5.47	9.07	25.33	15.14	16.11	12.57
	Na	3.66	7.25	28.21	6.99	7.78	12.55	109.90	6.28	6.61	11.63	23.44	13.32	14.49	5.24

Table B.3: Difference between the computed NSC in ppm with decontracted and contracted pcSseg-2 basis set for different methods and all systems of the benchmark set of the size $[X_6Y_{19}]^{13-/26-}$ or $[X_4Y_{10}]^{12-}$, respectively. The missing numbers are caused by calculation time and memory issues due to the high demand of the decontracted basis sets.

		HF	M06L	BLYP	PBE	TPSS	M06	B3LYP	PBE0	TPSSH	MP2	DSD-PBEP86	B2PLYP
	Br	-0.20	0.13	-0.05	-0.10	-0.18	0.03	-0.10	-0.15	-0.20			
Li	Cl	-0.07	0.36	0.09	0.05	-0.03	0.19	0.04	0.00	-0.05	0.07	0.02	0.02
	F	0.14	0.58	0.30	0.25	0.20	0.51	0.25	0.20	0.18	0.29	0.29	0.26
	Br		**-1.33**	-0.37	-0.38	-0.19		-0.40		-0.18			
Na	Cl	-0.35	**-1.42**	-0.49	-0.46	-0.19	-0.72	-0.53	-0.39	-0.20			
	F	-0.17	-0.84	-0.61	-0.62	-0.32	-0.35	-0.54	-0.43	-0.28	-0.10	-0.03	-0.22
	Br		-0.36	0.51	0.40	0.84			0.58	0.87			
K	Cl	0.99	-0.95	0.41	0.26	0.71	0.24	0.43	0.45	0.73			
	F	0.89	0.49	0.48	0.39	0.93	0.76	0.49	0.56	0.93	0.99		0.84
Mg	O	0.25	**-1.70**	-0.39	-0.36	0.26	**-1.64**	-0.30	-0.13	0.27			
	S	0.63	0.09	0.28	0.13	0.41	**1.30**	0.26	0.25	0.43			
Zn	S	**5.61**	**7.29**	**4.28**	**4.78**	**6.89**	**6.95**	**4.43**	**5.02**	**6.70**		**6.38**	**5.88**
	Se	**5.52**	**6.93**	**3.36**	**3.67**	**5.67**	**6.02**			**5.65**			
	K	-0.15	**-3.63**	-0.03	-0.13	-0.45	**-2.03**	-0.23	-0.22	-0.44		0.05	-0.01
F	Li	-0.26	-0.24	**1.78**	**1.88**	0.68	**-2.04**	**1.03**	**1.03**	0.54	-0.21	0.14	0.57
	Na	-0.11	**2.79**	**1.99**	**1.17**	0.42	**1.62**	**1.23**	0.60	0.32	0.13	0.26	0.68
	K	**1.04**	**3.31**	**1.60**	**1.52**	**2.33**	**3.55**	**1.39**	**1.40**	**2.17**			
Cl	Li	**1.37**	**5.62**	**2.35**	**1.93**	**3.01**	**2.62**	**1.96**	**1.68**	**2.76**	**1.33**	**1.43**	**1.61**
	Na	0.37	**8.85**	**1.03**	0.78	**2.01**		0.79	0.65	**1.84**			
	K		-0.04	**3.05**	**2.76**	**1.73**			**1.83**	**1.49**			
Br	Li	**-1.77**	**17.28**	**2.04**	**1.50**	**1.66**		**1.37**	0.80	**1.27**			
	Na		**15.72**	**2.22**	**2.39**	**2.46**	**-66.90**	**1.72**		**2.20**			

Table B.4: NMR NSCs in ppm for **a)** LiF, **b)** NaF, **c)** LiCl, **d)** NaCl, **e)** LiBr, and **f)** NaBr for the embedded and non-embedded systems with cluster size $[XY_6]^{5-}$ and $[X_6Y]^{5+}$ for different basis sets and methods.

a)		Lithium						Fluoride					
		embedded		non-embedded				embedded		non-embedded			
	pcSseg-X	HF	MP2	HF	MP2	CCSD	CCSD(T)	HF	MP2	HF	MP2	CCSD	CCSD(T)
$[LiF_6]^{5-}$	1	93.73	93.18	91.40	89.68	89.72	89.53	452.14	451.28	289.51	210.58	226.67	214.70
	2	93.71	92.85	93.47	92.71	92.68	92.53	441.45	443.10	335.01	242.85	274.40	247.82
	3	93.64	92.77	94.54	96.59	96.80	107.63	435.68	432.79	178.55	-459.63	-839.50	-5593.36
	4	93.27						431.72					
$[Li_6F]^{5+}$	1	94.92	94.72	94.96	94.78	94.78	89.53	441.68	448.29	438.41	444.95	445.04	445.24
	2	95.02	94.72	95.05	94.76	94.75	92.53	435.14	439.36	434.14	435.01	435.90	435.54
	3	95.04	94.72	95.07	94.86	94.87	94.84	435.76	435.26	433.54	432.15	433.33	432.60
	4	94.92						431.90					

b)		Sodium						Fluoride					
		embedded		non-embedded				embedded		non-embedded			
	pcSseg-X	HF	MP2	HF	MP2	CCSD	CCSD(T)	HF	MP2	HF	MP2	CCSD	CCSD(T)
$[NaF_6]^{5-}$	1	574.65	565.77	577.21	568.13	569.55	568.70	473.99	477.37	410.15	372.63	380.24	376.33
	2	573.82	563.67	581.27	573.80	575.66	574.48	450.43	453.37	398.17	352.69	370.77	359.56
	3	573.85	561.67	581.80	572.53	574.38	572.95	449.22	447.84	398.54	283.38	286.68	212.22
	4	573.81						445.45					
$[Na_6F]^{5+}$	1	614.26	612.30	614.06	612.21	612.54	612.31	467.54	473.57	464.71	470.83	469.66	470.22
	2	615.29	613.26	614.46	612.26	612.76	612.47	451.57	453.88	449.53	453.40	453.15	453.48
	3	614.75	611.77	613.92	610.82	611.28	610.98	449.79	448.60	448.13	448.87	448.69	448.51
	4	614.76						449.32					

c)		Lithium						Chloride					
		embedded		non-embedded				embedded		non-embedded			
	pcSseg-X	HF	MP2	HF	MP2	CCSD	CCSD(T)	HF	MP2	HF	MP2	CCSD	CCSD(T)
$[LiCl_6]^{5-}$	1	93.89	93.50	91.87	91.26	91.29	91.18	1086.26	1093.27	1031.97	1034.44	1034.10	1032.56
	2	93.51	92.81	92.10	91.34	91.42	91.29	1077.19	1089.81	1036.12	1038.59	1038.65	1035.98
	3	92.66	92.06	92.74	92.21	92.26	92.15	1079.26	1077.63	993.13	956.20	977.25	960.98
	4	92.81						1071.08					
$[Li_6Cl]^{5+}$	1	94.88	94.75	94.93	94.80	94.78	94.77	1102.19	1129.62	1106.86	1135.72	1133.12	1134.47
	2	94.85	94.63	94.87	94.65	94.62	94.61	1101.58	1119.50	1101.34	1120.37	1119.01	1120.57
	3	94.98	94.83	95.01	94.86	94.84	94.83	1099.32	1102.37	1102.36	1105.65	1105.87	1105.88
	4	94.86						1100.65					

d)

		Sodium						Chloride					
		embedded		non-embedded				embedded		non-embedded			
	pcSseg-X	HF	MP2	HF	MP2	CCSD	CCSD(T)	HF	MP2	HF	MP2	CCSD	CCSD(T)
$[NaCl_6]^{5-}$	1	570.73	564.21	574.48	568.65	568.79	567.91	1112.53	1123.94	1090.63	1098.23	1097.43	1096.96
	2	572.34	565.07	575.91	569.59	570.47	569.31	1105.53	1116.79	1086.15	1089.51	1089.30	1087.85
	3	571.33	562.68	575.14	567.17	568.48	567.12	1104.55	1105.88	1081.71	1073.23	1078.81	1074.29
	4	571.45						1096.67					
$[Na_6Cl]^{5+}$	1	612.94	611.97	612.47	611.44	611.43	611.32	1136.24	1163.85	1138.07	1167.28	1163.95	1166.26
	2	613.40	612.39	612.87	611.75	611.89	611.73	1125.73	1149.52	1126.03	1151.21	1148.53	1151.18
	3	613.24	611.47	612.71	610.84	611.00	610.82	1120.99	1125.58	1125.39	1130.69	1129.87	1130.50
	4	613.27						1124.84					

e)

		Lithium						Bromide					
		embedded		non-embedded				embedded		non-embedded			
	pcSseg-X	HF	MP2	HF	MP2	CCSD	CCSD(T)	HF	MP2	HF	MP2	CCSD	CCSD(T)
$[LiBr_6]^{5-}$	1			91.83	91.35	91.36	91.27			2914.86	2920.25	2919.00	2918.10
	2			92.07	91.33	91.40	91.27			2903.98	2900.21	2901.65	2897.56
	3			92.60	91.94					2825.12	2784.90		
	4												
$[Li_6Br]^{5+}$	1			94.89	94.77	94.75	94.74			3071.36	3104.03	3104.11	3107.66
	2			94.82	94.61	94.58	94.57			3039.44	3051.93	3051.17	3053.26
	3			94.97	94.84	94.81	94.80			3041.81	3045.64	3045.97	3045.83
	4												

f)

		Sodium						Bromide					
		embedded		non-embedded				embedded		non-embedded			
	pcSseg-X	HF	MP2	HF	MP2	CCSD	CCSD(T)	HF	MP2	HF	MP2	CCSD	CCSD(T)
$[NaBr_6]^{5-}$	1		572.03	566.66	566.81	566.03			3021.46	3030.64	3029.93	3029.25	
	2			572.97	566.92	567.81	566.63			2993.14	2992.51	2992.77	2991.16
	3			572.93	565.01					2980.14	2968.24		
	4												
$[Na_6Br]^{5+}$	1			612.13	611.27	611.22	611.10			3145.47	3181.58	3180.74	3186.11
	2			612.29	611.41	611.49	611.21			3089.87	3107.31	3105.40	3109.02
	3			612.22	610.54	610.62	610.46			3089.24	3095.73	3094.49	3095.29
	4												

Table B.5: Influence of basis set size on the relativistic effect for **a)** Na and **b)** Cl in NaCl. Computational level: two-component Hamiltonian: X2C[382, 383] with PBE0/dyall.ae2z. Computed with DIRAC19.

a)	Non-relativistic in ppm	Scalar Relativistic in ppm	Relativistic with SOC in ppm	ΔNon-relativistic: Scalar relativistic in %	ΔNon-relativistic: Relativistic with SOC in %
dyall.ae2z	602.7	611.8	605.3	1.51	0.43
dyall.ae3z	596.6	606.2	600.3	1.59	0.62
dyall.ae4z	597.6	607.1	598.3	1.61	0.13
b)	Non-relativistic in ppm	Scalar Relativistic in ppm	Relativistic with SOC in ppm	ΔNon-relativistic: Scalar relativistic in %	ΔNon-relativistic: Relativistic with SOC in %
dyall.ae2z	2168.5	2218	2209.4	2.28	1.88
dyall.ae3z	1917.8	1967.2	1959.3	2.58	2.17
dyall.ae4z	1741.8	1789.4	1781.6	2.73	2.28

Table B.6: Comparison of non-relativistic NSCs for **a)** metals and **b)** halides computed with different programs (ORCA and DIRAC19) and methods. The non-relativistic DIRAC19 results are obtained by a calculation with the speed of light = 2000 a.u. except LEVY-LEBLOND (already non-relativistic). Basis Set ORCA: pcSseg-2, Basis Set DIRAC19: dyall.*. Models are non-embedded. Functional: PBE0. All values in ppm.

a)	ORCA	DIRAC19			
	Non-relativistic	X2C		BSS	
	pcSseg-2	ae2z	ae3z	ae2z	ae3z
$[LiF_6]^{5-}$	91.0	115.1	157.0	115.3	121.2
$[LiCl_6]^{5-}$	90.5	141.7	155.2	98.5	97.5
$[LiBr_6]^{5-}$	90.3	147.9	168.5	97.9	95.7
$[NaF_6]^{5-}$	568.0	751.2	738.1	595.8	628.5
$[NaCl_6]^{5-}$	563.6	798.2	769.7	568.8	573.0
$[NaBr_6]^{5-}$	560.0	812.7	787.2	565.1	566.5
$[KF_6]^{5-}$	1226.3	1567.7	1542.2	1292.8	1298.3
$[KCl_6]^{5-}$	1182.0	1620.5	1596.9	1232.0	1281.2
$[KBr_6]^{5-}$	1178.6	1581.1	1607.7	1216.1	1238.5
$[MgO_6]^{10-}$	568.0	1037.7	1040.8	562.7	560.7
$[MgS_6]^{10-}$	579.7	1038.1	1043.4	595.3	590.5
$[ZnS_4]^{6-}$	1384.1	1880.4	2441.4	1498.8	1560.2
$[ZnSe_4]^{6-}$	1472.5	2050.4	1541.2	1571.7	1582.9

b)	ORCA	DIRAC19						
	Non-relativistic	X2C		BSS		LVCORR	LEVY-LEBLOND	URKBAL
	pcSseg-2	ae2z	ae3z	ae2z	ae3z	ae2z	ae2z	ae2z
$[Li_6F]^{5+}$	422.7	779.8	-362.1	424.0	423.4	299.6	-	425.6
$[Na_6F]^{5+}$	441.1	903.8	918.1	446.8	441.2	-	446.8	447.4
$[K_6F]^{5+}$	310.1	735.5	1578.3	346.3	307.9	-	346.3	349.7
$[Li_6Cl]^{5+}$	1089.7	1896.1	1342.9	1099.3	1095	838.7	1099.0	1100.2
$[Na_6Cl]^{5+}$	1120.2	1708.0	997.0	1142.6	1121.7	880.1	1142.3	1142.2
$[K_6Cl]^{5+}$	984.1	1804.4	2160.1	1042	985.8	780.8	1041.7	1043.4
$[Li_6Br]^{5+}$	3008.3	5062.8	3655.2	3041.9	3025.3	2674.5	3039	3041.9
$[Na_6Br]^{5+}$	3074.2	4567.9	2742.6	3129.1	3081.9	2758.3	3126.1	3126.5
$[K_6Br]^{5+}$	2842.7	4774.9	4300.6	2971.5	2847.2	2600.6	2968.5	2969.4

Table B.7: Total relativistic effect (difference between non-relativistic and relativistic calculation including spin-orbit coupling effect) for **a)** metals and **b)** halides computed with different methods. Level of theory: PBE0/dyall.*. Computed with DIRAC19. All values in ppm.

a)	two-component			
	X2C		BSS	
	ae2z	ae3z	ae2z	ae3z
$[LiF_6]^{5-}$	-0.9	0.6	0.4	0.5
$[LiCl_6]^{5-}$	-1.6	0.3	1.0	0.5
$[LiBr_6]^{5-}$	-6.0	1.2	3.1	1.3
$[NaF_6]^{5-}$	1.7	3.0	16.3	17.5
$[NaCl_6]^{5-}$	1.2	3.8	16.6	15.0
$[NaBr_6]^{5-}$	-8.8	5.4	19.5	12.8
$[KF_6]^{5-}$	18	15.8	86.8	89.2
$[KCl_6]^{5-}$	14.1	18.6	85.1	87.9
$[KBr_6]^{5-}$	7.1	13.9	81.3	79.1
$[MgO_6]^{10-}$	3.9	5.0	28.8	23.6
$[MgS_6]^{10-}$	4.3	-14.0	25.8	8.7
$[ZnS_4]^{6-}$	-92.8	-87.4	350.7	351.6
$[ZnSe_4]^{6-}$	-198.7	-333.2	483.6	471.9

b)	two-component				four-component	
	X2C		BSS		URKBAL	LVCORR
	ae2z	ae3z	ae2z	ae3z	ae2z	ae2z
$[Li_6F]^{5+}$	2.5	2.1	8.7	9.6	4.0	4.2
$[Na_6F]^{5+}$	3.2	7.5	8.9	12.3	3.4	-
$[K_6F]^{5+}$	3.6	20.0	9.2	13.1	1.6	-
$[Li_6Cl]^{5+}$	27.3	9.6	61.8	65.5	28.8	30.0
$[Na_6Cl]^{5+}$	20.8	7.4	62.0	66.8	29.4	30.9
$[K_6Cl]^{5+}$	21.4	27.0	61.6	68.6	27.5	28.7
$[Li_6Br]^{5+}$	320.7	106.6	568.9	583.7	294	299.8
$[Na_6Br]^{5+}$	257.3	71	572.1	587.2	300.8	306.4
$[K_6Br]^{5+}$	252.9	158.9	566.3	579.9	294.3	301.9

Table B.8: Scalar relativistic effect (difference between non-relativistic and relativistic calculation excluding spin-orbit coupling effect) for **a)** metals and **b)** halides computed with different methods. Level of theory DIRAC19: PBE0/dyall.*, relativity: spin free two-component Hamiltonians (X2C, BSS). All values in ppm.

a)	X2C		BSS	
	ae2z	ae3z	ae2z	ae3z
$[LiF_6]^{5-}$	0.0	0.2	0.3	0.4
$[LiCl_6]^{5-}$	-0.2	0.0	0.4	0.4
$[LiBr_6]^{5-}$	-0.8	0.1	0.5	0.4
$[NaF_6]^{5-}$	2.7	2.9	16.6	17.5
$[NaCl_6]^{5-}$	3.4	3.6	16.5	17.7
$[NaBr_6]^{5-}$	2.7	3.4	17.0	18.0
$[KF_6]^{5-}$	15.6	16.0	87.8	89.2
$[KCl_6]^{5-}$	17.8	19.5	88.5	89.1
$[KBr_6]^{5-}$	13.6	18.2	90.7	93.2
$[MgO_6]^{10-}$	5.6	7.2	20.8	20.8
$[MgS_6]^{10-}$	7.9	3.8	21.5	22.1
$[ZnS_4]^{6-}$	-68.3	-59.9	326.2	331.2
$[ZnSe_4]^{6-}$	-93.6	-140	337.6	340.1
b)	X2C		BSS	
	ae2z	ae3z	ae2z	ae3z
$[Li_6F]^{5+}$	3.0	0.8	8.7	9.5
$[Na_6F]^{5+}$	3.7	6.6	9.3	12.5
$[K_6F]^{5+}$	4.2	15.9	10.0	13.8
$[Li_6Cl]^{5+}$	29.2	11.7	62.1	65.3
$[Na_6Cl]^{5+}$	22.9	10.6	62.8	67.3
$[K_6Cl]^{5+}$	23.8	30.3	63.4	69.7
$[Li_6Br]^{5+}$	344.7	103.6	571.2	581.7
$[Na_6Br]^{5+}$	282.7	82.6	576.3	585.9
$[K_6Br]^{5+}$	284.5	190.0	571.8	579.0

Table B.9: Spin-orbit coupling effect (difference between relativistic calculations excluding and including spin-orbit coupling effects) for **a)** metals and **b)** halides computed with different methods. Level of theory DIRAC19: PBE0/dyall.*. All values in ppm.

a)	X2C		BSS	
	ae2z	ae3z	ae2z	ae3z
$[LiF_6]^{5-}$	-0.9	0.8	0.1	0.0
$[LiCl_6]^{5-}$	-1.4	0.2	0.6	0.1
$[LiBr_6]^{5-}$	-5.1	1.2	2.6	0.9
$[NaF_6]^{5-}$	-1.1	0.0	-0.3	0.0
$[NaCl_6]^{5-}$	-2.2	0.2	0.1	-2.7
$[NaBr_6]^{5-}$	-11.4	2.0	2.5	-5.2
$[KF_6]^{5-}$	2.4	-0.2	-1.0	0.0
$[KCl_6]^{5-}$	-3.8	-0.9	-3.4	-1.2
$[KBr_6]^{5-}$	-6.5	-4.2	9.4	-14.1
$[MgO_6]^{10-}$	-1.7	-2.2	8.0	2.8
$[MgS_6]^{10-}$	-3.6	-17.8	4.2	-13.5
$[ZnS_4]^{6-}$	-24.5	-27.5	24.5	20.4
$[ZnSe_4]^{6-}$	-105.1	-193.3	146.0	131.8
b)	X2C		BSS	
	ae2z	ae3z	ae2z	ae3z
$[Li_6F]^{5+}$	-0.5	1.3	0.0	0.1
$[Na_6F]^{5+}$	-0.5	0.9	-0.3	-0.3
$[K_6F]^{5+}$	-0.6	4.1	-0.8	-0.7
$[Li_6Cl]^{5+}$	-2.0	-2.1	-0.4	0.2
$[Na_6Cl]^{5+}$	-2.1	-3.2	-0.8	-0.5
$[K_6Cl]^{5+}$	-2.5	-3.3	-1.7	-1.2
$[Li_6Br]^{5+}$	-24.0	-3.1	-2.3	2.0
$[Na_6Br]^{5+}$	-25.4	-11.6	-4.3	1.4
$[K_6Br]^{5+}$	-31.6	-31.2	-5.4	0.9

Example Input Files Band Gaps

Example Input File TD-DFT

```
!B3PW91 DKH2 cc-pVTZ def2/J cc-pVTZ/C RIJCOSX NoSFitting RI-SOMF(1x)

%tddft
DoSOC true
Triplets true
MaxIter 500
NRoots 100
PrintLevel 3
end

%pointcharges "licl.pc"

*xyz 0 1
Li 28.21236 28.21236 28.21236
Cl 28.21236 28.21236 30.77712
Cl 25.64760 28.21236 28.21236
Cl 28.21236 25.64760 28.21236
Li 28.21236 25.64760 30.77712
Li 25.64760 28.21236 30.77712
Cl 25.64760 25.64760 30.77712
Li 25.64760 25.64760 28.21236
Li> 0.95 25.64760 28.21236 25.64760 NewECP "SDD" end
Li> 0.95 28.21236 25.64760 25.64760 NewECP "SDD" end
Li> 0.95 25.64760 25.64760 33.34188 NewECP "SDD" end
Li> 0.95 28.21236 28.21236 33.34188 NewECP "SDD" end
Li> 0.95 28.21236 23.08284 28.21236 NewECP "SDD" end
Li> 0.95 25.64760 23.08284 30.77712 NewECP "SDD" end
[...]
*
```

Example Input File bt-PNO-STEOM-CCSD

```
!RHF bt-PNO-STEOM-CCSD RI-SOMF(1x) RIJCOSX DKH2 cc-pVTZ def2/J cc-pVTZ/C NoSFitting

%mdci
SteomSOC true
iroot 1
MaxIter 500
nRoots 10
PrintLevel 3
DoLeft true
DoTDM true
NDav 50
DTol 1e-4
DLPNOLINEAR true
NEWDOMAINS true
DoEOMMP2 true
DoRECAN true
end

%pointcharges "licl.pc"

*xyz 0 1
Li 28.21236 28.21236 28.21236
Cl 28.21236 28.21236 30.77712
Cl 25.64760 28.21236 28.21236
Cl 28.21236 25.64760 28.21236
Li 28.21236 25.64760 30.77712
Li 25.64760 28.21236 30.77712
Cl 25.64760 25.64760 30.77712
Li 25.64760 25.64760 28.21236
Li> 0.95 25.64760 28.21236 25.64760 NewECP "SDD" end
Li> 0.95 28.21236 25.64760 25.64760 NewECP "SDD" end
Li> 0.95 25.64760 25.64760 33.34188 NewECP "SDD" end
Li> 0.95 28.21236 28.21236 33.34188 NewECP "SDD" end
Li> 0.95 28.21236 23.08284 28.21236 NewECP "SDD" end
Li> 0.95 25.64760 23.08284 30.77712 NewECP "SDD" end
[...]
*
```

Additional Information Band Gap Study

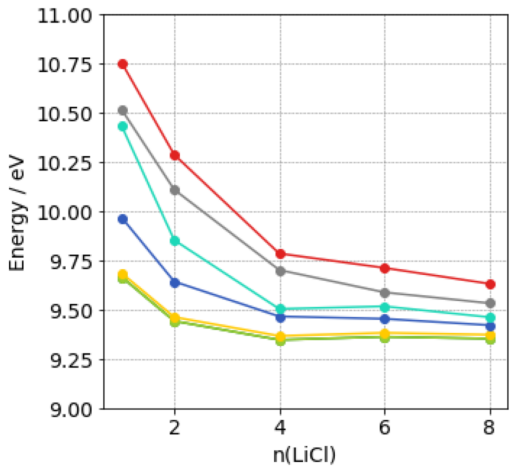

Figure B.7: bt-PNO-STEOM calculated excitations energies for clusters $[Li_nCl_n]^0$, n=1-4, 6, 8. green, yellowgreen, green, blue, turquoise, gray, and red lines represent excitations states with numbers 1, 2, 3, 10, 20, 30, and 40 respectively.

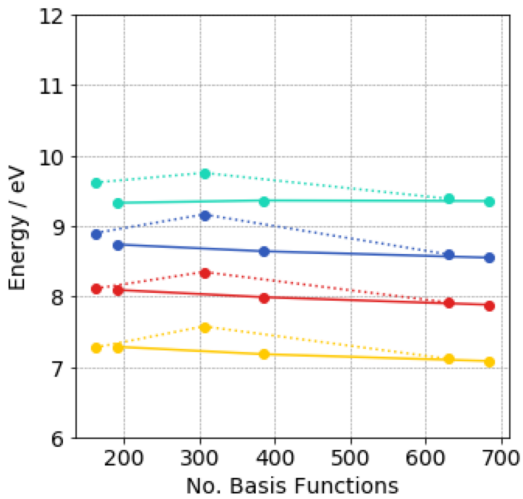

Figure B.8: Comparison of cc-pVXZ (solid line) and def2-XVP (dotted line) basis set types and sizes with different methods: BLYP (yellow), B3LYP (red), B2PLYP (blue), and bt-PNO-STEOM-CCSD (turquoise) calculated on cluster ($[Li_8Cl_8]^0$.

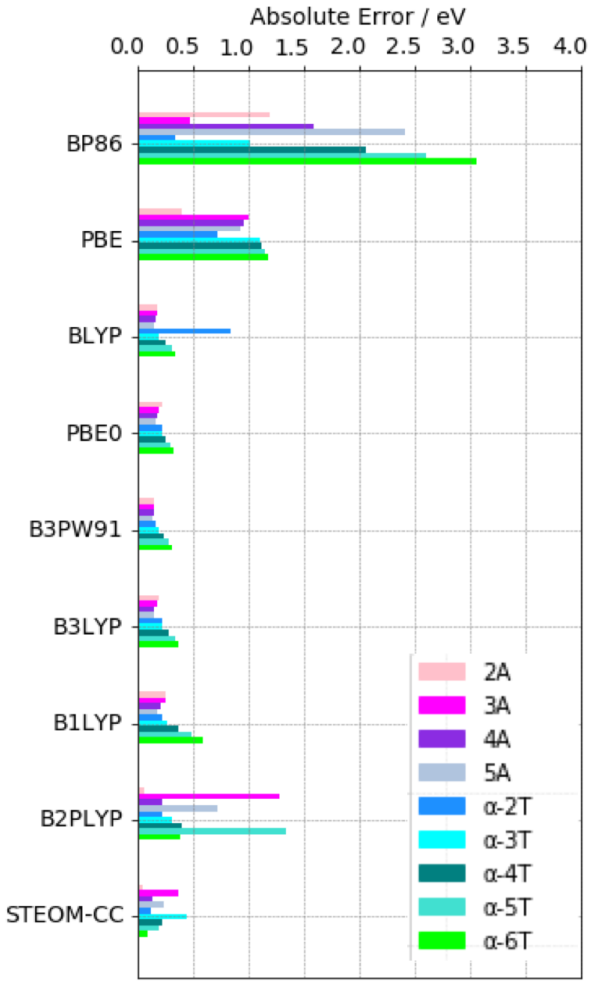

Figure B.9: Absolute errors in eV of the experimental vs. calculated fundamental band gaps computed with Δ-SCF/ DFT with different functionals and bt-PNO-STEOM-CCSD(STEOM-CC) for the organic semiconductor benchmark set.

Table B.10: TD-DFT and bt-PNO-STEOM-CCSD calculated optical band gaps in eV for all inorganic and organic systems of the benchmark set. Statistical evaluation of all quantities is given by means of mean absolute error (MAE) and maximum absolute errors (MaxAE).

	BP86	BLYP	PBE	B1LYP	B3LYP	B3PW91	PBE0	B2PLYP	STEOM-CC	Exp.
Organic Semiconductors										
2A	4.26	4.26	4.26	4.52	4.48	4.49	4.55	4.44	4.07	4.14
3A	3.10	3.11	3.11	3.44	3.39	3.39	3.46	3.54	3.50	3.20
4A	2.34	2.35	2.35	2.67	2.62	2.62	2.68	2.76	3.04	2.54
5A	1.81	1.82	1.82	2.13	2.09	2.08	2.14	2.22	2.50	1.84
α-2T	3.92	3.93	3.93	4.09	4.11	4.10	4.14	4.17	4.26	4.11
α-3T	3.14	3.15	3.15	3.33	3.34	3.34	3.38	3.42	3.57	3.49
α-4T	2.66	2.67	2.67	2.89	2.89	2.89	2.94	3.00	3.18	3.18
α-5T	2.33	2.34	2.34	2.61	2.59	2.59	2.65	2.73	2.95	2.98
α-6T	2.09	2.09	2.09	2.41	2.38	2.39	2.45	2.56	2.83	2.87
Inorganic Semiconductors										
LiF	8.31	8.43	8.53	9.61	9.83	9.71	9.96	10.07	11.41	11.60
LiCl	7.18	7.42	7.54	8.00	8.11	8.27	8.37	8.67	9.35	9.40
NaCl	6.42	6.62	6.78	7.28	7.40	7.59	7.64	8.11	8.81	8.97
LiBr	6.14	6.34	6.52	6.81	6.89	7.12	7.12	7.54	7.70	7.60
NaBr	5.73	5.94	6.12	6.46	6.56	6.79	6.82	7.36	7.54	7.50
MgO	4.21	4.46	4.56	5.25	5.41	5.47	5.67	5.47	6.32	6.21
MgS	1.95	2.07	2.19	2.69	2.83	2.99	3.02	3.14	4.55	4.78
MgSe(ZB)	1.61	1.71	1.75	2.27	2.40	2.50	2.55	2.69	3.75	3.90
MgSe(RS)	2.31	2.51	2.60	2.91	2.99	3.19	3.23	3.22	3.96	3.81
ZnS	2.41	2.50	2.52	3.11	3.26	3.32	3.39	3.44	4.01	3.78
ZnO	1.16	1.19	1.23	1.96	2.14	2.14	2.25	1.86	3.62	3.44
ZnSe	2.09	2.17	2.15	2.78	2.93	2.91	3.04	3.25	2.91	2.82
GeS	1.04	1.09	1.07	1.41	1.49	1.45	1.53	1.13	1.57	1.55
MAE	1.26	1.17	1.12	0.78	0.71	0.65	0.61	0.56	0.11	
MaxAE	3.29	3.17	3.07	2.09	1.95	1.89	1.76	1.64	0.23	

Table B.11: TD-DFT and bt-PNO-STEOM-CCSD calculated fundamental band gaps in eV for all organic systems of the benchmark set. Statistical evaluation of all quantities is given by means of mean absolute error (MAE) and maximum absolute errors (MaxAE).

	BP86	BLYP	PBE	B1LYP	B3LYP	B3PW91	PBE0	B2PLYP	STEOM-CC	Exp.
Organic Semiconductors										
2A	6.98	8.54	8.32	8.36	8.30	8.33	8.39	8.11	8.19	8.16
3A	6.97	7.50	6.67	6.69	6.65	6.67	6.74	7.78	6.87	6.51
4A	6.97	6.33	5.54	5.55	5.52	5.53	5.58	5.59	5.51	5.39
5A	6.98	5.49	4.72	4.73	4.70	4.71	4.74	5.28	4.80	4.58
α-2T	7.37	7.00	8.52	7.49	7.55	7.50	7.50	7.50	7.60	7.70
α-3T	7.01	7.10	6.19	6.22	6.18	6.22	6.26	6.31	6.44	6.01
α-4T	7.23	6.29	5.42	5.43	5.41	5.45	5.55	5.58	5.40	5.19
α-5T	7.22	5.77	4.92	4.91	4.89	4.95	5.10	5.95	4.80	4.63
α-6T	7.28	5.40	4.56	4.54	4.53	4.59	4.80	4.60	4.31	4.23
MAE	1.63	0.94	0.27	0.22	0.18	0.22	0.30	0.53	0.19	
MaxAE	3.05	1.17	0.82	0.31	0.30	0.36	0.57	1.32	0.43	

C Additional Information Part IV

Synthesis of Co_3O_4, Al_2CoO_4, and Co_2ZnO_4

The crystal structures used for the models in the Co_3O_4, Al_2CoO_4, and Co_2ZnO_4 band gap and XES studies in Chapter 5 were obtained from crystallographic measurements of the cobalt oxides synthesized as described subsequent. The same structures were used to measure the XES as well.

The spinel materials were synthesized in an enclosed spray-flame reactor as has been described previously.[557, 558] For all synthesized materials (Co_3O_4, Co_2ZnO_4 and Al_2CoO_4), metal nitrates were used as precursors: $Co(NO_3)_2{\cdot}6H_2O$ (Honeywell, >99.0% purity), $Zn(NO_3)_2{\cdot}6H_2O$ (AppliChem, 99.0 % purity) and $Al(NO_3)_3{\cdot}9H_2O$ (VWR Chemicals, >98.0 % purity). Ethanol (VWR, >99.9 % purity) and 2 ethylhexanoic acid (2-EHA) (Alfa Aesar, >99 % purity) were used as solvents. Using the respective metal nitrates in a total concentration of 0.2 molar, a solution was prepared for each material system using a mixture of ethanol (35 Vol.%) and 2-EHA (65 Vol.%).

Each corresponding solution was filled in a syringe pump and supplied to the reactor at a constant flow rate of 2 ml/min via a hollow needle located at the center of an external mixing two-fluid atomizing nozzle. A fine spray was formed from the solution by a flow of 7 slm of O_2 (Air Liquide, technical). The spray was ignited by a continuously burning premixed pilot flame (3 slm CH_4 (Air Liquide, N25, 99.5%) and 5 slm O_2), stabilized by a sheath-gas flow (140 slm, compressed air) added via a porous sintered bronze plate. The pressure in the reactor chamber was kept constant at 970 mbar abs., and an additional stream of quenching gas flow (230 slm, compressed air) was supplied downstream the reaction zone to control the reactor off-gas temperature to values below 130°C. After synthesis and in order to reach the desired crystallographic phases, the collected Co_3O_4 and Co_2ZnO_4 samples were heat-treated at 400°C for 2 h while the Al_2CoO_4 sample was heat-treated at 1000°C for 2 h under a continuous air flow (500 l/h) in a Nabertherm L 1/12/R6 muffle furnace.

Band Gap Study of Co_3O_4

Input Files for Band Gap Study of Co_3O_4

Broken-Symmetry TD-DFT Input File Example

```
!VeryTightSCF Ionic-Crystal-QMMM PBE0 RIJCOSX DKH2 DKH-def2-qzvpp def2/J def2-qzvpp/C

%scf maxiter 500
Flipspin 4,5
FinalMs 0.0
end

%tddft
  maxiter 500
  nroots 200
  PrintLevel 3
end

%qmmm
 QMAtoms {0:26} end
 ORCAFFFilename "2t4o.ORCAFF.prms"
  HFLayers 0
  ECPLayerECP "SDD"
  ECPLayers 3
  CONV_Charges false
  ENFORCETOTALCHARGE true
  CHARGE_TOTAL    0
  PrintLevel 4
end


*xyzfile -26 7 2t4o.xyz
```

EOM-CC with HF layer Input File Example

```
!Ionic-Crystal-QMMM UHF EOM-CCSD RIJCOSX DKH2 cc-pVQZ-DK def2/J cc-pVQZ/C RI-SOMF(1x)

%scf maxiter 500 end

%mdci
  iroot 1
  maxiter 500
  nroots 20
end


%qmmm
 QMAtoms {0} end
 ORCAFFFilename "1t.ORCAFF.prms"
  HFLayerAtoms {1:4} end
  ECPLayerECP "SDD"
  ECPLayers 3
  CONV_Charges false
  ENFORCETOTALCHARGE true
  CHARGE_TOTAL    0
  PrintLevel 4
end

*xyzfile 2 4 1t.xyz
```

SA-CASSCF with NEVPT2 Input File Example

```
!Ionic-Crystal-QMMM cc-pVQZ/C def2/J DKH2 cc-pVQZ-DK
!NoITER NormalPrint MOREAD NoLoewdin NoMulliken


%moinp "2t4o.gbw"


%casscf
nel 14
norb 10
nroots 200
mult 1
maxiter 100
PTMethod SC_NEVPT2
end

%qmmm
 QMAtoms {0:26} end
 ORCAFFFilename "2t4o.ORCAFF.prms"
  HFLayers 0
  ECPLayerECP "SDD"
  ECPLayers 4
  CONV_Charges false
  ENFORCETOTALCHARGE true
  CHARGE_TOTAL    0
  PrintLevel 4
end


*xyzfile -26 7 2t4o.xyz
```

MR-EOM-CC Input File Example

```
!MR-EOM Ionic-Crystal-QMMM cc-pVQZ/C def2/J DKH2 cc-pVQZ-DK
!NoITER NormalPrint MOREAD NoLoewdin NoMulliken

%moinp "1t.gbw"

%casscf
nel 7
norb 5
nroots 20
mult 4
maxiter 100
ActOrbs unchanged
end

%mrci
newblock 4*
nroots 20
 refs cas(7,5) end
end
soc
 dosoc true
end
end

%qmmm
 QMAtoms {0:4} end
 ORCAFFFilename "1t.ORCAFF.prms"
  HFLayers 0
  ECPLayerECP "SDD"
  ECPLayers 3
  CONV_Charges false
  ENFORCETOTALCHARGE true
  CHARGE_TOTAL    0
  PrintLevel 4
end


*xyzfile -6 4 1t.xyz
```

Table C.1: Overview of Co_3O_4 optical absorption experiments from the literature (1).

Reference	Material	Measurement	Wavelength range / eV	Absorption Bands/ eV	Assignment Absorption Bands	Band Gaps / eV	Assignment Band Gaps	Method
Cherkashin, 1969[482]	Ceramic	UV/Vis Spectrometer	-	0.81 1.50	-	-	-	-
Tanaka, 1979[500]	Polycrystalline sample, Ceramic	UV/Vis Spectrometer (self-build)	1.0-3.5	1.7 3.1	-	-	-	-
Belova, 1983[483]	0.1-0.5 μm Thin Film	Opt. Transmission (UV/Vis/NIR), Perkin-Elmer-spectrometer 450	0.5-6.1	0.87 1.70 2.85 5.39	e(Co(II)) $\rightarrow t_2$(Co(II)) e(Co(II) $\rightarrow 4s$(Co(II)) t_{2g}(Co(III)) $\rightarrow e_g$(Co(III)) $2p$(O) $\rightarrow 4s$(Co(III)) *Based on SCF XαSW, Tanabe-Sugano	-	-	-
Martens, 1985[484]	Ceramic: Pellets from powder (hot pressed)	Ellipsometer	0.7-5.5	0.80 1.60 2.65 4.40	Origin uncertain Transitions related to Co(III) *assigned due to substitution with Co in $CoFe_2O_4$	-	-	-
Cook, 1986[478]	Thin Film (polycrys-talline)	opt. Transmission (T) Cary-17, Ellipsometer (E) (300-1000n)	0.5-4.1	0.82(T) 0.93(T) 1.7(T)/1.6(E) 2.8(T)/2.7(E)	e(Co(II)) $\rightarrow t_2$(Co(II)) e(Co(II)) $\rightarrow e_g$(Co(III)) t_{2g}(Co(III)) $\rightarrow t_2$(Co(II)) $2p$(O) $\rightarrow t_2$(Co(II)) *based on Miedzinska	-	-	-
Murad, 1988[457]	0.1-0.2 μm Thin Film (spray pyrolysis)	Pye-Unciam SP8-100 spec-trophotomer	1.4-4.1	-	-	1.45 2.00 3.20	3x direct allowed BGs	Tauc relation

Table C.2: Overview of Co_3O_4 optical absorption experiments from the literature (2).

Reference	Material	Measurement	Wavelength range / eV	Absorption Bands/ eV	Assignment Absorption Bands	Band Gaps / eV	Assignment Band Gaps	Method
Schumacher, 1990[458]	0.1 μm Thin Film (sputtering)	Photorepsonse	1.5-4.1	-	-	1.5	Indirect BG (1A1→1T1 O_h Co^{3+}) *based on Martens	Tauc relation from quantum efficiency data
Varkey, 1993[459]	0.02-0.1 μm Thin Film	Philips PU 3700 spectrophotometer	1.4-4.1	-	-	1.65	Optical BG	Tauc Relation
Lenglet, 1994[479]	Thin Film (decomposition (D) of cobaltous nitrate vs. sol gel method (S))	Optical Spectroscopy	0.5>	0.85(D)/0.84(S) 0.95/0.93 1.85/1.85 3.45/3.35 4.80/4.70	-	-	-	-
Nkeng, 1995[480]	0.01-2 μm Thin Film (sputtering (SU) vs. spray pyrolysis (SY))	mUV/Vis/NIR reflectance spectroscopy (Lambda 9 Perkin-Elmer spectrometer)	0.5-6.2	0.82(SU)/0.84(SY) 0.93/0.95 1.70/1.95 2.80/3.55	-	-	-	-
Patil, 1996[460]	1.9 μm Thin Film (spray pyrolysis)	Hitachi 330 spectrophotometer	1.5-3.5	0.48 1.02 1.08 1.12 1.26 1.38	-	0.75 1.10 1.26 1.38 1.44 2.06	Indirect forbidden opt. BG Indirect allowed opt. BG Direct forbidden opt. BG Direct forbidden opt. BG Direct allowed opt. BG Direct allowed opt. BG	Tauc relation

Table C.3: Overview of Co_3O_4 optical absorption experiments from the literature (3).

Reference	Material	Measurement	Wavelength range / eV	Absorption Bands/ eV	Assignment Absorption Bands	Band Gaps / eV	Assignment Band Gaps	Method
Ruzakowski Athey, 1996[481]	0.015-0.022 μm Thin Filmn(Spray Pyrolysis)	Transmittance/ Ellipsometry J.A. Woollam Co., Inc. Rotating analyzer VASE	0.7-3.5	0.83 0.94 1.70 2.90	e(Co(II)) $\rightarrow t_2$(Co(II)) e(Co(II)) $\rightarrow e_g$(Co(III)) t_{2g}(Co(III)) $\rightarrow t_2$(Co(II)) $2p$(O) $\rightarrow t_2$(Co(II)) *based on Miedzinska	-	-	-
Cheng, 1998[467]	0.65 μm polycrystalline thin Film (CVD)	Shimazu spectrophotometer UV-140, Transmission	1.3-2.2	1.6-1.7 2.8-2.9	- LMCT	1.50-1.52 1.88-1.95	Co(III)-Co(II) O-Co(II) 2x direct allowed opt. BGs	Tauc relation
Barreca, 2001[471]	0.204-1.276 μm Thin Film (CVD)	Opt. Abs. UV-VIS-NIR dual beam spectrophotometer: Carry 5E (Varian)	0.6-4.1	0.82 0.98 1.70 2.48	e(Co(II)) $\rightarrow t_2$(Co(II)) e(Co(II)) $\rightarrow e_g$(Co(III)) $2p$(O) $\rightarrow e_g$(Co(III)) $2p$(O) $\rightarrow t_2$(Co(II)) *based on Nkeng, Belova, Cook	1.5 2.0	Subband inside "true" opt. BG, O 2p→Co(III) 3d "true" opt. BG, interband transitions (O 2p→Co(II) 3d)	Tauc relation
Kadam, 2001[461]	0.9(A)-1.7(B) μm Thin Film (PSPT)	Hitachi model-330 spectrophotometer	1.5-3.5	1.04(A)/0.88(B) 1.16(A)/1.08(B)	-	1.10(A)/0.98(B) 1.46(A)/1.42(B) 2.10(A)/2.02(B)	Indirect allowed opt. BG Direct allowed opt. BG Direct allowed opt. BG	Tauc relation
Pejova, 2001[462]	0.6 μm Thin Film (polycrystalline)	Hewlett Packard 8452A spectrophotometer (UV/vis)	1.5-4.0	-	-	2.2	Direct allow. opt. BG	Tauc relation

Table C.4: Overview of Co_3O_4 optical absorption experiments from the literature (4).

Reference	Material	Measurement	Wavelength range / eV	Absorption Bands/ eV	Assignment Absorption Bands	Band Gaps / eV	Assignment Band Gaps	Method
Kim, 2003[499]	1.0 μm Thin Film (sol-gel method)	Elipsometry (rottating analyzer)	1.5-4.0	1.65 2.40 2.80	t_{2g}(Co(III)) $\rightarrow$ t_2(Co(II)) $2p$(O) $\rightarrow$ e_g(Co(II)) $2p$(O) $\rightarrow$ t_2(Co(III)) *based on Miedzinska	-	-	-
Mane, 2003[463]	Thin Film (MOCVD)	UV/Vis Spectrophotometry (Hitachi UV-visible Spectrophotometer model U-300)	1.4-3.1	-	-	1.45 2.05	Direct allowed opt. BG Direct allowed opt. BG	Tauc relation
Gulino, 2003[464]	Thin Film (MOCVD)	UV/Vis Spectrometer (Beckman DU650)	1.2-3.5	-	-	1.48 2.19	Direct allowed opt. BG Direct allowed opt. BG	Tauc relation
Yamamoto, 2003[472]	0.0068/0.0136 μm Thin Film (sol-gel method)	opt. spectr. Hitachi Ltd., U-3500, IR opt. spectr. (Ando Electric Co. Ltd., AQ 6315A), white light (Ando Electric Co. Ltd., AQ 4303B)	0.5-3.5	0.75 0.90 1.70 3.00	-	0.80(0.7/1.0) 1.30 2.10	e(Co(II)) $\rightarrow$ t_2(Co(II)) t_{2g}(Co(III)) $\rightarrow$ t_2(Co(II)) $2p$(O) $\rightarrow$ t_2(Co(II)) *based on Miedzinska all three: direct allowed opt. BGs	Tauc relation

Table C.5: Overview of Co_3O_4 optical absorption experiments from the literature (5).

Reference	Material	Measurement	Wavelength range / eV	Absorption Bands/ eV	Assignment Absorption Bands	Band Gaps / eV	Assignment Band Gaps	Method
Bahlawane, 2004[473]	0.03-0.04 μm Thin Film (CVD)	UV–Vis spectrometer, UVIKON 860, KONTRON Instruments	1.5-4.1	1.69 3.02	-	1.43 2.15	t_{2g}(Co(III)) $\rightarrow$ t_2(Co(II)) $2p$(O) $\rightarrow$ t_2(Co(II)) *based on Miedzinska both: direct allowed opt. BGs	Tauc relation
Shinde, 2006[465]	0.8 μm Thin Film (Spray Pyrolysis)	Systonic Spectrophotometer-119	1.2-3.5	-	-	1.6 2.1	Indirect allowed opt. BG Direct allowed opt. BG	Tauc relation
Thota, 2009[474]	powder (nanocrystaline, sol-gel method)	UV-vis-NIR spectrophotometer (Varian based Cary 5000)	0.6-6.2	0.56 0.85 0.95 1.77 3.12	e(Co(II)) $\rightarrow$ t_2(Co(II)) e(Co(II)) $\rightarrow$ t_2(Co(II)) e(Co(II)) $\rightarrow$ e_g(Co(III)) t_2g(Co(III)) $\rightarrow$ t_2(Co(II)) $2p$(O) $\rightarrow$ t_2(Co(III)) *based on Lenglet, Kim, XRD	1.52 2.53	Opt. BG (subband located in energy gap), O$\rightarrow$Co(II) Opt. BG, O$\rightarrow$Co(III)	Tauc relation
Ngamou, 2010[466]	0.325 μm Thin Film (CVD)	Shimadzu UV-vis spectrophotometer	1.4-3.1	-	-	1.52 2.14	O$\rightarrow$Co(III) O$\rightarrow$Co(II)	Tauc relation
Louradi, 2011[468]	0.4-0.5 μm Thin Film (spray pyrolysis, T=300°C-500°C)	SHIMADZU 3101 PC UV-VIS-NIR spectrophotometer	0.5-4.1	-	-	1.48/1.51 2.08/2.11	T=300°C/T=500°C Both direct BGs	Tauc relation

Table C.6: Overview of Co_3O_4 optical absorption experiments from the literature (6).

Reference	Material	Measurement	Wavelength range / eV	Absorption Bands/ eV	Assignment Absorption Bands	Band Gaps / eV	Assignment Band Gaps	Method
Qiao, 2013[475]	0.017 μm Thin Film	opt. abs., Photoluminesence (PL)	0.5-6.2	0.7 1.6 2.2 (3.7) 4.4	Lowest energy band has three peaks (0.7-1.1 eV) DFT assigned	0.76/0.74(PL) 1.60	Fundamental BGs	Tauc relation
Waegle, 2014[476]	0.01-0.06 μm Thin Film (magnetron sputtering)	Shimadzu UV-2600 spectrohphot./ FT-IR Bruker Vertex 70V	0.7-3.0	0.82 0.94 1.66 2.84	e(Co(II)) $\rightarrow t_2$(Co(II)) e(Co(II)) $\rightarrow e_g$(Co(III)) t_{2g}(Co(III)) $\rightarrow t_2$(Co(II)) $2p$(O) $\rightarrow t_2$(Co(III)) *Miedzinska mentioned	(0.7) 1.6	Midgap (d-d trans., not named BG) BG	Beer's Law
Jiang, 2014[477]	0.01 μm Thin Film	UV/Vis-NIR	0.6-3.5	0.82 0.93 1.64 2.81	*based on XUV? (Extreme UV) Pathways 3.0 eV: $2p$(O) $\rightarrow e_{2g}$(Co(III))	1.6	Direct BG	-
Reddy, 2017[437]	Thin Film (sputtering)	UV-vis: Shimadzu UV-3600; UV-vis-NIR spectrophot.	1.0-4.1	-	-	1.4	BG	From UV/Vis (no further specification)
Lakehal, 2018[469]	0.256 μm Thin Film (deposited, sol gel method)	Shimadzu-1650 spectrophotometer	1.4-4.1	-	-	1.5 2.2	$2p$(O) $\rightarrow e_g$(Co(III)) $2p$(O) $\rightarrow t_2$(Co(II)) *assigned based on Lit. both: direct allowed opt. BGs	Tauc relation
Zhang, 2020[470]	0.15-0.18 μm Thin Film	Opt. Transimission Spectra	0.6-4.1	-	-	1.5	Direct opt. BG	Tauc Plot

Table C.7: Overview of Co_3O_4 band gap (BG) and absorption spectra calculations from the literature (1).

Reference	Model	Method	BGs & Excitation Energies / eV	BG Type/ Transition Character	Other Information
Belova, 1983[483]	• $[CoO_4]^{6-}$ & $[CoO_6]^{9-}$ cluster in electrostatic model • electrostatic model: average external field parameters determined by XPS data • "Watson spheres"	• SCF-XαSW (self-consistent field Xα (α = exchange parameter) scattered wave cluster method, spin restricted calculation • Orbital difference	0.80 2.18 2.61 5.67 6.39	Co(II)$e \rightarrow t_2$ Co(II) $e \rightarrow 4s$ Co(III) $t_{2g} \rightarrow e_g$ O $2p$ →Co(II) $4s$ O $2p$ →Co(III) $4s$	Co(III) might be high spin due to symmetry lowering
Belova, 1983[483]	• see above	• Spin polarized considerations derived from results of method above	0.87 1.38 2.18 2.61 5.67	Co(III) $e_g^{\alpha} \rightarrow t_{2g}^{\beta}$ Co(II) $t_2^{\alpha} \rightarrow 4s$ Co(II) $e \rightarrow 4s$ Co(III) $e_g^{\alpha} \rightarrow e_g^{\beta}$ O $2p \rightarrow$ Co(II) $4s$	
Miedzinska, 1987[501]	• Unit cell	• Semi-empirical form of MOs, VS1E • Orbital energies of isolated ion from empirical IPs • VS1E orbitals adjusted for Pauling electroneutrality effect → partial reduction $Co^{2+/3+}$& O^{2-} • Energy diagram via Wolfgang-Helmholtz approx. for $[Co^{2+}O_4^{2-}]$ and $[Co^{3+}O_6^{2-}]$; 6×$[Co^{2+}O_4^{2-}]$ combined to ligand group orbitals, overlap with 1× $[Co^{3+}O_6^{2-}]$	0.8 1.0 1.3 2.1	Co(II) $e \rightarrow t_2$ Co(II) t_2 →Co(III) e Co(III) t_{2g} →Co(II) t_2 O $2p$ →Co(II) t_2	Distortion removes orbital degeneracies

Table C.8: Overview of Co_3O_4 band gap (BG) and absorption spectra calculations from the literature (2).

Reference	Model	Method	BGs & Excitation Energies / eV	BG Type/ Transition Character	Other Information
Wang, 2006[491]	• Periodic Boundary Conditions	• Spin-polarized PAW calculation with energy cut-off: 550 eV using VASP • GGA & GGA+(U=3.3 eV)	0.7 1.6	GGA GGA+U	GGA: 2.39μ_B GGA+U: 2.67μ_B
Walsh, 2007[488]	• Co-Fe-Al oxide spinel systems • Periodic boundary conditions • 14 atom primitive spinel unit cell • special quasi-random structure (SQS) model for random occupation in inverse structure	• Spin-polarized and scalar relativistic PAW calculation with energy cut-off 500 eV using VASP • $6 \times 6 \times 6$ k-point grid for Brillouin zone • Gradient corrected DFT with the Co & Fe $3d$ ($3d$ highly correlated $\rightarrow$ U necessary) states treated with on-site correction for Coulomb interaction (DFT+U) • PBE+U with U tested from 2 to 5 eV $\rightarrow$ electronic structure quite independent, U=2 eV for Co $3d$ and U=3 eV for Fe $3d$ chosen because BGs in region of experimental data • BG determined from difference in DOS	Co_3O_4 1.23 1.51 1.67 Al_2CoO_4 2.32 2.61 2.65	Co_3O_4 $X \rightarrow X$ direct trans. $\Gamma \rightarrow X$ indirect trans. $\Gamma \rightarrow \Gamma$ direct trans. Al_2CoO_4 $X \rightarrow X$ direct trans. $\Gamma \rightarrow X$ indirect trans. $\Gamma \rightarrow \Gamma$ direct trans. Called Electronic BG VBM = mixture T_d Co $3d$ & O $2p$ CBM = O_h Co $3d$	• Electronic BG of Co_3O_4 and Fe_3O_4 do not change significantly if T_d sites replaced (M_2AlO_4 – inverse spinel); increase greater 1 eV if O_h sites replaced (MAl_2O_4 – normal spinel)

Table C.9: Overview of Co_3O_4 band gap (BG) and absorption spectra calculations from the literature (3).

Reference	Model	Method	BGs & Excitation Energies / eV	BG Type/ Transition Character	Other Information
Xu, 2009[486]	• Periodic boundary conditions	• Spin-polarized and geometry optimized PBE calculation and cut-off energy 4.5 Å and Fermi smearing of 0.01 Hartree using DMol[3] • Brillouin zone $5 \times 5 \times 5$ Monkhorst-Pack grids for bulk (k points) • Double-numerical basis with polarization functions (DNP): O all electron basis sets, ECPs for Co cores	1.75 (↑) 1.92 (↑) 2.06 (↑) 2.2 (↓) 2.9 (↓) 3.3	$X \rightarrow X$ direct gap O $2p$ →Co(II) t_2 $\Gamma \rightarrow X$ indirect gap $\Gamma \rightarrow \Gamma$ direct gap Co(III) t_{2g} →Co(II) t_2 O $2p$ →Co(II) t_2 O $2p$ →Co(III) e_g Co(III) t_{2g} →Co(II) t_2	• bulk shows antiferromagnetic properties • Antiferromagnetic Co(II) $= 2.631\mu_B$ • Strong hybridization of the Co^{3+} $3d$ with O $2p$
Chen, 2011[485]	• Periodic boundary conditions • 14-atom primitive unit cell of spinel structure • conventional cubic cell with 56 atoms and tetragonal supercell with 112 atoms	• Spin-polarized PAW calculation with cut-off energy of 120 Ry using Quantum Espresso package: DFT-GGA and GGA+U • $8 \times 8 \times 8$ k-point grid convcerged sampling of Brillouin zone • Use of norm conserving Troullier-Martins pseudopotantials • PBE+U with U(Co(II))=4.4 eV; U(Co(III))=6.7 eV and PBE0	PBE 0.30 0.75 0.94 1.39 PBE+U 1.96 2.41 2.81 3.25 1.67 2.02 2.16 PBE0 3.42	PBE $X \rightarrow X$ Direct BG $\Gamma \rightarrow X$ Indirect BG $X \rightarrow \Gamma$ Indirect BG $\Gamma \rightarrow \Gamma$ Direct BG PBE+U (4.4/6.7) $X \rightarrow X$ Direct BG $\Gamma \rightarrow X$ Indirect BG $X \rightarrow \Gamma$ Indirect BG $\Gamma \rightarrow \Gamma$ Direct BG PBE+U=4.4 PBE+U=5.9 PBE+U=6.7 PBE0 Minimum BG	• Valence band two subbands: lower energies dominated by O $2p$ and upper by Co^{3+} $3d$, smaller amounts of Co^{2+} present • Bottom of conduction band: Co^{2+} and Co^{3+} $3d$ • Co(II), PBE: 2.64 μ_B • Co(II), PBE+U: 2.84 μ_B • Co(II), PBE0: 2.90 μ_B

Table C.10: Overview of Co_3O_4 band gap (BG) and absorption spectra calculations from the literature (4).

Reference	Model	Method	BGs & Excitation Energies / eV	BG Type/ Transition Character	Other Information
Montoya, 2011[492]	• Periodic ab-initio	• PAW calculation (plane wave expansion truncated) with cut-off energy 550 eV with VASP • Brillioun zone integration: $6 \times 6 \times 6$ Monkhorst-Pack k-points grid • PBE; PBE+(U=3.3 eV)	0.1 1.6	PBE PBE+U	• PBE+U: $1.6\mu_B$
Qiao, 2013[475]	• Periodic boundary conditions	• DFT and DFT+U tested • DFT without U gives best structure • DOS • Orbital difference • Oscillator strength ($p \rightarrow d$ magnitudes stronger than $d \rightarrow d$) • U distorts band structure	0.83 0.95 1.04 1.64 1.84 2.62 3.66 4.69 5.8	Direct transitions (first is BG) Co(II) e_g →Co(II) $t_{2g}(\downarrow)$ Co(II) e_g →Co(III) $e_g(\downarrow)$ Co(II) e_g →Co(III) $e_g(\uparrow)$ Co(III) t_{2g} →Co(II) $t_{2g}(\downarrow)$ Co(III) t_{2g} →Co(III) e_g O $2p(I)$ →Co(II) $t_2(\downarrow)$ O $2p(I)$ →Co(III) e_g O $2p(II)$ →Co(II) $t_2(\downarrow)$ O $2p(II)$ →Co(III) e_g	• Co_3O_4 did not exhibit strong electron correlations; electronic structure well described by standard DFT • First five transitions pure $3d \rightarrow 3d$ transitions in homovalent Co or between two heterovalent Co, spin orientation depending • $3d \rightarrow 3d$ transitions forbidden for pure $3d$ bands; non-zero transition matrix element may result from hybridization of O $2p$ & Co $3d$ → relaxed parity selection rule

Table C.11: Overview of Co_3O_4 band gap (BG) and absorption spectra calculations from the literature (5).

Reference	Model	Method	BGs & Excitation Energies / eV	BG Type/ Transition Character	Other Information
Lima, 2014[487]	• Periodic boundary conditions	• Full-potential linear augmented plane wave (FP-LAPW) and geometry optimized calculation with cut-off energy of $K_{\max} = 8.0/R_{\mathrm{MT}}$ using WIEN2k • Charge density Fourier-expanded up to $G_{\max} = 14$ • k-point grid: $8 \times 8 \times 8$ Brillouin zone • PBE & mBJ (semilocal potential) & B3PW91 • TDOS, PDOS (total and partial electronic density of states) • Absorption curve: electric dipole-allowed transitions from the populated Kohn-Sham states	GGA-PBE 0.35 0.80 0.95 1.35 mBJ 2.84 3.00 3.20 3.40 B3PW91 1.55 2.00 2.40 2.80 1.86, 2.4, 2.9 (Abs. peaks)	GGA-PBE $X \rightarrow X$ Direct BG $\Gamma \rightarrow X$ Indirect BG $X \rightarrow \Gamma$ Indirect BG $\Gamma \rightarrow \Gamma$ Direct BG mBJ $X \rightarrow X$ Direct BG $\Gamma \rightarrow X$ Indirect BG $X \rightarrow \Gamma$ Indirect BG $\Gamma \rightarrow \Gamma$ Direct BG B3PW91 $X \rightarrow X$ Direct BG $\Gamma \rightarrow X$ Indirect BG $X \rightarrow \Gamma$ Indirect BG $\Gamma \rightarrow \Gamma$ Direct BG Dominated by Co(II) e_g →Co(II) t_{2g} Co(III) t_{2g} →Co(III) e_g	• Dominated by Co(II) e_g →Co(II) t_{2g} & Co(III) t_{2g} →Co(III) e_g • Superposition of both optical transitions • Calculations predict that crystal field splitting at both sides are of same magnitude
Kaptagay, 2015[495]	• periodic slab model (infinite in 2D) • bulk contains formula units, i.e., 14 ions	• PAW calculation with cut-off energy of 600 eV and including Methfessel-Paxton smearing with 0.1 eV using VASP • Monkhorst-Pack $4 \times 4 \times 4$ k point sampling • PBE+U(=3 eV)	1.60	BG	• Magnetic moment Co(II) 2.63 μ_B

Table C.12: Overview of Co_3O_4 band gap (BG) and absorption spectra calculations from the literature (6).

Reference	Model	Method	BGs & Excitation Energies / eV	BG Type/ Transition Character	Other Information
Singh, 2015[173]	• Periodic boundary conditions	• PAW calculations including core electrons with energy cut-off of 500 eV using VASP • PBE & PBE+U(Co(II)=4.4 eV/Co(III)=6.4 eV) & HSE06 (range-separated XC functional) • PBE & PBE+U: k points $8\times8\times8$; BZ: tetrahedron method (Blöchl) • HSE06: k points $4\times4\times4$, BZ: Gaussian smearing (width 0.01 eV) • HSE06: HF exchange 25%, 20%, 17%, 15%, 13%, 10%, 5% • Investigation of fundamental & opt. BG via dielectric tensor • G0W0 (perturbative non-self-consistent) & GW (self-consistent) • QSGW: quasiparticle self-consistent GW (Sc-GW0: QP eigenvalues & WF both updated in G & Sc-GW: QP eigenvalues & WF both updated in G & W) • Input WF & energies for G0W0 obtained from DFT calc. on bulk unit cell using PBE, PBE+U, HSE06 (5%) • G0W0: k point grid $4\times4\times4$ & q point mesh of response function: $2\times2\times2$	0.34 2.45 0.78 0.79 0.82 0.94 0.98 0.98	Direct BG PBE PBE+U HSE06 (5%) Sc-GW0 Indirect BG GW0 GW G0W0 Sc-GW	• linear dependency of BG on HF exchange • magnetic moments available

Table C.13: Overview of Co_3O_4 band gap (BG) and absorption spectra calculations from the literature (7).

Reference	Model	Method	BGs & Excitation Energies / eV	BG Type/ Transition Character	Other Information
Lima, 2016[496]	• Periodic boundary conditions • Normal spinel structure	• FP-LAPW calculation with and without SOC using WIEN2k • K points: $8 \times 8 \times 8$ • PBE & PBE+U & B3PW91	wo/wSOC 0.72/0.86 1.11/1.26 1.34/1.50 1.49/1.66 1.86/2.04 1.60/1.65 2.04/2.12 2.42/2.48	wo/wSOC B3PW91 ($\alpha = 5\%$) B3PW91 ($\alpha = 10\%$) B3PW91 ($\alpha = 13\%$) B3PW91 ($\alpha = 15\%$) B3PW91 ($\alpha = 20\%$) PBE+U=3.0/3.0 $Co^{2+/3+}$ PBE+U=4.4/4.4 PBE+U=4.4/6.7	wo/wSOC $2.33/2.33\mu_B$ $2.40/2.40\mu_B$ $2.43/2.43\mu_B$ $2.45/2.45\mu_B$ $2.49/2.49\mu_B$ $2.35/2.36\mu_B$ $2.40/2.38\mu_B$ $2.42/2.42\mu_B$
Zaki, 2018[489]	• Periodic Boundary Conditions	• PAW calculations with energy cut-off 380 eV using CASTEP program package, BG from PDOS • Monkhorst-Pack grid $6 \times 6 \times 6$ k-points • PBE+U = 3.5 eV (GGA-PBEsol+U)	1.26 1.77 1.61 2.22	$X \rightarrow X$ Direct BG $\Gamma \rightarrow X$ Indirect BG $X \rightarrow \Gamma$ Indirect BG $\Gamma \rightarrow \Gamma$ Direct BG	• Dielectric function available
Sousa, 2019[490]	• Periodic Boundary Conditions	• FP-LAPW calculations using WIEN2k & using SIESTA for magnetic property calculations • K point grid: $8 \times 8 \times 8$ • PBE & Becke-Johnson XC	0.35 0.06 1.33 0.96 2.60	PBE LDA B3PW91 BJ mBJ	$2.20\mu_B$ $1.94\mu_B$ $2.42\mu_B$ $2.26\mu_B$ $2.62\mu_B$

Table C.14: Overview of Co_3O_4 band gap (BG) and absorption spectra calculations from the literature (8).

Reference	Model	Method	BGs & Excitation Energies / eV	BG Type/ Transition Character	Other Information
Zhandun, 2020[493]	• Periodic Boundary Conditions	• PAW calculation with cut-off energy of 500 eV using VASP • $8 \times 8 \times 8$ Monkhorst-Pack mesh of k points • PBE & PBE+(U=4.5 eV) & G0W0	0.2 0.35 0.6	PBE PBE+U G0W0	
Cadi-Essadek, 2021[494]	• Periodic Boundary Conditions	• PAW calculation VASP • $8 \times 8 \times 8$ k point mesh • PBE & PBE+U • Long-range dispersion interaction DFT-D3	0.35 0.55 0.75 0.98 1.21 1.43 1.64 1.86 2.07 2.28 2.46	PBE+U=0.0 PBE+U=0.5 PBE+U=1.0 PBE+U=1.5 PBE+U=2.0 PBE+U=2.5 PBE+U=3.0 PBE+U=3.5 PBE+U=4.0 PBE+U=4.5 PBE+U=5.0	$2.27\mu_B$ $2.36\mu_B$ $2.43\mu_B$ $2.49\mu_B$ $2.53\mu_B$ $2.58\mu_B$ $2.61\mu_B$ $2.65\mu_B$ $2.68\mu_B$ $2.71\mu_B$ $2.73\mu_B$

Table C.15: Dependence of the optical excited state calculations on the basis set for the cobalt oxide models, here for the example cluster 1t, for different methods.

	State	def2-SVP	def2-TZVP	def2-QZVPP	cc-pVDZ	cc-pVTZ	cc-pVQZ	cc-pV5Z
PBE0	$3d \rightarrow 3d$ (1)	0.899	0.945	0.976	0.897	0.957	0.979	0.987
	$3d \rightarrow 3d$ (2)	1.736	1.744	1.763	1.718	1.749	1.766	1.773
	LMCT	6.386	6.74	6.653	6.085	6.629	6.681	6.695
EOM-CC	$3d \rightarrow 3d$ (1)	0.444	0.494	0.529	0.485	0.504	0.525	0.53
	$3d \rightarrow 3d$ (2)	1.699	1.751	1.733	1.759	1.731	1.748	1.755
	LMCT	7.471	7.422	7.478	7.255	7.395	7.61	7.7
SA-CASSCF	$3d \rightarrow 3d$ (1)	0.415	0.441	0.442	0.413	0.434	0.443	-
	$3d \rightarrow 3d$ (2)	0.717	0.763	0.764	0.712	0.748	0.766	-
	$3d \rightarrow 3d$ (3)	2.746	2.749	2.749	2.73	2.743	2.748	-
NEVPT2	$3d \rightarrow 3d$ (1)	0.481	0.545	0.547	0.5	0.539	0.55	-
	$3d \rightarrow 3d$ (2)	0.818	0.923	0.929	0.843	0.91	0.936	-
	$3d \rightarrow 3d$ (3)	2.406	2.351	2.262	2.356	2.281	2.235	-
MR-EOM-CC	$3d \rightarrow 3d$ (1)	0.449	0.487	0.537	0.428	0.471	0.487	-
	$3d \rightarrow 3d$ (2)	0.763	0.84	0.93	0.718	0.786	0.813	-
	$3d \rightarrow 3d$ (3)	2.324	2.21	2.284	2.228	2.152	2.144	-

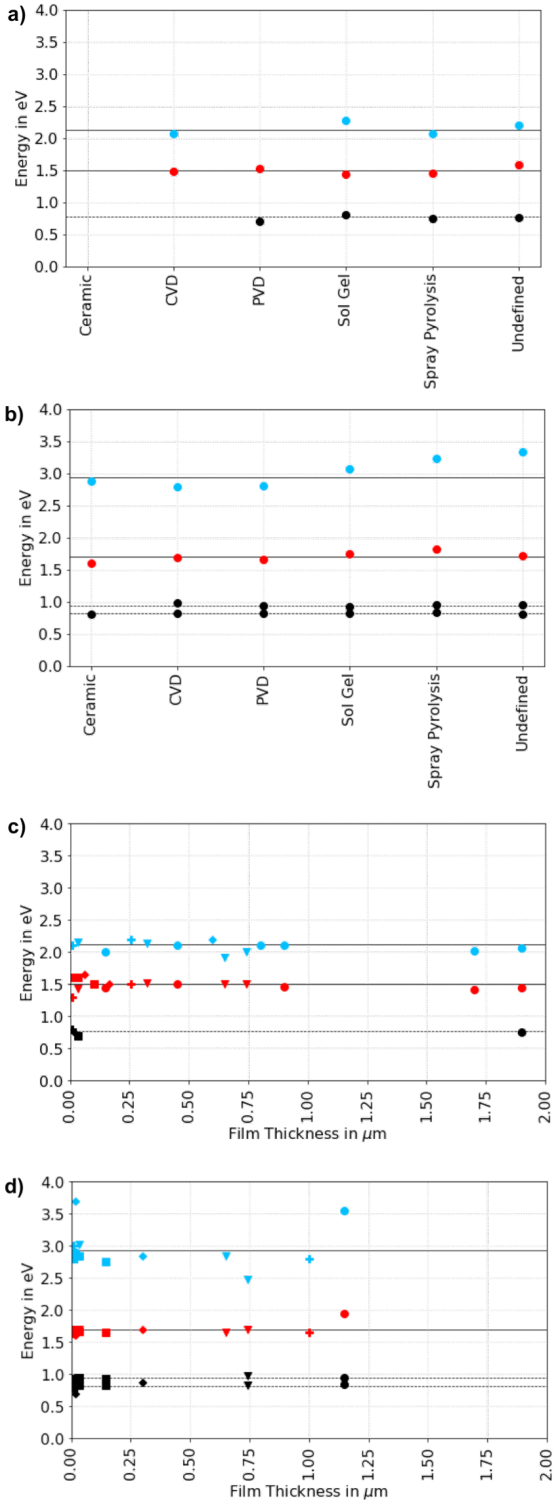

Figure C.1: Relation between method to prepare Co_3O_4 sample and experimental **a)** band gaps and **b)** absorption bands as well as relation between film thickness of Co_3O_4 thin films for **c)** band gaps and **d)** absorption bands with triangles symbolizing CVD, squares PVD, pluses sol gel, circles spray pyrolysis, and diamonds undefined prepared thin films.

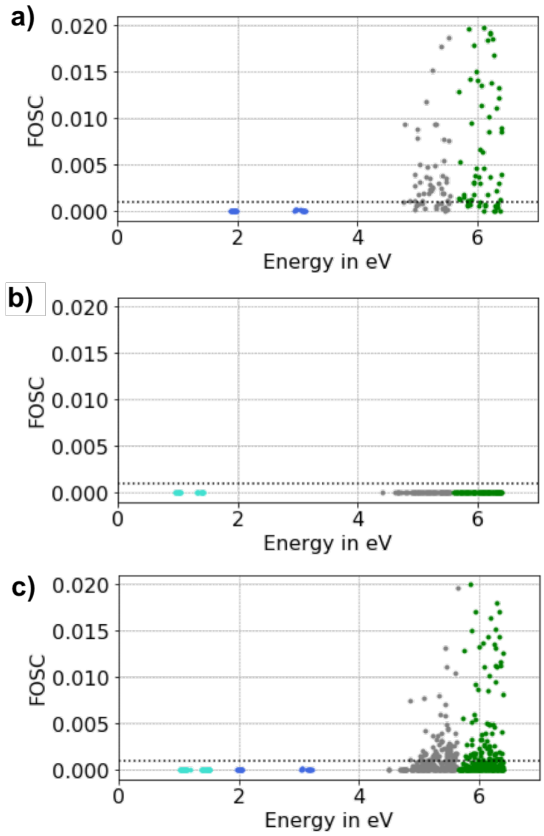

Figure C.2: Excited states of Co_2ZnO_4 for system size 2t4o computed with TD-DFT with **a)** only singlet, **b)** only triplet, and **c)** spin-orbit coupled states. Level of theory: PBE0/def2-QZVPP. Color code: Co(III) $3d$ $t_{2g} \rightarrow e_g$ triplet (turquoise) and singlet (blue) excitations, Co(III) $3d \rightarrow 3d$ Co(III) MMCT (gray), O $2p$ →Co(III) $3d$ LMCT (green)

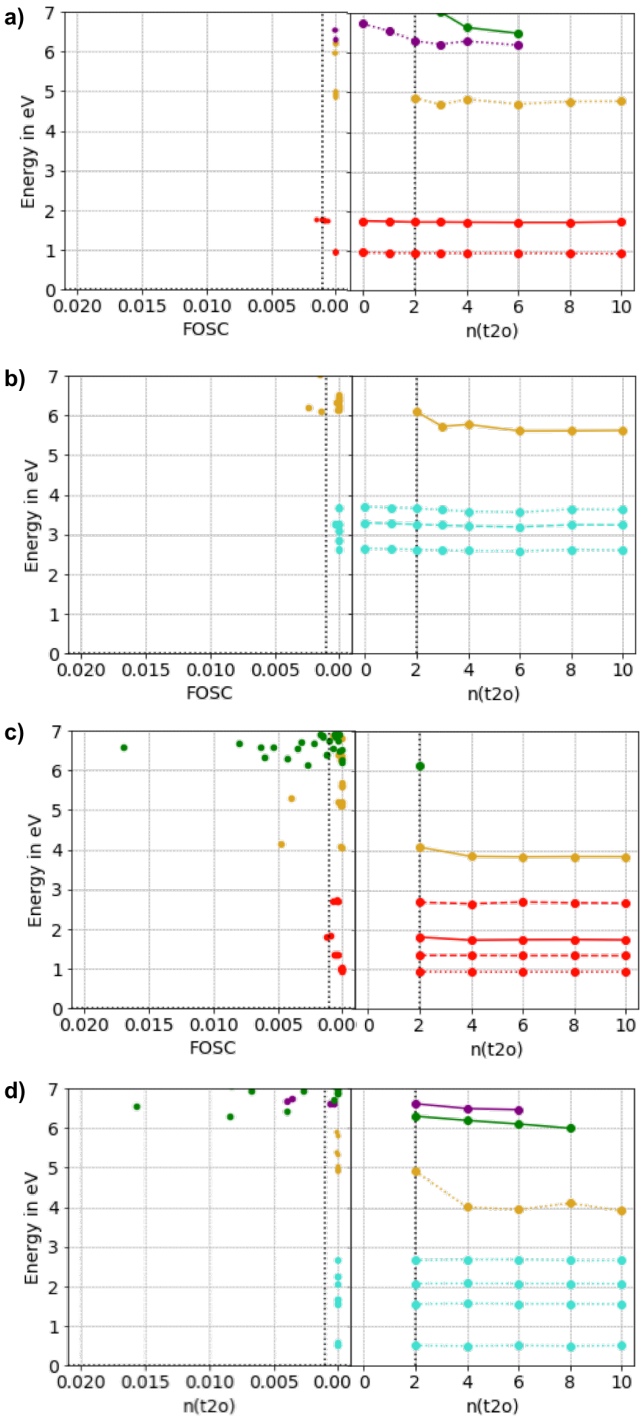

Figure C.3: Different TD-DFT approaches for calculating the excited states in Al_2CoO_4: **a)** high spin, **b)** high spin with spin slip, **c)** broken-symmetry, **d)** broken-symmetry with SF. Color code: Co(II) $3d$ $e \rightarrow t_2$ excitation (red), Co(II) $3d$ $e \rightarrow t_2$ excitation with spin flip (turquoise), Co(II)→Co(II) MMCT (yellow), O $2p$ →Co(II) $3d$ LMCT (green), Co(II) $3d \rightarrow 4s$ (purple); dark states (dotted line), "potentially" non-dark states (dashed line), non-dark states (solid line). Level of theory: PBE0/def2-QZVPP.

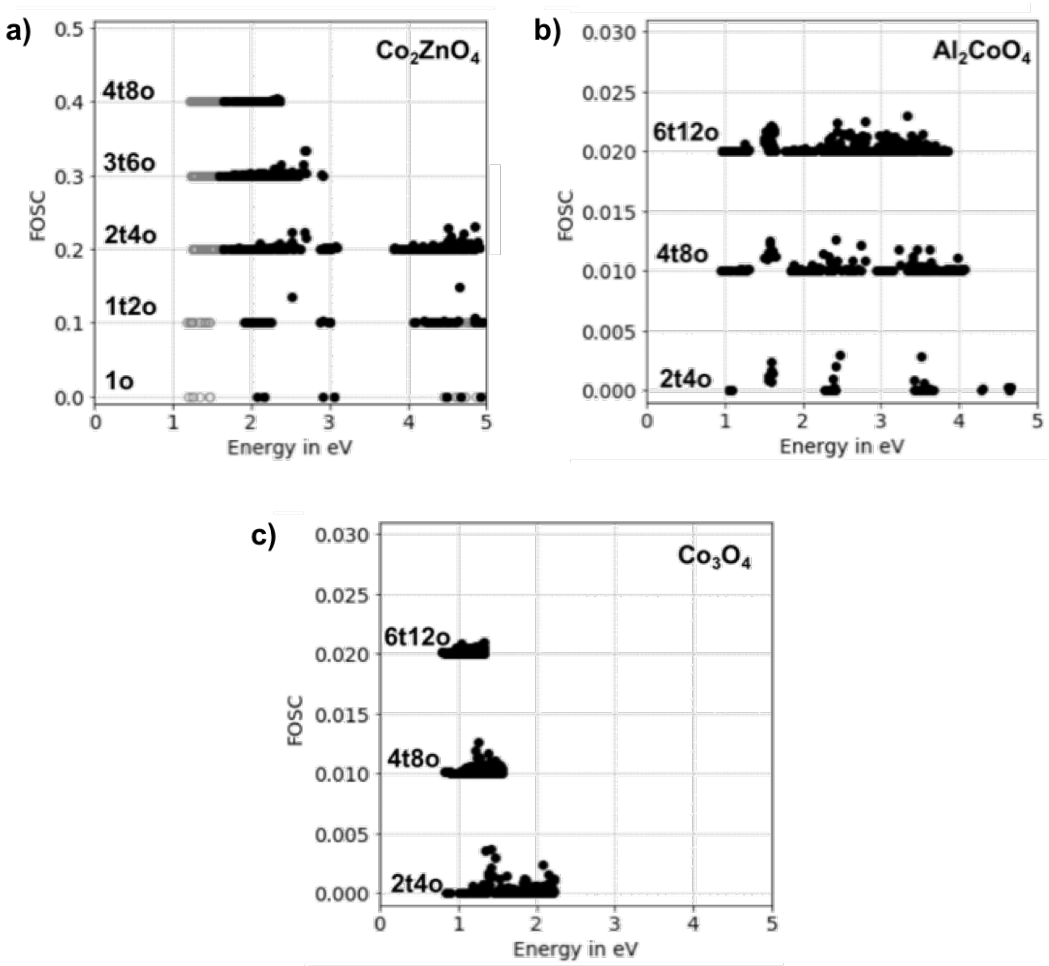

Figure C.4: Excited states of increasing system size computed with PBE/def2-QZVPP for **a)** Co_2ZnO_4, **b)** Al_2CoO_4, and **c)** Co_3O_4.

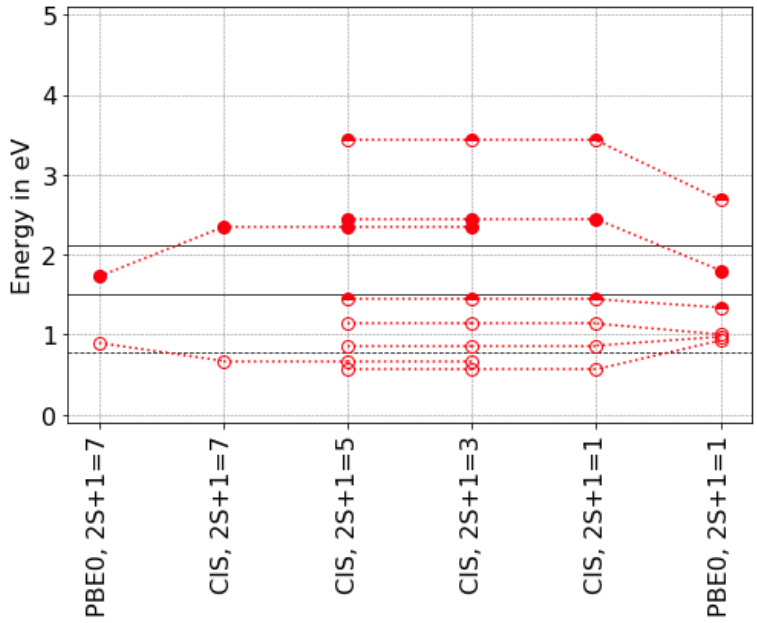

Figure C.5: First excited states of absorption bands of ligand field transitions in Al_2CoO_4 computed with system size 2t4o as high spin (2S+1=7), intermediate spins (2S+1=5 and 2S+1=3), and open singlet (2S+1=1) with PBE0 and CIS.

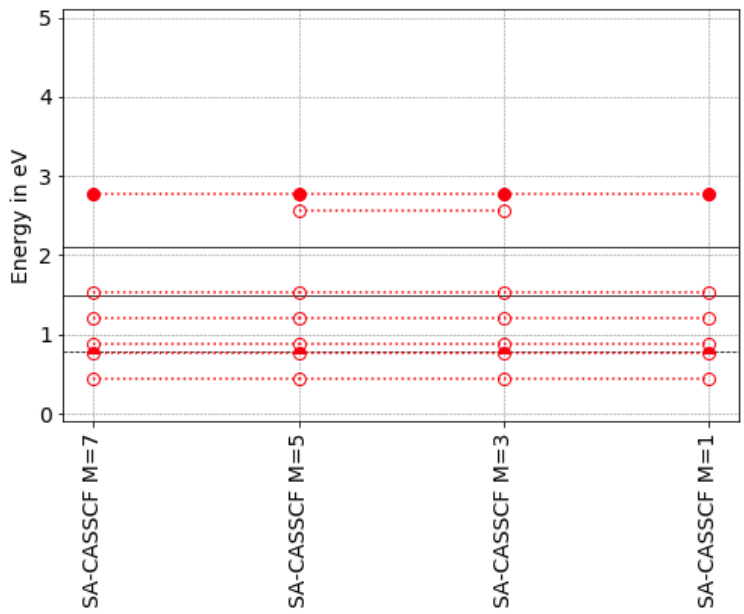

Figure C.6: First excited states of absorption bands originating from ligand field transitions in Al_2CoO_4 with system size 2t4o computed as high spin (2S+1=7), intermediate spins (2S+1=5 and 2S+1=3), and open singlet (2S+1=1) with SA-CASSCF.

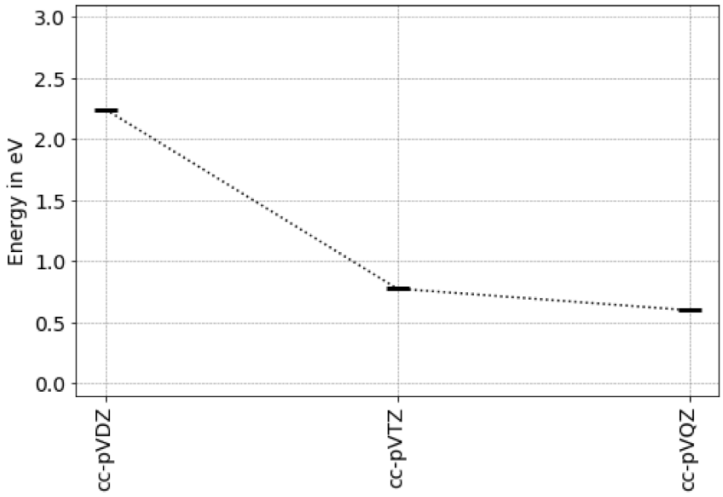

Figure C.7: Difference between "ionic" and "neutral" antiferromagnetic "ground states" with respect to the basis set size computed with NEVPT2 for cluster size 2t4o of the Al_2CoO_4 model.

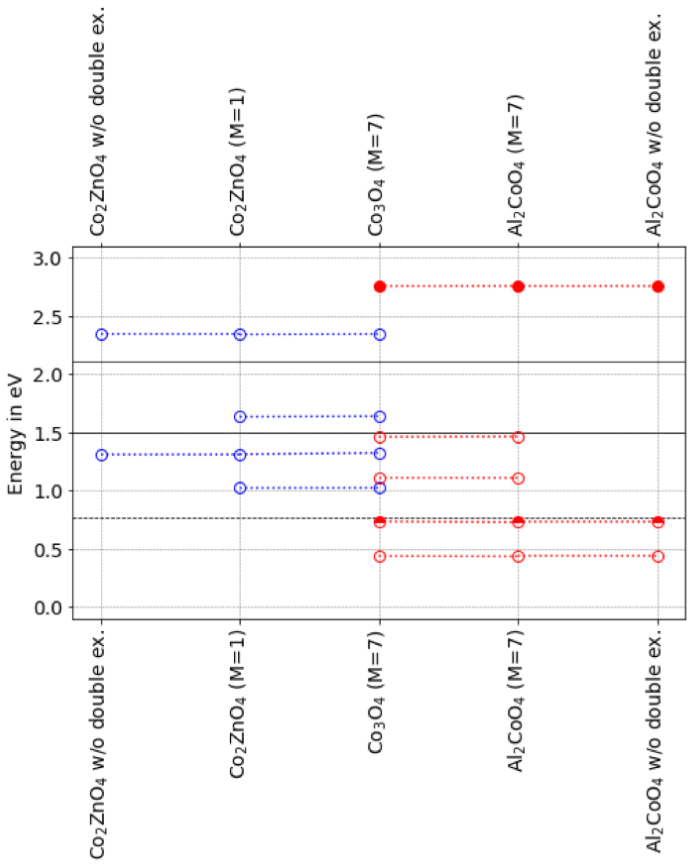

Figure C.8: Comparison of ICE-CI models of Al_2CoO_4, Co_2ZnO_4, and Co_3O_4 including states with oscillator strengths of zero (dark states). Oscillator strengths are taken from SA-CASSCF calcualtions with selected CSFs.

XES Studies of Co_3O_4

Experimental XES Measurements

The XES data collection was done at the PINK tender X-ray beamline at BESSY II. The PINK beamline is currently operated in commissioning mode. A considerable gain in fluorescence signal could be obtained by using a multilayer monochromator (∼100 eV band pass), and the energy of the incident beam was 8 keV. The beam size on the sample was 30 μm × 500 μm (V×H). All spectra were collected using an in-house-designed energy dispersive von Hamos spectrometer with a vacuum sample chamber environment (5 mbar working pressure). The analyser was set up in a vertical dispersion direction, taking advantage of the small vertical beam size to improve the energy resolution. A Si(620) crystal with a bending radius of R=250mm dispersed incoming fluorescence radiation onto an Eiger detector with a 75 μm ×

75 μm pixel size. The 80mm x 40mm detector chip accepted fluorescent radiation reflected from the crystal analyser under 76.3-68.3° Bragg angles that corresponded to an energy window of 7430-7770 eV.

The samples were packed as pure finely ground powder in a 1 mm thick aluminum sample holder covered with Kapton tape (38 m thick) and measured at room temperature. The energy was calibrated by measuring X-ray emission lines from 2 references loaded in the same configuration as the sample. As references, the $K\alpha$ lines from a Ni foil and the $K\beta_{1,3}$ from a Co foil were measured. The center of mass for the $K\alpha$ peaks (obtained from a fitting to a Voigt model), was calibrated to 7461.04 eV, 7478.26 eV and the maximum intensity of the $K\beta_{1,3}$ line was calibrated to 7649.45 eV. The resulting polynomial fit was used to calibrate the energies of the measured samples. The spectra were baseline corrected by applying a linear regression. They were also normalized in regard to the local maximum of the intensity of the $K\beta_{1,3}/K\beta'$ mainline and $K\beta_{2,5}/K\beta''$ VtC XES, respectively.

Example Input Files XES studies

Example Input One-Electron XES

```
! Ionic-Crystal-QMMM UKS BP86 DKH2 DKH-def2-tzvp AutoAux
!VeryTightSCF DEFGRID1 NormalPrint

%xes
Coreorb 0,0
Orbop 0,1
CoreOrbSOC 0,1
DoSOC true
end

%qmmm
  QMAtoms {0:6} end
  ORCAFFFilename "1o.ORCAFF.prms"
  HFLayers 0
  ECPLayerECP "SDD"
  ECPLayers 3
  CONV_Charges false
  ENFORCETOTALCHARGE true
  CHARGE_TOTAL    0
  PrintLevel 4
end


*xyzfile -9 1 1o.xyz
```

Example Input QRO Generation

```
! Ionic-Crystal-QMMM UKS BP86 DKH2 DKH-def2-tzvp VeryTightSCF
! SCFConv7 UNO DEFGRID1 Normalprint


%method SpecialGridAtoms 27
 SpecialGridIntAcc 7
 end

%qmmm
  QMAtoms {0:6} end
  ORCAFFFilename "1o.ORCAFF.prms"
  HFLayers 0
  ECPLayerECP "SDD"
  ECPLayers 3
  CONV_Charges false
  ENFORCETOTALCHARGE true
  CHARGE_TOTAL    0
  PrintLevel 4
end

*xyzfile -9 1 1o.xyz
```

Example Input CASCI XES

```
!Ionic-Crystal-QMMM autoaux DKH2 DKH-def2-tzvp
%method FrozenCore FC_NONE end
! NormalPrint
! MOREAD
! NoLoewdin NoMulliken

%moinp "1o.qro"

%scf
rotate {0,35,90} {12,36,90} {13,37,90} {14,38,90} end
end

%casscf
nel 13
norb 9
nroots 5000,5000,5000
mult 2,4,6
maxiter 1
refs
{1 2 2 2 2 2 2 0 0}
{2 1 2 2 2 2 2 0 0}
{2 2 1 2 2 2 2 0 0}
[…]
end
rel
Quad true
DoSOC true
XESSOC true
XASMOs 35
DoDTensor false
end
end

%method SpecialGridAtoms 27
 SpecialGridIntAcc 7
 end

%qmmm
  QMAtoms {0:6} end
  ORCAFFFilename "1o.ORCAFF.prms"
  HFLayers 0
  ECPLayerECP "SDD"
  ECPLayers 3
  CONV_Charges false
  ENFORCETOTALCHARGE true
  CHARGE_TOTAL    0
  PrintLevel 4
end

*xyzfile -8 2 1o.xyz
```

Additional Information Mainline XES Study

CSFs for the Co_2ZnO_4 mainline XES spectrum

Initial States

$$|0\rangle_I = |1s3p\bar{3p}3d_{t_{2g}}3\bar{d}_{t_{2g}}| \tag{C.1}$$

$$|Q_3^{3e_g}d_{t_{2g}} + \frac{1}{2}\rangle_I = \frac{1}{\sqrt{2}}(|1s3p\bar{3p}3d_{t_{2g}}3\bar{d}_{e_g}| - |1s3p\bar{3p}3d_{e_g}3\bar{d}_{t_{2g}}|) \tag{C.2a}$$

$$|Q_3^{3e_g}d_{t_{2g}} - \frac{1}{2}\rangle_I = \frac{1}{\sqrt{2}}(|\bar{1s}3p\bar{3p}3d_{t_{2g}}3\bar{d}_{e_g}| - |\bar{1s}3p\bar{3p}3d_{e_g}3\bar{d}_{t_{2g}}|) \tag{C.2b}$$

$$|D_3^{3e_g}d_{t_{2g}} + \frac{1}{2}\rangle_I = \frac{1}{\sqrt{6}}(|1s3p\bar{3p}3d_{t_{2g}}3\bar{d}_{e_g}| - |1s3p\bar{3p}3d_{e_g}3\bar{d}_{t_{2g}}| + 2|\bar{1s}3p\bar{3p}3d_{t_{2g}}3d_{e_g}|) \tag{C.3a}$$

$$|D_3^{3e_g}d_{t_{2g}} - \frac{1}{2}\rangle_I = \frac{1}{\sqrt{6}}(|\bar{1s}3p\bar{3p}3d_{t_{2g}}3\bar{d}_{e_g}| + |\bar{1s}3p\bar{3p}3d_{e_g}3\bar{d}_{t_{2g}}| + 2|\bar{1s}3p\bar{3p}3\bar{d}_{t_{2g}}3\bar{d}_{e_g}|) \tag{C.3b}$$

$$|C_3^{3e_g}d_{t_{2g}} + \frac{1}{2}\rangle_I = \frac{1}{\sqrt{2}}(|1s3p\bar{3p}3d_{t_{2g}}3\bar{d}_{e_g}| - |1s3p\bar{3p}3d_{e_g}3\bar{d}_{t_{2g}}|) \tag{C.4a}$$

$$|C_3^{3e_g}d_{t_{2g}} - \frac{1}{2}\rangle_I = \frac{1}{\sqrt{2}}(|\bar{1s}3p\bar{3p}3d_{t_{2g}}3\bar{d}_{e_g}| + |\bar{1s}3p\bar{3p}3d_{e_g}3\bar{d}_{t_{2g}}|) \tag{C.4b}$$

Final States

$$|A_{3p}^{1s} + \frac{1}{2}\rangle_F = |1s\bar{1s}3p3d_{t_{2g}}3\bar{d}_{t_{2g}}| \tag{C.5a}$$

$$|A_{3p}^{1s} - \frac{1}{2}\rangle_F = |1s\bar{1s}\bar{3p}3d_{t_{2g}}3\bar{d}_{t_{2g}}| \tag{C.5b}$$

$$|Q_3^{3e_g}d_{t_{2g}} + \frac{1}{2}\rangle_F = \frac{1}{\sqrt{2}}(|1s\bar{1s}3p3d_{t_{2g}}3\bar{d}_{e_g}| - |1s\bar{1s}3p3d_{e_g}3\bar{d}_{t_{2g}}|) \tag{C.6a}$$

$$|Q_3^{3e_g}d_{t_{2g}} - \frac{1}{2}\rangle_I = \frac{1}{\sqrt{2}}(|1s\bar{1s}\bar{3p}3d_{t_{2g}}3\bar{d}_{e_g}| - |1s\bar{1s}\bar{3p}3d_{e_g}3\bar{d}_{t_{2g}}|) \tag{C.6b}$$

$$|D_3^{3e_g} d_{t_{2g}} + \frac{1}{2}\rangle_I = \frac{1}{\sqrt{6}}(|1s\bar{1}s3p3d_{t_{2g}}3\bar{d}_{e_g}| - |1s\bar{1}s3p3d_{e_g}3\bar{d}_{t_{2g}}| + 2|1s\bar{1}s\bar{3}p3d_{t_{2g}}3d_{e_g}|) \tag{C.7a}$$

$$|D_3^{3e_g} d_{t_{2g}} - \frac{1}{2}\rangle_I = \frac{1}{\sqrt{6}}(|1s\bar{1}s\bar{3}p3d_{t_{2g}}3\bar{d}_{e_g}| + |1s\bar{1}s\bar{3}p3d_{e_g}3\bar{d}_{t_{2g}}| + 2|1s\bar{1}s\bar{3}p3\bar{d}_{t_{2g}}3\bar{d}_{e_g}|) \tag{C.7b}$$

$$|C_3^{3e_g} d_{t_{2g}} + \frac{1}{2}\rangle_I = \frac{1}{\sqrt{2}}(|1s\bar{1}s3p3d_{t_{2g}}3\bar{d}_{e_g}| - |1s\bar{1}s3p3d_{e_g}3\bar{d}_{t_{2g}}|) \tag{C.8a}$$

$$|C_3^{3e_g} d_{t_{2g}} - \frac{1}{2}\rangle_I = \frac{1}{\sqrt{2}}(|1s\bar{1}s\bar{3}p3d_{t_{2g}}3\bar{d}_{e_g}| + |1s\bar{1}s\bar{3}p3d_{e_g}3\bar{d}_{t_{2g}}|) \tag{C.8b}$$

CSFs for the Al_2CoO_4 mainline XES spectrum

Initial States

$$|Quint + 2\rangle_I = |1s3p\bar{3}p3d_e3\bar{d}_e3d_{t_2,1}3d_{t_2,2}3d_{t_2,3}| \tag{C.9a}$$

$$|Quint - 2\rangle_I = |\bar{1}s3p\bar{3}p3d_e3\bar{d}_e3\bar{d}_{t_2,1}3\bar{d}_{t_2,2}3\bar{d}_{t_2,3}| \tag{C.9b}$$

$$\begin{aligned}|Trip_0 + 1\rangle_I = \frac{1}{\sqrt{2}}(&|1s3p\bar{3}p3d_e3\bar{d}_e3\bar{d}_{t_2,1}3d_{t_2,2}3d_{t_2,3}| \\ &+|\bar{1}s3p\bar{3}p3d_e3\bar{d}_e3d_{t_2,1}3d_{t_2,2}3d_{t_2,3}|)\end{aligned} \tag{C.10a}$$

$$\begin{aligned}|Trip_0 - 1\rangle_I = \frac{1}{\sqrt{2}}(&1s3p\bar{3}p3d_e3\bar{d}_e3\bar{d}_{t_2,1}3\bar{d}_{t_2,2}3\bar{d}_{t_2,3}| \\ &+|\bar{1}s3p\bar{3}p3d_e3\bar{d}_e3d_{t_2,1}3\bar{d}_{t_2,2}3d_{t_2,3}|)\end{aligned} \tag{C.10b}$$

$$\begin{aligned}|Trip_1 + 1\rangle_I = \frac{1}{\sqrt{6}}(&2|1s3p\bar{3}p3d_e3\bar{d}_e3d_{t_2,1}3\bar{d}_{t_2,2}3d_{t_2,3}| \\ &-|1s3p\bar{3}p3d_e3\bar{d}_e3\bar{d}_{t_2,1}3d_{t_2,2}3d_{t_2,3}| \\ &-|\bar{1}s3p\bar{3}p3d_e3\bar{d}_e3d_{t_2,1}3d_{t_2,2}3d_{t_2,3}|)\end{aligned} \tag{C.11a}$$

$$\begin{aligned}|Trip_1 - 1\rangle_I = \frac{1}{\sqrt{6}}(&|1s3p\bar{3}p3d_e3\bar{d}_e3\bar{d}_{t_2,1}3\bar{d}_{t_2,2}3\bar{d}_{t_2,3}| \\ &+|\bar{1}s3p\bar{3}p3d_e3\bar{d}_e3d_{t_2,1}3\bar{d}_{t_2,2}3\bar{d}_{t_2,3}| \\ &-2|\bar{1}s3p\bar{3}p3d_e3\bar{d}_e3\bar{d}_{t_2,1}3d_{t_2,2}3\bar{d}_{t_2,3}|)\end{aligned} \tag{C.11b}$$

$$
\begin{aligned}
|Trip_2+1\rangle_I = \frac{1}{\sqrt{12}}(&3|1s3p\bar{3}\bar{p}3d_e3\bar{d}_e3d_{t_2,1}3d_{t_2,2}3\bar{d}_{t_2,3}| \\
&-|1s3p\bar{3}\bar{p}3d_e3\bar{d}_e3d_{t_2,1}3\bar{d}_{t_2,2}3d_{t_2,3}| \\
&-|1s3p\bar{3}\bar{p}3d_e3\bar{d}_e3\bar{d}_{t_2,1}3d_{t_2,2}3d_{t_2,3}| \\
&-|\bar{1}s3p\bar{3}\bar{p}3d_e3\bar{d}_e3d_{t_2,1}3d_{t_2,2}3d_{t_2,3}|)
\end{aligned}
\tag{C.11c}
$$

$$
\begin{aligned}
|Trip_2-1\rangle_I = \frac{1}{\sqrt{12}}(&|1s3p\bar{3}\bar{p}3d_e3\bar{d}_e3\bar{d}_{t_2,1}3\bar{d}_{t_2,2}3\bar{d}_{t_2,3}| \\
&+|\bar{1}s3p\bar{3}\bar{p}3d_e3\bar{d}_e3d_{t_2,1}3\bar{d}_{t_2,2}3\bar{d}_{t_2,3}| \\
&+|\bar{1}s3p\bar{3}\bar{p}3d_e3\bar{d}_e3\bar{d}_{t_2,1}3d_{t_2,2}3\bar{d}_{t_2,3}| \\
&-3|\bar{1}s3p\bar{3}\bar{p}3d_e3\bar{d}_e3d_{t_2,1}3d_{t_2,2}3d_{t_2,3}|)
\end{aligned}
\tag{C.11d}
$$

Final States

$$
|Quint+2\rangle_F = |1s\bar{1}s3p3d_e3\bar{d}_e3d_{t_2,1}3d_{t_2,2}3d_{t_2,3}| \tag{C.12a}
$$

$$
|Quint-2\rangle_F = |1s\bar{1}s\bar{3}\bar{p}3d_e3\bar{d}_e3\bar{d}_{t_2,1}3\bar{d}_{t_2,2}3\bar{d}_{t_2,3}| \tag{C.12b}
$$

$$
\begin{aligned}
|Trip_0+1\rangle_F = \frac{1}{\sqrt{2}}(&|1s\bar{1}s3p3d_e3\bar{d}_e3\bar{d}_{t_2,1}3d_{t_2,2}3d_{t_2,3}| \\
&+|1s\bar{1}s\bar{3}\bar{p}3d_e3\bar{d}_e3d_{t_2,1}3d_{t_2,2}3d_{t_2,3}|)
\end{aligned}
\tag{C.13a}
$$

$$
\begin{aligned}
|Trip_0-1\rangle_F = \frac{1}{\sqrt{2}}(&1s\bar{1}s3p3d_e3\bar{d}_e3\bar{d}_{t_2,1}3\bar{d}_{t_2,2}3\bar{d}_{t_2,3}| \\
&+|1s\bar{1}s\bar{3}\bar{p}3d_e3\bar{d}_e3d_{t_2,1}3\bar{d}_{t_2,2}3d_{t_2,3}|)
\end{aligned}
\tag{C.13b}
$$

$$
\begin{aligned}
|Trip_1+1\rangle_I = \frac{1}{\sqrt{6}}(&2|1s\bar{1}s3p3d_e3\bar{d}_e3d_{t_2,1}3\bar{d}_{t_2,2}3d_{t_2,3}| \\
&-|1s\bar{1}s3p3d_e3\bar{d}_e3\bar{d}_{t_2,1}3d_{t_2,2}3d_{t_2,3}| \\
&-|1s\bar{1}s\bar{3}\bar{p}3d_e3\bar{d}_e3d_{t_2,1}3d_{t_2,2}3d_{t_2,3}|)
\end{aligned}
\tag{C.14a}
$$

$$
\begin{aligned}
|Trip_1-1\rangle_I = \frac{1}{\sqrt{6}}(&|1s\bar{1}s3p3d_e3\bar{d}_e3\bar{d}_{t_2,1}3\bar{d}_{t_2,2}3\bar{d}_{t_2,3}| \\
&+|1s\bar{1}s\bar{3}\bar{p}3d_e3\bar{d}_e3d_{t_2,1}3\bar{d}_{t_2,2}3\bar{d}_{t_2,3}| \\
&-2|1s\bar{1}s\bar{3}\bar{p}3d_e3\bar{d}_e3\bar{d}_{t_2,1}3d_{t_2,2}3\bar{d}_{t_2,3}|)
\end{aligned}
\tag{C.14b}
$$

$$
\begin{aligned}
|Trip_2+1\rangle_I = \frac{1}{\sqrt{12}}(3|1s\bar{1}s3p3d_e3\bar{d}_e3d_{t_2,1}3d_{t_2,2}3\bar{d}_{t_2,3}| \\
-|1s\bar{1}s3p3d_e3\bar{d}_e3d_{t_2,1}3\bar{d}_{t_2,2}3d_{t_2,3}| \\
-|1s\bar{1}s3p3d_e3\bar{d}_e3\bar{d}_{t_2,1}3d_{t_2,2}3d_{t_2,3}| \\
-|1s\bar{1}s3\bar{p}3d_e3\bar{d}_e3d_{t_2,1}3d_{t_2,2}3d_{t_2,3}|)
\end{aligned}
\tag{C.14c}
$$

$$
\begin{aligned}
|Trip_2-1\rangle_I = \frac{1}{\sqrt{12}}(|1s\bar{1}s3p3d_e3\bar{d}_e3\bar{d}_{t_2,1}3\bar{d}_{t_2,2}3\bar{d}_{t_2,3}| \\
+|1s\bar{1}s3\bar{p}3d_e3\bar{d}_e3d_{t_2,1}3\bar{d}_{t_2,2}3\bar{d}_{t_2,3}| \\
+|1s\bar{1}s3\bar{p}3d_e3\bar{d}_e3\bar{d}_{t_2,1}3d_{t_2,2}3\bar{d}_{t_2,3}| \\
-3|1s\bar{1}s3\bar{p}3d_e3\bar{d}_e3d_{t_2,1}3d_{t_2,2}3d_{t_2,3}|)
\end{aligned}
\tag{C.14d}
$$

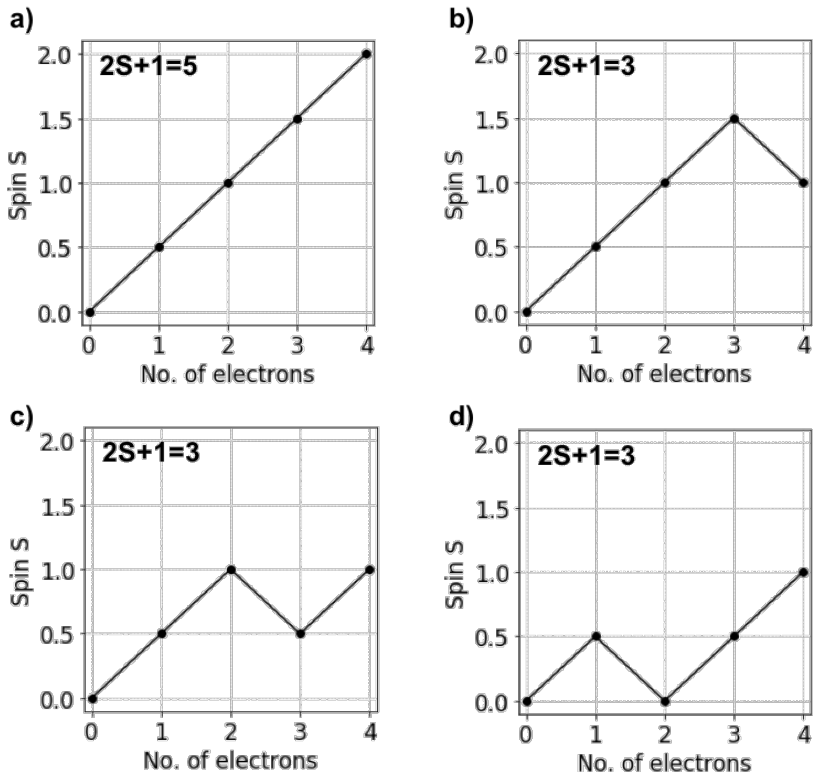

Figure C.9: Spin branching diagrams representing 4e4o CSFs coupling to **a)** 2S+1=5 and **b)-d)** 2S+1=3.

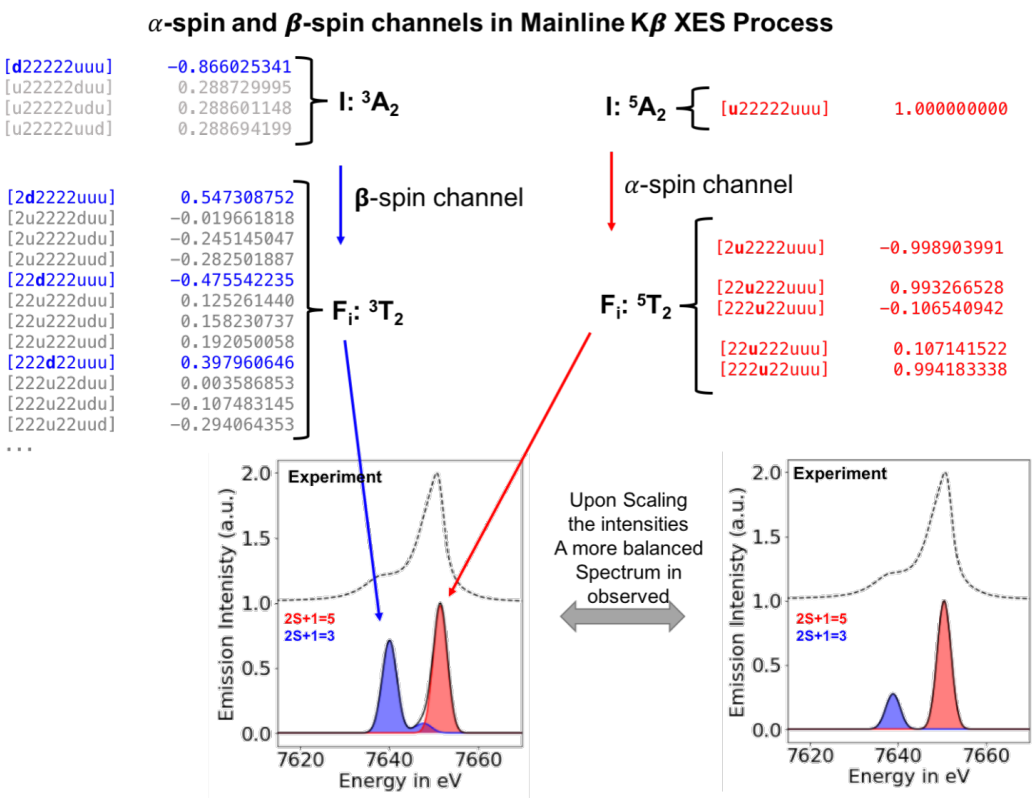

Figure C.10: Example for overmixing of α and β emission pathways in the CI for cluster model 1t of Al_2CoO_4.

List of Abbreviations

AO Atomic Orbital

BG Band Gap

BR Boundary Region

BS Broken-Symmetry

bt-PNO back-transformed pair-natural-orbitals

calc. Calculated

CAS Complete Active Space

CC Coupled Cluster

CI Configuration Interaction

CN Coordination Number

CSF Configuration State Function

DFT Density Functional Theory

DLPNO Domain Localized Pair Natural Orbital

EA Electron Affinity

ECP Electrostatic Core Potentials

EE Excitation Energy

EOM Equation of Motion

exp. Experimental

FS Final State

GS Ground State

HF Hartree-Fock

IP Ionization Potential

IS Initial State

MO Molecular Orbital

MR Multi-Reference

NMR Nuclear Magnetic Resonance

NSC Nuclear Shielding Constant

o Octahedral

opt. Optical

PC Point Charge

pot. Potential

QC Quantum Cluster

QM/MM Quantum Mechanics/Molecular Mechanics

QRO Quasi-Restricted Orbitals

ref. Reference

SA State-Averaged

SCe Supercell

SCl Spherical Cluster

SOC Spin-Orbit Coupling

STEOM Similarity-Transformed-Equation-of-Motion

t Tetrahedral

trans. Transport

VtC Valence-to-Core

XAS X-Ray Absorption Spectroscopy

XES X-Ray Emission Spectroscopy

List of Figures

2.1 A schematic representation from a unit cell (= one cube) to ever larger supercells to an "infinite" crystal. 12

2.2 Total potential energy (black), Coulomb potential (blue), and repulsion potential (red) of an interaction between a cation and an anion as a function of their distance r/r_0, where r_0 is their equilibrium distance. 13

2.3 One-dimensional charge array with alternating positive and negative charges and the resulting Coulomb potential of the first charge on the left. Figure inspired by ref. [87]. 14

2.4 **a)** Unit cell and supercell of NaCl in the rock salt structure. **b)** The Madelung constant of an ion in the center of a rock salt supercell with increasing supercell size in terms of the number of Na^+ and Cl^- ions. 15

2.5 MO diagram of a diatomic NaCl molecule. 18

2.6 **a)** Schematic representation of the valence band formation from the HOMO and the conduction band formation from the LUMO for NaCl. **b)** Orbital picture of NaCl models with increasing cluster sizes. Level of theory: HF/def2-tzvp, clusters modeled with the electrostatic embedded cluster approach. 19

2.7 **a)** Band structure and **b)** Density of States (DOS) from a periodic calculation compared to **c)** "Density of States" generated from **d)** the orbitals of a non-periodic calculation of NaCl with system size $[Na_{32}Cl_{32}]^0$. Reduced and modified band structure and density of states data taken from ref. [104]. 21

3.1 Electrostatic embedded cluster model for NaCl with the QC (quantum cluster: atomic structure in the center, green: Cl and purple: Na), the BR (boundary region, red), and the PC (point charge field, small dots) field. 26

3.2 Schematic protocol for the creation of an electrostatic embedded cluster model using data from a CIF to create a supercell and the resulting QC, BR, and PC field. 29

3.3 Sample excerpts from a possible input file for ORCA_CrystalPrep, generated via "geninput" with ORCA_CrystalPrep and modified accordingly. 31
3.4 Example input file (left) and the corresponding point charge file (right) for a "simple" electrostatic embedded cluster calculation with ORCA for the example of an embedded $[Na_4Cl_4]^0$ cluster. 33
3.5 Typical workflow for a calculation protocol that follows the "simple" electrostatic embedded cluster approach to model a crystal. 34
3.6 Typical workflow for a calculation protocol that uses the Ionic-Crystal-QM/MM environment in ORCA to model a crystal. 35
3.7 Example input file (top), corresponding xyz file (bottom left), and force field file (bottom right) for an electrostatically embedded cluster calculation using Ionic-Crystal-QM/MM in ORCA for the example of an $[Na_4Cl_4]^0$ cluster. 36
3.8 Different QC sizes of NaCl (rock salt structure) for the supercell approach (SCe) and spherical cluster approach (SCl). 40
3.9 Convergence of the energy of the HOMO-LUMO gap for increasing SCe (red) and SCl (blue) NaCl clusters with (solid line) and without (dashed line) electrostatic embedding environment. 41
3.10 Construction of a "QC + HF" cluster model with $[Na_6Cl_{19}]^{13-}$ as the QC, extended to $[Na_{63}Cl_{62}]^+$ with HF layers, and corresponding ORCA input files for the "simple" embedding approach (left) and Ionic-Crystal-QM/MM (right). Color code: Part of QC treated with HF (blue). . . . 42
3.11 Different QC sizes for ZnS (zinc blende structure) for the supercell approach (SCe) and spherical cluster approach (SCl). 43
3.12 Different QC sizes for Co_3O_4 (spinel structure) for the spherical cluster approach (SCl). The abbreviation "t" stands for tetrahedral and represents a tetrahedral unit $[Co(II)O_4]^{6-}$ and the "o" stands for octahedral and represents a distorted octahedral unit $[Co(III)O_6]^{9-}$. 44
3.13 Different BR sizes defined by ECP layers around the QC examples $[Na_4Cl_4]^0$ and $[NaCl_6]^{5-}$. 45
3.14 Change in kinetic energy T for **a)** the total system and **b)** average per electron with increasing number of ECP layers for the systems $[Na_4Cl_4]^0$ (turquoise), $[Na_{32}Cl_{32}]^0$ (blue), $[Na_6Cl]^{5+}$ (gray), $[NaCl_6]^{5-}$ (red), and $[Na_6Cl_{19}]^{13-}$ (yellow). 46

3.15 Energy change of **a)** the HOMO-LUMO gap, **b)** the HOMO, and **c)** the LUMO with increasing number of ECP layers for systems $[Na_4Cl_4]^0$ (turquoise), $[Na_{32}Cl_{32}]^0$ (blue), $[Na_6Cl]^{5+}$ (gray), $[NaCl_6]^{5-}$ (red), and $[Na_6Cl_{19}]^{13-}$ (yellow). 47
3.16 Change in potential energy V with increasing number of lattice points for $[Na_4Cl_4]^0$ (turquoise) and $[Na_{32}Cl_{32}]^0$ (blue). 48
3.17 **a)** Color code of the different atomic positions in a QC for the example of $[Na_{32}Cl_{32}]^0$ in the rock salt structure showing the tip (blue), edge (purple), surface (gray), and bulk (red). **b)** Charge distribution within the QC $[Na_{32}Cl_{32}]^0$ when the applied charge of ECPs and PCs is too low (±0.6, circle with filled bottom), matches the charges of the QC (±0.92, filled circle), and is too high (±1.2, circle with filled top). Charges calculated with CHELPG. Level of theory: PBE/def2-tzvp. . 49
3.18 Dependence of CHELPG, Mulliken, Loewdin, and Hirshfeld charges on **a)** the basis set size (method: PBE); Color code: def2-SVP (gray), def2-TZVP (red), def2-QZVPP (yellow), cc-pVDZ (turquoise), cc-pVTZ (blue), cc-pVQZ (brown), cc-pV5Z (black) and **b)** the level of theory (basis set: def-TZVP); Color code: average GGA (gray), average hybrid functional (red), double-hybrid functional B2PLYP (yellow), DLPNO-CCSD (turquoise), Hartree-Fock (blue); Cluster example: $[Na_4Cl_4]^0$. The specific GGA and hybrid functionals and there calculated charges can be found in Figure A.4 on page 313 in the appendix. 52
3.19 Linear regression of the applied charges vs. the average charges in the QC to find the point where the applied and QC charges match for the example $[Na_{32}Cl_{32}]^0$. Level of theory: PBE/def2-TZVP. 53
3.20 Convergence of the optimized charge with cluster size for a series of electrostatically embedded NaCl QCs in the SCe approach. Level of theory: PBE/def2-TZVP. 53
3.21 Comparison of the optimized charges for the electrostatically embedded QC $[Na_6Cl_{19}]^{13-}$ with and without HF layers. Level of theory: PBE/def2-tzvp + HF/LANL2DZ. Color Code: HF atoms (blue). . . . 54
3.22 Dependence of the HOMO-LUMO gap of $[Na_{32}Cl_{32}]^0$ on different applied charges. Level of theory: HF/def2-tzvp. 55

5.1 Schematic representation of an absorption and emission process. . . 69
5.2 The electromagnetic spectrum and the types of excited states caused by electromagnetic waves of different wavelengths λ/ frequencies ν. 69

6.1 Orbital diagram of exemplary selected ground and excited state determinants. 73
6.2 Schematic representation of the construction of the orbital space for CASSCF/CASCI (left) and RASSCF/RASCI (right) calculations. . . . 78

7.1 Schematic representation of the excitation process between spin states in NMR spectroscopy. 87

8.1 Schematic representation of the optical (opt.) and transport (trans.) band gaps (BG) in a solid-state system. Nomenclature: IP = ionic potential, EA = electron affinity, E_B = exciton binding energy, E_0 = ground state energy, E_1 = first excited state energy. Figure inspired by ref. [239]. 93
8.2 Schematic representation of the expected errors symbolized by arrows of different sizes in comparison for different single-reference methods for the calculation of **a)** optical (opt.) and **b)** transport (trans.) band gaps (BG). Nomenclature: GS = ground state, HL gap = HOMO-LUMO gap. 99
8.3 **a)** Schematic representation of the XES process resulting as a secondary process from a K-edge XAS and **b)** the corresponding XES spectra. Figure inspired by ref. [62]. 101

9.1 Benchmark set of inorganic and organic semiconductors and insulators. 107
9.2 Excitation scheme of **a)** LiCl and **b)** ZnS adopted in a one-electron picture assuming an O_h ligand field coordination environment around Li or Cl centers and a T_d one around the Zn or S centers. Color-coded arrows: dipole-allowed transitions (green solid arrows), dipole-forbidden transitions (red dashed arrows). 112

10.1 Nomenclature for the example of the quantum clusters $[Na_{32}Cl_{32}]^0$ and $[Na_{19}Cl_{44}]^{25-}$. Centers with different chemical environments are denoted with color code: tip (blue), edge (purple), surface (grey), and bulk (red). Small spheres: Na, large spheres: Cl. 118
10.2 NSCs vs. electrostatic charges (CHELPG) for the different Na sites in the quantum cluster ($[Na_{32}Cl_{32}]^0$) treated within the electrostatic embedded cluster approach (full circles) or as a bare neutral cluster (non-embedded, empty circles). Color code: tip (blue), edge (purple), surface (grey), and bulk (red). 119

10.3 NSCs of Na (left) and Cl (right) in NaCl for a sequence of **a)** and **b)** bare SCe clusters (dashed line) and **c)** and **d)** embedded SCe (dotted line) and SCl clusters (solid line). **e)** and **f)** Comparison of NSCs of bare (dashed line) and embedded SCe (dotted line) and embedded SCl clusters (solid line) at the bulk cluster position. Color code: tip (blue), edge (purple), surface (gray), and bulk (red). Level of theory: PBE/pcSseg-2. 121
10.4 NSCs of **a)** Na and **b)** Cl for NaCl for a sequence of embedded SCe (dotted line) and SCl (solid line) clusters. Color code: tip (blue), edge (purple), surface (grey), and bulk (red). Level of theory: MP2/pcSseg-1. 125
10.5 NSCs of **a)** Na in embedded $[NaCl_6]^{5-}$ and **b)** Cl in embedded $[Na_6Cl]^{5+}$ clusters for increasing pcSseg-X basis set size calculated with PBE (yellow), PBE0 (red), DSD-PBEP86 (blue), and MP2 (turquoise). . . . 126
10.6 NSCs of Na in embedded $[NaCl_6]^{5-}$ computed with **a)** PBE and **b)** MP2 and Cl in embedded $[Na_6Cl]^{5+}$ computed with **c)** PBE and **d)** MP2 calculated with contracted (solid line) and decontracted (dashed line) basis sets: pcSseg-X (turquoise), def2-XVPP (red), and cc-pVXZ (blue). 127
10.7 NSCs of **a)** Na in non-embedded $[NaCl_6]^{5-}$ and **b)** Cl in non-embedded $[[Na_6Cl]^{5+}$ for different methods. Dashed blue line: PBE, PBE0, DSD-PBEP86, and solid red line: HF, MP2, CCSD, CCSD(T). Basis set: pcSseg-2. 128
10.8 NSCs (left, primary y-axis) of the halides Y in $[M_6Y_{19}]^{13-}$ for **a)** $[M_6F_{19}]^{13-}$, **b)** $[M_6Cl_{19}]^{13-}$, and **c)** $[M_6Br_{19}]^{13-}$ vs. experimental chemical shifts δ (right, secondary y-axis). Basis set: pcSseg-3. 133
10.9 NSCs (left, primary y-axis) of the alkali metals M in $[M_6Y_{19}]^{13-}$ for **a)** $[Li_6Y_{19}]^{13-}$, **b)** $[Na_6Y_{19}]^{13-}$, and **c)** $[K_6Y_{19}]^{13-}$ vs. experimental chemical shifts δ (right, secondary y-axis). Basis set: pcSseg-3. 135
10.10 NSCs (left, primary y-axis) of the metals in **a)** $[Mg_6Y_{19}]^{26-}$ and **b)** $[Zn_4Y_{10}]^{12-}$ vs. experimental chemical shifts δ (right, secondary y-axis). Basis set: pcSseg-3. 136
10.11 Absolute errors of calculated vs. experimental chemical shifts δ computed with different methods for **a)** halides, **b)** alkali metals, and **c)** magnesium and zinc. Basis set: pcSseg-3. 138

11.1 Calculation results of the first excited states of $[Li_nCl_n]^0$ (n=1-4, 6 and 8) with bt-PNO-STEOM-CCSD for charges equal to 1.05 (gray), 0.95 (turquoise) and 0.85 (blue) and with B3PW91 for charges equal to 1.05 (yellow), 0.95 (red) and 0.85 (green). Red dashed line: experiment. . . 145
11.2 Calculations of the first excited states of LiCl with the SCe approach ($[Li_nCl_n]^0$, n=1-4, 6, 8) with bt-PNO-STEOM-CCSD (turquoise) and B3PW91 (yellow) and with the SCl approach ($[LiCl_6]^{5-}$, $[Li_2Cl_{10}]^{8-}$, $[Li_4Cl_{16}]^{12-}$ and $[Li_6Cl_{19}]^{13-}$) with bt-PNO-STEOM-CCSD (blue) and B3PW91 (red). Red dashed line: experiment. 146
11.3 Comparison of cc-pVXZ basis set sizes with different methods BLYP (yellow), B3LYP (red), B2PLYP (blue), and bt-PNO-STEOM-CCSD (turquoise) for ($[Li_8Cl_8]^0$. Dashed line: extrapolated basis functions for bt-PNO-STEOM-CCSD. 148
11.4 Difference between first singlet and triplet excited states (blue) and between first singlet excited state and first excited state including SOC (red) for **a)** $[Li_8Cl_8]^0$ and for **b)** $[Zn_4S_{10}]^{12-}$. 151
11.5 CIS, TD-DFT, and bt-PNO-STEOM-CCSSD (STEOM-CC) calculated energy difference between first excited state and HOMO-LUMO gap ($\Delta E_{LR}^{S_0 \rightarrow S_1} - \Delta\epsilon^{HL}$) for the case of $[Li_8Cl_8]^0$ (blue) and $[Zn_4S_{10}]^{12-}$ (red) clusters. 152
11.6 Experimental versus calculated band gap energies with **a)** and **b)** PBE, **c)** and **d)** B3PW91, and **e)** and **f)** bt-PNO-STEOM-CCSD (STEOM-CC) for LiCl (left) for cluster sizes $[Li_nCl_n]^0$ with n=1-4, 6 and 8 and for ZnS (right) for cluster sizes $[ZnS_4]^{6-}$, $[Zn_2S_7]^{10-}$ and $[Zn_4S_{10}]^{12-}$. Color code: experiment (dashed red line), first excited state (turquoise line), HOMO-LUMO gap (solid blue line), periodic DFT results (dashed black[12] and gray[11] line). 153
11.7 Absolute errors in eV of the experimental vs. TD-DFT and bt-PNO-STEOM-CCSD (STEOM-CC) computed optical band gap. 155

13.1 Crystal structures of the spinel cobalt oxides: **a)** Co_3O_4, **b)** $Co(III)_2ZnO_4$, and **c)** $Al_2Co(II)O_4$. Local view of the **d)** T_d symmetric $[MO_4]^{6-}$ (M=Co(II) or Zn) and **e)** D_{3d} symmetric $[MO_6]^{9-}$ (M=Co(III) or Al) building units. Color code: Co(III) (blue), Co(II) (purple), Al (turquoise), Zn (gray). . 169
13.2 Cluster model size 3t6o of Co_3O_4 with the respective electronic structure of the $3d$ orbitals of the Co(II) and Co(III) centers. 170

13.3 Cluster model the "toy" model 3t6o-$Al_2Cu(II)O_4$ with three tetrahedral Cu(II) centers with the respective electronic structures of the centers' $3d$ orbitals regarding the "neutral" and "ionic" antiferromagnetic states. The symmetries of the centers locally and with respect to each other are indicated (T_d, C_s, or C_{2v}). 173
13.4 Visualization of **a)** the canonical singly occupied MOs of the Cu(II)-Cu(II) interacting centers in 3t6o type of clusters in C_{2v} symmetry referring to the symmetric as $\psi_g(b_2) = \frac{1}{\sqrt{2}}(d^A_{yz} + d^B_{yz})$ and the antisymmetric as $\psi_u(b_2) = \frac{1}{\sqrt{2}}(d^A_{yz} - d^B_{yz})$ and **b)** the pseudo-localized broken-symmetry magnetic orbitals of C_{2v} symmetry referring to as $\alpha = \frac{1}{\sqrt{2}}(\psi_g + \psi_u)$ and $\beta = \frac{1}{\sqrt{2}}(\psi_g - \psi_u)$. 174
13.5 MO diagrams of **a)** the ferromagnetic, **b)** the antiferromagnetic "neutral", and **c-d)** the antiferromagnetic "ionic" states of symmetries $^{1,3}A_1$. 176
13.6 Possible **a)** ferromagnetic and **b)** "neutral" or **c)** "ionic" antiferromagnetic states concerning the $3d$ orbitals of two tetrahedral Co(II) sites. 179

14.1 Overview of experimental **a)** absorption bands[467, 471–484, 499, 500] and **b)** band gaps[437, 457–477] found in literature. Empty circles: indirect band gaps. Filled circles: direct band gaps. Cross: forbidden gaps. Colors indicate different energy ranges of the absorption bands and the corresponding band gaps. 184
14.2 Overview on calculated band gaps found in literature.[173, 485, 490–496] Unfilled circles: indirect band gaps. Filled circles: direct band gaps. Green circles: band gaps including SOC. 189
14.3 Overview on calculated band gaps found in literature including more than one band gap.[485–489] 191
14.4 Schematic representation of excited states in the one electron picture for **a)** $[Co(III)O_6]^{9-}$ (O_h/ D_{3d}) and **b)** $[Co(II)O_4]^{6-}$ (T_d). Dashed red lines: dipole-forbidden transitions, solid green lines: dipole-allowed transitions. 196
14.5 TD-DFT convergence scheme of Co_2ZnO_4 with PBE0/DKH-def2-tzvp. The left side of the figure shows all excited states for model size 2t4o, while the right side shows the convergence of only the first excited state of each absorption band with cluster size. Color code: Co(III) $3d$ $t_{2g} \rightarrow e_g$ triplet (turquoise) and singlet (blue) excitations, Co(III) $3d \rightarrow 3d$ Co(III) MMCT (gray), O $2p$ →Co(III) $3d$ LMCT (green); dark states (dotted line), "potentially" non-dark states (dashed line), non-dark states (solid line). 199

14.6 **a)** Standard TD-DFT and **b)** broken-symmetry TD-DFT convergence scheme of Al_2CoO_4 with PBE0/DKH-def2-tzvp. The left side of the figures shows all excited states for model size 2t4o, while the right side shows the convergence of only the first excited state of each absorption band with cluster size. Color code: Co(II) $3d$ $e \rightarrow t_2$ excitations (red), Co(II)→Co(II) MMCT (yellow), O $2p$ →Co(II) $3d$ LMCT (green); dark states (dotted line), "potentially" non-dark states (dashed line), non-dark states (solid line). 201

14.7 **a)** Broken-symmetry TD-DFT convergence scheme of Co_3O_4. The left side of the figure shows all excited states for model size 2t4o, while the right side shows the convergence of only the first excited state of each absorption band with cluster size. **b)** Co ligand field excitations of Co_3O_4 (left) vs. [Co_2ZnO_4 + Al_2CoO_4] (right). Color code: Co(II) $3d$ $e \rightarrow t_2$ (red), Co(III) $3d$ $t_{2g} \rightarrow e_g$ triplet (turquoise) & singlet (blue) excitations, Co(III)→Co(III) MMCT (gray), Co(II)→Co(II) MMCT (yellow), Co(II)→Co(III) MMCT (black); dark states (dotted line), "potentially" non-dark states (dashed line), non-dark states (solid line). Level of theory: PBE0/DKH-def2-tzvp 203

14.8 Results of first excited states belonging to different absorption bands for TD-DFT for **a)** Co_2ZnO_4 and b) Al_2CoO_4 for cluster size 4t8o (Exception: EOM-CC, cluster sizes are 1o and 1t, respectively). Basis sets: def2-QZVPP for TD-DFT and CIS, cc-pVQZ for EOM-CC. Color code: Co(II) $3d$ $e \rightarrow t_2$ (red), Co(III) $3d$ $t_{2g} \rightarrow e_g$ triplet (turquoise) & singlet excitations (blue), Co(III)→Co(III) MMCT (gray), Co(II)→Co(II) MMCT (yellow). Dark states (empty circle), “potentially” non-dark states (half-filled circles), non-dark states (filled circles). 206

14.9 Calculation results of the first excited triplet (turquoise) and singlet (blue) states of absorption bands originating from ligand field transitions in the isolated Co(III) site 1o in terms of single configurational methods (PBE0, EOM-CC, CIS) and with multiconfigurational/-reference methods (SA-CASSCF, NEVPT2, MR-EOM-CC, ICE-CI). Dark states (empty circle), “potentially” non-dark states (half-filled circles), non-dark states (filled circles). 210

14.10 Calculation results of the first excited triplet (turquoise) and singlet (blue) states of absorption bands originating from ligand field transitions in cluster sizes 1o and 1t2o of Co_2ZnO_4 computed with ICE-CI, SA-CASSCF, and NEVPT2. Dark states (empty circle), “potentially” non-dark states (half-filled circles), non-dark states (filled circles). . . 212

14.11 Calculation results of the first excited states of absorption bands originating from ligand field transitions in the single Co(II) site 1t in terms of single-reference methods (PBE0, EOM-CC, CIS), and with multiconfigurational/-reference methods (SA-CASSCF, NEVPT2, MR-EOM, ICE-CI). Dark states (empty circle), “potentially” non-dark states (half-filled circles), non-dark states (filled circles). 213
14.12 Calculated first excited states of absorption bands orginating from ligand field transitions in Al_2CoO_4 with system size 1t as high spin (2S+1=4) and 2t4o computed for "neutral" (red) and "ionic" (purple) antiferromagnetic states (2S+1=1) with SA-CASSCF and NEVPT2. Dark states (empty circle), “potentially” non-dark states (half-filled circles), non-dark states (filled circles). 215
14.13 Calculated first excited states of absorption bands originating from ligand field transitions in Al_2CoO_4 for cluster size 2t4o with **a)** "neutral" and **b)** "ionic" antiferromagnetic description and 1t with Co centers that are formally Co(I), Co(II), and Co(III) with NEVPT2 and MR-EOM-CC. Dark states (empty circle), “potentially” non-dark states (half-filled circles), non-dark states (filled circles). 216
14.14 Comparison of calculated first excited states of overlapping absorption bands originating from ligand field transitions in multiconfigurational models of Co_3O_4, Al_2CoO_4, and Co_2ZnO_4. Dark states (empty circle), “potentially” non-dark states (half-filled circles), non-dark states (filled circles). Color code: tetrahedral Co $3d$ $e \rightarrow t_2$ excitation for “neutral” (red) and for "ionic" (purple) antiferromagnetic states, octahedral Co $3d$ $t_{2g} \rightarrow e_g$ triplet (turquoise) and singlet (blue) excitations. 219
14.15 Results of first excited states of absorption bands originating from ligand field transitions for mulifconfiguration/-reference methods for **a)** Co_2ZnO_4 and **b)** Al_2CoO_4. Color code: tetrahedral Co $3d$ $e \rightarrow t_2$ excitation for “neutral” (red) and for "ionic" (purple) antiferromagnetic states, octahedral Co $3d$ $t_{2g} \rightarrow e_g$ triplet (turquoise) and singlet (blue) excitations. 221

15.1 Experimental Co $K\beta_{1,3}/K\beta'$ mainline XES spectra of Co_3O_4 (black), $Co(III)_2ZnO_4$ (blue), and $Al_2Co(II)O_4$ (red) for **a)** normalized to themselves; **b)** compared to each other; **c)** $Co(III)_2ZnO_4$ and $Al_2Co(II)O_4$ shown with prefactors representing the Co(III):Co(II) site ratio in Co_3O_4 compared to the combined spectrum (gray) and Co_3O_4. **d)** Difference spectrum between Co_3O_4 and the combined $Co(III)_2ZnO_4$ and $Al_2Co(II)O_4$ $K\beta_{1,3}/K\beta'$ mainline XES spectrum. 231

15.2 **a) – c)** Experimental Co $K\beta_{1,3}/K\beta'$ mainline XES spectrum of Co_3O_4 (black), $Co(III)_2ZnO_4$ (blue), and $Al_2Co(II)O_4$ (red) spinel solids with different prefactors regarding the intensity of the cobalt oxide derivatives and the respective sum of $Co(III)_2ZnO_4$ and $Al_2Co(II)O_4$ (dotted gray line). **d)** & **e)** Difference spectra between Co_3O_4 and the summed-up spectra $Co(III)_2ZnO_4$ and $Al_2Co(II)O_4$ with respective prefactors. 231

15.3 Convergence of the computed one-electron (top) and CASCI (bottom) $K\beta_{1,3}/K\beta'$ mainline XES spectrum employing increasing cluster sizes of **a)** and **d)** Co_3O_4, **b)** and **e)** Al_2CoO_4 as well as **c)** and **f)** Co_2ZnO_4. Dashed line: experiment. 233

15.4 Calculated $K\beta_{1,3}/K\beta'$ mainline XES spectra using the one-electron approach for the 2t4o type cluster model of **b)** Co_3O_4, **c)** $Co(III)_2ZnO_4$, and **d)** $Al_2Co(II)O_4$ shown in **a)**. The color coded subspectra correspond to the contributions of the individual Co centers as emission centers according to the color code given by the 2t4o model in **a)**. Color code: subspectra corresponding to tetrahedral Co(II) (red and orange) and distorted octahedral Co(III) sites (blue, cyan, turquoise, and green). Black line: total spectrum. The spectra are normalized with respect to the maximum intensity of the spectrum of Co_3O_4 as shown in **b)**. 234

15.5 Schematic representation of the $K\beta_{1,3}/K\beta'$ mainline XES emission process as a secondary independent process of the core-ionization of the $1s$ metal orbital by XAS. The XES process includes radiative spontaneous emission from the $1s$ core-ionized initial state to the $3p$ core-ionized final states and non-radiative optical Auger processes. . 237

15.6 CASCI XES calculated $K\beta_{1,3}/K\beta'$ mainline XES spectrum for the toy model $[Cu(II)O_4]^{6-}$. Color code of multiplets: yellow (2S+1=1), blue (2S+1=3). 240

15.7 Predominant electron configurations and term symbols of the core-ionized initial and final states reached by the $K\beta_{1,3}/K\beta'$ mainline XES in the case of the low spin octahedral Co(III) sites in Co_2ZnO_4. . 243
15.8 CASCI computed $K\beta_{1,3}/K\beta'$ mainline XES spectra considering final states with $1s^s3p^53d^6_{t_{2g}}3d^0_{e_g}$ electron configuration of symmetry $^2T_{1u}$ originating from the low spin octahedral Co(III) sites. Color code of multiplets: turquoise (2S+1=2). 244
15.9 Predominant electron configurations and term symbols of the core-ionized initial and final states reached by the $K\beta_{1,3}/K\beta'$ mainline XES in the case of hypothetical intermediate spin state octahedral Co(III) sites in Co_2ZnO_4. 245
15.10 $K\beta_{1,3}/K\beta'$ mainline XES spectra considering final states with electron configuration $1s^s3p^53d^5_{t_{2g}}3d^1_{e_g}$ originating from hypothetical octahedral Co(III) sites with an intermediate spin state with **a)** being the uncorrected CASCI and **b)** being the core-ionized initial state corrected spectrum. Color code of multiplets: turquoise (2S+1=2), orange (2S+1=4). 246
15.11 Predominant electron configurations and term symbols of the core-ionized initial and final states reached by the $K\beta_{1,3}/K\beta'$ mainline XES in the case of the low spin core-ionized initial and low and intermediate spin final states originating from octahedral Co(III) sites in Co_2ZnO_4. 247
15.12 Experimental (dashed line) vs. total CASCI calculated $K\beta_{1,3}/K\beta'$ mainline XES spectra employing a) one-photon relation of Equation 15.1 and b) two-photon relation of Equation 15.5. The spectra are analyzed in terms of parent non-relativistic final states, belonging to low spin $1s^23p^53d^6_{t2g}3d^0_{eg}$ electron configuration of symmetry $^2T_{1u}$ as well as intermediate spin $1s^23p^53d^5_{t2g}3d^1_{eg}$ electron configurations of symmetry $^{2,4}[A_{1u}, A_{2u}, T_{1u}, T_{2u}]$. Color code of multiplets: $2S + 1 = 2$ (turquoise). 249
15.13 Experimental (dotted line) vs. CASCI calculated $K\beta_{1,3}/K\beta'$ mainline XES spectra of the octahedral Co(III) site representing Co_2ZnO_4 for **a)** considering all possible final states with no excited electrons in the $3d$ orbitals (bottom panel) and with excited electrons within the $3d$ orbitals (second panel from bottom) and for **b)** with scaling of the LFT parameters $1s3d$ and $3p3d$ in the total CASCI spectrum calculated using AILFT for different scalings of the exchange $G^{1,3}_{3p3d}$ Slater-Condon integrals from their initial values (∼15.6 and 9.5 eV). 251

15.14 Predominant electron configurations and term symbols of the core-ionized initial and final states reached by the $K\beta_{1,3}/K\beta'$ mainline XES in the case of high spin tetrahedral Co(II) sites in Al_2CoO_4. . . . 252
15.15 CASCI calculated $K\beta_{1,3}/K\beta'$ mainline XES spectra considering final states with $1s^s3p^53d_e^43d_{t_2}^3$ electron configuration of symmetry $^{3,5}T_2$ belonging to high spin tetrahedral Co(II) sites in Al_2CoO_4. **a)** Uncorrected calculation result, **b)** calculation result without the doub-triplet initial states, and **c)** calculation result without the doub-triplet initial states and the incorrect contributions from the α emission pathway. Color code for multiplets: blue (2S+1=3), red (2S+1=5). 253
15.16 Predominant electron configurations and term symbols of the core-ionized initial and final states reached by the $K\beta_{1,3}/K\beta'$ mainline XES process in the case of high spin tetrahedral Co(II) sites in Al_2CoO_4 including final states with ligand field excitations. 255
15.17 Experimental (dashed line) vs. total CASCI computed $K\beta_{1,3}/K\beta'$ mainline XES spectra considering all possible final states originating from high spin tetrahedral Co(II) sites in Al_2CoO_4. **a)** Uncorrected calculation result, **b)** calculation result without the doub-triplet initial states, and **c)** calculation result without the doub-triplet initial states and the incorrect contributions from the α emission pathway. Color code for multiplets: blue (2S+1=3), red (2S+1=5). 256
15.18 Experimental (dashed line) vs. total CASCI computed $K\beta_{1,3}/K\beta'$ mainline XES spectrum of high spin tetrahedral Co(II) sites in Al_2CoO_4 based of LFT parameters from $1s3d$ and $3p3d$ AILFT calculations computed for different scalings of the exchange $G^{1,3}_{3p3d}$ Slater-Condon integrals from their initial values ($\sim$16.9 and 9.8 eV). 257
15.19 Experimental (dotted line) versus CASCI calculated $K\beta_{1,3}/K\beta'$ mainline XES spectra (solid black line) for the 2t4o type of clusters for Co3O4. The computed spectra are analyzed in terms of dominating subspectra arising Co(III)-D_{3d} and Co(II)-T_d centers in 1:2 ratio, as well as dominating 2S+1=2 (turquoise), 2S+1=4 (orange) and 2S+1=3 (blue), 2S+1=5 (red) multiplicities respectively. 258

16.1 Experimental Co $K\beta_{2,5}/K\beta''$ VtC XES spectra of Co_3O_4 (black), $Co(III)_2ZnO_4$ (blue), and $Al_2Co(II)O_4$ (red) for **a)** normalized to themselves; **b)** compared to each other; **c)** $Co(III)_2ZnO_4$ and $Al_2Co(II)O_4$ shown with prefactors representing the Co(III):Co(II) site ratio in Co_3O_4 compared to the combined spectrum (gray) and Co_3O_4. **d)** Difference spectrum between Co_3O_4 and the combined $Co(III)_2ZnO_4$ and $Al_2Co(II)O_4$ $K\beta_{2,5}/K\beta''$ VtC XES spectrum. 264
16.2 Gaussian fit of experimental Co $K\beta_{2,5}/K\beta''$ VtC XES spectra of **a)** $Al_2Co(II)O_4$, **b)** $Co(III)_2ZnO_4$, and **c)** Co_3O_4 spinel solids. 265
16.3 Convergence of computed one-electron DFT (top) and CASCI (bottom) $K\beta_{2,5}/K\beta''$ VtC XES spectra with increasing cluster sizes for: **a)** and **d)** Co_3O_4, **b)** and **e)** Al_2CoO_4, and **c)** and **f)** Co_2ZnO_4. Dashed line: experimental spectrum. 266
16.4 One-electron DFT calculated $K\beta_{2,5}/K\beta''$ VtC XES spectra for cluster size 2t4o shown in **a)** of **b)** Co_3O_4, **c)** $Co(III)_2ZnO_4$, and **d)** $Al_2Co(II)O_4$. Subspectra represent contributions from individual Co centers in the 2t4o structure, indicated by the color code shown in **a)**. Color code: subspectra of tetrahedral Co(II) (red and orange) and octahedral Co(III) (gray, turquoise, green, and blue) sites and total spectrum (black). Spectra are normalized to the total spectrum of Co_3O_4 in **b)**. 268
16.5 One-electron DFT calculated $K\beta_{2,5}/K\beta''$ VtC XES spectrum for cluster size 2t4o of Co_3O_4 (solid black line) compared to experiment (dashed line). Colored spectra indicate the dominant contributions in terms of single electron decays as shown in figure. 269
16.6 The one-electron DFT calculated $K\beta_{2,5}/K\beta''$ VtC XES spectra (black solid line) for cluster size 2t4o for different cobalt sites compared to experiment (dashed line). Contributions from tetrahedral Co(II) sites from **a)** Co_3O_4 and **b)** $Al_2Co(II)O_4$. Contributions from distorted octahedral Co(III) sites in **c)** Co_3O_4 and **d)** $Co(III)_2ZnO_4$. All spectra are normalized to the total calculated $K\beta_{2,5}/K\beta''$ VtC XES spectrum of Co_3O_4 (solid gray line). Colored spectra indicate the dominant contributions in terms of single electron decays as indicated in the figure. 270

16.7 **a)** Diagram of the electron decays with the symmetries of the states contributing to the $K\beta_{2,5}/K\beta''$ VtC XES of the tetrahedral site [Cu(II)O_4]$^{6-}$. **b)** Corresponding CASCI spectrum, highlighting the one-electron decays. Color code: O $2s$ $\rightarrow$ Cu(II) $1s$ (gray), O $2p$ $\rightarrow$ Cu(II) $1s$ light blue, Cu(II) $3d$ $\rightarrow$ $1s$ (red). Underlying multiplets, singlet (yellow) and triplets (blue), of the CASCI calculated spectrum for final states **c)** without and **d)** with $3d$ excited electrons. 273

16.8 Possible "neutral" and "ionic" antiferromagnetic states of three interacting Cu centers (cluster size 3t6o). Color code: "spectator" centers (black), "emissive" center (red) after core-ionization. 277

16.9 Energetic ordering and state mixing of **a)** ground states and **b)** core-ionized initial states in different antiferromagnetic states. Color code: "neutral" antiferromagnetic states (blue), "ionic" antiferromagnetic states with the "emissive" center in a $3d^9$ electron configuration (orange), "ionic" antiferromagnetic states with the "emissive" center in a $3d^8$ or $3d^{10}$ electron configuration (gray). 279

16.10 Diagram of the electron decays and symmetries of the final states contributing to the $K\beta_{2,5}/K\beta''$ VtC XES spectra involving the $3d$ orbitals of the "emissive" center and the $3d$ orbitals involved in the antiferromagnetic coupling between the "spectator" centers Cu^A/Cu^B, originating from a **a)** "neutral" and **b)** "ionic" antiferromagnetic core-ionized state. Color-coded arrows: O $2s$ $\rightarrow$Cu(II) $1s$ (gray), O $2p$ $\rightarrow$Cu(II) $1s$ (light blue), Cu(II) $3d$ $\rightarrow$ $1s$ (red) electron decays. 281

16.11 **a)** Total (top panel) CASCI calculated $K\beta_{2,5}/K\beta''$ VtC XES for cluster size 3t6o of Al_2Cu(II)O_4 with subspectra originating from "neutral" (bottom panel) and "ionic" (middle panel) antiferromagnetic final states. Contributing one-electron decays are highlighted in different colors. Color code: O $2s$ $\rightarrow$Cu(II) $1s$ (gray), O $2p$ $\rightarrow$Cu(II) $1s$ (light blue), Cu(II) $3d$ $\rightarrow$Cu(II) $1s$ (red) electron decays. **b)** State weights of the contributing "neutral" and "ionic" antiferromagnetic states to the total spectrum in **a)**. Color code: "neutral" (blue) and "ionic" (gray) antiferromagnetic states. Numbers 1 to 6 denote the six energy groups. 282

16.12 Core-ionized initial states and possible electron decays in Al_2CoO_4 relevant to the $K\beta_{2,5}/K\beta''$ VtC XES process for different cluster sizes: **a)** high spin single-center case (1t) and **b)** to **d)** antiferromagnetic three-center cases (3t6o). For the three-center case, the "spectator" centers are in **b)** a "neutral" antiferromagnetic state, **c)** an "ionic" antiferromagnetic state with one electron exchanged by superexchange, and **d)** an "ionic" antiferromagnetic state with two electrons exchanged by superexchange. Color-coded arrows: O $2s$ →Co(II) $1s$ (gray), O $2p$ →Co(II) $1s$ (light blue), Co(II) $3d \rightarrow 1s$ (red) electron decays. . . . 284
16.13 Cluster size 5t12o, representing a "neutral" antiferromagnetic system with four Co(II) "spectator" centers (blue) forming a "cage" around the "emissive" Co(II) center (green). 286
16.14 Potential 3t6o subsystems with a central "emissive" Co(II) center (green) and two neighboring "spectator" Co(II) centers (blue) in cluster 5t12o. 287
16.15 Core-ionized initial states and possible electron decays in Co_2ZnO_4 relevant to the $K\beta_{2,5}/K\beta''$ VtC XES process for different cluster sizes: **a)** low spin single-center case (1o) and **b)** diamagnetic two-center case (1t2o). Color-coded arrows: O $2s$ →Co(III) $1s$ (gray), O $2p$ →Co(III) $1s$ (light blue), Co(III) $3d \rightarrow 1s$ (red) electron decays. 288
16.16 CASCI calculated spectra of Co_2ZnO_4: **a)** electron decay contributions for cluster sizes 1o (bottom panel) and 2t4o (middle panel) compared to the experimental spectrum (top panel, dashed line). Color code: O $2s$ →Co(III) $1s$ (gray), O $2p$ →Co(III) $1s$ (light blue) electron decays. **b)** Comparison of the Gaussian fit of the CASCI calculated spectrum for cluster size 2t4o (bottom panel) with the experimental Gaussian fit (top panel). 290
16.17 CASCI calculated orbital bands for cluster sizes 1o, 1t2o, and 2t4o. Color code: O $2s$ (gray), O $2p$ (light blue), Co(III) $3d$ (red) orbitals. . . 291
16.18 CASCI calculated spectra of Al_2CoO_4 compared to the experimental spectrum (top panel) for increasing cluster sizes 1t (bottom panel), 2t4o (second from bottom panel), and 3t6o (second from top panel, dashed line), where all Co(II) centers are in a local high spin $3d^7$ electron configuration. Spectra cutouts in circles: spectral region visualized with lower Gaussian broadening of the plotted spectrum (weighting is 1.0 instead of 3.5). Color code: O $2s$ →Co(II) $1s$ (gray), O $2p$ →Co(II) $1s$ (light blue), Co(II) $3d \rightarrow 1s$ (red) electron decays. . . 292

16.19 CASCI calculated spectra of Al_2CoO_4 showing the electron decay contributions for cluster size 3t6o representing model size "5t12o". The "spectator" centers generate pairs of "neutral" (bottom panel) and "ionic" antiferromagnetic states with one (middle panel) or two (top panel) electrons exchanged via superexchange. Color code: O $2s$ →Co(II) $1s$ (gray), O $2p$ →Co(II) $1s$ (light blue), Co(II) $3d \rightarrow 1s$ (red) electron decays. 294
16.20 Components of the $K\beta''$ feature originating from O $2s$ →Co(II) $1s$ electron decays (gray) and their relevance in the antiferromagnetic scenarios in the "5t12o" model with two exchanged electrons. Panel A shows features originating from O $2s$ orbitals not associated with the "spectator" centers, panel B associated with the "spectator" center with reduced and panel C increased effective charge. The top two panels show the respective summed-up features. 295
16.21 CASCI calculated spectra of Al_2CoO_4 in the "5t12o" model. **a)** Weighted contributions of subspectra with final states including "spectator" centers in "neutral" (0 electrons exchanged, bottom panel) and "ionic" antiferromagnetic states with one (second from bottom) and two (middle panel) electrons exchanged via superexchange, along with the total spectrum (second from top) and the experimental spectrum (top panel, dashed line), highlighting the underlying electron decays. Color code: O $2s$ →Co(II) $1s$ (gray), O $2p$ →Co(II) $1s$ (light blue), Co(II) $3d \rightarrow 1s$ (red) electron decays. **b)** Comparison of the Gaussian fit of the total CASCI spectrum (bottom panel) with the experimental Gaussian fit (top panel). 297
16.22 Comparison of CASCI $K\beta_{2,5}/K\beta''$ VtC XES spectra generated from the thought experiment (lower panel), where two 2t4o spectra were shifted along the axis to fit the upper (blue) and lower (red) energy double-peak features, the "5t12o" model (middle panel), and the experimental spectrum (upper panel, dashed line). 299
16.23 Comparison of the Gaussian fit of the experiment (top panel) with the computed $K\beta_{2,5}/K\beta''$ VtC XES spectrum of Co_3O_4 (second from top), which was generated as the sum of the ratio 2: 1 ratio representing the Co(III):Co(II) ratio in Co_3O_4 from the normalized CASCI calculated $K\beta_{2,5}/K\beta''$ VtC XES spectra of Co_2ZnO_4 (second from bottom) and Al_2CoO_4 (bottom panel). 300

A.1 Keyword list for ORCA_CrystalPrep (1). 310

A.2 Keyword list for ORCA_CrystalPrep (2). 311
A.3 Template input file for ORCA_CrystalPrep. 312
A.4 Dependence of CHELPG, Mulliken, Loewdin, and Hirshfeld charges on the level of theory (basis set: def-TZVP). Color code: GGA functionals: BLYP (black), PBE (lightgray), BP86 (darkorange); hybrid functionals: B3LYP (darkred), B1LYP (gold), PBE0 (deepskyblue), double-hybrid functionals: B2PLYP (mediumblue); wavefunction-based method: DLPNO-CCSD (lightsteelblue), HF (purple); Cluster example: $[Na_4Cl_4]^0$.313

B.1 Different QC sizes for GeS (orthorhombic structure) for the supercell approach (SCe) in the electrostatic embedded cluster model. 314
B.2 PBE/pcSseg-2 computed NMR NSCs of Mg (left) and S (right) for MgS by employing a sequence of embedded SCe (dotted line) and SCl (solid line) type clusters for the different atom positions in the cluster. Color code: tip (blue), edge (purple), surface (grey), and bulk (red). 317
B.3 Computed NMR NSCs of Na in $[NaCl_6]^{5-}$ (left) and Cl $[Na_6Cl]^{5+}$ (right) with respect to method and dependent on the basis set size of pcSseg-X for non-embedded (top) and embedded (bottom) clusters. Dashed line: PBE, PBE0, HF, DSD-PBEP86, solid line: HF, MP2, CCSD, CCSD(T). Color code: X=1 (blue), X=2 (red), X=3 (turquoise), X=4 (yellow) . . . 318
B.4 Influence of the model size (non-embedded) on the relativistic effects for F, Cl, Br, (left) and Na (right) in NaF (top), NaCl (center), and NaBr (bottom). Color code: difference between non-relativistic NSC and scalar relativistic NSC (scalar relativistic effect) (blue), difference between non-relativistic NSC and total relativistic NSC (total relativistic effect = scalar relativistic effect + SOC) (red), difference between scalar relativistic NSC and total relativistic NSC (spin-orbit coupling effect) (turquoise). Level of theory: two-component Hamiltonian: X2C with PBE0/dyall.ae2z. Computed with DIRAC19. 319
B.5 Absolute errors in ppm of calculated vs. experimental chemical shifts with different methods for alkali metals with **a)** alkali metal chlorides and **b)** alkali metal bromides being the standard reference. Basis set: pcSseg-3. 320
B.6 Absolute errors in ppm of calculated vs. experimental chemical shifts with different methods for halides with **a)** lithium halides and **b)** potassium halides being the standard reference. Basis set: pcSseg-3. . 321

B.7 bt-PNO-STEOM calculated excitations energies for clusters $[Li_nCl_n]^0$, n=1-4, 6, 8. green, yellowgreen, green, blue, turquoise, gray, and red lines represent excitations states with numbers 1, 2, 3, 10, 20, 30, and 40 respectively. 333
B.8 Comparison of cc-pVXZ (solid line) and def2-XVP (dotted line) basis set types and sizes with different methods: BLYP (yellow), B3LYP (red), B2PLYP (blue), and bt-PNO-STEOM-CCSD (turquoise) calculated on cluster ($[Li_8Cl_8]^0$. 333
B.9 Absolute errors in eV of the experimental vs. calculated fundamental band gaps computed with Δ-SCF/ DFT with different functionals and bt-PNO-STEOM-CCSD(STEOM-CC) for the organic semiconductor benchmark set. 334

C.1 Relation between method to prepare Co_3O_4 sample and experimental **a)** band gaps and **b)** absorption bands as well as relation between film thickness of Co_3O_4 thin films for **c)** band gaps and **d)** absorption bands with triangles symbolizing CVD, squares PVD, pluses sol gel, circles spray pyrolysis, and diamonds undefined prepared thin films. 356
C.2 Excited states of Co_2ZnO_4 for system size 2t4o computed with TD-DFT with **a)** only singlet, **b)** only triplet, and **c)** spin-orbit coupled states. Level of theory: PBE0/def2-QZVPP. Color code: Co(III) $3d$ $t_{2g} \rightarrow e_g$ triplet (turquoise) and singlet (blue) excitations, Co(III) $3d \rightarrow$ $3d$ Co(III) MMCT (gray), O $2p$ →Co(III) $3d$ LMCT (green) 357
C.3 Different TD-DFT approaches for calculating the excited states in Al_2CoO_4: **a)** high spin, **b)** high spin with spin slip, **c)** broken-symmetry, **d)** broken-symmetry with SF. Color code: Co(II) $3d$ $e \rightarrow t_2$ excitation (red), Co(II) $3d$ $e \rightarrow t_2$ excitation with spin flip (turquoise), Co(II)→Co(II) MMCT (yellow), O $2p$ →Co(II) $3d$ LMCT (green), Co(II) $3d \rightarrow 4s$ (purple); dark states (dotted line), "potentially" non-dark states (dashed line), non-dark states (solid line). Level of theory: PBE0/def2-QZVPP. . . . 358
C.4 Excited states of increasing system size computed with PBE/def2-QZVPP for **a)** Co_2ZnO_4, **b)** Al_2CoO_4, and **c)** Co_3O_4. 359
C.5 First excited states of absorption bands of ligand field transitions in Al_2CoO_4 computed with system size 2t4o as high spin (2S+1=7), intermediate spins (2S+1=5 and 2S+1=3), and open singlet (2S+1=1) with PBE0 and CIS. 360

C.6 First excited states of absorption bands originating from ligand field transitions in Al_2CoO_4 with system size 2t4o computed as high spin (2S+1=7), intermediate spins (2S+1=5 and 2S+1=3), and open singlet (2S+1=1) with SA-CASSCF. 360
C.7 Difference between "ionic" and "neutral" antiferromagnetic "ground states" with respect to the basis set size computed with NEVPT2 for cluster size 2t4o of the Al_2CoO_4 model. 361
C.8 Comparison of ICE-CI models of Al_2CoO_4, Co_2ZnO_4, and Co_3O_4 including states with oscillator strengths of zero (dark states). Oscillator strengths are taken from SA-CASSCF calcualtions with selected CSFs. 362
C.9 Spin branching diagrams representing 4e4o CSFs coupling to **a)** 2S+1=5 and **b)-d)** 2S+1=3. 369
C.10 Example for overmixing of α and β emission pathways in the CI for cluster model 1t of Al_2CoO_4. 370

List of Tables

3.1 Overview of ECPs of class SDD for all elements used in this work. . . 45
3.2 Overview of four different definitions of atomic charges (q) for atom A. 51

6.1 Description of operators in the Hartree-Fock equation shown in the atomic unit notation.[183, 187, 188] 74

8.1 Approximated oscillator strengths of allowed, partly allowed, and forbidden states.[234] 91

9.1 Overview of all systems of the benchmark set, their space groups abbreviated with RS for Rock Salt (Fm-3m), ZB for Zinc Blende (F-43m) and OR for Orthorhombic, bond lengths in Å, information about participation in studies, calculated charges and experimental (exp.) parameters. NMR shift (δ) in ppm[270–273] and optical band gap (opt. BG) in eV (value in brackets: chosen reference). 109
9.2 Overview of organic semiconductor benchmark set including their crystal structure and optical (opt.) and fundamental (fund.) band gaps (BG) in eV. 110

10.1 Computed NSCs in ppm of Na and Cl in $[NaCl_6]^{5-}$ and $[Na_4Cl_4]^0$ with different electrostatic environments. Level of theory: PBE/pcSseg-2. 117
10.2 Cluster sizes that were employed to compute the DFT and MP2 NMR parameters. 123
10.3 Difference of NSCs of M in ppm computed with pcSseg-2 between $[MY_6]^{5-}$ and $[M_6Y_{19}]^{13-}$. Bolt values are significant errors. 124
10.4 Non-relativistic computed NCSs and two-component Hamiltonian BSS relativistic correction for a series of non-embedded model systems for **a)** metals and **b)** halides without embedding. Level of Theory: PBE0/dyall.ae3z. 130

10.5 **a)** Mean absolute error and **b)** mean deviation for the different methods and nuclei. Color code: worst two values (red) and best two values (blue) for each nucleus. Basis set: pcSseg-3. Range of chemical shift for each nucleus is $\Delta\delta$ and approximate magnitude computed nuclear shielding constants ∼NSC. All values in ppm. 140

11.1 Cluster sizes employed to compute the optical band gaps of the different inorganic crystals. 147

11.2 Performance of various DFT functionals in the framework of Δ-SCF/DFT and TD-DFT vs. bt-PNO-STEOM-CC for calculating the optical and fundamental band gap energies in eV of Anthracene (3A) with LR meaning linear response (TD-DFT or STEOM-CC) and HL is HOMO-LUMO gap. 149

13.1 Detailed description of the employed cobalt oxide models within the embedded cluster approach in terms of the QC compositions, the number of ECPs in the BR and the number of point charges in the PC region. 171

14.1 Transition character of specific excited states and their energy based on calculation results from literature[475, 483, 486, 487, 501]. Transition energy in eV. 192

14.2 Orbital symmetries of $3d$ orbitals and whether the transition between the $3d$ orbitals of the nearest tetrahedral and octahedral cobalt centers is a dipole-allowed transition, considering that they have either C_s or C_{2v} symmetry to each other. 197

15.1 Calculated $\Delta E(K\beta_{1,3} - K\beta')/(4G^1_{pd} + 42G^3_{pd})$ splittings for a variety of $K\beta_{1,3}/K\beta'$ mainline XES final state electron configurations in tetrahedral (T_d) Co(II) and octahedral O_h Co(III) centers as a function of the e^2 and t^2 covalency reduction factors. 242

B.1 Comparison of experimental[118, 119, 266] and periodic[267] bond lengths in Å for different crystals. 314

B.2 Difference between NSC in ppm calculated with contracted pcSseg-2 and pcSseg-3 basis sets for different methods and all systems of the benchmark set of the size $[X_6Y_{19}]^{13-/26-}$ or $[X_4Y_{10}]^{12-}$. 322

B.3 Difference between the computed NSC in ppm with decontracted and contracted pcSseg-2 basis set for different methods and all systems of the benchmark set of the size $[X_6Y_{19}]^{13-/26-}$ or $[X_4Y_{10}]^{12-}$, respectively. The missing numbers are caused by calculation time and memory issues due to the high demand of the decontracted basis sets. 323
B.4 NMR NSCs in ppm for **a)** LiF, **b)** NaF, **c)** LiCl, **d)** NaCl, **e)** LiBr, and **f)** NaBr for the embedded and non-embedded systems with cluster size $[XY_6]^{5-}$ and $[X_6Y]^{5+}$ for different basis sets and methods. 324
B.5 Influence of basis set size on the relativistic effect for **a)** Na and **b)** Cl in NaCl. Computational level: two-component Hamiltonian: X2C[382, 383] with PBE0/dyall.ae2z. Computed with DIRAC19. 326
B.6 Comparison of non-relativistic NSCs for **a)** metals and **b)** halides computed with different programs (ORCA and DIRAC19) and methods. The non-relativistic DIRAC19 results are obtained by a calculation with the speed of light = 2000 a.u. except LEVY-LEBLOND (already non-relativistic). Basis Set ORCA: pcSseg-2, Basis Set DIRAC19: dyall.*. Models are non-embedded. Functional: PBE0. All values in ppm. . . 327
B.7 Total relativistic effect (difference between non-relativistic and relativistic calculation including spin-orbit coupling effect) for **a)** metals and **b)** halides computed with different methods. Level of theory: PBE0/dyall.*. Computed with DIRAC19. All values in ppm. 328
B.8 Scalar relativistic effect (difference between non-relativistic and relativistic calculation excluding spin-orbit coupling effect) for **a)** metals and **b)** halides computed with different methods. Level of theory DIRAC19: PBE0/dyall.*, relativity: spin free two-component Hamiltonians (X2C, BSS). All values in ppm. 329
B.9 Spin-orbit coupling effect (difference between relativistic calculations excluding and including spin-orbit coupling effects) for **a)** metals and **b)** halides computed with different methods. Level of theory DIRAC19: PBE0/dyall.*. All values in ppm. 330
B.10 TD-DFT and bt-PNO-STEOM-CCSD calculated optical band gaps in eV for all inorganic and organic systems of the benchmark set. Statistical evaluation of all quantities is given by means of mean absolute error (MAE) and maximum absolute errors (MaxAE). 335
B.11 TD-DFT and bt-PNO-STEOM-CCSD calculated fundamental band gaps in eV for all organic systems of the benchmark set. Statistical evaluation of all quantities is given by means of mean absolute error (MAE) and maximum absolute errors (MaxAE). 336

C.1 Overview of Co_3O_4 optical absorption experiments from the literature (1). 341
C.2 Overview of Co_3O_4 optical absorption experiments from the literature (2). 342
C.3 Overview of Co_3O_4 optical absorption experiments from the literature (3). 343
C.4 Overview of Co_3O_4 optical absorption experiments from the literature (4). 344
C.5 Overview of Co_3O_4 optical absorption experiments from the literature (5). 345
C.6 Overview of Co_3O_4 optical absorption experiments from the literature (6). 346
C.7 Overview of Co_3O_4 band gap (BG) and absorption spectra calculations from the literature (1). 347
C.8 Overview of Co_3O_4 band gap (BG) and absorption spectra calculations from the literature (2). 348
C.9 Overview of Co_3O_4 band gap (BG) and absorption spectra calculations from the literature (3). 349
C.10 Overview of Co_3O_4 band gap (BG) and absorption spectra calculations from the literature (4). 350
C.11 Overview of Co_3O_4 band gap (BG) and absorption spectra calculations from the literature (5). 351
C.12 Overview of Co_3O_4 band gap (BG) and absorption spectra calculations from the literature (6). 352
C.13 Overview of Co_3O_4 band gap (BG) and absorption spectra calculations from the literature (7). 353
C.14 Overview of Co_3O_4 band gap (BG) and absorption spectra calculations from the literature (8). 354
C.15 Dependence of the optical excited state calculations on the basis set for the cobalt oxide models, here for the example cluster 1t, for different methods. 355

Bibliography

1. Cox, N. *et al.* Electronic structure of the oxygen-evolving complex in photosystem II prior to O-O bond formation. *Science* **345,** 804 (6198 2014).
2. Ye, S., Geng, C.-Y., Shaik, S. & Neese, F. Electronic structure analysis of multistate reactivity in transition metal catalyzed reactions: the case of C–H bond activation by non-heme iron(iv)–oxo cores. *Physical Chemistry Chemical Physics* **15,** 8017–8030 (21 2013).
3. Pantazis, D. A., Ames, W., Cox, N., Lubitz, W. & Neese, F. Two Interconvertible Structures that Explain the Spectroscopic Properties of the Oxygen-Evolving Complex of PhotosystemII in the S2 State. *Angewandte Chemie International Edition* **51,** 9935–9940 (39 2012).
4. Ye, S. & Neese, F. Nonheme oxo-iron(IV) intermediates form an oxyl radical upon approaching the C–H bond activation transition state. *Proceedings of the National Academy of Sciences* **108,** 1228 (4 2011).
5. Lancaster, K. M. *et al.* X-ray Emission Spectroscopy Evidences a Central Carbon in the Nitrogenase Iron-Molybdenum Cofactor. *Sci.* **334,** 974–977 (6058 2011).
6. Petrenko, T. *et al.* Characterization of a Genuine Iron(V)Nitrido Species by Nuclear Resonant Vibrational Spectroscopy Coupled to Density Functional Calculations. *Journal of the American Chemical Society* **129,** 11053–11060 (36 2007).
7. Berry, J. F. *et al.* An Octahedral Coordination Complex of Iron(VI). *Science* **312,** 1937 (5782 2006).
8. Schöneboom, J. C., Neese, F. & Thiel, W. Toward Identification of the Compound I Reactive Intermediate in Cytochrome P450 Chemistry: A QM/MM Study of Its EPR and Mössbauer Parameters. *Journal of the American Chemical Society* **127,** 5840–5853 (16 2005).
9. Maganas, D., Trunschke, A., Schlögl, R. & Neese, F. A unified view on heterogeneous and homogeneous catalysts through a combination of spectroscopy and quantum chemistry. *Faraday Discussions* **188,** 181–197 (0 2016).

10. Neese, F., Atanasov, M., Bistoni, G., Maganas, D. & Ye, S. Chemistry and Quantum Mechanics in 2019: Give Us Insight and Numbers. *J. Am. Chem. Soc.* **141,** 2814–2824 (7 2019).

11. Crowley, J. M., Tahir-Kheli, J. & Goddard, W. A. Resolution of the Band Gap Prediction Problem for Materials Design. *J. Phys. Chem. Lett.* **7,** 1198–1203 (7 2016).

12. Garza, A. & Scuseria, G. Predicting Band Gaps with Hybrid Density Functionals. *J. Phys. Chem. Lett.* **7,** 4165–4170 (20 2016).

13. Heyd, J., Peralta, J., Scuseria, G. & Martin, R. Energy band gaps and lattice parameters evaluated with the Heyd-Scuseria-Ernzerhof screened hybrid functional. *J. Chem. Phys.* **123,** 174101 (17 2005).

14. Perdew, J. & Ruzsinszky, A. Density-functional energy gaps of solids demystified. *Eur. Phys. J. B.* **91,** 108 (1–5) (6 2018).

15. Perdew, J. *et al.* Understanding band gaps of solids in generalized Kohn–Sham theory. *Proc. Natl. Acad. Sci. USA* **114,** 2801–2806 (11 2017).

16. Chan, M. & Ceder, G. Efficient Band Gap Prediction for Solids. *Phys. Rev. Lett.* **105,** 196403 (19 2010).

17. Heyd, J., Scuseria, G. & Ernzerhof, M. Hybrid functionals based on a screened Coulomb potential. *J. Chem. Phys.* **118,** 8207–8215 (18 2003).

18. Moussa, J., Schultz, P. & Chelikowsky, J. Analysis of the Heyd-Scuseria-Ernzerhof density functional parameter space. *J.Chem. Phys.* **136,** 204117 (1–10) (20 2012).

19. Perdew, J. P. Density Functional Theory and the Band Gap Problem. *Int. J. Quantum Chem.* **19,** 497–523 (1986).

20. Khmelevskyi, S., Kresse, G. & Mohn, P. Correlated excited states in the narrow band gap semiconductor FeSi and antiferromagnetic screening of local spin moments. *Phys. Rev. B* **98,** 125205 (1–8) (12 2018).

21. Schimka, L. *et al.* Accurate surface and adsorption energies from many-body perturbation theory. *Nat. Mater.* **9,** 741–744 (9 2010).

22. Booth, G., Grüneis, A., Kresse, G. & Alavi, A. Towards an exact description of electronic wavefunctions in real solids. *Nature* **493,** 365–370 (7432 2012).

23. Kubas, A. *et al.* Surface Adsorption Energetics Studied with "Gold Standard" Wave-Function-Based Ab Initio Methods: Small-Molecule Binding to TiO2(110). *J. Phys. Chem. Lett.* **7,** 4207–4212 (20 2016).

24. Grüneis, A. *et al.* Natural Orbitals for Wave Function Based Correlated Calculations Using a Plane Wave Basis Set. *J. Chem. Theory Comput.* **7,** 2780–2785 (9 2011).

25. Spencer, J. & Alavi, A. Efficient calculation of the exact exchange energy in periodic systems using a truncated Coulomb potential. *Phys. Rev. B: Condens. Matter Mater. Phys.* **77,** 193110 (1–4) (19 2008).

26. Grüneis, A., Marsman, M. & Kresse, G. Second-Order Møller-Plesset Perturbation Theory Applied to Extended Systems. II. Structural and Energetic Properties. *J. Chem. Phys.* **133,** 074107 (1–11) (7 2010).

27. Marsman, M., Grüneis, A., Paier, J. & Kresse, G. Second-Order Møller-Plesset Perturbation Theory Applied to Extended Systems. I. Within the Projector-Augmented-Wave Formalism Using a Plane Wave Basis Set. *J. Chem. Phys.* **130,** 184103 (1–10) (18 2009).

28. Hunt, R., Szyniszewski, M., Prayogo, G., Maezono, R. & Drummond, N. Quantum Monte Carlo calculations of energy gaps from first principles. *Phys. Rev. B* **98,** 075122 (1–22) (7 2018).

29. McClain, J. *et al.* Spectral functions of the uniform electron gas via coupled-cluster theory and comparison to the GW and related approximations. *Phys. Rev. B: Condens. Matter Mater. Phys.* **93,** 235139 (1–6) (23 2016).

30. McClain, J., Sun, Q., Chan, G.-L. & Berkelbach, T. Gaussian-Based Coupled-Cluster Theory for the Ground-State and Band Structure of Solids. *J. Chem. Theory Comput.* **13,** 1209–1218 (3 2017).

31. Zaleśny, R., Papadopoulos, M. G., Mezey, P. G. & Leszczynski, J. *Linear-Scaling Techniques in Computational Chemistry and Physics: Methods and Applications* (Springer, Netherlands, 2011).

32. Pisani, C. *et al.* Periodic local MP2 method for the study of electronic correlation in crystals: Theory and preliminary applications. *J. Comput. Chem.* **29,** 2113–2124 (13 2008).

33. Usvyat, D., Sadeghian, K., Maschio, L. & Schütz, M. Geometrical frustration of an argon monolayer adsorbed on the MgO (100) surface: An accurate periodic *ab initio* study. *Phys. Rev. B* **86,** 045412 (4 2012).

34. Hirata, S., Grabowski, I., Tobita, M. & Bartlett, R. Highly accurate treatment of electron correlation in polymers: coupled-cluster and many-body perturbation theories. *Chem. Phys. Lett.* **345,** 475–480 (5–6 2001).

35. Hirata, S., Podeszwa, R., Tobita, M. & Bartlett, R. Coupled-cluster singles and doubles for extended systems. *J. Chem. Phys.* **120,** 2581–2592 (6 2004).

36. Sun, J. & Bartlett, R. Second-order many-body perturbation-theory calculations in extended systems. *J. Chem. Phys.* **104,** 8553–8565 (21 1996).

37. Ayala, P., Kudin, K. & Scuseria, G. Atomic orbital Laplace-transformed second-order Møller-Plesset theory for periodic systems. *J. Chem. Phys.* **115,** 9698–9707 (21 2001).

38. Boese, A. & Sauer, J. Accurate Adsorption Energies of Small Molecules on Oxide Surfaces: Co-Mgo(001). *Phys. Chem. Chem. Phys.* **15,** 16481–16493 (2013).

39. Stodt, D., Noei, H., Hattig, C. & Wang, Y. A combined experimental and computational study on the adsorption and reactions of NO on rutile TiO2. *Phys. Chem. Chem. Phys.* **15,** 466–472 (2 2013).

40. Pöhlchen, M. & Staemmler, V. AbInitio Calculations for the Adsorption of Small Molecules on Metal Oxide Surfaces. I. Cluster Calculations for Carbon Monoxide CO on Nickel Oxide NiO(100). *J. Chem. Phys.* **97,** 2583–2592 (1992).

41. Libisch, F., Huang, C. & Carter, E. Embedded Correlated Wavefunction Schemes: Theory and Applications. *Acc. Chem. Res.* **47,** 2768–2775 (9 2014).

42. Kotliar, G. *et al.* Electronic Structure Calculations with Dynamical Mean-Field Theory. *Rev. Mod. Phys.* **78,** 865–951 (3 2006).

43. Sun, Q. & Chan, G.-C. Quantum Embedding Theories. *Acc. Chem. Res.* **49,** 2705–2712 (12 2016).

44. Riplinger, C. & Neese, F. An efficient and near linear scaling pair natural orbital based local coupled cluster method. *J. Chem. Phys.* **138,** 034106 (3 2013).

45. Helmich, B. & Hättig, C. Local pair natural orbitals for excited states. *J. Chem. Phys.* **135,** 214106 (2011).

46. Helmich, B. & Hättig, C. A pair natural orbital implementation of the coupled cluster model CC2 for excitation energies. *J. Chem. Phys.* **139,** 084114 (2013).

47. Helmich, B. & Hättig, C. A pair natural orbital based implementation of ADC(2)-x: Perspectives and challenges for response methods for singly and doubly excited states in large molecules. *Comput. Theor. Chem.* **1040–1041,** 35–44 (2014).

48. Dutta, A., Neese, F. & Izsák, R. Towards a pair natural orbital coupled cluster method for excited states. *J. Chem. Phys.* **145,** 034102 (1–8) (3 2016).

49. Dutta, A., Neese, F. & Izsák, R. Speeding up equation of motion coupled cluster theory with the chain of spheres approximation. *J. Chem. Phys.* **144,** 034102 (1–12) (3 2016).

50. Dutta, A., Nooijen, M., Neese, F. & Izsák, R. Exploring the Accuracy of a Low Scaling Similarity Transformed Equation of Motion Method for Vertical Excitation Energies. *J. Chem. Theory Comput.* **14,** 72–91 (1 2018).

51. Dittmer, A., Izsák, R., Neese, F. & Maganas, D. Accurate Band Gap Predictions of Semiconductors in the Framework of the Similarity Transformed Equation of Motion Coupled Cluster Theory. *Inorg. Chem.* **58,** 9303–9315 (2019).

52. Shafei, R. *et al.* Electronic and Optical Properties of Eu2+-Activated Narrow-Band Phosphors for Phosphor-Converted Light-Emitting Diode Applications: Insights from a Theoretical Spectroscopy Perspective. *Journal of the American Chemical Society* **144,** 8038–8053 (18 2022).

53. Pollock, C., Delgado-Jaime, M., Atanasov, M., Neese, F. & DeBeer, S. K beta Mainline X-ray Emission Spectroscopy as an Experimental Probe of Metal-Ligand Covalency. *J. Am. Chem. Soc.* **136,** 9453–9463 (26 2014).

54. Cutsail III, G. & DeBeer, S. Challenges and Opportunities for Applications of Advanced X-ray Spectroscopy in Catalysis Research. *ACS Catal.* **12,** 5864–5886 (10 2022).

55. Pantazis, D. Meeting the Challenge of Magnetic Coupling in a Triply-Bridged Chromium Dimer: Complementary Broken-Symmetry Density Functional Theory and Multireference Density Matrix Renormalization Group Perspectives. *J. Chem. Theory Comput.* **15,** 938–948 (2 2019).

56. Neese, F. Definition of corresponding orbitals and the diradical character in broken symmetry DFT calculations on spin coupled systems. *J. Phys. Chem. Solids* **65,** 781–785 (4 2004).

57. Barone, V. *et al.* Magnetic Interactions in Phenyl-Bridged Nitroxide Diradicals: Conformational Effects by Multireference and Broken Symmetry DFT Approaches. *J. Phys. Chem. A* **113,** 15150–15155 (52 2009).

58. Krewald, V. *et al.* The Protonation States of Oxo-Bridged Mn-IV Dimers Resolved by Experimental and Computational Mn K Pre-Edge X-ray Absorption Spectroscopy. *Inorg. Chem.* **52,** 12904–12914 (22 2013).

59. Krewald, V. *et al.* Metal oxidation states in biological water splitting. *Chemical Science* **6,** 1676–1695 (3 2015).

60. Lassalle-Kaiser, B. *et al.* Experimental and Computational X-ray Emission Spectroscopy as a Direct Probe of Protonation States in Oxo-Bridged Mn-IV Dimers Relevant to Redox-Active Metalloproteins. *Inorg. Chem.* **52,** 12915–12922 (22 2013).

61. Bjornsson, R. *et al.* Identification of a spin-coupled Mo(III) in the nitrogenase iron–molybdenum cofactor. *Chemical Science* **5,** 3096–3103 (8 2014).

62. Kowalska, J. & DeBeer, S. The role of X-ray spectroscopy in understanding the geometric and electronic structure of nitrogenase. *Biochim. Biophys. Acta. Mol. Cell. Res.* **1853,** 1406–1415 (6 2015).

63. Sharma, S. & Chan, G.-L. Spin-adapted density matrix renormalization group algorithms for quantum chemistry. *J. Chem. Phys.* **136,** 124121 (12 2012).

64. Chilkuri, V. & Neese, F. Comparison of many-particle representations for selected-CI I: A tree based approach. *J. Comput. Chem.* **42,** 982–1005 (14 2021).

65. Chilkuri, V. & Neese, F. Comparison of Many-Particle Representations for Selected Configuration Interaction: II. Numerical Benchmark Calculations. *J. Comput. Chem.* **17,** 2868–2885 (5 2021).

66. Li Manni, G., Smart, S. D. & Alavi, A. Combining the Complete Active Space Self-Consistent Field Method and the Full Configuration Interaction Quantum Monte Carlo within a Super-CI Framework, with Application to Challenging Metal-Porphyrins. *J. Chem. Theory Comput.* **12,** 1245–1258 (3 2016).

67. Sharma, S., Sivalingam, K., Neese, F. & Chan, G.-L. Low-energy spectrum of iron–sulfur clusters directly from many-particle quantum mechanics. *Nat. Chem.* **6,** 927–933 (10 2014).

68. Lunghi, A. & Totti, F. The Role of Anisotropic Exchange in Single Molecule Magnets: A CASSCF/NEVPT2 Study of the Fe4 SMM Building Block [Fe2(OCH3)2 (dbm)4] Dimer. *Inorganics* **4,** 28 (1–11) (4 2016).

69. Chilkuri, V. G., DeBeer, S. & Neese, F. Ligand Field Theory and Angular Overlap Model Based Analysis of the Electronic Structure of Homovalent Iron–Sulfur Dimers. *Inorg. Chem.* **59,** 984–995 (2 2020).

70. Dobrautz, W., Weser, O., Bogdanov, N. A., Alavi, A. & Li Manni, G. Spin-Pure Stochastic-CASSCF via GUGA-FCIQMC Applied to Iron–Sulfur Clusters. *J. Chem. Theory Comput.* **17,** 5684–5703 (9 2021).

71. Hoffmann, R. How Chemistry and Physics Meet in the Solid State. *Angew. Chem. Int. Ed.* **26,** 846–878 (9 1987).

72. Ihm, J. Total energy calculations in solid state physics. *Rep. Prog. Phys.* **51,** 105–142 (105 1988).

73. Daga, L., Civalleir, B. & Maschio, L. Gaussian Basis Sets for Crystalline Solids: All-Purpose Basis Set Libraries vs System-Specific Optimizations. *J. Chem. Theory Comput.* **16,** 2192–2201 (4 2020).

74. Grimme, S. & Schreiner, P. Computational Chemistry: The Fate of Current Methods and Future Challenges. *Angew. Chem. Int. Ed.* **57,** 4170–4176 (16 2018).

75. Olejniczak, M., Bast, R. & Gomes, A. On the calculation of second-order magnetic properties using subsystem approaches in a relativistic framework. *Phys. Chem. Chem. Phys.* **19,** 8400–8415 (2017).

76. Weber, J. & Schmedt auf der Günne, J. Calculation of NMR Parameters in Ionic Solids by an Improved Self-Consistent Embedded Cluster Method. *Phys. Chem. Chem. Phys.* **12,** 583–603 (2010).

77. Jacob, C. & Visscher, L. Calculation of Nuclear Magnetic Resonance Shielding constants Using Frozen-Density Embedding. *J. Chem. Phys.* **125,** 194104 (1–11) (19 2006).

78. Wesolowski, T., Shedge, S. & Zhou, X. Frozen-Density Embedding Strategy for Multilevel Simulations of Electronic Structure. *Chem. Rev.* **115,** 5891–5928 (12 2015).

79. Hartman, J., Balaji, A. & Beran, G. Improved Electrostatic Embedding for Fragment-Based Chemical Shift Calculations in Molecular Crystals. *J. Chem. Theory Comput.* **13,** 6043–6051 (12 2017).

80. Kubas, A., Verkamp, M., Vura-Weis, J., Neese, F. & Maganas, D. Restricted Open-Shell Configuration Interaction Singles Study on M- and L-edge X-ray Absorption Spectroscopy of Solid Chemical Systems. *J. Chem. Theory Comput.* **14,** 4320–4334 (8 2018).

81. Stodt, D., Noei, H., Hättig, C. & Wang, Y. A Combined Experimental and Computational Study on the Adsorption and Reactions of NO on Rutile TiO2. *Phys. Chem. Chem. Phys.* **15,** 466–472 (2013).

82. Hoffmann, R. *Solids and Surfaces: A Chemist's View of Bonding in Extended Structures* 6–7 (VCH Publishers Inc., New York, US, 1988).

83. Dittmer, A., Stoychev, G., Maganas, D., Auer, A. & Neese, F. Computation of NMR Shielding Constants for Solids Using an Embedded Cluster Approach with DFT, Double-Hybrid DFT, and MP2. *J. Chem. Theory Comput.* **16,** 6950–6967 (2020).

84. Atkins, P., de Paula, J. & Keeler, J. *Atkins' Physical Chemistry* 11th ed., 641–645 (Oxford University Press Inc., New York, USA, 2018).

85. Szabo, A. & Ostlund, N. *Modern Quantum Chemistry - Introduction to Advanced Electronic Structure Theory* 46–64 (Dover Publications, Inc., New York, USA, 1982).

86. Atkins, P., de Paula, J. & Keeler, J. *Atkins' Physical Chemistry* 11th ed., 35 (Oxford University Press Inc., New York, USA, 2018).

87. Atkins, P., de Paula, J. & Keeler, J. *Atkins' Physical Chemistry* 11th ed., 662 (Oxford University Press Inc., New York, USA, 2018).

88. Madelung, E. Das elektrische Feld in Systemen von regelmäßig angeordneten Punktladungen. *Phys. Z.* **19,** 524–533 (1919).

89. Hoppe, R. Madelung Constants. *Angew. Chem. Int. Ed.* **5,** 95–106 (1 1966).

90. Szabo, A. & Ostlund, N. *Modern Quantum Chemistry - Introduction to Advanced Electronic Structure Theory* 43–45 (Dover Publications, Inc., New York, USA, 1982).

91. Atkins, P. & Friedman, R. *Molecular Quantum Mechanics* 5th ed., 20–26 (Oxford University Press Inc., New York, USA, 2011).

92. Cramer, C. *Essentials of Computational Chemistry* 2nd ed., 105–128 (John Wiley Sons, Ltd, West Sussex, England, 2004).

93. Atkins, P. & Friedman, R. *Molecular Quantum Mechanics* 5th ed., 69–96 (Oxford University Press Inc., New York, USA, 2011).

94. Leach, A. *Molecular Modelling - Principles and Applications* 2nd ed., 54–74 (Prentice Hall, UK, 2001).

95. Szabo, A. & Ostlund, N. *Modern Quantum Chemistry - Introduction to Advanced Electronic Structure Theory* 180–190 (Dover Publications, Inc., New York, USA, 1982).

96. Roothaan, C. New Developments in Molecular Orbital Theory. *Revs. Modern Phys.* **23,** 69–89 (2 1951).

97. Harris, D. & Bertolucci, M. *Symmetry and Spectroscopy - An Introduction to Vibrational and Electronic Spectroscopy* 245–252 (Dover Publications, Inc., New York, USA, 1989).

98. Atkins, P. & Friedman, R. *Molecular Quantum Mechanics* 5th ed., 262–285 (Oxford University Press Inc., New York, USA, 2011).

99. Mulliken, R. Electronic Population Analysis on LCAO–MO Molecular Wave Functions. I. *J. Chem. Phys.* **23,** 1833–1840 (10 1955).

100. Atkins, P., de Paula, J. & Keeler, J. *Atkins' Physical Chemistry* 11th ed., 656–673 (Oxford University Press Inc., New York, USA, 2018).

101. Atkins, P. & Friedman, R. *Molecular Quantum Mechanics* 5th ed., 286–291 (Oxford University Press Inc., New York, USA, 2011).

102. Atkins, P., de Paula, J. & Keeler, J. *Atkins' Physical Chemistry* 11th ed., 271 (Oxford University Press Inc., New York, USA, 2018).

103. Leach, A. *Molecular Modelling - Principles and Applications* 2nd ed., 141–153 (Prentice Hall, UK, 2001).

104. Accessed: 15-11-2022. `http://dipc.ehu.es/frederiksen/inelastica/index.php/NaCl`.

105. Pople, J. & Beveridge, D. *Approximate Molecular Orbital Theory* 1–30 (McGraw-Hill Inc., U.S.A., 1970).

106. Harris, D. & Bertolucci, M. *Symmetry and Spectroscopy - An Introduction to Vibrational and Electronic Spectroscopy* 130–134 (Dover Publications, Inc., New York, USA, 1989).

107. Krylov, A. From orbitals to observables and back. *J. Chem. Phys.* **153,** 080901 (1–15) (2020).

108. Dohn, A. Multiscale electrostatic embedding simulations for modeling structure and dynamics of molecules in solution: A tutorial review. *Int. J. Quantum Chem.* **120,** e26343 (1–22) (21 2020).

109. Van Mourik, T. First–principles quantum chemistry in the life sciences. *Philos. Trans. R. Soc. London A* **362,** 2653 (1825 2004).

110. Momma, K. & Izumi, F. VESTA 3 for three-dimensional visualization of crystal, volumetric and morphology data. *J. Appl. Crystallogr.* **44,** 1272–1276 (2011).

111. Macrae, C. *et al.* Mercury 4.0: from visualization to analysis, design and prediction. *J. Appl. Crystallogr.* **53,** 226–235 (2020).

112. Dovesi, R. *et al.* Quantum-mechanical condensed matter simulations with CRYSTAL. *WIREs Comput. Mol. Sci.* **8,** e1360 (4 2018).

113. Hanwell, M. *et al.* Avogadro: An advanced semantic chemical editor, visualization, and analysis platform. *J. Cheminform.* **4,** 17 (1 2012).

114. Avogadro development team. *Avogadro: an open-source molecular builder and visualization tool.* version any. 2012–2022. `http://avogadro.cc/`.

115. Jmol development team. *Jmol: an open-source Java viewer for chemical structures in 3D* version any. 2004–2022. `http://www.jmol.org/`.

116. E.F., P. *et al.* UCSF Chimera–a visualization system for exploratory research and analysis. *J. Comput. Chem.* **25,** 1605–1612 (13 2004).

117. Chimera development team. *UCSF Chimera* version any. 2004–2022. `https://www.rbvi.ucsf.edu/chimera`.

118. Gražulis, S. *et al.* Crystallography Open Database - an Open-Access Collection of Crystal Structures. *J. Appl. Crystallogr.* **42,** 726–729 (2009).

119. Gražulis, S. *et al.* Crystallography Open Database (Cod): An OpenAccess Collection of Crystal Structures and Platform for World-Wide Collaboration. *Nucleic Acids Res.* **40,** D420–D427 (2012).

120. Fuentealba, P., Preuss, H., Stoll, H. & von Szentpály, L. A proper account of core-polarization with pseudopotentials: single valence-electron alkali compounds. *J. Chem. Phys. Lett.* **89,** 418–422 (5 1982).

121. Peterson, K. Systematically convergent basis sets with relativistic pseudopotentials. I. Correlation consistent basis sets for the post-d group 13–15 elements. *J. Chem. Phys.* **119,** 11099–11112 (2003).

122. Peterson, K. A., Figgen, D., Goll, E., Stoll, H. & Dolg, M. Systematically convergent basis sets with relativistic pseudopotentials. II. Small-core pseudopotentials and correlation consistent basis sets for the post-d group 16–18 elements. *J. Chem. Phys.* **119,** 11113–11123 (21 2003).

123. Lim, I. S., Schwerdtfeger, P., Metz, B. & Stoll, H. All-electron and relativistic pseudopotential studies for the group 1 element polarizabilities from K to element 119. *J. Chem. Phys.* **122,** 104103–104112 (10 2005).

124. Figgen, D., Rauhut, G., Dolg, M. & Stoll, H. Energy-consistent pseudopotentials for group 11 and 12 atoms: adjustment to multi-configuration Dirac–Hartree-Fock data. *Chem. Phys.* **311,** 227–244 (1-2 2005).

125. Fuentealba, P., Stoll, H., von Szentpály, L., Schwerdtfeger, P. & Preuss, H. On the reliability of semi-empirical pseudopotentials: simulation of Hartree-Fock and Dirac-Fock results. *J. Phys. B: At. Mol. Phys.* **16,** L323–L328 (11 1983).

126. Stoll, H., P. Fuentealba, P. S., Flad, J. & von Szentpály L.and Preuss, H. Cu and Ag as one-valence-electron atoms: CI results and quadrupole corrections for Cu2, Ag2, CuH, and AgH. *J. Chern. Phys.* **81,** 2732–2736 (6 1984).

127. Fuentealba, P., Szentpaly, L., Preuss, H. & Stoll, H. Pseudopotential calculations for alkaline-earth atoms. *J. Phys. B: At. Mol. Opt. Phys.* **18,** 1287–1296 (1985).

128. Dolg, M., Wedig, U., Stoll, H. & Preuss, H. Energy-Adjusted Abinitio Pseudopotentials for the 1st-Row Transition-Elements. *J. Chem. Phys.* **86,** 866–872 (2 1987).

129. Igel-Mann, G., Stoll, H. & Preuss, H. Pseudopotentials for main group elements (IIIa through VIIa). *Mol. Phys.* **65,** 1321–1328 (1988).

130. Bergner, A., Dolg M.and Küchle, W. & Stoll H.and Preuss, H. Abinitio energy-adjusted pseudopotentials for elements of groups 1317. *Mol. Phys.* **80,** 1431–1441 (1993).

131. Schautz, F., Flad, H.-J. & Dolg, M. Quantum Monte Carlo study of Be2 and group 12 dimers M2 (M = Zn, Cd, Hg). *Theor. Chem. Acc.* **99,** 231–240 (1998).

132. Metz, B., Stoll, H. & Dolg, M. Small-core multiconfiguration-Dirac–Hartree–Fock-adjusted pseudopotentials for post-d main group elements: Application to PbH and PbO. *J. Chem. Phys.* **113,** 2563–2569 (7 2000).

133. Mulliken, R. Electronic Population Analysis on LCAO–MO Molecular Wave Functions. II. Overlap Populations, Bond Orders, and Covalent Bond Energies. *J. Chem. Phys.* **23,** 1841–1846 (10 1955).

134. Mulliken, R. Electronic Population Analysis on LCAO-MO Molecular Wave Functions. III. Effects of Hybridization on Overlap and Gross AO Populations. *J. Chem. Phys.* **23,** 2338–2342 (10 1955).

135. Löwdin, P. On the Non-Orthogonality Problem Connected with the Use of Atomic Wave Functions in the Theory of Molecules and Crystals. *J. Chem. Phys.* **18,** 365–375 (3 1950).

136. Cusachs, L. & Politzer, P. On the problem of defining the charge on an atom in a molecule. *Chem. Phys. Lett.* **1,** 529–531 (11 1968).

137. Breneman, C. & Wiberg, K. Determining Atom-Centered Monopoles from Molecular Electrostatic Potentials. The Need for High Sampling Density in Formamide Conformational Analysis. *J. Comput. Chem.* **11,** 361–373 (3 1990).

138. Hirshfeld, F. Bonded-atom fragments for describing molecular charge densities. *Theor. Chim. Acta* **44,** 129–138 (1977).

139. Szabo, A. & Ostlund, N. *Modern Quantum Chemistry - Introduction to Advanced Electronic Structure Theory* 151–152 (Dover Publications, Inc., New York, USA, 1982).

140. Mao, J. Atomic Charges in Molecules: A Classical Concept in Modern Computational Chemistry. *Postdoc J* **2,** 15–18 (2 2014).

141. Chirlian, L. & Miller Francl, M. Atomic Charges Derived from Electrostatic Potentials: A Detailed Study. *J. Comput. Chem.* **8,** 894–905 (6 1987).

142. Weigend, F. & Ahlrichs, R. Balanced basis sets of split valence, triple zeta valence and quadruple zeta valence quality for H to Rn: Design and assessment of accuracy. *Phys. Chem. Chem. Phys.* **7,** 3297–3305 (18 2005).

143. Aravena, D., Neese, F. & Pantazis, D. Improved Segmented All-Electron Relativistically Contracted Basis Sets for the Lanthanides. *J. Chem. Theory Comput.* **12,** 1148–1156 (3 2016).

144. Dunning T. H., J. Gaussian Basis Sets for Use in Correlated Molecular Calculations. I. The Atoms Boron Through Neon and Hydrogen. *J. Chem. Phys.* **90,** 1007–1023 (2 1989).

145. Kern, C. & Karplus, M. Analysis of Charge Distributions: Hydrogen Fluoride. *J. Chem. Phys.* **40,** 1374–1389 (5 1964).

146. Wiberg, K. & Rablen, P. Comparison of Atomic Charges Derived via Different Procedures. *J. Comput. Chem.* **14,** 1504–1518 (12 1993).

147. Leach, A. *Molecular Modelling - Principles and Applications* 2nd ed., 155–158 (Prentice Hall, UK, 2001).

148. Kresse, G. & Furthmüller, J. Efficient iterative schemes for ab initio total-energy calculations using a plane-wave basis set. *Phys. Rev. B* **54,** 11169–11 186 (16 1996).

149. Lippert, G., Hutter, J. & Parrinello, M. A hybrid Gaussian and plane wave density functional scheme. *Mol. Phys.* **92,** 477–488 (3 1997).

150. Nagy, B. & Jensen, F. Basis Sets in Quantum Chemistry. *Rev. Comp. Chem.* **30,** 93–150 (2017).

151. Peterson, K. A. & Hill, J. G. *Annual Reports in Computational Chemistry* 47–74 (Elsevier, Netherlands, 2018).

152. Peintinger, M. F., Oliveira, D. V. & Bredow, T. Consistent Gaussian Basis Sets of Triple-zeta Valence with Polarization Quality for Solid-State Calculations. *J. Comput. Chem.* **34,** 451–459 (6 2013).

153. Laun, J., Vilela Oliveira, D. & Bredow, T. Consistent gaussian basis sets of double-and triple-zeta valence with polarization quality of the fifth period for solid-state calculations. *J. Comput. Chem.* **39,** 1285–1290 (19 2018).

154. Vilela Oliveira, D., Laun, J., Peintinger, M. F. & Bredow, T. BSSE-correction scheme for consistent gaussian basis sets of doubleand triple-zeta valence with polarization quality for solid-state calculations. *J. Comput. Chem.* **40,** 2364–2376 (27 2019).

155. Jensen, F. Polarization Consistent Basis Sets: Principles. *J. Chem. Phys.* **115,** 9113–9125 (20 2001).

156. Liakos, D. & Neese, F. Improved Correlation Energy Extrapolation Schemes Based on Local Pair Natural Orbital Methods. *J. Phys. Chem. A* **116,** 4801–4816 (19 2012).

157. Atkins, P. & Friedman, R. *Molecular Quantum Mechanics* 5th ed., 302–307 (Oxford University Press Inc., New York, USA, 2011).

158. Varga, K. & Pantelides, S. Lagrange-function approach to real-space order-N electronic-structure calculations. *Phys. Stat. Sol. B* **243,** 1110–1120 (5 2006).

159. Mazurek, A., Szeleszczuk, L. & Pisklak, D. Periodic DFT Calculations—Review of Applications in the Pharmaceutical Sciences. *Pharmaceutics* **12,** 415 (1–29) (5 2020).

160. Lee, K., Yu, J. & Morikawa, Y. Comparison of localized basis and plane-wave basis for density-functional calculations of organic molecules on metals. *Phys. Rev. B* **75,** 045402 (1–5) (4 2007).

161. Lehtola, S. Curing basis set overcompleteness with pivoted Cholesky decompositions. *J. Chem. Phys.* **151,** 241102 (1–5) (24 2019).

162. Hill, G. Gaussian basis sets for molecular applications. *J. Quantum Chem.* **113,** 21–34 (1 2012).

163. Shepherd, J., Grüneis, A., Booth, G., Kresse, G. & Alavi, A. Convergence of many-body wavefunction expansions using a plane wave basis: from the homogeneous electron gas to the solid state. *Phys. Rev. B* **86,** 035111 (1–14) (3 2012).

164. Zhou, Y., Gull, E. & Zgid, D. Material-Specific Optimization of Gaussian Basis Sets against Plane Wave Data. *J. Chem. Theory Comput.* **17,** 5611–5622 (9 2021).

165. Lowe, J. & Peterson, K. *Quantum Chemistry* 3rd ed., 358–372 (Elsevier, England, 2006).

166. Harrison, N. An Introduction to Density Functional Theory. `https://www.imperial.ac.uk/media/imperial-college/research-centres-and-groups/computational-materials-science/teaching/DFT_NATO.pdf` (2001).

167. Riplinger, C. & Neese, F. An efficient and near linear scaling pair natural orbital based local coupled cluster method. *J. Chem. Phys.* **138,** 034106 (2013).

168. Riplinger, C., Sandhoefer, B., Hansen, A. & Neese, F. Natural triple excitations in local coupled cluster calculations with pair natural orbitals. *J. Chem. Phys.* **139,** 134101 (2013).

169. Roos, B., Taylor, P. & Sigbahn, P. A complete active space SCF method (CASSCF) using a density matrix formulated super-CI approach. *Chem. Phys.* **48,** 157–173 (2 1980).

170. Roos, B. The complete active space SCF method in a fock-matrix-based super-CI formulation. *Int. J. Quantum Chem.* **14,** 175–189 (1980).

171. Sigbahn, P., Almlöf, J., Heiberg, A. & Roos, B. The complete active space SCF (CASSCF) method in a Newton–Raphson formulation with application to the HNO molecule. *J. Chem. Phys.* **74,** 2384–2396 (4 1981).

172. Benavides-Riveros, C., Lathiotakis, N. & Marques, M. Towards a formal definition of static and dynamic electronic correlations. *Phys. Chem. Chem. Phys.* **19,** 12655–12664 (2017).

173. Singh, V., Kosa, M., Majhi, K. & Major, D. T. Putting DFT to the Test: A First-Principles Study of Electronic, Magnetic, and Optical Properties of Co3O4. *J. Chem. Theory Comput.* **11,** 64–72 (1 2015).

174. Barone, V. *et al.* Computational molecular spectroscopy. *Nat. Rev. Methods Primers* **1,** 35 (1–26) (2021).

175. Grunenberg, J. *Computational Spectroscopy - Methods, Experiments and Applications* (Wiley-VCH Verlag GmbH Co. KGaA, Weinheim, Germany, 2010).

176. Harris, D. & Bertolucci, M. *Symmetry and Spectroscopy - An Introduction to Vibrational and Electronic Spectroscopy* 1–4 (Dover Publications, Inc., New York, USA, 1989).

177. Harris, D. & Bertolucci, M. *Symmetry and Spectroscopy - An Introduction to Vibrational and Electronic Spectroscopy* 62–92 (Dover Publications, Inc., New York, USA, 1989).

178. Atkins, P., de Paula, J. & Keeler, J. *Atkins' Physical Chemistry* 11th ed., 237–245 (Oxford University Press Inc., New York, USA, 2018).

179. Harris, D. & Bertolucci, M. *Symmetry and Spectroscopy - An Introduction to Vibrational and Electronic Spectroscopy* 310–330 (Dover Publications, Inc., New York, USA, 1989).

180. Atkins, P. & Friedman, R. *Molecular Quantum Mechanics* 5th ed., 191–206 (Oxford University Press Inc., New York, USA, 2011).

181. Atkins, P. & Friedman, R. *Molecular Quantum Mechanics* 5th ed., 437–472 (Oxford University Press Inc., New York, USA, 2011).

182. Atkins, P. & Friedman, R. *Molecular Quantum Mechanics* 5th ed., 407–417 (Oxford University Press Inc., New York, USA, 2011).

183. Atkins, P. & Friedman, R. *Molecular Quantum Mechanics* 5th ed., 295–302 (Oxford University Press Inc., New York, USA, 2011).

184. Szabo, A. & Ostlund, N. *Modern Quantum Chemistry - Introduction to Advanced Electronic Structure Theory* 205–210 (Dover Publications, Inc., New York, USA, 1982).

185. Atkins, P. & Friedman, R. *Molecular Quantum Mechanics* 5th ed., 235–239 (Oxford University Press Inc., New York, USA, 2011).

186. Young, D. *Computational Chemistry: A Practical Guide for Applying Techniques to Real World Problems* 19–28 (John Wiley Sons, Inc., New York, USA, 2001).

187. Szabo, A. & Ostlund, N. *Modern Quantum Chemistry - Introduction to Advanced Electronic Structure Theory* 111–115 (Dover Publications, Inc., New York, USA, 1982).

188. Atkins, P. & Friedman, R. *Molecular Quantum Mechanics* 5th ed., 253 (Oxford University Press Inc., New York, USA, 2011).

189. Piela, L. *Ideas of Quantum Chemistry* 389–504 (Elsevier, Oxford, England, 2014).

190. Atkins, P. & Friedman, R. *Molecular Quantum Mechanics* 5th ed., 307–312 (Oxford University Press Inc., New York, USA, 2011).

191. Piela, L. *Ideas of Quantum Chemistry* 525–533 (Elsevier, Oxford, England, 2014).

192. Cremer, D. & He, Z. Analysis of coupled cluster methods - IV. Size-extensive quadratic CI methods - quadratic CI with triple and quadruple excitations. *Theor. Chim. Acta* **88,** 47–67 (1994).

193. Malmqvist, P.-A., Rendell, A. & Roos, B. The Restricted Active Space Self-Consistent-Fleld Method, Implemented with a Split Graph Unitary Group Approach. *J. Phys. Chem.* **94,** 5477–5482 (14 1990).

194. Szabo, A. & Ostlund, N. *Modern Quantum Chemistry - Introduction to Advanced Electronic Structure Theory* 322–327 (Dover Publications, Inc., New York, USA, 1982).

195. Atkins, P. & Friedman, R. *Molecular Quantum Mechanics* 5th ed., 176–184 (Oxford University Press Inc., New York, USA, 2011).

196. Szabo, A. & Ostlund, N. *Modern Quantum Chemistry - Introduction to Advanced Electronic Structure Theory* 350–353 (Dover Publications, Inc., New York, USA, 1982).

197. Atkins, P. & Friedman, R. *Molecular Quantum Mechanics* 5th ed., 313–315 (Oxford University Press Inc., New York, USA, 2011).

198. Angeli, C., Cimiraglia, R., Evangelisti, S., Leininger, T. & Malrieu, J.-P. Introduction of n-electron valence states for multireference perturbation theory. *J. Chem. Phys.* **114,** 10252–10264 (23 2001).

199. Angeli, C., Cimiraglia, R. & Malrieu, J.-P. N-electron valence state perturbation theory: a fast implementation of the strongly contracted variant. *Chem. Phys. Lett.* **350,** 297–305 (3–4 2001).

200. Angeli, C., Cimiraglia, R. & Malrieu, J.-P. N-electron valence state perturbation theory: a fast implementation of the strongly contracted variant. *J. Chem. Phys.* **117,** 9138–9153 (20 2002).

201. Andersson, K., Malmqvist, P.-Å., Roos, B., Sadlej, A. & Wolinski, K. Second-Order Perturbation Theory with a CASSCF Reference Function. *J. Phys. Chem.* **94,** 5483–5488 (1990).

202. Andersson, K., Malmqvist, P.-A. & Roos, B. Second-Order Perturbation Theory with a CASSCF Reference Function. *J. Phys. Chem.* **96,** 1218–1226 (2 1992).

203. Pathak, S., Lang, L. & Neese, F. A dynamic correlation dressed complete active space method: Theory, implementation, and preliminary applications. *J. Chem. Phys.* **147,** 234109 (1–17) (23 2017).

204. Bartlett, R. & Musiał, M. Coupled-cluster theory in quantum chemistry. *Rev. Mod. Phys.* **79,** 291–352 (1 2007).

205. Pinski, P., Riplinger, C., Valeev, E. & Neese, F. Sparse maps: A systematic infrastructure for reduced-scaling electronic structure methods. I. An efficient and simple linear scaling local MP2 method that uses an intermediate basis of pair natural orbitals. *J. Chem. Phys.* **143,** 034108 (2015).

206. Riplinger, C., Pinski, P., Becker, U., Valeev, E. & Neese, F. Sparse maps: A systematic infrastructure for reduced-scaling electronic structure methods. II. Linear scaling domain based pair natural orbital cluster theory. *J. Chem. Phys.* **144,** 024109 (2016).

207. Saitow, M., Becker, U., Riplinger, C., Valeev, E. & Neese, F. A new near-linear scaling, efficient and accurate, open-shell domainbased local pair natural orbital coupled cluster singles and doubles theory. *J. Chem. Phys.* **146,** 164105 (2017).

208. Hohenberg, P. & Kohn, W. Inhomogeneous Electron Gas. *Phys. Rev.* **136,** 864–871 (3B 1964).

209. Kohn, W., Becke, A. & Parr, R. Density Functional Theory of Electronic Structure. *J. Phys. Chem.* **100,** 12974–12980 (31 1996).

210. Atkins, P. & Friedman, R. *Molecular Quantum Mechanics* 5th ed., 317–323 (Oxford University Press Inc., New York, USA, 2011).

211. Perdew, J. & Schmidt, K. Jacob's ladder of density functional approximations for the exchange-correlation energy. *AIP Conf. Proc.* **577,** 1–20 (1 2001).

212. Perdew, J. P., Burke, K. & Ernzerhof, M. Generalized Gradient Approximation Made Simple. *Phys. Rev. Lett.* **77,** 3865–3868 (18 1996).

213. Becke, A. Density-Functional Exchange-Energy Approximation with Correct Asymptotic-Behaviour. *Phys. Rev. A* **38,** 3098–3100 (1988).

214. Lee, C., Yang, W. & Parr, R. LYP Functional. *Phys. Rev. B* **37,** 785 (1988).

215. Perdew, J. Erratum: Density-functional approximation for the correlation energy of the inhomogeneous electron gas. *Phys. Rev. B* **34,** 7406 (10 1986).

216. Tao, J., Perdew, J., Staroverov, V. & Scuseria, G. Climbing the Density Functional Ladder: Nonempirical Meta-Generalized Gradient Approximation Designed for Molecules and Solids. *Phys. Rev. Lett.* **91,** 146401 (1–4) (14 2003).

217. Zhao, Y. & Truhlar, D. The M06 suite of density functionals for main group thermochemistry, thermochemical kinetics, noncovalent interactions, excited states, and transition elements: Two new functionals and systematic testing of four M06-class functionals and 12 other functionals. *Theor Chem Acc.* **120,** 215–241 (1–3 2006).

218. Becke, A. Density-Functional Thermochemistry. III. The Role of Exact Exchange. *J. Chem. Phys.* **98,** 5648–5652 (1993).

219. Adamo, C. & Barone, V. Toward reliable density functional methods without adjustable parameters: The PBE0 model. *J. Chem. Phys.* **110,** 6158–6169 (13 1999).

220. Perdew, J., Tao, J., Staroverov, V. & Scuseria, G. Meta-generalized Gradient Approximation: Explanation of a Realistic Nonempirical Density Functional. *J. Chem. Phys.* **120,** 6898–6911 (2004).

221. Tao, J., Perdew, J., Staroverov, V. & Scuseria, G. Climbing the Density Functional Ladder: Nonempirical Meta–Generalized Gradient Approximation Designed for Molecules and Solids. *Phys. ReV. Lett.* **91,** 146401 (1–4) (14 2003).

222. Perdew, J. *et al.* Atoms, Molecules, Solids, and Surfaces: Applications of the Generalized Gradient Approximation for Exchange and Correlation. *Phys. Rev. B: Condens. Matter* **46,** 6671–6687 (1992).

223. Grimme, S. Semiempirical Hybrid Density Functional with Perturbative Second-Order Correlation. *J. Chem. Phys.* **124,** 034108 (1–16) (3 2006).

224. Kozuch, S., Gruzman, D. & Martin, J. DSD-BLYP: A General Purpose Double Hybrid Density Functional Including Spin Component Scaling and Dispersion Correction. *J.Chem. Phys. C* **114,** 20801–20808 (48 2010).

225. Kozuch, S. & Martin, J. Spin-Component-Scaled Double Hybrids: An Extensive Search for the Best Fifth-Rung Functionals Blending DFT and Perturbation Theory. *J. Comput. Chem.* **34,** 2327–2344 (27 2013).

226. Kozuch, S. & Martin, J. DSD-PBEP86: In Search of the Best Double-Hybrid Dft with Spin-Component Scaled MP2 and Dispersion Corrections. *Phys. Chem. Chem. Phys.* **13,** 20104–20107 (2011).

227. Piela, L. *Ideas of Quantum Chemistry* 130–132 (Elsevier, Oxford, England, 2014).

228. Douglas, M. & Kroll, N. Quantum electrodynamical corrections to the fine structure of helium. *Ann. Phys.* **82,** 89–155 (1 1974).

229. Hess, B. Relativistic electronic-structure calculations employing a two-component no-pair formalism with external-field projection operators. *Phys. Rev. A* **33,** 3742–3748 (6 1986).

230. Atkins, P., de Paula, J. & Keeler, J. *Atkins' Physical Chemistry* 11th ed., 488–508 (Oxford University Press Inc., New York, USA, 2018).

231. Wolinski, K., Hinton, J. & Pulay, P. Efficient Implementation of the Gauge-Independent Atomic Orbital Method for NMR Chemical Shift Calculations. *J. Am. Chem. Soc.* **112,** 8251–8260 (23 1990).

232. Charpentier, T. The PAW/GIPAW Approach for Computing NMR Parameters: A New Dimension Added to NMR Study of Solids. *Solid State Nucl. Magn. Reson.* **40,** 1–20 (2011).

233. Jensen, F. Segmented Contracted Basis Sets Optimized for Nuclear Magnetic Shielding. *J. Chem. Theory Comput.* **11,** 132–138 (1 2015).

234. Harris, D. & Bertolucci, M. *Symmetry and Spectroscopy - An Introduction to Vibrational and Electronic Spectroscopy* 330–341 (Dover Publications, Inc., New York, USA, 1989).

235. Maganas, D., DeBeer, S. & Neese, F. A Restricted Open Configuration Interaction with Singles Method To Calculate Valence-to-Core Resonant X-ray Emission Spectra: A Case Study. *Inorg. Chem.* **56,** 11819–11836 (19 2017).

236. Bernadotte, S., Atkins, A. & Jacob, C. Origin-independent calculation of quadrupole intensities in X-ray spectroscopy. *J. Chem. Phys.* **137,** 204106 (1–15) (20 2012).

237. Roemelt, M. & Neese, F. Excited States of Large Open-Shell Molecules: An Efficient, General, and Spin-Adapted Approach Based on a Restricted Open-Shell Ground State Wave function. *J. Phys. Chem. A* **117,** 3069–3083 (14 2013).

238. Manne, R. & Åberg, T. Koopmans' theorem for inner-shell ionization. *Chem. Phys. Lett.* **7,** 282–284 (2 1970).

239. Bredas, J. Mind the gap! *Mater. Horiz.* **1,** 17–19 (2014).

240. Makuła, P., Pacia, M. & Macyk, W. How To Correctly Determine the Band Gap Energy of Modified Semiconductor Photocatalysts Based on UVVis Spectra. *J. Phys. Chem. Lett.* **9,** 6814–6817 (23 2018).

241. Seo, D.-K. & Hoffmann, R. Direct and indirect band gap types in one-dimensional conjugated or stacked organic materials. *Theor. Chem. Acc.* **102,** 23–32 (1999).

242. Strehlow, W. & Cook, E. Compilation of Energy Band Gaps in Elemental and Binary Compound Semiconductors and Insulators. *Phys. Chem. Ref. Data* **2,** 163–199 (1 1973).

243. Wang, L.-M. Relationship between Intrinsic Breakdown Field and Bandgap of Materials. *2006 25th International Conference on Microelectronics,* 576–579 (2006).

244. Quaschning, V. *Understanding Renewable Energy Systems* 2nd ed. (Routledge Taylor Francis Group, New York, USA, 2016).

245. Serway, R. & Jewett, J. *Physics for Scientists and Engineers with Modern Physics* 8th ed., 1315–1317 (Cengage Learning, Los Angeles, USA, 2010).

246. Bartlett, R. & Ranasinghe, D. The power of exact conditions in electronic structure theory. *Chem. Phys. Lett.* **669,** 54–70 (2017).

247. Haduke, R. & Bartlett, R. Communication: Can excitation energies be obtained from orbital energies in a correlated orbital theory? *J. Chem. Phys.* **149,** 131101 (1–7) (13 2018).

248. Koopmans, T. Ordering of Wave Functions and Eigenenergies to the Individual Electrons of an Atom. *Physica* **1,** 104–113 (1933).

249. Kowalczyk, T., Yost, S. & Voorhis, T. Assessment of the SCF density functional theory approach for electronic excitations in organic dyes. *J. Chem. Phys.* **134,** 054128 (5 2011).

250. Casida, M. Time-dependent density-functional theory for molecules and solids. *J. Mol. Struct.* **914,** 3–18 (2009).

251. Dreuw, A. & M., H.-G. Failure of Time-Dependent Density Functional Theory for Long-Range Charge-Transfer Excited States: The Zincbacteriochlorin-Bacteriochlorin and BacteriochlorophyllSpheroidene Complexes. *J. Am. Chem. Soc.* **126,** 4007–4016 (12 2004).

252. Tsuneda, T., Singh, R. K. & Nakata, A. Relationship between orbital energy gaps and excitation energies for long-chain systems. *J. Comput. Chem.* **37,** 1451–1462 (16 2016).

253. Bartlett, R. Coupled-cluster theory and its equation-of-motion extensions. *Wiley Interdiscip. Rev. Comput. Mol. Sci.* **2,** 126–138 (1 2012).

254. Bartlett R. J.and Musiał, M. Coupled-cluster theory in quantum chemistry. *Rev. Mod. Phys.* **79,** 291–352 (1 2007).

255. Nooijen, M. & Bartlett, R. Similarity transformed equation-of-motion coupled-cluster theory: Details, examples, and comparisons. *J. Chem. Phys.* **107,** 6812–6830 (17 1997).

256. Dutta, A. K., Saitow, M., Demoulin, B., Neese, F. & Izsak, R. A domain-based local pair natural orbital implementation of the equation of motion coupled cluster method for electron attached states. *J. Chem. Phys.* **150,** 164123 (16 2019).

257. Dutta, A., Saitow, M., Demoulin, B., Neese, F. & Izsák, R. A domain-based local pair natural orbital implementation of the equation of motion coupled cluster method for electron attached states. *J. Chem. Phys.* **150,** 164123 (2019).

258. Reining, L. The GW approximation: content, successes and limitations. *WIREs Comput. Mol. Sci.* **8,** e1344 (2017).

259. Blase, X., Duchemin, I., Jacquemin, D. & Loos, P.-F. The Bethe-Salpeter Equation Formalism: From Physics to Chemistry. *J. Phys. Chem. Lett.* **11,** 7371–7382 (2020).

260. Nooijen, M. *et al.* Communication: Multireference equation of motion coupled cluster: A transform and diagonalize approach to electronic structure. *J. Chem. Phys.* **140,** 081102 (8 (1–5) 2014).

261. Bergmann, U. & Glatzel, P. X-ray emission spectroscopy. *Photosynth. Res.* **102,** 255–266 (2009).

262. Manne, R. & Åberg, T. Koopmans' theorem for inner-shell ionization. *Chem. Phys. Lett.* **7,** 282–284 (2 1970).

263. Lee, N., Petrenko, T., Bergmann, U., Neese, F. & DeBeer, S. Probing Valence Orbital Composition with Iron K X-ray Emission Spectroscopy. *J. Am. Chem. Soc.* **132,** 9715–9727 (28 2010).

264. Beckwith, M. A. *et al.* Manganese K beta X-ray Emission Spectroscopy As a Probe of Metal-Ligand Interactions. *Inorg. Chem.* **50,** 8397–8409 (17 2011).

265. Shermer, M. How To Be Open-Minded Without Your Brains Falling Out. *J. Thought* **38,** 33–48 (2 2003).

266. Downs, R. T. & Hall-Wallace, M. The American Mineralogist Crystal Structure Database. *Am. Mineral.* **88,** 247–250 (2003).

267. Haas, P., Tran, F. & Blaha, P. Calculation of the lattice constant of solids with semilocal functionals. *Phys. Rev. B* **8,** 085104 (1–10) (2009).

268. Maganas, D. *et al.* First principles calculations of the structure and V L-edge X-ray absorption spectra of V2O5 using local pair natural orbital coupled cluster theory and spin–orbit coupled configuration interaction approaches. *Phys. Chem. Chem. Phys.* **15,** 7260–7276 (19 2013).

269. Maganas, D., DeBeer, S. & Neese, F. Restricted Open-Shell Configuration Interaction Cluster Calculations of the L-Edge X-ray Absorption Study of TiO2 and CaF2 Solids. *Inorg. Chem.* **53,** 6374–6385 (13 2014).

270. Hayashi, S. & Hayamizu, K. Accurate determination of NMR chemical shifts in alkali halides and their correlation with structural factors. *Bull. Chem. Soc. Jpn.* **63,** 913–919 (1990).

271. Dupree, R. & Smith, M. Solid-state Magnesium-25 NMR Spectroscopy. *J. Chem. Soc., Chem. Commun.,* 1483–1485 (1988).

272. Pallister, P., Moudrakovski, I. & Ripmeester, J. Mg-25 ultra-high field solid state NMRspectroscopy and first principles calculations of magnesium compounds. *Phys. Chem. Chem. Phys.* **11,** 11487–11500 (2009).

273. Bastow, T. & Stuart, S. NMR Study of the Zinc Chalcogenides (ZnX, X = O, S, Se, Te). *Phys. Stat. Soli. B* **145,** 719–728 (2 1988).

274. Piacentini, M., Lynch, D. & Olson, C. Thermoreflectance of LiF between 12 and 30 eV. *Phys. Rev. B* **13,** 5530–5543 (12 1976).

275. Roessler, D. & Walker, W. Optical Constants of Magnesium Oxide and Lithium Fluoride in the Far Ultraviolet. *J. Opt. Soc. Am.* **57,** 835–836 (6 1967).

276. Roy, G., Singh, G. & Gallon, T. The electron energy loss spectra of some alkali halides in the band gap region. *Surf. Sci.* **152–153,** 1042–1050 (2 1985).

277. Roessler, D. & Walker, W. Electronic spectrum of crystalline lithium fluoride. *J. Phys. Chem. Solids* **28,** 1507–1515 (8 1967).

278. Pantelides, S. Electronic excitation energies and the soft-x-ray absorption spectra of alkali halides. *Phys. Rev. B* **11,** 2391–2411 (6 1975).

279. DeSalvo, R., Sheik-Bahae, M., Said, A., Hagan, D. & van Stryland, E. Z-scan measurements of the anisotropy of nonlinear refraction and absorption in crystals. *Opt. Lett.* **18,** 194–196 (3 1993).

280. Baldini, G. & Bosacchi, B. Optical Properties of Na and Li Halide Crystals at 55 °K. *Phys. Stat. Sol.* **38,** 325–334 (1 1970).

281. Roessler, D. & Walker, W. Electronic Spectra of Crystalline NaCl and KCl. *Phys. Rev* **166,** 599–606 (3 1968).

282. Miyata, T. & Tomiki, T. Optical Studies of NaCl Single Crystals in 10 eV Region II. The Spectra of Conductivity at Low Temperatures, Absorption Constant and Energy Loss. *J. Phys. Soc. Jpn.* **24,** 1286–1302 (6 1968).

283. Haensel, R. *et al.* Photoemission Measurement on NaCl in the Photon Energy Range 32-50 eV. *Phys. Rev. Lett.* **23,** 530–532 (10 1969).

284. Fröhlich, D. & Staginnus, B. New Assignment of the Band Gap in the Alkali Bromides by Two-Photon Spectroscopy. *Phys. Rev. Lett.* **19,** 496–498 (9 1967).

285. Williams, M. & Arakawa, E. Optical Properties of Single-Crystal Magnesium Oxide. *J. Appl. Phys.* **38,** 5272–5276 (13 1967).

286. Heo, S. *et al.* Band gap and defect states of MgO thin films investigated using reflection electron energy loss spectroscopy. *AIP Adv.* **5,** 077167 (1–8) (7 2015).

287. Roessler, D. & Walker, W. Electronic Spectrum and Ultraviolet Optical Properties of Crystalline MgO. *Phys. Rev.* **159,** 733–738 (3 1967).

288. Cox, P. & Williams, A. Surface excitons on ionic crystals. *Surf. Sci.* **175,** L782–L786 (2 1986).

289. Chayed, N. *et al.* Optical Band Gap Energies of Magnesium Oxide (MgO) Thin Film and Spherical Nanostructures. *AIP Conf. Proc.* **1400,** 328–332 (1 2011).

290. Suemune, I., Uesugi, K., Suzuki, H., Nahiki, H. & Arita, M. Low-Dimensional II–VI Semiconductor Structures: ZnSe/MgS Superlattices and CdSe Self-Organized Dots. *Phys. Stat. Sol. B* **202,** 845–856 (2 1997).

291. Davidson, I., Moug, R., Izdebski, F., Bradford, C. & Prior, K. Determination of the band-gap of MgS and MgS-rich Zn1xMgxSySe1y alloys from optical transmission measurements. *Phys. Stat. Sol. B* **247,** 1396–1398 (6 2010).

292. Okuyama, H., Nakano, K., Miyajima, T. & Akimoto, K. Epitaxial Growth of ZnMgSSe on GaAs Substrate by Molecular Beam Epitaxy. *Jpn. J. Appl. Phys.* **30,** L1620–L1623 (9B 1991).

293. Jobst, B., Hommel, D., Lunz, U., Gerhard, T. & Landwehr, G. E0 band-gap energy and lattice constant of ternary Zn1xMgxSe as functions of composition. *Appl. Phys. Lett.* **69,** 97–99 (1 1996).

294. Puls, J., Rabe, M., Siarkos, A. & Henneberger, F. Excitonic properties of ZnSe/(Zn,Mg)Se quantum wells: A model study of the tensile-strain situation. *Phys. Rev. B* **57,** 14749–14757 (23 1998).

295. Litz, M. *et al.* Epitaxy of Zn1 xMgxSeyTe1 y on (100)InAs. *J. Cryst. Growth* **159,** 54–57 (1–4 1996).

296. Lunz, U. *et al.* The energy gap of epitaxial layers as a function of composition and temperature. *Semicond. Sci. Technol.* **12,** 970–973 (1997).

297. Vögele, B. *et al.* The influence of magnesium on p-type doping and optoelectronic properties of Zn1xMgxSe-based heterostructures. *J. Cryst. Growth* **201–202,** 950–953 (1999).

298. Wörz, M. *et al.* Gap Energies, Exciton Binding Energies and Band Offsets in Ternary ZnMgSe Compounds and ZnSe/ZnMgSe Heterostructures. *Phys. Stat. Sol. B* **202,** 805–816 (2 1997).

299. Okuyama, H., Kishita, Y. & Ishibashi, A. Quaternary alloy Zn1xMgxSySe1y. *Phys. Rev. B* **57,** 2257–2263 (4 1998).

300. Srikant, V. & Clarke, D. On the optical band gap of zinc oxide. *J. Appl. Phys.* **83,** 5447–5451 (10 1998).

301. Theis, D. Wavelength-modulated reflectivity spectra of ZnSe and ZnS from 2.5 to 8 eV. *Phys. Stat. Sol. B* **79,** 125–130 (1 1977).

302. Tran, T., Park, W., Tong, W., Kyi M.M. Wagner, B. & Summers, C. Photoluminescence properties of ZnS epilayers. *J. Appl. Phys.* **81,** 2803 (6 1997).

303. Kim, C. & Sivananthan, S. Optical properties of ZnSe and its modeling. *Phys. Rev. B* **53,** 1475–1484 (3 1996).

304. Pelucchi, E. *et al.* Structural and electronic properties of wide band gap Zn1xMgSe alloys. *J. Appl. Phys.* **95,** 4184–4192 (8 2004).

305. Adachi, S. & Taguchi, T. Optical properties of ZnSe. *Phys. Rev. B* **43,** 9569–9577 (12 1991).

306. Wiley, J., Breitschwerdt, A. & Schönherr, E. Optical absorption band edge in single-crystal GeS. *Solid State Commun.* **17,** 355–359 (3 1975).

307. Eymard, R. & Otto, A. Optical and electron-energy-loss spectroscopy of GeS, GeSe, SnS, and SnSe single crystals. *Phys. Rev. B* **16,** 1616–1623 (4 1977).

308. Elkorashy, A. Optical constants of germanium sulphide single crystal by interference method. *Phys. B: Condens. Matter* **21,** 171–180 (2 1988).

309. Chen, M. *et al.* Anthracene-based semiconductors for organic field-effect transistors. *J. Mater. Chem. C* **6,** 7416–7444 (28 2018).

310. Hummer, K. & Ambrosch-Draxl, C. Electronic properties of oligoacenes from first principles. *Phys. Rev. B* **72,** 205205 (1–10) (20 2005).

311. Deleuze, M., Claes, L., Kryachko, E. & François, J.-P. Benchmark theoretical study of the ionization threshold of benzene and oligoacenes. *J. Chem. Phys.* **119,** 3106–3119 (6 2003).

312. Modelli, A., Mussoni, L. & Fabbri, D. Electron Affinities of Polycyclic Aromatic Hydrocarbons by Means of B3LYP/6-31+G* Calculations. *J. Phys. Chem. A* **110,** 6482–6486 (20 2006).

313. Sun, H. & Autschbach, J. Electronic Energy Gaps for -Conjugated Oligomers and Polymers Calculated with Density Functional Theory. *J. Chem. Theory Comput.* **10,** 1035–1047 (3 2014).

314. Stoychev, G., Auer, A., Izsák, R. & Neese, F. Self-Consistent Field Calculation of Nuclear Magnetic Resonance Nuclear shielding Constants Using Gauge-Including Atomic Orbitals and Approximate Two-Electron Integrals. *J. Chem. Theory Comput.* **14,** 619–637 (2 2018).

315. Dietschreit, J. *et al.* Predicting19F NMR Chemical Shifts: A Combined Computational and Experimental Study of a Trypanosomal Oxidoreductase–Inhibitor Complex. *Angew. Chem. Int. Ed.* **59,** 12669–12673 (31 2020).

316. Bellotti, E. Computational electronics of wide-bandgap semiconductors. *Proc. SPIE, Physics and Simulation of Optoelectronic Devices XI* **4986,** 589–594 (2003).

317. Laskowski, R., Blaha, P. & Tran, F. Assessment of DFT Functionals with NMR Chemical Shifts. *Phys. Rev. B: Condens. Matter* **87,** 195130 (1–8) (19 2013).

318. De Wijs, G. A. *et al.* NMR Shielding constants from Density Functional Perturbation Theory: GIPAW Versus All-Electron Calculations. *J. Chem. Phys.* **146,** 064115 (1–11) (6 2017).

319. Pickard, C. & Mauri, F. All-Electron Magnetic Response with Pseudopotentials: NMR Chemical Shifts. *Phys. Rev. B: Condens. Matter* **63,** 245101 (1–13) (24 2001).

320. Hartman, J., Kudla, R., Day, G., Mueller, L. & Beran, G. Benchmark Fragment-Based 1H, 13C, 15N and 17O Chemical Shift Predictions in Molecular Crystals. *Phys. Chem. Chem. Phys.* **18,** 21686–21709 (2016).

321. Sebastiani, D. & Rothlisberger, U. Nuclear Magnetic Resonance Chemical Shifts from Hybrid DFT QM/MM Calculations. *J. Phys. Chem. B* **108,** 2807–2815 (9 2004).

322. Krykunov, M., Ziegler, T. & van Lenthe, E. Implementation of a Hybrid DFT Method for Calculating NMR Shieldings Using Slater-Type Orbitals with SpinOrbital Coupling Included. Applications to 187Os, 195Pt, and 13C in Heavy-Metal Complexes. *J. Phys. Chem. A* **113,** 11495–11500 (43 2009).

323. Schimka, L. *et al.* Accurate Surface and Adsorption Energies from Many-Body Perturbation Theory. *Nat. Mater.* **9,** 741–744 (2010).

324. Booth, G., Grüneis, A., Kresse, G. & Alavi, A. Towards an Exact Description of Electronic Wavefunctions in Real Solids. *Nature* **493,** 365–370 (2012).

325. Usvyat, D., Sadeghian, K., Maschio, L. & Schütz, M. Geometrical Frustration of an Argon Monolayer Adsorbed on the Mgo (100) Surface: An Accurate Periodic Study. *Phys. Rev. B: Condens. Matter* **86,** 045412 (1–13) (4 2012).

326. McClain, J., Sun, Q., Chan, G.-L. & Berkelbach, T. Gaussian-Based Coupled-Cluster Theory for the Ground-State and Band Structure of Solids. *J. Chem. Theory Comput.* **13,** 1209–1218 (2017).

327. Usvyat, D., Maschio, L. & Schütz, M. Periodic and fragment models based on the local correlation approach. *WIREs Compu. Mol. Sci.* **8,** e1357 (1–27) (4 2018).

328. Ditchfield, R. Self-consistent perturbation theory of diamagnetism. *Mol. Phys.* **27,** 789–807 (1974).

329. Häser, M., Ahlrichs, R., Baron, H., Weis, P. & Horn, H. Direct computation of second-order SCF properties of large molecules on workstation computers with an application to large carbon clusters. *Theor. Chim. Acta* **83,** pages455–470 (1992).

330. Grimme, S. *et al.* Fully Automated Quantum-Chemistry-Based Computation of Spin–Spin-Coupled Nuclear Magnetic Resonance Spectra. *Angew. Chem. Int. Ed.* **56,** 14763–14769 (2017).

331. Wolff, S. & Ziegler, T. Calculation of DFT-GIAO NMR shifts with the inclusion of spin-orbit coupling. *J. Chem. Phys.* **109,** 895–905 (3 1998).

332. Stoychev, G., Auer, A. & Neese, F. Efficient and Accurate Prediction of Nuclear Magnetic Resonance Shielding Tensors with Double-Hybrid Density Functional Theory. *J. Chem. Theory Comput.* **14,** 4756–4771 (2018).

333. Gauss, J. Effects of electron correlation in the calculation of nuclear magnetic resonance chemical shifts. *J. Chem. Phys.* **99,** 3629–3643 (5 1993).

334. Kollwitz, M. & Gauss, J. A direct implementation of the GIAO-MBPT(2) method for calculating NMR chemical shifts. Application to the naphthalenium and anthracenium ions. *Chem. Phys. Lett.* **260,** 639–646 (5–6 1996).

335. Kollwitz, M., Häser, M. & Gauss, J. Non-Abelian point group symmetry in direct second-order many-body perturbation theory calculations of NMR chemical shifts. *J. Chem. Phys.* **108,** 8295–8301 (20 1998).

336. Gauss, J. GIAO-MBPT(3) and GIAO-SDQ-MBPT(4) Calculations of Nuclear Magnetic Shielding Constants. *Chem. Phys. Lett.* **229,** 198–203 (3 1994).

337. Gauss, J. & Stanton, J. Coupled-Cluster Calculations of Nuclear Magnetic Resonance Chemical Shifts. *J. Chem. Phys.* **103,** 3561–3577 (9 1995).

338. Gauss, J. & Stanton, J. Gauge Invariant Calculation of Nuclear Magnetic Shielding Constants at the Coupled-Cluster Singles and Doubles Level. *J. Chem. Phys.* **102,** 251–253 (1 1995).

339. Gauss, J. & Stanton, J. Perturbative Treatment of Triple Excitations in Coupled Cluster Calculations of Nuclear Magnetic Shielding Constants. *J. Chem. Phys.* **104,** 2574–2583 (7 1996).

340. Flaig, D. *et al.* Benchmarking Hydrogen and Carbon NMR Chemical Shifts at HF, DFT, and MP2 Levels. *Chem. Theory Comput.* **10,** 572–578 (2014).

341. Helgaker, T. *et al.* Recent Advances in Wave Function-Based Methods of Molecular-Property Calculations. *Chem. Rev.* **112,** 543–631 (2012).

342. Gauss, J. & Werner, H. NMR Chemical Shift Calculations within Local Correlation Methods: The GIAO-LMP2 Approach. *Phys. Chem. Chem. Phys.* **2,** 2083–2090 (2000).

343. Loibl, S. & Schütz, M. NMR Shielding Tensors for Density Fitted Local Second-Order Møller-Plesset Perturbation Theory Using Gauge Including Atomic Orbitals. *J. Chem. Phys.* **137,** 084107 (2012).

344. Ochsenfeld, C., Kussmann, J. & Koziol, F. Ab Initio NMR Spectra for Molecular Systems with a Thousand and More Atoms: A Linear-Scaling Method. *Angew. Chem. Int. Ed.* **43,** 4485–4489 (2004).

345. Kussmann, J. & Ochsenfeld, C. Linear-Scaling Method for Calculating Nuclear Magnetic Resonance Chemical Shifts Using Gauge-Including Atomic Orbitals within Hartree-Fock and Density-Functional Theory. *J. Chem. Phys.* **127,** 054103 (1–16) (5 2007).

346. Beer, M., Kussmann, J. & Ochsenfeld, C. Nuclei-Selected Nmr Shielding Calculations: A Sublinear-Scaling Quantum-Chemical Method. *J. Chem. Phys.* **134,** 074102 (1–15) (7 2011).

347. Keal, T. & Tozer, D. The Exchange-Correlation Potential in Kohn–Sham Nuclear Magnetic Resonance Shielding Calculations. *J. Chem. Phys.* **119,** 3015–3024 (2003).

348. Reimann, S. *et al.* The importance of current contributions to shielding constants in density-functional theory. *Phys. Chem. Chem. Phys.* **17,** 18834–18842 (28 2015).

349. Hunger, M. In situ NMR spectroscopy in heterogeneous catalysis. *Catal. Today* **97,** 3–12 (1 2004).

350. Laws, D., Bitter, H.-M. & Jerschow, A. Solid-State NMR Spectroscopic Methods in Chemistry. *Angew. Chem. Int. Ed.* **41,** 3096–3129 (17 2002).

351. Neese, F. The Orca Program System. *WIREs: Comput. Mol. Sci.* **2,** 73–78 (2012).

352. Eichkorn, K., Treutler, O., Öhm, H., Häser, M. & Ahlrichs, R. Auxiliary Basis Sets to Approximate Coulomb Potentials. *Chem. Phys. Lett.* **240,** 283–290 (1995).

353. Neese, F., Wennmohs, F., Hansen, A. & Becker, U. Efficient, Approximate and Parallel Hartree–Fock and Hybrid DFT Calculations. A 'Chain-of-Spheres' Algorithm for the Hartree–Fock Exchange. *Chem. Phys.* **356,** 98–109 (2009).

354. Izsák, R. & Neese, F. An Overlap Fitted Chain of Spheres Exchange Method. *J. Chem. Phys.* **135,** 144105 (1–11) (14 2011).

355. Weigend, F. Hartree-Fock Exchange Fitting Basis Sets for H to Rn. *J. Comput. Chem.* **2,** 167–175 (2006).

356. Weigend, F., Häser, M., Patzelt, H. & Ahlrichs, R. RI-MP2: optmized auxilary basis sets and demonstration of efficiency. *Chem. Phys. Let.* **294,** 143–152 (1998).

357. Hättig, C. Optimization of auxiliary basis sets for RI-MP2 and RI-CC2 calculations: Core–valence and quintuple-f basis sets for H to Ar and QZVPP basis sets for Li to Kr. *Phys. Chem. Chem. Phys.* **7,** 59–66 (2005).

358. Furness, J. *et al.* Current Density Functional Theory Using Meta-Generalized Gradient Exchange-Correlation Functionals. *J. Chem. Theory Comput.* **11,** 4169–4181 (2015).

359. Tellgren, E. *et al.* Non-perturbative calculation of molecular magnetic properties within current-density functional theory. *J. Chem. Phys.* **140,** 034101 (1–11) (3 2014).

360. Lee, A., Handy, N. & Colwell, S. The density functional calculation of nuclear shielding constants using London atomic orbitals. *J. Chem. Phys.* **103,** 10095–10109 (1995).

361. Malkin, V., Malkina, O., Casida, M. & Salahub, D. Nuclear Magnetic Resonance Shielding Tensors Calculated with a Sum-over-States Density Functional Perturbation Theory. *J. Am. Chem. Soc.* **116,** 5898–5908 (1994).

362. Reimann, S. *et al.* The importance of current contributions to shielding constants in density-functional theory. *Phys. Chem. Chem. Phys.* **17,** 18834–18842 (2015).

363. Perdew, J. Density-Functional Approximation for the Correlation-Energy of the Inhomogeneous Electron-Gas. *Phys. Rev. B* **33,** 8822–8824 (1986).

364. Perdew, J., Ernzerhof, M. & Burke, K. Rationale for Mixing Exact Exchange with Density Functional Approximations. *J. Chem. Phys.* **105,** 9982–9985 (1996).

365. Stanton, J., Gauss, J., Harding, M., Szalay, P. & et al. CFOUR, a quantum chemical program package. `For%20the%20current%20version,%20see%20www.cfour.de` (accessed Nov. 2019).

366. Barysz, M., Sadlej, A. & Snijders, J. Nonsingular two/one-component relativistic Hamiltonians accurate through arbitrary high order in 2. *Int. J. Quantum Chem.* **65,** 225–239 (1997).

367. Barysz, M. & Sadlej, A. Two-component methods of relativistic quantum chemistry: from the Douglas±Kroll approximation to the exact two-component formalism. *J. Mol. Struct. (Theochem.)* **573,** 181–200 (2001).

368. Barysz, M. & Sadlej, A. Infinite-order two-component theory for relativistic quantum chemistry. *J. Chem. Phys.* **116,** 2696–2704 (2002).

369. Iliaš, M., Jensen, H., Kello, V., Roos, B. & Urban, M. Theoretical study of PbO and the PbO anion. *Chem. Phys. Lett* **408,** 210–215 (4–6 2005).

370. Dyall, K. Relativistic double-zeta, triple-zeta, and quadruple-zeta basis sets for the 4s, 5s, 6s, and 7s elements. *J. Phys. Chem. A* **113,** 12638–12644 (45 2009).

371. Dyall, K. Core correlating basis functions for elements 31–118. *Theor. Chem. Acc.* **131,** 1217 (1–11) (2012).

372. Dyall, K. An exact separation of the spin-free and spin-dependent terms of the Dirac–Coulomb–Breit Hamiltonian. *J. Chem. Phys.* **100,** 2118–2127 (1994).

373. Maldonado, A. & Aucar, G. Relativistic and Electron-Correlation Effects on the Nuclear Magnetic Resonance Shieldings of Molecules Containing Tin and Lead Atoms. *J. Phys. Chem. A* **118,** 7863–7875 (2014).

374. Dračínský, M., Unzueta, P. & Beran, G. Improving the accuracy of solid-state nuclear magnetic resonance chemical shift prediction with a simple molecular correction. *Phys. Chem. Chem. Phys.* **21,** 14992–15000 (2019).

375. Flaig, D. *et al.* Benchmarking Hydrogen and Carbon NMR Chemical Shifts at HF, DFT, and MP2 Levels. *J. Chem. Theory Comput.* **10,** 572–578 (2 2014).

376. Olejniczak, M., Bast, R., Saue, T. & Pecul, M. A simple scheme for magnetic balance in four-component relativistic Kohn–Sham calculations of nuclear magnetic resonance shielding constants in a Gaussian basis. *J. Chem. Phys.* **136,** 014108 (1–13) (1 2012).

377. Kaupp, M., Malkin, O. & Malkin, V. Interpretation of 13C NMR chemical shifts in halomethyl cations. On the importance of spin-orbit coupling and electron correlation. *Chem. Phys. Lett.* **265,** 55–59 (1–2 1997).

378. Kaupp, M., Malkin, O., Malkin, V. & Pyykkö, P. How Do Spin–Orbit-Induced Heavy-Atom Effects on NMR Chemical Shifts Function? Validation of a Simple Analogy to Spin–Spin Coupling by Density Functional Theory (DFT) Calculations on Some Iodo Compounds. *Chem. Eur. J.* **4,** 118–126 (1998).

379. Kaupp, M. *Calculation of NMR and EPR Parameters* (Wiley-VCH Verlag GmbH Co. KGaA, Weinheim, 2004).

380. Autschbach, J. *High Resolution NMR Spectroscopy: Understanding Molecules and their Electronic Structures* (Elsevier, Oxford, 2013).

381. Vícha, J., Novotny, J., Komorovsky, S., Straka, M. & Kaupp, M. Relativistic Heavy-Neighbor-Atom Effects on NMR Shifts: Concepts. *Chem. Rev.* **120,** 7065–7103 (2020).

382. Iliaš, M. & Saue., T. An infinite-order two-component relativistic Hamiltonian by a simple one-step transformation. *J.Chem. Phys.* **126,** 064102 (2007).

383. Knecht, S. & Saue, T. X2Cmod: A modular code for Exact-Two-Component Hamiltonian Transformations with contributions from M. Ilias, H. J. Aa. Jensen and M. Repisky (2010–2013).

384. Visscher, L. Approximate molecular relativistic Dirac-Coulomb calculations using a simple Coulombic correction. *Theor. Chem. Acc.* **98,** 68–70 (1997).

385. Aucar, I., Gómez, S. S., Melo, J. I., Giribert, C. C. & Ruiz de Azúa, M. Theoretical study of the nuclear spin-molecular rotation coupling for relativistic electrons and non-relativistic nuclei. II. Quantitative results in HX (X=H,F,Cl,Br,I) compounds. *J. Chem. Phys.* **138,** 134107 (2013).

386. Lévy-Leblond, J.-M. Nonrelativistic particles and wave equations. *Commun. Math. Phys.* **6,** 286–311 (1967).

387. Gromov, O., Kuzin, S. & Golubeva, E. Performance of DFT methods in the calculation of isotropic and dipolar contributions to 14N hyperfine coupling constants of nitroxide radicals. *J. Mol. Model.* **25,** 93 (1–10) (2019).

388. Medvedev, M., Bushmarinov, I., Sun, J., Perdew, J. & Lyssenk, K. Density functional theory is straying from the path toward the exact functional. *Science* **355,** 49–52 (2017).

389. Witwicki, M. Density functional theory and ab initio studies on hyperfinecoupling constants of phosphinyl radicals. *Int. J. Quantum Chem.* **118,** e25779 (2018).

390. Jin, Y. & Bartlett, R. The QTP family of consistent functionals and potentials in Kohn-Sham density functional theory. *J.Chem. Phys.* **145,** 034107 (1–10) (3 2016).

391. Ganyushin, D. & Neese, F. First-principles calculations of zero-field splitting parameters. *J. Chem. Phys.* **125,** 024103 (1–11) (2 2006).

392. Neese, F. Efficient and accurate approximations to the molecular spin-orbit coupling operator and their use in molecular g-tensor calculations. *J. Chem. Phys.* **122,** 034107 (1–13) (3 2005).

393. Neese, F. A spectroscopy oriented configuration interaction procedure. *J. Chem. Phys.* **119,** 9428–9443 (18 2003).

394. Dunning, T. Gaussian basis sets for use in correlated molecular calculations. I. The atoms boron through neon and hydrogen. *J. Chem. Phys.* **90,** 1007–1023 (2 1989).

395. Eichkorn, K., Treutler, O., Öhm, H., Häser, M. & Ahlrichs, R. Auxiliary basis sets to approximate Coulomb potentials. *Chem. Phys. Lett.* **240,** 283–290 (4 1995).

396. Neese, F., Wennmohs, F., Hansen, A. & Becker, U. Efficient, approximate and parallel Hartree–Fock and hybrid DFT calculations. A 'chain-of-spheres' algorithm for the Hartree–Fock exchange. *Chem. Phys.* **356,** 98–109 (1–3 2009).

397. Accessed: 11-07-2023. `https://cerncourier.com/a/viewpoint-theory-in-the-computer-age`.

398. Zakzeski, J., Bruijnincx, P. C. A., Jongerius, A. L. & Weckhuysen, B. M. The Catalytic Valorization of Lignin for the Production of Renewable Chemicals. *Chem. Rev.* **110,** 3552–3599 (6 2010).

399. Zakzeski, J., Bruijnincx, P. C. A. & Weckhuysen, B. M. In situ spectroscopic investigation of the cobalt-catalyzed oxidation of lignin model compounds in ionic liquids. *Green Chem.* **13,** 671–680 (3 2011).

400. Makwana, V. D., Son, Y.-C., Howell, A. R. & Suib, S. L. The Role of Lattice Oxygen in Selective Benzyl Alcohol Oxidation Using OMS-2 Catalyst: A Kinetic and Isotope-Labeling Study. *J. Catal.* **210,** 46–52 (1 2002).

401. Schlögl, R. Selective Oxidation: From a Still Immature Technology to the Roots of Catalysis Science. *Top. Catal.* **59,** 1461–1476 (17 2016).

402. Grasselli, R. K. Fundamental Principles of Selective Heterogeneous Oxidation Catalysis. *Top. Catal.* **21,** 79–88 (1 2002).

403. Anke, S. *et al.* Selective 2-Propanol Oxidation over Unsupported Co3O4 Spinel Nanoparticles: Mechanistic Insights into Aerobic Oxidation of Alcohols. *ACS Catal.* **9,** 5974–5985 (7 2019).

404. Tian, Z. Y. *et al.* Low-temperature deep oxidation of olefins and DME over cobalt ferrite. *Proc. Combust. Inst.* **35,** 2207 (2015).

405. Urdă, A., Herraïz, A., Rédey, Á. & Marcu, I. C. Co and Ni ferrospinels as catalysts for propane total oxidation. *Catal. Commun.* **10,** 1651 (2009).

406. Mountapmbeme Kouotou, P. *et al.* Structure–activity relation of spinel-type Co–Fe oxides for low-temperature CO oxidation. *Catal. Sci. Technol.* **4,** 3359 (2014).

407. Xie, X., Li, Y., Liu, Z. Q., Haruta, M. & Shen, W. Low-temperature oxidation of CO catalysed by Co3O4 nanorods. *Nature* **458,** 746 (2009).

408. Thomas, J. *et al.* Synthesis of cobalt ferrite nanoparticles by constant pH co-precipitation and their high catalytic activity in CO oxidation. *New J. Chem.* **41,** 7356 (2017).

409. Evans, G. *et al.* Particle size–activity relationship for CoFe2O4 nanoparticle CO oxidation catalysts. *J. Mater. Chem.* **18,** 5518 (2008).

410. Chagas, C. A., Souza, E. F. d., Carvalho, M. C. N. A. d., Martins, R. L. & Schmal, M. Cobalt ferrite nanoparticles for the preferential oxidation of CO. *Appl. Catal. A* **519,** 139 (2016).

411. Lukashuk, L. *et al.* Operando XAS and NAP-XPS studies of preferential CO oxidation on Co3O4 and CeO2-Co3O4 catalysts. *J. Catal.* **1,** 344 (2016).

412. Bahlawane, N. *et al.* Tailoring the properties and the reactivity of the spinel cobalt oxide. *Phys. Chem. Chem. Phys.* **11,** 9224 (2009).

413. Tian, Z. Y., Tchoua Ngamou, P. H., Vannier, V., Kohse-Höinghaus, K. & Bahlawane, N. Catalytic oxidation of VOCs over mixed Co–Mn oxides. *Appl. Catal. B* **125,** 117–118 (2012).

414. Ortega, K. F. *et al.* Topotactic Synthesis of Porous Cobalt Ferrite Platelets from a Layered Double Hydroxide Precursor and Their Application in Oxidation Catalysis. *Chem.-Eur. J.* **23,** 12443 (2017).

415. Zafeiratos, S. *et al.* Methanol oxidation over model cobalt catalysts. *J. Catal.* **269,** 309 (2010).

416. Anke, S. *et al.* Selective 2-Propanol Oxidation over Unsupported Co3O4 Spinel Nanoparticles: Mechanistic Insights into Aerobic Oxidation of Alcohols (2021).

417. Mate, V. R., Shirai, M. & Rode, C. V. Heterogeneous Co3O4 catalyst for selective oxidation of aqueous veratryl alcohol using molecular oxygen. *Catal. Commun.* **33,** 66–69 (2013).

418. Wu, Y., Ruirui, S. & Cen, J. Facile Synthesis of Cobalt Oxide as an Efficient Electrocatalyst for Hydrogen Evolution Reaction. *Front. Chem.* **8,** 386 (2020).

419. Kärkäs, M. D., Verho, O., Johnston, E. V. & Åkermark, B. Artificial Photosynthesis: Molecular Systems for Catalytic Water Oxidation. *Chem. Rev.* **114,** 11863–12001 (2014).

420. Ma, J. *et al.* Application of Co3O4-based materials in electrocatalytic hydrogen evolution reaction: A review. *Int. J. Hydrog. Energy* **45,** 21205–21220 (41 2020).

421. Budiyanto, E. *et al.* Impact of Single-Pulse, Low-Intensity Laser Post-Processing on Structure and Activity of Mesostructured Cobalt Oxide for the Oxygen Evolution Reaction. *ACS Appl. Mater. Interfaces* **13,** 51962–51973 (44 2021).

422. Gawali, S. R. *et al.* Role of cobalt cations in short range antiferromagnetic Co3O4 nanoparticles: a thermal treatment approach to affecting phonon and magnetic properties. *Sci. Rep.* **8,** 249 (1 2018).

423. Shepit, M., Paidi, V. K., Roberts, C. A. & van Lierop, J. Competing ferro- and antiferromagnetic exchange drives shape-selective Co3O4 nanomagnetism. *Sci. Rep.* **10,** 20990 (1 2020).

424. Böhl *et al.* Colored Pigments. *Industrial Inorganic Pigments,* 99–162 (2005).

425. Perry, N. H. *et al.* Co3O4–Co2ZnO4 spinels: The case for a solid solution. *J. Solid State Chem.* **90,** 143–149 (2012).

426. Rong, F. *et al.* Zinc-cobalt oxides as efficient water oxidation catalysts: the promotion effect of ZnO. *J. Mater. Chem. A* **3,** 4010–4017 (7 2015).

427. Huang, X. C. *et al.* Electronic structure and p-type conduction mechanism of spinel cobaltite oxide thin films. *Phys. Rev. B* **100** (11 2019).

428. Wang, X. Y. *et al.* Geometrical-Site-Dependent Catalytic Activity of Ordered Mesoporous Co-Based Spinel for Benzene Oxidation: In Situ DRIFTS Study Coupled with Raman and XAFS Spectroscopy. *ACS Catal.* **7,** 1626–1636 (3 2017).

429. Yan, G. & Sautet, P. Surface Structure of Co3O4 (111) under Reactive Gas-Phase Environments. *ACS Catal.* **9,** 6380–6392 (7 2019).

430. Budiyanto, E. *et al.* Tailoring Morphology and Electronic Structure of Cobalt Iron Oxide Nanowires for Electrochemical Oxygen Evolution Reaction. *ACS Appl. Energy Mater.* **3,** 8583–8594 (9 2020).

431. Yu, M. Q. *et al.* Dual Role of Silver Moieties Coupled with Ordered Mesoporous Cobalt Oxide towards Electrocatalytic Oxygen Evolution Reaction. *Angew. Chem. Int. Ed.* **59,** 16544–16552 (38 2020).

432. Anke, S. *et al.* On the reversible deactivation of cobalt ferrite spinel nanoparticles applied in selective 2-propanol oxidation. *J. Catal.* **382,** 57–68 (2020).

433. Chai, G. T. *et al.* Spinel Co3O4 oxides-support synergistic effect on catalytic oxidation of toluene. *Appl. Catal. A-General,* 614 (2021).

434. Kanazawa, T. *et al.* Cobalt Aluminate Spinel as a Cocatalyst for Photocatalytic Oxidation of Water: Significant Hole-Trapping Effect. *ACS Catal.* **10,** 4960–4966. (9 2020).

435. Ma, L. *et al.* High Spin State Promotes Water Oxidation Catalysis at Neutral pH in Spinel Cobalt Oxide. *Ind. Eng. Chem. Res.* **57,** 1441–1445 (5 2018).

436. Petitto, S. C., Marsh, E. M., Carson, G. A. & Langell, M. A. Cobalt oxide surface chemistry: The interaction of CoO(100), Co3O4(110) and Co3O4(111) with oxygen and water. *J. Mol. Catal. A Chem.* **281,** 49–58 (1–2 2008).

437. Reddy, K. P., Jain, R., Ghosalya, M. K. & Gopinath, C. S. Metallic Cobalt to Spinel Co3O4-Electronic Structure Evolution by Near-Ambient Pressure Photoelectron Spectroscopy. *J. Phys. Chem. C* **121,** 21472–21481 (39 2017).

438. Yuan, C., Liu, S. Y., Wang, Z. Q. & Wang, G. Y. Catalytic oxidation of low concentrations of vinyl chloride over spinel-type Co3O4 catalysts. *React. Kinet. Mech. Catal.* **125,** 757–771 (2 2018).

439. Ghosh, S. *et al.* Role of dilution on the electronic structure and magnetic ordering of spinel cobaltites. *Phys. Rev. B* **98** (23 2018).

440. Rushiti, A., Hattig, C., Wen, B. & Selloni, A. Structure and Reactivity of Pristine and Reduced Spinel CoFe2O4 (001)/(100) Surfaces. *J. Phys. Chem. C* **125,** 9774–9781 (18 2021).

441. Kox, T., Spohr, E. & Kenmoe, S. Impact of Solvation on the Structure and Reactivity of the Co3O4 (001)/H2O Interface: Insights From Molecular Dynamics Simulations. Frontiers In Energy Research. **8** (2020).

442. Chen, L. *et al.* Intrinsic ferromagnetic coupling in Co3O4 quantum dots activatedby graphene hybridization. *Appl. Phys. Lett.* **108,** 252402 (25 2016).

443. Xing, L. & Prewitt, C. High-Temperature X-Ray-Diffraction Study of Co3o4 - Transition from Normal to Disordered Spinel. *Phys. Chem. Miner.* **17,** 168–172 (2 1990).

444. Roth, W. The magnetic structure of Co3O4. *J. Phys. Chem. Solids* **25,** 1–10 (1 1964).

445. Harris, D. & Bertolucci, M. *Symmetry and Spectroscopy - An Introduction to Vibrational and Electronic Spectroscopy* 5–6 (Dover Publications, Inc., New York, USA, 1989).

446. Summerville, R. H. & Hoffmann, R. Tetrahedral and other M2L6 transition metal dimers. *J. Am. Chem. Soc.* **98,** 7240–7254 (23 1976).

447. Calzado, C., Angeli, C., Taratiel, D., Caballol, R. & Malrieu, J.-P. Analysis of the magnetic coupling in binuclear systems. III. The role of the ligand to metal charge transfer excitations revisited. *J. Chem. Phys.* **131,** 044327 (2009).

448. De Loth, P., Cassoux, P., Daudey, J. & Malrieu, J. Ab initio direct calculation of the singlet-triplet separation in cupric acetate hydrate dimer. *J. Am. Chem. Soc.* **103,** 4007–4016 (14 1981).

449. Hay, P., Thibeault, J. & Hoffmann, R. Orbital Interactions in Metal Dimer Complexes. *J. Am. Chem. Soc.* **97,** 4884–4899 (1975).

450. Britz, A. *et al.* Site-Selective Real-Time Observation of Bimolecuar Electron Transfer in a Photocatalytic System Using L-Edge X-Ray Absorption Spectroscopy. *Chem. Phys. Chem.* **22,** 693–700 (7 2021).

451. Kupfer, B. *et al.* Thin Film Co3O4/TiO2 Heterojunction Solar Cells. **5,** 1401007 (1 2014).

452. Majhi, K. *et al.* Combinatorial Investigation and Modelling of MoO3 Hole-Selective Contact in TiO2|Co3O4|MoO3 All-Oxide Solar Cells. *Adv. Mater. Interfaces* **3,** 1500405 (1 2015).

453. Zhang, Y. *et al.* Synthesis and Characterization of Spinel Cobaltite (Co3O4) Thin Films for Function as Hole Transport Materials in Organometallic Halide Perovskite Solar Cells. *ACS Appl. Energy Mater.* **3,** 3755–3769 (2020).

454. Ge, B. *et al.* Self-Organized Co3O4-SrCO3 Percolative Composites Enabling Nanosized Hole Transport Pathways for Perovskite Solar Cells. *Adv. Funct. Mater.* **31,** 2106121 (46 2021).

455. Majhi, K. *et al.* Co3O4 Based All-Oxide PV: A Numerical Simulation Analyzed Combinatorial Material Science Study. *J. Phys. Chem. C* **120,** 9053–9060 (17 2016).

456. Qiao, L. *et al.* Nature of the band gap and origin of the electro-/photo-activity of Co3O4. *J. Mater. Chem. C* **1,** 4628–3633 (2013).

457. Murad, W. A., Al-Shamari, S. M., Al-Khateeb, F. H. & Misho, R. H. Band Gap Measurements of Co304 Thin Films Prepared by the Method of Chemical Spray Pyrolysis. *Phys. Stat. Sol. (a)* **106,** 143–146 (1988).

458. Schumacher, L., Holzhueter, I. B., Hill, I. R. & Dignam, M. J. Semiconducting and Electrocatalytic Properties of Sputtered Cobalt Oxide Films. *Electrochim. Acta* **35,** 975–984 (6 1990).

459. Varkey, A. J. & Fort, A. F. A chemical method for preparation of cobalt oxide thin films. *Sol. Energy Mater. Sol. Cells* **31,** 277–282 (1993).

460. Patil, P. S., Kadam, L. D. & Lokhande, C. D. Preparation and characterization of spray pyrolysed cobalt oxide thin films. *Thin Solid Films* **272,** 29–32 (1996).

461. Kadam, L. D. & Patil, P. S. Thickness-dependent properties of sprayed cobalt oxide thin films. *Mater. Chem. Phys.* **68,** 225–232 (2001).

462. Pejova, B., Isahi, A., Najdoski, M. & Grozdanov, I. Fabrication and characterization of nanocrystalline cobaltoxide thin films. *Mater. Res. Bull.* **36,** 161–170 (2001).

463. Mane, A. U. & Shivashankar, S. A. MOCVD of cobalt oxide thin films: dependence of growth, microstructure, and optical properties on the source of oxidation. *J. Cryst. Growth* **254,** 368–377 (3-4 2003).

464. Gulino, A., Fiorito, G. & Fragalà, I. Deposition of thin films of cobalt oxides by MOCVD. *J. Mater. Chem.* **13,** 861–865 (2003).

465. Shinde, V. R., Mahadik, S. B., Gujar, T. P. & Lokhande, C. D. Supercapacitive cobalt oxide (Co3O4) thin films by spray pyrolysis. *Appl. Surf. Sci.* **252,** 7487–7492 (20 2006).

466. Ngamou, P. H. T. & Bahlawane, N. Influence of the Arrangement of the Octahedrally Coordinated Trivalent Cobalt Cations on the Electrical Charge Transport and Surface Reactivity. *Chem. Mater.* **22,** 4158–4165 (2010).

467. Cheng, C.-S., Serizawa, M., Sakata, H. & Hirayma, T. Electrical conductivity of Co3O4 films prepared by chemical vapour deposition. *Mater. Chem. Phys.* **53,** 225–230 (1998).

468. Louradi, A. *et al.* Characterization of cobalt oxide thin films prepared by a facile spray pyrolysis technique using perfume atomizer. *J. Alloys Compd.* **509,** 9183–9189 (37 2011).

469. Lakehal, A. *et al.* Structural, optical and electrical properties of Ni-doped Co3O4 prepared via Sol-Gel technique. *Mater. Res.* **21,** e20170545 (3 2018).

470. Zhang, Y. *et al.* Synthesis and Characterization of Spinel Cobaltite (Co3O4) Thin Films for Function as Hole Transport Materials in Organometallic Halide Perovskite Solar Cells. *ACS Appl. Energy Mater.* **3,** 3755–3769 (2020).

471. Barreca, D. *et al.* Composition and Microstructure of Cobalt Oxide Thin Films Obtained from a Novel Cobalt(II) Precursor by Chemical Vapor Deposition. *Chem. Mater.* **13,** 588–593 (2 2001).

472. Yamamoto, H., Tanaka, S. & Hirao, K. Effects of substrate temperature on nanostructure and band structure of sputtered Co3O4 thin films. *J. Appl. Phys.* **93,** 4158–4162 (7 2003).

473. Bahlawane, N., Fischer Rivera, E., Kohse-Höinghaus, K., Brechling, A. & Kleineberg, U. Characterization and tests of planar Co3O4 model catalystsprepared by chemical vapor deposition. *Appl. Catal. B* **53,** 245–255 (2004).

474. Thota, S., Kumar, A. & Kumar, J. Optical, electrical and magnetic properties of Co3O4 nanocrystallites obtained bythermal decomposition of sol–gel derived oxalates. *Mater. Sci. Eng. B* **164,** 30–37 (2009).

475. Qiao, L. *et al.* Nature of the band gap and origin of the electro-/photo-activity of Co3O4. *J. Mater. Chem. C* **1,** 4628–3633 (2013).

476. Waegle, M. M., Doan, H. Q. & Cuk, T. Long-Lived Photoexcited Carrier Dynamics of d–d Excitations in Spinel Ordered Co3O4. *J. Phys. Chem. C* **118,** 3426–2432 (2014).

477. Jiang, C.-M., Baker, L. R., Lucas, J. M., Vura-Weis, J. & Alivisatos, A. P. Characterization of Photo-Induced Charge Transfer and Hot Carrier Relaxation Pathways in Spinel Cobalt Oxide (Co3O4). *J. Phys. Chem. C* **118,** 22774–22784 (2014).

478. Cook, J. G. & van der Meer, M. P. The optical properties of sputtered Co3O4 films. *Thin Solid Films* **144,** 165–176 (2 1986).

479. Lenglet, M. & Jørgensen, C. K. Reinvestigation of the optical properties of Co3O4. *Chem. Phys. Lett.* **229,** 616–620 (1994).

480. Nkeng, P. *et al.* Characterization of Spinel-Type Cobalt and Nickel Oxide Thin Films by X-Ray Near Grazing Diffraction, Transmission and Reflectance Spectroscopies, and Cyclic Voltammetry. *J. Electrochem. Soc.* **142,** 1777–1783 (6 1995).

481. Ruzakowski Athey, P., Urban III, F. K., Tabet, M. F. & McGahan, W. A. Optical properties of cobalt oxide films deposited by spray pyrolysis. *J. Vac. Sci. Technol. A* **14,** 685–692 (3 1996).

482. Cherkashin, A. & Vilesov, F. Diffuse Reflection Spectra of some Nickel and Cobalt Oxides. *Sov. Phys. Solid State* **11,** 1068 (1969).

483. Belova, I. D. *et al.* Co(III) Ions High-Spin Configuration in Nonstoichiometric Co3O4 Films. *Solid State Commun.* **47,** 577–584 (8 1983).

484. Martens, J. W. D., Peeters, W. L. & van Noort, H. M. Optical, Magneto-Optical and Mössbauer Spectroscopy on Co3+ Substituted Cobalt Ferrite Co2+Fe2-xCo3-xO4 (O<x<2). *J. Phys. Chem. Solids* **46,** 411–416 (1985).

485. Chen, J., Wu, X. & Selloni, A. Electronic structure and bonding properties of cobalt oxide in the spinel structure. *Phys. Rev. B* **83,** 245204 (2011).

486. Xu, X.-L., Chen, Z.-H., Li, Y., Chen, W.-K. & Li, J.-Q. Bulk and surface properties of spinel Co3O4 by density functional calculations. *Surf. Sci.* **603,** 653–658 (4 2009).

487. Lima, A. Interpretation of the optical absorption spectrum of Co3O4 with normal spinel structure from first principles calculations. *J. Phys. Chem. Solids* **75,** 148–152 (1 2014).

488. Walsh, A. *et al.* Structural, magnetic, and electronic properties of the Co-Fe-Al oxide spinel system: Density-functional theory calculations. *Phys. Rev. B* **76,** 165119 (2007).

489. Zaki, N. *et al.* Theoretical study of structural, electronic and magnetic properties of the T spinel Co3O4 under the pressure from 0 to 30 GPa. *Int. J. Eng. Technol.* **7,** 121–125 (2018).

490. Sousa, O., Lima, J., Lima, A. & Lalic, M. V. Theoretical study of structural, electronic and magnetic properties of the T spinel Co3O4 under the pressure from 0 to 30 GPa. *J. Magn. Magn. Mater* **484,** 21–30 (2019).

491. Wang, L., Maxisch, T. & Ceder, G. Oxidation energies of transition metal oxides within the GGA+U framework. *Phys. Rev. B* **73** (2006).

492. Montoya, A. & Haynes, B. Periodic density functional study of Co3O4 surfaces. *Chem. Phys. Lett.,* 63–68 (2011).

493. Zhandun, V. & Nemtsev, A. Ab initio study of the magnetic, optical and electronic properties of spinel Co3O4 within DFT and GW approaches. *J. Magn. Magn. Mater.* **499,** 166306 (2020).

494. Cadi-Essadeka, A. *et al.* DFT+U Study of the Electronic, Magnetic and Mechanical Properties of Co, CoO, and Co3O4. *S. Afr. J. Chem.* **74** (2021).

495. Kaptagay, G., Inerbaeva, T., Mastrikovb, Y., Kotominb, E. & Akilbekova, A. Water interaction with perfect and fluorine-doped Co3O4 (100) surface. *Solid State Ion.* **277,** 77–82 (2015).

496. Lima, A. Density functional theory study on the magnetic properties of Co3O4 with normal spinel structure. *J. Phys. Chem. Solids* **91,** 86–89 (2016).

497. Morosan, E., Natelson, D., Nevidomskyy, A. H. & Si, Q. Strongly Correlated Materials. *Adv. Mater.* **24,** 4896–4923 (2012).

498. Izyumov, Y. A. & Kurmaev, E. Z. Materials with strong electron correlations. *Phys.-Usp.* **51,** 23–56 (2008).

499. Kim, K. J. & Park, Y. R. Optical investigation of charge-transfer transitions in spinel Co3O4. *Solid State Commun.* **127,** 25–28 (2003).

500. Tanaka, T. Optical Constants of Polycrystalline 3d Transition Metal Oxides in the Wavelength Region 350 to 1200 nm. *Jpn. J. Appl. Phys.* **18,** 1043–1047 (6 1979).

501. Miedzinska, K., Hollebone, B. & Cook, J. An assigment of the optical absorption spectrum of mixed valence Co3O4 spinel films. *J. Phys. Chem. Solids* **48,** 649–656 (7 1987).

502. Quintanilla, J. & Hooley, C. The strong-correlations puzzle. *Phys. World* **22,** 32–37 (6 2009).

503. Neese, F., Wennmohs, F., Becker, U. & Riplinger, C. The ORCA quantum chemistry program package. *J. Chem. Phys.* **152,** 224108 (1–18) (22 2020).

504. Brandenburg, J., Bannwarth, C., Hansen, A. & Grimme, S. B97-3c: A revised low-cost variant of the B97-D density functional method. *J. Chem. Phys.* **148,** 064104 (1–13) (6 2018).

505. Grimme, S., Hansen, A., Ehlert, S. & Mewes, J.-M. r2SCAN-3c: A "Swiss army knife" composite electronic-structure method. *J. Chem. Phys.* **154,** 064103 (1–18) (6 2021).

506. Casanova-Páez, M. & Goerigk, L. Time-Dependent Long-Range-Corrected Double-Hybrid Density Functionals with Spin-Component and Spin-Opposite Scaling: A Comprehensive Analysis of Singlet–Singlet and Singlet–Triplet Excitation Energies. *J. Chem. Theory Comput.* **17,** 5165–5186 (8 2021).

507. Casanova-Páez, M., Dardis, M. & Goerigk, L. B2PLYP and B2GPPLYP: The First Two Double-Hybrid Density Functionals with Long-Range Correction Optimized for Excitation Energies. *J. Chem. Theory Comput.* **15,** 4735–4744 (9 2019).

508. Orlandi, G. & Siebrand, W. Mechanisms of vibronic intensity borrowing. *Chem. Phys. Lett.* **15,** 465–468 (4 1972).

509. Maganas, D., Kowalska, J., Van Stappen, C., DeBeer, S. & Neese, F. Mechanism of L2,3-edge x-ray magnetic circular dichroism intensity from quantum chemical calculations and experiment—A case study on V(IV)/V(III) complexes. *J. Chem. Phys.* **152,** 114107 (1–15) (11 2019).

510. Ganyushin, D. & Neese, F. First-principles calculations of magnetic circular dichroism spectra. *J. Chem. Phys.* **128,** 114117 (1–13) (11 2008).

511. Noodleman, L. Valence bond description of antiferromagnetic coupling in transition metal dimers. *J. Chem. Phys.* **74,** 5737–5743 (10 1981).

512. Noodleman, L. & Davidson, E. R. Ligand spin polarization and antiferromagnetic coupling in transition metal dimers. *Chem. Phys.* **109,** 131–143 (1 1986).

513. DeBeer George, S. & Neese, F. Calibration of Scalar Relativistic Density Functional Theory for the Calculation of Sulfur K-Edge X-ray Absorption Spectra. *Inorg. Chem.* **49,** 1849–1853 (4 2010).

514. Chandrasekaran, P. *et al.* Sensitivity of X-ray Core Spectroscopy to Changes in Metal Ligation: A Systematic Study of Low-Coordinate, High-Spin Ferrous Complexes. *Inorg. Chem.* **52,** 6286–6298 (11 2013).

515. Delgado-Jaime, M. U. *et al.* Identification of a Single Light Atom within a Multinuclear Metal Cluster Using Valence-to-Core X-ray Emission Spectroscopy. *Inorg. Chem.* **50,** 10709–10717 (21 2011).

516. Lancaster, K. M., Finkelstein, K. D. & DeBeer, S. K beta X-ray Emission Spectroscopy Offers Unique Chemical Bonding Insights: Revisiting the Electronic Structure of Ferrocene. *Inorg. Chem.* **50,** 6767–6774 (14 2011).

517. Glatzel, P. & Bergmann, U. High resolution 1s core hole X-ray spectroscopy in 3d transition metal complexes - electronic and structural information. *Coordination Chemistry Reviews* **249,** 65–95 (1–2 2005).

518. Rovezzi, M. & Glatzel, P. Hard x-ray emission spectroscopy: a powerful tool for the characterization of magnetic semiconductors. *Semiconductor Science And Technology* **29** (2 2014).

519. Beckwith, M. A. *et al.* Manganese K beta X-ray Emission Spectroscopy As a Probe of Metal-Ligand Interactions. *Inorg. Chem.* **50,** 8397–8409 (17 2011).

520. Mathe, Z. *et al.* Calcium Valence-to-Core X-ray Emission Spectroscopy: A Sensitive Probe of Oxo Protonation in Structural Models of the Oxygen-Evolving Complex. *Inorg. Chem.* **58,** 16292–16301 (23 2019).

521. Pollock, C. J., Delgado-Jaime, M. U., Atanasov, M., Neese, F. & DeBeer, S. K beta Mainline X-ray Emission Spectroscopy as an Experimental Probe of Metal-Ligand Covalency. *J. Am. Chem. Soc.* **136,** 9453–9463 (26 2014).

522. Pollock, C. J., Lancaster, K. M., Finkelstein, K. D. & DeBeer, S. Study of Iron Dimers Reveals Angular Dependence of Valence-to-Core X-ray Emission Spectra. *Inorg. Chem.* **53,** 10378–10385 (19 2014).

523. DeBeer George, S., Petrenko, T. & Neese, F. Inorg. Chim. Acta. **361,** 965 (2008).

524. Rees, J. A., Martin-Diaconescu, V., Kovacs, J. A. & DeBeer, S. X-ray Absorption and Emission Study of Dioxygen Activation by a Small-Molecule Manganese Complex. *Inorg. Chem.* **54,** 6410–6422 (13 2015).

525. DeBeer George, S., Petrenko, T. & Neese, F. *J. Phys. Chem. A.* **112,** 12936 (2009).

526. Lee, N., Petrenko, T., Bergmann, U., Neese, F. & DeBeer, S. Probing Valence Orbital Composition with Iron K X-ray Emission Spectroscopy. *J. Am. Chem. Soc.* **132,** 9715–9727 (28 2010).

527. Roemelt, M., Maganas, D., DeBeer, S. & Neese, F. A combined DFT and restricted open-shell configuration interaction method including spin-orbit coupling: Application to transition metal L-edge X-ray absorption spectroscopy. *J. Chem. Phys.* **138,** 204101 (1–22) (20 2013).

528. Roemelt, M. *et al.* Manganese K-Edge X-Ray Absorption Spectroscopy as a Probe of the Metal–Ligand Interactions in Coordination Compounds. *Inorg. Chem.* **51,** 680–687 (1 2011).

529. Lancaster, K. M. *et al.* X-ray Emission Spectroscopy Evidences a Central Carbon in the Nitrogenase Iron-Molybdenum Cofactor. *Sci.* **334,** 974 (6058 2011).

530. Ament, L. J. P., van Veenendaal, M., Devereaux, T. P., Hill, J. P. & van den Brink, J. Resonant inelastic x-ray scattering studies of elementary excitations. *Rev. Mod. Phys.* **83,** 705–767 (2 2011).

531. Solomon, E. I. Spectroscopic Methods in Bioinorganic Chemistry: Blue to Green to Red Copper Sites. *Inorg. Chem.* **45,** 8012–8025 (20 2006).

532. Rees, J. A. *et al.* The Fe–V Cofactor of Vanadium Nitrogenase Contains an Interstitial Carbon Atom. *Angew. Chem. Int. Ed.* **54,** 13249–13252 (45 2015).

533. Askari, A. B. *et al.* In situX-ray emission and high-resolution X-ray absorption spectroscopy applied to Ni-based bimetallic dry methane reforming catalysts. *Nanoscale* **12,** 15185–15192 (28 2020).

534. Saveleva, V. A. *et al.* Potential-Induced Spin Changes in Fe/N/C Electrocatalysts Assessed by In Situ X-ray Emission Spectroscopy. *Angew. Chem. Int. Ed.* **60,** 11707–11712 (21 2021).

535. Holden, W. M., Seidler, G. T. & Cheah, S. Sulfur Speciation in Biochars by Very High Resolution Benchtop K X-ray Emission Spectroscopy. *J. Phys. Chem. A* **122,** 5153–5161 (23 2018).

536. Stein, J. L. *et al.* Probing Surface Defects of InP Quantum Dots Using Phosphorus K and K X-ray Emission Spectroscopy. *Chem. Mater.* **30,** 6377–6388 (18 2018).

537. Zimmermann, P. *et al.* Modern X-ray spectroscopy: XAS and XES in the laboratory. *Coord. Chem. Rev.* **423** (2020).

538. Malzer, W. *et al.* A laboratory spectrometer for high throughput X-ray emission spectroscopy in catalysis research. *Rev. Sci. Instrum.* **89,** 113111 (11 2018).

539. Lee, N., Petrenko, T., Bergmann, U., Neese, F. & DeBeer, S. Probing Valence Orbital Composition with Iron K X-ray Emission Spectroscopy. *J. Am. Chem. Soc.* **132,** 9715–9727 (2010).

540. Beckwith, M. A. *et al.* Manganese K X-ray Emission Spectroscopy As a Probe of Metal Ligand Interactions. *Inorg. Chem.* **50,** 8397–8409 (2011).

541. Lafuerza, S., Carlantuono, A., Retegan, M. & Glatzel, P. Chemical Sensitivity of K and K X-ray Emission from a Systematic Investigation of Iron Compounds. *Inorg. Chem.* **59,** 12518–12535 (17 2020).

542. Maganas, D., DeBeer, S. & Neese, F. A Restricted Open Configuration Interaction with Singles Method To Calculate Valence-to-Core Resonant X-ray Emission Spectra: A Case Study. *Inorg. Chem.* **56,** 11819–11836 (19 2017).

543. Maganas, D. *et al.* First principles calculations of the structure and V L-edge X-ray absorption spectra of V2O5 using local pair natural orbital coupled cluster theory and spin-orbit coupled configuration interaction approaches. *Phys. Chem. Chem. Phys.* **15,** 7260–7276 (19 2013).

544. Pantazis, D. A., Chen, X.-Y., Landis, C. R. & Neese, F. All-Electron Scalar Relativistic Basis Sets for Third-Row Transition Metal Atoms. *J. Chem. Theory Comput.* **4,** 908–919 (2008).

545. Stoychev, G. L., Auer, A. A. & Neese, F. Automatic Generation of Auxiliary Basis Sets. *J. Chem. Theory Comput.* **13,** 554–562 (2017).

546. Hess, B. A. Applicability of the no-pair equation with free-particle projection operators to atomic and molecular structure calculations. *Phys. Rev. A* **32,** 756–763 (1985).

547. Jansen, G. & Hess, B. A. Revision of the Douglas-Kroll transformation. *Phys. Rev. A* **39,** 6016–6017 (11 1989).

548. Wolf, A., Reiher, M. & Hess, B. A. The generalized Douglas–Kroll transformation. *J. Chem. Phys.* **117,** 9215–9226 (20 2002).

549. Neese, F. Importance of Direct SpinSpin Coupling and Spin-Flip Excitations for the Zero-Field Splittings of Transition Metal Complexes: A Case Study. *J. Am. Chem. Soc.* **128,** 10213–10222 (2006).

550. Von Barth, U. & Grossmann, G. The effect of the core hole on x-ray emission spectra in simple metals. *Solid State Commun.* **32,** 645–649 (8 1979).

551. Błachucki, W. *et al.* Inception of electronic damage of matter by photon-driven post-ionization mechanisms. *Struct. Dyn.* **6,** 024901 (2 2019).

552. Kramers, H. & Heisenberg, W. Über die Streuung von Strahlung durch Atome. *Z. Phys.* **31,** 681–708 (1 1925).

553. Neese, F., Petrenko, T., Ganyushin, D. & Olbrich, G. Advanced aspects of ab initio theoretical optical spectroscopy of transition metal complexes: Multiplets, spin-orbit coupling and resonance Raman intensities. *Coord. Chem. Rev.* **251,** 288–327 (3 2007).

554. Pauncz, R. *Spin Eigenfunctions* (Springer, Boston (MA), USA, 1979).

555. Grabenstetter, J. E., Tseng, T. J. & Grein, F. Generation of genealogical spin eigenfunctions. *Int. J. Quantum Chem.* **10,** 143–149 (1 1976).

556. Hoijtink, G. J. The influence of paramagnetic molecules on singlet-triplet transitions. *Mol. Phys.* **3,** 67–70 (1 1960).

557. Angel, S. *et al.* Spray-flame synthesis of La(Fe, Co)O3 nano-perovskites from metal nitrates. *AlChE J.* **66,** e16748 (1 2020).

558. Hardt, S., Wlokas, I., Schulz, C. & Wiggers, H. Impact of Ambient Pressure on Titania Nanoparticle Formation During Spray-Flame Synthesis. *J. Nanosci. Nanotechnol.* **15,** 9449–9456 (12 2015).